

AD-A273 394

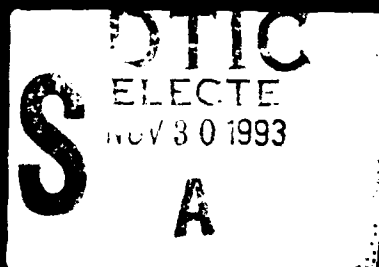


VOLUME 310

Ferroelectric Thin Films III

EDITORS

Edward R. Myers
Bruce A. Tuttle
Seshu B. Desu
Poul K. Larsen



This document has been approved
for public release and sale; its
distribution is unlimited.

Ferroelectric Thin Films III

Symposium held April 13-16, 1993, San Francisco, California, U.S.A.

DTIC QUALITY INSPECTED 8

EDITORS:

Edward R. Myers

National Semiconductor Corporation
Santa Clara, California, U.S.A.

Bruce A. Tuttle

Sandia National Laboratories
Albuquerque, New Mexico, U.S.A.

Seshu B. Desu

Virginia Polytechnic Institute
Blacksburg, Virginia, U.S.A.

Poul K. Larsen

Philips Research Laboratories
The Netherlands

Acquisition	
NTIS	✓
DTIC	✓
Unrestricted	✓
Available	✓
By	
Date	
Availability	
Dist	
A-1	

93-29190



MRS

MATERIALS RESEARCH SOCIETY
Pittsburgh, Pennsylvania

93 11 29 075

This work relates to Department of Navy Grant N00014-93-1-0400 issued by the Office of Naval Research. The United States Government has a royalty-free license throughout the world in all copyrightable material contained herein.

Single article reprints from this publication are available through
University Microfilms Inc., 300 North Zeeb Road, Ann Arbor, Michigan 48106

CODEN: MRSPDH

Copyright 1992 by Materials Research Society.
All rights reserved.

This book has been registered with Copyright Clearance Center, Inc. For further information, please contact the Copyright Clearance Center, Salem, Massachusetts.

Published by:

Materials Research Society
9800 McKnight Road
Pittsburgh, Pennsylvania 15237
Telephone (412) 367-3003
Fax (412) 367-4373

Library of Congress Cataloging in Publication Data

Ferroelectric thin films III : symposium held April 13-16, 1993, San Francisco, California, U.S.A. / editors, Bruce A. Tuttle, Edward R. Myers, Seshu B. Desu, Poul K. Larsen

p. cm.—(Materials Research Society symposium proceedings ; v. 310)
Includes bibliographical references and index.

ISBN: 1-55899-206-5

1. Ferroelectric thin films—Congresses. I. Tuttle, Bruce A. II. Myers, Edward R. III. Desu, Seshu B. IV. Larsen, Poul K. V. Title: Ferroelectric thin films three. VI. Series: Materials Research Society symposium proceedings ; v. 310.

TA418.9.T45F48 1993
621.3815'2—dc20

93-41489
CIP

Manufactured in the United States of America

Contents

PREFACE	xi
ACKNOWLEDGMENTS	xii
MATERIALS RESEARCH SOCIETY SYMPOSIUM PROCEEDINGS	xiv
PART I: NOVEL CHARACTERIZATION TECHNIQUES	
MICROSTRUCTURAL EVOLUTION OF $Pb(Zr,Ti)O_3$ CERAMICS USING ELECTRON PARAMAGNETIC RESONANCE W.L. Warren, B.A. Tuttle, R.W. Schwartz, W.F. Hammetter, D.C. Goodnow, J.T. Evans, Jr., and J.A. Bullington	3
OXYGEN TRACER DIFFUSION IN SOL-GEL DERIVED $Pb(Zr,Ti)O_3$ THIN FILMS John J. Vajo, L.A. Momoda, S.B. Wong, and G.S. Kamath	9
ORIENTED LEAD ZIRCONATE TITANATE THIN FILMS: CHARACTERIZATION OF FILM CRYSTALLIZATION James A. Voigt, B.A. Tuttle, T.J. Headley, M.O. Eatough, D.L. Lamppa, and D. Goodnow	15
PHYSICOCHEMICAL AND MICROSTRUCTURAL CHARACTERIZATION OF RF SPUTTERING MAGNETRON $Pb(Zr,Ti)O_3$ THIN FILMS F. Varniere, E. Cattani, B. Eakim, H. Achari, and B. Agius	23
IMAGING OF FERROELECTRIC DOMAINS IN $KTiOPO_3$ SINGLE CRYSTALS BY SYNCHROTRON X-RAY TOPOGRAPHY S. Wang, M. Dudley, L.K. Cheng, J.D. Bierlein, and W. Bindloss	29
PART II: DEVICE MATERIALS SCIENCE	
*PIEZOELECTRIC AND CAPACITATIVE MICROACTUATORS AND DEVICES M. Sayer, D. Barrow, L. Zou, C.V.R. Vasant Kumar, R. Noteboom, D.A. Knapik, D.W. Schindel, and D.A. Hutchins	37
TUNABLE DIELECTRIC AND PIEZOELECTRIC CHARACTERISTICS OF LEAD MAGNESIUM NIOBATE TITANATE RELAXOR THIN FILMS J. Chen, Q. Zhang, and L.E. Cross	47
PYROELECTRIC PROPERTIES OF LEAD BASED FERROELECTRIC THIN FILMS A. Patel, D.A. Tossell, N.M. Shorrocks, R.W. Whatmore, and R. Watton	53
ELECTRICAL PROPERTIES OF SOL-GEL PZT THIN FILMS FOR DECOUPLING CAPACITOR APPLICATIONS Robert W. Schwartz, D. Dimos, S.J. Lockwood, and V.M. Torres	59
FIBER OPTIC PHASE AND POLARIZATION MODULATOR UTILIZING A TRANSPARENT PIEZOFILM WITH INDIUM TIN OXIDE COATING V.S. Sudarshanam, S.B. Desu, and R.O. Claus	65
MATERIALS CHARACTERIZATION OF NONDESTRUCTIVE READOUT NONVOLATILE MEMORY DEVICES Bruce A. Tuttle, Dale C. McIntyre, Carleton H. Seager, Terry J. Garino, William L. Warren, Joseph T. Evans, and Robert W. Waldman	71

*Invited Paper

INTEGRATED PYROELECTRIC INFRARED SENSOR USING PVDF THIN FILM DEPOSITED BY ELECTRO-SPRAY METHOD Ryouji Asahi, Jiro Sakata, Osamu Tabata, Midori Mochizuki, Susumu Sugiyama, and Yasunori Taga	79
---	----

PART III: OPTOELECTRONIC DEVICES AND PROPERTIES

*PHOTO-INDUCED AND ELECTROOPTIC PROPERTIES OF (Pb,La)(Zr,Ti)O ₃ FILMS D. Dimos, W.L. Warren, and B.A. Tuttle	87
THE APPLICATION OF OPTICAL INTERFEROMETRY TO THE STUDY OF FIELD-INDUCED EFFECTS IN BULK AND THIN FILM FERRO- ELECTRICS Keith L. Lewis and Kathleen F. Dexter	99
REVERSIBLE PHOTO-INDUCED CURRENTS IN EPITAXIAL Pb(Zr _{0.52} Ti _{0.48})O ₃ THIN FILMS J. Lee, S. Esayan, J. Prohaska, and A. Safari	107
PROGRESS TOWARD VIABLE EPITAXIAL OXIDE FERROELECTRIC WAVEGUIDE HETEROSTRUCTURES ON GaAs D.K. Fork, J.J. Kingston, G.B. Anderson, E.J. Tarsa, and J.S. Speck	113
CHEMICAL VAPOR DEPOSITION OF EPITAXIAL BaTiO ₃ FILMS FOR FREQUENCY DOUBLING DEVICES Peter C. Van Buskirk, Gregory T. Stauf, Robin Gardiner, Peter S. Kirilin, B. Bihari, J. Kumar, and G. Gallatin	119

PART IV: PROCESS INTEGRATION

REACTIVE ION ETCHING OF Pt/PbZr _x Ti _{1-x} O ₃ /Pt INTEGRATED FERROELECTRIC CAPACITORS J.J. Van Glabbeek, G.A.C.M. Spierings, M.J.E. Ulenaers, G.J.M. Dormans, and P.K. Larsen	127
REACTIVE ION ETCHING OF PbZr _x Ti _{1-x} O ₃ AND RuO ₂ THIN FILMS Dilip P. Vijay, Seshu B. Desu, and Wei Pan	133
CHEMICALLY ASSISTED ION-BEAM ETCHING OF SOL-GEL DERIVED PZT, PLZT AND LiTaO ₃ THIN FILMS FOR SILICON BASED DEVICE INTEGRATION P.F. Baude, C. Ye, and D.L. Polla	139
EPITAXIAL FERROELECTRIC HETEROSTRUCTURES OF ISOTROPIC METALLIC OXIDE (SrRuO ₃) AND Pb(Zr _{0.52} Ti _{0.48})O ₃ C.B. Eom, R.B. Van Dover, Julia M. Phillips, R.M. Fleming, R.J. Cava, J.H. Marshall, D.J. Werder, C.H. Chen, and D.K. Fork	145
IMPACT OF BACKEND PROCESSING ON INTEGRATED FERROELECTRIC CAPACITOR CHARACTERISTICS P.D. Maniar, R. Moazzami, R.E. Jones, A.C. Campbell, and C.J. Mogab	151
DEPOSITION, STRUCTURAL CHARACTERIZATION, AND BROADBAND (1KHz-40GHz) DIELECTRIC BEHAVIOR OF BaTi _{2-x} O ₃ THIN FILMS W.-T. Liu, S. Cochrane, P. Beckage, D.B. Knorr, T.-M. Lu, J.M. Borrego, and E.J. Rymaszewski	157

*Invited Paper

PART V: DEGRADATION AND MODELLING

- *CORRELATIONS AMONG DEGRADATIONS IN LEAD ZIRCONATE
TITANATE THIN FILM CAPACITORS** 165
In K. Yoo, Seshu B. Desu, and Jimmy Xing
- ENERGY RELEASE DUE TO DOMAIN FORMATION IN THE STRAINED
EPITAXY OF MULTIVARIANT FILMS** 179
W. Pompe, X. Gong, Z. Suo, and J.S. Speck

PART VI: CHARACTERIZATION OF FERROELECTRIC THIN FILM-ELECTRODE INTERFACES

- BOTTOM ELECTRODES FOR HIGH DIELECTRIC OXIDE COMPOUNDS:
EFFECTS ON CRYSTALLIZATION OF LEAD CONTAINING FERRO-
ELECTRICS** 189
A. Grill, D. Beach, C. Smart, and W. Kane
- FERROELECTRIC La-Sr-Co-O/Pb-Zr-Ti-O/La-Sr-Co-O HETERO-
STRUCTURES ON SILICON: RELIABILITY TESTING** 195
R. Ramesh, T. Sands, V.G. Keramidas, and D.K. Fork
- EFFECTS OF PLATINUM ELECTRODE STRUCTURES ON CRYSTALLINITY
AND ELECTRICAL PROPERTIES OF MOD-PREPARED PZT CAPACITORS** 201
Dennis J. Eichorst and Cynthia J. Baron
- ELECTRON MICROSCOPY STUDY OF THE INFLUENCE OF THE
ADHESION LAYER FOR Pt ELECTRODE ON THE MICROSTRUCTURE
OF SOL-GEL CRYSTALLIZED PZT** 209
Vidya Kaushik, Papu Maniar, Andrew Campbell, Robert Jones,
Reza Moazzami, C. Joseph Mogab, Robert Hance, and Ronald Pyle
- TEXTURED $\text{Pb}(\text{Zr}_{0.54}\text{Ti}_{0.46})\text{O}_3$ THIN FILMS WITH $\text{YBa}_2\text{Cu}_3\text{O}_{7.5}$ AND
YTTRIA-STABILIZED ZIRCONIA BUFFER LAYERS ON (001) Si** 215
Tsvetanka Zheleva, P. Tiwari, and J. Narayan

PART VII: CHEMICAL VAPOR DEPOSITION

- *ORGANOMETALLIC CHEMICAL VAPOR DEPOSITION OF LEAD
ZIRCONATE-TITANATE THIN FILMS** 223
M. de Keijser, P.J. van Veldhoven, and G.J.M. Dormans
- MOCVD GROWTH AND STRUCTURE OF PbTiO_3 THIN FILMS** 235
Y. Gao, G. Bai, K.L. Merkle, H.L.M. Chang, and D.J. Lam
- METALLORGANIC CHEMICAL VAPOR DEPOSITION (MOCVD) OF
TITANIUM-BASED FERROELECTRIC THIN FILMS** 241
Warren C. Hendricks, Seshu B. Desu, Jie Si, and Chien H. Peng
- PLASMA ENHANCED METALORGANIC CHEMICAL VAPOR DEPOSITION
OF CONDUCTIVE OXIDE ELECTRODES FOR FERROELECTRIC BaTiO_3
CAPACITORS** 249
Jiming Zhang, Guang-Ji Cui, Douglas Gordon, Peter Van Buskirk,
and John Steinbeck
- GROWTH AND CHARACTERIZATION OF FERROELECTRIC $\text{Pb}(\text{Zr,Ti})\text{O}_3$
THIN FILMS BY MOCVD USING A 6 INCH SINGLE WAFER CVD
SYSTEM** 255
Masaru Shimizu, Masashi Fujimoto, Takuma Katayama,
Tadashi Shiosaki, Kenichi Nakaya, Mitsuru Fukagawa, and
Eiki Tanikawa

*Invited Paper

PART VIII: SPIN PYROLYSIS OF THIN FILMS

CRYSTALLIZATION BEHAVIOR AND ELECTRICAL PROPERTIES OF WET-CHEMICALLY DEPOSITED LEAD ZIRCONATE TITANATE THIN FILMS	263
S. Merklein, D. Sporn, and A. Schönecker	
PREFERRED ORIENTATIONS FOR SOL-GEL DERIVED PLZT THIN LAYERS	269
Toshihiko Tani, Zhengkui Xu, and David A. Payne	
SOLUTION CHEMISTRY OPTIMIZATION OF SOL-GEL PROCESSED PZT THIN FILMS	275
Steven J. Lockwood, R.W. Schwartz, B.A. Tuttle, and E.V. Thomas	
MICROSTRUCTURAL CHARACTERIZATION OF SOL-GEL DERIVED LEAD TITANATE DEPOSITED ON SILICA	281
Joseph M. Schwartz, Lorraine Falter Francis, and Lanny D. Schmidt	
SUBSTRATE INFLUENCED NUCLEATION AND CRYSTALLIZATION OF LiNbO_3 THIN FILMS MADE BY SOL-GEL	287
Vikram Joshi, Debasis Roy, and Martha L. Mecartney	
PREPARATION AND CHARACTERIZATION OF SOL-GEL DERIVED HETEROEPITAXIAL LiNbO_3 AND LiTaO_3 THIN FILMS	293
Keiichi Nashimoto	

PART IX: NIOBIUM AND BARIUM BASED FERROELECTRICS

*GROWTH, MICROSTRUCTURES AND OPTICAL PROPERTIES OF KNbO_3 THIN FILMS	301
Thomas M. Graettinger, P.A. Morris, R.R. Woolcott, F.C. Zumsteg, A.F. Chow, and A.I. Kingon	
FORMATION OF BaMgF_4 FILMS ON Pt/MgO , Si AND GaAs SUBSTRATES	313
Kouji Aizawa, Tatsuya Ichiki, and Hiroshi Ishiwara	
FERROELECTRIC PROPERTIES OF a -AXIS TEXTURED BaTiO_3 THIN FILMS	319
H.A. Lu, L.A. Wills, B.W. Wessels, X. Zhan, J.A. Helfrich, and J.B. Ketterson	
PREPARATION AND CHARACTERIZATION OF EPITAXIAL KNbO_3 THIN FILMS BY A SOL-GEL METHOD	325
Hidehiro Endo and M.J. Cima	

PART X: MATERIALS AND PROCESSES

LOW TEMPERATURE PREPARATION OF BaTiO_3 FILMS ON SILICON	333
M.E. Pilleux and V.M. Fuenzalida	
MICROSTRUCTURAL CHANGES DUE TO PROCESS CONDITIONS IN SOL-GEL DERIVED KNbO_3 THIN FILMS	339
G.J. Derderian, J.D. Barrie, K.A. Aitchison, P.M. Adams, and M.L. Mecartney	
EPITAXIAL GROWTH OF $\text{Pt}(001)$ THIN FILMS ON $\text{MgO}(001)$ UNDER OXIDIZING CONDITIONS	345
G. Cui, P.C. Van Buskirk, J. Zhang, C.P. Beetz, Jr., J. Steinbeck, Z.L. Wang, and J. Bentley	

*Invited Paper

AEROSOL ROUTES TO PEROVSKITE PHASE MIXED METAL OXIDES C.D. Chandler, Q. Powell, M.J. Hampden-Smith, and T.T. Kodas	351
FERROELECTRIC THIN FILMS VIA SOL-GEL PROCESSING OF SINGLE-SOURCE PRECURSORS C.D. Chandler, M.J. Hampden-Smith, and R.W. Schwartz	357
DRY ETCHING OF PZT FILMS IN AN ECR PLASMA Barbara Charlet and Kerrie E. Davies	363
TRANSMISSION ELECTRON MICROSCOPY OF PZT THIN-FILMS PREPARED BY A SOL-GEL TECHNIQUE Supapan Seraphin, Dan Zhou, G. Teowee, J.M. Boulton, and D.R. Uhlmann	369
CURRENT STATUS OF AND RECENT RESULTS ON GROUP 2 SOURCE COMPOUNDS FOR VAPOR PHASE EPITAXY OF FERROELECTRIC THIN FILMS William S. Rees, Jr., Henry A. Luten, Michael W. Carris, Celia R. Caballero, Werner Hesse, and Virgil L. Goedken	375
PART XI: CHARACTERIZATION	
EXAMINATION OF TITANIUM OXIDES, LEAD OXIDES AND LEAD TITANATES USING X-RAY DIFFRACTION AND RAMAN SPECTROSCOPY Lynnette D. Madsen and Louise Weaver	385
OPTICALLY INDUCED PARAMAGNETIC DEFECTS IN PbTiO_3 SINGLE CRYSTALS W.L. Warren, B.A. Tuttle, B.N. Sun, Y. Huang, and D.A. Payne	391
DEPOSITION OF DIELECTRIC THIN FILMS BY ATOMIC LAYER EPITAXY AND THEIR APPLICATION FOR ELECTROLUMINESCENCE DISPLAYS Dong Heon Lee, Yong Soo Cho, Jeon Kook Lee, and Hyung Jin Jung	397
PRISM-FILM COUPLING IN ANISOTROPIC PLANAR WAVEGUIDES OF EPITAXIAL (101) RUTILE THIN FILMS C.M. Foster, S.-K. Chan, H.L.M. Chang, R.P. Chiarello, and D.J. Lam	403
THE DEFECT STRUCTURE OF BaTiO_3 THIN FILMS L.A. Wills and B.W. Wessels	409
A MODEL OF THE METAL-FERROELECTRIC-METAL CAPACITOR G. Teowee and D.R. Uhlmann	415
EFFECT OF Zr/Ti RATIO ON THE FATIGUE AND RETENTION BEHAVIOR OF SOL-GEL DERIVED PZT FILMS G. Teowee, J.M. Boulton, M.N. Orr, C.D. Baertlein, R.K. Wade, D.P. Birnie III, and D.R. Uhlmann	423
A NOVEL METHOD FOR DETERMINING THE CURIE TEMPERATURE OF FERROELECTRIC FILMS Chi Kong Kwok and Seshu B. Desu	429
STUDY OF PbTiO_3 FORMATION KINETICS BY AN IN-SITU STRESS MEASUREMENT TECHNIQUE Chen C. Li and Seshu B. Desu	435

ELECTRICAL PROPERTIES OF AMORPHOUS THIN FILMS OF FERROELECTRIC OXIDES PREPARED BY SOL-GEL TECHNIQUE Yuhuan Xu, Ren Xu, Chih-Hsing Cheng, and John D. Mackenzie	441
FERROELECTRIC THIN FILMS INTENDED FOR ELECTRONIC DEVICE APPLICATIONS A. Patel, E.A. Logan, R. Nicklin, N.B. Hasdell, R.W. Whatmore, and M. Uren	447
PART XII: SPUTTER DEPOSITION	
*SPUTTERING OF LEAD-BASED FERROELECTRICS K. Iijima, N. Nagao, T. Takeuchi, I. Ueda, Y. Tomita, and R. Takayama	455
PZT THIN FILMS ON A LEAD TITANATE INTERLAYER PREPARED BY rf MAGNETRON SPUTTERING P.H. Ansari and A. Safari	467
ULTRA-THIN SPUTTERED PZT FILMS FOR ULSI DRAMs Jiyoung Kim, C. Sudhama, Rajesh Khamankar, and Jack Lee	473
PART XIII: PULSED LASER AND OTHER VAPOR DEPOSITION TECHNIQUES	
EFFECTS OF PROCESS PARAMETERS ON THE ABLATED FLUX CHARACTERISTICS DURING PULSED-LASER ABLATION OF LEAD ZIRCONATE TITANATE (PZT) D.J. Lichtenwalner, O. Auciello, R. Dat, R. Barnes, A.F. Schreiner, O.E. Hankins, and A.I. Kingon	481
PREPARATION OF SrTiO_3 THIN FILMS BY ECR AND THERMAL MOCVD P-Y. Lesaichere, H. Yamaguchi, T. Sakuma, Y. Miyasaka, M. Yoshida, and A. Ishitani	487
AUTHOR INDEX	495
SUBJECT INDEX	499

*Invited Paper

Preface

This symposium showcased the advancement in processing technology and basic scientific understanding of ferroelectric thin films. The conference highlighted the use of novel materials science analysis techniques to characterize ferroelectric thin film materials and devices and to relate the nanoscale features and responses detected by these techniques to ferroelectric, electrooptic and piezoelectric properties. Examples of newer material analysis techniques included atomic force microscopy, electron spin resonance, high resolution transmission electron microscopy, combined Rutherford backscattering-nuclear reaction analysis and the use of optical interferometry to provide a three dimensional representation of field induced displacement.

There was a strong emphasis in this proceedings regarding process integration issues and the advancement of new electrode materials. While the development of electrode processing techniques and the resulting electrical and optical properties of ferroelectric thin films were reported, relationships to and characterization of ferroelectric film microstructures were stressed. Numerous dry etching techniques were presented for ferroelectric thin films, electrodes and diffusion barriers. Excellent ferroelectric thin film properties were demonstrated for thin films fabricated by production scale metallorganic chemical vapor deposition processes. Finally, the development of the first fully integrated commercial pyroelectric infrared ferroelectric thin film sensor was reported.

This symposium proceedings presents the latest technical information on ferroelectric thin films from academia, government organizations and industry. It highlights advances made during the past 18 months, since the last Ferroelectric Thin Films symposium held at the Fall 1991 MRS meeting, and provides insight into the current trends emerging for this exciting technology.

The papers in this proceedings volume were presented at the Materials Research Society Spring 1993 Ferroelectric Thin Films III Symposium held in San Francisco, CA on April 16-20.

Edward R. Myers
Bruce A. Tuttle
Seshu B. Desu
Poul K. Larsen

September 1993

Acknowledgments

The symposium chairs would like to acknowledge the contributing and invited authors for the outstanding quality of their presentations and proceeding manuscripts. The invited speakers included:

D.B. Dimos	M. de Keijser
T.M. Graettinger	K.S. Grabovski
K. Iijima	A.I. Kingon
M. Sayer	N. Setter
I.K. Yoo	

In addition, the symposium organizers are indebted to the session chairs for their effort in overseeing the sessions, guiding subsequent discussions and reviewing the manuscripts.

The symposium chairs wish to express their appreciation to the following organizations who provided financial support, enabling us to present the Ferroelectric Thin Films III symposium.

Raytheon Company
Office of Naval Research
Advanced Research Projects Agency
National Semiconductor
Radiant Technologies, Inc.
Bellcore
Sandia National Laboratories

The symposium organizers wish to extend a special thanks to Dr. Jane Alexander and the Advanced Research Projects Agency for supporting the first Ferro-electric Thin Films Student Awards. Student award winners were:

Leo Archer	Garo Derderian
Vikram Joshi	Jai-Chan Lee
Lynnette Madsen	Mauricio Pilleux
Joseph Schwartz	Laura Wills
Michael Vestal	

A special thanks is reserved for the Materials Research Society and their staff, as well as the Spring 1993 Meeting Chairs for the development of another outstanding conference.

MATERIALS RESEARCH SOCIETY SYMPOSIUM PROCEEDINGS

- Volume 279—Beam-Solid Interactions—Fundamentals and Applications, M.A. Nastasi, N. Herbots, L.R. Harriott, R.S. Averback, 1993, ISBN: 1-55899-174-3
- Volume 280—Evolution of Surface and Thin Film Microstructure, H.A. Atwater, E. Chason, M. Grabow, M. Lagally, 1993, ISBN: 1-55899-175-1
- Volume 281—Semiconductor Heterostructures for Photonic and Electronic Applications, D.C. Houghton, C.W. Tu, R.T. Tung, 1993, ISBN: 1-55899-176-X
- Volume 282—Chemical Perspectives of Microelectronic Materials III, C.R. Abernathy, C.W. Bates, D.A. Bohling, W.S. Hobson, 1993, ISBN: 1-55899-177-8
- Volume 283—Microcrystalline Semiconductors—Materials Science & Devices, Y. Aoyagi, I. T. Canham, P.M. Fauchet, I. Shimizu, C.C. Tsai, 1993, ISBN: 1-55899-178-6
- Volume 284—Amorphous Insulating Thin Films, J. Kamicki, R.A.B. Devine, W.L. Warren, M. Matsumura, 1993, ISBN: 1-55899-179-4
- Volume 285—Laser Ablation in Materials Processing—Fundamentals and Applications, B. Braren, J. Dubowski, D. Norton, 1993, ISBN: 1-55899-180-8
- Volume 286—Nanophase and Nanocomposite Materials, S. Komarneni, J.C. Parker, G.J. Thomas, 1993, ISBN: 1-55899-181-6
- Volume 287—Silicon Nitride Ceramics—Scientific and Technological Advances, I.W. Chen, P.F. Becher, M. Mitomo, G. Petzow, I.S. Yen, 1993, ISBN: 1-55899-182-4
- Volume 288—High Temperature Ordered Intermetallic Alloys V, I. Baker, J.D. Whittenberger, R. Darolia, M.H. Yoo, 1993, ISBN: 1-55899-183-2
- Volume 289—Flow and Microstructure of Dense Suspensions, L.J. Struble, C.F. Zukoski, G. Mantland, 1993, ISBN: 1-55899-184-0
- Volume 290—Dynamics in Small Confining Systems, J.M. Drake, D.D. Awschalom, J. Klafter, R. Kopelman, 1993, ISBN: 1-55899-185-9
- Volume 291—Materials Theory and Modelling, P.D. Bristowe, J. Broughton, J.M. Newsam, 1993, ISBN: 1-55899-186-7
- Volume 292—Biomolecular Materials, S.T. Case, J.H. Waite, C. Viney, 1993, ISBN: 1-55899-187-5
- Volume 293—Solid State Ionics III, G.A. Nazri, J.-M. Tarascon, M. Armand, 1993, ISBN: 1-55899-188-3
- Volume 294—Scientific Basis for Nuclear Waste Management XVI, C.G. Interrante, R.T. Pabalan, 1993, ISBN: 1-55899-189-1
- Volume 295—Atomic-Scale Imaging of Surfaces and Interfaces, D.K. Biegelson, D.S.Y. Tong, D.J. Smith, 1993, ISBN: 1-55899-190-5
- Volume 296—Structure and Properties of Energetic Materials, R.W. Armstrong, J.J. Gilman, 1993, ISBN: 1-55899-191-3

MATERIALS RESEARCH SOCIETY SYMPOSIUM PROCEEDINGS

- Volume 297—Amorphous Silicon Technology—1993, E.A. Schiff, M.J. Thompson, P.G. LeComber, A. Madan, K. Tanaka, 1993, ISBN: 1-55899-193-X
- Volume 298—Silicon-Based Optoelectronic Materials, R.T. Collins, M.A. Tischler, G. Abstreiter, M.L. Thewalt, 1993, ISBN: 1-55899-194-8
- Volume 299—Infrared Detectors—Materials, Processing, and Devices, A. Appelbaum, L.R. Dawson, 1993, ISBN: 1-55899-195-6
- Volume 300—III-V Electronic and Photonic Device Fabrication and Performance, K.S. Jones, S.J. Pearton, H. Kanber, 1993, ISBN: 1-55899-196-4
- Volume 301—Rare-Earth Doped Semiconductors, G.S. Pomrenke, P.B. Klein, D.W. Langer, 1993, ISBN: 1-55899-197-2
- Volume 302—Semiconductors for Room-Temperature Radiation Detector Applications, R.B. James, P. Siffert, T.E. Schlesinger, L. Franks, 1993, ISBN: 1-55899-198-0
- Volume 303—Rapid Thermal and Integrated Processing II, J.C. Gelpey, J.K. Elliott, J.J. Wortman, A. Ajmera, 1993, ISBN: 1-55899-199-9
- Volume 304—Polymer/Inorganic Interfaces, R.L. Opila, A.W. Czanderna, F.J. Boerio, 1993, ISBN: 1-55899-200-6
- Volume 305—High-Performance Polymers and Polymer Matrix Composites, R.K. Eby, R.C. Evers, D. Wilson, M.A. Meador, 1993, ISBN: 1-55899-201-4
- Volume 306—Materials Aspects of X-Ray Lithography, G.K. Celler, J.R. Maldonado, 1993, ISBN: 1-55899-202-2
- Volume 307—Applications of Synchrotron Radiation Techniques to Materials Science, D.L. Perry, R. Stockbauer, N. Shinn, K. D'Amico, L. Terminello, 1993, ISBN: 1-55899-203-0
- Volume 308—Thin Films—Stresses and Mechanical Properties IV, P.H. Townsend, J. Sanchez, C-Y. Li, T.P. Weihs, 1993, ISBN: 1-55899-204-9
- Volume 309—Materials Reliability in Microelectronics III, K. Rodbell, B. Filter, P. Ho, H. Frost, 1993, ISBN: 1-55899-205-7
- Volume 310—Ferroelectric Thin Films III, E.R. Myers, B.A. Tuttle, S.B. Desu, P.K. Larsen, 1993, ISBN: 1-55899-206-5
- Volume 311—Phase Transformations in Thin Films—Thermodynamics and Kinetics, M. Atzmon, J.M.E. Harper, A.L. Greer, M.R. Libera, 1993, ISBN: 1-55899-207-3
- Volume 312—Common Themes and Mechanisms of Epitaxial Growth, P. Fuoss, J. Tsao, D.W. Kisker, A. Zangwill, T.F. Kuech, 1993, ISBN: 1-55899-208-1
- Volume 313—Magnetic Ultrathin Films, Multilayers and Surfaces/Magnetic Interfaces—Physics and Characterization (2 Volume Set), C. Chappert, R.F.C. Farrow, B.T. Jonker, R. Clarke, P. Grünberg, K.M. Krishnan, S. Tsunashima/E.E. Marinero, T. Egami, C. Rau, S.A. Chambers, 1993, ISBN: 1-55899-211-1
- Volume 314—Joining and Adhesion of Advanced Inorganic Materials, A.H. Carim, D.S. Schwartz, R.S. Silberglitt, R.E. Loehman, 1993, ISBN: 1-55899-212-X
- Volume 315—Surface Chemical Cleaning and Passivation for Semiconductor Processing, G.S. Higashi, E.A. Irene, T. Ohmi, 1993, ISBN: 1-55899-213-8

PART I

Novel Characterization Techniques

MICROSTRUCTURAL EVOLUTION OF $\text{Pb}(\text{Zr,Ti})\text{O}_3$ CERAMICS USING ELECTRON PARAMAGNETIC RESONANCE

W. L. WARREN*, B. A. TUTTLE*, R. W. SCHWARTZ*, W. F. HAMMETTER*,
D. C. GOODNOW*, J. T. EVANS, Jr.**, and J. A. BULLINGTON**

*Materials and Process Sciences Center, Sandia National Laboratories, Albuquerque, NM 87185-5800

**Radiant Technologies Inc., 1009 Bradbury Ave., Albuquerque, NM 87106

ABSTRACT

Using electron paramagnetic resonance (EPR) we have followed the microstructural evolution with temperature of lead zirconate titanate (PZT) ceramics from the amorphous to the perovskite phase. A number of paramagnetic point defects were identified (Carbon, Pb^{+3} , and Ti^{+3}) while traversing the evolution of these ceramics during various heat treatments both before and after optical illumination. Perhaps the most important finding is that the Pb^{+3} and Ti^{+3} centers can only be optically created in the perovskite materials, thereby, showing that they are not associated with the amorphous or the pyrochlore phases. It is also found that EPR signals attributed to carbon radicals are present in fairly high concentrations ($4 \times 10^{17}/\text{cm}^3$) if the solution chemistry derived PZT materials are annealed in an oxygen deficient ambient (0.1% O_2) at 650°C .

INTRODUCTION

Perovskite films of $\text{Pb}(\text{Zr,Ti})\text{O}_3$ (PZT) are of widespread interest because of the many microelectronic and opto-electronic applications for which these films could improve performance [1,2]. Basic research on the processing and electrical properties of these ferroelectric thin films is relevant if these materials are to be used in microelectronic devices [3,4].

We have investigated the nature of defects in virgin and ultra-violet (UV) illuminated sol-gel derived PZT ceramics annealed at different temperatures using electron paramagnetic resonance (EPR). The UV-excitation was necessary to transform some of the defects into their EPR-active state. We find that the EPR-centers observed are strongly dependent on the anneal temperature and/or crystalline phase of the PZT as well as the anneal ambient. The three major paramagnetic defects observed include Pb^{+3} [5] and Ti^{+3} [6] ions, and a resonance attributed to carbon dangling bonds. It is found that the Pb^{+3} and Ti^{+3} centers are only created in the perovskite phase, and thus, appear to be an inherent feature of the perovskite phase. The carbon dangling bonds are shown to be present in fairly large densities ($4 \times 10^{17}/\text{cm}^3$) in PZT materials annealed at relatively high temperatures (650°C) in an oxygen deficient ambient. A density this large may strongly affect the materials' electronic properties.

EXPERIMENTAL PROCEDURE

PZT gel derived particles were fabricated using a solution chemistry technique similar to that described by Yi and Sayer [7]. Alkoxide derived solutions (0.25 M) were synthesized from precursors of lead (II) acetate trihydrate, titanium tetraisopropoxide and zirconium n-butoxide-butanol with additions of acetic acid, deionized water and methanol. While PZT 53/47 gel derived particles were used in this phase evolution study, single phase perovskite gel derived particles were fabricated and characterized using EPR for PZT compositions with Zr/Ti stoichiometries that ranged across the PZT phase diagram. The alkoxide solutions were placed in glass containers and dried at 50°C for 12 h to remove excess solvent. The PZT 53/47 gels

were then placed in Pt lined alumina crucibles and heated at 1°C/min. in air to either 300, 450, 650 or 800°C which resulted in PZT microstructures containing systematically varying assemblages of amorphous, pyrochlore, and perovskite phases as determined by X-ray and scanning electron microscopy (SEM). Single phase perovskite gel derived PZT particles of other Zr/Ti stoichiometries were obtained by heat treating at either 650 or 800°C. While the PZT 53/47 samples annealed at 300 and 450°C were kept at temperature for 24, or 48 hrs, particles annealed at 650 and 800°C were held at temperature for 30 min. The presence of carbon dangling bonds in the 300°C and 450°C gels made precise EPR measurements difficult. Therefore, after the 50°C drying operation, subsequent gels were heated to 300°C and then mechanically reduced to less than 50 µm in particle size. These finer gel-derived particles were heat treated at 350, 400, and 500°C for 24 hrs, substantially less carbon was detected and the perovskite crystallization temperature appeared to be lowered.

Systematic variation of the volume fraction of phases in PZT gels is critical to the proper interpretation of the EPR results. For the coarser particles, both X-ray diffraction analysis and scanning electron microscopy (SEM) indicated that the gel particles annealed at 300°C were completely amorphous and that PZT 53/47 gel particles annealed at 650 and 800°C were single phase perovskite. Relatively uniform, equiaxed grains on the order of 1 µm were observed for the 800°C samples. No evidence of minor phases were detected by SEM analysis. If such minor phases do exist, we conservatively estimate that they are less than 1% by volume of these two gels. Integrated peak height intensity ratios indicated that the coarse gel particles heat treated at 450°C contained approximately equal amounts of pyrochlore and perovskite phases. Previous studies have shown that X-ray diffraction often substantially underestimates the volume percent of pyrochlore phase in chemically prepared PZT materials [8,9]. Unfortunately, because of the heterogeneous nucleation of perovskite phase in the 450°C particles, it was impossible to quantify the volume fractions of each phase by SEM.

The X-ray diffraction patterns of fine gel-derived particles heat treated at 350, 400 and 500°C are shown in Fig. 1, respectively. While the diffraction patterns indicated that the 350°C gel consisted of three phases: pyrochlore, perovskite, and PbO, the 400°C particles consisted of two phases: perovskite and pyrochlore. (There may actually be some undetectable (by X-ray) amorphous phase in the triphasic sample.) The 500°C gel-derived particles were single phase perovskite by X-ray diffraction. In this paper, the samples corresponding to the 300, 350, 400, and 500°C anneals will be termed amorphous, triphasic, diphasic, and perovskite, respectively. Once again, accurate determination of the volume fraction of each phase using SEM analysis was not successful. Nonetheless, it is very evident that the volume fraction of perovskite phase increases with annealing temperature.

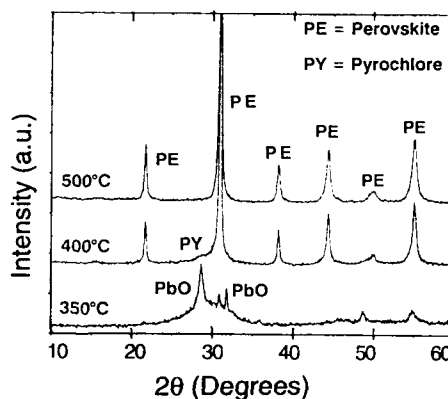


FIG. 1. X-ray diffraction patterns for PZT samples annealed at 350, 400, and 500°C in air for 24 hrs.

Some of the PZT gels were also annealed in an oxygen deficient, or reducing ambient (0.1% O_2) at 650°C. Both massicot (orthorhombic phase) and litharge (tetragonal phase) commercial PbO powder, were also investigated. Enhancement of the volume percentage of the tetragonal phase was prepared by annealing the massicot PbO powder at 800°C in air for 1 hr.

The EPR measurements were made on a Bruker ESP-300E X-band spectrometer at 25K. An Oriel 100 W Hg arc lamp was used in conjunction with a 3.4 eV narrow-band interference filter for the room temperature monochromatic illumination of the PZT and PbO powders. Following the UV illumination, the samples were quickly cooled (30 sec) to 25K.

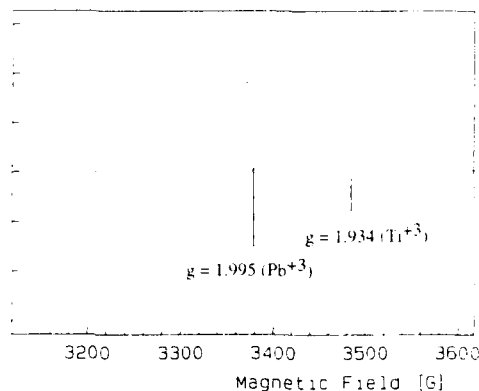
RESULTS AND DISCUSSION

Figure 2 shows that optical illumination creates both Pb^{+3} and Ti^{+3} centers in single phase perovskite PZT 53/47 materials. In other publications it was demonstrated that the optically induced EPR signal at $g = 1.995$ is due to Pb^{+3} [5] by observation of the very large nuclear hyperfine interaction of the 21.1% abundant $I = 1/2$ ^{207}Pb nuclei. The other EPR signal at $g = 1.934$ was found to be due to Ti^{+3} centers by a combined EPR/optical absorption spectroscopy study [6]. It was found that the Ti^{+3} centers are partly responsible for the absorption at 2.6 eV, which is a characteristic crystal field splitting energy of Ti^{+3} ions in many materials [10]. In order to show that the optically induced Pb^{+3} and Ti^{+3} centers are only a feature of the perovskite structure, we now investigate the response of UV-illumination on the (1) diphasic (pyrochlore and perovskite) and (2) amorphous phases of PZT, as well as the (3) litharge and (4) massicot phases of PbO. The results are summarized in Table I. Table I supports our ascertainment that these optically induced EPR centers are only associated with the perovskite structure, and hence, are not due to a small undetectable (by SEM, X-ray) pyrochlore or amorphous phase(s) in the 'single phase' perovskite materials. These results also effectively demonstrate that the defect center is not associated with excess PbO in the perovskite ceramics; if this was the case, then we would expect to observe large UV-induced EPR signals in the pure PbO samples, which simply did not occur.

It should be mentioned that UV-illumination did create very small Pb^{+3} signal in the sample annealed at 350 and 400°C in air, i.e., the ones we term triphasic and diphasic, respectively. The density of the Pb^{+3} signal was only a very small fraction (3-10%) of that observed in the UV-illuminated single phase perovskite sample. We believe that the paramagnetism in these samples result from a small amount of embedded perovskite phase that is present. Consistent with this argument, recall from the X-ray diffraction patterns (Figs. 1(a and b)) that these particular samples do indeed contain some perovskite phase. Following our earlier argument, if these defects were associated with the pyrochlore or amorphous phases, then we would expect to observe the largest density of EPR centers in either the amorphous, triphasic, or diphasic samples, which again did not occur. However, note that the Pb^{+3} density does increase with annealing temperature as does the perovskite phase.

Therefore, it appears as though the Pb^{+3} center can be described as a hole trapped on a corner Pb^{+2} ion in the perovskite lattice, and the Ti^{+3} center is simply an electron trapped at the central Ti^{+4} ion in the perovskite lattice. To further substantiate this point, we have also been able to show that Pb^{+3} centers are created in single crystals of $PbTiO_3$ [11]; this argues that the defects are not necessarily located at the grain boundaries in the polycrystalline ceramics investigated here. On a similar note, it is found that Pb^{+3} centers are optically induced in every Ti/Zr stoichiometry that we have explored in the PZT system (0/100, 5/95, 10/90, 25/75, 48/52, 53/47, 56/44, 75/25, 90/10, and 100/0) [12]. We believe that these collective results provide strong evidence that holes being trapped at Pb^{+2} centers are germane to the Pb-based perovskite ferroelectrics.

Fig. 2. EPR trace showing that UV-light creates Pb^{+3} and Ti^{+3} centers in perovskite PZT.



	Material	Phase	Pb ⁺ 3 or Ti ⁺ 3 centers
Table I. Formation of UV-activated EPR centers for various PZT and PbO phases.	PZT	amorphous	NO
	PZT	triphasic	YES (3% density)
	PZT	diphasic	YES (10% density)
	PZT	perovskite	YES
	PbO	litharge	NO
	PbO	massicot	NO

At this juncture we now turn to the observation of an extrinsic defect center in solution-derived PZT which we ascribe to carbon dangling-bonds. These particular defect centers were observed without optically illuminating any of the ceramics, i.e., they are present in the virgin materials. This resonance is observed in the amorphous PZT materials annealed at 300°C in air as illustrated in Fig. 3 (a). The concentration of carbon dangling bonds is $3 \times 10^{16}/\text{cm}^3$. We ascribe this resonance to a carbon dangling bond since its zero-crossing g value of 2.0024 and peak-to-peak linewidth is characteristic of carbon radicals in many different materials [13,14]. Consistent with the carbon radical assignment, it should be noted that the amorphous powder was visually black. Evidently, the 300°C anneal in air is not sufficient to oxidize all the residual organics. These observations also suggest that the oxidation process in part involves unpaired spins on carbon atoms. The carbon radicals observed here are not bonded to hydrogen, i.e., methyl radicals, since these centers would produce characteristic hydrogen nuclear hyperfine splittings [13,15].

We find that annealing the PZT powders at $T > 400^\circ\text{C}$ in air tends to further oxidize the carbon dangling bonds as shown in Fig. 3 (b) and (c); these samples were annealed at 400 and 650°C, respectively. To get rid of the carbon radicals at $T < 400^\circ\text{C}$ it was necessary to anneal the PZT gel powders for extended periods of time (roughly 12 hrs).

Trace 3 (d) shows a very large EPR signal which we again ascribe to carbon dangling bonds ($4 \times 10^{17}/\text{cm}^3$) in PZT samples annealed at 650°C in an *oxygen deficient* ambient (0.1% O_2).

The spin resonance features are essentially identical to that observed in Trace 3 (a); consistent with this carbon assignment, the sample was again visually black. (The PZT powder annealed at 650°C in air was a yellowish-orange color.) To further confirm the carbon radical identification we investigated the microwave saturation characteristics of the $g = 2.0024$ resonance in the PZT to that of strong pitch, i.e., a carbon EPR standard. The results are plotted in Fig. 4. As shown the microwave saturation characteristics are essentially identical between the two. This provides further evidence for our carbon dangling-bond assignment.

Fig. 3 EPR traces of PZT corresponding to the (a) amorphous, (b) diphasic, and (c) perovskite phases all annealed in air. Trace (d) was for a PZT powder annealed at 650°C in 0.1% O₂.

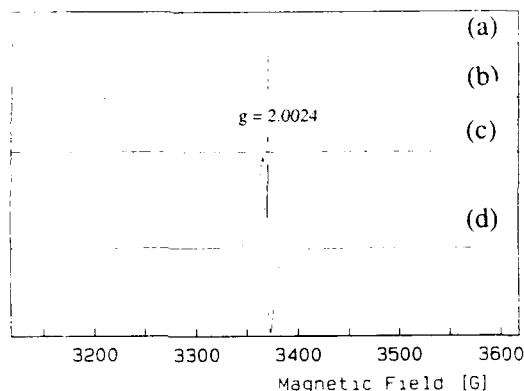
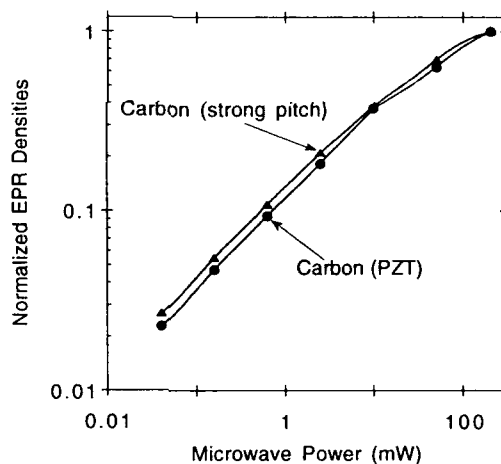


Fig. 4 Microwave saturation characteristic for the PZT sample annealed in a reducing ambient (0.1% O₂/650°C) and strong pitch, a carbon EPR standard.



The observation of carbon radicals may be of interest when considering the effects of annealing ambient on solution derived PZT electronic properties. It should be mentioned that large paramagnetic carbon densities can certainly effect the materials' electronic properties, and should be considered as a possible candidate for any observed degradation of PZT films annealed in a reducing atmosphere.

CONCLUSIONS

We have been able to determine that the optically induced Pb^{+3} and Ti^{+3} centers are associated with the perovskite phase of PZT. This result, coupled with our earlier observations on Pb^{+3} centers [5,11,12], strongly suggests that this center is inherent to Pb-based perovskite ferroelectrics. This study has also shown that if the PZT ceramics are annealed in a reducing ambient, even at relatively high temperatures (650°C), carbon radicals are present in fairly high densities.

ACKNOWLEDGMENTS

We would like to thank G. E. Pike, C. H. Seager, D. Dimos, and D. M. Smyth for many useful discussions during the course of this work. This work performed in part at Sandia National Laboratories was supported by the U. S. Department of Energy under contract DE-AC04-76DP00789.

REFERENCES

1. P.K. Larsen, R. Cuppens, and G.A.C.M. Spierings, *Ferroelectrics*, 128, 265 (1992).
2. D. Dimos and R.W. Schwartz, *MRS Symp. Proc.*, Vol. 243, 73 (1992).
3. R.W. Schwartz, B.C. Bunker, D. Dimos, R.A. Assink, B.A. Tuttle, D.R. Tallant, and L.A. Weinstock, *Integ. Ferroelectrics*, 2, 243 (1992).
4. S. Li, R.A. Condrate, Sr., and R.M. Spriggs, *Spectroscopy Lett.*, 21, 969 (1988).
5. W.L. Warren, B.A. Tuttle, P.J. McWhorter, F.C. Rong and E.H. Poindexter, *Appl. Phys. Lett.*, 62 (1993).
6. W.L. Warren, C.H. Seager, D. Dimos, and E.J. Friebele, *Appl. Phys. Lett.*, 61, 2530 (1992).
7. G. Yi, Z. Wu, and M. Sayer, *J. Appl. Phys.*, 64, 2717 (1988).
8. B.A. Tuttle, R.W. Schwartz, D.H. Doughty, and J.A. Voight, *MRS Symp. Proc.*, Vol. 200, 159 (1990).
9. A.H. Carim, B.A. Tuttle, D.H. Doughty, and S.L. Martinez, *J. Am. Cer. Soc.*, 74, 1455, (1991).
10. S. Arafa and F. Assabghy, *J. Appl. Phys.*, 45, 5269 (1974).
11. W.L. Warren, B.A. Tuttle, S.N. Sun, Y. Huang, and D.A. Payne, *MRS Symp. Proc.*, (1993), these proceedings
12. W.L. Warren, B.A. Tuttle, and J. Robertson, *J. Am. Cer. Soc.*, submitted.
13. R.A.B. Devine and A. Tissier, *J. Appl. Phys.*, 69, 2480 (1991).
14. G. Kordas, *MRS Symp. Proc.*, Vol. 61, 419 (1986).
15. J.E. Wertz and J. R. Bolton, "Electron Spin Resonance" (Chapman Hall, NY, 1986).

OXYGEN TRACER DIFFUSION IN SOL-GEL DERIVED Pb(Zr,Ti)O₃ THIN FILMS

JOHN J. VAJO, L.A. MOMODA, S.B. WONG AND G.S. KAMATH
Hughes Research Laboratories, 3011 Malibu Canyon Road, Malibu, CA 90265

ABSTRACT

We have studied oxygen diffusion in thin films of Pb(Zr,Ti)O₃ on Pt/Ti/SiO₂/Si <100> multilayer substrates using ¹⁸O as a tracer. The PZT films were synthesized using the sol-gel technique and crystallized in air at 650° C for 30 minutes. Diffusion experiments were conducted in one atmosphere of ¹⁸O₂ at temperatures between 400-600° C, the extent of exchange was monitored using secondary ion mass spectrometry. Exchange profiles were modeled using solutions of the diffusion equation with boundary conditions for a layer with finite thickness. Significant exchange (>60%) of ¹⁶O by ¹⁸O was measured after treatment under conditions similar to those used for crystallization. At low levels of exchange, oxygen diffusion does not follow a simple Fickian profile and differences exist between nominally identical films. These results suggest that oxygen exchange is sensitive to the film's microstructure.

INTRODUCTION

The effect of defect chemistry on the electrical device performance of lead zirconate titanate thin films (PZT), especially for nonvolatile memory applications, has been a subject of recent interest [1,2]. Charged defects such as oxygen vacancies have been suspected as the origin of switching fatigue and high film conductance. Previous studies have shown that oxygen diffusion can readily occur in the perovskite based ceramics and single crystals [3-5] and the results of some recent work suggest that an oxygen annealing atmosphere does improve the device performance of ferroelectric thin films [6]. In our study, oxygen exchange in sol-gel derived PZT thin films was investigated using an ¹⁸O₂ tracer and depth profiling with secondary ion mass spectrometry (SIMS) to measure diffusion profiles for oxygen. We have determined the diffusion characteristics of oxygen in the films and we have found that oxygen tracer diffusion can be used as a characterization technique which exposes subtle differences in the defect chemistry and the microstructure of the film.

EXPERIMENTAL PROCEDURES

PZT thin films of nominal composition Pb(Zr_{0.3}Ti_{0.7})O₃ were synthesized from lead (IV) acetate, zirconium n-butoxide and titanium isopropoxide precursors using the sol-gel method [7]. Three layers of the sol were spin coated onto a multilayer substrate consisting of 250 nm Pt/100 nm Ti/1000 nm SiO₂ on Si<100>. Each layer was pyrolyzed for 5 minutes at 300° C to remove most of the water and solvents from the film. The entire three layer stack, ~280 nm thick, was then heat treated at 650° C for 30 minutes in air to promote crystallization. The films were air quenched after the heat treatment. The achievement of a polycrystalline tetragonal perovskite structure was verified by x-ray diffraction analysis.

Oxygen diffusion into the films was studied using ¹⁸O₂ (98.6% isotopic purity) as a tracer. The films were annealed in a sealed ampule that consisted of a 30 cm quartz tube with a 1 cm x 0.5 cm rectangular cross section connected to a 400 cm³ ballast volume that remained outside the furnace at room temperature. The ballast volume maintained a constant atmospheric pressure (± 10%) of ¹⁸O₂ in the ampule between 25° C and 900° C. The samples were heat treated by inserting the ampule into a preheated furnace for various periods of time.

Secondary ion mass spectrometry (SIMS) and Auger electron spectroscopy (AES) measurements were performed in a Perkin-Elmer 595/600 system with a PHI 3500 SIMS II attachment. SIMS profiles were obtained using 3.0 keV Ar⁺ primary ions (40° angle of incidence, 300 nA current, 100 μm spot) rastered over ~ 1 mm² area with only the central 4% being analyzed. ¹⁶O and ¹⁸O negative secondary ions as well as other positive secondary ions species were monitored.

PZT film thicknesses were determined by profilometer measurements of craters sputtered down to the PZT/Pt interface.

RESULTS

Figure 1 shows an AES sputtered depth profile of a typical PZT/Pt/Ti/SiO₂/Si structure after crystallization in air for 30 minutes at 650° C. The profile shows the initial composition of the PZT/electrode/substrate structure used for the ¹⁸O₂ exchange measurements. There are several important features to the profile. As reported previously [8], the surface of the PZT layer is enriched in Pb and depleted in Ti suggesting a PbO rich surface. Within the limits imposed by the analysis conditions, the PZT/Pt interface is sharp. In contrast, the Pt/Ti interface is broader which may indicate intermixing of the Pt and Ti layers during crystallization or which may be an artifact of the sputtering process. Significant diffusion of Pt into the Ti layer is, however confirmed by the observation of a Pt containing phase seen within the Ti layer at a sputtering time of ~76 minutes. The most obvious effect of heating the layers is that after crystallization, the Ti layer is oxidized. Although the atomic concentrations are approximate, the predicted composition is close to TiO₂. This effect has been observed previously for Pt/Ti and other PZT electrode structures [9,10]. Obviously, the properties of the PZT layer could be altered by migration of oxygen from the PZT layer to the Ti layer during crystallization.

After heating in ¹⁸O₂, the fraction of ¹⁸O in the PZT layer, ($f(^{18}\text{O})$), was determined from SIMS sputtered depth profiles using the expression

$$f(^{18}\text{O}) = \frac{I(^{18}\text{O})}{I(^{18}\text{O}) + I(^{16}\text{O})} \quad (1)$$

where $I(x)$ is the SIMS intensity of the species x . Exchange data are shown in Figure 2 for three ¹⁸O₂ heat treatment conditions and for a sample not treated in ¹⁸O₂. Without treatment, $f(^{18}\text{O}) \approx 0.002$ which is approximately the natural abundance of ¹⁸O. Therefore, there are no

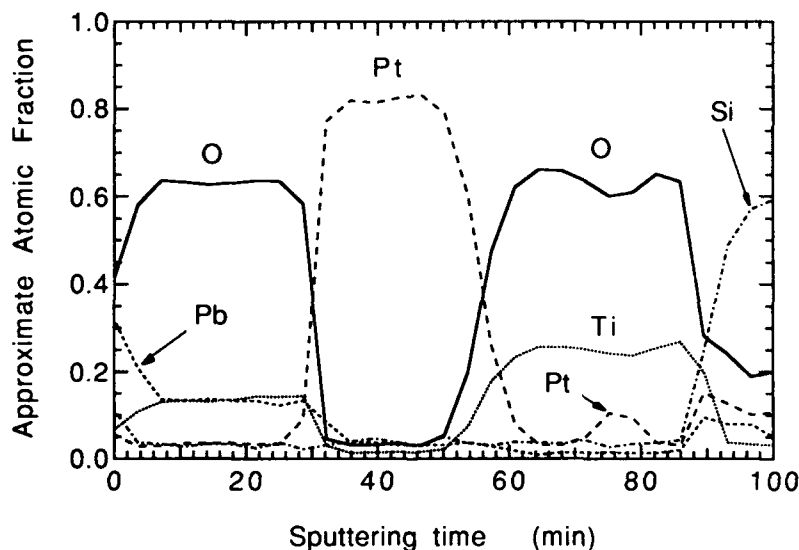


Figure 1. Auger depth profile of a PZT film after crystallization at 650° C for 30 minutes. The Zr signal which overlaps with the Pt signal has been omitted for clarity.

detectable interferences in $I(^{18}\text{O})$ from sources such as H_2O which is generated during the sol-gel process. After treatment in $^{18}\text{O}_2$ at 600°C for 30 minutes there is $>60\%$ exchange throughout the PZT film, Figure 2. Since these conditions are similar to those used for crystallization (in this work, 650°C for 30 minutes) the exchange illustrated in Figure 2 indicates that any oxygen lost from the PZT film can be simultaneously replenished from the gas phase. More generally, this result implies that exchange of oxygen in the PZT film with oxygen in the gas phase occurs during crystallization.

The exchange of oxygen into the oxidized Ti layer was also monitored and in all cases was found to be small. For example, treatment at 600°C for 30 minutes, for which $>60\%$ exchange occurs in the PZT layer, results in $<2\%$ exchange in the Ti layer (data not shown). This result demonstrates that oxidation of the Ti layer reaches completion during crystallization and that oxygen in the Ti layer is kinetically more stable than oxygen in the PZT layer.

At the PZT surface $f(^{18}\text{O})$ does not equal the gas phase atomic fraction (0.99). This result indicates that there is a kinetic barrier to oxygen incorporation (dissociation) at the PZT surface. The extent to which the barrier is related to the deviations from the nominal composition, as shown in Figure 1, is being studied.

The depth distributions of $f(^{18}\text{O})$ were modeled using Fick's laws. For a layer with finite thickness, the solution of the diffusion equation yields

$$f(^{18}\text{O}) = C_0 \sum_{j=0}^{\infty} (-1)^j \left[\operatorname{erfc} \left(\frac{a(2j+1) + (x-a)}{2(Dt)^{1/2}} \right) + \operatorname{erfc} \left(\frac{a(2j+1) - (x-a)}{2(Dt)^{1/2}} \right) \right] \quad (2)$$

where C_0 is the fraction of ^{18}O at the PZT surface, a is the PZT film thickness, x is the depth measured from the PZT surface, D (cm^2/sec) is the diffusion coefficient, t is the $^{18}\text{O}_2$ treatment time, and erfc is the complementary error function [1]. For each exchange measurement, C_0 and D were adjusted to best fit the measured profiles. Curves calculated using the first three

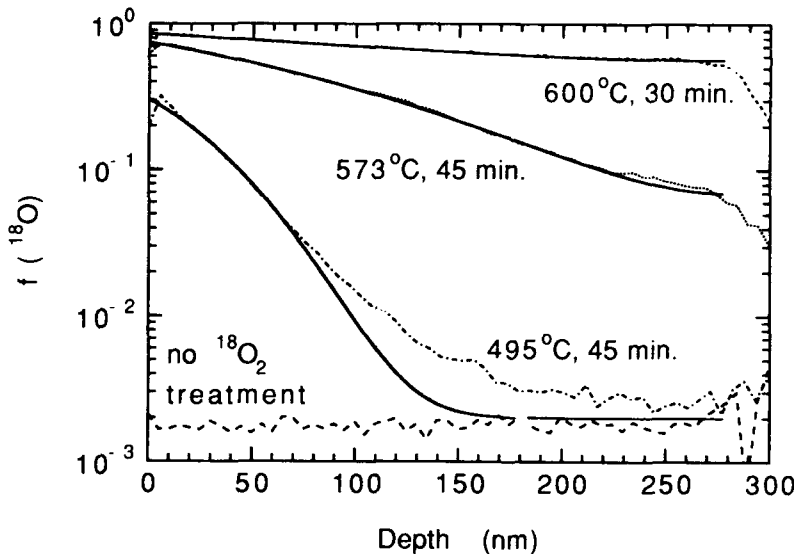


Figure 2. Fraction of ^{18}O in PZT as a function of depth for three sample following heat treatments in $^{18}\text{O}_2$ and for an untreated sample. Solid lines are results of model calculations using equation (2).

terms in equation 2 are shown in Figure 2.

In cases where the extent of exchange is large, $> 10\%$ throughout the film, the Fickian model describes the exchange well. In particular, there is no noticeable effect of the variation in composition near the surface (see Figure 1) on the extent of oxygen exchange. In cases where the extent of exchange falls below $\sim 5\%$, deviations from the model behavior occur. The deviations are relatively small. For example, for treatment at 495°C for 45 minutes (Figure 2), the model fails to account for only 5% of the oxygen atoms exchanged.

Diffusion coefficients, determined by fitting equation 2 to the $f(^{18}\text{O})$ profiles for temperatures from 400°C to 600°C , are plotted in Arrhenius form in Figure 3. The behavior is linear with an activation energy, E_{diff} , of $54 \pm 4\text{ kcal/mol}$ ($2.3 \pm 0.2\text{ eV}$) and a diffusion prefactor $D_0 = 10^{0.6 \pm 1.0}\text{ cm}^2/\text{sec}$.

In Figure 4, the exchange of oxygen into three different but nominally identical films are compared after simultaneous treatment at 445°C for 180 minutes. The extent of exchange is similar for all three films with minor differences. The differences between the films increase as the level of exchange decreases with increased depth. For the profiles shown in Figure 4, the total fraction of oxygen atoms exchanged varies between 6% and 8%.

DISCUSSION

Figure 1 demonstrates that the Ti electrode layer oxidizes during crystallization of the PZT film. The origin of the oxygen atoms which are eventually bound in the Ti layer is of interest because the oxygen vacancy concentration affects the electrical properties of the PZT film. One possible source of oxygen is the SiO_2 layer since, on a thermodynamic basis, Ti will react with SiO_2 to form TiO_2 and Ti silicides [12]. From Figure 1, it does not appear that a distinct Ti silicide layer is formed indicating that the crystallization conditions were not favorable for the Ti to react with SiO_2 . A second source of oxygen for oxidation of the Ti layer is the PZT layer. This mechanism would involve oxygen diffusion through the intervening Pt layer. Loss of oxygen from the PZT layer would be expected to alter adversely the electrical properties of the PZT. However, Figure 2 illustrates that any oxygen lost from the PZT layer can be replenished with oxygen from the gas phase.

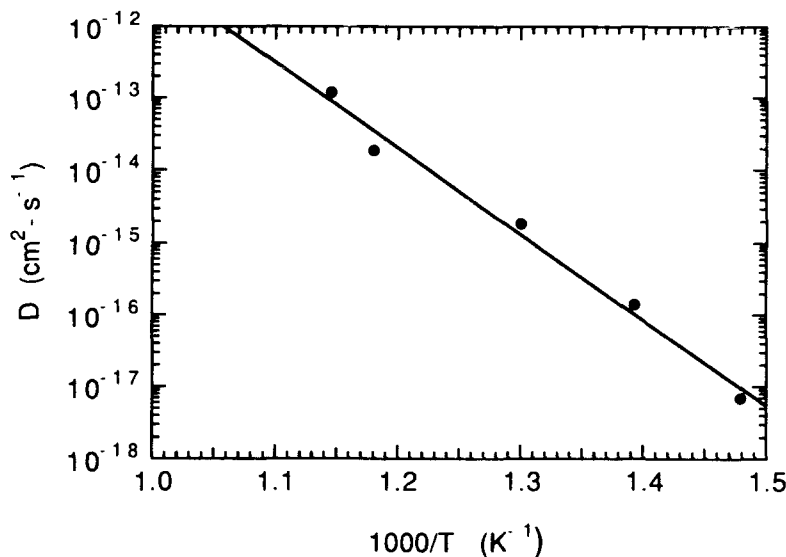


Figure 3. Arrhenius plot of diffusion coefficients determined from numerical fits to equation (2).

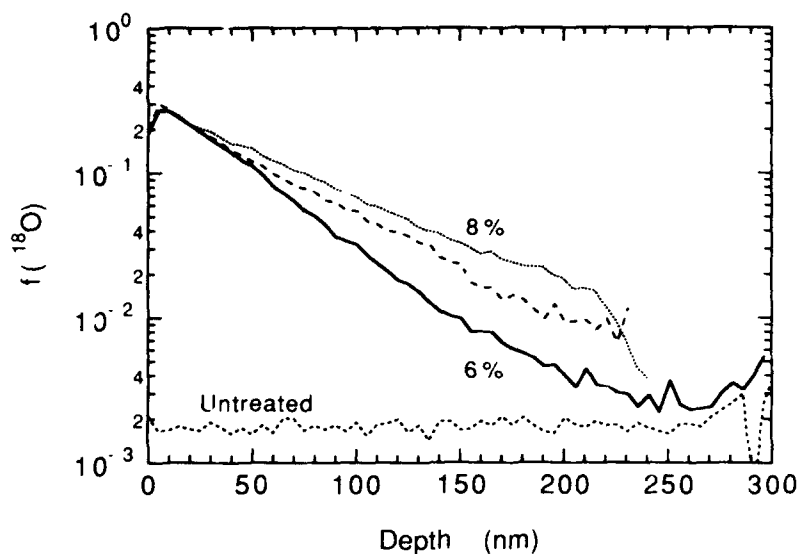


Figure 4. Fraction of ^{18}O as a function of depth following treatment in $^{18}\text{O}_2$ at 445°C for 180 minutes for three similarly processed films.

The observation of significant oxygen exchange under conditions similar to those used for crystallization implies that during crystallization, the concentration of oxygen in the PZT film is in equilibrium or near equilibrium with oxygen in the gas phase. Thus, changes in the partial pressure of oxygen will affect the oxygen vacancy concentration, $[V_{\text{O}}]$, in the PZT film. This conclusion has been confirmed by the measurements of the electrical characteristics of films annealed at various oxygen partial pressures [6]. In addition, $[V_{\text{O}}]$ will depend on the temperature of crystallization as well as on the rate of cooling following crystallization. A rapid cooling would be expected to "freeze-in" the $[V_{\text{O}}]$ present at the crystallization temperature. If the temperature is lowered slowly, the $[V_{\text{O}}]$ will adjust until the kinetics become too slow to keep pace with the decreasing temperature. The extent to which these processing variations alter electrical properties and whether or not variations in crystallization conditions can be observed using oxygen exchange measurements are being studied.

The model calculations using equation (2) shown in Figure 2 assume that the diffusion constant is independent of depth throughout the PZT film. This assumption appears to be justified for profiles with $> 5\%$ exchange throughout the film by the excellent agreement between the model calculations and the measured profiles. However, deviations occur when the level of exchange falls below $3\text{--}5\%$. In these cases, the model calculations underestimate the measured extent of exchange indicating that there are faster, although minor, diffusion mechanisms. Since the PZT films are polycrystalline, diffusion along grain boundaries may account for the differences between model calculations and the experimental measurements. Secondary electron micrographs of the PZT surface clearly show individual grains with an average diameter of ~ 100 nm. Assuming the individual grains are relatively smooth and the oxygen spacing within the lattice is 0.4 nm (JCPDS card #33-784), the fraction of oxygen atoms associated with the grain boundaries is $\sim 2\%$. This value is approximately equal to the fraction of oxygen atoms that are not accounted for by the Fickian model. Certainly other mechanisms are possible, any mechanism in which the diffusion constant varies with depth could account for the measured exchange profiles. A diffusion constant that depends on the local microstructure (grain boundaries, defects) and, therefore, on depth may actually be expected for a polycrystalline thin film on a heterosubstrate.

Regarding the diffusion parameters measured in our study, the high E_a and D_0 values seem to be consistent with those expected for oxygen diffusion in an easily dissociated perovskite lattice. That is, thermal dissociation of PbO from the lattice is a likely vacancy diffusion mechanism for the PZT thin films. The 54.4 kcal/mol activation energy measured is higher than values which have been attributed to a cationic displacement mechanism typically seen in perovskite ferroelectrics (~ 20 kcal/mole) [4], and is more likely due to a higher energy thermal dissociation mechanism. The activation energy for the thermal dissociation of a BaTiO_3 ceramic has been determined to be ~ 100 kcal/mole at temperatures of $>1000^\circ\text{C}$. In our PZT thin films, the dissociation mechanism seems to occur at much lower temperatures.

The differences in oxygen exchange between films shown in Figure 4 are similar to the deviations from the Fickian behavior discussed above and may be due to differences in microstructures. If differences in oxygen exchange can be correlated with electrical properties, such differences could provide a sensitive technique to monitor the microstructure of PZT thin films.

CONCLUSIONS

To summarize, significant oxygen exchange occurs in sol-gel derived PZT thin films heated in $^{18}\text{O}_2$ under conditions typically used for crystallization. A Fickian diffusion model with $D_0 = 10^{0.6} \text{ cm}^2/\text{sec}$ and $E_{\text{diff}} = 54$ kcal/mol can account for the measured diffusion profiles for levels of exchange $\geq 5\%$. For levels of exchange $\leq 5\%$, deviations from Fickian behavior were observed. We believe that the variations are related to differences in microstructure and grain boundary diffusion.

REFERENCES

- [1] D. M. Smyth, *Ferroelectrics* **116**, 117 (1991).
- [2] J.F. Scott and C. A. Paz de Araujo, *Science* **246**, 1400 (1989).
- [3] A. Yamiji, *J. Am. Ceram. Soc.* **58**, 152 (1975).
- [4] S. Shirasaki, H. Yamamura, H. Haneda, K. Kakegawa and J. Moori, *J. Chem. Phys.* **73**, 4640 (1980).
- [5] A. Hasegawa, S. Fujitsu, K. Koumoto and H. Yanagida, *Japan. J. Appl. Phys.* **30**, 1252 (1991).
- [6] C.K. Kwok and S.B. Desu in *Ferroelectric Thin Films II*, edited by A.I. Kingon, E.R. Myers and B. Tuttle (Mater. Res. Soc. Proc. **243**, Boston, MA, 1992) pp. 393.
- [7] R.W. Schwartz, R. A. Assink and J.T. Headley in *Ferroelectric Thin Films II*, edited by A.I. Kingon, E.R. Myers and B. Tuttle (Mater. Res. Soc. Proc. **243**, Boston, MA, 1992) pp. 245.
- [8] B.D. Qu, Y.G. Wang, W.L. Zhong, K.M. Wang and Z.L. Wang, *J. Appl. Phys.* **71**, 3467 (1992).
- [9] A. Grill, W. Kane, J. Viggiano, M. Brady and R. Laibowitz, *J. Mat. Res.* **7**, 3260 (1992).
- [10] J.O. Olowolafe, R.E. Jones, Jr., A.C. Campbell, R.I. Hegde, C.J. Mogab and R.B. Gregory, *J. Appl. Phys.* **73**, 1764 (1993).
- [11] B. Tuck, *Introduction to Diffusion in Semiconductors*, (Peter Peregrinus Ltd., England, 1974), p. 25.
- [12] R. Pretorius, J.M. Harris and M.A. Nicolet, *Solid State Electronics* **21**, 667 (1978).

ORIENTED LEAD ZIRCONATE TITANATE THIN FILMS: CHARACTERIZATION OF FILM CRYSTALLIZATION

JAMES A. VOIGT, B. A. TUTTLE, T. J. HEADLEY, M. O. EATOUGH, D. L. LAMPPA,
AND D. GOODNOW
Sandia National Laboratories, P.O. Box 5800, Albuquerque, NM 87185.

ABSTRACT

Through systematic variation of film processing temperature and time, we have characterized the pyrochlore to perovskite crystallization process of solution-derived PZT 20/80 thin films. The ≈ 3000 Å thick films were prepared by spin deposition using $\langle 100 \rangle$ single crystal MgO as the film substrate. By controlled rapid thermal processing, films at different stages in the perovskite crystallization process were prepared with the tetragonal PZT 20/80 phase being $\langle 100 \rangle / \langle 001 \rangle$ oriented relative to the MgO surface. An activation energy for the conversion process of 326 kJ/mole was determined by use of an Arrhenius expression using rate constants found by application of the method of Avrami. The activation energy for formation of the PZT 20/80 perovskite phase of the solution-derived films compared favorably with that calculated from data by Kwok and Desu [1] for sputter-deposited 3500 Å thick PZT 55/45 films. The similarity in activation energies indicates that the energetics of the conversion process is not strongly dependent on the method used for film deposition.

INTRODUCTION

The ability to control the microstructural properties of ferroelectric (FE) thin films is of critical importance to many applications. In non-volatile memory applications, for example, the grain size in the polycrystalline FE film should be substantially smaller than device feature sizes to insure uniform electrical performance throughout the memory. Although recently the characterization of FE film microstructures has been the subject of much study [2], relatively little work has been done to develop an understanding of the nucleation and growth processes involved in the formation of the FE perovskite phase [1,3,4].

Most FE films are prepared by first depositing a precursor film containing constituent metal ions in the desired stoichiometry using a standard film deposition technique, such as chemical vapor deposition or solution coating. The precursor film, which can be amorphous as deposited, is then often converted to the crystalline desired FE phase by a thermal processing operation. For the lead zirconate titanate, PZT, system, it is well documented that the FE perovskite phase crystallizes out of a nanocrystalline pyrochlore matrix that forms during the initial stages (low temperatures) of the thermal processing step [5-7]. The resulting microstructure of the FE PZT film is dramatically influenced by the zirconium to titanium ratio [5,8]. Films with a high zirconium content tend to form large perovskite grain structures (on the size scale of several microns) that are often called rosettes due to their resemblance to spherulitically grown particles. Titanium rich films, on the other hand, typically have much smaller, often submicron grain sizes indicating much higher nucleation rates. Other factors, including precursor film structure [6,9] and the substrate material [10], can also influence film microstructure. As an example for the film preparation process used in this study, PZT films prepared and processed identically (i.e., $\langle 100 \rangle$ MgO substrates, processed at 650°C for 10 min in flowing oxygen) but with zirconium to titanium ratios of 40:60 and 20:80 had average grain sizes of 2 μm [10] and 0.7 μm , respectively, as determined by the lineal intercept method using a multiplicative factor of 1.

In this paper, we describe initial results of our work on characterizing the conversion of solution-derived PZT thin films from the nanocrystalline pyrochlore phase to the perovskite phase. A high titanium content composition (PZT 20/80) was chosen in order to study the crystallization process when nucleation rates are higher and finer grained microstructures are produced than for near-morphotropic phase boundary compositions. Single crystal MgO substrates were used so that the processes involved in the formation oriented of PZT films could

This work performed at Sandia National Laboratories, supported by the U. S. Department of Energy under contract number DE-AC04-76DP00789.

be investigated. Also, the tetragonal form of the PZT 20/80 phase allowed us to readily characterize ferroelectric domain structure as a function of film processing conditions [11]. Finally, our results on high titanium, solution-derived PZT thin films could be compared with work by Kwok and Desu [1] on the kinetics of the conversion of sputter-deposited PZT thin films near the morphotropic phase boundary (PZT 55/45).

EXPERIMENTAL

PZT 20/80 films were fabricated by spin-coating (3000 rpm for 30 seconds) using a solution prepared by the inverted mixing order process developed by Schwartz et al. [12] which is a modification of a hybrid solution deposition process developed by Sayer and coworkers [13]. Excess lead (5 mole %) was added to be consistent with previous work on preparation of oriented PZT films [10,14]. To obtain oriented growth, <100> single crystal MgO with an epitaxial surface finish was used as the substrate. The substrates were heat treated at 400°C in air for 10 minutes prior to film deposition. Films were decomposed using a 5 minute heat treatment at 300°C on a hot plate. Three film layers were deposited to produce films with a thickness of ≈ 3000 Å. Film crystallization was carried out using a rapid thermal processing, RTP, system (AET/Addax, Model RMV4, Milpitas, CA). For a more detailed discussion of the film preparation process see Tuttle et al. [10].

RESULTS AND DISCUSSION

We have used rapid thermal processing to obtain thin films at different stages of conversion to the PZT 20/80 perovskite phase. Figure 1 shows thermal cycles used for processing films at 500°C for 30 sec and 10 min. Within the constraints of the RTP system software, the heating rate was programmed to be as close to 160°C/sec as possible for all of the thermal processing cycles used in this study.

In general, the film surface reached the programmed soak temperature within six seconds of the programmed time with little or no over shoot as measured by the temperature controlling thermocouple located on the film surface. Sample cooling varied depending on processing temperature and time (see Figure 1) due to the thermal mass of the quartz furnace chamber of the RTP system. All samples, however, cooled through the PZT 20/80 Curie temperature ($\approx 450^\circ\text{C}$) at a relatively constant rate of 8°C/sec regardless of the processing condition.

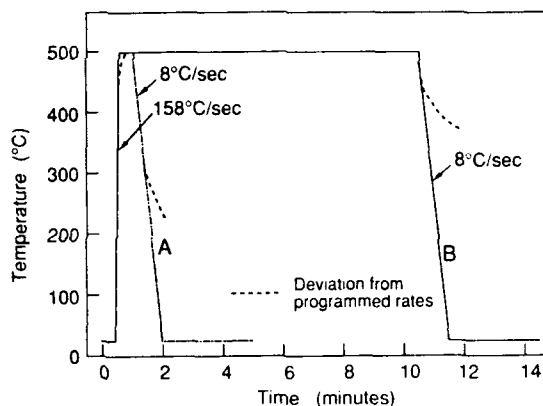


Fig. 1. Rapid thermal processing (RTP) schedules including deviations from programmed temperatures: A) 500°C for 30 s. and B) 500°C for 600 s.

As has been discussed earlier, the perovskite phase forms by a solid state conversion of a nanocrystalline pyrochlore phase that forms rapidly during film heating at temperatures above 400°C. This is illustrated in Figure 2 where x-ray diffraction results for films processed using the heating schedules in Figure 1 are shown. The x-ray results show that the film processed at 500°C for 30 sec is mainly the pyrochlore phase with only a trace amount of perovskite present. After 10 min at 500°C the x-ray diffraction results show that the film has been fully converted to a highly <001>/<100> oriented perovskite. The high degree of orientation is shown by the low

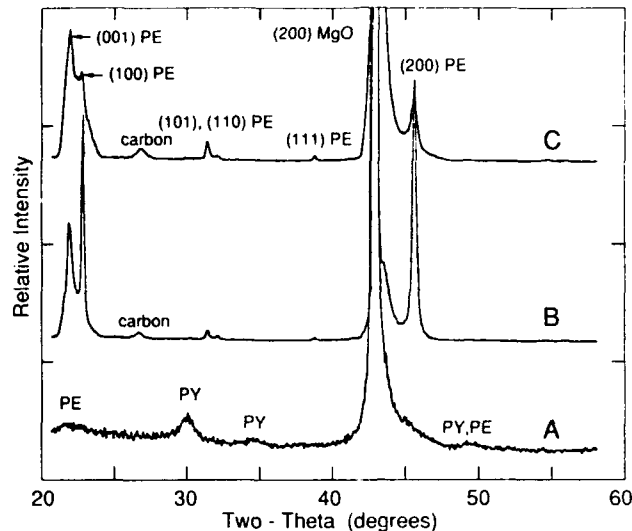


Fig. 2. X-ray diffraction patterns of ≈ 300 -nm-thick PZT 20/80 films on $\langle 100 \rangle$ single crystal MgO processed under the following conditions: A) 500°C, 30 s (intensity is $\times 5$), B) 500°C, 600 s, and C) 550°C, 30 s (PE = perovskite, PY = pyrochlore, carbon presence due to prior SEM analysis).

intensity of the normally major $\langle 110 \rangle$ diffraction peak. The splitting of the $\langle 001 \rangle$ and $\langle 100 \rangle$ peaks is expected due to the tetragonal structure of the PZT 20/80 phase. The much greater intensity of the $\langle 100 \rangle$ diffraction peak relative to that of the $\langle 001 \rangle$ peak is due to the film/MgO stress relationship as the film cools through the Curie point [14].

The extreme temperature sensitivity to the pyrochlore to perovskite transformation is shown by comparison of the x-ray diffraction results for a film processed at 550°C for 30 sec (Figure 2) to those already discussed that were processed at 500°C. After 30 seconds at 550°C the film is completely converted to perovskite where as it took approximately 10 minutes at 500°C to get the same level of conversion, as determined by x-ray diffraction. Kinetic information on the pyrochlore/perovskite transformation only could be obtained up to 525°C; above this temperature the transformation was too fast to be accurately controlled by the RTP system. The fast kinetics of the transformation process at moderate temperatures is related to the high titanium content of the films used in this study. For comparison, Kwok and Desu [1] show x-ray results for the conversion of sputter-deposited PZT 55/45 films in which a significant amount of pyrochlore remains even after 15 min at 550°C.

Figure 3 is a backscattered electron, BSE, photomicrograph of a partially transformed PZT 20/80 film. The high contrast between the perovskite phase (lighter) and the pyrochlore phase (darker) results from the density difference between the two phases. The higher density of the perovskite phase causes a higher flux of backscattered electrons resulting in a brighter BSE image. The figure shows the characteristic circular single crystal perovskite grains that grow out of the pyrochlore matrix. The single crystal form of these grains is shown more clearly using plan view transmission electron microscopy as illustrated in Figure 4. The domain structure within the perovskite grains are easily seen as is the uniform fine scale structure of the pyrochlore matrix material. It should be noted that the pyrochlore matrix consisted of a single nanocrystalline phase; in contrast to the diphasic pyrochlore matrix that has been reported for films with higher zirconium to titanium ratios [5,7].

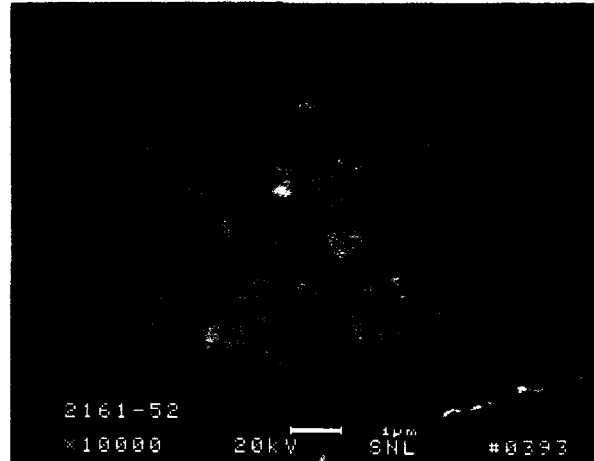


Fig. 3. Back scattered electron (BSE) photomicrograph of oriented PZT 20/80 thin film processed for 60 s at 525°C (lighter regions are circular, single crystal perovskite grains growing out of pyrochlore matrix).



0.5 µm

Fig. 4. Bright-field transmission electron photomicrograph of typical perovskite single crystal grain that has grown out of pyrochlore matrix during PZT 20/80 crystallization process.

The transformation process was characterized at a constant temperature, T , by application of the Johnson-Mehl-Avrami equation [15,16],

$$X(t) = 1 - \exp[-(Kt)^N] \quad (1)$$

where $X(t)$ is the volume fraction of perovskite formed after time, t , K is the rate constant, and N is the growth exponent. Image analysis of BSE photomicrographs was used to determine $X(t)$.

It was assumed that the area fraction determined by image analysis was equal to a film's volume fraction of perovskite. Because of limitations in resolution of the BSE images and the error introduced in assuming that the perovskite phase is uniformly distributed throughout the thickness of the film, the results of the use of the Avrami method to analyze the conversion process are somewhat qualitative. Taking the log of equation 1 twice results in a linear expression where the slope and the y-intercept are equal to N and $N \ln(K)$, respectively, when $\ln\{\ln[1/(1-X)]\}$ is plotted versus $\ln(t)$. Figure 5 shows such a plot for films processed at 475, 500, and 525°C. The data show the expected linear relationship with an average growth exponent of 2.04.

This value is similar to that found for sputter-deposited PZT 55/45 thin films ($N_{ave} = 2.23$) [1] and also for the crystallization of sol gel-derived titania thin films ($N_{ave} = 1.76$) [17].

The rate constants determined by the Avrami analysis were used to calculate an overall activation energy, E_a , for the solid state phase transformation using the Arrhenius expression,

$$K = A \exp(-E_a/kT) \quad (2)$$

where k is Boltzmann's constant and A is related to the activation entropy for the process [18]. A value of 326 kJ/mole was found for the activation energy from the linear relationship shown in Figure 6. Again, this is in reasonable agreement with the data of Kwok and Desu on sputter-deposited PZT 55/45 [1], where an E_a of 248 kJ/mole was calculated using equations 1 and 2. For comparison, Shaikh and Vest found an activation energy of about 84 kJ/mole for the formation of $PbTiO_3$ powder from organometallic precursors [19].

A difference in overall activation energies for the PZT 20/80 and PZT 55/45 thin films can be expected for several reasons. The overall activation energy for crystallization is a function of the activation energies

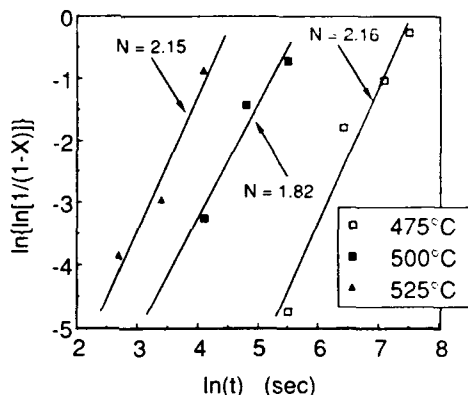


Fig. 5. Plot of $\ln\{\ln[1/(1-X)]\}$ vs. $\ln(t)$.

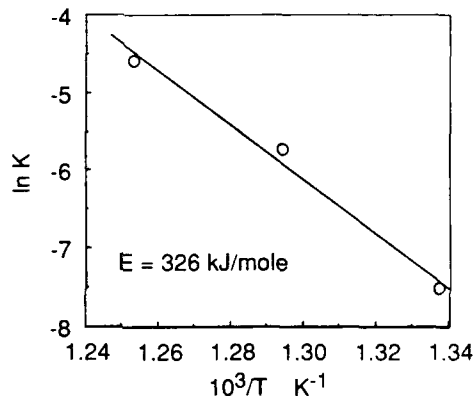


Fig. 6. The inverse temperature dependence of the rate constant K .

of nucleation and growth. The functional form of this relationship is dependent on the mode of the transformation (e.g., $E_a = E_{\text{nucleation}} + (N-1)E_{\text{growth}}$ for constant nucleation rate and linear two-dimensional growth) [20]. As discussed earlier, the zirconium to titanium ratio strongly influences the perovskite nucleation and growth processes. These observations indicate that the energetics of the nucleation and growth processes, and thus the overall activation energy for crystallization, should be dependent on composition. The effect of composition on the activation energy of thin film crystallization has been shown previously for the crystallization of amorphous Ge/Si films on SiO₂ by Edelman and coworkers [21]. They found that E_a varied for Ge_xSi_{1-x} from 299 kJ/mole to 193 kJ/mole for x going from 1 to 0 where E_a was calculated based on the induction time for nucleation. It is expected that E_a for PZT thin films should decrease with increasing titanium content. This conclusion is based on previous observations that nucleation rates increase with increasing titanium and, also, by the fact that the kinetics of the conversion for the PZT 20/80 films was faster than that of the PZT 55/45 films for a fixed temperature (see discussion of x-ray diffraction results). Unfortunately that is the opposite of what is reported here. The inconsistency is no doubt related to the inaccuracy in the method used to determine the volume fraction of perovskite which was the same for both studies discussed here. For example, the activation energies are statistically the same if an error of only about 15% is assumed. The fact that different film deposition methods (solution versus sputtering) and substrates (<100> MgO versus Pt coated single crystal Si) were used in the two studies also makes direct comparisons difficult.

SUMMARY

The overall activation energy for the solid state transformation of nanocrystalline pyrochlore to perovskite for solution-derived PZT 20/80 thin films was determined. The value is in reasonable agreement with previously published data on sputter-deposited PZT 55/45 thin films. This result indicates that the energetics of the transformation process are not greatly different despite the differences in deposition method, substrate material, and composition. In order to do a quantitative comparison of the effect of these variables on the conversion kinetics, a more accurate technique is required to determine the fraction of film converted to the perovskite phase. Our results on the microstructural development of the perovskite phase in PZT 20/80 thin films in terms of nucleation and growth will be presented in a future publication.

ACKNOWLEDGEMENTS

We would like to thank B. McKenzie (SEM), F. A. Greulich (image analysis), A. Kilgo (image analysis), M. Gonzales (x-ray diffraction), and T. Tribble (TEM sample preparation) for their contributions to this project.

REFERENCES

1. C. K. Kwok and S. B. Desu in *Ferroelectric Films*, edited by A. S. Bhalla and K. M. Nair (Ceram. Trans. 25, Amer. Ceram. Soc., Westerville, OH, 1992) pp.85-96.
2. (a) *Ferroelectric Thin Films*, edited by E. R. Myers and A. I. Kingon (Mater. Res. Soc. Proc. 200, Pittsburgh, PA, 1990); (b) *Ferroelectric Thin Films II*, edited by A. I. Kingon, E. R. Myers and B. A. Tuttle (see Ref. 2(a), 1992); and (c) *Ferroelectric Films*, see Ref. 1.
3. K. Chen and J. Mackenzie in *Better Ceramics Through Chemistry IV*, edited by B. J. J. Zelinsky, C. J. Brinker, D. E. Clark, and D. R. Ulrich (Mater. Res. Soc. Proc. 180, Pittsburgh, PA, 1990) pp. 663-668.
4. S. H. Rou, T. M. Graettinger, A. F. Chow, C. N. Soble, II, D. J. Lichenwalner, O. Auciello, and A. I. Kingon, see Ref. 2(b), pp. 81-91; D. Barrow, C. V. R. Vasant Kumar, R. Pascual, and M. Sayer, *ibid.* pp. 113-122; C. Peng and S. B. Desu, *ibid.*, pp. 335-344.
5. L. N. Chapin and S. A. Myers, see Ref. 2(b), pp. 153-58.
6. C. C. Hsueh and M. L. McCartney, J. Mater. Res. 6, 2208 (1991).
7. B. A. Tuttle, T. J. Headley, B. C. Bunker, R. W. Schwartz, T. J. Zender, C. L. Hernandez, D. C. Goodnow, R. J. Tissot, J. Michael, and A. H. Carim, J. Mater. Res. 7, 1876 (1992).

8. C. K. Kwok and S. B. Desu, *J. Mater. Res.* **8**, 339 (1993).
9. R. W. Schwartz, R. A. Assink, and T. J. Headley, see Ref. 2(b), pp. 245-254.
10. B. A. Tuttle, J. A. Voigt, D. C. Goodnow, D. L. Lamppa, T. J. Headley, M. O. Eatough, G. Zender, R. D. Nasby, and S. M. Rodgers, *J. Amer. Ceram. Soc.* **76** (6), 1573 (1993).
11. T. J. Headley, B. A. Tuttle, and J. A. Voigt (unpublished).
12. R. W. Schwartz, B. C. Bunker, D. Dimos, R. A. Assink, D. R. Tallant, I. Weinstock, and D. M. Haaland in Proc. of 3rd Int. Symp. on Integrated Ferroelectrics, (1991) pp. 535-46.
13. G. Yi, Z. Wu, and M. Sayer, *J. Appl. Phys.* **64** (5), 2717 (1988).
14. B. A. Tuttle, J. A. Voigt, T. J. Garino, D. C. Goodnow, R. W. Schwartz, D. L. Lamppa, T. J. Headley, and M. O. Eatough in Proc. of the 8th IEEE Int. Symp. on Appl. of Ferroelectrics, edited by M. Liu, A. Safari, A. I. Kingon, and G. Haertling (IEEE, Piscataway, NJ, 1992) pp. 344-48.
15. W. A. Johnson and R. F. Mehl, *Trans. Metall. Soc. AIME*, **135**, 416 (1939).
16. M. Avrami, *J. Chem. Phys.*, **7** (12), 1103 (1939); **8** (2), 212 (1940); **9** (2) 177 (1941).
17. G. J. Exarhos and M. Aloï, *Thin Solid Films* **193/194**, 42 (1990).
18. G. J. Exarhos and W. M. Risen, Jr., *J. Amer. Ceram. Soc.* **57** (9), 401 (1974).
19. A. S. Shaikh and G. M. Vest, *J. Amer. Ceram. Soc.* **69** (9), 682 (1986).
20. S. Rangantahan and M. Von Heimendahl, *J. Mater. Sci.*, **16**, 2401 (1981).
21. F. Edelman, Y. Komen, S. S. Iyer, J. Heydenreich, and D. Baither, *Thin Solid Films*, **222**, 57 (1992).

PHYSICOCHEMICAL AND MICROSTRUCTURAL CHARACTERIZATION OF RF SPUTTERING MAGNETRON $\text{Pb}(\text{Zr,Ti})\text{O}_3$ THIN FILMS

F. VARNIERE, E. CATTAN, B. EAKIM, H. ACHARD* and B. AGIUS
Institut Universitaire de Technologie, Université de Paris Sud (XI), Plateau du Moulon,
BP127, 91403 ORSAY CEDEX, FRANCE. *LETI Département de Microélectronique 85 X,
38041 GRENOBLE CEDEX, FRANCE

ABSTRACT

Lead zirconate titanate thin films were deposited on Pt/TiN/BPSG/Si structures by sputtering an oxide target of nominal composition $\text{Pb}(\text{Zr}_{0.55}\text{Ti}_{0.45})\text{O}_3$ or PZT in argon plasma. The PZT films were deposited at different pressures and different substrate temperatures ranging from floating temperature to 400°C ; the thicknesses of the sputtered films were in the 15-720 nm range. The absolute and relative cation and oxygen compositions of the thin films were determined by a new method based on the simultaneous use of Rutherford Backscattering Spectroscopy (RBS) and Nuclear Reaction Analysis (NRA) induced by a deuteron beam. The total deposition rate and atomic ones are observed as a function of the substrate temperature and pressure. Therefore the dependence of film composition on pressure and substrate temperature is discussed.

Post-deposition annealing studies and ferroelectric properties are presented. The values of the remanent polarization, P_r , were in the range $5\text{--}7\text{ }\mu\text{C}/\text{cm}^2$, the coercitive field, E_c , between 15 and 25 kV/cm and the dielectric constant, ϵ_r , evaluated from capacitance measurements around 1200, depending on the process parameters.

INTRODUCTION

Recently, lead zirconate-titanate (PZT) thin films have attracted considerable attention for application to cell capacitors for dynamic random access memories (DRAMs), due to their high dielectric constant, and for use in non volatile-RAMs, due to their reversible large spontaneous polarization. Thin films of PZT based ferroelectrics have been prepared by various methods such as sol-gel process [1], RF magnetron sputtering [2], ion beam sputtering [3] etc. Among these, sputtering techniques have been the most successful and, particularly, single-target RF magnetron sputtering of oxide powder targets [4-5]. This method exhibits some advantages which include its simplicity in device fabrication, its high deposition rates over large substrate areas and its ability to operate at floating temperature. However, this method has also some disadvantages such as generation of surface damages which can be minimised by using low power density and composition differences in the films with respect to the nominal target composition; these differences are mainly due to the instability of the plasma during the sputtering process.

In this investigation, we have studied a sputtering method in order to get precise control of film composition, with the aim to reach the nominal target stoichiometry, $\text{Pb}(\text{Zr}_{0.55}\text{Ti}_{0.45})\text{O}_3$. The composition of the films is determined, with an accuracy better than $\pm 2\%$, by using a recently developed analytical technique based on the simultaneous use of Rutherford Backscattering Spectrometry (RBS) and Nuclear Reaction Analysis (NRA) [6-7]. Some PZT films are deposited on Pt/TiN/BPSG/Si and annealed in conditions which lead to the formation of the perovskite structure. Preliminary results on structural (X-Ray diffraction) and electrical measurements on these films are presented.

EXPERIMENTAL PROCEDURES

The PZT thin films have been prepared using a conventional rf-magnetron sputtering with a ceramic target under various conditions. The substrates are (100)p-silicon wafers with a BPSG thermally oxidized layer 800 nm of thickness. A TiN film with a thickness of 100 nm has been deposited on the BPSG/Si-wafer as an intermediate layer between the BPSG film and the lower electrode which is a (111) oriented Pt thin film (200 nm thick) deposited by dc magnetron sputtering. No pretreatment was performed for the Pt/TiN/BPSG/Si substrates prior to the sputter deposition of the PZT films. The sputtering conditions of PZT are shown in Table I.

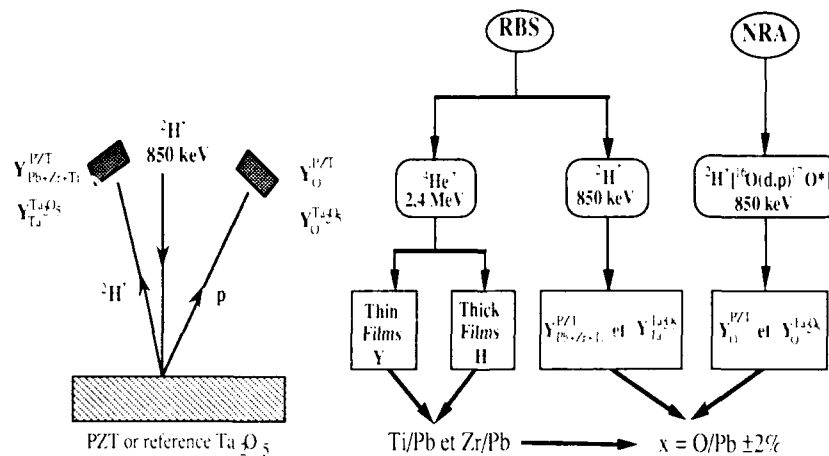
Table I. Sputtering conditions for PZT deposition.

Target diameter	100 mm
Target-substrate spacing	70 mm
Sputtering gas	100% Ar
Base pressure	10^{-5} Pa
Power supply frequency	13.56 MHz
Input power	70 - 100 W
Gas pressure	0.5-3 Pa
Deposition mode	Static
Deposition rate	6 nm/min at 70W
Deposition temperature	Floating-400°C

sition is deduced from the ratio of plateau heights, and the precision of the measurements is estimated to be in the range $\pm 2-3\%$.

For the determination of the oxygen stoichiometry, we used $^{16}\text{O}(\text{d},\text{p})^{17}\text{O}^*$ nuclear reaction with a 850 keV deuteron beam and simultaneously we registered the RBS spectrum of the deuterons backscattered by the elements present in the film and in the Si substrate. The ratio of the NRA proton peak integrals from oxygen to the cationic RBS integral is a measure of the oxygen stoichiometry, once compared to a similar ratio from a standard target, measured in the same conditions (Table II). The reference target is a thermally oxidized tantalum thin layer (Ta_2O_5) on Si.

Table II. Schematic diagram of the composition analysis of the PZT films



The oxygen stoichiometry x is given by the equation :

$$x = 5/2 \left(\frac{\sum \text{Ta}}{\sum \text{Pb} + \text{Zr} + \text{Ti}} \right) \cdot \left(\frac{^{16}\text{O} \sum \text{Pb}(\text{Zr}, \text{Ti}) \text{O}_3}{^{16}\text{O} \sum \text{Ta}_2\text{O}_5} \right)$$

The precision on the oxygen stoichiometry depends mainly on the statistical errors on the peak integrals, i.e. $\pm 2-3\%$. The results are beam dose independent.

The crystal structure of the films was examined by an X-ray diffraction (XRD) method. For electrical measurements, Pt thin films were deposited as an upper electrode with a diameter of 0.6 mm at room temperature. The D-E hysteresis curve was observed using a Radiant Technologies Model RT66A ferroelectric test equipment.

The deposition rate is determined from the film thickness measured by a profilometer. The composition is measured on 50-800 nm-thick films with nuclear microanalysis in their RBS and NRA modes.

The cationic composition is determined by $^4\text{He}^+$ RBS at 2.4 MeV (Table II). For thin films (<250 nm), the Zr, Ti, and Pb peaks are well separated from each other, and the cation composition can be determined from the ratios of peak integrals of each metallic element, normalized to the electron cloud corrected Rutherford cross section. The precision is better than $\pm 2\%$. For thick films, the relative cation compo-

RESULTS AND DISCUSSION

A. Deposition rate. Figure 1 shows a three dimensional parametric representation of the variation of the total deposition rate with pressure and substrate temperature. The deposition rate increases as a function of the pressure and decreases with the temperature, but it is practically constant for a given pressure between 100°C and 200°C. Zirconium and titanium do not take part in this deposition rate decrease with the temperature, and stay practically constant. On the other hand, oxygen and overall the lead content in the film affect the final composition (Figure 2). This decrease is attributed to the surface mobility of the incident film material and to a reduced sticking coefficient of these components with the temperature. A typical deposition rate is 6 nm/min.

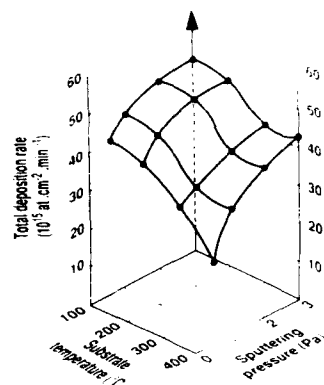


Figure 1 : Three dimensional parametric variations of the deposition rate of PZT thin films with substrate temperature and sputtering pressure.

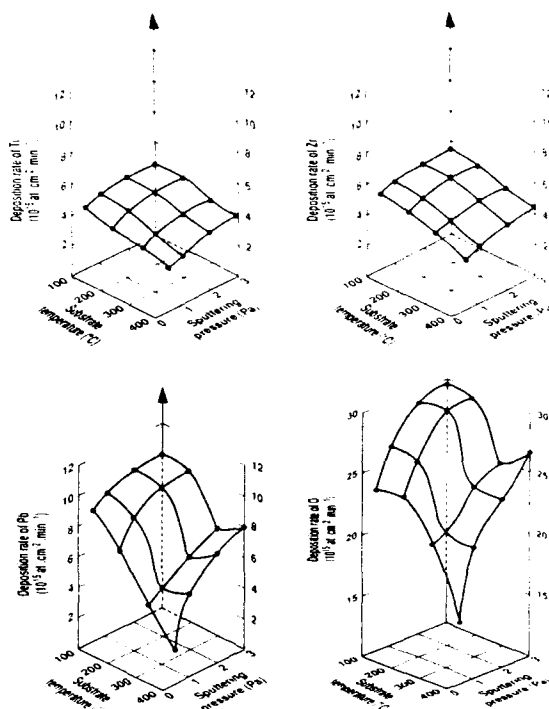


Figure 2 : Three dimensional parametric variations of the different atomic deposition rates of PZT films with substrate temperature and sputtering pressure.

B. Film composition.

The dependence of film composition on pressure and substrate temperature is shown in Figure 3. Film composition is represented by the atomic ratios of Zr/Pb, Ti/Pb, Zr/Ti and O/Pb. Also, $\text{Pb}(\text{Zr}_{0.55}\text{Ti}_{0.45})\text{O}_3$ target composition is shown by horizontal dashed lines.

Pressure. The Zr/Pb and Ti/Pb ratios of the films are found to change with sputtering gas pressure. When the film is sputtered at a lower gas pressure, the lead content in the sputtered film is less than that of the target. It approaches the target composition as the pressure is increased. On the other hand, the Zr/Ti ratios of the films are almost equal to that of the target, irrespective of the sputtering gas pressure.

These compositional changes may be caused by the following mechanism. At a lower gas pressure, preferential re-sputtering of lead atoms is caused by fast negative ions and neutrals traversing the sputtering system without collision and bombarding the substrate. The energy of these fast particles is attenuated by gas phase collisions, so re-sputtering decreases with increasing pressure. At pressures values as high as 3 Pa, the mean free path of sputtered atoms and ions is on the order of a few millimeters and compositional changes are suppressed.

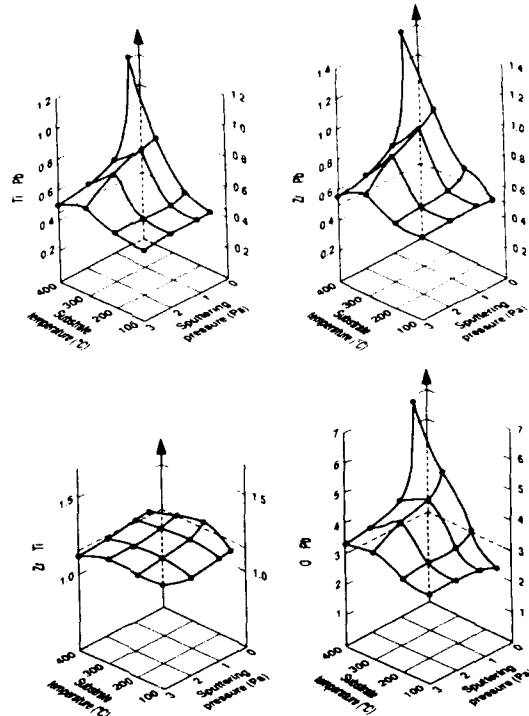


Figure 3 : Three dimensional parametric variation of the composition of sputtered PZT thin films with substrate temperature and sputtering pressure.

Temperature. Figure 3 clearly indicates that the Zr/Ti ratio is not influenced by the temperature deposition until 400°C. Lead content decreases rapidly with the deposition temperature especially at low pressures and induces an important cationic modification. In the same time the oxygen content decreases but not as fast as the lead content (especially at 0.5 Pa). Hence, we observe a particularly large value for the oxygen composition compared to the metallic elements. Presently, we don't have a satisfactory explanation for the stabilisation in the total deposition rate for 2 and 3 Pa between 300°C and 400°C.

As-grown thin films deposited from a stoichiometric PZT target at a pressure of 3 Pa for varying substrate temperatures below 200°C exhibit good composition, further studies were made on such films.

Thickness. Figure 4 shows the dependence of film composition on the film thickness. The cation and oxygen stoichiometries are to be constant and similar to that of the target in the film thickness range (15 - 720 nm). This behaviour could be seen as surprising in terms of the lead surface constancy because, the sputtering time for growing thicker films being long (60-120 nm), we could expect localized surface temperatures of the target to change and can affect the target surface composition. Such phenomenon may then result in modifying the sputtering yields with time, mainly in the case of lead. Thus, taking into account all the factors influencing the composition, films have been grown under the optimized sputtering conditions mentioned in table I for their structural and electrical characterization.

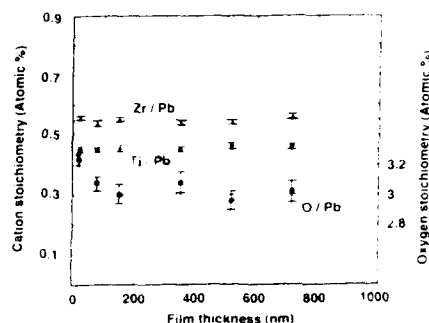


Figure 4 : Variation of composition of PZT films with the film thickness (rf power : 70 W, argon pressure : 3 Pa). Dashed lines correspond to target composition.

C. Structural nature

The structural nature of films is evaluated by the X-ray diffraction method. The X-ray diffraction patterns of the films annealed in H_2/Ar at different temperatures (540-560-600-640 °C) for 120 min are shown in Figure 5a. The crystalline structures of the obtained films are influenced by the annealing temperatures. As the annealing temperature is increased, crystal structure of the film changes from amorphous (for as-deposited films), through pyrochlore (540 °C), and a mixture of pyrochlore and perovskite (600 °C), to single-phase perovskite (640 °C). Annealing experiments in just argon, indicated that there was sufficient oxygen in the as-deposited film to form the perovskite structure.

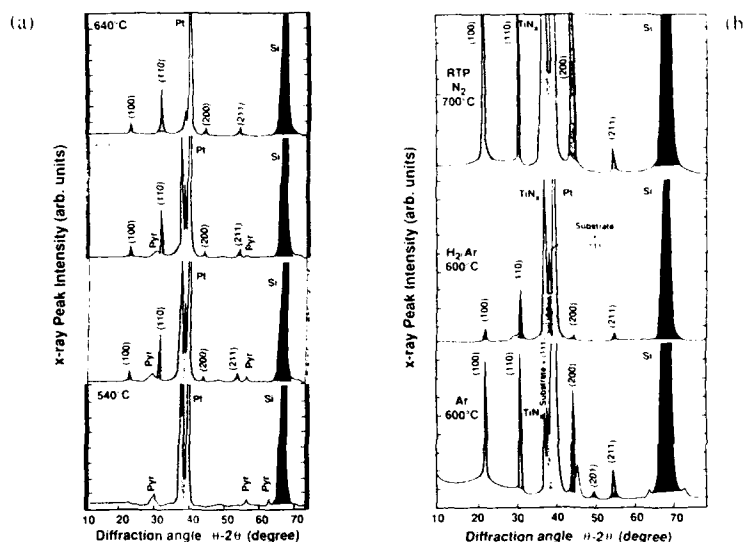


Figure 5 : X-ray diffraction patterns of a 450 nm PZT film (a) after different annealing temperatures (b) subjected to different thermal processing conditions.

Such standard processing temperature, in the range 600-700 °C for 1-2 hours, could destroy the performance of the existing devices such as MOSFET including the doping profile and metallization. Rapid thermal processing (RTP) has been developed very fast in recent years to reduce the thermal budget, and improve the thin film properties in VLSI process. Figure 5b shows a first comparison between these two different techniques; we have to improve our RTP results.

D. Ferroelectric properties

Most of the perovskite $\text{Pb}(\text{Zr}_{0.55}\text{Ti}_{0.45})\text{O}_3$ thin films annealed in argon atmosphere at 640 °C for 120 min show ferroelectric hysteresis characteristics. Figure 6 shows a D-E hysteresis loop of the 450 nm-thick film. Typical values of remanent polarization (P_r) of tetragonal films are ranged from 5 to 10 $\mu\text{C}/\text{cm}^2$. Coercitive fields (E_c) films are 20-30 kV/cm.

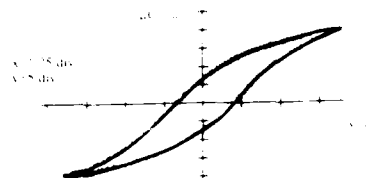


Figure 6 : Typical set of pulsed hysteresis loop at 5 V for thin film (450 nm) annealed in Ar.

CONCLUSION

PZT thin films in the thickness range 15-720 nm with improved ferroelectric properties have been obtained by rf magnetron sputtering of $\text{Pb}(\text{Zr,Ti})\text{O}_3$ target. The kinetics of the sputtering process and the effect of sputtering parameters on film composition and deposition rate have been studied.

Films deposited at low pressure (0.5 Pa) exhibit low oxygen concentration and low oxygen composition. For higher deposition pressures (3 Pa) films are stoichiometric.

The mechanism of non reactive sputtering PZT target on a pure argon was presented. Complete thermalization of the sputtered species is necessary to obtain a good control composition. In our case, this demands deposition at high sputtering pressure (3 Pa) with the substrates being maintained at a substrate-target distance of 7 cm. A virtual source is then formed between the cathode and the substrates and some of the sputtered material can return to the sputtering source.

Post-deposition annealing in Ar at 600 °C for 2 hours resulted in PZT films with perovskite structure.

ACKNOWLEDGMENT

This work was supported by Alcatel and by CNRS (GDR 86). F. Laugier (LETI) is thanked for his technical assistance in providing the X-ray analysis. G. Chevrier is thanked for useful X-ray discussions.

REFERENCES

- 1-G. Yi, Z. Wo, and M. Sayer, *J. Appl. Phys.*, **64** (5), 2717, (1988).
- 2-S.B. Krupanidhi, N. Maffei, M. Sayer, and K. El-Aassal, *J. Appl. Phys.*, **54**, 6601, (1983).
- 3-M.S. Ameen, T.M. Graettinger, S.H. Rou, H.N. Al-Shareef, K.D. Gifford, O. Auciello, and A.I. Kingon, *Mat. Res. Soc. Symp. Proc.*, **200**, 65, (1990).
- 4-E. Cattán, B. Agius, H. Achard, J.P. Joly, *Ferroelectrics*, **128**, 25, (1992).
- 5-K. Genivas, M. Sayer, *J. Appl. Phys.*, **64** (3), 1484, (1988).
- 6-J.C. Cheang Wong, Jian Li, C. Ortega, J. Siejka, G. Vizkelethy and Y. Lemaître, *Nucl. Instr. and Meth. in Physics Research B* (1991).
- 7-E. Cattán, B. Agius, H. Achard, J.P. Joly, J.C. Cheang Wong, C. Ortega, J. Siejka, *Mat. Res. Soc. Symp. Proc.*, **243**, 173, (1992).

IMAGING OF FERROELECTRIC DOMAINS IN KTiOPO_4 SINGLE CRYSTALS BY SYNCHROTRON X-RAY TOPOGRAPHY

S. Wang,* M. Dudley,* L.K. Cheng,** J.D. Bierlein,** and W. Bindloss**

*Dept. of Materials Science and Engineering, SUNY at Stony Brook, NY 11794-2275.

**E.I. du Pont de Nemours & Company, Inc., Experimental Station, Central R&D Dept., P.O. Box 80306, Wilmington, DE 19880-0306.

ABSTRACT

The application of synchrotron white beam X-ray topography to the study of ferroelectric domain structures in hydrothermally grown potassium titanyl phosphate (KTiOPO_4 ; KTP) single crystals is reported. The domain walls can be exclusively imaged on topographs with selected diffraction vectors and X-ray wavelengths, while images of other defects, such as dislocations, inclusions and surface scratches, can be simultaneously made very diffuse. The topographic images correspond well with electrostatic toning images. X-ray topography readily reveals the three dimensional shapes of the domain walls. There are two contributions to domain wall contrast: one is fringe-like which can be interpreted in terms of the dynamical theory of X-ray diffraction, and the other is diffuse strain contrast arising from long range strain associated with the wall. These two contributions can be observed simultaneously or separately depending on the diffraction conditions. The long range strain is thought to be associated with the curvature of the domain walls. It appears that the main components of the displacement field associated with this strain are directed approximately perpendicular to the domain wall.

INTRODUCTION

Potassium titanyl phosphate (KTiOPO_4 ; KTP) is a well known nonlinear optical material with many applications in frequency conversion and electro-optics [1]. Specifically, its broad temperature bandwidth, wide angular acceptance and high damage threshold have made KTP the best crystal for the frequency doubling of Nd-based lasers operating near $1\mu\text{m}$. The recent demonstration of blue light generation using quasi-phase matching in KTP [2] and the successful growth of other KTP-related crystals (e.g. KTiAsO_4) [3] further broaden these materials' commercial application to include optical data storage, pollution control and remote sensing.

KTP crystallizes in the noncentrosymmetric orthorhombic space group $\text{Pn}2_1\text{a}$ with lattice parameters, $a=12.8\text{ \AA}$, $b=10.6\text{ \AA}$ and $c=6.4\text{ \AA}$, and is ferroelectric with polar axis along the crystallographic b axis [4]. High quality single crystals can be readily grown by both the high temperature flux method [5] and the hydrothermal method [6, 7]. Since the crystals are ferroelectric, multiple domain regions are often found, which are detrimental to device performance. Therefore it is important to have a technique capable of revealing the domain configurations. To date, the only techniques reported for revealing domains in KTP crystals are the piezoelectric [8], electro-optic [8], pyroelectric [8] and electrostatic toning [9] techniques.

Despite two earlier X-ray topographic studies [10, 11], much remains unknown about the structural details of extended defects in KTP and their effects on crystal properties. In particular no X-ray topographic observation of ferroelectric domains in KTP has been reported, although topographic observations of ferroelectric domains have been reported for other materials such as barium titanate [12] and lithium ammonium sulfate [13]. As

part of a systematic effort to better understand the role of extended defects in KTP using Synchrotron White Beam X-ray Topography (SWBXT, for a review of the technique see [14]), we have embarked upon a detailed study of ferroelectric domains therein. In this paper, we report the first X-ray topographic observation of ferroelectric domains in hydrothermally grown KTP crystals. The multi-domain KTP crystal to be discussed has also been studied by the electrostatic toning technique thus allowing the results of the topographic study to be independently checked and justified. It should be noted that, whereas the toning technique only gives information on the surface intersections of the domain walls, X-ray topography unambiguously reveals the three dimensional shapes of the ferroelectric domains. The diffraction conditions required for exclusively imaging domain configurations in KTP crystals are discussed.

EXPERIMENTAL

A commercial hydrothermally-grown KTP crystal was used in this study. The crystal was grown under high temperature (600°C) and pressure ($\approx 25\text{ kpsi}$) conditions from a potassium phosphate mineralizer [6, 7]. The crystal grows nearly exclusively along the $[011]$ and $[0\bar{1}1]$ directions at a rate of $\approx 1\text{ mm/s/decade-week}$. The b -plate used in this experiment was cut from the end-cap of the as-grown crystal. The large face of the plate measured around 10 mm by 6 mm , and the plate thickness was around 0.7 mm . This crystal plate was selected for study due to its low dislocation density and well defined ferroelectric domains. The b -surfaces of the crystal were polished to optical flatness using standard polishing compounds, and no special chemical etching was used.

Examination by optical microscopy revealed several scratches on both surfaces of the plate, leftover from the polishing process. The crystal was then examined using the electrostatic toning technique [9]. In this technique the crystal is quickly cooled by placing it in contact with a dry ice/acetone mixture to develop a pyroelectric charge field which mimics the domain reversals in the crystal. A liquid suspension of electrostatic toner is then applied to decorate this charge field rendering the domains visible. A possible disadvantage of the toning technique is that the thermal shock experienced by the crystal may cause damage to the crystal. The fact that X-ray topography is nondestructive (provided proper precautions are taken - see next paragraph) may make it a preferable alternative for the visualization of ferroelectric domains in these crystals.

SWBXT experiments were carried out on the Stony Brook Topography Station, beam-line X-19C, at the National Synchrotron Light Source (NSLS), Brookhaven National Laboratory. It has been observed that the relatively highly absorbed, longer wavelength components in the white X-ray beam can lead to potential problems with radiation damage. This damage can cause a coloration of the transparent crystals through a color-center mechanism, which is obviously undesirable for an optical crystal. However, this problem can be completely avoided if one selectively removes these more highly absorbed longer wavelength components from the incident spectrum by employing a filter consisting of few hundred micrometers of aluminum, thus shifting the peak of the source spectrum from around 0.8 \AA to about 0.45 \AA . Under these conditions, no coloration is observed while exposure times on the Kodak SR-5 X-ray film (resolution better than $5\mu\text{m}$) were still only about 15 seconds in the transmission geometry. In order to avoid harmonic contamination due to the broad spectral range of the incident X-rays [15], the diffraction wavelengths were chosen to be between 0.3 \AA and 0.5 \AA .

Note that the lattice parameters defined earlier are consistent with the convention adopted in previous X-ray topographic studies of KTP [10, 11]. This convention can be related to the more commonly used optical convention [1] by permuting the b and c axes.

RESULTS

The overall defect distribution in the crystal can be observed on the X-ray topograph shown in Fig. 1(a), where dislocations, denoted by **D**, inclusions, indicated by **I** and some scratches on the surface, marked by **S**, can be easily identified. The dislocations, which are straight growth dislocations do not lie along low index directions and are neither of pure edge nor pure screw character, and as expected do not disappear on any strong reflections.

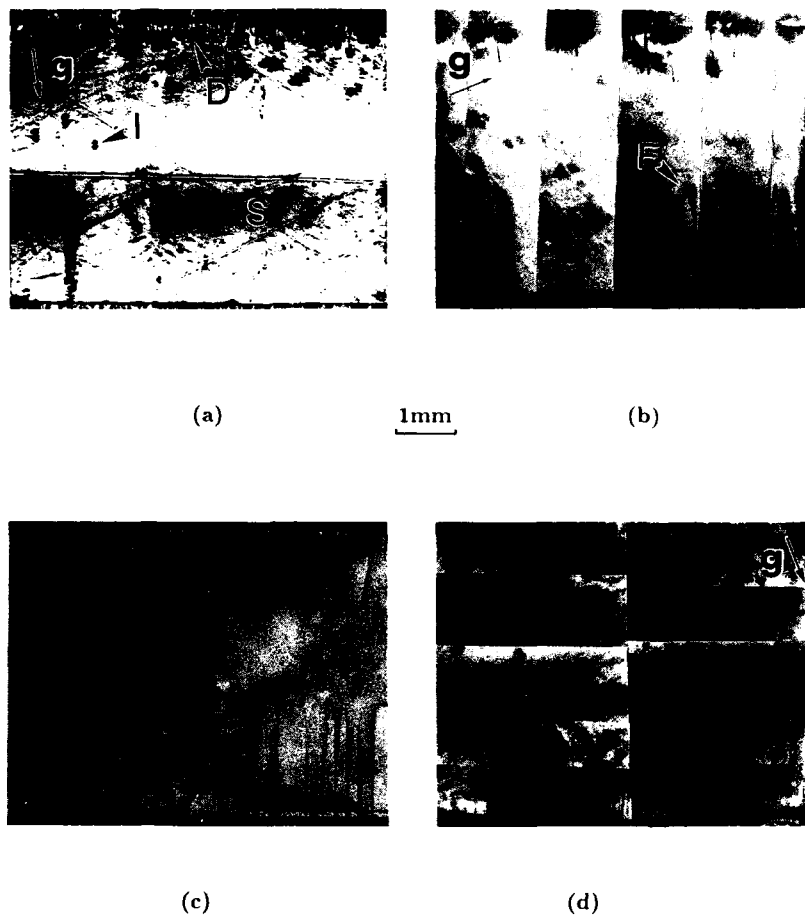


Figure 1. Synchrotron white beam X-ray topographs and a toning image of a hydrothermally grown KTP single crystal, (a) $g=(107)$, $\lambda=0.35\text{\AA}$, (b) $g=(401)$, $\lambda=0.50\text{\AA}$, (c) the toning pattern and (d) $g=(401)$, $\lambda=0.32\text{\AA}$.

This is in agreement with previous topographic observations in flux grown KTP crystals [10.

11], although the growth morphologies compared to those in hydrothermally grown crystals are considerably different. Other than the growth dislocations, a number of inclusions are visible as well as some surface scratches due to residual polishing damage.

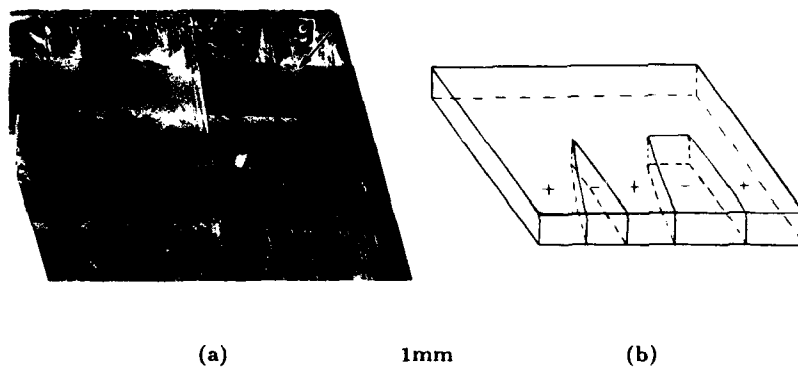


Figure 2. (a) Synchrotron X-ray topograph ($g=(\bar{2}1\bar{2})$, $\lambda=0.25\text{\AA}$) showing the 3D shapes of the domains in the same crystal as in Fig. 1, (b) a schematic drawing of the 3D shapes of two typical domain walls in this crystal.

The topograph shown in Fig. 1(b), a relatively weak reflection, shows very diffuse contrast from the crystal defects, as expected. The only well defined contrast features are the dark lines indicated by F, associated with ferroelectric domain walls. This image shows an exact correspondence with the toning image shown in Fig. 1(c), confirming the observation. By comparing the topographs in Figures 1(a) and (b) two components to the domain wall image can be identified. A broad, diffuse image, corresponding to strain contrast, overlapping with a narrow, sharp image corresponding to interference-fringe contrast from the domain wall itself. Extinction of the strain contrast is observed when the reflecting plane normal is perpendicular to the domain wall normal.

By tilting the crystal so that the domain walls have wider projection widths on the detector, the fringes resulting from the domain walls become more pronounced, as shown in Fig. 1(d) and Fig. 2(a). The three dimensional shapes of the domain walls are also easily deduced from such images, as shown schematically in Fig. 2(b). While there are large areas of domain wall parallel to the (100) plane, the wall actually curves either side of this plane. Domains sometimes converge to a line, while other times they are truncated leaving a region of (001) domain wall.

DISCUSSION

Under low absorption conditions, when the product of the linear absorption coefficient and crystal thickness, μt , is less than unity (which is the case for all the topographs discussed in the previous section), reflections which are appropriate for imaging defects such as dislocations are usually of low index and high structure factor. This is because the rocking curve widths of such reflections are among the largest available, which in turn give

sharp and well defined images of defects such as dislocations, which under low μt conditions are produced primarily by the "direct" image mechanism. Such direct images are shown on the topographs in both Fig. 1(a) and Fig. 2(b). However, the proper diffraction conditions for exclusively imaging the ferroelectric domain structures are expected to be somewhat different because the direct image contrast due to the lattice strains in the vicinity of the domain boundary may overwhelm the less intense fringe contrast due to dynamical effects occurring at the boundary itself. This latter type of contrast is expected to be possible on all low μt reflections (i.e. all reflections discussed in this paper). Since, the strain due to the existence of the domain walls is expected to be much less than that due to other crystal defects, such as dislocations, inclusions and surface scratches, the direct image of this strain field is not expected to be discernible on strong, low strain sensitivity reflections. However, as strain sensitivity increases, as we go to weaker and weaker reflections, this strain field is expected to become apparent, with its image becoming broader and broader, until in the limit of an extremely weak reflections it becomes so broad and diffuse as to no longer be clearly discernible. In SWBXT, a large number of reflections with a large range of rocking curve widths is routinely obtained, so that the above observations are readily tested, and examination of Fig. 1 and Fig. 2 shows that these observations are in fact confirmed.

The ferroelectric domain walls are planar defects which can be treated as inversion twin boundaries. The phase shift between the original wavefields and wavefields newly created upon crossing such boundaries is given as [16], $\delta_{hkl} = 2\pi \mathbf{g} \cdot \mathbf{u} + \alpha_{hkl}$, where \mathbf{g} is the diffraction vector, \mathbf{u} is the fault vector associated with the boundary, and α is the difference between the phase angles of the structure factors of the two regions of crystal joined at the boundary. Since fringe contrast due to the phase shift has been observed on the topographs for which the α factors are calculated to be zero (as determined by the space group [17]), e.g. Fig. 1(b) and (d), the \mathbf{u} vectors are determined to be non-zero for the domains. A detailed analysis and discussion of the possible values of this displacement vector is to be presented elsewhere.

The situation for KTP ferroelectric domain walls is complicated by the fact that the walls are generally curved. Since the fault vectors associated with the domain walls are expected to lie along major crystallographic directions, long range strains in the vicinity of domain wall may thus be attributed to the lattice relaxation associated with the necessity for the boundaries to "zig-zag" back and forth from one low index (low energy) plane to another. The displacement vectors of such long range strains were found to be perpendicular to the domain walls, as can be seen on the topographs in Fig. 1. Strains due to the anti-parallel spontaneous polarizations at a domain wall [12] are not expected to be operative since all the domain walls observed in this crystal are parallel to the polar axis.

CONCLUSIONS

Ferroelectric domains in hydrothermally grown KTP single crystals have been studied by SWBXT. Judicious choice of diffraction conditions enables the domain walls to be imaged exclusively. The three dimensional shapes of the domain walls can be unambiguously deduced from the X-ray topographs. The displacement vectors of the long range strains associated with the curved domain wall structures are found to be approximately perpendicular to the domain walls.

ACKNOWLEDGMENTS

Research supported by E.I. DuPont de Nemours & Company, Inc. Topography carried out at the Stony Brook Synchrotron Topography Beamline, X-19C, at the NSLS, which is supported by DOE.

REFERENCES

1. J.D. Bierlein and H. Vanherzeeke, *J. Opt. Soc. Am.* **B6**, 622 (1989).
2. C.J. van der Poel, J.D. Bierlein, J.B. Brown and S. Colak, *Appl. Phys. Lett.* **57**, 2074 (1990).
3. L.K. Cheng, J.D. Bierlein and A.A. Ballman, *J. Cryst. Growth*, **110**, 697 (1991).
4. I. Tardjman, R. Masse and J.C. Gritel, *Z. Kristal.* **139**, 103 (1974).
5. G.M. Loiacono and R.A. Stolzenberger, *Appl. Phys. Lett.* **53**, 1498 (1988).
6. G. Gashurov and R.F. Belt in *Tunable Solid State Lasers for Remote Sensing*, edited by R.L. Byer, E.K. Gustafson, R. Trebino, (Springer-Verlag, 1984), p. 119.
7. F. Ahmed, R.F. Belt and G. Gashurov, *J. Appl. Phys.* **60**, 839 (1986).
8. J.D. Bierlein and F. Ahmed, *Appl. Phys. Lett.* **51**, 1322 (1987).
9. F. Laurell, M.G. Roelofs, W. Bindloss, H. Hsiung, A. Suna, and J.D. Bierlein, *J. Appl. Phys.* **71**, 4664 (1992).
10. R.J. Bolt, H. de Haas, M.T. Sebastian and H. Klapper, *J. Cryst. Growth* **110**, 587 (1991).
11. P.J. Halfpenny, L. O'Neill, J.N. Sherwood, G.S. Simpson, A. Yokotani, A. Miyamoto, T. Sasaki, and S. Nakai, *J. Cryst. Growth* **113**, 722 (1991).
12. N. Akaba, S. Susuki and M. Takagi, *J. Phys. Soc. Japan* **46**, 1583 (1979).
13. H. Klapper, *Prog. Crystal Growth and Charact.* **14**, 367 (1987).
14. J. Miltat in *Characterization of Crystal Growth Defects by X-ray Methods*, edited by B.K. Tanner and D.K. Bowen, (Plenum, New York, 1980) pp. 401-420.
15. M. Hart, *J. Appl. Cryst.* **8**, 436 (1975).
16. J. Chikawa, *J. Appl. Cryst.* **1**, 165 (1968).
17. *International Tables for X-Ray Crystallography*, Vol. I, (Kynoch, Birmingham, 1952) p. 392.

PART II

Device Materials Science

PIEZOELECTRIC AND CAPACITATIVE MICROACTUATORS AND DEVICES

M.SAYER, D.BARROW, L.ZOU AND C.V.R.VASANT KUMAR, R.NOTEBOOM,
D.A.KNAPIK, D.W.SCHINDEL AND D.A.HUTCHINS*

Department of Physics, Queen's University, Kingston, ON Canada K7L 3N6

Department of Engineering, University of Warwick, Warwick, England

ABSTRACT

Ultrasonic transducers, microactuators and resonators using sol gel PZT films, polymer membranes and silicon machining techniques can take the form of cantilevers, membranes, and array sensors. Static deflections in simple electrode configurations for PZT films supported on silicon or silicon nitride membranes are of the order of $1\text{ }\mu\text{m}$, while larger deflections can be developed under ac and resonant excitation. High frequency acoustic actuators using capacitive excitation of polymer films have been used to evaluate the performance of piezoelectric sensors.

INTRODUCTION

In recent years, there has been increasing interest in silicon micromachined structures for functional applications [1]. Combining micromachined silicon with piezoelectric and ferroelectric thin films has resulted in novel microdevices ranging from membrane pressure sensors [2], cantilever or bimorph accelerometers [3] and microvalves [4], high displacement actuators [5] to piezoelectric micromotors [6]. Active damping of resonating structures has significant technical applications [7]. The objectives of current technology are well exemplified by micromachined sensors developed by D.L.Polla et al at the University of Minnesota [2]. In these vertically integrated sensors, a $<1\text{ }\mu\text{m}$ thick PZT sensing film is created above an air gap over a preamplifier MOSFET integrated into silicon. Significant findings from the Minnesota group are that the piezoelectric properties of the films as measured in such microdevices are comparable to those of the bulk material [8].

High quality PZT films of thickness from 1 to $10\text{ }\mu\text{m}$ have been prepared on silicon on 6" diameter silicon wafers using sol gel methods [9,10].



Figure 1 a) cross-section of a multilayer PZT film $7\text{ }\mu\text{m}$ in thickness on platinum/titanium/silicon with a gold top contact. b) surface and edge morphology of a $10\text{ }\mu\text{m}$ thick PZT film on platinum/Ti/Si.

Figure 1 (a) shows a cross-section of a $7\text{ }\mu\text{m}$ thick sol gel film prepared by multiple spin coating of a platinum coated silicon wafer. Each coat is $0.1\text{ }\mu\text{m}$ thick, the layers are fired to 400°C between each coat, and a final rapid thermal anneal is carried out for 30s at 650°C to fully crystallize the material into a perovskite form which can be made piezoelectric by poling. Figure 1(b) shows the edge and surface morphology of a multi-coated film $10\text{ }\mu\text{m}$ thick. Little evidence is seen for layering originating from the processing technique, and crystallisation occurs throughout the bulk of the material.

In order to make large area films of this thickness a major requirement is to minimise the degree of internal residual stress. The effect of internal stress is well illustrated in the fabrication of 20 PZT layers on a $1\text{ }\mu\text{m}$ silicon membrane etched into a silicon wafer [9].

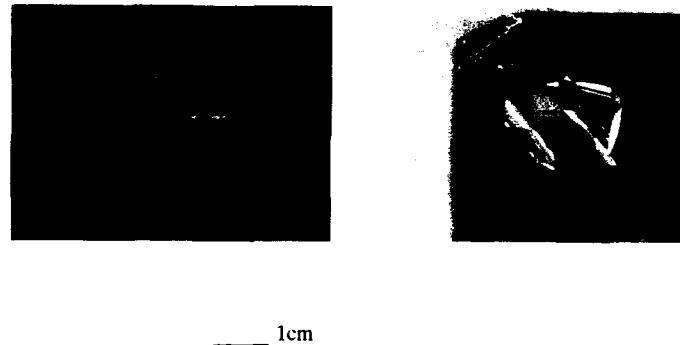


Figure 2 20 layers of PZT formed on a $1\text{ }\mu\text{m}$ thick silicon membrane etched into a thicker silicon wafer a) with a satisfactory level of internal stress, b) when the internal stress exceeds the fracture strength of the silicon membrane.

If the processing is appropriate (Fig 2(a)) the films can be readily achieved with no mechanical distortion. However, if stress builds up, the fracture strength of the supporting silicon is exceeded, and the film ruptures with severe coiling of the membrane. This occurs during hot plate firing rather than during rapid thermal processing. The development of stress results from a number of processes including the diffusion of oxidation products from the film during firing, the nature of the sol gel process itself, and stresses due to thickness variations within the film. While major efforts have been previously made to prepare thick films in single layers [11], multilayer coatings prepared by automated deposition of thinner films now seem to be more effective because of the increased efficiency of the release of oxidation by-products. Thick films are also easier to prepare on large area silicon wafers. This is likely due to the increased uniformity of film thickness in such large area samples.

Given that PZT films of 1 to $20\text{ }\mu\text{m}$ thickness and of areas μm^2 to m^2 appear to be feasible by sol gel or MOD methods, it has been of interest to consider the need for films to carry out macroscopic functions such as acoustic sensing and large area actuation, and which can be used to fabricate structures whose vibrational amplitude can be controlled by active damping. This paper examines the possibilities for such devices using piezoelectric thin films, estimates the potential for their implementation, and calculates the thickness of the piezoelectric film which is required. In a related technology, micromachined capacitive devices used to assess the operation of the ferroelectric structures are described.

DEVICE STRUCTURES

a) Membrane Structures

Flexible membranes are of particular interest for ink jet printing, as resonating structures for chemical sensors, and potentially as acoustic transducers or high frequency microphones. In principle, it would be ideal if these could be completely self-supported, but a supporting membrane has been necessary to date. Such supporting structures include $1\text{ }\mu\text{m}$ silicon membranes etched into silicon wafers [12] or silicon nitride membranes which have been fabricated in silicon by conventional photolithography and chemical etching [13]. The structure of such devices is shown in Figure 3 (a), while Figure 3 (b) shows the upper and lower views of a $150\text{ }\mu\text{m}$ wide x 2 mm long slot covered with $1\text{ }\mu\text{m}$ silicon nitride supporting a PZT layer. This membrane is etched into a $170\text{ }\mu\text{m}$ thick $\langle 110 \rangle$ silicon wafer. Structures fabricated on large area (up to 1 cm^2) silicon membranes are shown in Figure 2.

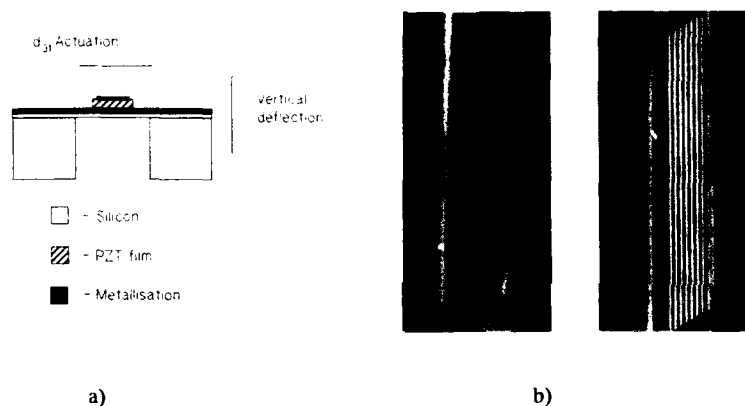
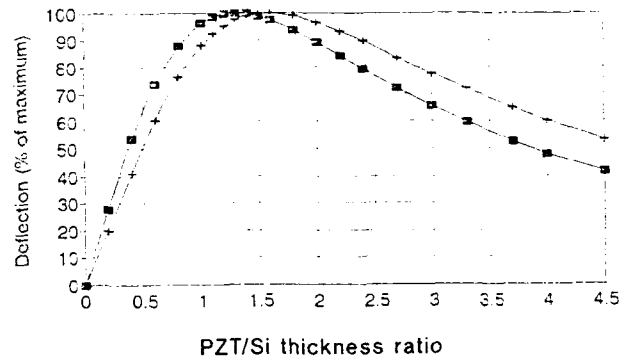


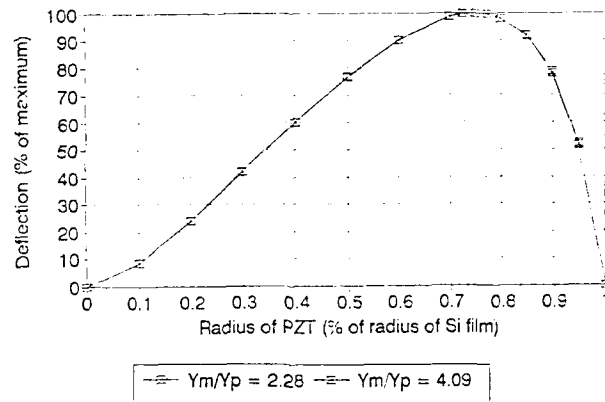
Figure 3: a) Membrane structures incorporating PZT thin films. The active region of the PZT film may be set either by etching the PZT, or by the extent of the upper electrode. b) Silicon nitride membrane structures chemically etched in $170\text{ }\mu\text{m}$ thick $\langle 110 \rangle$ silicon wafers [13]. A silicon wafer coated with silicon nitride is etched from one side. The insets show the upper and lower side of the slots. The slot is $150\text{ }\mu\text{m}$ x $50\text{ }\mu\text{m}$. Membranes which have been achieved are shown in the insets. The picture on the right hand side shows an upper electrode viewed through the membrane.

Calculations have been made of the displacement of the centre of a circular membrane as the result of a voltage applied across the PZT film. The action is set by the stress in the plane of the membrane induced by a field applied to the top and bottom electrode. This results from the d_{31} strain coefficient of the PZT film. In the calculation, the membrane is assumed to be clamped at its edges by the bulk silicon. The main parameters of the problem are the thickness and elastic properties of the film compared to those of the supporting membrane, and the area of the stressed PZT compared to the area of the membrane.

The predicted performance is shown in Figures 4 and 5. The deflection at the centre of the membrane is shown for silicon nitride and silicon membranes respectively. The ratio of Young's Modulus for the respective membrane and the PZT film are 4.09 and 2.28.



(a): Deflection as a function of relative film thickness



(b): Deflection as a function of actuator radius relative to membrane radius.

Figure 4: Vertical deflection at the centre of a membrane/PZT structure in which the ratio of Young's Modulus is as shown. The ordinate is the deflection relative to the maximum value achievable under given driving conditions.

The maximum deflection occurs for a PZT film thickness of about 1.5 times the supporting membrane thickness when the radius of the actuator is about 0.75 of the full radius of the membrane. This implies that the thickness of PZT required to deflect actuated systems based on $1\mu\text{m}$ thick silicon or silicon nitride membranes is of the order of $1.5\mu\text{m}$. This is easily feasible using current fabrication technology.

Figure 5 shows the deflection predicted for a $1\mu\text{m}$ thick silicon membrane 5mm in radius with a PZT film transducer of the optimum thickness and radius

fabricated on its face. The maximum amplitude of static deflection will be limited to about 0.2mm with the limit being set by the limiting tensile stress in the silicon membrane of approximately 300 MPa.

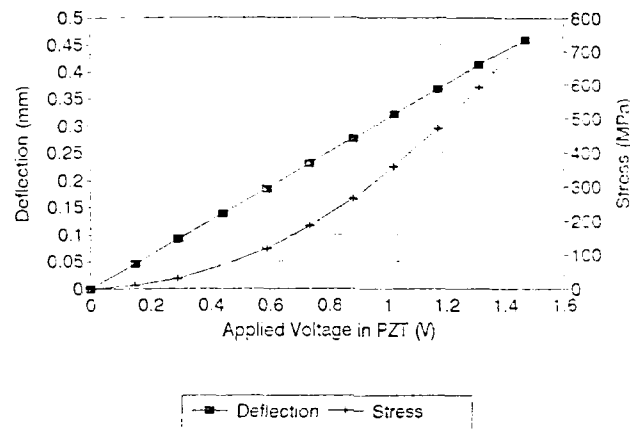


Figure 5: Static deflection versus applied voltage for a 1.3 μm thick PZT film on a silicon. Young's Modulus ratio $Y_w/Y_p = 2.28$, Poisson's ratio for the membrane = 0.279 and for the PZT = 0.295. PZT strain coefficient $d_{31} = -93.5 \times 10^{-12}$ C/N and piezoelectric coupling constant $k_p = 0.52$.

b) Resonant Structures - An Ultrasonic Phased Array

Resonant structures require a film thickness which equals $\lambda/2$ or $\lambda/4$ of the wavelength of sound at the operating frequency depending on the coupling conditions at the interface to the substrate. For impedance matching to a conventional 50 ohm source, the area of the transducer should also be given by $50 = 1/\omega C$, where ω is the angular frequency of operation and C is the capacitance of the transducer [1]. Calculations based on the velocity of sound in bulk PZT suggest that the half wave resonant frequencies for bulk wave transducers 5-20 μm thick lie in the range of 450 - 100 MHz, while the quarter wave resonance frequency is half this value. Because of attenuation in the surrounding media at these frequencies, such transducers have received little attention. However, many medical imaging applications exist if this frequency can be reduced to the 50-100 MHz range. Again depending on the coupling conditions, the thickness of PZT required lies in the range of 20-40 μm . Based on the films and fabrication procedures discussed above, the development of such films is now approaching feasibility. The design of a 50 MHz phased array for skin imaging where the objective is to examine structures located within approximately 1 mm of the skin surface is shown in Fig.6.

The 50 MHz transducer consists of multiple elements spaced between 5-8 μm apart with the design of an individual element shown in Fig.7. The structure has to take into account acoustic impedance matching both to the substrate and to the aqueous propagation medium. This is achieved using a 32 μm thick lower aluminum layer and an upper 11 μm thick layer of the organic piezoelectric PVDF for acoustic impedance matching. The system is designed as a set of overlapping layers with the PZT being deposited by a sol gel process,

and PVDF sheets of appropriate thickness being epoxied onto the final structure. The individual elements can then be diced by fine line laser ablation to form the individual elements. In this case, a PZT layer thickness of $30\text{ }\mu\text{m}$ will be required to produce a 50 MHz transducer with a $30\text{ }\mu\text{m}$ resolution in the forward direction. Layers of this thickness still are in advance of current fabrication technology, but do now appear to be within the bounds of possibility.

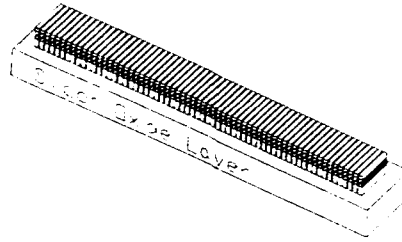


Figure 6: Design of a 50 MHz ultrasonic phased array for acoustic imaging. The interelement spacing is $5\text{ }\mu\text{m}$.

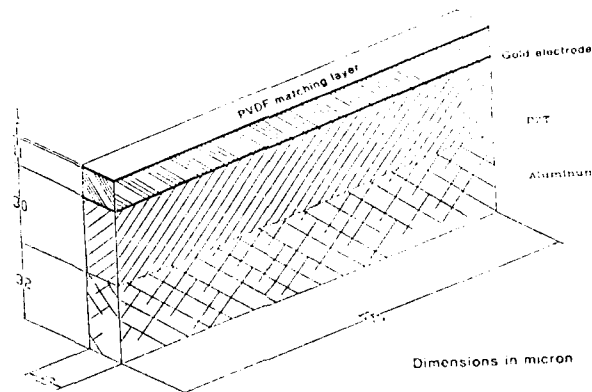


Figure 7: Individual element design. The PZT is fabricated on a lower acoustic matching layer of aluminum, with an upper $11\text{ }\mu\text{m}$ layer of PVDF matching to the propagation medium. In practice a thin coating of polyimide would be required over the upper electrode structure in order to provide electric insulation.

The performance predicted for this structure using a model created by R.Krimholz, D.Leedom and G.Mattaei [14] is shown in Fig. 8. Figure 8(a) shows that the resonant frequency response of the structure will peak at 50 MHz, while Figure 8(b) shows that the angular resolution, defined by the point at which the intensity is $1/2$ of its maximum value, on the axis of the transducer at a distance of 4 mm is 2° and the depth of field is $150\text{ }\mu\text{m}$. This would provide adequate resolution for many skin imaging purposes.

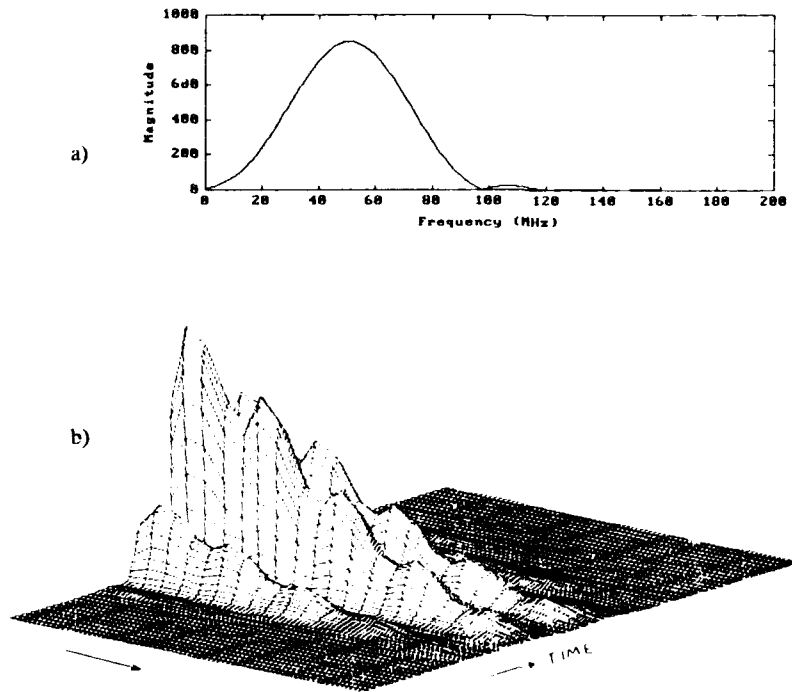


Figure 8: Predicted response of an ultrasound imaging sensor based on a $30\text{ }\mu\text{m}$ PZT film with aluminum and PVDF matching layers. a) frequency response, b) spatial sensitivity.

c) Piezoelectric Cantilever Beams

A cross-section of a bimorph cantilever structure is shown in Fig.9. A simple calculation of the expected displacement of the free end of the cantilever assuming d_{31} excitation is given in equation (1) [15]. The d_{31} strain coefficient of thin film PZT can be determined directly from equation (1) by measuring the vibration of the end of the beam.

$$D = Z(r,k)(L/h)^2 d_{31}V \quad (1)$$

where Z is a response function depending on r , the ratio of the substrate thickness to the film thickness and k , the ratio of the Young's moduli of the substrate and the film. In this equation L is the length of the cantilever and h is the thickness of the film.

An interesting application of this structure would be in actively damped systems, where an electrode pattern can define a sensor and actuator on the structure. When the structure is exposed to unwanted vibrations, the sensor will produce a signal which can be inverted and sent to the actuator to oppose the vibrations.

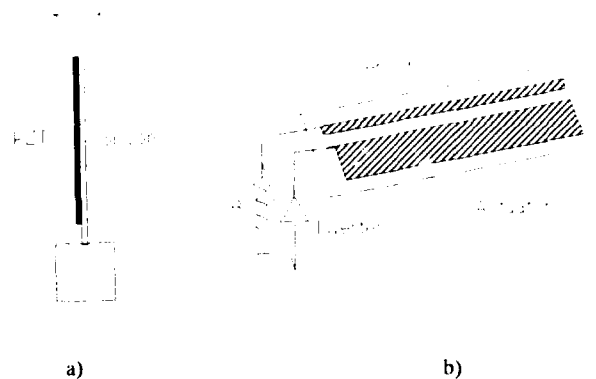


Figure 9: a) Bimorph structure fabricated into silicon. b) Actively damped structure showing part of the film used as a sensor, part as an actuator.

The scale of the structure shown in Figure 9 b) can extend, in principle, from the micron scale to large macroscopic dimensions. For example, critical damping can be achieved in an aluminum beam 1mm thick aluminum beam, 20 m long and 10 cm wide, using a 4 μm thick PZT film [16]. Thus the piezoelectric film thickness does not appear to be an issue. Film thicknesses of the order of 1-5 μm are adequate for most actuator purposes.

3. Capacitance Sensors

The direct measurement of deflections in the above structures is often difficult, requiring interferometric or capacitive techniques. A convenient technique for investigation has resulted from the development of high sensitivity, large frequency bandwidth capacitive sensors using micromachining methods [17]. The principle is shown in Fig. 10.

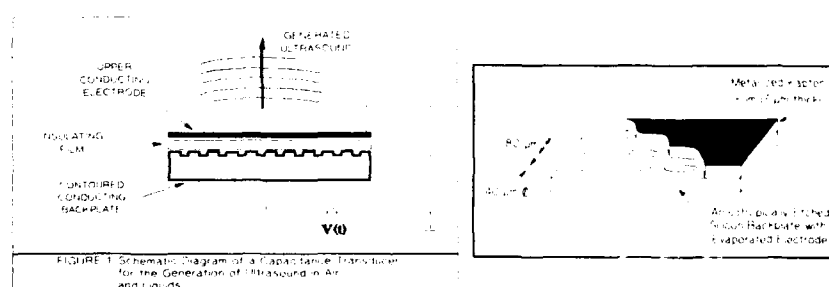


Figure 10: Capacitance sensors using polymer films and a micromachined backplate a) basic structure, b) form of backplate using a spin coated polyimide film.

An insulating film separates a front electrode from a silicon backplate. The impact of ultrasound on the film causes capacitance variation which can be detected electrically. An increase in sensitivity is caused by the use of a micromachined backplate which serves to create cavity resonators behind the film. The form of the cavity is shown in Figure 11. Initial work used thin kapton sheets as the insulating film, but more recent studies have employed spin coated polyimide. These produce sensors with a flat frequency response out to 2 MHz for airborne ultrasonics.

a) Application to Piezoelectric Structures

Piezoelectric elements including a bimorph cantilever and a membrane actuator were driven at various frequencies in air. The generated acoustic wave was detected by a capacitance sensor located approximately 1 cm from the piezoelectric element. The response of a silicon/thin film PZT cantilever structure to a 10 kHz sinusoidal voltage is shown in Fig. 12. The cantilever is 1 cm long, 0.5 mm wide and the PZT film is 2 microns thick. The system sensitively generates and detects air borne acoustic waves.

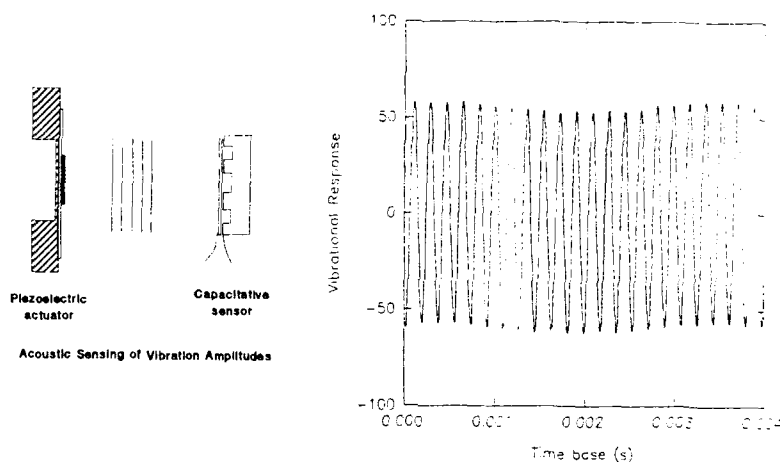


Figure 12. Vibrational response of silicon/PZT film cantilever structure to a 10 kHz sinusoidal voltage measured using a capacitive sensor.

5. Conclusions

Multi-layer sol gel PZT coatings now provide a reproducible fabrication technology for thick PZT layers at least up to 10 μm in thickness. Key criteria are to maintain uniform film thickness during processing, and to minimise film stresses by an appropriate choice of sol gel process. Many of these requirements are compatible with the spin coating of large area silicon wafers for ferroelectric memory.

6. Acknowledgements

This work was supported by the Premier's Technology Fund of the Province of Ontario acting through the Ontario Centre for Materials Research, and also by the Natural Sciences and Engineering Research Council of Canada. Discussions with P.R. Hosington and E.R. Moynihan of Spectra Inc., Hanover, NH are appreciated. Part of the work originated in the engineering physics theses of D.A. Knapik, R.P. Noteboom and J.W. Langelaan.

7. References

- [1] M.Sayer, 1991 Ultrasonics Symposium Proceedings, IEEE, Piscataway 1991, 595
- [2] D.L.Polla, Proc. 1992 Int. Symp. Appl. Ferroelect. Greenville, NC. (in press)
- [3] K.E.Petersen, IEEE Trans. Electron Devices 1982, 500
- [4] H.Van Lintel, F. van der Pohl and S.Boustra, Sensors and Actuators, 15, 153 (1988)
- [5] W.P.Robbins, D.L.Polla and D.E.Glumac, IEEE Trans. Ultrason. Ferroelectr. and Freq. Control, 38, 455 (1991)
- [6] K.R.Udayakuma, S.F.Bart, A.M.Flynn, J.Chen, L.S.Tavrow, L.E.Cross, R.A.Brooks and D.J.Erich, Proc. IEEE Micro Electromechanical Systems, Nara, Japan 109 (1991)
- [7] C.R.Fuller and G.P.Gibbs, J.Intell.Mater.Syst.Struct. 1,189 (1991)
- [8] C-C. Hsueh, T.Tamagawa, C.Ye, A.Helgeson and D.L.Polla, Proc. IEEE Micro Electromechanical Systems, Nara, Japan 114 (1991)
- [9] G.Yi and M.Sayer, Amer.Ceram.Bull. 70,1173 (1991)
- [10] C.V.R.Vasant Kumar and M.Sayer, to be published (1993)
- [11] G.Yi and M.Sayer, Proc. 1992 Int. Symp. Appl. Ferroelect., Greenville, NC. (in press)
- [12] Virginia Semiconductor Inc., Fredericksburg, Virginia 22401
- [13] M.Sayer, C.V.R.Vasant Kumar, D.Barrow, Li Zou and D.T.Amm, Proc. MRS. Symp. 243,39 (1991)
- [14] R.Krimholtz, D.Leedom and G.Matthaei, Electron.Letts. 6, 256 (1970)
- [15] J.G.Smits and T.K.Cooney, Ferroelectrics 119, 89 (1991)
- [16] J.Langelaan, B.Sc thesis, Queen's University 1991 (unpublished)
- [17] D.W.Schindel, D.A.Hutchins, L.Zou and M.Sayer, Proc. IEE Conf. on Acoustic Sensing and Imaging, London, 1993

Tunable Dielectric and Piezoelectric Characteristics of Lead Magnesium Niobate Titanate Relaxor Thin Films

J. CHEN, Q. ZHANG AND L.E. CROSS

Materials Research Laboratory
The Pennsylvania State University
University Park, PA 16802

ABSTRACT

Ferroelectric relaxor thin films $\text{Pb}[(\text{Mg}_{1/3}\text{Nb}_{2/3})_{0.9}\text{Ti}_{0.1}]\text{O}_3$ (90PMN10PT) have been fabricated by the sol-gel technique. The dielectric, piezoelectric and electrostrictive characteristics have been investigated. Experimental results show that the dielectric permittivity and effective piezoelectric coefficients of the films can be tuned by varying dc bias fields which offers the useful features in designing smart micro transducer and actuator systems. Dielectric constants of the films are in the range of 5000 to 6000. The electric field induced strain is on the order of 10^{-3} , and the maximum effective d_{33} coefficient of 90PMN10PT films is as large as 265 pC/N at 31 kV/cm. The electrostrictive coefficient Q_{11} is on the order of $1.2 \times 10^{-2} \text{ m}^4/\text{C}^2$ and M_{11} is $3.5 \times 10^{-16} \text{ m}^2/\text{V}^2$.

INTRODUCTION

In the past few years, development activity in microactuators has focused primarily on three technologies: electrostatic, thermal and piezoelectric effects. In addition to being the candidate materials for high density and nonvolatile computer memory cells, ferroelectric thin films have recently been shown to be promising materials for microsensor and microactuator applications. Combined with silicon technology, ferroelectric micro sensors and actuators have a great potential in many application areas[1,2]. However, until recently there has been little attention given to the piezoelectric characteristics of ferroelectric thin films. Compositions of lead magnesium niobate titanate (PMNPT) at the PMN side of the phase diagram are ferroelectric relaxor oxide ceramics, which have a high dielectric permittivity over a broad temperature range and high electrostriction. Among the many compositions, 90PMN10PT has the highest dielectric permittivity and the largest electrostriction at room temperature which make it a desirable composition for practical applications [3-5]. The major advantages of PMNPT relaxors for sensor and actuator applications are their nonlinear electrical and electromechanical properties which includes high dielectric permittivity and piezoelectric coefficient; these properties are strongly dependent on electric fields. The lack of any significant hysteresis behavior makes the properties reproducible; no poling is required which simplifies the material processing. Based on these advantages, PMNPT ferroelectric relaxors have been widely used in multilayer capacitors, transducers, sensor/actuators and smart material systems[6,7]. Recently, a few attempts have been made to fabricate PMN and PMNPT thin films because of their potential applications in microelectronics. However, the electrical properties of these films were significantly inferior to their ceramic counterparts[8-10]. The major challenge is to form the desired perovskite structure without pyrochlore phase which will be detrimental to the electric properties. It was found that the rapid thermal annealing technique can enhance the perovskite phase formation and improve the electric properties of PMNPT films near the morphotropic phase boundary (with PMN/PT composition of 65/35) [11].

This study focuses on the fabrication and characterization of ferroelectric relaxor thin films (90PMN10PT) and for first time, reports the piezoelectric and electrostrictive characteristics of PMNPT thin films.

EXPERIMENTAL

90PMN10PT thin films were prepared by the sol-gel process. The solution started with lead acetate trihydrate, $\text{Pb}(\text{CH}_3\text{COO})_2 \cdot 3\text{H}_2\text{O}$, magnesium ethoxide, niobium ethoxide, and titanium isopropoxide. Lead acetate trihydrate was dissolved in 2-methoxyethanol solvent and distilled at 124 °C, the boiling point of 2-methoxyethanol solvent, to remove the water of hydration. Magnesium ethoxide and niobium ethoxide were mixed and dissolved in 2-methoxyethanol solvent; these two precursor solutions were mixed in a dry box with titanium isopropoxide and refluxed at ~70 °C for 10 hours. After cooling, a few percent of formate was added into the solution to prevent cracking of the films. The films were deposited on platinum coated silicon wafers by multi-step spin-coating of partially hydrolyzed alkoxide-based solutions. The films were annealed in a rapid thermal annealing facility (Heat Pulse 210T). Annealing temperatures between 750-850 °C were desirable. X-ray diffraction analysis utilizing $\text{CuK}\alpha$ radiation showed that the films consisted of a single perovskite phase at room temperature. For annealing temperatures lower or higher than this temperature range, pyrochlore phases readily formed. Although these films were prepared at higher temperatures than that of PZT films, but because of the short annealing period (10-30 seconds), the total thermal budget of the process still remained low.

Dielectric properties were measured by a HP 4192A impedance analyzer. Hysteresis loops were used to evaluate the ferroelectric properties of the films by using a modified Sawyer-Tower circuit. The field induced piezoelectric and electrostrictive coefficients were characterized by measuring the electric field induced strain in the films. A laser interferometer was used to measure the displacement of the film caused by the field induced strain as a function of driving electric field. The details of experimental setup have been described elsewhere [12]. In practice, only effective or clamped piezoelectric behavior can be evaluated because thin films are deposited on the substrates. However, unlike ceramic actuators and transducers, piezoelectric or electrostrictive thin films usually work under stressed or clamped boundary conditions. Therefore, the effective piezoelectric or electrostrictive behaviors are of more technical significance.

RESULTS AND DISCUSSION

Figure 1 shows the polarization hysteresis loop for 580 nm thick 90PMN10PT films, a remanent polarization of 6 $\mu\text{C}/\text{cm}^2$ and coercive field of 15 kV/cm have been measured respectively under a maximum field of 270 kV/cm.

The dielectric permittivity of 90PMN10PT thin films were measured under a weak electric field. Figure 2 shows that the highest dielectric permittivity was approximately 5800 at a field of 178 V/cm. The high field dielectric properties were characterized as a function of dc electric bias field. The dielectric permittivity exhibits a strong dc bias field dependence. Figure 2 also shows that when the dc bias electric field is ramped from 0 to 10 V in a 580 nm thick film, the dielectric constant dropped from 5800 to 800. The effect of field dependent dielectric permittivity will also be manifested in the field induced piezoelectric and electrostrictive properties of the thin films.

The field induced piezoelectric and electrostrictive coefficients were characterized by measuring the electrically induced strain in the films. Usually ferroelectric relaxors with composition 90PMN10PT have a very weak piezoelectric effect at room temperature because the depolarization temperature is at about 15 °C and permittivity maximum temperature lies near 45 °C which implies that the material has a pseudo-cubic structure at room temperature. However, its diffuse phase transition nature and large induced polarization make bulk PMNPT relaxor materials exhibit a large and electric field tunable electromechanical strain [7]. The strain level is comparable to normal ferroelectric materials, such as PZT, without the troublesome

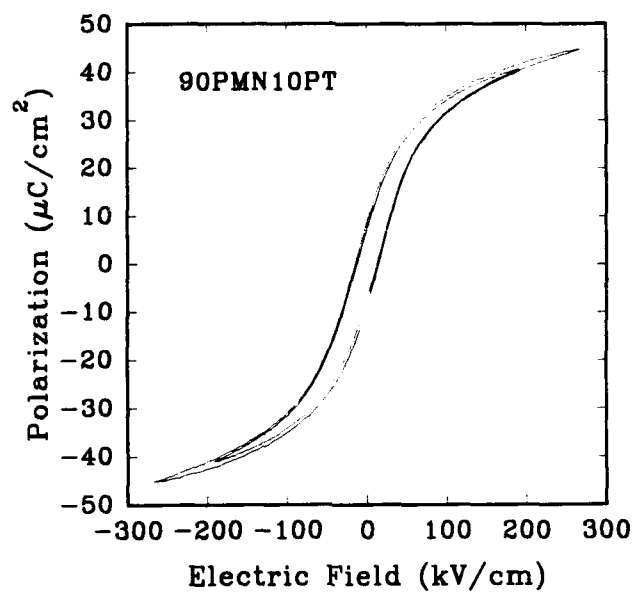


Fig.1 Polarization P versus applied field E for 90PMN10PT Thin films

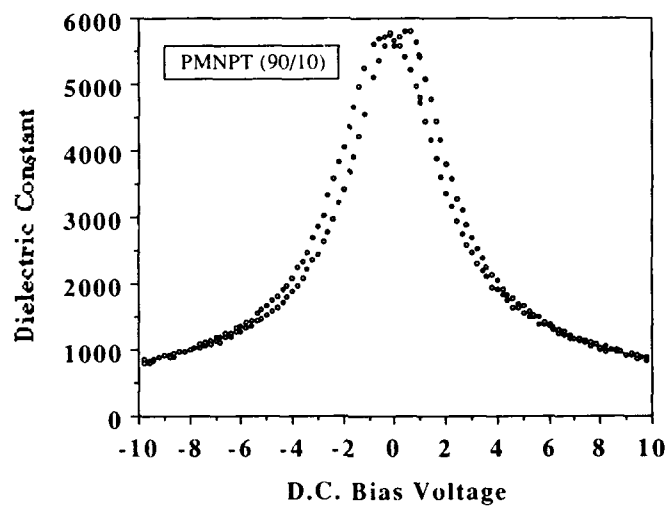


Fig.2 Dielectric Permittivity of 90PMN10PT films varies with d.c. bias fields

hysteresis behavior which is a severe drawback of most normal piezoelectric materials for actuator applications. These advantages are vital also in the thin film form. Figure 3 illustrates the effective piezoelectric coefficient of PMNPT(90/10) thin films under different dc electric bias conditions. The field induced piezoelectric response can vary over a wide range under external dc electric field. The piezoelectric effect is small for biases less than 0.1 V (1.7 kV/cm), as low as 27 pC/N in Figure 3, but as the dc bias is increased, the effective piezoelectric coefficient increases linearly and reaches its maximum (265 pC/N) at 1.8 V, which corresponds to a field level of 31 kV/cm. This maximum effective d_{33} piezoelectric coefficient is even larger than that of PZT thin films (223 pC/N)[14]. After the maximum value, the effective piezoelectric d_{33} coefficient decreases slightly with increasing dc bias field, which may reflect the fact that field induced polarization approaches its saturation value and dielectric permittivity tends to decrease remarkably.

The above experimental analysis has been cast in terms of linear electromechanical effects, the piezoelectric coefficients have been assumed constant under constant bias fields; therefore, the field induced strain is a linear function of the driving field; all other higher order effects, such as electrostriction, are assumed too small to be taken into consideration. However, when there is no dc bias field (the induced piezoelectric effect becomes very weak) and/or a sufficiently high field is applied to the 90PMN10PT thin film, the higher order effects, such as electrostriction, become a significant part of the induced strain. The nonlinear electromechanical effects are therefore no longer negligible.

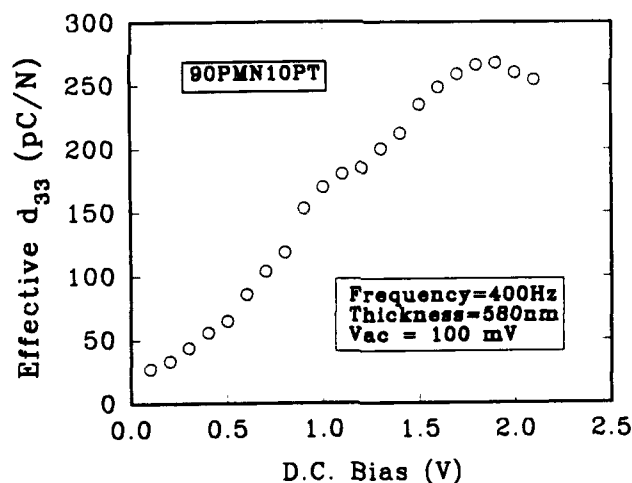


Fig. 3 Effective piezoelectric d_{33} coefficients of 90PMN10PT films are a function of d.c. bias fields

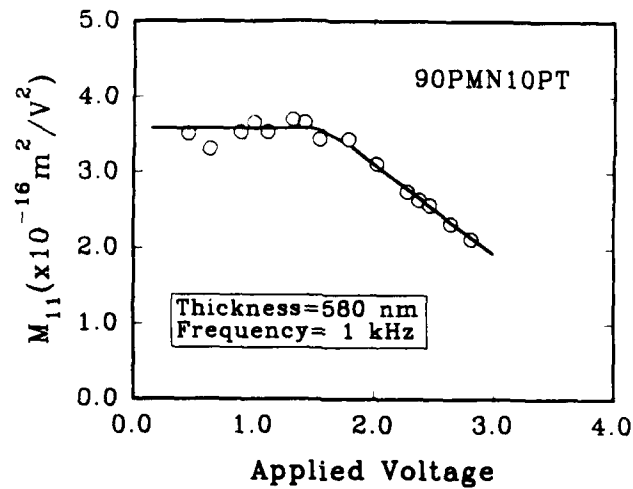


Fig. 4 Effective piezoelectric M_{11} coefficients of 90PMN10PT films are a function of d.c. bias fields

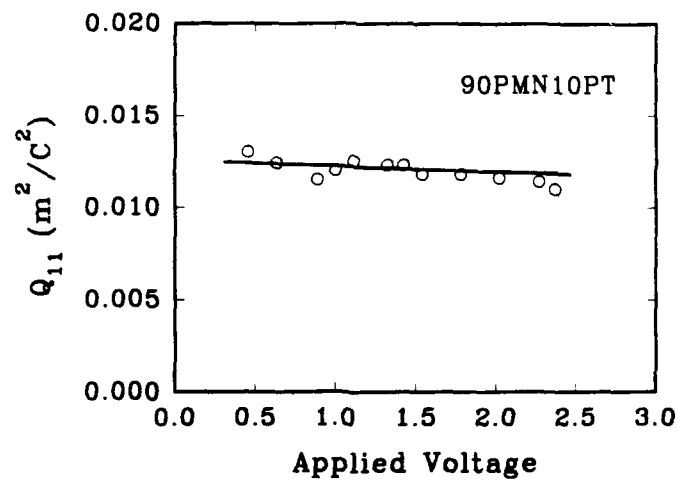


Fig. 5 Effective piezoelectric Q_{11} coefficients of 90PMN10PT films are a function of d.c. bias fields

There are three nonvanishing polarization (or electric field) related electrostriction coefficients in a cubic perovskite material (m3m), Q_{11} , Q_{12} and Q_{44} (or M_{11} , M_{12} and M_{44}). The longitudinal and transverse coefficients can be expressed as

$$Q_{ij} = \frac{1}{2} \left(\frac{\partial^2 x_j}{\partial P_i^2} \right) \quad \text{or} \quad M_{ij} = \frac{1}{2} \left(\frac{\partial^2 x_j}{\partial E_i^2} \right) \quad ij = 1, 2$$

where x_j is the polarization P_i (or electric field E_i) induced strain. From these relations the electrostrictive coefficients can be obtained.

Effective electrostrictive coefficients were evaluated by the measurement of field induced strain. Effective electrostrictive M_{11} coefficient has been calculated from the curve of strain and plotted in Figure 4. The low field value of M_{11} ($3.5 \times 10^{-16} \text{ m}^2/\text{V}^2$) compared favorably to that of bulk ceramics ($M_{11} = 5.5 \times 10^{-16} \text{ m}^2/\text{V}^2$ at 30°C , [3,7,13]). At low electric fields M_{11} is nearly constant, however, at high electric fields the M_{11} coefficient is no longer constant and shows a strong field dependence. The electrostrictive coefficient Q_{11} is almost independent of electric field; the induced strain is proportional to the square of polarization (P^2), Q_{11} was $1.2 \times 10^{-2} \text{ m}^4/\text{C}^2$ (Figure 5) which is comparable with the bulk ceramic value. The maximum strain level generated by the electrostrictive effect is on the order of 10^{-3} in the films. These results are consistent with those obtained on PMNPT bulk ceramic materials.

CONCLUSIONS

In summary, PMNPT relaxor thin films have excellent piezoelectric properties. The field induced strain is as high as 10^{-3} . The dielectric permittivity and effective piezoelectric coefficient can be significantly tuned by application of a dc bias field. The small strain hysteresis and large effective piezoelectric coefficients ($d_{33} = 265 \text{ pC/N}$) and effective electrostrictive coefficients [$Q_{11} = 1.5 \times 10^{-2} \text{ m}^4/\text{C}^2$ and $M_{11} = 3.5 \times 10^{-16} \text{ m}^2/\text{V}^2$] suggest that this material is well suited for micro transducer and actuator applications.

References

1. K.R. Udayakumar, J. Chen, Keith G. Brooks and L.E. Cross in *Ferroelectric Thin Films II*, eds. by A.I. Kingon and E.R. Myers, (Mater. Res. Soc. Proc. 243, Pittsburgh, PA, 1991) pp. 49
2. W. Tjhen, T. Tamagawa, C. P. Ye, C.C. Hsueh, P. Schiller, and D.L. Polla, *Proc. IEEE Micro Electro Mechanical Systems Workshop*, 114 (1991)
3. Shoichiro Nomura and Kenji Uchino, *Ferroelectrics*, 41, 117 (1982)
4. S. J. Jang, K. Uchino, S. Nomura, and L. E. Cross, *Ferroelectrics* 27, 31 (1980)
5. S. L. Swartz and T. R. Shrout, *Mater. Res. Bull.* 17, 1245 (1982)
6. W. Y. Pan, W. Y. Gu, D. J. Taylor and L. E. Cross, *Jpn. J. Appl. Phys.* 28(4), 653 (1989)
7. Shoichiro Nomura and Kenji Uchino, *Ferroelectrics*, 50, 197 (1983)
8. L. F. Francis, Y. J. Oh, and D. A. Payne, *J. Mater. Sci.* 25, 5007 (1990)
9. K. Okuwada, M. Imai and K. Kakuno, *Jpn. J. Appl. Phys.* 28, L1271 (1989)
10. L. F. Francis and D. A. Payne in *Ferroelectric Thin Films*, eds. by A.I. Kingon and E.R. Myers, (Mater. Res. Soc. Proc. 200, Pittsburgh, PA, 1990) pp. 149
11. K.R. Udayakumar, J. Chen, P.J. Schuele, V. Kumar, S. B. Krupanidhi and L.E. Cross, *Appl. Phys. Lett.* 60(10), 1187 (1992)
12. Q. Zhang, W. Pan, and L. E. Cross, *J. Appl. Phys.* 63, 2490 (1988)
13. Q. Zhang, W. Pan, A. Bhalla, and L. E. Cross, *J. Am. Ceram. Soc.*, 72 [4] 599, (1989)
14. J. Chen, and L. E. Cross, to be submitted

PYROELECTRIC PROPERTIES OF LEAD BASED FERROELECTRIC THIN FILMS

A. PATEL, D.A. TOSSELL, N.M. SHORROCKS, R. W. WHATMORE AND R. WATTON*
 GEC-Marconi Materials Technology Ltd, Caswell, Towcester, Northants, NN12 8EQ, UK
 *DRA, St Andrews Road, Malvern Worcs, WR14 3PS, UK

ABSTRACT

Lead based thin ferroelectric films have been prepared using both sol-gel and dual ion beam sputtering (DIBS) processes. Material compositions within the PbTiO_3 and PLZT system have been deposited by both techniques onto metallised silicon. By using a standard sol-gel prepared solution, modified with acetylacetone and spin-coating, $1\mu\text{m}$ thick fully perovskite layers, were obtained at low temperature (450°C) with some preferred orientation. The grain size was in the range $0.2\text{--}0.4\mu\text{m}$. A dielectric constant of 400 and a reversible pyroelectric coefficient of $1.2 \times 10^{-4}\text{Cm}^{-2}\text{K}^{-1}$ were obtained. In contrast, a range of capping layers (SiO_2 , Al_2O_3 , BPSG) on silicon have been investigated using the DIBS process. Highly crystalline (100) and (111) films were readily produced at temperatures in excess of 550°C , at a growth rate of $0.3\mu\text{m}/\text{hour}$. Control of stoichiometry has also been studied in detail, by sputtering of a composite metal-ceramic target with a high energy Kr beam and by bombarding the growing film with a low energy oxygen ion-beam. Dielectric constants of 200-300, losses below 0.015 and resistivities above $10^{10}\Omega\text{m}$ have been achieved. A pyroelectric coefficient of the order of $2.5 \times 10^{-4}\text{Cm}^{-2}\text{K}^{-1}$, pre-poled for a La-doped film on BPSG capped Si was obtained, which did not increase significantly on poling.

INTRODUCTION

The sensing of long wavelength infra-red radiation is of growing interest for a wide range of applications, from the detection of flames for fire alarms to the detection through emitted heat for intruders and thermal imaging applications.

The two wavebands of particular interest are from 3 to $5\mu\text{m}$ and 8 to $14\mu\text{m}$ and both correspond to regions of low atmospheric absorption, and the latter is considered to be of particular interest as it corresponds to the peak in black body radiation spectrum for bodies at around 300K . Compared to normal photo-effect sensors, ie, those based on GaAs or $\text{Hg}_x\text{Cd}_{1-x}\text{Te}$, ferroelectric sensors can be operated at ambient temperatures, requiring low power and cheap detector technologies¹. Pyroelectricity², the release of charge due to a materials change in temperature occurs in polar materials. As a group within the polar materials, ferroelectric crystals exhibit the largest effects and hence have been the subject of intensive research³. Because the pyroelectric signal voltage which is proportional to the temperature variation of the element, increases with a decrease in the element thickness and hence heat capacity, it therefore follows that a thin film up to $10\mu\text{m}$ thick would be desirable as a pyroelectric sensor element. A wide array of thin film deposition techniques have been investigated such as MOCVD⁴, sol-gel⁵, RF⁶ and ion-beam sputtering⁷. In particular, full monolithic integration of such films with silicon or GaAs would yield significant advantages in terms of increased speeds, reduced voltages and improved response. In this paper, we report the use of the sol-gel and the emerging PVD technique of dual ion beam sputtering (DIBS) for the synthesis of undoped PbTiO_3 (PT) and La-doped $(\text{Pb}_{1-x}\text{La}_x)\text{TiO}_3$ (PLT) where $x \approx 0\text{--}0.2$. The PbTiO_3 family of materials are attractive as detector material⁸ because they show large pyroelectric coefficients P , small dielectric constant ϵ_r and small temperature coefficient of P . Poling of pure PbTiO_3 , however, requires the application of high electric fields. The addition of La⁹ has been shown to lower the T_c and the tetragonality, leading to a drop in the coercive field whilst maintaining good levels of polarisation.

EXPERIMENTAL PROCEDURE

The precursors used to prepare the sol-gel deposition solution consisted of lead acetate trihydrate, titanium n-butoxide and lanthanum acetate in 2-methoxyethanol as a solvent.

The preparation procedure was based on the technique originally proposed by Budd et al¹⁰, however, the final stock solution, nominally 0.6M was further modified with acetylacetone (acac). The addition of acac decreased the tendency for premature hydrolysis and also improved the film quality and surface wetting characteristics. A typical process schematic is shown in Figure 1. The concentration of the deposition solutions was adjusted to up to 0.3M by suitable additions of 2-methoxyethanol, and were used without any prehydrolysis. The films were typically spin-coated at 2000rpm/30 secs and a bake every 3 layers at 170°C, followed by a bake at 450°C every 6 layers. The thickness per layer obtained after firing was about 0.03µm.

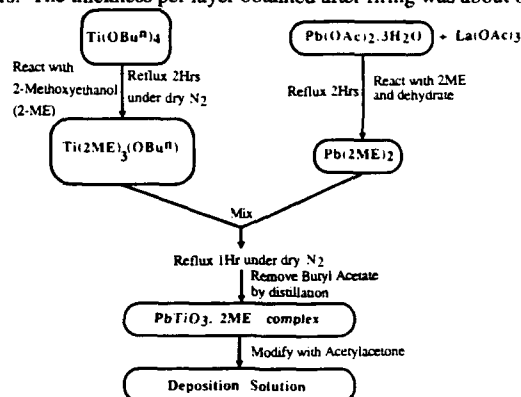


Figure 1. Schematic of sol-preparation.

The PVD deposition system consisted of a Nordiko 3450 DIBS system, Figure 2. The system has been described fully previously⁷, except that the argon sputtering beam has been replaced by a heavier krypton beam. The DIBS process has a number of advantages, including low pressure deposition, low film contamination, good film adhesion, high film density and refractive index. For PLT deposition, an adjustable composite target has been developed and is depicted in Figure 3. Pieces of ceramic lead oxide and PLT are fixed to a titanium backing plate. By suitable variation of the configuration, films of the desired stoichiometry were obtained. The substrate temperature was in the range 500-600°C, and the growth rate of 0.33µm/hour was typically obtained and this was largely independent of target configuration and substrate temperature.

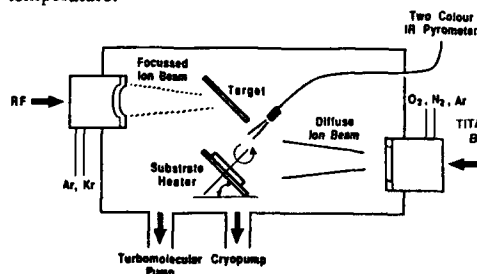


Figure 2 DIBS Sputtering System.

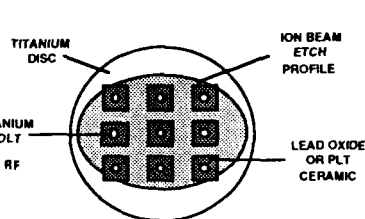


Figure 3. Adjustable Composite Target

In both cases, films were deposited on platinum (1000Å) coated silicon provided with a thermal oxide barrier layer or BPSG. The films were characterised by a number of techniques, including X-ray diffraction (XRD) using $\text{Cu}\alpha$ radiation, electron probe microanalysis (EPMA) and scanning electron microscopy (SEM) and (STEM). Electrical properties were determined using a Wayne Kerr 6425 LCR meter. Hysteresis loop measurements were performed on a Radiant Technologies RT66A thin film tester. The pyroelectric coefficients were calculated from

the ac current produced by modulating the substrate temperature at frequencies from 5 to 50 mHz. Poling was limited to a temperature maximum of 150°C and to fields up to 10^7Vm^{-1} .

RESULTS AND DISCUSSION

An X-ray diffractogram trace for a PT film grown at 450°C from solution is shown in Figure 4, indicating the expected tetragonal phase. The calculated c/a ratio was determined to be 1.056 which is close to the value of bulk PT (1.06). The intensity of the (001) and (101) lines decrease with increase in the thermal treatment up to 700°C. Similarly, a PLT film with $x = 0.1$, deposited at 450°C gave a very highly preferred (111) orientated film as shown in Figure 5. Apart from the (111) the only other line present is the (100). This is not unexpected as the La would favour reduced tetragonality and thus the intrinsic favouring of a particular orientation for a given stress state. Also, the film was expected to lattice match the highly preferred (111) platinum bottom electrode.

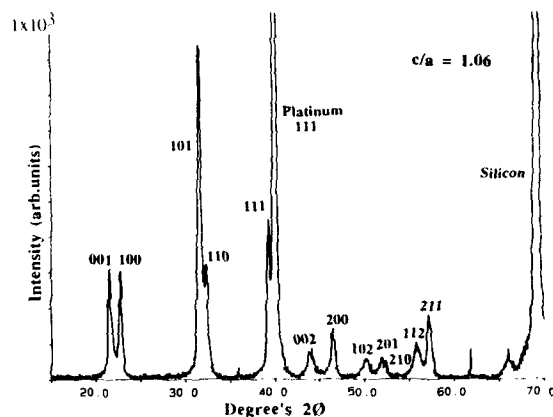


Figure 4. X-ray diffractogram for a sol-derived PT film

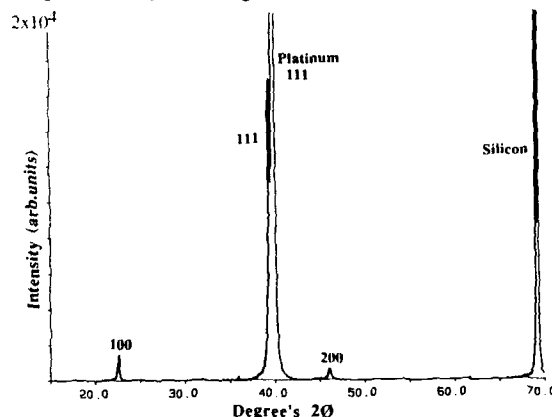


Figure 5. X-ray diffractogram for a sol-derived PLT film

La-doping also favours the (111) orientation in films grown using the DIBS system. A typical trace is shown in figure 6 for a film grown at a temperature of 500-600°C. The deposition of DIBS PT films occurs above the Curie temperature of 490°C, and the degree of stress at T_c can greatly influence and fix the observed orientation after cooling. The majority of

the PT films produced show a tendency towards (100) orientation, however capping the silicon with an amorphous alumina layer does force the orientation towards (001) as compared with plain silicon. For La doped films, higher temperature ($\sim 600^\circ\text{C}$) favours (100) whereas lower temperature ($\sim 550^\circ\text{C}$) favours (111). It should be noted that there is no gradual changeover from (100) to (111); mixed (100)/(111) films do not occur. It seems that at higher temperature, a critical stress is exceeded that enables the film to overcome the restraint of being matched to the (111) Pt.

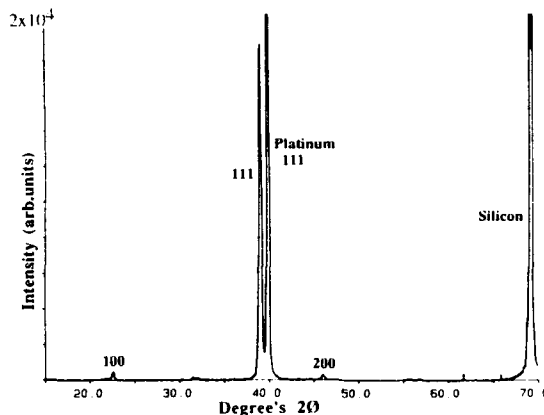


Figure 6. X-ray diffractogram for a DIBS derived PLT film

The structure of the sol-gel films is illustrated in Figures 7 and 8 for PT and PLT, respectively. Individual strata corresponding to the intermediate baking at 450°C can clearly be seen. The grain size was determined to be $\leq 0.1\mu\text{m}$ across. The surface was also composed of smooth areas interspaced with small 'blisters', which were probably caused by stress relief. In contrast, the PLT film (7(b)) showed a smooth surface with a columnar through film structure confirming the high preferred (111) orientation seen by XRD. The grain structure was again small ($< 0.2\mu\text{m}$).

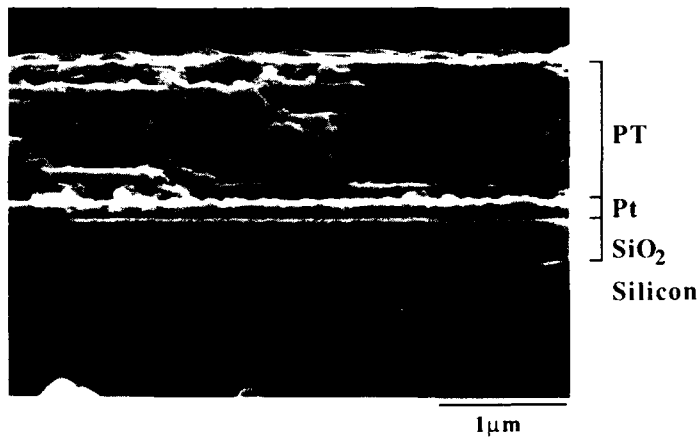


Figure 7. SEM cross-section of a PT film on Pt/SiO₂/Si, showing "strata"

Although the strata corresponding to individual bakes was not observed by SEM, these were clearly seen when the sample was examined by high resolution TEM. It is thought that these 'strata' could be responsible for the weak pyro-activity seen in PLT films even after poling at high fields.

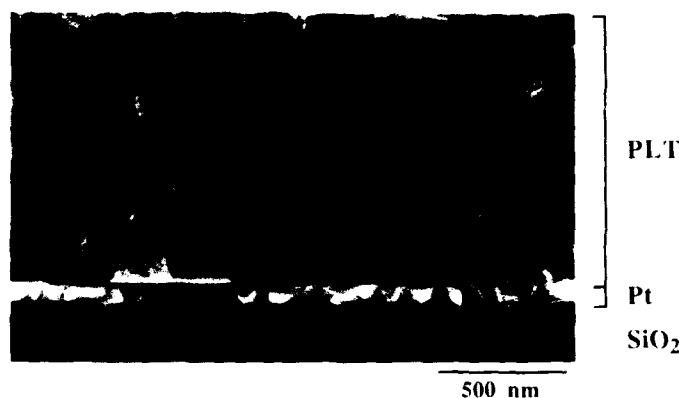


Figure 8. SEM cross-section of a PLT film on Pt/SiO₂/Si, indicating the columnar structure

Similar SEM and TEM examination of DIES films indicated smooth surfaces for both PT and PLT films, with La giving films with better optical properties. Cross-sectional SEM examination of a PLT film again showed a columnar grain morphology and no visible porosity. Also, the grain diameter (200nm) seems fairly constant through the film thickness through matching the Pt grain diameter which is of the order of 100-150nm and then undergoing limited grain growth.

PYROELECTRIC MEASUREMENTS

Samples for characterisation were prepared by first evaporating Cr/Au or Pt dots (1-2mm diameter) onto the surface of the film through a shadow mask. The bottom electrode in the case of sol-gel films was exposed by etching away the film at a corner. Contact to the bottom and top electrodes was made by silver epoxy wire bonds. The dielectric constant and loss (1kHz) measured on the sol-gel PT films ranged from 100-200 and 0.8-2%, respectively for film thicknesses of 0.3-1μm. The PLT films, however, gave ϵ_r values of ≥ 400 with losses of ~5%. In both cases the resistivity was up to $10^{10}\Omega\text{m}$. The measured maximum pyroelectric coefficient obtained for PT was $1.45 \times 10^{-4}\text{C/m}^2/\text{K}$ after poling at up to $18\text{V}/\mu\text{m}$, which is in good agreement with that obtained to Kani et al⁵. The PLT film, however, gave a low value of $6 \times 10^{-5}\text{C/m}^2/\text{K}$, this may be a consequence of the 'strata' in the films causing localised breakdown. None of the sol-gel films showed any pre-pole pyroelectric activity. The DIBS films gave similar dielectric constants but reversed losses for PT and PLT; values of 200-300 and $\leq 1.5\%$ for the PLT. The resistivity value was $>10^{10}\Omega\text{m}$. The PLT films did, however, show pre-pole pyroelectric activity with values up to $2.5 \times 10^{-4}\text{C/m}^2/\text{K}$ which remained unchanged on poling. These films had greater breakdown fields and poling at $15 \times 10^6\text{Vm}^{-1}$ gave 85% reversal of the pyro-response. This corresponds to a figure of merit F_D (1kHz) ($P/C_r\sqrt{\epsilon_0\epsilon_r\tan\delta}$) of $2.2 \times 10^{-5}\text{Pa}^{-1/2}$. Films from both deposition systems yielded slim and non-saturating hysteresis loops (with an apparent Pr of 0.1-0.2μC/cm² and E_c of 10kV/cm). This is not surprising as previous studies¹¹ have shown that very high fields up to 500kV/cm at 1kHz

were required to switch PT films.

CONCLUSIONS

The present work has demonstrated that good quality highly crystalline lead titanate and La-doped lead titanate films can be readily deposited at low temperatures (450-600°C) using the sol-gel and by the DIBS processes. Both processes give highly (111) oriented films on metallised silicon, and showed good pyroelectric behaviour. With further development, this method is likely to become a preferred route for the preparation of integrated large area 2-D arrays for IR detectors.

ACKNOWLEDGEMENTS

This work has been carried out with the support of the Defence Research Agency, Ministry of Defence.

REFERENCES

1. R.W. Whatmore, *Ferroelectrics* 118, 241 (1991).
2. S.T. Lui and D. Long, *Proc. IEEE* 66 (1), 14 (1978).
3. R. Watton, *Ferroelectrics* 91, 87-108 (1989).
4. C.J. Brierley, C. Trundle, L. Considine, R.W. Whatmore and F.W. Ainger, *Ferroelectrics* 91, 181-192 (1989).
5. K. Kani, H. Murakami, K. Watari, A. Tsuzuki and Y. Torii, *J. Mats. Sci. Letts.* 11, 1605-1607 (1992).
6. R. Takayama, Y. Tomita, K. Iijima and I. Ueda, *J. Appl. Phys.* 61 (1), 411 (1987).
7. D.A. Tossell, N.M. Shorrocks, J.S. Obhi and R.W. Whatmore, *Ferroelectrics* 134, 297-302 (1992).
8. C. Ye, T. Tamagawa and D.L. Polla, *J. Appl. Phys.* 70 (10), 5538-5543 (1991).
9. K. Keizer, G.J. Lansink and A.J. Burggraf, *J. Phys. Chem. Solids.* 39, 59-63 (1978).
10. K.D. Budd, S.K. Dey and D.A. Payne, *Br. Ceram. Proc.*, 36, 107-21 (1985).
11. C. Ye, T. Tamagawa, Y. Lin and D.L. Polla, *Mat. Res. Soc. Symp. Proc.*, 243, 61-66 (1992).

ELECTRICAL PROPERTIES OF SOL-GEL PZT THIN FILMS FOR DECOUPLING CAPACITOR APPLICATIONS

ROBERT W. SCHWARTZ,*[†] D. DIMOS,* S. J. LOCKWOOD,* AND V. M. TORRES*

* Sandia National Laboratories, Materials and Process Sciences Center, P.O. Box 5800, Albuquerque, NM 87185-5800

[†] Advanced Materials Laboratory, 1001 University Blvd., SE Suite 100
Albuquerque, NM 87106

ABSTRACT

The successful development of PZT thin films for decoupling capacitor devices places stringent requirements on the dielectric and leakage properties of the films. We have characterized these properties for PZT thin films with compositions near the morphotropic phase boundary prepared by a sol-gel process. Capacitors were fabricated from films with thicknesses varying from 0.4 to 1.2 μm . For zero applied bias, the dielectric constants of these films were in the range of 800 to 1200. The room temperature dielectric constant was observed to decrease by $\sim 25\%$ with the application of a 5 V bias. We have also characterized the interrelationships between temperature, applied bias, and dielectric constant. The capacitors exhibited asymmetry in their leakage and breakdown characteristics with bias sign, as well as non-linear I-V behavior. Breakdown fields for undoped PZT 53/47 films were typically in the range of 750 kV/cm.

We have also studied the effects of La and Nb donor doping on the leakage behavior of PZT 50/50 thin films. Doping with 2 to 5 mol % of either La or Nb resulted in a reduction in film leakage current by a factor of 10^3 . Leakage currents of the highly doped materials were approximately $2 \times 10^{-9} \text{ A/cm}^2$ under an applied field of $\sim 65 \text{ kV/cm}$ at a temperature of 125°C .

INTRODUCTION

Lead zirconate titanate ($\text{PbZr}_x\text{Ti}_{1-x}\text{O}_3$; PZT) thin films are of immense technological interest for a diversity of electronic applications because of the unique dielectric, ferroelectric, piezoelectric, pyroelectric, and electrooptic responses that they display when subjected to an applied electric field. Applications under consideration include: decoupling capacitors, DRAMs,[1] nonvolatile memories,[2] piezoelectric micromotors,[3] infrared detectors,[4] and electrooptic storage media.[5] While a variety of physical and chemical deposition approaches have been used to fabricate PZT thin films, one method that has been used extensively is sol-gel processing,[6] because of the low capital investment costs and the ease of integration with standard semiconductor processing technologies. Solution deposition approaches also allow for enhanced compositional control, especially for multicomponent material systems such as PZT, PLZT (La-doped PZT) and PNZT (Nb-doped PZT).

While many of the applications mentioned above, especially nonvolatile memories and DRAMs, have received considerable attention, the use of ceramic thin films for decoupling capacitor applications appears to have been relatively neglected. Since decoupling capacitors reside close to the integrated circuit (IC), they serve to decouple the IC from the power supply, and thus, provide a local source, or sink, of charge. Also, by having the capacitor close to the IC, input inductance can be significantly reduced, resulting in potentially higher operational frequencies.[7] Because the primary material requirements for decoupling capacitor applications are high permittivity, low dielectric loss and high resistivity, PZT thin films would appear to be well suited to this application. Furthermore, since this is a nonswitching application, fatigue issues, which have presented a significant problem in the development of PZT thin films for nonvolatile memory applications, are not an important factor.

In this paper, we report on our investigations of the potential use of donor doped PZT thin films for decoupling capacitor devices. Currently, ceramic chip capacitors are most often used in this application.[7] However, since ceramic thin films allow for a still greater level of package integration, further increases in operational frequencies and packaging densities may be possible. We selected PZT thin films for this investigation because of our previous experience with thin films of these compositions, and because of various reports which indicate that PZT materials retain high dielectric constants and low dielectric losses up to frequencies of at least

1 GHz.[8-10] We also discuss the effects of donor doping on thin-film leakage characteristics, bias effects on dielectric response, and general characteristics of thin-film breakdown. While the results reported are for discrete thin-film capacitors, our eventual goal is the direct integration of the PZT thin-film capacitors onto the integrated circuit or package.

EXPERIMENTAL

The ceramic thin films of the present study were prepared using a sol-gel process that we have reported on previously.[11,12] Briefly, 0.4 M PZT, PLZT and PNZT solutions were prepared from carboxylate and alkoxide precursors. PZT solutions were prepared by first adding titanium isopropoxide to zirconium butoxide. Acetic acid was then added followed by addition of methanol and lead (IV) acetate. At this point, the solution was heated to dissolve the lead precursor. Subsequent additions of methanol, acetic acid and water completed the solution preparation process. Lanthanum was incorporated into the solutions as lanthanum acetate and niobium was incorporated as niobium ethoxide. The lanthanum acetate was added to the solution batch at the same time as the lead precursor, while the niobium ethoxide was added to the solution with the other B-site alkoxide compounds. Thin films were prepared by spin-casting onto Pt/Ti/SiO₂/Si substrates at 3000 rpm for 30 seconds. Following deposition, the films were heat treated for 5 minutes at 300°C for organic pyrolysis. Crystallization, after every fourth layer, was accomplished by heat treatment at 650°C for 30 minutes. A 15°C/min ramp rate was used. Top platinum electrodes (1.0 - 2.0 mm diameter) were deposited by sputtering using a shadow mask.

Dielectric constant and loss were characterized using an HP 4194 impedance analyzer with an oscillation level of 0.02 volts. Low oscillation levels were used to minimize contributions due to domain switching. Dielectric properties were tested both with and without applied bias. For temperature dependent property measurements, a Signatone dc controlled power supply hot stage was used for sample heating. Leakage characteristics were determined using a Keithley 286 source measurement unit interfaced through an IEEE bus to a personal computer. Electrical property results are given for top and bottom electrode thicknesses of 0.3 μ m, although we are presently using much thicker electrodes (1.5 μ m) to minimize the effective series resistance of the capacitor devices.

RESULTS AND DISCUSSION

The first part of this study focused on the effects of thin-film stoichiometry on room temperature dielectric constant. Results for this relationship are shown in Figure 1. In general, the behavior of the PZT thin films paralleled that of the bulk ceramic materials;[13] the maximum dielectric constants were observed for compositions near the morphotropic phase boundary. Interestingly, as previously reported by Watanabe [14] and Klee,[15] the dielectric constants of our thin films were typically greater than those of the bulk materials. This effect is possibly related to the fine grain size of the thin films compared to the bulk materials. The PZT films were characterized by a columnar growth morphology with an average grain size of 100 - 150 nm. Dielectric losses for the thin films were in the range of 0.015 - 0.030, irrespective of the composition. Because of the high dielectric constants observed for PZT 50/50 ($k' \sim 1200$) and PZT 53/47 ($k' \sim 1000$) our investigation focused on these compositions. Although these are strongly hysteretic compositions, decoupling capacitors are designed to suppress voltage fluctuations, and therefore, to operate at a relatively constant bias level (e.g., 5 V). Consequently, the use of hysteretic compositions does not present an operational problem. After identifying the compositions of interest we proceeded with our study of other electrical properties pertinent to device development.

One key material characteristic for capacitor applications is the temperature dependence of the dielectric constant in the operational temperature regime of interest. Results are presented in Figure 2 for the temperature dependence of k' , from 25°C to 125°C, for a PZT 53/47 thin film. Under zero applied bias, there is a fairly strong dependence of dielectric constant on temperature, with dielectric constant increasing by approximately 50% between 25 to 125°C. This behavior is representative of other compositions we have investigated.[16] With an applied bias of +5 V, however, the temperature dependence of k' is decreased and is more suitable for capacitor applications. Under this applied bias, dielectric constant only increases by about 20% over the

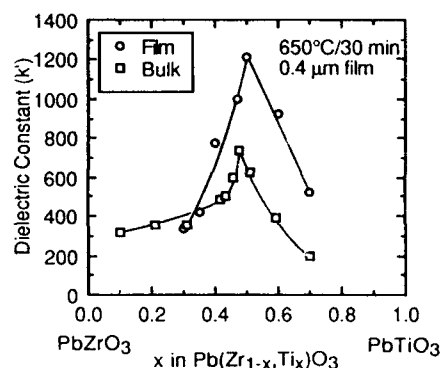


Fig. 1. Effect of PbZrO_3 - PbTiO_3 ratio on the 25°C dielectric constant for thin film and bulk ceramics. (Bulk data - Ref. 13)

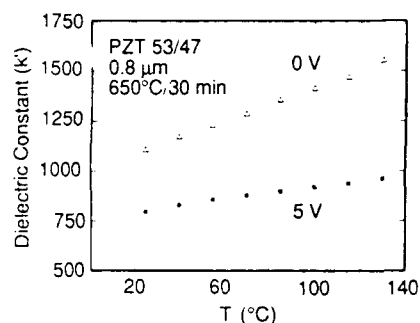


Fig. 2. Temperature and field dependence of the dielectric constant of a PZT 53/47 thin film.

same temperature range, varying from ~ 800 to ~ 950 . Capacitor performance under these conditions would thus meet the Z 5U classification. The applied bias corresponds to an applied electric field of ~ 62.5 kV/cm.

In addition to characterization of the thin-film dielectric properties we have also studied their current vs. time (I-t) and current vs. voltage (I-V) behavior. A typical I-t response is given in Figure 3 for a film held at 95°C, subjected to a +30 V bias. Upon application of the voltage, there occurs a high current transient response, followed by a slow decay in leakage current to a steady-state value. The time required to reach steady state is dependent on both the temperature and the applied voltage, although in general, times of 30 minutes or greater, are required. Possible explanations for I-t behavior have been discussed previously by other authors.[17] The films also exhibited non-linear I-V behavior under applied electric fields from 25 - 125 kV/cm.

In an attempt to decrease the magnitude of the leakage currents of the films, we have studied incorporation of both A- and B-site donor dopants into the films. Results for 0.4 and 0.77 μm PLZT thin films are given in Figure 4 for lanthanum additions ranging from 0.1 to 5.0 mol %. Leakage currents are reported for an applied electric field of 65 kV/cm at a measurement temperature of 125°C, 30 minutes after the application of the voltage. The values represent essentially steady-state current flows. Undoped PZT 50/50 exhibited a leakage current of $\sim 2 \times 10^{-6}$ A/cm². The addition of 0.1 - 0.5 mol % La resulted in a slight decrease in leakage current to $\sim 4 \times 10^{-7}$ A/cm². Further increases in lanthanum doping resulted in still further

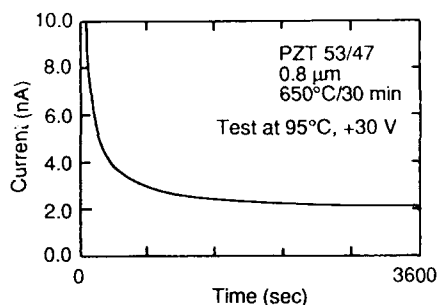


Fig. 3. Typical I-t response of a 0.8 μm PZT 53/47 thin film.

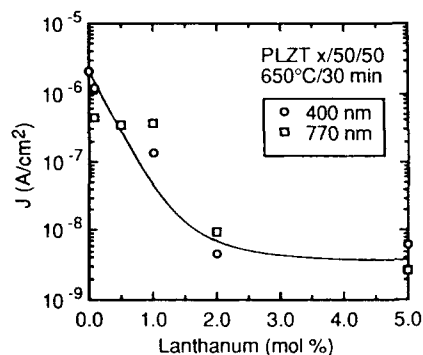


Fig. 4. Effect of lanthanum doping on the leakage currents of PLZT x/50/50 thin films.

improvements in leakage currents, the 0.77 μm , 5.0 mol % lanthanum doped film (PLZT 5/50/50) displayed a leakage current of 2.5×10^{-9} , i.e., an improvement of around 10^3 compared to our nominal, undoped PZT 50/50 thin film. This behavior is interesting for two reasons. First, it demonstrates that dramatically improved leakage performance is possible in these thin films by incorporating an A-site donor dopant. Second, the amount of lanthanum that must be added to obtain this improvement is significantly greater than would be necessary to charge compensate acceptor impurities. Lead vacancies are also acceptors which need to be charge compensated to minimize the carrier concentration, thus, the present results would seem to imply that the films contain a high vacancy concentration (~ 1 at. %). Experiments are in progress to study the conductivity behavior of lanthanum doped PZT films prepared from solutions that incorporate higher levels of excess lead precursor.

Microstructural observations using SEM have indicated that the film microstructure does not appear to vary with lanthanum doping. Examination of ferroelectric hysteresis loops displayed the expected trend with increasing lanthanum content; hysteresis loops became slimmer and coercive field and remanent polarization decreased. These observations indicate that the lanthanum is indeed being incorporated into the perovskite structure. We are presently estimating film density by measuring the refractive indices of the films using ellipsometry, to determine if increasing film density can explain the observed decrease in leakage current with increased lanthanum doping. Dielectric constant and loss were relatively independent of lanthanum doping level and no systematic effect of doping on these properties was observed.

Niobium doping yielded similar results to those observed for lanthanum doping. Results are illustrated in Figure 5. While a doping level of 0.1 mol % resulted in a decrease in the leakage current by about a factor of five, a 5.0 mol % doping level resulted in a leakage current that was $\sim 10^3$ less than the undoped PZT 50/50 thin film. Again, the doping level required to obtain a maximum increase in resistivity is relatively high. Analysis of Figures 4 and 5 shows that, in fact, the curves for La and Nb doping fall almost directly on top of each other. Thus, doping with either A- or B-site donor species results in increased film resistivity.

The calculated resistivities of the PLZT thin films are compared to the reported values for the bulk ceramics [18] in Figure 6. Due to the non-linear I-V characteristics of the thin films, a true assessment of the resistivities from the available data is difficult. Because of this, effective thin-film resistivities were calculated by dividing the leakage current by the applied electric field of 65 kV/cm, at a measurement temperature of 125°C. Thus, the present plot at least gives a feeling for the magnitude of thin-film resistivities compared to bulk materials. Due to the more demanding test conditions for the films compared to the bulk ceramics (100°C, 0.1 kV/cm), it would appear that the measured resistivities of the thin films are at least as high as the values for bulk ceramics. As observed for bulk ceramics, increased lanthanum doping resulted in higher resistivity.

To predict the reliability characteristics of the thin films we have recently begun to study the breakdown characteristics of the films under various time/temperature conditions. A voltage

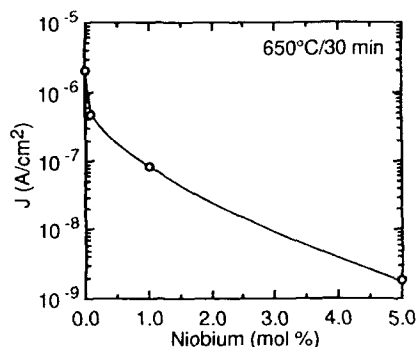


Fig 5. Effect of doping level on the leakage characteristics of 0.8 μm niobium doped PZT 50/50 thin films.

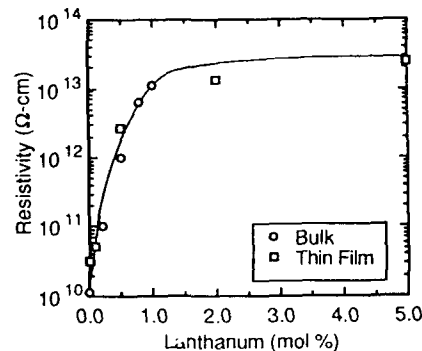


Fig 6. Resistivities of PLZT bulk ceramics and PLZT x/50/50 thin films. (Bulk ceramic data - Ref. 18)

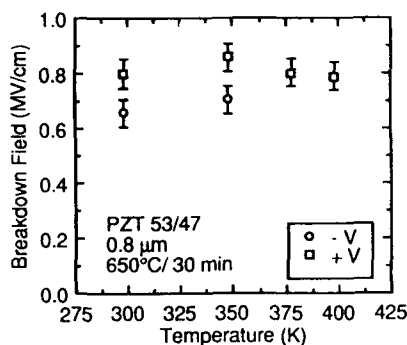


Fig. 7 Effect of temperature on dielectric breakdown strength for both bias directions with a 5 second step duration; 0.8 μ m PZT.

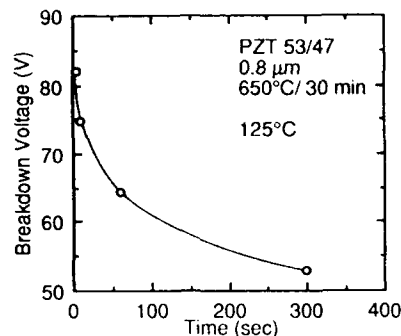


Fig. 8 Effect of step duration on measured breakdown strength at 125°C; 0.8 μ m PZT 53/47.

staircase program with varied step durations was used; 2 V step heights were employed. Based on the model of Klein [19], it would be predicted that higher temperatures and longer duration steps would result in lower breakdown strengths. Results for the effects of temperature and bias are presented in Figure 7 for 5 second duration voltage steps. Individual results represent the average of a minimum of six measurements. Surprisingly, over the temperature range studied, breakdown field was relatively independent of temperature. The average value of EBD was ~ 800 kV/cm for positively biased samples, i.e., those samples where the top electrode was biased positively with respect to the bottom electrode. The absence of a temperature effect could potentially be related to the relatively short step duration. Preliminary studies with longer duration (10 to 60 minute) steps indicate that higher temperatures in fact result in lower breakdown strengths. Temperature effects on the breakdown strength of 0.4 μ m films, for longer duration voltage steps, have also been reported previously by Moazzami. [20] He reported that increasing temperature from 85°C to 150°C resulted in a decrease in the time-to-breakdown from $\sim 4 \times 10^4$ seconds to $\sim 1 \times 10^3$ seconds, for an applied electric field of 750 kV/cm. These values are slightly greater than our measured values, although differences in testing procedures may be partially responsible for this variation.

Bias direction also affected breakdown strength. Capacitors under negative bias exhibited lower breakdown fields than those biased positively. This effect, shown in Figure 7, was observed at room temperature and 75°C. The breakdown strength of the negatively biased capacitors varied from 650 to 700 kV/cm.

Voltage step duration effects on breakdown strength were also noted and results are shown in Figure 8 for a 0.8 μ m PZT 53/47 thin film tested at 125°C. While pulse durations of 5 seconds resulted in film breakdown strengths > 1 MV/cm, 300 second pulses yielded apparent breakdown strengths of ~ 650 kV/cm. These results fit the model proposed by Klein [19] and are in qualitative agreement with those of Moazzami. [20] Similar experiments at 25 and 75°C yielded analogous results. While further pulse duration experiments are required for accurate estimates of reliability, by plotting the pulse duration versus reciprocal breakdown field, it appears that reasonable device lifetimes, $> 10^8$ seconds (10 years), are expected.

CONCLUSIONS

The electrical properties of donor-doped PZT thin films have been characterized with the aim of evaluating these materials for decoupling capacitor applications. The dielectric properties of the films, $k \sim 800 - 1000$ and $\tan \delta \sim 0.02$, appear reasonable for this application. We have also characterized the conductivity behavior of the doped and undoped PZT thin films. Leakage currents required a relatively long time to reach steady state and I-V characteristics were typified by non-linear behavior. Thin film resistivity was dramatically improved by the incorporation of

either A- or B-site donor dopants. Compared to our nominal PZT 50/50 material, an improvement in leakage current by a factor of 10^3 was observed for films with doping levels of 5 mol %. Thin-film dielectric properties were relatively unaffected by doping. Finally, to begin to predict capacitor reliability performance, we have started to study the effects of temperature and step duration on breakdown field. As predicted, longer duration voltage steps yielded lower effective breakdown field. Acceptable device lifetimes are expected.

ACKNOWLEDGEMENT

This work was supported by the U.S.DOE under contract DE-AC04-76DP00789. We would also like to acknowledge the technical assistance of Christine Roth and Joe Kubas.

REFERENCES

1. L. H. Parker, and A. F. Trasch, IEEE Circuits and Devices Magazine, 1990, 17.
2. J. F. Scott and C. A. Paz de Araujo, Science, **246**, 1400 (1989).
3. K. R. Udayakumar, J. Chen, K. G. Brooks, L. E. Cross, A. M. Flynn, and D. J. Ehrlich, in Ferroelectric Thin Films II, edited by A. I. Kingon, E. R. Myers and B. Tuttle, (Mat. Res. Soc. Symp. Proc., **243**, Pittsburgh, PA, 1992) pp. 49-54.
4. C. Ye, T. Yamagawa, Y. Lin, and D. L. Polla, in Ferroelectric Thin Films II, edited by A. I. Kingon, E. R. Myers and B. Tuttle, (Mat. Res. Soc. Symp. Proc., **243**, Pittsburgh, PA, 1992) pp. 61-66.
5. C.E. Land, J.Am. Ceram. Soc., **71** (11), 905 (1988).
6. See for example, Ferroelectric Thin Films II edited by A. I. Kingon, E. R. Myers and B. Tuttle, (Mat. Res. Soc. Symp. Proc., **243**, Pittsburgh, PA, 1992).
7. J. Galvagni, AVX Technical Report, AVX Corporation, Myrtle Beach, SC.
8. O. Kersten and G. Schmidt, Ferroelectrics, **67**, 191 (1986).
9. J. Chen, K. R. Udayakumar, K. G. Brooks, and L. E. Cross, IEEE ISAF Proc., 1992, 182.
10. M. T. Lanagan, J. H. Kim, S-J. Jang, and R. E. Newnham, J. Am. Ceram. Soc., **71** (4), 311 (1988).
11. R. W. Schwartz, B. C. Bunker, D. B. Dimos, R. A. Assink, B. A. Tuttle, D. R. Tallant, and I. A. Weinstock, Int. Ferroelectrics, **2**, 243 (1992).
12. R. A. Assink and R. W. Schwartz, Chem. of Mater., **5** (4), 511 (1993).
13. B. Jaffe, R. S. Roth, and S. Marzullo, J. Res. Nat. Bur. Stds., **55**, 239 (1955).
14. H. Watanabe, T. Mihara, and C. A. Paz de Araujo, Proc. 3rd. Intl. Symp. Int. Ferro., 1991, 139.
15. M. Klee and R. Waser, in Ferroelectric Thin Films II, edited by A. I. Kingon, E. R. Myers and B. Tuttle, (Mat. Res. Soc. Symp. Proc., **243**, Pittsburgh, PA, 1992) pp. 437-442.
16. R. W. Schwartz, D. Dimos, and B. A. Tuttle, to be submitted to J. Am. Ceram. Soc.
17. X. Chen and A. I. Kingon, presented at the 5th Intl. Symp. Int. Ferro., Colorado Springs, CO, April, 1993.
18. L. Wu, T-S. Wu, C-C. Wei, and H-C. Liu, J. Phys. C: Sol. Stat. Phys., **16**, 2823 (1983).
19. N. Klein, "Electrical Breakdown in Solids," in Advances in Electronics and Electron Physics, (Academic Press, **26**, New York, 1969).
20. R. Moazzami, C. Hu, and W. H. Shephard, IEEE IRPS, 1990, 231.

FIBER OPTIC PHASE AND POLARIZATION MODULATOR UTILIZING A TRANSPARENT PIEZOFILM WITH INDIUM TIN OXIDE COATING

V.S.SUDARSHANAM *, S. B. DESU ** and R.O.CLAUS *

*Virginia Polytechnic Institute and State University, Fiber and Electro Optics Research Center,
Bradley Department of Electrical Engineering, Blacksburg, VA 24061-0111.

**Virginia Polytechnic Institute and State University, Department of Materials Science and
Engineering, Blacksburg, VA 24061-0111.

ABSTRACT

A fiber optic phase and polarization modulator is presented in which a thin transparent piezoelectric polyvinylidene fluoride film with indium tin oxide electrode metallization is placed directly in the path of the output of a single mode fiber. Experimental characterization is presented in terms of the linearity of response, phase shifting coefficient, and frequency response for two arrangements differing in the boundary clamping conditions. Many applications to fiber optic switches, intensity modulators and demultiplexers are indicated.

INTRODUCTION

Optical interferometric systems of the bulk optic, holographic or fiber optic kinds commonly utilize phase and polarization modulators ¹⁻⁴ as an integral part for phase calibration, and for implementation and testing of several detection schemes that extract the measured signal from optical, electronic and mechanical noise. In preference to using bulk optic components, in-line fiber optic phase and polarization modulators have been devised wherein the light remains guided within the fiber in the interaction region of the modulator. This confinement within the fiber reduces the intensity loss due to insertion of the modulator. For instance, interaction with an externally induced modulation is commonly achieved by bonding the fiber onto a piezoelectric PZT cylinder or a thin strip of polyvinylidene fluoride (PVF₂) film ¹⁻⁴. Though the insertion loss is reduced, the presence of the epoxy as a medium of transfer of strain from the strictive element to the fiber introduces large nonlinearity of response and reduces the efficiency of strain transfer, thus limiting the phase shifting coefficient (PSC) and dynamic range³. This happens because of the different elastic parameters of the fiber, the piezofilm and the epoxy. These negative factors become more pronounced when long fiber lengths, and hence more epoxied regions, are used to increase the phase and polarization modulation⁴. Moreover, these strictive elements, utilizing multiple fiber passes, occupy appreciable space so that compactness is not achieved⁴. Whereas, in such modulators, time- dependent modulation alone has been considered, certain applications require spatial modulation⁵ as well. This paper presents a fiber optic phase and polarization modulator utilizing a piezoelectric PVF₂ film with optically transparent metal electrodes made of indium tin oxide coating. The modulator is characterized for the linearity of response, frequency response and phase shifting coefficient both for phase as well as polarization modulation. The modulator is tested using a combined Mach-Zehnder- Fabry-Perot configuration. Compared to several meters of fiber interaction length, utilized in other existing modulator configurations, a single thin film of ~ 50 μm is shown to provide a phase shifting coefficient of the same order of magnitude. Varied applications involving controllable concurrent spatial and temporal, and phase and polarization modulation are indicated.

(a) Mach-Zehnder interferometer setup. A He Ne laser (633 nm) is connected to a directional coupler (A, B, C, D). The signal path (D) goes through an intensity modulator (Fabry-Perot output) to a detector (D). The reference path (B, C) goes through a reference fiber, an index matching liquid, a beam splitter, a piezofilm, and a detector (D) to produce a fringe pattern on a screen.

(b) Direct view of the piezofilm. A piezofilm is shown with a metal washer glued to it, connected to an ST connector. Dimensions of 6 mm and 1 cm are indicated.

transmissivity of the piezofilm was higher in the 1300 nm range, a He-Ne laser at 633nm was used for convenience. The fiber on port C was terminated in an ST connector which was butt-coupled to the Indium Tin Oxide coated Piezofilm (ITOP). A thin circular metal washer to which the ITOP was bonded (see Fig.1(b)) enabled well defined boundary clamping conditions and resonance frequencies. A firm contact between the fiber and the ITOP was ensured by forming a small depression of the ITOP and verified by a microscope. Though the size of the ITOP needed was not more than the dimensions of the fiber itself, easy assemblage and mounting involved using a larger ITOP. Another configuration, differing in that the fiber did not end in the ST connector, was studied but not pursued because the PSC was relatively less though the phase shift varied linearly with the applied voltage. The fiber end on the port B was terminated in index matching oil to cut off back reflections. The ITOP acts as a phase modulator in the outgoing direction of the port C with the phase shift measured by means of the Mach Zehnder (MZ) configuration, while it would form an extrinsic Fabry Perot (FP) interferometer output in the reflection mode in the direction of detector D2. The transmission FP output seen at detector D1 would be negligible in intensity compared to the directly transmitted fiber output. The phase shift measured by the J_{1-4} method² for a number of trials was 1.374 ± 0.01 rad for an input voltage of 10.5 V. Figure 2 shows the phase shift by the J_{1-4} method as a function of the input voltage at 2 kHz for the FP case. The least squares fit to the plot shown is $(f = -0.0004 \text{ V}^2 + 0.131 \text{ V} + 0.0008)$, indicating a linear phase shifting coefficient (PSC) of 0.131 rad/Vp. Figure 3 shows the frequency response measured in the FP mode. The normalized output reaches a peak at a frequency of ~7.4 kHz. In comparison to the significant resonance peak of the FPF²⁻⁴ which is mostly in the range of 3-4 kHz, this presents a better suitability to fiber sensor applications where a higher frequency of

operation is preferred to overcome low-frequency noise. That the back-reflected output from the FP interferometer must present a phase shift that is double that of the phase shift in the direct output from the MZ case was confirmed by the combined Mach-Zehnder-Fabry

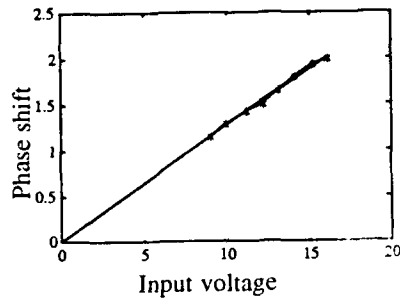


Fig. 2. Linearity of phase shift with voltage.

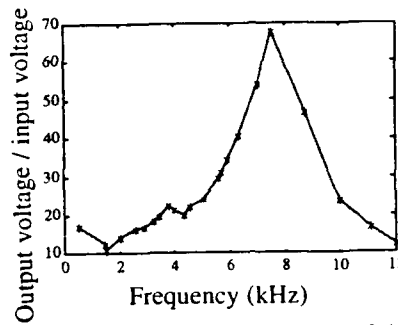


Fig. 3. Frequency response of the phase shift.

Perot configuration. Figure 4 (a) shows the output of the MZ interferometer while Fig.4 (b) shows the FP output. The voltage readings shown in Fig.4 correspond to the amplitude of the fundamental frequency component as shown by the arrows (2 kHz in a and b, and 7.4 kHz in c and d). Similar amplitudes at the next three harmonics of the fundamental frequency for each frame can be read by moving the cursor in the oscilloscope. The phase shift for each frame is then calculated from the four amplitude readings by utilizing the J1..J4 method² of direct linear phase measurement. The phase shift at 2 kHz for these two outputs are determined by the J1..J4 method to be 0.97 rad and 1.923 rad respectively. This was further confirmed at the resonance frequency of 7.4 kHz shown for the MZ and FP cases in Figs.4(c) and (d) respectively. The phase shifts respectively were 1.67 rad and 3.23 rad for an input voltage of

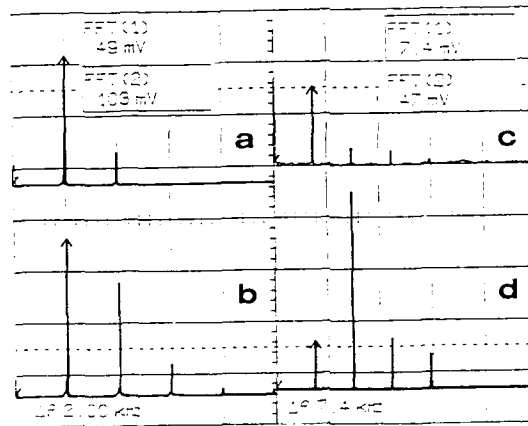


Fig.4. FFT of the output of (a) the Mach Zehnder interferometer and (b) the Fabry Perot interferometer for phase shift at 2 kHz, and (c) the Mach Zehnder interferometer and (d) the Fabry Perot interferometer for phase shift at resonance of 7.4 kHz. The voltage readings indicate the amplitude of the fundamental frequency for each frame.

6.57 Vp. Thus the utility of the phase modulator for the Mach Zehnder interferometric configuration has also been demonstrated. Further, as the resonance frequency is reached the PSC becomes larger with the result that a PSC of 0.508 rad/Vp was recorded for the frequency of 7.4 kHz. The PSC of 1.77rad/Vp-m for the FPF configuration² reported earlier was obtained by utilizing one meter of fiber interaction length. In comparison to this, the interaction length here is the thickness, ~ 50 nm, of the ITOP itself. Comparing these values, the performance of the ITOP direct modulator configuration presented is much superior to the performance of the FPF configuration. Also, a single piezofilm alone has been utilized in the demonstration here whereas a stack of piezofilms, bonded together with an optically transparent epoxy, can be used to multiply the phase shift produced. For this purpose, it is also possible to form by chemical deposition a multilayer element consisting of alternate films of ITO and PVF₂ to avoid the use of epoxy.

The optical birefringence⁶ exhibited by the PVF₂ piezofilm can be effectively utilized to fabricate polarization modulators with high efficiency. The ITOP fiber optic polarization modulator was tested in the arrangement of the Mach Zehnder configuration shown in Fig.1(a) after blocking the output from port B. A half wave plate was introduced after the polarized laser source and an analyzer after the ITOP on port C. The ST connector was moved away from the ITOP so that the two were not in contact. This was done to compare the frequency response with that determined earlier, and find the effect of mechanical loading of the ITOP by the connector. An input voltage at the frequency of 8.4 kHz was given to the piezofilm. Figure 5 shows the effect of bringing in the analyzer and removing it subsequently, demonstrating that the plot shown is indeed due to polarization modulation and not due to any reflection-related interference effects. Concurrent phase modulation does not contribute to the plot because the signal dies out on removing the analyzer. Figure 6 shows the frequency response of the ITOP

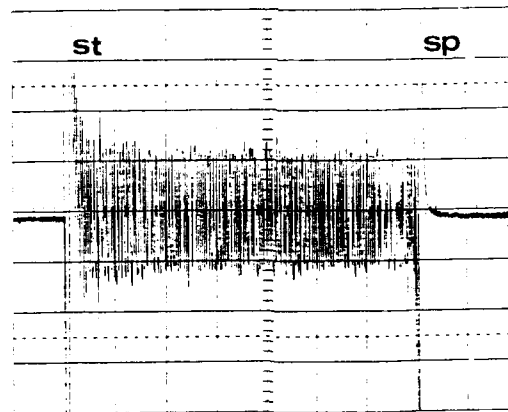


Fig.5. Instantaneous output of the ITOP modulator when the analyzer is inserted (St) and removed subsequently (Sp).

polarization modulator in terms of the normalized output voltage as a function of the input frequency. It is seen that the significant resonance peak occurs at 8.4 kHz which corresponds to the resonance peak at 7.4 kHz in the loaded condition. This change in the resonance frequency between the unloaded and the loaded conditions was as expected. Figure 7 shows the variation of the output voltage at the fundamental frequency of 8.4 kHz as a function of the input voltage. To achieve this, an experimental study of the effect on the modulation depth for variation of the half wave plate angle and the analyzer angle was conducted, and optimum angles for the half wave plate and the analyzer were chosen for maximum polarization modulation depth. Thus, both polarization and phase modulation with the ITOP modulator have been demonstrated.

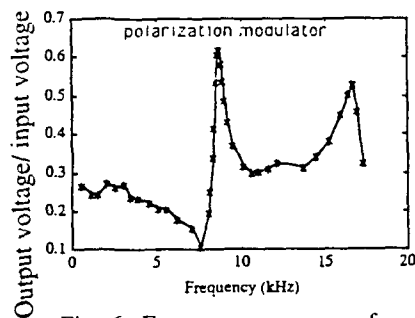


Fig. 6. Frequency response of polarization modulation.

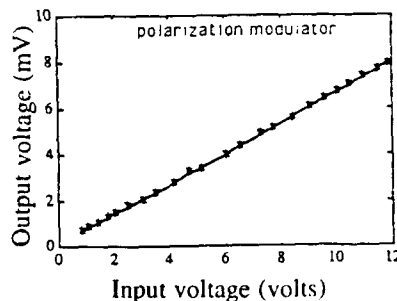


Fig. 7. Linearity of the output voltage with input voltage, at 8.4 kHz.

APPLICATIONS

The ITOP based direct phase modulator can be used in fiber interferometers of the Mach-Zehnder, the Fabry Perot as well as the Michelson configurations for the generation of a carrier phase/ polarization modulation or for active control of the phase difference biasing the interferometer at the quadrature point. The capability of producing a spatial distribution of the phase/ polarization modulation leads to interesting applications for fiber interferometric sensors where two modes supported by the fiber that differ in the spatial distribution of their electromagnetic field complex amplitude are utilized. This device can thus be used to generate a differential spatial phase modulation along with time-dependent phase modulation facilitating detection of several physical parameters. The transparent piezofilm has significant applications in fiber optic switches and intensity modulators⁷ utilized in communication and sensor systems. Given the attractive features of PVF₂ compared to ceramic PLZT or liquid crystals, a great potential exists for the development of PVF₂ based switches and demultiplexers for both single mode and multimode fiber systems.

ACKNOWLEDGEMENT

This work was partially supported by the Center for Innovative Technology, Virginia Polytechnic Institute and State University. The authors thank David Port of Atochen Sensors for providing the ITPO sample.

REFERENCES

1. R.P.De Paula and E.L.Moore, Proc. SPIE, **478**, 3, 1984.
2. V.S.Sudarshanam and K.Srinivasan, Opt.Lett. **14**, 140, 1989.
3. V.S.Sudarshanam and K.Srinivasan, J.Appl.Phys. **68**, 1975, 1990.
4. V.S.Sudarshanam and R.O.Claus, " Frequency response and phase shift nonlinearity of a cylindrical PVDF film based fiber optic phase modulator", J.Lightwave Technol., (accepted for publication, April 1993 issue).
5. T.Sato, Y.Ueda, and O.Ikeda, Appl.Opt. **20**, 343, 1981.
6. R.J.Shuford, A.F.Wilde, J.J.Ricca, and G.R.Thomas, Polymer Engg. Sci. **16**, 25, 1976.
7. Z.K.Ioannidis, I.P. Giles, and C.Bowry, Appl.Opt. **30**, 328, 1991.

MATERIALS CHARACTERIZATION OF NONDESTRUCTIVE READOUT NONVOLATILE MEMORY DEVICES

Bruce A. Tuttle, Dale C. McIntyre, Carleton H. Seager, Terry J. Garino, and William L. Warren, Sandia National Laboratories, Albuquerque, NM 87185
Joseph T. Evans and Robert W. Waldman, Radiant Technologies, Inc., Albuquerque, NM 87109

ABSTRACT

Prototype ferroelectric thin film, nonvolatile memory, nondestructive readout (NDRO), semiconductor devices have been fabricated. The "1" and "0" logic states of these prototype devices are in principle determined by the modulation of the conductivity of a semiconductor film channel by the polarization state of the underlying ferroelectric thin film layer. Programmed resistance ratios of the two logic states of 5:1 are demonstrated. While the best performance to date has been achieved for devices that have a 40 nm In_2O_3 film covering a 300 nm thick PZT 20/80 layer, we also develop criteria for selecting semiconductor films that will improve performance for this NDRO device design. Among the other semiconductor films that are characterized with respect to this criteria are boron doped Ge, ZnO and aluminum doped ZnO. It is demonstrated that by appropriate donor doping of ZnO films the effects of intrinsic defects are masked and that process temperatures can be extended by 300°C.

INTRODUCTION

The principal advantage of NDRO ferroelectric thin film semiconductor memories is that there is substantially less chance of bit error readings than for their conventional destructive readout (DRO) counterparts. During the read operation in a conventional two transistor / two capacitor DRO cell design, several operations occur while the bit line or bit line bar capacitor is switched to the opposite polarization state of the initial read. Typically, these operations consist of driving the ferroelectric capacitor to its opposite polarization state, reading the state with the sense amplifier, driving the bit line or bit line bar line to the rails (typically 5 volts), and then setting the drive line back to zero volts to restore the initial polarization state of the capacitor. The time interval for these operations ranges from 100 ns to 500 ns, depending on cell design and timing circuitry. If an event, such as, a power outage or a radiation burst occurs during this time interval, a bit error reading is quite likely to occur.

Figure 1 is a schematic diagram of the type of nondestructive readout nonvolatile memory device that is discussed in this paper. Device operation is determined by the conductivity of the semiconductor film that is deposited on the PZT film layer. For an n-type semiconductor film, if the polarization vector is oriented towards the semiconductor film (pointing up in Figure 1, $+P_R$) one would expect that the majority carrier (electron) concentration is enhanced and the conductivity of the film increases. Conversely, if the ferroelectric is switched to the opposite polarization state ($-P_R$), one would expect that the electron concentration is reduced in the semiconductor film and conductivity decreases. The logic state is read by monitoring the current flowing in the semiconductor film; and thus, the ferroelectric polarization state is not reversed during the read operation. For maximum difference in the "1" and "0" resistance states, a semiconductor film thickness of approximately 50 nm is used. While inadequate coverage of the PZT film surface is obtained if the semiconductor film is much thinner than 50 nm, the resistance difference may be reduced for thicker films. The ITO layer decreases the contact resistance between the top Pt electrode and the In_2O_3 thin film, thereby increasing the programmed resistance ratio.

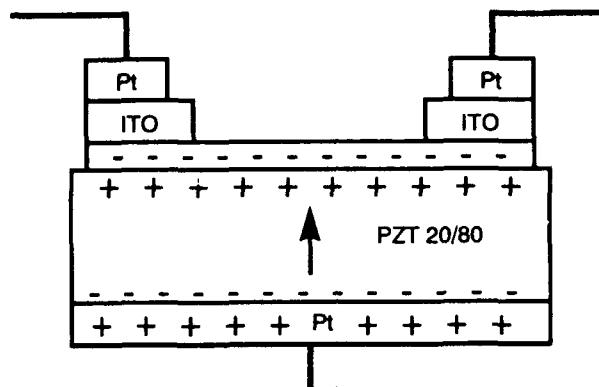


FIG. 1. Schematic diagram of NDRO device.

The concept of modulating semiconductor film conductivity by an underlying ferroelectric was considered by Morris¹ and Zuleeg and coworkers² in the mid-1960's. We have based much of our work on subsequent publications by Crawford³ and Taylor⁴ in the 1970's. Crawford³ demonstrated that the conductivity of a SnO_2 film could be changed by approximately four orders of magnitude by the polarization state of an underlying PZT based bulk ceramic. Taylor⁴ outlined the process by which semiconductor film conductivity could be modulated by $\text{Bi}_4\text{Ti}_3\text{O}_{12}$ films or bulk ceramics. He also suggested the use of these structures for nonvolatile semiconductor memories. The ready availability in the late 1980's of solution derived PZT thin films,⁵ led Evans and Bullington^{6,7} to the development of circuitry and device structure that would make commercial NDRO ferroelectric thin film devices realizable.

Our work is one of the first reports of the NDRO operation and characteristics of solution derived-PZT film // semiconductor film composites. We present preliminary data concerning film composite chemical interactions after the composite has been subjected to simulated process temperatures. Further, we describe the semiconductor film properties necessary for optimization of NDRO device performance, and show both material and electrical characterization of a number of semiconductor film // ferroelectric film composites. We demonstrate that resistivities obtained for semiconductor film // PZT film composites are consistent with measurements of mobility and carrier concentration obtained for semiconductor films deposited on fused silica substrates as a function of process temperature.

Finally, we acknowledge that the assumption, which is implicitly made throughout this paper, that the sole mechanism responsible for NDRO device characteristics is the modulation of bulk semiconductor film resistivity by the underlying ferroelectric film is too simplistic. Among the many effects that can have substantial impact on real device characteristics are electrode // semiconductor film contact potentials, semiconductor film // ferroelectric film interface states, and charge injection⁸ into trap states in the ferroelectric film. The emphasis of our work is materials characterization, as such, a detailed discussion of the nuances of NDRO operation and the mechanisms responsible for this behavior are outside the scope of this paper.

EXPERIMENTAL PROCEDURE

Prototype NDRO devices were fabricated using solution chemistry derived $\text{Pb}(\text{Zr,Ti})\text{O}_3$ thin films and electron beam deposited In_2O_3 thin films or RF Magnetron sputter deposited Ge, ZnO or Al doped ZnO thin films. For the prototypes, the PZT 20/80 films were deposited using a process similar to the hybrid solution deposition procedure developed by Gi and Sayer.⁹ Crystallization treatments of 650°C for 1 hour were used. Indium oxide films were fabricated by electron beam evaporating In at 10^{-6} Torr and then oxidizing the In film at 400°C in air. ZnO and Ge films were RF sputter deposited after the base pressure of the system was cryopumped to less than 10^{-7} Torr and with a target to substrate distance of 5 cm. Although ZnO films were RF magnetron sputtered using many deposition conditions, the two types of Al doped ZnO films discussed in this paper were deposited with a ring magnetron target, Ar gas, a sputter deposition rate of 50 nm/min, and pressures of either 10 mT and 25 mT. Al doped ZnO films deposited at 10mT pressure had an order of magnitude lower resistivity, 2×10^{-3} ohm-cm compared to 2×10^{-2} ohm-cm, than films deposited at 25 mT. The Al doped ZnO target contained 2 weight percent Al_2O_3 , which corresponds to a doping level of 0.32 atom percent Al in ZnO. Germanium films were RF magnetron sputter deposited with a planar target at 20 mT Ar pressure. The Ge sputtering target was doped with boron to a resistivity of 0.01 ohm-cm. Fused silica or PZT films deposited on platinized silicon wafers were used as the substrates for electrical characterization of semiconductor films.

Interfacial reactions between the semiconductor film and the PZT film can have a substantial impact on device performance. In addition to conventional blanket wafer sections on platinized silicon wafers, 2.5 cm X 2.5 cm photolithographically defined areas on 10 cm (4") diameter prototype device wafers were also investigated. These large areas consisting of multiple film depositions were annealed at temperatures ranging from 300°C to 650°C to determine the extent of interaction. Auger electron spectroscopy (AES), Secondary ion mass spectroscopy (using ^{17}O to minimize charging effects) and transmission electron microscopy were among the techniques used to characterize film structure, microchemistry and interfacial reactions.

An array of electrical test measurements was used to characterize prototype devices, blanket semiconductor film // PZT film structures and individual semiconductor films. Typically, prototype device characterization was performed with 2 ms pulses, 8 volt write pulses, 0.4 volt drain to source read pulses. Similar "1" and "0" state resistivities were obtained with 5 μs pulses using arbitrary waveform generators. Four point I-V measurements were used to initially characterize semiconductor films after deposition. Hall Effect and four point I-V measurements were performed on structures consisting of an 1.1 cm X 1.1 cm square of material with Au electrodes deposited on the corners. While traditional Van der Pauw analysis was used to reduce the data obtained from four point I-V measurements, fourier transform techniques were used to enhance signal to noise ratios in the Hall effect measurements for low mobility samples. Hall effect measurements were performed with magnetic fields up to 0.77 T and with dc electrical bias. Both Hall effect and four point I-V measurements were made over the temperature range from 40K to 295K. Ambient Seebeck measurements confirmed that all of the semiconductor films in this study were n-type.

RESULTS AND DISCUSSION

The choice of a semiconductor film for NDRO devices is severely restricted by a combination of both processing and electrical requirements. First, the film composite must be insensitive to process environments, such as, glass encapsulation, metallization anneal, and packaging environments. The film's electrical resistivity should also be relatively constant over the operating temperature range, -55°C to 125°C for military applications, so that the currents sensed are of the same order of magnitude. Because of the constraints of device geometry - typical dimensions of a semiconductor film channel are $10\text{ }\mu\text{m} \times 10\text{ }\mu\text{m} \times 50\text{ nm}$ - it is important that the resistivity be on the order of 0.01 ohm-cm . If the film resistivity is less than 0.01 ohm-cm , then there is an improper match to the CMOS series resistance (approximately 3000 ohms). In many cases, this will result in the resistance difference between "1" and "0" states to be rather limited. Programmed resistance ratios on the order of 2:1 to 10:1 are desirable. The programmed resistance ratio is defined as the ratio of the resistance in the high resistance state to the resistance of the low resistance state. If the resistance ratio is less than 2:1, then it is difficult to discriminate between "1" and "0" logic states. If the resistance ratio is much greater than 10:1, then the device write speed is compromised by the large RC time constant of the device.

Our primary technique for determining the suitability of a semiconductor film for NDRO devices was to deposit a candidate semiconductor film on a PZT film and then anneal the composite at 600°C or 650°C for 1 hour in air. These annealing conditions were chosen to roughly approximate the aforementioned process temperature environments. After the anneal, the electrical properties and interfacial reactions of the film composite were then analyzed. This approach reduces an essentially infinite number of semiconductor thin film candidates to a very small number.

Chemical reaction between the semiconductor film and the PZT film at temperature eliminates many films from consideration for NDRO devices. An example of extensive chemical reaction is shown in Figure 2 for a Ge film deposited on a PZT 40/60 film layer. While Auger electron spectra indicate substantial interdiffusion of Ge and O for the film annealed at 600°C , Ge and O profiles are relatively sharp for the film annealed at 350°C . Corresponding electrical resistivity measurements indicated film resistivities that were orders of magnitude outside the desired specifications. Diffusion of oxygen from the annealing atmosphere into the Ge film, which may be preferential along grain boundaries, may also have contributed to the substantial change in resistivity. In contrast, the Auger electron spectra of the prototype wafer materials analysis area for an In_2O_3 thin film deposited on PZT 20/80 and annealed at 650°C for 1 hour indicates that massive interdiffusion of In into the PZT layer has not occurred and that the oxygen content of the In_2O_3 film did not change appreciably upon annealing. Further, the resistivity of this film was adequate for NDRO device operation. While determination of Sn diffusion was at the limits of AES detectability, diffusion of Sn from the $\text{In}_{1-x}\text{Sn}_x\text{O}_3$ interface contact layer into the In_2O_3 film was detected by SIMS analysis. Diffusion of Sn into other layers was below the levels of SIMS detectability for this analysis structure. Functional prototypes were fabricated from this $\text{ITO}/\text{In}_2\text{O}_3/\text{PZT}$ composite structure.

Zinc oxide was another semiconductor film material that did not exhibit extensive chemical reaction with PZT after a 650°C air anneal. ZnO films deposited on PZT 53/47 layers showed no significant reaction by optical microscopy after annealing at 650°C for 1 hour. Further, Pt electrodes were deposited on top of the composite and essentially identical ferroelectric properties ($P_R = 25\text{ }\mu\text{C}/\text{cm}^2$ and $E_c = 40\text{ kV}/\text{cm}$) were obtained for the annealed composite as for the virgin ferroelectric film. Four point resistivities on the order of 0.1 ohm-cm were obtained for as deposited ZnO films on fused silica. However, prototype devices fabricated using

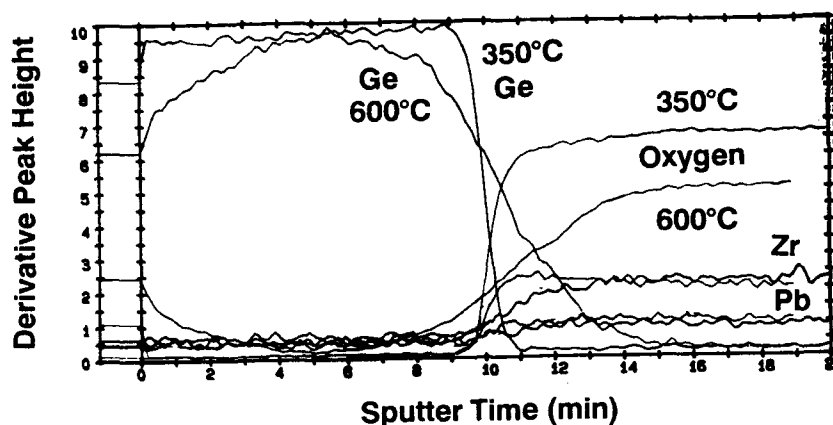


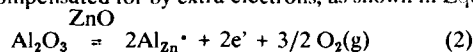
FIG. 2. Auger Electron Spectra for Ge // PZT 40/60 composites annealed at 350°C and 600°C

ZnO films and annealed at 400°C in air had resistivities orders of magnitude too high for device applications. We attribute this behavior to the decrease in oxygen vacancy concentration in the vicinity of the grain boundaries after the 400°C anneal. The majority carrier (electron) concentration is reduced, as shown in equation 1, and the

$$\text{O}_o = \text{V}_o^{\bullet\bullet} + 2e' + 1/2 \text{O}_2(\text{g}) \quad (1)$$

conductivity decreases. We acknowledge that there is still some uncertainty whether zinc interstitials or oxygen vacancies are the primary property controlling intrinsic defects for ZnO, but for the purposes of the present discussion it is inconsequential.

Our strategy for making ZnO films more insensitive to process temperatures is to extrinsically dope the ZnO films to such concentration as to mask the effects of the intrinsic defects. The effect of increasing resistivity with annealing temperature is shown in Figure 3, for both an Al doped ZnO film and a ZnO films with no additions. These films were deposited on fused silica substrates and were 500 nm and 100 nm thick, respectively. The Al doped ZnO film was deposited at a pressure of 10 mT. The resistivity is measured at ambient after the films were annealed for 1 hour at the temperature plotted on the graph. The resistivity of the ZnO film with no purposefully added dopants increased by two orders of magnitude after a 300°C anneal, consistent with prototype device measurements. ZnO films with 0.32 atomic percent Al additions had an as deposited resistivity of approximately 10^{-3} ohm-cm, which is two orders of magnitude less than that of the as deposited film. The decrease in resistivity is attributed to the substitution of an Al ion on a Zn site, which is compensated for by extra electrons, as shown in Equation 2.



While Al doped ZnO films were less sensitive to annealing temperatures than ZnO films with no purposefully added dopants, a substantial increase in resistivity was observed after annealing at 500°C. Specifically, after a 400°C anneal, the Al doped ZnO film resistivity has increased by less than a factor of five, but after annealing at 500°C, the resistivity has increased by two orders of magnitude.

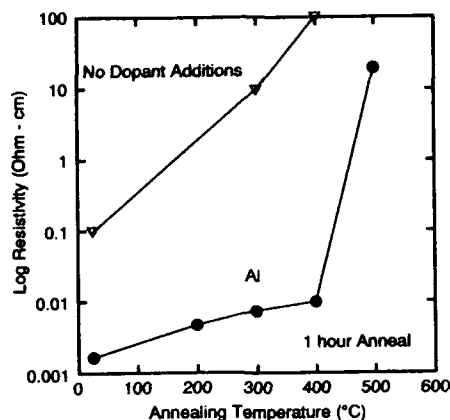


FIG. 3. Ambient resistivity of ZnO and Al doped ZnO films after 1 hour anneal in air at temperature.

We attribute this increase in resistivity with annealing temperature to the oxidation of Al at the grain boundaries, which increases the effective impedance of the grain boundaries. Previously, it has been shown¹⁰ that the grain size of ZnO varistors doped with Al is substantially less than that for varistors with no Al additions, suggesting the active presence of Al at grain boundary interfaces in ZnO based materials. Further, Hall effect measurements were obtained for two Al doped ZnO films, one of which was not annealed and the other which was annealed at 300°C in air for 1 hour. The electron mobility substantially decreases and the carrier concentration remains essentially constant with annealing, which further supports the above hypothesis. This implies that if a ZnO film could be made with a suitable dopant, one that would not result in the formation of potential barriers to transport at grain boundaries after annealing, a process temperature insensitive semiconductor film could be developed for PZT thin film NDRO devices.

Van der Pauw analyses of four point I-V measurements as a function of temperature, from 40K to 295K, were performed on both In_2O_3 and Al doped ZnO films. Resistivity vs. temperature relationships for the two films are depicted in Figure 4. The resistivity magnitude of both the Al doped ZnO film and the indium oxide film are similar at 295K being 0.027 and 0.011 ohm-cm, respectively. The Al doped ZnO film was deposited at a pressure of 25 mT, in an attempt to achieve a resistivity closer to the desired value for NDRO devices, and has an order of magnitude higher resistivity than the ZnO film deposited at 10 mT. A similar percentage change in resistivity, on the order of 30%, is measured from 40K to 295K for both the In_2O_3 and Al doped ZnO films. The two films also exhibit similar behavior as a function of annealing temperature as both films have an approximately 30 fold increase in resistivity after annealing in the temperature range of 300°C to 400°C.

The reason for the resistivity increases upon annealing are substantially different for the two films. The In_2O_3 film shows a significant change in carrier concentration after the anneal, while the Al doped ZnO film carrier concentration remains essentially constant ($\approx 2.7 \times 10^{20} \text{ cm}^{-3}$). Interestingly, the measured Al doped ZnO film carrier concentration is very close to the calculated value of $2 \times 10^{20} \text{ cm}^{-3}$ for 0.32 at.% Al doped ZnO, which is the nominal target composition. After the anneal, the carrier concentration of the In_2O_3 film decreased from an initial value of $1.3 \times 10^{21} \text{ cm}^{-3}$ to $6.3 \times 10^{18} \text{ cm}^{-3}$ with a Hall mobility of approximately $1 \text{ cm}^2/\text{V}\cdot\text{sec}$ being measured before and after the anneal. The Hall mobility of the Al doped ZnO film decreases from an initial value of $1.6 \text{ cm}^2/\text{V}\cdot\text{sec}$ to $0.048 \text{ cm}^2/\text{V}\cdot\text{sec}$ after annealing. The Hall mobility is larger than the conductivity mobility by a factor f , which is approximately 1.9 for the case of ionized impurity scattering.

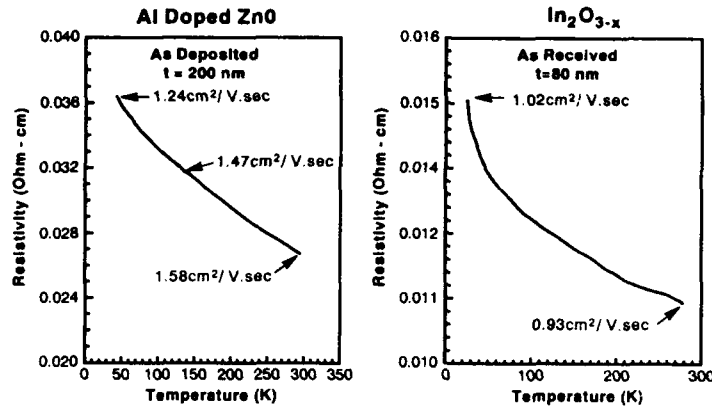


FIG. 4. Resistivity of Al doped ZnO and In_2O_3 films as a function of temperature from 40K to 295K.

Prototype devices have been made with both In_2O_3 and Al doped ZnO resistor channels. Channel dimensions were either $10\ \mu\text{m} \times 10\ \mu\text{m}$ or $30\ \mu\text{m} \times 30\ \mu\text{m}$ depending on the mask set used. As deposited Al doped ZnO devices (10 mT deposition pressure) had resistivities that were an order of magnitude less than those of the as deposited In_2O_3 film devices, as predicted from electrical resistivity measurements on glass slides. For a typical In_2O_3 based NDRO device that was annealed at 400°C , we achieved a low resistance state of 50,000 ohms (0.25 ohm-cm) and a high resistance state of 250,000 ohms (1.25 ohm-cm) for a programmed resistance ratio of 5:1. While 2 ms pulses were used for these measurements, 0.4 volts was applied across the semiconductor film to obtain resistance readings. We obtained essentially identical programmed resistance ratios using sequences of 5 μs pulses from arbitrary waveform generators and monitoring current.

SUMMARY

While functioning prototype NDRO devices have been fabricated, more work is required to develop semiconductor film - ferroelectric thin film composites that are more insensitive to process environments. Semiconductor film selection for NDRO devices was based on three criteria: 1) no chemical reaction with underlying PZT films at process temperatures, 2) appropriate ambient electrical resistivity (approximately 0.01 ohm-cm), and 3) minimal variation of electrical properties after simulated process temperature anneals. While the high mobility¹¹ ($1900\ \text{cm}^2/\text{V}\cdot\text{sec}$) of boron doped Ge films is attractive for NDRO devices, AES spectra indicate that chemical reactivity of Ge/PZT composites in process environments may be a significant problem. Hall effect measurements indicated that after a 400°C anneal in air, the carrier concentrations of In_2O_3 films decreased from $1.3 \times 10^{21}\ \text{cm}^{-3}$ to $6.3 \times 10^{18}\ \text{cm}^{-3}$; whereas, the carrier concentration of Al doped ZnO films annealed at 300°C was essentially the same as that measured at ambient. However, the mobility of the Al doped ZnO films decreased by three orders of magnitude after the anneal, resulting in similar resistance increases for both films after annealing. Nonetheless, functioning prototype devices based on either In_2O_3 or Al doped ZnO films were fabricated. Glass passivated NDRO devices based on In_2O_3 had programmed resistance ratios greater than 5:1.

ACKNOWLEDGEMENTS

The authors acknowledge the support of DOE under CRADA contract SC-1075 for this work. The authors also acknowledge the efforts of Dave Goodnow, Mark Harrington, Wayne Buttry, Paul Grandon, Steve Rodgers, Jean Greene, Gerald Nelson, Duane Dimos, Herb Tardy and Robert Nasby.

REFERENCES

1. J.L. Moll and Y. Tarui, IEEE Trans-Electron Devices, ED10, 328 (1963).
2. R. Zuleeg and H.H. Weider, Solid State Electronics, 9, 657 (1966).
3. J.C. Crawford, Ferroelectrics, 1, 23-30 (1970).
4. G.W. Taylor, Ferroelectrics, 18, 17-20 (1978).
5. K. Budd, S. Dey, and D. Payne, Brit. Ceram. Soc. Proceedings, 36, 107-20 (1985).
6. J.T. Evans and J.A. Bullington, U.S. Patent No. 5 070 385 (3 December 1991).
7. J.T. Evans and J.A. Bullington, U.S. Patent No. 5 119 329 (2 June 1992).
8. H. Buhay, S. Sinharoy, W. Kasner, M. Francombe, D. Lampe and E. Stepke, Appl. Phys. Lett., 58 14 1470-2 (1991).
9. G. Yi, Z. Wu, and M. Sayer, J. Appl. Phys., 64 (5), 1 2717-24 (1988).
10. B. Tuttle, MRS Bulletin, 12 [7] 40-5 (1987).
11. B.G. Streetman, Solid State Electronic Devices, Prentice-Hall, Englewood Cliffs, N.J., 443 (1972).

INTEGRATED PYROELECTRIC INFRARED SENSOR USING PVDF THIN FILM DEPOSITED BY ELECTRO-SPRAY METHOD

RYOJI ASAH, JIRO SAKATA, OSAMU TABATA,
MIDORI MOCHIZUKI, SUSUMU SUGIYAMA AND YASUNORI TAGA
Toyota Central Research and Development Laboratories, Inc.
Nagakute-cho, Aichi-gun, Aichi-ken, 480-11, Japan.

ABSTRACT

A pyroelectric infrared sensor using a poly(vinylidene fluoride) (PVDF) thin film has been integrated with a read-out circuit on a silicon substrate. The PVDF thin film with a thickness of 1-2 μm was deposited on the sensing area by an electro-spray (ESP) method. A form I crystal and a large pyroelectric coefficient of $4 \text{ nCcm}^{-2}\text{K}^{-1}$ were observed just after the deposition without any poling treatments. The fabrication process of the sensor was based on a standard MOS LSI process and a polysilicon sacrificial layer etching technique. In order to reduce the heat capacitance and the thermal conduction, the PVDF thin film was supported on a thin Si_3N_4 membrane structure formed by etching a part of the silicon substrate under the sensing area. The sensor with a sensing area of $400 \times 400 \mu\text{m}^2$ had a responsivity of 98 V/W, a detectivity of $1.4 \times 10^7 \text{ cmHz}^{1/2}\text{W}^{-1}$, an NEP of $2.9 \times 10^{-9} \text{ Hz}^{-1/2}\text{W}$ at a frequency of 100 Hz and a time constant of 1.3 msec.

INTRODUCTION

In the last several years, much attention has been concentrated on room-temperature-operatable two-dimensional and integrated infrared sensors from a view point of their wide applications. Pyroelectric infrared sensors, which detect a change of dipole moment when a temperature at the sensing area is changing, are more advantageous because of their high sensitivity. Conventional pyroelectric two-dimensional array sensors previously reported were hybrid constructions consisting of a bulk material, such as a zirconate ceramics [1] or a LiTaO_3 single crystal [2], and a silicon substrate in which read-out circuits were formed. Recently, a pyroelectric two-dimensional array sensor using a PLTO thin film on a MgO substrate connected with separate read-out circuits by bonding wires was reported [3]. However, pyroelectric thin films deposited on a silicon substrate have been desired. This is because the integration of the pyroelectric thin film with the read-out circuits can easily solve the problems caused by thermal crosstalk between sensor elements, connections between detector arrays and read-out circuits, and the low sensitivity of each small sensor element [4,5].

A poly(vinylidene fluoride) (PVDF) thin film is a very suitable material for two-dimensional devices because of its small thermal conductivity and its ability to be easily patterned by photolithographic technology [6]. The PVDF shows ferroelectric behavior in a form I crystal. Since the form I crystal of the PVDF can be obtained from a form II crystal by stretching a film and applying a very high electric field [7], the PVDF sheet has been glued to a silicon substrate to integrate the sensor with the read-out circuits [8,9]. On the other hand, its copolymers such as P(VDF-TrFE) can be easily fabricated on a silicon substrate by the spin coating technique, since they possess the form I crystal under any crystallization condition. Nevertheless, poling treatments are still needed in order to have adequate dipole arrangement in the copolymers [10]. Since unevenness of the pyroelectricity or breakdown was often caused by the poling treatment because of thickness variation or pinholes in the film, it has been difficult to obtain a thin P(VDF-TrFE) film having uniformity and a large pyroelectric coefficient on a silicon substrate.

This paper presents a PVDF pyroelectric infrared sensor integrated with a read-out circuit onto a silicon chip. The features of this sensor are as follows: (1) An electro-spray (ESP) method [11] was used to deposit the PVDF thin film on the silicon substrate. (2) The fabrication technique was based on silicon LSI technology combined with micromachining technology using a polysilicon sacrificial layer technique. The preparation of the PVDF thin film, the fabrication and characteristics of the sensor are described.

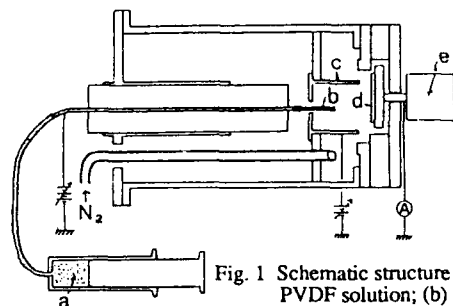


Fig. 1 Schematic structure of an ESP deposition apparatus: (a) PVDF solution; (b) needle; (c) cylindrical electrode; (d) substrate; (e) motor.

PREPARATION OF PVDF THIN FILMS

The schematic structure of an ESP deposition apparatus is shown in Fig. 1. A PVDF solution of 0.2 wt.% in an organic solvent such as dimethylformamide (DMF) is charged by applying an electric voltage of 8-15 kV between the needle and the electrode of the substrate. The distance between the needle and the substrate is 10-25 mm. The charged droplets of the PVDF solution are transported from the needle to the substrate by the electric field. In order to focus and control the direction of the droplets of the PVDF solution, a biased cylindrical electrode enclosing the path of the PVDF solution is arranged. On the way to the substrate, most of the solvent is vaporized by dry nitrogen which is made to flow in the opposite direction to the droplets. Subsequently, polymers of the PVDF along with the residual solvent are deposited on the electrode of the substrate. The deposition is carried out under atmospheric pressure and around room temperature. For improvement in the uniformity of the film, the substrate is rotated. The electrode of the substrate is electrically connected to the ground through the axis of a motor. The ion current shunted to the ground is monitored during the deposition.

Figure 2 shows an XPS spectrum of the PVDF film deposited on a silicon substrate. There were two peaks at 287.9 and 292.0 eV assigned to CH_2 and CF_2 respectively, and no other peaks assigned to CF and CF_3 were observed. The height of the two peaks were almost same. These results indicate that the PVDF film mainly consists of $\text{CH}_2\text{-CF}_2$ structure, and decomposition hardly occurs during the ESP deposition process. While, decomposition often arose from the ionization and heating to high temperatures needed for vaporization. The crystal forms and orientations of the PVDF film were identified by IR reflection absorption spectroscopy (IRRAS) method with p- and s-polarized lights as shown in Fig. 3. In this case PVDF film was deposited on the silicon substrate on which Al layer was formed. The bands at 470, 510 and 1280 cm^{-1} assigned to the form I crystal were observed, while those at 490, 530, 610 and 795 cm^{-1} assigned to the form II were not observed [12]. Figure 3 also shows evident dichroism in the spectra; a very intense band at 1280 cm^{-1} in the spectrum with p-polarized light decayed when s-polarized light was used. The band at 1280 cm^{-1} is assigned to CF_2 symmetric stretching vibration of the form I crystal. From these results the form I crystal is stable in the PVDF film deposited by the ESP method, and the CF_2 dipoles in the films are perpendicularly oriented to the substrate. It is considered that the orientation of the form I is attributed to the applied field during film deposition, and the CF_2 dipoles are aligned along the applied field. The another advantage of the ESP method is that these characteristics were commonly found in the cases using any kinds of substrate.

The pyroelectric coefficient λ versus the ion current during the ESP deposition is shown in Fig. 4. The ion current was varied by changing the applied voltage and distance between the needle and the substrate. The pyroelectric coefficient increased with an increase in the ion current. For an ion current above $3\text{ }\mu\text{A}$, a large pyroelectric coefficient of $4\text{ nCcm}^{-2}\text{K}^{-1}$ was obtained. The IR spectra in Fig. 5 indicate the stability of the form I crystal in a deposited film after heat treatments at 90-160 °C for 30 min. The form I crystals in the PVDF did not vanish up to 160 °C. Though the heat treatment caused a reduction of the pyroelectric coefficient, the reduction was within 15 % after the heat treatment at 120 °C, which is a typical temperature

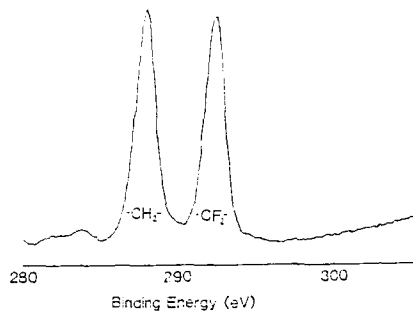


Fig. 2. XPS spectrum of PVDF film prepared by the ESP method.

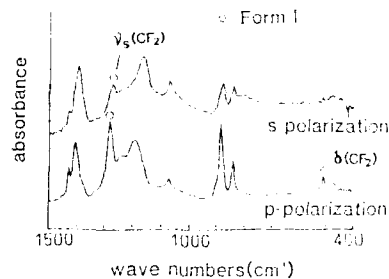


Fig. 3. IR spectra of the PVDF film measured by the IRRAS method.

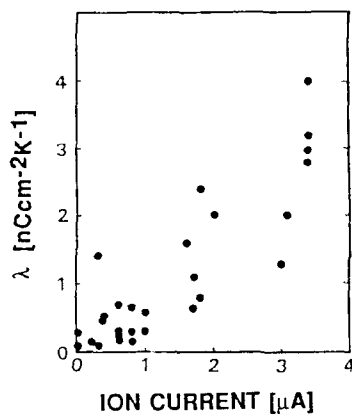


Fig. 4. Ion current dependence of the pyroelectric coefficient.

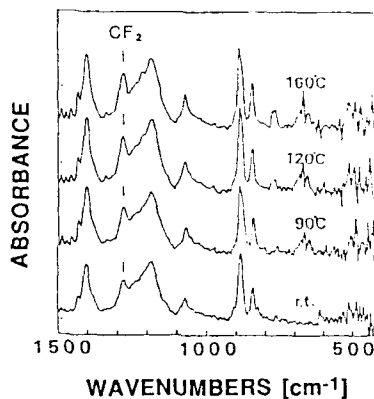


Fig. 5. Stability of the form I crystal after heat treatments at 90-160 °C.

encountered in the photolithography process. Furthermore, the PVDF film could be etched by O_2 reactive ion etching (RIE) without reducing the pyroelectric coefficient. From the above results, it was revealed that the PVDF film prepared by the ESP method can be applied to the integration with the read-out circuits on a silicon substrate.

STRUCTURE AND FABRICATION OF THE SENSOR

Figure 6 shows the schematic cross-sectional structure of the sensor. Figure 7 is the photograph of the fabricated infrared sensor chip before forming an absorbent. The sensor element with a sensing area of $400 \times 400 \mu m^2$ and MOS FETs are integrated on a silicon substrate. In order to reduce the thermal capacitance of the sensor elements and the thermal conduction from the sensor element to the substrate, the sensor element has a membrane structure supported by Si_3N_4 with a thickness of 150 nm. This membrane structure was formed by silicon anisotropic etching. A number of etch holes with a diameter of $10 \mu m$ and an interval of $25 \mu m$ were made in the membrane. These holes were needed to uniformly etch a part of silicon substrate under the sensor area, as well as to reduce the thermal capacitance and thermal conduction of the membrane. Designing the diameter, D , and the interval, I , of the holes was required to avoid the concentration of the stress around the holes which often

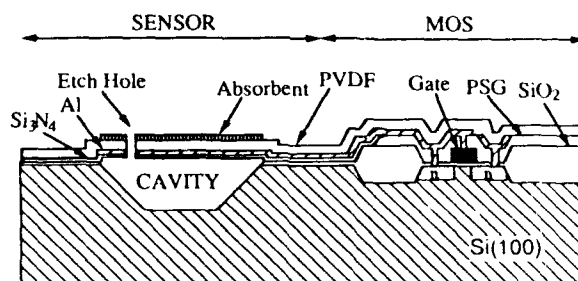


Fig. 6. Schematic cross-sectional structure of the sensor.

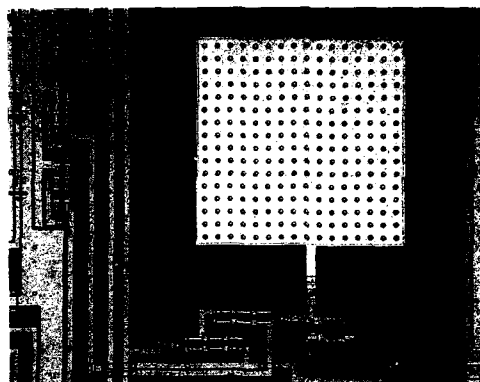


Fig. 7. Photograph of the fabricated infrared sensor chip (before forming an absorbent).

causes the membrane to break during anisotropic etching. The maximum stress over the membrane with the holes was designed to be much less than the fracture strength of Si_3N_4 by the finite element method. A PVDF thin film was formed on the Al lower electrode on the membrane using the ESP method. The typical thickness of the PVDF was 1-2 μm . The upper electrode, Au-black, which functions as an absorbent of infrared-rays, was formed on the top of the sensor element. The Au-black absorbed over 90 % of infrared-rays with the wavelength ranging from 2 to 20 μm . The lower electrode was electrically connected to the gate of the MOS FET, and the upper electrode was connected to the ground. Note that the thicknesses of the PVDF and the Au-black are not essential for the thermal isolation of the sensor because of their low thermal conductivities. Due to this thermal isolation structure, the temperature of the sensor element is effectively changed by incident infrared-rays.

The fabrication process was based on a standard MOS LSI process and the polysilicon sacrificial layer technique [13,14]. The key points of the sensor process were how to prevent damage to the sensor element and its read-out circuits during the deposition of the PVDF. First, the charged droplets of the PVDF solution with their high kinetic energy sometimes physically damaged to the thin membrane. This problem was solved by optimization of the ESP conditions, e.g. the applied voltage and the distance between the needle and the substrate. Second, the charged droplets caused charging of the surface of the silicon substrate, and it often gave rise to breaking down the gate oxides of the MOS FETs. This problem was avoided by connecting a diode-connected MOS FET with a threshold voltage of 0.5-0.7 V to

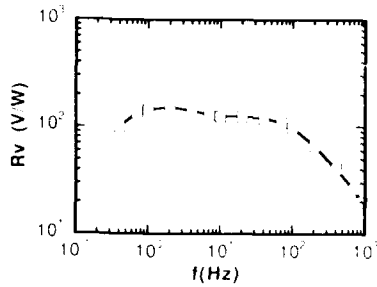


Fig. 8. Frequency dependence of the voltage responsivity.

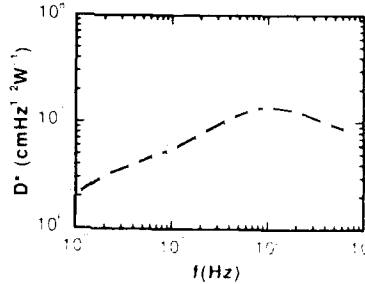


Fig. 9. Frequency dependence of the normalized detectivity.

the gate electrode. It shunts the charge of the gate electrode to the ground during the deposition. When the sensor operates, it serves as an input resistor whose value of resistivity can be adjustable by the channel doping. A typical resistivity value was $3 \times 10^{10} \Omega$ at an output voltage from the PVDF capacitance ranging within ± 1 mV.

CHARACTERISTICS OF THE SENSOR

The fabricated sensors were irradiated with chopped infrared radiation from a blackbody furnace at 500 K. The output signals were impedance-transferred by on-chip MOS FETs and measured by the spectrum analyzer (HP Model 3582A).

Figure 8 shows the frequency dependences of the voltage responsivity R_v . A flat net frequency response was obtained over wide range of frequencies. The frequency dependences of the R_v is expressed as follows:

$$R_v = \frac{\epsilon A \lambda \omega R}{G} \left[\frac{1}{1 + (\omega \tau_e)^2} \right]^{1/2} \left[\frac{1}{1 + (\omega \tau_t)^2} \right]^{1/2}$$

where ϵ is the emissivity, A is the sensing area, ω is the chopping frequency, R is the electrical resistivity, G is the thermal conductivity, τ_e is the electrical time constant and τ_t is the thermal time constant. The measured electrical time constant associated with rise-times in the lower frequency region was 180 msec that was comparable to the calculated value of 230 msec from sensor design. The thermal time constant associated with fall-times in the higher frequency region was 1.3 msec. Small thermal capacity of the membrane structure has succeeded in the small thermal time constant. The measured voltage responsivity and noise behavior were used to calculate the normalized detectivity which can be used to compare the performance with different kinds of detector. The normalized detectivity D^* is defined as

$$D^* = \frac{R_v}{V_n} \sqrt{A \cdot \Delta f}$$

where V_n is the noise voltage and Δf is the amplifier bandwidth. The frequency dependency of D^* is shown in Fig. 9. The maximum value of D^* was placed at the frequency associated with the thermal time constant because the slope of the R_v in the higher region was larger than that of V_n . The maximum value of D^* was $1.4 \times 10^7 \text{ cmHz}^{1/2} \text{ W}^{-1}$ at 100 Hz. The fundamental characteristics of the fabricated integrated pyroelectric infrared sensor using PVDF thin film deposited by the ESP method is summarized in Table I. The noise equivalent power NEP was defined as

$$\text{NEP} = \frac{V_n}{R_v \sqrt{\Delta f}}$$

Table I: Characteristics of the PVDF infrared sensor.

Sensing Area (μm^2)	400 x 400
PVDF Thickness (μm)	2
Pyroelectric Coefficient ($\text{nCcm}^{-2}\text{K}^{-1}$)	2-4
Responsivity (V/W)	98 (100Hz)
Detectivity ($\text{cmHz}^{1/2}\text{W}^{-1}$)	1.4×10^7 (500,100,1)
NEP ($\text{Hz}^{-1/2}\text{W}$)	2.9×10^{-9} (500,100,1)
Thermal Time Constant (msec)	1.3

SUMMARY

The results of this study are summarized as follows: (1) A PVDF thin film has been deposited on a silicon substrate by an ESP method. The PVDF thin film had a large pyroelectric coefficient without a poling treatment. The pyroelectric coefficient increased with an increase in the ion current monitored during the deposition. For ion currents above $3 \mu\text{A}$, a large pyroelectric coefficient of $4 \text{ nCcm}^{-2}\text{K}^{-1}$ was obtained. (2) A pyroelectric infrared sensor using a PVDF thin film has been integrated with a read-out circuit on a silicon substrate. The PVDF thin film was supported on a thin Si_3N_4 membrane structure formed by etching a part of the silicon substrate under the sensing area. The sensor with a sensing area of $400 \times 400 \mu\text{m}^2$ had a responsivity of 98 V/W, a detectivity of $1.4 \times 10^7 \text{ cmHz}^{1/2}\text{W}^{-1}$, an NEP of $2.9 \times 10^{-9} \text{ Hz}^{-1/2}\text{W}$ at a frequency of 100 Hz and a time constant of 1.3 msec.

The features of the sensor including the structure and the fabrication technique offer considerable advantages in the performance, productivity and realization of an one-chip two-dimensional infrared sensor.

ACKNOWLEDGEMENT

The authors wish to thank Device Development Lab. in Toyota Central R&D Laboratories, Inc. for their help in fabrication of the sensors.

REFERENCES

1. R. Watton *et al.*, SPIE 510 Infrared Technology X, 139 (1984).
2. M. Okuyama *et al.*, Tech. Digest of Transducers'87 (1987).
3. Y. Tomita *et al.*, Tech. Digest of the 8th Sensor Symp., 59 (1989).
4. M. Okuyama *et al.*, Jpn. J. Appl. Phys. Suppl. **21**, 1 (1982).
5. C. Ye *et al.*, Sensors and Actuators A, **35**, 77 (1992).
6. T. L. Cheeks *et al.*, J. Vac. Sci. Technol. **5** (4), Jun/Aug, 1917 (1987).
7. A. J. Lovinger, Jpn. J. Appl. Phys. Suppl. **24**, 2 (1985).
8. W. V. Munch *et al.*, Sensors and Actuators A, **25-27**, 167 (1991).
9. P. C. A. Hammes *et al.*, Sensors and Actuators A, **32**, 396 (1992).
10. A. Lee *et al.*, Thin Solid Films, **181**, 245 (1989).
11. J. Sakata *et al.*, Thin Solid Films, **195**, 175 (1991).
12. T. Takahashi *et al.*, Appl. Phys. Lett. **37** (9), 1 Nov, 791 (1980).
13. M. Suzuki *et al.*, Tech. Digest of the 9th Sensor Symp., 71 (1990).
14. O. Tabata *et al.*, Proc. of the 2nd Int. Symp. on Micro Machine and Human Science, 163 (1991).

PART III

Optoelectronic Devices and Properties

PHOTO-INDUCED AND ELECTROOPTIC PROPERTIES OF $(\text{Pb},\text{La})(\text{Zr},\text{Ti})\text{O}_3$ FILMS

D. DIMOS, W.L. WARREN, and B.A. TUTTLE
Sandia National Laboratories, Albuquerque, NM 87185

ABSTRACT

Photo-induced changes in the hysteresis behavior of sol-gel derived $\text{Pb}(\text{Zr},\text{Ti})\text{O}_3$ (PZT) and $(\text{Pb},\text{La})(\text{Zr},\text{Ti})\text{O}_3$ (PLZT) films have been characterized. The film photosensitivity has been evaluated with respect to the magnitude of the effects, the time response and the spectral dependence. Photo-induced hysteresis changes exhibit a stretched-exponential time dependence, which implies a dispersive mechanism. The spectral dependence is strongly peaked at the band edge (~ 3.4 eV), which indicates that generation of electron-hole pairs in the material is critical. The photo-induced hysteresis changes are reproducible and stable, which indicates that the controlling charge traps are stable. However, improvements in film photosensitivity will be required to develop these materials for optical memory applications.

INTRODUCTION

There is an increasing demand today for devices capable of storing and processing large quantities of optical information, including random-access optical memories, image comparators, and spatial light modulators (SLMs). Ferroelectric thin films, especially those based on PLZT solid solutions, exhibit photoferroelectric and electrooptic responses that make them good candidate materials for many optical-information storage, display and processing applications [1-5]. To store optically-generated information, light is used, in possible combination with an applied bias, to locally change the polarization state of the film. For optical readout, the polarization-dependent birefringence can be used to modulate the reflected (or transmitted) light intensity.

There have been many studies of electrooptic responses in PZT and PLZT films, which show that thin-film electrooptic properties are comparable to PLZT ceramics of similar compositions. Furthermore, the size of the electrooptic effects in films should be sufficient for optical readout with good signal-to-noise, especially if enhanced by using suitable etalon techniques [6]. In addition, photo-induced effects for optical storage have been extensively studied in PLZT ceramics [7-10]; however, relatively little has been reported about comparable effects in ferroelectric films [11-12]. Consequently, photo-induced responses in PZT and PLZT films have been studied with an emphasis on optical-information storage applications.

In this paper, photo-induced changes in the hysteresis behavior of sol-gel derived PZT and PLZT films are reported for various compositions, substrate types, and electrode materials. The various types of photo-induced effects and their magnitudes are discussed. An initial evaluation of the photosensitivity with respect to the time response and the spectral dependence is also presented. Since the photo-induced responses are intimately related to charge trapping, electron paramagnetic resonance (EPR) has been used to examine photo-induced charge traps. All of these studies provide important information about the photoferroelectric mechanisms in PLZT films and give a starting point for considering device performance.

EXPERIMENTAL

PZT and PLZT films were fabricated by spin coating using a metal alkoxide solution; the precursors were lead (IV) acetate, lanthanum acetate, zirconium butoxide butanol, and titanium isopropoxide. A comprehensive description of the procedure has been previously published [13,14]. The desired film thickness was achieved by depositing multiple layers. After each layer was deposited, a 300°C bake was used to drive off volatile organics. Both oxidized silicon wafers and MgO single crystals were used as substrates. The base electrode was either Pt or RuO_x ($x \leq 2$), which gave four different substrate types: Pt/Ti/SiO₂/Si, RuO_x/Ti/SiO₂/Si, Pt/MgO, and RuO_x/Ti/MgO; the Ti layer was to promote adhesion. For the Pt/MgO samples, the Pt was deposited at approximately 600°C to achieve a high degree of [100] orientation. The films on Si substrates were fired at 650°C for about 30 min. The films on MgO substrates were processed using rapid thermal annealing to 650°C; a highly-oriented [001] PZT film was obtained with the oriented Pt electrode. Both procedures yielded films that were essentially single-phase perovskite and had columnar microstructures with a lateral grain size of 100-150 nm. Films in excess of 500 nm thick were prepared by firing after every 4 layers to avoid cracking during densification.

Top electrodes (1-3 mm diameter) were sputter deposited to establish a parallel-plate capacitor geometry. To allow investigation of photo-induced effects, optically-transparent indium tin oxide (ITO) or thin, semi-transparent metal films were used for the top electrodes. A 10 nm thick Pt film was typically used for the top electrode, since Pt gave the most reproducible electrical properties; however, thin Au (10 nm), RuO_x (20 nm), and ITO (150 nm) electrodes were also used for comparison.

Hysteresis loops for the films were measured using the Radiant Technologies RT-66A tester. A 200 W Oriel Hg arc lamp in combination with narrow band interference filters was used to generate light at 336, 365, 404, and 436 nm. An argon ion laser was used to produce 457 nm illumination. The illumination intensity was adjusted using neutral density filters. An Ealing optical shutter, which also triggered a voltage supply, was used to control the exposure time. The EPR measurements were made on an X-band Bruker ESP-300E spectrometer at 25K. An optical-access microwave cavity was used for in-situ illumination experiments. Accurate g factors were determined by a frequency counter and an NMR Gaussmeter.

RESULTS

PHOTO-INDUCED EFFECTS

There are two primary phenomena exhibited by PZT and PLZT films that can be used to store optically-generated information. The first type of photo-induced effect common to all PZT and PLZT films studied is illustrated in Fig. 1. The sample for Fig. 1 is an 810 thick Pb(Zr_{0.53}Ti_{0.47})O₃ (PZT 53/47) film on Pt/Ti/SiO₂/Si. To examine the effect of illumination, the electroded region is initially poled to negative remanence, $-P_r$, where the bottom electrode is at ground with respect to the top electrode. The capacitor is then illuminated with band-gap light (365 nm) through a semi-transparent (12 nm thick) Pt top electrode and biased at +2.5 V, which is near the switching threshold. After a 10 sec exposure with bias, the hysteresis response (solid line) has been altered to exhibit both a clear suppression in the switchable polarization and a noticeable change in the coercive voltage, V_c . The solid curve, which is the new steady-state response, is obtained following several post-illumination hysteresis cycles. This procedure is used because some recovery of the dynamic polarization range, ΔP_s , occurs during the first few

cycles. The change in remanent polarization from the unilluminated to the illuminated response, which is most apparent for this sample at $-P_r$, can be the basis of an optical storage device. The reduction in the value of ΔP_s can be regarded as a photo-induced analog of fatigue. A photo-induced fatigue effect similar to that seen in the thin-film samples is also observed when storing optical images in bulk-ceramic samples of PLZT [9,15].

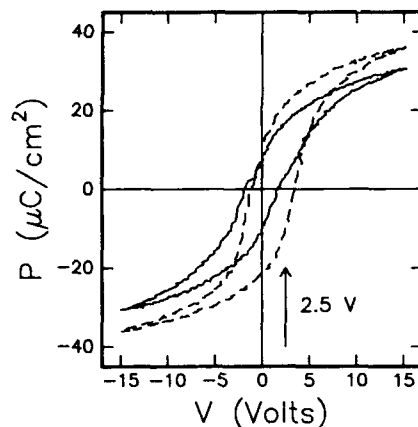


Figure 1. Photo-induced suppression of ΔP by partial switching. PZT 53/47 (810 nm) film on Pt/Ti/SiO₂/Si. ---- initial response. — loop after optical writing. $V = +2.5$ V, $t = 10$ sec, $\lambda = 365$ nm, $I = 25$ mW/cm².

The compressed loops have been positioned on the polarization axis to reflect a symmetric suppression of the switchable polarization about $P=0$. A fairly symmetric reduction of ΔP_s has been demonstrated using an electrooptic technique to determine the absolute polarization [15]. The position of the compressed thin-film loops contrasts the behavior observed in PLZT bulk ceramics, where the photo-induced reduction in ΔP is very asymmetric [9,15]. The amount by which ΔP_s and ΔP_r are suppressed is a sensitive function of bias voltage and is maximized by partially switching the material with a bias just below V_c . The initial hysteresis response can be restored by illuminating the sample with a saturating bias of the opposite sign ($-V_s$). Some recovery of ΔP_s (ΔP_r) also occurs due to illumination at $+V_s$, but the restoration is typically incomplete.

The other phenomenon exhibited by all films is a photo-induced shift of the hysteresis loop along the voltage axis, as illustrated in Fig. 2. The sample in this case is a PLZT 6/20/80 (6 at % La) on Pt/Ti/SiO₂/Si. The two curves for $+V_s$ and $-V_s$ were obtained after biasing the sample at $+15$ V and -15 V, respectively, with concurrent band-gap illumination. This translation of the hysteresis loop implies that a photo-induced, space-charge field has been introduced into the film. The two states produced with the saturating voltages are stable and reproducible end-point states. A pure voltage shift, without optical fatigue, is observed for biases that cause complete switching in contrast to the behavior seen in Fig. 1, which is observed for biases that lead only to partial switching. The magnitude of the maximum shift in coercive voltage, ΔV_c , was measured for a variety of film thicknesses, compositions, electrode materials, and substrate type. It was found that the value of ΔV_c increased with increasing thickness and that for

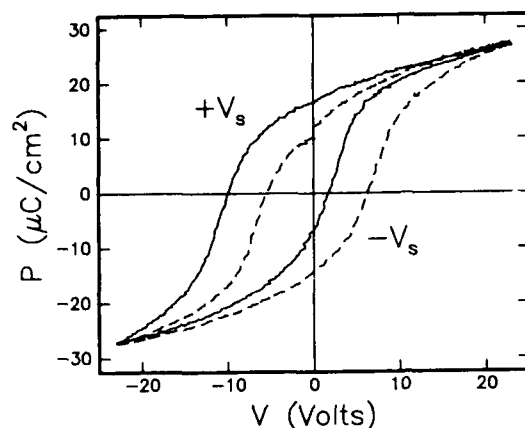


Figure 2. Photo-induced voltage shift indicating the presence of a space-charge field. PLZT 6/20/80 film ($1.06 \mu\text{m}$) on Pt/Ti/SiO₂/Si. --- $-V_s$ (-15 V). — $+V_s$ ($+15 \text{ V}$). $\lambda = 365 \text{ nm}$, $I = 25 \text{ mW/cm}^2$, 20 sec .

a given thickness range, its value did not depend strongly on film composition, electrode material, or substrate type.

Films with relatively square hysteresis loops were used to examine the dependence of the photo-induced voltage shift on the polarization state, as illustrated in Fig. 3. This sample is a 420 nm thick PZT 40/60 film on Pt/MgO. A fairly square hysteresis loop is obtained since the film is both highly oriented and compressively stressed, due to the thermal expansion mismatch with the substrate [16,17]. The loops associated with the two saturating bias states ($+V_s$, $-V_s$) are shown. In addition, Fig. 3 shows the loop obtained after a sample which displayed the $-V_s$ behavior was switched to $+P_r$ and then illuminated at zero bias. The hysteresis loop obtained this way is almost identical to that obtained with a positive saturating bias and light. This result shows that the voltage shift is a direct consequence of the polarization state of the material rather than being a direct function

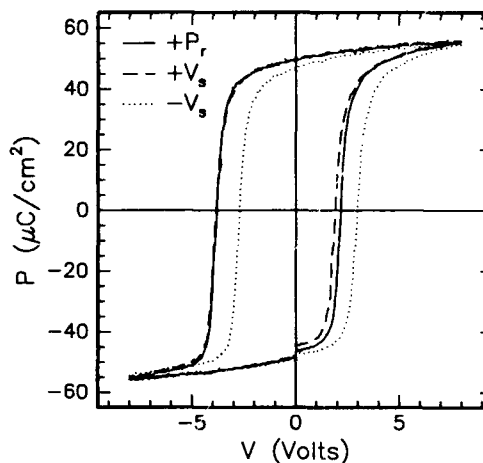


Figure 3. Photo-induced voltage shift for $+P_r$, $+V_s$, $-V_s$. PZT 40/60 film on Pt/MgO (420 nm). $|V_s| = 7 \text{ V}$, $\lambda = 365 \text{ nm}$, $I = 25 \text{ mW/cm}^2$, $t = 20 \text{ sec}$.

of the applied bias. This conclusion is consistent with the observation that the value of ΔV_c does not increase with increasing bias as long as the bias is sufficient to cause complete switching.

KINETIC RESPONSE

Evaluating the time dependence of the photo-induced effects yields mechanistic information and is critical when considering possible device performance. The kinetic response of the voltage-shift effect previously described (Figs. 2 & 3) was determined by measuring the change in coercive voltage obtained when switching from one end-point state to the other as a function of exposure time. Figure 4 illustrates a typical result, which was obtained for a 780 nm thick PZT 40/60 film on oriented Pt/MgO. For each measurement, the sample capacitor was first switched to the negative end-point state using 365 nm light and a bias of -9V applied for 30 sec. Several hysteresis loops were then run to allow for some recovery and to make sure that the initial response was always the same. The 365 nm light and a bias of +9V were then applied concurrently for different periods of time. Finally, several hysteresis loops were run to determine ΔV_c .

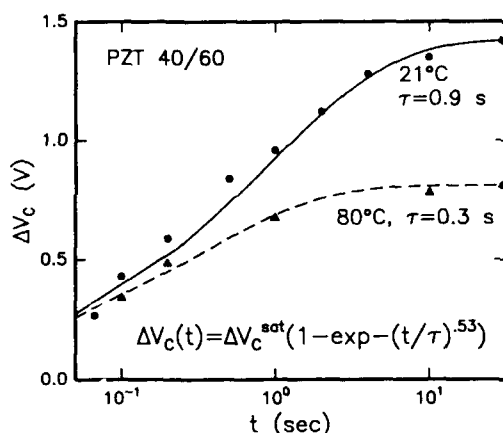


Figure 4. Voltage shift as a function of exposure time for a PZT (40/60) film (780 nm) on Pt/MgO. $\lambda = 365$ nm, $I = 25$ mW/cm². The lines are fits to the stretched exponential function (Eq. 1).

In general, the voltage-shift kinetics follow a stretched-exponential function of the form,

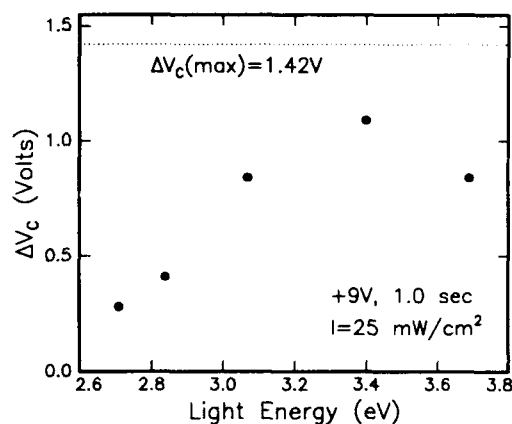
$$\Delta V_c(t) = \Delta V_c^{\text{sat}} [1 - \exp(-(t/\tau)^\beta)] \quad (1)$$

The stretched-exponential dependence is indicative of a dispersive mechanism. Both the stretching parameter, β , and the relaxation time, τ , vary somewhat for different samples; τ is also a function of temperature, illumination wavelength, and light intensity. For the conditions used in Fig. 4 ($T = 21^\circ\text{C}$, $\lambda = 365$ nm, and $J = 25$ mW/cm²), the stretching parameter had a value of $\beta = 0.53$ and a relaxation time of $\tau = 0.9$ sec. The relaxation time decreased to $\tau = 0.3$ sec by increasing the temperature to 80°C . The relaxation time also exhibited a sublinear dependence on the light intensity over the range of 5-25 mW/cm². The complete time dependence for the optical-fatigue effect was not characterized; however, a relaxation time of ~ 1 sec is consistent with observations.

SPECTRAL RESPONSE

Another critical aspect of the photosensitivity is the spectral dependence. The spectral dependence of the voltage-shift effect has been evaluated by measuring the value of ΔV_c obtained during a 1 sec exposure with bias using a fixed light intensity. Figure 5 shows a typical result obtained with the 780 nm thick PZT 40/60 film; the writing bias was +9V and the intensity was 25 mW/cm². The maximum coercive voltage shift, $\Delta V_c(\text{max}) = 1.42$ V, is obtainable for all five wavelengths given enough time. Therefore, the peak response at 365 nm is equivalent to a minimum in the relaxation time. The main point is that the intrinsic photosensitivity decreases dramatically as a function of energy below the band edge (~3.4 eV).

Figure 5. Voltage shift as a function of illumination energy for a 1 sec exposure. $I = 25 \text{ mW/cm}^2$, $V_s = 9\text{V}$.



DISCUSSION

The photo-induced changes in hysteresis can be qualitatively accounted for by considering the interaction between internal fields due to the polarization charge and photo-generated carriers. Initially, the situation that occurs due to a saturating bias will be considered. A reasonable domain configuration for an unoriented, columnar film that has been completely switched is schematically depicted in Fig. 6. The arrow head represents the positive terminating end of the spontaneous dipole. The internal charge separation gives rise to a strong depolarizing field. Charge redistribution in the external circuit acts to compensate the polarization charge and, thus, reduce the depolarizing field. However, this charge compensation is typically incomplete. Illuminating the ferroelectric with band-gap light generates electron-hole pairs. The internal depolarizing field acts as a bias to redistribute the photo-generated carriers (+, -), as illustrated. Significant charge redistribution is evidenced by the appearance of a transient photocurrent upon illumination. Trapping of this charge stabilizes the present domain configuration over the oppositely oriented one, which is equivalent to introducing a space-charge field, as shown. This space-charge field leads to the observed voltage shift of the hysteresis loop.

Since the principal polarization discontinuity occurs at the top and bottom electrode interfaces, the internal compensating charge will be trapped near these interfaces. By assuming that essentially all the trapped

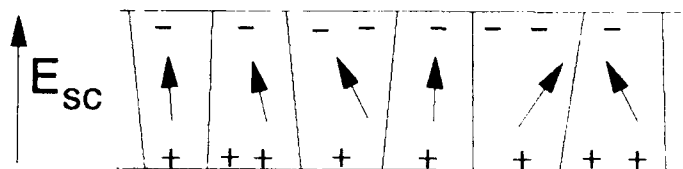


Figure 6. Schematic diagram showing the dipole orientation due to a saturating bias and the internal compensating charge.

charge is at or near the interfaces, ΔV_c is approximately given by,

$$\Delta V_c = (Q_+(\text{bottom}) + Q_-(\text{top})) * t / \epsilon \epsilon_0, \quad (2)$$

where Q is the charge/unit area and t is the film thickness. For comparable films, the value of ΔV_c is expected to increase linearly with thickness, which has been experimentally observed [15]. Equation 2 can then be used to calculate the effective charge/unit area. For the 780 nm thick PZT 40/60 sample on MgO, $\Delta V_c = 1.42$ V and $\epsilon = 1000$. Assuming $Q_+ = Q_-$, then the effective density of trapped charge near each interface is roughly $5 \times 10^{12}/\text{cm}^2$, which is less than 0.1% of the available sites. However, it should also be noted that even though Eq. 2 assumes trapping of both electrons and holes, the phenomenon observed can be sufficiently explained by trapping of primarily one charged species.

The photo-induced fatigue of Fig. 1 can be accounted for by considering the situation that occurs due to partial switching at intermediate biases. Figure 7 depicts a possible domain configuration for a sample with a macroscopic remanent polarization of roughly zero. Photo-generated charge accumulates at domain boundaries with a large polarization discontinuity. This trapped charge inhibits these domains from reorienting. By "locking" the orientation of certain domains, the switchable polarization is reduced.

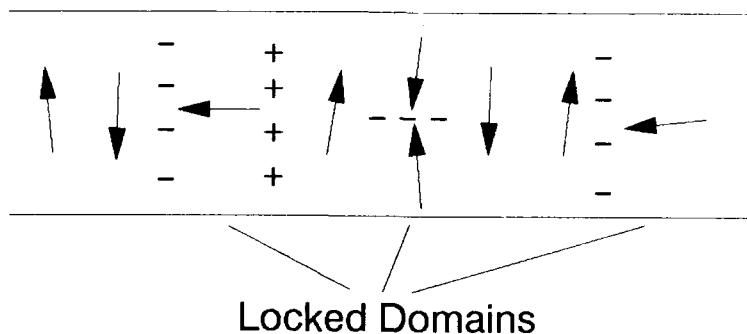


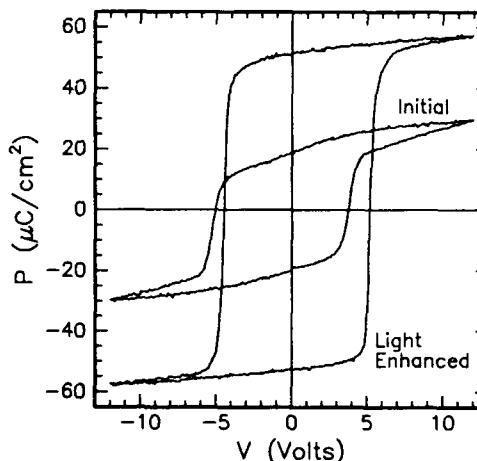
Figure 7. Schematic diagram showing a possible domain configuration for $P \approx 0$ and the trapped, compensating charge at domain boundaries.

In addition, illumination may allow domain configurations to be established which would ordinarily be unachievable. For example, the head-to-head domain orientation, which may be possible in thicker films, would normally be energetically unfavorable. However, this configuration would be stabilized by trapped electrons, as shown.

Restoration of the suppressed loop requires near-band-gap illumination to generate new carriers, which can recombine with the trapped charge, and an applied bias to reorient the previously locked domains. An alternative approach would have been to use sub-band-gap illumination to photo-excite the trapped charge out of the trapping centers. Since this approach has not worked, the gap states created by the trapped charge evidently have no optical cross-section. This observation is also consistent with the previously discussed drop in efficiency for the photo-induced effects at wavelengths much below the band edge.

A photo-induced improvement in the initial hysteresis response of films has also been commonly observed. Our most dramatic example of this behavior, which was obtained on the previously described 780 nm thick PZT 40/60 on Pt/MgO, is illustrated in Fig. 8. The initial hysteresis loop of a typical capacitor exhibited low values for P_r and P_s compared to the anticipated response for a highly-oriented, compressed film. Improvement to the light-enhanced loop was achieved with band-gap light and a bias of -8 V for 20 sec. The observation of a photo-induced improvement in hysteresis suggests the presence of processing-induced trapped charge in films. The presence of a large amount of trapped charge in this PZT 40/60 sample was not unreasonable since it was fabricated by rapid thermal annealing using quartz lamps. In addition, this sample, which was annealed twice, displayed a much bigger improvement in the hysteresis than a similar, but thinner sample, which required only one anneal. This difference may be due to the internal interface formed by the initial firing of the thicker film, which could provide an excellent location for charge trapping.

Figure 8. Light-enhanced improvement of the initial hysteresis behavior of a PZT 40/60 film on Pt/MgO.
 $\lambda = 365$ nm, $I = 25$ mW/cm²,
 $V = -8$ V, 20 sec.



The time response may be controlled by the carrier mobility or the charge-trapping kinetics. If charge migration is rate limiting, the stretched exponential behavior indicates a dispersive transport mechanism. The hole mobility is anticipated to be relatively low due to an abundance of shallow hole traps [18,19]. Alternatively, the trapping kinetics of one or both carrier types into the deeper, more stable traps may be rate limiting for optical storage. In either case, the stretched-exponential kinetics implies a distribution of trapping energies.

The nature of the charge traps have been investigated because of the critical role they play in the photo-induced effects for optical storage. EPR measurements have been done on hot-pressed, ceramic samples of PLZT 7/65/35 [20] and on sol-gel derived powders of various compositions [21]. With band-gap illumination, two-types of charged defects are produced. These defects have been identified as Pb^{3+} and Ti^{3+} [20], as illustrated in Fig. 9b, which is the EPR spectrum for a UV-illuminated PZT 7/65/35 ceramic plate. The Pb^{3+} center is a hole trapped at a Pb^{2+} site; this trapping center is shallow and hence metastable at room temperature [19]. The Ti^{3+} center is an electron trapped at a Ti^{4+} site. Although the Ti^{3+} center is not observed for all samples, the Pb^{3+} center is found for all compositions. It is interesting to note that the creation kinetics of these EPR centers also follows a stretched-exponential function, with a stretching parameter (β) similar to that obtained for the voltage-shift kinetics. This similarity may suggest that both phenomenon are controlled by a common process, such as dispersive carrier transport.

However, there is no obvious relationship between these traps centers and the optical storage effects. Both the Pb^{3+} and the Ti^{3+} centers are easily photo-bleached for a range of sub-band-gap wavelengths, as shown in Fig. 7c for a light energy of 2.3 eV. However, photobleaching of these defect centers does not effect the hysteresis loops. Consequently, these

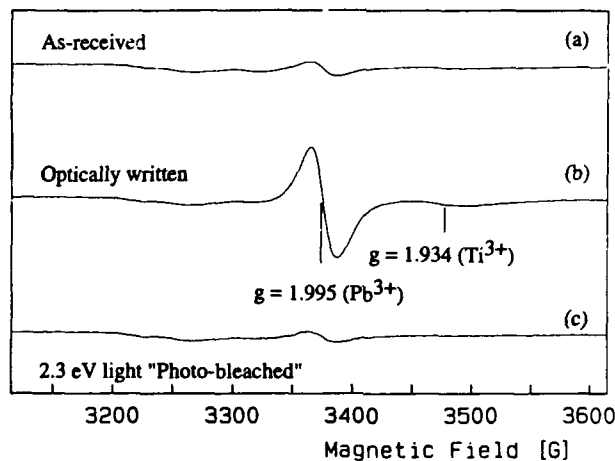


Figure 9. EPR spectra for a PLZT 7/65/35 transparent ceramic sample. The optically written state corresponds to illumination with 365 nm light.

traps can not be the stable ones which control the photo-induced hysteresis changes, which makes sense since they are shallow traps. The lack of any other paramagnetic centers suggest that charges may be trapped as pairs. This situation occurs in systems where the pair trapping is stabilized by a lattice relaxation [22-24]. While it is possible to speculate about the role of various deep defect centers, such as lead vacancies, the critical trapping sites for optical storage effects have not been identified. It is also important to emphasize that the behavior of defects in bulk and powder samples is expected to be the same as for thin films.

CONSIDERATIONS FOR OPTICAL STORAGE DEVICES

The primary requirement for an optical memory or optically-addressable device, such as an SLM, is that light can be used to produce a discernable change in the state of the material. Both types of photo-induced hysteresis changes observed in PLZT films are large and reproducible enough to provide the basis for an optical memory technology. A simple operational scheme for a digital optical memory is illustrated in Fig. 10. Initially the entire sample is reset to the positive curve (+) by switching to $+P_r$ and illuminating. The film is then electrically switched to $-P_r$ with no light. Individual bits are switched to the negative curve (-) by illuminating them one at a time; this procedure allows the bits to be completely defined by the optical addressing process. However, both the illuminated and unilluminated bits are still at $-P_r$. To read the stored information, a bias is applied that partially switches the (+) bits while leaving the (-) bits at $-P_r$. In this case, a pulse of 3.7 V switches the (+) bits to $P_r = 0$. This step illustrates the advantage of having a material with a sharp switching threshold. A longer wavelength laser with polarizing optics can be used to differentiate these two states based on the electrooptic response of the material. Since these films exhibit an electrooptic response which is roughly quadratic with respect to polarization ($\Gamma \propto P^2$) [6], the two

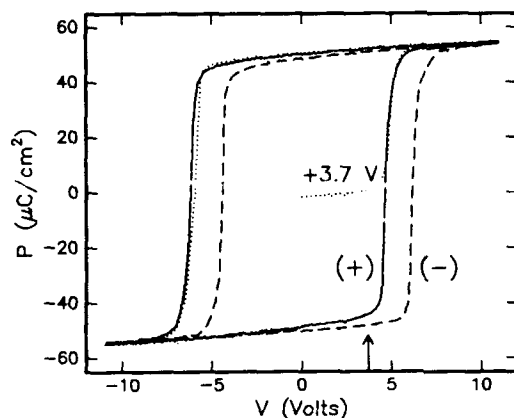


Figure 10. Photo-induced hysteresis response for operation of an optical memory. The arrow corresponds to 3.7 V, which switches the (+) state bits to $P_r = 0$.

desireable end-point states are $P_r = |P_r(\max)|$ and $P_r = 0$. Selective erasure can be accomplished by electrically switching the film to $+P_r$ and illuminating the bits to be reset, which puts them back on the (+) curve.

While a few different operational mechanisms could be implemented to make a working optical memory using PZT or PLZT films, a number of issues

need to be addressed to produce a competitive technology. To compete with existing hard disk technologies, the time response for writing information needs to be improved by roughly two orders of magnitude. Consequently, it is critical to determine the rate-limiting process and to develop strategies for modifying the response time. An optical-memory medium should also be compatible with solid-state lasers ($\lambda = 700\text{-}800\text{ nm}$). Significant improvements in the photosensitivity at longer wavelengths can be anticipated based on the improvements achieved in PLZT ceramics by ion implantation [25]. For high-density optical memories, the minimum bit size needs to be evaluated. The bit resolution may depend on both the grain size and the lateral spreading of photo-induced carriers. Finally, the issues common to ferroelectric nonvolatile memories, such as long-term retention, fatigue, and polarization-state imprinting, need to be considered in relation to an optically-addressed, optically-read memory.

CONCLUSIONS

Two different photo-induced changes in hysteresis behavior have been characterized in PZT and PLZT films. The observed effects are controlled by the trapping of charge at the near surface region or at internal domain boundaries. Charge is trapped in very stable centers, which display no paramagnetic signature and, thus, have not yet been identified. A photo-induced improvement in initial hysteresis behavior also demonstrates the presence of processing-induced space charge. The photo-induced voltage shift exhibits a stretched-exponential time dependence, which implies a dispersive mechanism. The relaxation times improve with increasing intensity and increasing temperature, but remain fairly long ($\tau > 0.1\text{ sec}$).

Both of the observed photo-induced hysteresis changes could be used to devise a working optical memory; however, there are many issues that need to be resolved to develop a competitive technology. First, the photosensitivity needs to be significantly improved with respect to both the time and spectral dependence. Improvements in the intrinsic photosensitivity of films can be anticipated from chemical doping or ion implantation. Confirming these anticipated improvements will be critical to the development of ferroelectric film optical memories. Second, the minimum bit size needs to be evaluated as compared to the diffraction limit. Third, issues common to ferroelectric memories, such as long-term retention, fatigue, and polarization-state imprinting, need to be considered in relation to an optically-addressed, optically-read memory.

ACKNOWLEDGEMENTS

This work was supported by the Office of Naval Research and the U.S. Department of Energy under contract DE-AC04-76DP00789. The authors would like to acknowledge C.H. Seager, R.W. Schwartz, and J.A. Bullington for helpful discussions and thank D. Goodnow and J. Kubas for technical assistance.

REFERENCES

1. B.A. Tuttle, MRS Bull., 12, [5], 40 (1987).
2. A.R. Tanguay, Opt. Eng., 24, [1], 2 (1985).
3. C.E. Land, Ceram. Trans., 11, 343 (1990).
4. A. Ersen, S. Krishnakumar, V. Oztuz, J. Wang, C. Fan, S. Esener, and S.H. Lee, Appl. Opt., 31, 3950 (1992).
5. S.J. Martin, M.A. Butler, C.E. Land, Elec. Lett., 24, 1486 (1988).
6. D. Dimos, C.E. Land, and R.W. Schwartz, Ceram. Trans., 25, 323 (1992).
7. C.E. Land and P.S. Peercy, Ferroelectrics, 22, 677 (1978).
8. J.W. Burgess, R.J. Hurditch, C.J. Kirkby, and G.E. Scrivener, Appl. Opt., 15, 1550 (1976).
9. P.J. Chen and C.E. Land, J. Appl. Phys., 51, 4961 (1980).
10. C.E. Land, J. Am. Ceram. Soc., 71, 905 (1988).
11. D. Dimos and R.W. Schwartz, Mat. Res. Soc. Symp. Proc., 243, 73 (1992).
12. C.E. Land, J. Am. Ceram. Soc., 72, 2059 (1989).
13. R.W. Schwartz, B.C. Bunker, D. Dimos, R.A. Assink, B.A. Tuttle, D.R. Tallant, and I.A. Weinstock, Int. Ferroelectrics, 2, 243 (1992).
14. R.A. Assink and R.W. Schwartz, Chem. of Mater., Accepted for publication (1993).
15. D. Dimos, W.L. Warren, C.H. Seager, B.A. Tuttle, and R.W. Schwartz, submitted to J. Appl. Phys.
16. B.A. Tuttle, J.A. Voigt, T.J. Garino, D.C. Goodnow, R.W. Schwartz, D.L. Lamppa, T.J. Headley, and M.O. Eatough, Proc. of the 8th IEEE ISAF '92, 344.
17. B.A. Tuttle, J.A. Voigt, and T.J. Headley, accepted for publication J. Am. Ceram. Soc., 76, (1993).
18. V.V. Prisedsky, V.I. Shishkovsky, V.V. Klimov, Ferroelectrics, 17, 469 (1978).
19. J. Robertson, W.L. Warren, D. Dimos, B.A. Tuttle, and D.M. Smyth, submitted to Appl. Phys. Lett.
20. W.L. Warren, C.H. Seager, D. Dimos, and E.J. Friebele, Appl. Phys. Lett., 61, 2530 (1992).
21. W.L. Warren, B.A. Tuttle, P.J. McWhorter, F.C. Rong, and E.H. Poindexter, Appl. Phys. Lett., 62, 482 (1993).
22. W.L. Warren, J. Kanicki, F.C. Rong, E.H. Poindexter, and P.J. McWhorter, Appl. Phys. Lett., 61, 216 (1992).
23. R.A. Street and N.F. Mott, Phys. Rev. Lett., 35, 1293 (1975).
24. P.W. Anderson, Phys. Rev. Lett., 34, 953 (1975).
25. C.E. Land and P.S. Peercy, Ferroelectrics, 45, 25 (1982).

THE APPLICATION OF OPTICAL INTERFEROMETRY TO THE STUDY OF FIELD-INDUCED EFFECTS IN BULK AND THIN FILM FERROELECTRICS

KEITH L LEWIS AND KATHLEEN F DEXTER

Defence Research Agency, St Andrews Road, Malvern, Worcs. WR14 3PS, UK

ABSTRACT

A study is reported of field-induced effects in ferroelectric materials using optical interferometry. One of the techniques used is based on the use of a WYKO TOPO3 system and provides a three dimensional representation of field-induced displacement. The information provided is supplemented by optical transmission measurements on thin sections of material fabricated to allow interference fringing to be seen. Initial work has centred on the characterisation of ceramic PLZT material. Both transverse and longitudinal electrode configurations have been studied and have highlighted the magnitude of the effects possible and the importance of electrostrictive processes in determining the direction of deformation. These can result in anomalously high strain gradients over distances of the order of 50-100µm. This behaviour is compared with that found for preliminary samples of thin film ferroelectric materials.

1 INTRODUCTION

Significant interest is currently being shown in the exploitation of ferroelectric materials for a wide variety of applications, including microactuators, microsensors, miniature valves, micromotors, dynamic memory devices, optical modulators etc. The performance levels achievable are controlled by fundamental electro-elastic and electrostrictive processes, and ultimately by the properties of microscopic polar domains in the material. Thin film ferroelectric materials also exhibit effects that are significantly smaller than those encountered in the corresponding bulk material [1], [5]. The nature of this difference is currently of concern, particularly in the case of devices being developed for optical applications. In addition, fatigue effects in devices used for capacitor or memory devices may well be related to the high levels of strain introduced by the applied field. As a necessary prerequisite to the understanding and identification of the various effects possible in such materials, a study has been carried out of the changes in surface topography and/or optical constants in various device geometries as a function of applied field using optical interferometry.

2 EXPERIMENTAL

The interferometric measurements have been carried out using a WYKO TOPO3 system. This is best suited to the study of small spatial regions (ca 1000µm square) and has an ultimate spatial resolution of 0.3µm. It has been supplemented by optical reflection and transmission measurements on thin sections of material fabricated to allow interference fringing to be seen. The WYKO system comprises a phase shifting interferometer designed around a highly stable optical microscope. Light reflected from the object being measured interferes with light reflected from an internal reference surface, which can be moved by a PZT translator. The shifting fringe patterns are recorded by a CCD array and interpreted by a dedicated computer to provide a topographic representation of the surface. The work described here exploits the use of the instrument in a differential mode, in which an image is produced by digital subtraction of two optical phase arrays. The first is that of the device surface under zero bias, whilst the second is that of the same device area under the influence of an applied DC field.

Material has been examined using both transverse and longitudinal electrode geometries. The two electrode configurations are shown in the figure 1. Initial measurements were made using a thinned wafer of ceramic (9.65,35) PLZT. This material is typical of that used for electro-optic modulator applications, with a composition near the ferroelectric-antiferroelectric phase boundary. Surface electrodes were deposited by thermal evaporation (for aluminium) or by RF magnetron sputtering (for indium-tin oxide), using contact masks as appropriate to the device geometry required.

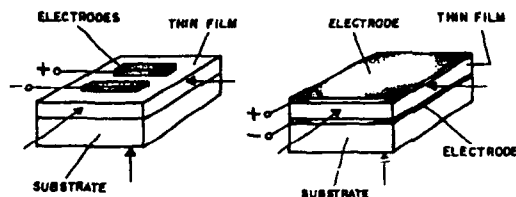


Figure 1 Schematic diagram showing transverse and longitudinal electrode configurations.

The expected deformation modes for the transverse case are shown in figure 2, which highlights the variation in optical indicatrix produced as a result of the applied field.

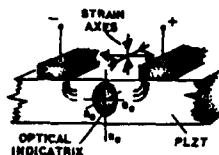


Figure 2 Schematic diagram showing deformation modes in an electrostrictive materials such as PLZT

The dominant strain effect to be expected is the expansion of material along a direction parallel to the applied field, with an accompanying contraction in a direction perpendicular to the field. The respective deformation modes are d_{33} and d_{31} respectively. The refractive index would be expected to increase along the axis perpendicular to the field, resulting for example in a phase shift which could be exploited in a resonant filter design. The anisotropy in refractive index gives rise to a birefringence which can be seen by examining the sample between crossed polarisers oriented at 45° to the axis of the electrodes. The situation is reversed in the longitudinal case, where the dominant strain axis is now perpendicular to the plane of the PLZT wafer. The applied field causes a dilatational effect, but the refractive index of the material is reduced correspondingly.

Deformation processes found in regions of the material close to surface electrodes may well be significantly different to those described above. The field intensity in such regions is high, with a component varying in direction away from the conductor. This can give rise to localised regions of high strain which could enhance or detract from the net optical phase change produced.

3 FREE STANDING BULK PLZT

The measured deformation across a $240\mu\text{m}$ wide transverse electrode gap formed on a $300\mu\text{m}$ thick free-standing PLZT wafer is as shown in figure 3. The plot shows the net differential effect of the field at the ends of the electrode and is obtained by digital subtraction of the two optical phase arrays, before and after application of the field. The dominant effect is an upward displacement of the electrodes, with a net downward shift of the PLZT in the gap itself. These relative displacements are clearly seen in comparison with the flat reference surface of unbiased material provided towards the rear of the area examined. The polarity of the field does not affect the direction of deformation. A line-scan along the surface of the PLZT (figure 4(a)), running along the $738\mu\text{m}$ mesh line from the unbiased region at the rear of

the scanned area towards the material present between the electrodes, clearly shows the contraction produced in the PLZT as a result of the field. The variation of PLZT displacement with applied voltage (figure 4(b)) clearly indicates quadratic behaviour. Upward movement of the electrode is largely a result of the vertical orientation of the field lines immediately below the surface. The displacement is also enhanced by processes of material deformation accompanying the transverse dilation of PLZT within the gap.

The high strain produced at the edge of the electrodes can cause cracking of the PLZT at high levels of applied field. This effect is often preceded by delamination of the electrode, usually starting at one end and running along the gap with a wave-like motion.

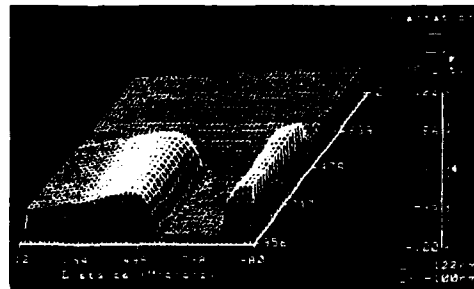


Figure 3 Displacement (in nm) measured by non-contact optical interferometry across the end of a 240 μm wide transverse electrode gap at a field of 2.5 V/ μm .

The effect of material clamping can be important. The displacement shown in figures 3 and 4 was measured for a free PLZT wafer, but the shift of interferometric fringes with application of field also indicated a deformation of the wafer in a bending mode. This results from the fact that the field is non-uniform throughout the thickness of the wafer, with material at the top of the wafer, near the electrodes, expanding further than that at the bottom, where significant electrical shielding occurs. The radius of curvature produced is very large (1-2 metres) but can be compensated for during the digital subtraction of the optical phase fields.

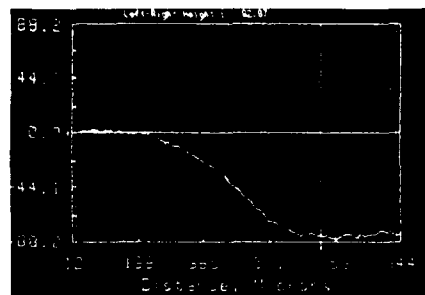


Figure 4(a) Line scan of the surface of the PLZT shown in figure 1, running in a direction parallel to the electrodes. The region to the left of the cursor has no field applied, whilst that to the right of the cursor is influenced by a field of 2.5 V/ μm .

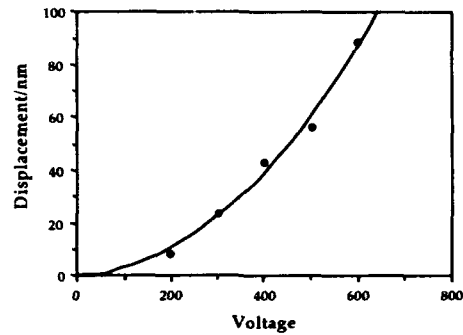


Figure 4(b) Variation of PLZT displacement with applied voltage

4 BULK PLZT WAFER BONDED TO A RIGID SUBSTRATE

Since the magnitude of d_{33} is greater than that of d_{31} , it would be expected that the highest sensitivity to applied field would be obtained for longitudinal device configurations. To assess the feasibility of this, a simple Fabry-Perot etalon was constructed by cementing a wafer of PLZT to an ITO-coated glass substrate, and thinning the PLZT by lapping and polishing to achieve a cavity thickness of about $80\mu\text{m}$. The top of the PLZT was then coated with ITO and the device assessed in reflection, utilising the residual Fresnel reflection losses at the PLZT/air interface to form the boundary of the resonant cavity (figure 5).

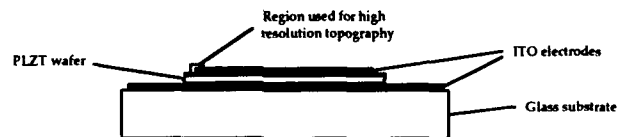


Figure 5 Schematic diagram showing configuration of simple etalon

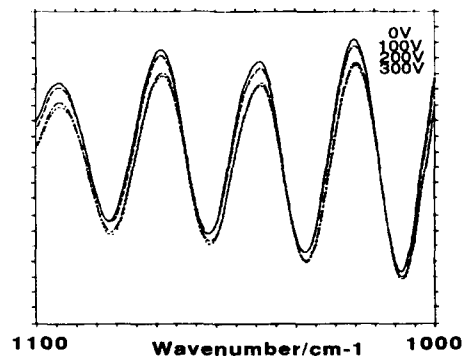


Figure 6 Variation in optical reflectivity produced by longitudinal application of electric field to thinned ceramic PLZT wafer.

The variation in reflectance of such a device, measured at wavelengths near $10\mu\text{m}$ is shown in figure 6. This shows that very little optical phase change is produced, although there is significant change in amplitude of the interference bands formed by the resonant cavity.

The implication is that the effect of dilation produced by the d_{33} mode is almost exactly balanced by the reduction in refractive index produced. The fall in amplitude of the interference fringing shown in figure 6 certainly implies a refractive index grading effect with a reduction in refractive index in a region close to the surface electrodes, presumably as a result of space-charge effects. An attempt has been made to explore the origin of these effects in more detail, by examining the region close to the edge of the upper surface electrode shown in figure 5 using the WYKO interferometer. The deformation measured at an applied field of only $0.8\text{V}/\mu\text{m}$ is shown in figure 7. As in the case of figures 3 and 4, this plot shows the differential effect of applying the field and at high resolution clearly shows the effect of fringing fields and field non-uniformity, with an upward displacement of the edge of the electrode and associated downward displacement of the adjacent PLZT which has no field applied to it. Some hysteresis is apparent, with indications of quadratic behaviour as shown in figure 8.

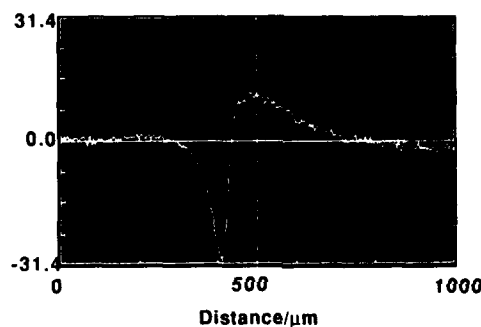


Figure 7 Deformation produced at the edge of the upper ITO electrode shown in figure 5. The position of the edge of the electrode is at $450\mu\text{m}$ and it extends to the right hand side of the plot from that point.

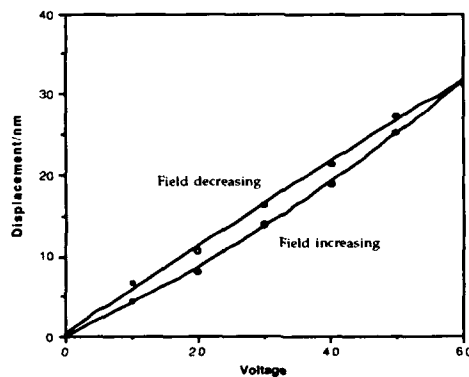


Figure 8 Hysteresis effect found for bare PLZT near the edge of a longitudinal configuration electrode. Displacements are negative and correspond to the minimum shown in figure 7.

It is clear that the various effects occurring are complex in nature and may be related to the composition and crystallinity of the constituent ferroelectric material. It is also significant that some of the behaviour observed may be related to the clamping effect at the adhesive bond between the thin wafer and the glass substrate.

5 THIN FILM DEVICES

A study has also been carried out of various film/substrate combinations with transverse electrodes using the WYKO interferometer. This configuration was chosen because of its reliability and its freedom from pinhole effects arising from defects in relatively large areas of the ferroelectric thin film material. Samples examined included perovskite phase material produced by the cluster magnetron technique previously described [2], by pulsed plasma deposition [3] and by dual ion beam sputtering [4]. Whilst the study of bulk material in an interferometer is simplified by the absence of optical phase change on reflection, the same is not true in the thin film case where the phase change is defined by the optical constants of the film/substrate ensemble. The WYKO computer software can interpret the effect of changing refractive index, but in the event it was found that the dominant effect produced under DC field application was the bending mode previously found in the thicker ceramic samples. The direction of movement was always the same, with a concave radius of curvature produced when the field was applied across transverse electrodes. It is clear that the films exhibit electro-elastic properties, but the sense of the deformation is opposite to that expected for a positive d_{33} , which would place the film into compression when the field was applied, with an ensuing convex deformation. These processes may be related to the clamping effect of the substrate and imply that extended planar structures may never achieve the same performance levels as bulk material. More success is likely to be obtained using discrete active device areas defined by micromachining.

In some films, deformation effects were seen using the WYKO under DC conditions close to the edges of electrodes. These are different to those found in bulk material and are on a much smaller dimensional scale. Spectroscopic measurements on the material present in the gap, carried out using an optical multichannel analyser fitted to the microscope indicate the absence of any fringe movement as a result of the applied DC field. However, when optical measurements are made on thin film devices between crossed polarisers using transverse electrodes, the effects of field-induced birefringence can be used to modulate an optical source at AC frequencies above 4Hz. At lower frequencies the response falls off, dropping to zero at DC levels. It is currently believed that the frequency dependence of the modulation reflects the material being permanently polarised at low excitation frequencies, so that the atoms in the lattice no longer move with the applied field and cause a refractive index shift. At higher frequencies, less opportunity is available to set up permanent space-charge fields in the material and the polar domains present in the material follow the variations in applied field. Many of these issues are being addressed in current studies.

6 CONCLUSIONS

The technique of optical interferometry can be applied to the study of the fundamental electro-elastic and electrostrictive processes in ferroelectric materials. Deformation processes measured in free-standing PLZT ceramic with applied field are easily understood, but can give rise to unexpected forms of behaviour when substrate clamping effects are introduced. The behaviour of thin film devices is dominated by such clamping effects under DC excitation, but at higher frequencies can be used as for optical modulator applications. The frequency dependence of the modulation reflects the material being permanently polarised at low excitation frequencies, so that the atoms in the lattice no longer move with the applied field and cause a refractive index shift.

7 ACKNOWLEDGMENTS

The authors are indebted to J E Chadney for assistance with the fabrication of electrode structures.

8 REFERENCES

1. H Adachi, T Mitsuyu, O Yamazaki and K Wasa: J Appl Phys **60** 736 (1986)
2. K F Dexter, K L Lewis and J E Chadney: Proc IEEE International Symposium on the Application of Ferroelectrics, Aug 1992, Greenville, USA
3. I P Llewelyn, R A Heinecke, K L Lewis and K F Dexter: Ferroelectrics **133** 85-90 (1992)
4. D A Tossell, J S Obhi, N M Shorrocks, A Patel and R W Whatmore: Proc IEEE International Symposium on the Application of Ferroelectrics, Aug 1992, Greenville, USA
5. A Mukherjee, S R J Brueck and A Y Wu: Optics Letters **15** 151 (1990)

REVERSIBLE PHOTO-INDUCED CURRENTS IN EPITAXIAL Pb(Zr_{0.52}Ti_{0.48})O₃ THIN FILMS

J. LEE, S. ESAYAN, J. PROHASKA AND A. SAFARI

Department of Ceramic Science and Engineering, Rutgers-The State University of New Jersey, Piscataway, NJ 08855-0909, USA.

ABSTRACT

The pyroelectric and photogalvanic effects have been studied extensively in epitaxial Pb(Zr_{0.52}Ti_{0.48})O₃ (PZT) thin films. For the first time, photo-induced currents, which were completely reversible by electrical voltage, were observed in ferroelectric thin films. The photo-induced currents exhibited transient and steady state components. The transient component, in turn, consisted of two components with fast (<1 μ s) and slow (~hours) relaxation times. The mechanisms of the photo-induced currents in PZT films and their possible application in non-destructive readout ferroelectric memory are discussed.

INTRODUCTION

Recently, ferroelectric thin films were extensively studied because of their application for non-volatile memories¹. The conventional readout process in such memory elements requires polarization switching at each readout, which results in ferroelectric fatigue and reliability issues. On the other hand, there have been a few studies to find a new mechanism for reading information from the ferroelectric memory without polarization switching using the field-effect transistor (FET) structure²⁻³. Such a non-destructive readout memory simplifies circuit design and alleviates stringent requirement on fatigue of ferroelectric thin films. Another possibility for non-destructive readout memory has been realized in bulk ferroelectric ceramics using the polarization-dependent photovoltage⁴. Therefore, the study of the photo-induced current in ferroelectric thin films is of great interest for construction of a new type of thin film ferroelectric memory. Photo-induced currents were previously studied on polycrystalline thin films^{5,6}. In this paper, the behaviors of pyroelectric and photogalvanic currents in epitaxially grown Pb(Zr_{0.52}Ti_{0.48})O₃ (PZT) thin films were studied extensively.

EXPERIMENTAL PROCEDURES

PZT films with the thickness of 0.5 μ m and with the polar c-axis perpendicular to the substrate surface were epitaxially grown in a high vacuum system on Y₁Ba₂Cu₃O_x (YBCO) coated SrTiO₃ substrates by pulsed laser ablation. Detailed experiment and ferroelectric properties of the epitaxial PZT films were reported elsewhere^{7,8}. Ferroelectric film capacitors were constructed with the Pt circular top electrode with the diameter of 0.6 mm. Platinum top electrodes were sputtered with the thickness of 400 Å and were expected to have 5 % transmission of incident illumination⁵. The P-E hysteresis loop of the PZT films were measured with hysteresis bridge circuit. A continuous (CW) and pulsed lasers were used for photoresponse of Pt/PZT/YBCO structure. For the photoresponse of the PZT films under steady-state illumination, the light from a He-Ne laser ($\lambda = 623$ nm, 5 mW) with the polarization in the a-b plane of the film was directed along the polar c-axis. An electrometer was used to detect the photocurrent generated from the film and the signal was recorded with a chart recorder. For the photoresponse of the PZT films on laser pulse illumination, a Q-switch Nd: YAG laser ($\lambda = 1064$ nm) with a 300 ns pulse duration and 100 Hz repetition rate was used. The photocurrents were measured by an oscilloscope with 50 Ω input impedance.

RESULTS AND DISCUSSION

The resistance and capacitance of Pt/PZT/YBCO structures were in the range of 10⁸ - 10⁹ Ω and 3-4 nF, respectively. Coercive field strength of PZT films estimated by the dielectric hysteresis loop measurement was ~ 53 kV/cm, corresponding to the coercive

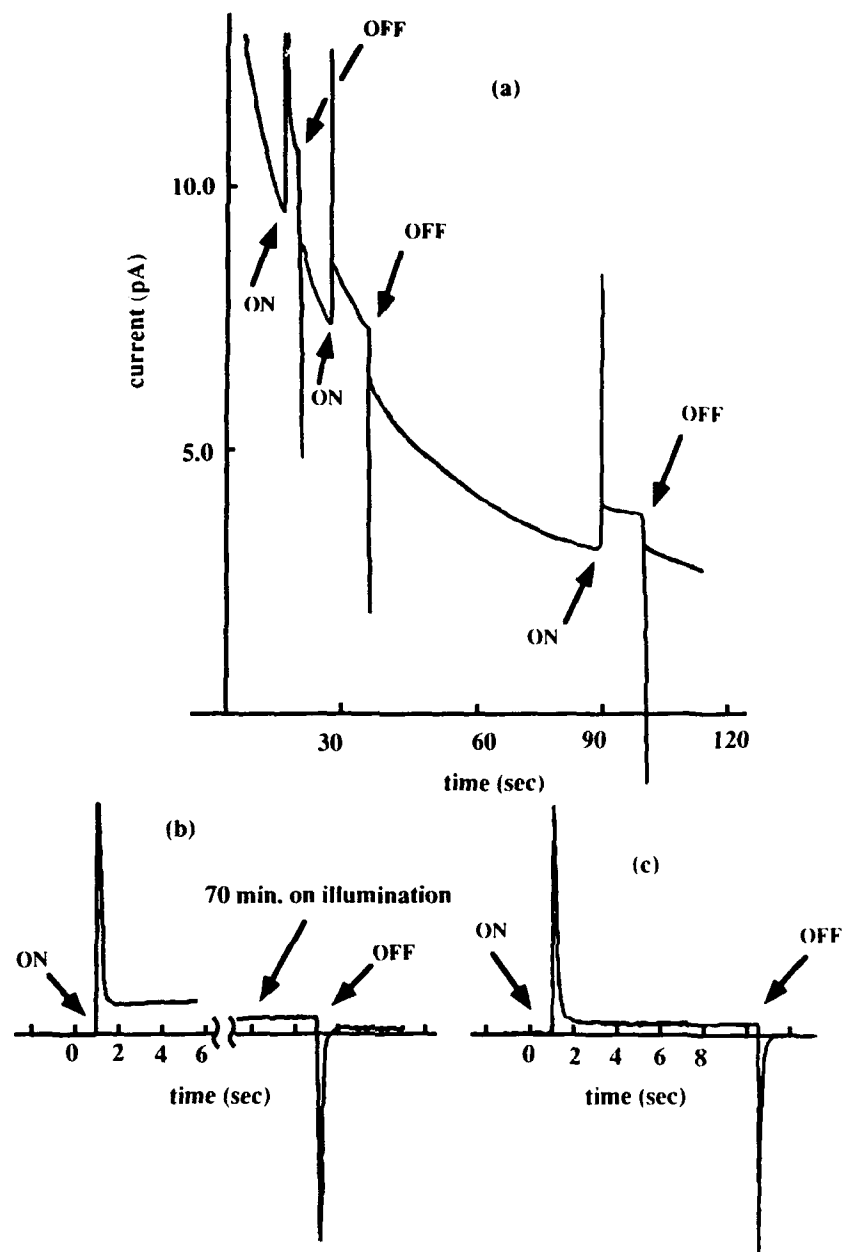


Figure 1. Current versus time for the Pt/PZT/YBCO structure with semi-transparent Pt top electrode (a) immediately after being poled by 5 V, (b) after the dark current was completely relaxed and (c) after the slow transient photocurrent disappeared after an extended time of illumination.

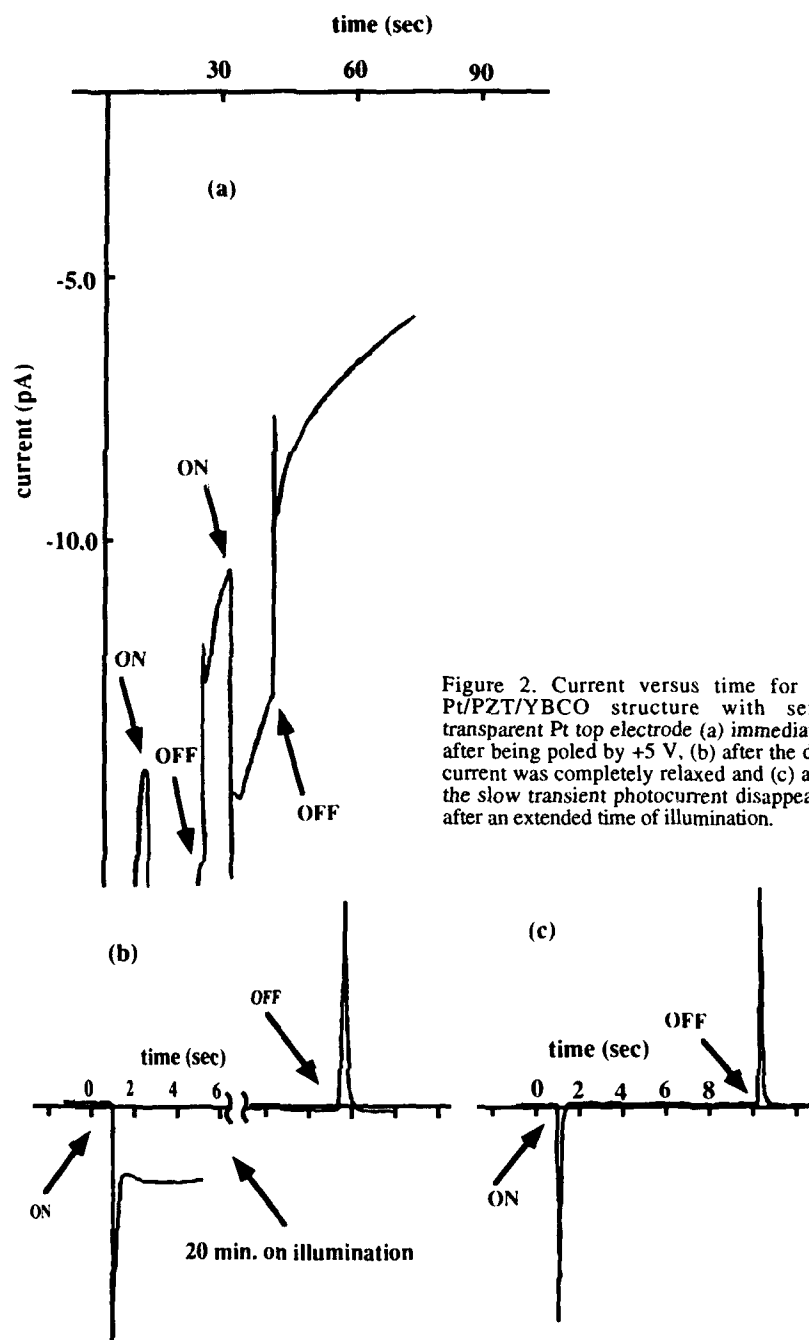


Figure 2. Current versus time for the Pt/PZT/YBCO structure with semi-transparent Pt top electrode (a) immediately after being poled by +5 V, (b) after the dark current was completely relaxed and (c) after the slow transient photocurrent disappeared after an extended time of illumination.

voltage of ~ 2.7 V. First, the photoresponse of the PZT films under steady-state illumination were studied. The laser irradiation has induced a current in the P/PZT/YBCO structure which has both steady-state and transient components, as shown in figure 1 and 2. It is important to point out that the transient component of current consists of fast and slow components. Both figures 1 and 2 show that the slow component of the current has 1-2 hours relaxation time. Dark leakage currents of 10^{-9} - 10^{-10} A were measured after applying 5 V dc switching voltage or 100 μ sec long pulse. This current gradually decreased and finally disappeared in an hour. Figure 1 and 2 show currents obtained in the dark state and under illumination immediately after polarization switching, and photocurrents after an extended time of illumination.

After applying a negative switching voltage, the photo-induced currents increased markedly, followed by a decay to a steady-state value on the order of an hour. It was noted that the behavior of the photo-induced current depends on duration of light illumination. Figure 1 and 2 show that the ratio of the fast and slow components of the transient photocurrent depends on the value of decaying dark current. After the leakage current and the slow decaying photocurrent disappeared, the remaining photocurrents consisted of the fast transient and small steady-state components (figure 1). For the positive switching voltage, the value of the slow transient component of the photocurrent was higher than that of the negative switching voltage. The photocurrent had only the fast transient component after relaxation (figure 2).

From the phenomenological point of view, thermal and photo-induced currents which are dependent of the direction of the remanent polarization can be represent by :

$$J_i = S[(\partial P_s / \partial T + \alpha_i c_{ik} d_{ik}) \partial T / \partial t + \beta_{ijk} \partial (E_j^* \omega E_k^* \omega) / \partial t + \chi_{ijk} (E_j^* \omega E_k^* \omega)] \quad (1)$$

where S is area of electrode; $\partial T / \partial t$ is the temperature time derivative; P_s is a spontaneous polarization; $E^* \omega$ is the electric field of optical radiation and α_i , c_{ik} and d_{ik} are the coefficient of thermal expansion, stiffness and piezoelectricity, respectively. β_{ijk} and χ_{ijk} are optical dc (rectification) and photogalvanic coefficients, respectively. The first term in equation (1) represents the pyroelectric effect (primary and secondary). The second and third terms represent photo-induced currents due to optical dc and photogalvanic effects⁹. As shown in equation (1), the currents due to pyroelectric or optical dc effect have a transient character. On the other hand, the photogalvanic current has a steady-state character. Equation (1) also shows that all components of current along the polar axis change their sign upon polarization switching. In addition to being polarization-dependent, there are a few other possible mechanisms for the polarization-independent steady-state current. These include contact potential at the electrode-ferroelectric interface and other surface effects.

Analysis of experimental results using equation (1) indicates that the completely reversible fast transient photocurrent is due to the pyroelectric and/or optical dc effects. The source of the slow transient photocurrent is probably connected with screening of spontaneous polarization by localized charge in the traps originating from impurities or defects¹⁰. Excitation of photocarriers changes the condition of filling of the impurity levels (traps) in the forbidden band. As a result, the screening conditions are changed, simultaneously, changing the value and distribution of the internal field in the PZT film. Slow relaxation of the photocurrent under continuous illumination possibly indicates that multiple trapping deep levels are involved in the screening process. The Maxwell relaxation time ($\tau = \epsilon \epsilon_0 / 4\pi \sigma$) of the PZT films estimated from I-V measurement is on the order of a second, where σ is a conductivity. However, slow relaxation of the transient photocurrent occurred on the order of an hour. The discrepancy between the relaxation times estimated from I-V measurement and those observed in transient photocurrent is probably due to inhomogeneity in the materials¹⁰ or the difference between volume resistance and surface resistance of the PZT films.

Based on the mechanism we propose for the slow transient photocurrent, the dc leakage current can affect the screening condition as well as the depolarization field. Figures 1 and 2 show that the slow transient photocurrents decrease with the decaying dark current. Slow decay of the dark current is probably due to long relaxation of ionic drift which is predominant in conduction of perovskite-based ferroelectrics in the high electric

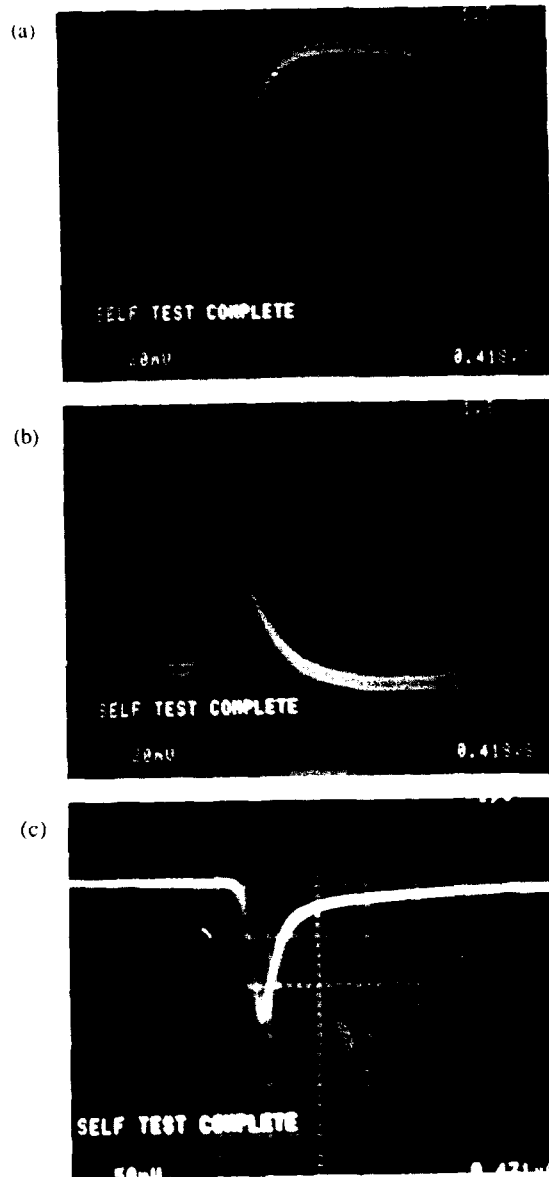


Figure 3. Photoresponse of epitaxial PZT films under pulse laser illumination, (a) after being poled by -5 V and (b) after being poled by 5 V, and (c) photoresponse of Si photodiode for laser pulse.

field ($\sim 10^5$ V/cm)¹¹. Photocarriers may change the screening condition through recharging defects, possibly oxygen vacancies or Pb vacancies, which can be carriers for the dark current in PZT films. The change in screening condition makes an additional contribution to the slow transient photocurrent.

As for the steady-state current, the experimental results show that it consists of both photogalvanic current and the current due to contact potential, as shown in figure 1 and 2. At the negative switching voltage, both currents had the same sign and a net current followed. On the other hand, the polarization-dependent photogalvanic current changed its direction at the positive switching voltage. As a result, currents due to photogalvanic effect and contact potential cancel out each other and the net steady-state current was almost zero.

We obtained pyroelectric and photogalvanic currents from epitaxial PZT films whose direction was dependent on the direction of the remanent polarization. In the ferroelectric memory elements, the logic unit (0,1) are determined by the direction of the remanent polarization. Therefore, using light sources, we could generate currents whose signs are determined by the direction of polarization. As a result, one can optically read the information which is written in the ferroelectric memory element with an excellent signal-to-noise ratio.

As for the time dependence of the photocurrents due to the slow transient component, it is possible to eliminate its effect by using a pulse laser illumination. Experiments using the Q-switch Nd:YAG laser (figure 3) shows that a 100 mV photoresponse was measured for a pulse laser input of $\sim 10^4$ W/cm². Furthermore by comparison, the temporal behaviors of the laser pulse and response (figure 3) are nearly identical. After applying a 5 V switching voltage, the polarity of the photoresponse is changed, as shown in figure 3 a and b. It is important to point out that unlike to the steady-state illumination, the pulse laser photoresponse did not show any delay after switching, and remained unchanged after a few hours illumination. For the photogalvanic and optical dc effects, the operation speed of memory element is mainly determined by the relaxation times of hot photoelectron and photo-induced nonlinear polarization, which is limited to 10^{-11} - 10^{-14} s. It is therefore possible to realize the non-destructive optical readout with the $<10^{-11}$ s operation speed.

SUMMARY

The pyroelectric and photogalvanic currents completely reversible by electric voltage were observed in epitaxial $\text{Pb}(\text{Zr}_{0.52}\text{Ti}_{0.48})\text{O}_3$ thin films. The mechanism of photo-induced current and the possibility to construct the ferroelectric memory with a non-destructive readout capability on the basis of the reversible current were discussed.

We would like to thank the Center for Ceramic Research and Glen Howatt Lab. for their financial supports.

REFERENCES

1. J. F. Scott and C. A. Pas de Araujo, *Science* 246, 1400 (1989).
2. S. Sinharoy, H. Buhay, M. H. Francombe, W. J. Takei, N. J. Doyle, J. H. Rieger, D. R. Lampe and E. Stepke, *J. Vac. Sci. Technol.* A9, 409 (1991).
3. S. Sinharoy, H. Buhay, W. H. Kasner, M. H. Francombe, D. R. Lampe and E. Stepke, *Appl. Phys. Lett.* 58, 1470 (1991).
4. P. S. Brody, *Appl. Phys. Lett.* 38, 153 (1981).
5. P. S. Brody and B. J. Rod, *Proceedings of 3rd Internal Symposium on Integrated Ferroelectrics*, Colorado Springs, Colorado, 1991, p. 251.
6. S. Tharkoor, A. P. Tharkoor and S. E. Bernacki, *Proceedings of 3rd International Symposium on Integrated Ferroelectrics*, Colorado Springs, Colorado, 1991, p. 262.
7. G. Yu, A. Boikov, S. K. Esayan, Z. G. Ivanov, G. Orosso, T. Claeson, J. Lee and A. Safari, *Appl. Phys. Lett.* 61, 528 (1992).
8. J. Lee, L. Johnson, A. Safari, R. Ramesh, T. Sands, H. Gilchrist and V. G. Keramidas, *Appl. Phys. Lett.*, to be published.
9. B. I. Sturman and V. M. Fridkin, *The Photovoltaic and Photorefractive Effects in Noncentrosymmetric Materials*, Gordon and Breach Science Publishers, 1992.
10. V. M. Fridkin, *Photoferroelectrics*, Springer-Verlag, New-York, 1979.
11. D. M. Smyth, *Ferroelectrics*, 116, 117 (1991).

PROGRESS TOWARD VIABLE EPITAXIAL OXIDE FERROELECTRIC WAVEGUIDE HETEROSTRUCTURES ON GaAs

D. K. Fork,* J. J. Kingston,* G. B. Anderson,* E. J. Tarsa,** and J. S. Speck**

*Xerox Palo Alto Research Center, 3333 Coyote Hill Road, Palo Alto, CA 94304

**Materials Department, University of California, Santa Barbara, CA 93106

ABSTRACT

Discoveries within the last two years have created possibilities for the fabrication of epitaxial oxide heterostructures on GaAs substrates. In particular, magnesium oxide, MgO, may have broad applications, including its use as a cladding layer in optical waveguides. This report expands upon earlier work by revealing additional epitaxial structures involving lithium niobate which have been grown. There are now five known variants of Z-lithium niobate on GaAs: direct Z-cut growth on GaAs (111)A or B, Z-cut growth on MgO (111) GaAs (111)A or B, and Z-cut growth on MgO (111) GaAs (001). Broad in-plane misalignment (about 15°) characterizes the latter structure, whereas the former possesses a textural width of 3° to 5° in the plane. All structures contain internal boundaries resulting from 180° rotations about the Z-axis. A critical issue for any ferroelectric heterostructure is its integrity in the presence of thermally induced tensile strain. Approaches to the mitigation of thin film fracture are discussed and a novel approach to strain relief via ridge waveguide fabrication is reported.

INTRODUCTION

Monolithic combination of GaAs based light sources with oxide ferroelectric thin film waveguide devices is as yet a distant goal, due to the lack of viable waveguide structures and processing methods, but is a goal pursued in several laboratories due to the potential advantages of such intimately interconnected hybrid devices. Progress toward meeting such a goal includes the following considerations. Confined optical modes are needed, hence a cladding layer of low index must be provided to separate the semiconductor ($n \approx 3.8$) from the ferroelectric ($n \approx 2.2$). The uniaxial or biaxial nature of ferroelectrics (LiNbO₃, BaTiO₃, PbTiO₃, KNbO₃ etc.) implicitly requires either highly oriented or epitaxial films to permit usage of tensor properties and to minimize light scattering. Waveguides place a premium on minimizing surface roughness, because thickness variations cause losses and/or propagation constant variations depending on their spatial frequency.¹ Integration with Si or GaAs imposes limits on processing temperature, material passivity, thermal expansion effects, and in most cases, the dielectric and ferroelectric characteristics which are intimately tied to film crystallinity and composition.

The previous MRS symposium on ferroelectric thin films (FTF II) marked the first report of epitaxial MgO thin films on GaAs (001).² Therein, the MgO layer was shown to permit the growth of epitaxial BaTiO₃ films, suggesting usefulness for optical and memory applications. Since then, three additional epitaxial relations were produced, as in Table I, which lists the currently demonstrated epitaxial oxides on GaAs. These are yttria-stabilized zirconia (YSZ),² indium-oxide,³ and magnesium oxide.^{2,4-6} (Oriented lead titanate growth has been reported on gallium arsenide with evidence for lead interdiffusion.⁷) Table I illustrates the large impact of pulsed laser deposition (PLD) on the development of this research, however, it remains true that the best propagation figures in ferroelectric oxide thin films have been in sputtered thin films.

Of potential optical waveguide cladding materials, YSZ has a higher refractive index than MgO (2.16 vs. 1.7) and is less chemically stable on GaAs than MgO,² making it a less desirable material. (Lower index implies stronger mode confinement, thinner minimum layer thickness, and higher intensity for a given power.)

Indium oxide, In₂O₃, would be a very interesting epitaxial waveguide cladding material, given its low index ($n=1.80$) and ability to be doped with Sn into a transparent conductor. In₂O₃ films on InAs/GaAs (001) currently reported have (111) faceting,³ causing more surface roughness than is tolerable in optical waveguides.

MgO is an interesting candidate as a waveguide cladding material since it is a substrate for a variety of epitaxial oxide ferroelectrics, such as LiNbO_3 , BaTiO_3 , PbTiO_3 , KNbO_3 etc. As in Table I, MgO can be grown in four crystallographies, which may prove useful for inducing various crystallographies essential to exploiting the tensor optical properties of the above and other complex oxides. Detailed mechanisms underlying the epitaxial variants of MgO on GaAs are not available, however, the cube-on-cube crystallographies appear to derive from initiating growth from a 'bare' or oxide free GaAs surface.^{2,6} Sulfur terminated GaAs (001) was used in the electron beam deposition process which generated the (110) || (001) variant.⁴ The (111) || (001) variant of MgO on GaAs grew in the presence of incomplete surface oxide desorption.⁵

Table I. Currently known epitaxial oxides on gallium arsenide

Material	Crystal System	Out-of-Plane Orientation	In-Plane Orientation	Method	Lattice Mismatch	Ref.
YSZ	Fluorite	(001) (001)	(100) (100)	PLD	-9.5%	[2]
In_2O_3	Bixbyite	(001) (001)	(100) (100)	PLD	2.27%	[3]
MgO	NaCl	(001) (001)	(100) (100)	PLD	-0.65%	[2]
MgO	NaCl	(110) (001)	(110) (110)	EB	-0.65%	[4]
MgO	NaCl	(111) (001)	$\pm(110) (110)$	PLD	-0.65%	[5]
MgO	NaCl	(111) (111)	(110) (110)	PLD	-0.65%	[6]
PLZT*	Perovskite	(110) (001)		Sput.	2.06, -27.8%	[7]
LiNbO_3	trigonal R3c	(001) (111)	(110) <211>	PLD	-0.86%	[6]

Abbreviations: PLD=pulsed laser deposition, EB=electron beam deposition, Sput.=sputter deposition. *In-plane orientation not reported.

In addition to the epitaxial cladding oxides mentioned above, the approach to waveguide cladding using *oriented* complex oxide growth on amorphous SiO_2 has been investigated at length,⁸ and may provide a route to optical integration.

GROWTH PROCESS

The PLD technique employed at Xerox is as follows. A 308 nm, 17 ns pulse length XeCl excimer laser [Lambda Physik EMG 103] generates a laser energy density of 0.8 to 1.3 J/cm² on 0.5 inch targets. The target-to-substrate distance is 50 mm; the base pressure is 2×10^{-7} Torr. We used LiNbO_3 single crystals as sources. LiNbO_3 films grew in conditions ranging from 525 °C to 825 °C and 1 to 200 mTorr O_2 . MgO films with the cube-on-cube crystallography were grown from Mg metal targets to reactively produce MgO in 5×10^{-6} Torr O_2 at 350 °C. Targets were mounted on a PolyGun source [Kurt J. Lesker Co.] which places 10 targets on a rotating polygon. The GaAs substrate was heated radiatively while temperature was monitored by a thermocouple near the lamp which reads higher than the substrate. Si doped GaAs (111)A (Ga terminated) and (111)B (As terminated) wafers, 6×6 mm square, were degreased and immersed for 30 seconds in either $\text{H}_2\text{SO}_4:\text{H}_2\text{O}_2:\text{H}_2\text{O} = 10:1:1$ or for 10 seconds in $\text{H}_2\text{O}_2:\text{H}_3\text{PO}_4:\text{H}_2\text{O} = 3:1:50$. The former is a stronger etch, (microns per minute versus .08 to .1 microns per minute); both produced comparable x-ray spectra. Substrates were then rinsed in deionized water, ethanol, spin-dried with ethanol in flowing N_2 , and introduced into the deposition chamber. The substrate was heated at 680 °C (600 °C by pyrometer) for 2 min in vacuum before deposition to sublimate surface oxides.

MgO/GaAs of the (111) || (001) variant was grown at UC Santa Barbara as in Ref. [5] using a 248 nm KrF excimer laser to deposit MgO from a pressed MgO powder

target using an energy density of $\sim 2 \text{ J cm}^{-2}$. GaAs (001) substrates were degreased and sequentially etched in $\text{NH}_4\text{OH}:\text{H}_2\text{O}_2:\text{H}_2\text{O}$ (35:15:70) and $\text{HCl}:\text{H}_2\text{O}$ (1:1) solutions and then soaked for 3 min. in DI water to form a uniform native oxide layer. Reflection high energy electron diffraction (RHEED) monitored the substrate surface during the oxide desorption at 590 °C. MgO was grown in 1.2×10^{-4} Torr O_2 and 430 °C following the appearance of a characteristic non-GaAs [110] azimuth RHEED pattern.⁵

RESULTS AND DISCUSSION

Fig. 1 shows a $\text{Cu K}\alpha$ X-ray θ - 2θ diffraction scan of a 100 nm LiNbO_3 film grown at 625 °C and 10 mT $\text{P}(\text{O}_2)$ with a 75 nm MgO interlayer on GaAs (111)B. Peaks are indexed to LiNbO_3 (006) and (0012), MgO (111) and (222), and GaAs (111) and (222). Films grown without the MgO interlayer, had identical x-ray spectra except for the missing MgO reflections. Rocking curve widths in ω characterize the out-of-plane misalignment of the grains and were typically 1.0 and 1.2 degrees for the MgO and LiNbO_3 layers respectively. The instrument resolution, determined on a Z-cut LiNbO_3 single crystal was 0.2 degrees. The d spacing of the (0012) reflection deviated from bulk values in a manner consistent with Li deficiency and could be corrected with Li-rich targets as discussed previously.⁶

X-ray diffraction ϕ -scans measure in-plane texture and crystallography. Fig. 2 overlays ϕ scans of GaAs {202}, MgO {200} and LiNbO_3 {104} planes. In-plane epitaxial relationships are LiNbO_3 [110] // GaAs [211] & [211] with and without the MgC layer (note the {104} reflections occur every 60°). This crystallography may be equivalently stated as LiNbO_3 having its Y-cut direction along GaAs <110> directions and X-cut along GaAs <211>. ϕ -widths were typically 2.8° and 4.5° for MgO and lithium niobate respectively. The ϕ resolution was 0.5° as measured on GaAs (202). Although the films contains 180° boundaries and broad in-plane texture, these characteristics do not inherently produce optical losses since they do not mix non-equal components of the dielectric tensor. The same crystallographies and characteristic rocking curves occurred in films on GaAs (111)B and (111)A.

Figure 3 shows a θ - 2θ diffraction scan of a 100 nm LiNbO_3 film grown on MgO (111)/GaAs (001) which was grown via the partial oxide desorption process described above. The lithium niobate diffraction shows a predominantly Z-cut orientation, with peak broadening, which is indicative of disorder, most likely caused by Li deficiency. The MgO diffraction indicates predominantly (111) texture, however, there is also a (50 times) weaker reflection due to MgO (002), indicating that the film contains at least a small amount of non-(111) oriented material. Rocking curve widths in ω are about 1.8 and 2.0 degrees for MgO and lithium niobate respectively, indicating that the out-of-plane misalignment is about double that grown on GaAs (111).

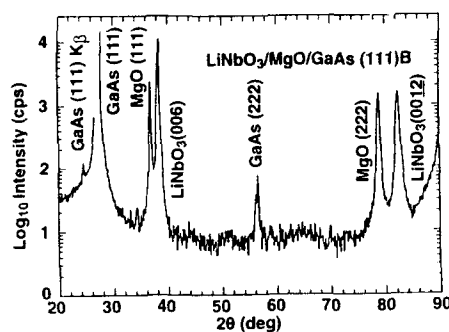


Figure 1. X-ray θ - 2θ scan of LiNbO_3 on GaAs (111)B with MgO (111) cladding.

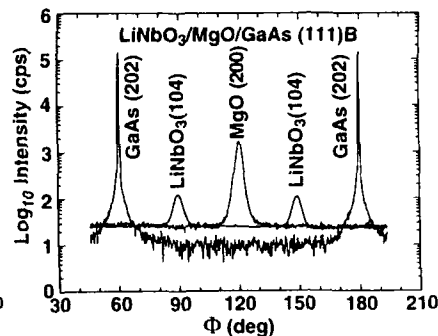


Figure 2. X-ray ϕ -scans of LiNbO_3 on GaAs (111)B with MgO (111) cladding.

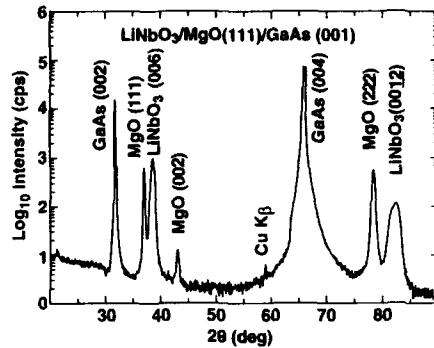


Figure 3. X-ray θ - 2θ scan of LiNbO_3 on GaAs (001) with an MgO (111) cladding.

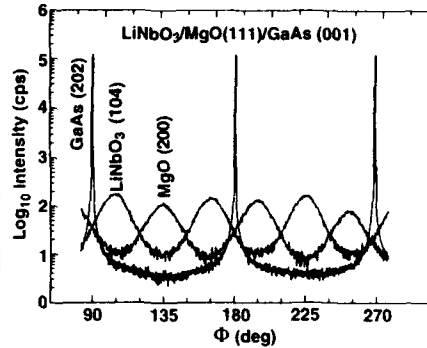


Figure 4. X-ray ϕ -scans of LiNbO_3 on GaAs (001) with MgO (111) cladding.

Figure 4 shows a series of phi scans of GaAs {202}, MgO {200} and LiNbO_3 {104} planes taken on the same film as in Figure 3. Peaks in the MgO phi scan occur every 60 degrees, illustrating the two-fold in-plane relationship of MgO to GaAs . Peaks in the lithium niobate phi scan also occur every 60 degrees, as was observed on GaAs (111) (Fig. 2), however we note here that given the two-fold relationship of LiNbO_3 on MgO (111), and the two-fold relationship of MgO (111) on GaAs (001), four inequivalent LiNbO_3 in-plane relationships are expected in the film, which form two pairs of reflections which can be distinguished in the phi scan. We also note that the width of the peaks in phi is 4 to 5 times broader than on GaAs (111), indicating many large angle grain boundaries in the film. The effect of such large angle grain boundaries on the optical properties has not been previously studied, although as suggested above, grain boundaries produced by rotations about the optic axis should be less harmful than boundaries resulting from grains with relative tilts of their optic axes.

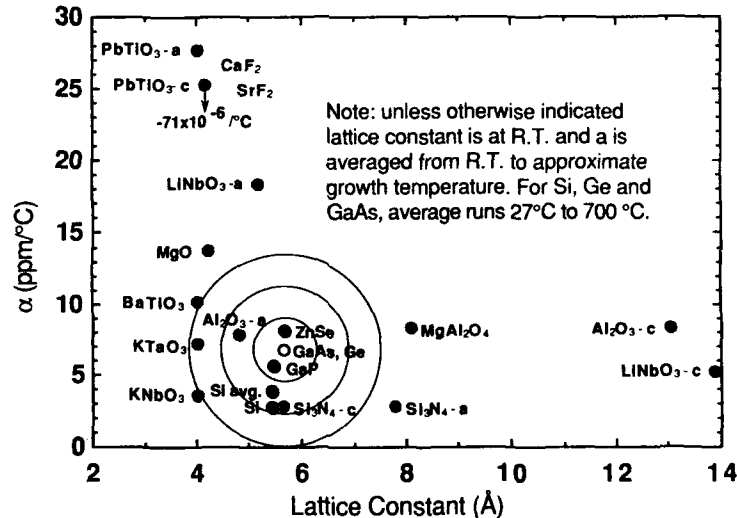


Figure 5. Potential waveguide and cladding materials arranged by lattice constant and thermal expansivity.

Whereas many of the current results in prototype oxide waveguide structures on GaAs are in $\text{LiNbO}_3/\text{MgO}/\text{GaAs}$, the general implementation potentially includes a wide variety of materials. Figure 5 is a scatter plot of potential materials arranged by lattice constant and thermal expansion constant. It is apparent that the elevated growth temperatures on GaAs will result in tensile strain of varying degrees at room temperature in most of the materials listed. As reported previously,⁶ fracture was observed in thick (600 nm) $\text{LiNbO}_3/\text{MgO}/\text{GaAs}$ (111) bilayers. There are several approaches to mitigating the fracture problem. If it is permissible to sacrifice the properties of the substrate, a more expansive substrate may be selected. Alternately, materials other than MgO and/or LiNbO_3 may be grown provided they have suitable intrinsic and thin film properties. If these options are unsuitable, a third alternative is to grow thin layers below the (not very well characterized) critical thickness for fracture. This may however produce waveguides for which the desired frequency is below the cutoff. Finally, a fourth alternative described here is to seek structural features which mitigate fracture. A promising strain relief structure, that also meets the requirement of lateral mode confinement, is the ridge waveguide. In the limit of a tall, narrow ridge, tensile stress along the waveguide induces contraction in the plane normal to the guide via the Poisson effect. The tensile stress is, in effect, applied uniaxially rather than biaxially. In the two limits, the stress σ for a given strain ϵ is,

$$\sigma_b = \epsilon/[E(1-\nu)] \quad (\text{biaxial case}); \quad \sigma_u = \epsilon/E \quad (\text{uniaxial case}),$$

where E is the Young's modulus and ν is the Poisson ratio. For a Poisson ratio of 1/3, a 33% stress reduction results in the limit of tall, narrow ridges, which is significant given that the critical thickness for fracture typically scales as σ^{-2} .

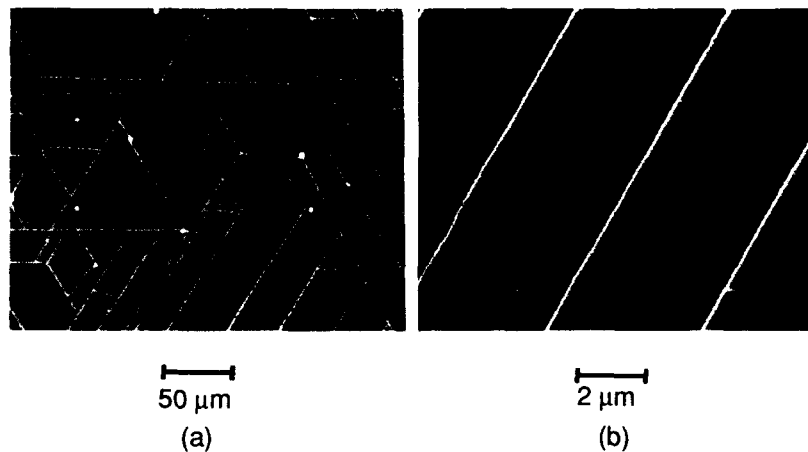


Figure 6. Fractured planar film (a) and unfractured film (b) grown on ridges.

Figure 6 compares scanning electron micrographs of a fractured planar structure and a ridge waveguide array of 1 μm ridges on 2 μm centers. It is evident that although these structures have comparable thickness, (500 nm LiNbO_3 on 100 nm MgO), only the planar structure is beyond its critical thickness. This was also confirmed via broad area surveys by optical and electron microscopy.

Figure 7. Cross section TEM of 500 nm $\text{LiNbO}_3/100 \text{ nm MgO/GaAs (111)B}$.

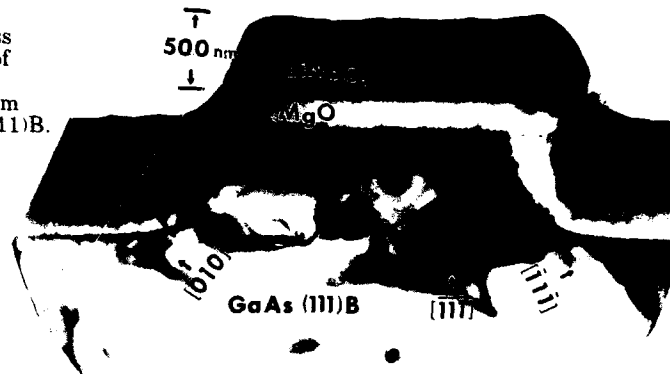


Figure 7 is a cross section transmission electron micrograph (TEM) of the ridge structure in Figure 6. Dislocations occur in the GaAs in response to the compression induced by the oxide layers. The sidewalls of this particular ridge are faceted into $\{010\}$ (right) and $\{101\}$ (left) crystal planes by the chemical etching process. This may be undesirable for waveguide fabrication, and if so, may be circumvented by alternate etching processes. The faceting does however illustrate the varying degree of MgO sticking on these differing crystal cleavages. In particular, the MgO does not stick readily to the $\{100\}$ type plane, which is in qualitative agreement with the high mobilities of MgO molecules on the $\{100\}$ face of MgO discussed in Ref. [7].

SUMMARY

Among the many requirements for viable epitaxial ferroelectric oxide heterostructure waveguides on GaAs, crystallographic control and thicknesses appropriate for guided modes are essentials. This report has illustrated five variants of epitaxial lithium niobate on GaAs substrates, and presents an approach to extending the critical thickness for thin film fracture via ridge waveguides.

We thank Rose Donaldson, and Brent Krusor of Xerox PARC for technical assistance. This work has been supported in part by the Department of Commerce Advanced Technology Program (70NANB2H1241).

REFERENCES

1. Dietrich Marcuse, Bell Sys. Tech. J. p. 3187, Dec. 1969.
2. K. Nashimoto, D. K. Fork and T. H. Geballe, Appl. Phys. Lett. **60**, 1199 (1992).
3. E. J. Tarsa, J. H. English, and J. S. Speck, Appl. Phys. Lett. **62**, 2332 (1993).
4. L. S. Hung, L. R. Zheng, and T. N. Blanton, Appl. Phys. Lett. **60**, 3129 (1992).
5. E. J. Tarsa, M. De Graef, D. R. Clarke, A. C. Gossard, and J. S. Speck, J. Applied Physics **73**, 3276 (1993).
6. D. K. Fork and G. B. Anderson, Proc. Mater. Res. Soc. Symp. on Pulsed Laser Deposition, Fall Meeting, Dec. 1992, Boston, MA (accepted); Appl. Phys. Lett. (accepted).
7. M. Ishida, S. Tsuji, K. Kimura, H. Matsunami, and T. Tanaka, J. Cryst. Growth **45**, 393 (1978).
8. A. B. Wegner, S. R. J. Brueck and A. Y. Wu, Ferroelectrics, **116**, 195 (1991).
9. S. Yadavalli, M. H. Yang, and C. P. Flynn, Phys. Rev. B **41**, 7961 (1990).

CHEMICAL VAPOR DEPOSITION OF EPITAXIAL BaTiO₃ FILMS FOR

FREQUENCY DOUBLING DEVICES, Peter C. Van Buskirk, Gregory T. Stauf, Robin Gardiner, Peter S. Kirlin, Advanced Technology Materials, Danbury, CT., B. Bihari, J. Kumar, University of Massachusetts-Lowell, G. Gallatin.

ABSTRACT

Ferroelectric materials such as BaTiO₃ are notable for their nonlinear optical and electrical properties. Optical frequency doubling in thin films integrated with compact semiconductor laser pumped solid state lasers is an attractive candidate for high efficiency generation of blue light. Chemical vapor deposition (CVD) using a single liquid source has been used to grow BaTiO₃ films on MgO. X-ray diffraction in the pole figure configuration indicates the films to be epitaxial, and rocking curves had FWHM = 0.7°. An optical scatterometer ($\lambda = 633$ nm.) has been used to identify deposition conditions that result in the lowest scatter losses. This paper describes these results as well as *waveguide designs to enhance the second harmonic generation efficiency in epitaxial BaTiO₃ films on MgO.*

Introduction

Although BaTiO₃ has exceptionally high second harmonic generation d-coefficients¹, conventional phase matching using birefringence in bulk crystals is difficult.² Propagation of light in thin film waveguides offers several advantages, including high power densities³ and the ability to phase match the incident and second harmonic wavelengths by engineering the waveguide structure to establish appropriate relations between their propagation constants.

Figure 1 illustrates various degrees of freedom in the design of thin film SHG devices. The simplest (1a) involves near-normal incidence; this configuration was used to characterize the BaTiO₃ films deposited in this effort and the results will be described below. Efficiency in a SHG-based device is defined as the square of the product of the optical intensity in power per unit area multiplied by the optical path length. The near-normal geometry in Fig. 1a is relatively inefficient because the optical path length is small, and for c-axis oriented films the electric field vector is difficult to align with the largest electro-optic tensor elements because of Snell's law. The first level of improvement involves setting up a guided wave in the film, either with a prism or grating coupler, thus increasing the optical path length. Phase matching the incident and harmonic optical fields can be achieved by selecting the substrate and waveguide thickness such that twice the propagation constant of the incident wavelength guided mode equals the propagation constant of the harmonic guided mode. Next, one can design a grating which will both couple in primary radiation and couple back out the second harmonic radiation at a different angle. Finally, figure 1b shows a waveguide structure which has been optimized for SHG efficiency by both phase matching and maximizing the resonant enhancement of the optical fields by the choice of the grating design parameters. A preliminary design will utilize a very low amplitude (≈ 100 Å) grating fabricated in either the MgO substrate or in the surface of the BaTiO₃ film. The grating period will be approximately 0.4 μ m to suppress diffraction into higher orders. Formation of features this size will require holographic exposure and ion milling. Development of computer code to predict the magnitude of the resonant enhancement is in progress and will be described in a future publication.

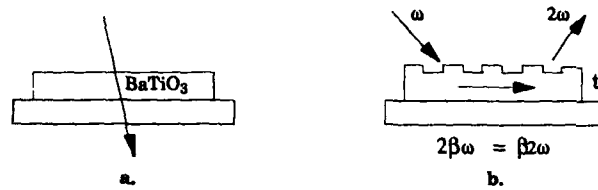


Figure 1. Thin film configurations for second harmonic generation in optically non-linear thin films (described in the text). 1b shows a waveguide structure which has been designed for efficient SHG by phase matching and creates resonant enhancement of the optical fields by optimizing the grating design.

Substrate selection

A variety of factors must be considered in design of a thin film frequency doubler. Substrate selection is perhaps the most important since it influences both the properties of the BaTiO_3 film and the degree of confinement due to the refractive index relationships.⁴ In general the better the chemical compatibility and lattice matching, the fewer the defects in an epitaxial film, resulting in lower optical losses and larger d-coefficients. SrTiO_3 is a good choice from this viewpoint; on the other hand, its refractive index is so close to BaTiO_3 that a prohibitively thick BaTiO_3 film ($> 1 \mu\text{m}$) would be required to support waveguiding.⁵ Therefore we have selected MgO as the substrate ($n \sim 1.73$) as a compromise between minimizing lattice mismatch and achieving a reasonable refractive index difference (to minimize film thickness). Figure 2 shows calculated propagation constants β as a function of BaTiO_3 film thickness for the $\text{MgO}/\text{BaTiO}_3/\text{air}$ configuration. The propagation constants are calculated⁶ for TE polarized $1.064 \mu\text{m}$ (2β) and TM polarized $0.532 \mu\text{m}$ (β) wavelengths, corresponding to the Nd:YAG laser incident beam and the frequency doubled output, respectively.

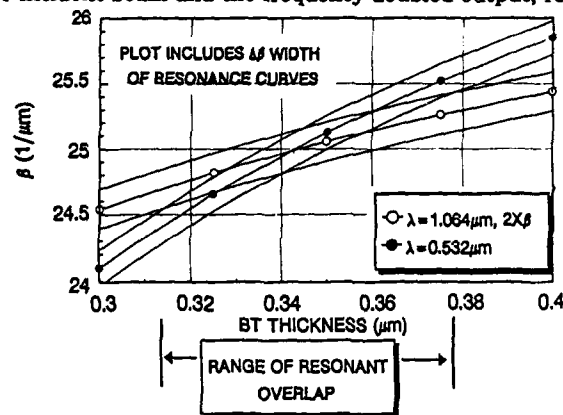


Figure 2. Propagation constants β as a function of BaTiO_3 film thickness for the $\text{MgO}/\text{BaTiO}_3/\text{air}$ waveguide configuration. Phase matching can be achieved by selecting the BaTiO_3 thickness such that $2\beta_\omega = \beta_{2\omega}$, corresponding to $0.34 \mu\text{m}$.

Chemical vapor deposition of BaTiO₃

Metal organic chemical vapor deposition (MOCVD) offers the potential for epitaxial film growth over large areas and at rates appropriate for device manufacturing. The BaTiO₃ films were grown in an inverted vertical reactor described previously,⁷ on (100) MgO substrates that were preannealed in oxygen at 1100 °C. The quartz reactor tube had a cylindrical configuration, and the gas inlet, substrate mounting and gas outlet were coaxial with the walls of the reactor. The substrate faced downward and was held against an inductively heated SiC susceptor by a pyrolytic boron nitride mask. A substrate temperature of 840 °C with gas flows in the reactor of 300 sccm Ar and 900 sccm O₂ and a total pressure of 2.2 torr gave a growth rate of about 0.3 μm/hr.

Titanium bis-isopropoxide bis(thd) and Ba(thd)₂-tetraglyme adduct were used as the source reagents and were delivered to the reactor at a combined rate of 0.7 μmol/min using a liquid delivery approach described in previous publications.^{8,9} Briefly, organic solutions containing the organometallic source complexes were delivered by a high precision liquid pump to a heated vaporizer assembly. The gaseous precursors were then transported to the reactor by an Ar carrier gas through heated manifolds. The major advantage of the liquid delivery approach is that liquids can be mixed just prior to vaporization; besides the simplicity of this approach the ability to make slight composition adjustments via computer control makes this approach highly desirable. Once the process has been optimized, simultaneous delivery of all the cation species to the substrates via a single solution is possible, which is inherently superior to separate precursor manifolds in terms of both film stoichiometry and system complexity. This technique has been successfully used by ATM for growth of BaSrTiO₃ and YBaCuO and other materials.¹⁰ The controlled delivery of relatively involatile CVD precursors offered by this technique opens the doors to a broad range of CVD processes, especially those which employ simultaneous delivery of several compounds.

BaTiO₃ physical properties

Films deposited under the conditions described above were typically smooth and featureless when imaged by SEM at 10⁴ x. At present films of the target 0.34 μm thickness are deposited using process timing to control thickness and this method results in thickness control of approximately ±5%.¹¹

X-ray diffraction in the Bragg-Brentano geometry revealed films deposited on MgO [100] to be essentially single [100] orientation, with trace levels of [110] and [111] orientations present with some variability. The reason for the presence of these misorientations is not known, although slight misalignment of the polishing lap with respect to the crystal axes of the substrate may result, after annealing, in steps which promote growth of misoriented material.¹² XRD pole figure analysis for a representative sample shows four-fold symmetry indicating the film to have an epitaxial relationship with the MgO surface Figure 3.

The diffraction line at 45.3° does not display the splitting expected for non-degenerate [200] and [002] lattice spacings, although bulk BaTiO₃ is tetragonal at room temperature. It is possible that the relatively small dimension of the BaTiO₃ normal to the surface effectively suppresses the tetragonal structure at room temperature; this result is familiar for fine-grained BaTiO₃ and has been characterized as the 'superparaelectric' phase.^{13,14} Clamping effects are known

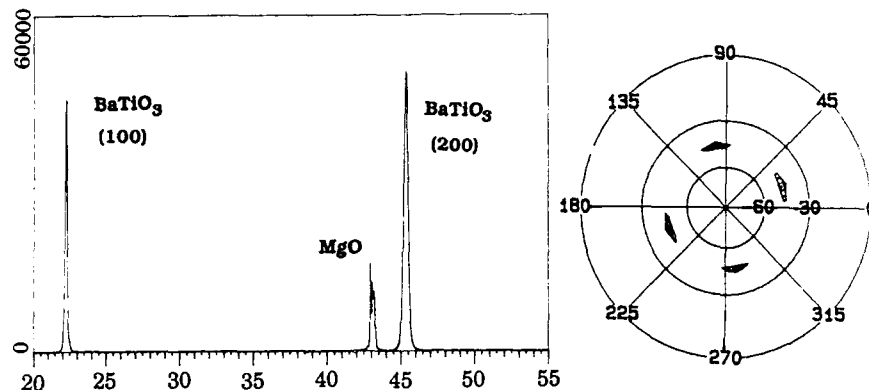


Figure 3. X-ray-diffraction, BaTiO₃/MgO. Left: the BaTiO₃ film is single phase, highly [200] oriented. Right: [110] pole figure reveals four-fold symmetry, indicating epitaxy.

to dramatically alter the non-linear optical response in bulk crystals and this may be an important effect in epitaxial thin films.¹⁵ Since these effects could perturb the refractive index of BaTiO₃ thin films relative to the bulk values used for the calculations in Figure 2, ellipsometry will be used to directly measure refractive indexes in our films to choose final target thicknesses.

BaTiO₃ optical properties

A simple apparatus was set up to make comparative measurements of the scatter resulting from the BaTiO₃/MgO samples. Changes in scattered light intensity gave us a simple, non-destructive way of looking at the optical quality of a film grown under certain conditions. A He-Ne laser ($\lambda = 633$ nm.) was directed at the BaTiO₃/MgO samples at a 45° angle of incidence.¹⁶ A Si detector¹⁷ was used to measure the intensity of scatter out of the specular reflected beam, at a range of off-specular angles from approximately 5-45°. Experiments were conducted to examine the effects of substrate annealing and deposition temperature on the scattered light intensity. We found that samples with similar XRD spectra could have significantly different scattering properties. Of most interest was the dependence of scatter on substrate preparation and substrate temperature. Samples of BaTiO₃/MgO on annealed substrates were found to have about 70% the scatter of samples on unannealed substrates. While relatively small on the logarithmic scale often used to describe optical scatter, this difference was repeatable for samples of this type prepared in the same deposition run.

Scatter also had a distinctive dependence on deposition temperature (Figure 4). Films grown on both cleaved and polished MgO substrates displayed the lowest scatter at approximately 850°C. More scatter at lower temperatures can be

explained when one examines the x-ray spectra of films grown at lower temperatures, which show substantially less intense peaks, even though the optical thicknesses were about the same. This indicates that either amorphous or fine-grained BaTiO_3 was present, not surprising at lower temperatures, either of which could cause increased scatter. Higher scatter due to higher deposition temperatures is slightly more difficult to explain; x-ray peak intensities did drop somewhat from those at 850°C , but the reason is unknown. Profilometer surface roughness measurements did not show any good correlation to increased light scatter, so it may be a bulk grain boundary or defect phenomenon rather than a surface roughness effect. TEM for these samples is underway in an effort to explain these phenomenon. Reductions in light scatter should result in decreased wave-guiding losses in the BaTiO_3 film.

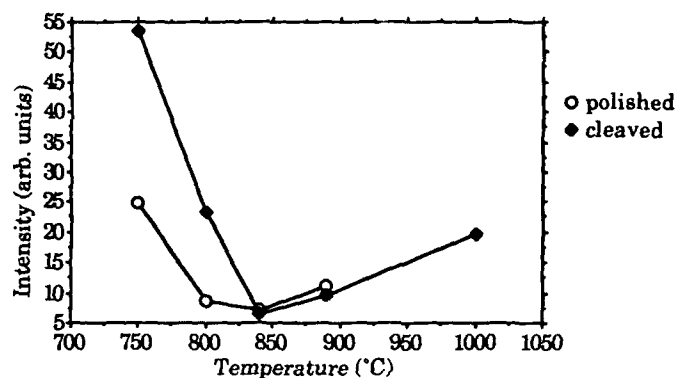


Figure 4. Relative scatter vs. deposition temperature. BaTiO_3 films on both cleaved and polished MgO had minimum scatter at approximately 850°C deposition temperature.

Poling procedures for the BaTiO_3 are under development. Poling involves putting an electric field across the sample, often with a needle or filament (corona poling) and in some cases heating it above the Curie temperature to align ferroelectric domains. We believe the as-grown material has some net domain orientation, since SHG d-coefficients as high as 0.7 pm/V (d_{15}) have been measured in unpoled films. This value is more than an order of magnitude below the value of the bulk material, and it is likely due to the unpoled state of the films as well as likely clamping effects which suppress SHG generation in a domain. Future work will focus on determining poling and deposition conditions to minimize these effects, and on fabrication of grating structures to enhance the efficiency of SHG in BaTiO_3 films.

Conclusions

A design for a thin film based frequency doubler, using the high second harmonic generation coefficient of BaTiO_3 , has been presented. This will require a material of high optical quality for low-loss wave-guiding, correct thickness to achieve phase-matching and optimum grating parameters to resonantly enhance SHG in the film. High quality BaTiO_3 films have been grown by CVD utilizing

simultaneous delivery of metalorganic precursors in a single liquid solution. Pole figure x-ray scans revealed that these films are (100) oriented and epitaxial on (100) MgO. Light scattering measurements indicated that (1) pre-annealing MgO substrates in oxygen before deposition improved optical quality of the BaTiO₃ films, and (2) the optimum film deposition temperature lies around 850 °C. Future work will focus on optimizing the effective d-coefficients of the BaTiO₃ films and on fabricating grating structures to enhance the SHG efficiency.

Acknowledgments

This work has been funded by the SDIO and contracted by the Naval Ocean Surveillance Center (Contract # N66001-92-C-7008).

- 1 Landolt-Bornstein Numerical Data and Functional Relationships in Science and Technology, New Series, III/11, Hellwege, K.H., ed., pp. 682, 685 (1979)
- 2 Non-critical phase matching (Type II) is disallowed in uniaxial materials with 4mm symmetry, and critical phase matching (Type I) is possible only at wavelengths greater than $\lambda = 2.0\mu$. Private communication with Keith Kendall, Pennsylvania State University.
- 3 "Desirability of electro-optic materials for guided-wave optics", Holman, R.L., Johnson, L.M., Skinner, D.P., *Optical Eng.*, 26(2), pp. 134-142 (1987)
- 4 Subsequent technical obstacles may include photorefractive effects ("optical damage") and difficulties in microlithographic fabrication of the structures.
- 5 At $\lambda = 1.06\mu$ for bulk single crystals, $n_{BT} = 2.322$ and $n_{ST} = 2.315$. A related problem is the magnitude of both the SrTiO₃ and BaTiO₃ refractive indices compared to air at the outer interface. A high index film deposited on top of the BaTiO₃ can reduce its required thickness, but adds undesirable complexity.
- 6 "Properties and applications of layered grating resonances", Gallatin, G.M., *SPIE Proc. Vol. 815*, 158 (1987)
- 7 "Microstructure of BaTiO₃ Thin Films Grown by Reduced-pressure CVD", Van Buskirk, P.C., Gardiner, R., Kirlin, P.S., *Proceedings, MRS Fall Meeting (1990)*, Boston MA., to be published
- 8 "Single Liquid Source Plasma Enhanced Metalorganic Chemical Vapor Deposition of High-quality YBa₂Cu₃O_{7-x} Thin Films", Jiming Zhang, Robin A. Gardiner, Peter S. Kirlin, Robert W. Boerstler, and John Steinbeck, *Appl. Phys. Lett.* 61, 2884 (1992).
- 9 "MOCVD growth of BaTiO₃ in an 8" single wafer CVD system", Van Buskirk, P.C., Gardiner, R., Kirlin, P.S., Krupanidhi, S.B., *Proceedings, 8th Int. Symp. Applications of Ferroelectrics*, August 31-Sept. 2, 1992, Greenville SC, 340-343
- 10 In addition, we have used this technique to deposit BaTiO₃, TlBaCaCuO, LaSrCoO₃, Cr₂O₅, MgAl₂O₄, Y₂O₃-ZrO₂ (YSZ) and PbLaZrTiO₃. We have also demonstrated reagent delivery for CVD of Ta₂O₅ and Cu.
- 11 An optical reflectance thickness monitor may be used if it becomes necessary for more precise control.
- 12 Communication with Angus Kingon, NCSU.
- 13 "Dependence of the Crystal Structure on Particle Size in Barium Titanate", Uchino, K., Sadanaga, E., Hirose, T., *J American Ceramic Society*, 72(8), 1558
- 14 "Dielectric properties of fine-grained barium titanate ceramics", Arlt, G., Hennings, D., de With, G., *J. Appl. Phys.*, 58(4) 1620-1625 (1985)
- 15 *Ibid.* Ref. 1.
- 16 The back surface of each sample was roughened on 600 grit sandpaper and painted black to reduce contribution of the back surface to the signal.
- 17 The detector was used in a photoconductive mode, and a beam chopper and lock-in amplifier were used to reduce noise.

PART IV

Process Integration

REACTIVE ION ETCHING OF $\text{Pt/PbZr}_{0.53}\text{Ti}_{0.47}\text{O}_3/\text{Pt}$ INTEGRATED FERROELECTRIC CAPACITORS

J.J. VAN GLABBEK, G.A.C.M. SPIERINGS, M.J.E. ULENAERS, G.J.M. DORMANS AND P.K. LARSEN

Philips Research Laboratories, P.O.Box 80.000, 5600 JA Eindhoven, The Netherlands

Abstract

Dry etching of a $\text{Pt/PbZr}_{0.53}\text{Ti}_{0.47}\text{O}_3/\text{Pt}$ (Pt/PZT/Pt) ferroelectric capacitor stack with CF_4/Ar plasmas with a reactive ion etching process for the fabrication of micrometer-sized integrated ferroelectric capacitors is described. The etch rate for both Pt and PZT is determined as a function of the process settings: Power, pressure and CF_4/Ar gas flow ratio. A chemical enhancement of the etch rate is found for PZT. It is shown that it is possible to etch the Pt/PZT/Pt ferroelectric capacitor stack in a CF_4/Ar plasma in a single lithographic process using patterning by photoresist masking. Redeposition processes occurring during etching are described.

1. Introduction

High-density ferroelectric random-access memory devices^{1,2} will require very small ferroelectric capacitors, having areas of the order of $(\text{sub})\mu\text{m}^2$. For preparing such small capacitors etching techniques have to be developed, preferentially using a minimum number of processing steps. With wet-chemical etching, using diluted HF-based solvents,³ it is not possible to pattern the ferroelectric film to such small dimensions. Also, wet etching of Pt-based electrodes is not viable. Consequently, capacitor size minimization requires the development of reliable anisotropic dry etching methods such as plasma etching and Reactive Ion Etching (RIE), enabling the structuring of ferroelectric capacitors preferentially in a single photolithographic process step.

Reactive ion and plasma etching of PZT and La-doped PZT (PLZT) has already been described by Poor and Fleddermann⁴ and Saito *et al.*⁵ The first authors report on plasma etching in mixed CF_4/HCl plasmas at elevated substrate temperatures. The latter authors describe structuring a sputtered PZT film in CCl_4 plasmas using photoresist as a masking material. Reactive ion-beam etching of Pt has been described by Novotny.⁶ In this paper the patterning of a complete ferroelectric capacitor stack consisting of a Pt bottom electrode, PZT and a Pt top electrode in a single process step is described.

2. Experimental

2.1. Pt and PZT film deposition

A 70 nm thick Pt bottom electrode is sputter deposited on 10 cm diameter oxidized silicon wafers provided with a thin Ti adhesion layer. Both as-deposited and post-annealed bottom electrodes were prepared.⁷ The electrode preparation process and the effect of the electrode on the PZT deposited on top of it have been described recently in detail.⁷ In this investigation three different PZT materials were etched:

- $\text{PbZr}_{0.53}\text{Ti}_{0.47}\text{O}_3$ films prepared by spin-coating using a modified sol-gel process.^{8,9} Each spin-coated layer is fired at 600°C and the final 290 nm stack is annealed at 700°C .
- $\text{PbZr}_{0.35}\text{Ti}_{0.65}\text{O}_3$ films prepared with a process similar to that used for $\text{PbZr}_{0.53}\text{Ti}_{0.47}\text{O}_3$.

The film thickness was 280 nm.

- c) $\text{PbZr}_{0.57}\text{Ti}_{0.43}\text{O}_3$ films prepared by OMCVD on as-deposited Pt bottom electrodes as described by Dormans *et al.*¹⁰ The film thickness was 350 nm.

The Pt top electrodes were sputter-deposited using the same process conditions as for the bottom electrode. The Pt top electrodes were not annealed.

2.2. Reactive ion etching equipment

The Pt/PZT/Pt stacks were etched in a Alcatel Gir 300 reactive ion etch system. The machine was a single wafer parallel plate etching apparatus equipped with a load-lock and a laser end point detection system. The experiments described here were all done with an RF working frequency of 13.56 MHz without substrate heating and with mixtures of CF_4 and Ar used as etching gases. Heating of the substrate occurred during the etching process caused by the bombardment of ions on the surface.¹¹ For other materials it was observed that ion bombardment induced heating does not change the etch rate.¹²

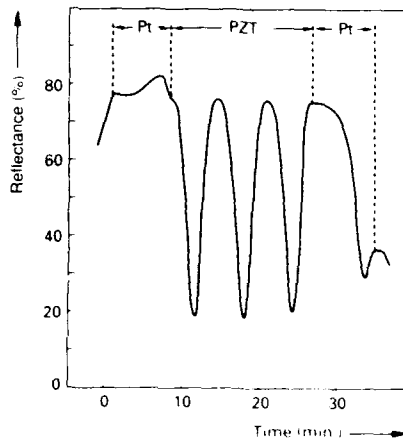


Fig. 1. An example of the changes in reflectivity during etching of a Pt/PZT/Pt stack.

2.3. Etch rate measurement

The etch rate was determined by measuring the time necessary to remove the Pt or PZT film with the laser end point detection system. The film thickness was determined by a surface scan method (Alphastep 200). Figure 1 shows an example of the reflectance of the wafer surface as a function of etching time. The typical reflectance changes indicating the Pt/PZT and PZT/Pt transitions are also shown. These transitions were determined by inspecting the wafers etched for times corresponding with these specific points on the reflectance curve.

3. Etching of PZT and Pt films

The influence of the various RIE process conditions on the etch rate were studied for Pt on sol-gel $\text{PbZr}_{0.53}\text{Ti}_{0.47}\text{O}_3$ films and for PZT on annealed Pt films. The investigations included the effect of RF power setting, pressure in the system during etching and the CF_4 -Ar gas flow ratio of the gas fed into the reactor.

Figure 2 shows for PZT as well as for Pt etched in CF_4 -Ar (4:1) that the etch rates increased with the RF power setting. As the power increased, both the flux of ions to the substrate and their energy increased.^{11,12} The increase in etch rate with power therefore indicates that for both materials the rate was predominantly determined by the ion bombardment and that the flow of fluorine containing species was not rate limiting. Similar increases of the etch rate with RF power setting have been observed in this machine for other materials, e.g. SiO_2 (See Table I).

Figure 3 shows the dependence of the etch rate on the CF_4 -Ar gas flow ratio of the gas

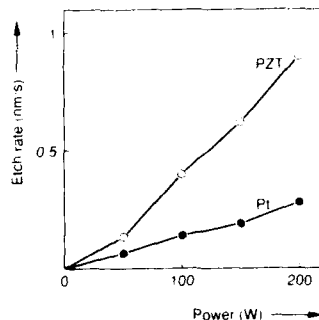


Fig. 2. The etch rate for PZT (\circ) and Pt (\bullet) as a function of RF power using a CF_4 -Ar gas flow ratio 4:1. Total gas flow rate was 20 sccm and pressure was 1 Pa.

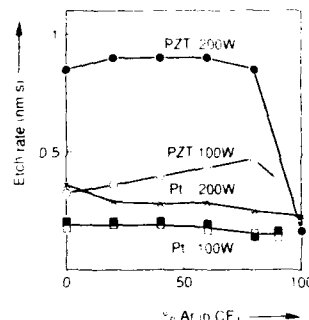


Fig. 3. PZT and Pt etch rate as a function of the CF_4 -Ar gas flow ratio at 1 Pa and 100 and 200W RF power setting. The etch rate for Pt is given for both bottom (\square) and top electrode (\blacksquare).

fed into the etch system. The etch rate for both PZT and Pt was nearly constant, with a about a factor 5 higher etch rate for PZT. Only in 100% Ar, the etch rate for PZT is comparable to that of Pt which shows that, as expected, in Ar both materials were removed by the ion bombardment of Ar^+ ions. When a small quantity of CF_4 is added to the plasma, the ion bombardment induced damage (e.g. bond rupture) increasing the probability of a chemical reaction of the PZT with fluorine reactive species present at the PZT surface. The fact that larger quantities of CF_4 did not increase the etch rate also shows that the flow of fluorine species was not rate determining. There is no chemical enhancement for Pt and the etching is caused by ion-bombardment only. This was also shown in reactive ion beam sputter experiments for Pt in a CF_3Cl -Ar mixtures.⁶

Figure 3 also shows that the etch rate for the bottom Pt-electrode and the top Pt-electrode material is the same. This means that in this respect the bottom electrode was not effected by the heating processes necessary for making the PZT films.

The dependence of the etch rate for both materials on the total pressure in the etch chamber was also studied. In general an increase in pressure decreases the ion bombardment energy and increases the flux. For PZT the etch rate decreases with pressure, confirming that the rate was determined by the ion-bombardment. For Pt, a maximum at about 4 Pa is found. At higher pressures (>5 Pa), a redeposition of material on the wafer surface was clearly observable. This resulted in a decrease of the etch rate for both Pt and PZT and in an increase in roughness of the PZT.

3.1. Effect of PZT composition and morphology.

Table 1 gives at four RF power settings the etch rate for the three types of PZT and for the other materials relevant to the fabrication of integrated ferroelectric capacitors. The etch rates for sol-gel $\text{PbZr}_{0.33}\text{Ti}_{0.67}\text{O}_3$ and $\text{PbZr}_{0.35}\text{Ti}_{0.65}\text{O}_3$ were identical while that for the OMCVD material is about 20% lower. This could be caused by the higher density of the OMCVD material compared to the sol-gel material. A higher porosity could give more chemical reactive sites thus increasing the chemical enhancement for the sol-gel compared to the OMCVD films. Similar decreases in etch rate with increased density has been observed for SiO_2 prepared by CVD techniques and annealed at different temperatures.¹³

Table I

The etch rate for PZT, Pt, photoresist and SiO_2 in nm/min at four RF power settings. The pressure is 1 Pa, the CF_4 -Ar gas flow ratio is 4:1 and the total flow rate is 20 sccm. The different PZT materials are discussed in the text.

	50 W	100 W	150 W	200 W
$\text{PbZr}_{0.53}\text{Ti}_{0.47}\text{O}_3$, sol-gel	10	19	30	44
$\text{PbZr}_{0.35}\text{Ti}_{0.65}\text{O}_3$, sol-gel	11	19	33	47
$\text{PbZr}_{0.57}\text{Ti}_{0.43}\text{O}_3$, OMCVD	-	17	25	33
Pt	3	5	8	10
Photoresist	29	-	-	-
SiO_2	-	37	50	-

4. Ferroelectric stack patterning

The ferroelectric capacitors were fabricated from the blanket Pt/PZT/Pt stack using a photolithographic process. A masking layer was deposited on top of the stack to protect the underlying Pt/PZT/Pt sandwich from being removed in the etching process. It is essential that after etching the masking material can be removed without damaging the etched structures. Organic photoresists, oxides and metals can be used as masking materials for RIE. Here we only discuss results using organic photoresists.

In IC technology, an organic photoresist materials is preferred because it can easily be applied by spin-coating and, in principle, easily removed, e.g. by stripping in a solvent or in an O_2 plasma etcher and it does not require additional process steps. The possibility to make use of a organic photoresist in the structuring of a ferroelectric capacitor is important in effecting a simple technology with the same basic technologies as used in IC fabrication.

4.1. Photoresist behaviour in CF_4/Ar plasmas

The photoresist (HPR204, Shipley) is spun on the ferroelectric stack, resulting in a 1.6 μm thick film. After exposure and development small photoresist patterns are obtained. During RIE, the photoresist mask layer interacted with the plasma in different ways, resulting in degradation of the mask. Observed effects are etching, thermal degradation and redeposition processes, which are discussed below.

1. The data from Table I show that the photoresist was etched at a faster rate than Pt and PZT. Consequently, the photoresist film has to be substantially thicker than the Pt/PZT/Pt stack.
2. During reactive ion etching, the wafers are heated by the ion bombardment, depending on the etching conditions. Excessive photoresist heating results in melting effects and locally this leads to much thinner photoresist film and the possibility of damage to the underlying Pt during RIE. Excessive heating can also cause carbonization of the photoresist, which makes it difficult to remove the photoresist by dissolving it in organic solvents.
3. The relatively low volatility of the fluorides and the formation of teflon-like products

can cause redeposition of the photoresist material during etching. At the edge of the photoresist areas, the low impact angle of the ion flux allows the build up of the redeposited material.

Using RIE conditions that minimize the heating effects on the photoresist (low RF power setting (50W) and low pressure (1 Pa)), Table I shows that the ratio between the etch rate for photoresist and PZT was about 3 and that of photoresist and Pt was about 10. This would mean that for a stack with a 70 nm Pt bottom and top electrode and 290 nm PZT a photoresist film of at least $2.1\text{ }\mu\text{m}$ is necessary to protect the underlying material. It was found, however, that $1.6\text{ }\mu\text{m}$ was sufficient, leaving a $0.2\text{ }\mu\text{m}$ photoresist film after etching. Because the etch rate for the photoresist was determined separately, and not in combination with PZT or Pt, this can only be explained by assuming that the photoresist was modified when etched simultaneously with Pt and PZT by reaction products resulting in an decrease of the etch rate.

After photoresist stripping the thin edge of redeposited material was clearly observable. The redeposited material cannot be removed using standard photoresist stripping solvents or O_2 plasmas. Using solvents at elevated temperatures with ultrasonic agitation it was possible to remove this redeposited material almost completely.

4.2. Ferroelectric capacitor etching.

In order to study how the etching proceeds during the structuring of the Pt/PZT/Pt stack, the process was stopped at intervals so the etched structures could be investigated. Figure

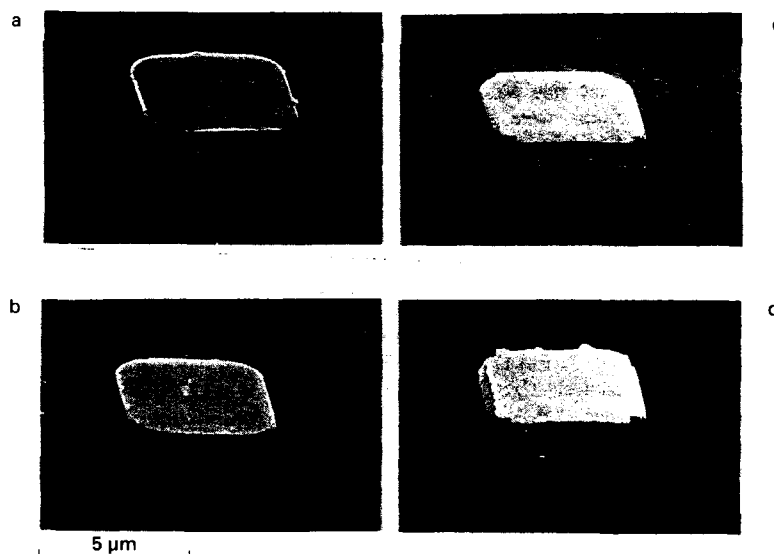


Fig. 4. SEM micrograph made after different stages in the reactive ion etching of a Pt/PZT/Pt stack for the preparation of a $5 \times 5\text{ }\mu\text{m}^2$ capacitor (sol-gel PZT 53/47). Etching conditions: 1 Pa, 50 W, CF_4 -Ar gas flow ratio 4:1. a) Pt top electrode etched; b) 50% of the PZT film etched; c) the complete PZT film etched; d) After etching the bottom Pt electrode.

4 shows how, as the etching proceeds, the capacitor was gradually formed. The photoresist was stripped using the solvent at elevated temperatures with ultrasonic agitation, as discussed above.

Figure 4a shows the situation when only the Pt top electrode is etched and the surface of the $\text{PbZr}_{0.53}\text{Ti}_{0.47}\text{O}_3$ is bare. Atomic Force Microscopy measurements show that the PZT surface had height variations of about 10-20nm. The distribution of these variations corresponds with the surface morphology of the PZT shown in Fig. 4a. These inhomogeneities are related to the crystallization process of the $\text{PbZr}_{0.53}\text{Ti}_{0.47}\text{O}_3$ films used in this study,^{8,9} and are found at the edges of the crystals growing in the amorphous as-deposited sol-gel film. Figure 4b and 4c shows the etched structure after 50% and 100% of the PZT film has been etched, respectively. The 70nm bottom electrode is still continuous after PZT etching because the thickness inhomogeneities are small (< 5 nm) when transferred into the Pt. Figure 4d shows the completely etched capacitor after the etching of the Pt bottom electrode. A relatively smooth, homogeneous-looking SiO_2 surface is obtained (Fig. 4d), with a surface roughness determined by AFM to be similar to or smaller than that of the PZT as expected from the somewhat higher etch rate of SiO_2 as compared to PZT.

5. Conclusion

The preparation of micrometer-sized integrated Pt/PZT/Pt ferroelectric capacitors has been demonstrated using anisotropic reactive ion etching in a CF_4/Ar plasma. The etch rate for Pt was determined by ion-bombardment, while for PZT a large chemical enhancement was found. This allowed for selective etching of the PZT and a stop of the etching process at the Pt bottom electrode. Conventional photoresist can be used as masking material provided that the power of the plasma is low. During etching, a redeposition of etching products occurred at the side wall of the photoresist mask. This deposit was difficult to remove; the best results were obtained using solvents at elevated temperatures with ultrasonic agitation. Removing etch deposits still requires further process optimization.

References

1. J.F. Scott and C.A. Araujo, *Science* **246**, 1400 (1989).
2. P.K. Larsen, R. Cuppens and G.A.C.M. Spierings, *Ferroelectrics* **128**, 265 (1992).
3. S. Mancha, *Ferroelectrics* **135**, 131 (1992).
4. M.R. Poor and C.B. Fleddermann, *J. Appl. Phys.* **70**, 3385 (1991).
5. K. Saito, J.H. Choi, T. Fukuda and M. Ohue, *Jpn. J. Appl. Phys.* **31**, L1260 (1992).
6. Z. Novotny, *Electrotech. Cat.* **41** (1990) 39 (Chem. Abstr. **135**, 50576 (1990)).
7. G.A.C.M. Spierings, J.B.A. van Zon, M. Klee and P.K. Larsen, *Integrated Ferroelectrics* (in press).
8. G.A.C.M. Spierings, M.J.E. Ulenaers, G.L.M. Kampschöer, H.A.M. van Hal and P.K. Larsen, *J. Appl. Phys.* **70**, 2290 (1991).
9. M. Klee, R. Eusemann, R. Waser and H. van Hal, *J. Appl. Phys.* **71**, 1566 (1992).
10. G.J.M. Dormans, M. de Keijser and P.J. van Veldhoven, *Mat. Res. Soc. Symp. Proc.* **243**, 203 (1992).
11. R.J. Visser, *J. Vac. Sci. Technol.* **A7**, 189 (1989).
12. R.J. Visser and J.A.G. Baggerman, *Proc. 9th Int. Symp. on Plasma Chemistry 1989*, Vol. II, p. 1039.
13. F. Gualandris, G.U. Pignatelli, S. Rojas and J. Scannell, *J. Vac. Sci. Technol.* **B3**, 1604 (1985).

REACTIVE ION ETCHING OF $\text{PbZr}_{1-x}\text{Ti}_x\text{O}_3$ AND RuO_2 THIN FILMS

DILIP P. VIJAY, SESHU B. DESU, WEI PAN

Department of Materials Science and Engineering, Virginia Polytechnic Institute and State University,
Blacksburg VA 24061

ABSTRACT

In this work, we have identified a suitable etch gas (CCl_2F_2) for Reactive Ion Etching (RIE) of PZT thin films on RuO_2 electrodes. The etch rate and anisotropy have been studied as a function of etching conditions. The effect of gas pressure, RF power and O_2 concentration on the etch rate have been determined. It was found that ion bombardment effects are primarily responsible for the etching of both PZT and RuO_2 thin films. Etch rates of the order of 20-30 nm/min were obtained for PZT thin films under low gas pressure and high RF power conditions. The etch residues and the relative etch rates of the components of the PZT solid solution were determined using XPS. The results show that the etching of PbO is the limiting factor in the etch process. For RuO_2 thin films, etch rates of the order of 8-10 nm/min were obtained when O_2 was added to the etch gas.

INTRODUCTION

Lead Zirconate Titanate (PZT) ferroelectric thin films are potential candidates for nonvolatile and dynamic random access memory applications as a result of their promising electrical properties and applicability in a wide range of temperatures. However, several problems need to be overcome before the integration of a PZT ferroelectric thin film capacitor into the existing semiconductor VLSI. Some of these issues include the degradation of the ferroelectric capacitor and the need for improvement of the existing processing techniques to obtain the optimum properties¹.

One of the key processing issues involved in the integration of PZT thin film based capacitors into the existing VLSI is the etching of these films and the associated electrodes. It is preferable to use the Reactive Ion Etching (RIE) for VLSI applications because of the large etch anisotropy, high resolution and the high etch uniformity that they offer². For RIE of PZT thin films, it is important to identify a suitable etch gas that can etch all three components of the PZT solid solution- PbO , ZrO_2 and TiO_2 - at reasonable etch rates and a common etch gas for both the electrodes and the ferroelectric material so as to facilitate stack capacitor etching.

Recently, there has been a considerable amount of interest in conductive oxides such as RuO_2 for electrodes in PZT thin film capacitors³ as a result of their reduced fatigue. We have therefore chosen to use RuO_2 electrodes for PZT thin film capacitors. Poor et al.⁴ have reported plasma etching of PLT thin films in CF_4 and HCl plasmas. However, to obtain high etch rates, substrate heating was necessary in their process. Saito et al.⁵ have etched RuO_2 using Reactive Ion Etching with a CF_4/O_2 plasma. In this study, we have examined the feasibility of using $\text{CCl}_2\text{F}_2/\text{O}_2$ as an etch gas for RIE of PZT thin film capacitors. The trends in the etch rates of these films have been studied as a function of etch parameters such as RF power, gas pressure, gas flow rate and percentage O_2 content in the chamber. The etch residues at the end of the etch process have been studied using XPS.

EXPERIMENTAL PROCEDURE

Thin films of PZT (53/47) were deposited to a thickness of 180-200 nm on Pt (500 nm) coated Si/SiO_2 substrates using the sol-gel/spin coating method. The PZT precursor was prepared from a metallorganic solution (0.4M) of lead acetate, zirconium n-propoxide and titanium iso-propoxide dissolved in acetic acid and n-propanol. The method of preparing the precursor is similar to that suggested by Yi et al⁶; more details regarding the method of preparation can be obtained from this reference. The coated films were annealed at 600°C for 30 min to form the PZT perovskite phase.

RuO_2 thin films were reactively sputtered to a thickness of 200 nm onto Si_3SiO_5 in an argon-oxygen ambient at a gas pressure of 10 mTorr and a substrate temperature of 200°C. The films were etched after suitable masking using positive photoresist in a RIE-1C (Samco) etcher. The thickness of material etched was determined using a WYKO 3D profilometer. The surface composition before and after the etch was determined using XPS and the etch anisotropy was evaluated using SEM.

RESULTS AND DISCUSSION

Since the PZT solid solution consists of three components (PbO , ZrO_2 and TiO_2), the overall etch rate is dependent on the Zr/Ti ratio and the concentration of excess lead. This is because of the differing volatilities of the fluorides and chlorides of the constituent elements. In this study we have examined the etch characteristics of only PZT films with compositions close to the morphotropic phase boundary. No substrate heating was used to avoid the loss of lead from the masked areas which could result in degradation of the films at high temperatures. The etching was performed on water cooled substrate holders (less than 100°C) to avoid excessive heating from the plasma. The critical etch parameters studied were the gas pressure, RF power and the effect of O_2 addition to the CCl_2F_2 plasma. Since the objective was to etch the complete ferroelectric stack capacitor in a single run, the etch rate of RuO_2 was also studied under the same conditions as the PZT films. The range of the values of the parameters were chosen so as to observe the general trends in etching of these films with varying conditions. The parameter values were also limited by the stability of the plasma.

Figure 1 shows the trend in etch rate of PZT films with increasing flow rate of CCl_2F_2 gas in the etch chamber. The flow rate of the gas in the chamber was not independent of the gas pressure and therefore its effect on the etch rate is a direct indication of the gas pressure effects. For the flow rate regime investigated, the gas pressure variation was typically 80-200 mTorr. The etching was performed at fixed RF power values of 150 W and 200 W. As can be seen from Figure 1, the etch rate decreases with increasing flow rate of the gas. Also, at low flow rates, higher etch rates are observed at higher RF power. The RF power does not have any significant effect on the etch rate at high flow rates. Typical etch rates obtained under conditions of low flow rates and high power were in the range of 20-30 nm/min. The decreasing trend of the etch rate with increasing flow rate indicates that the primary mechanism of etching in these films is by ion bombardment. At high gas pressures/flow rate there is a decrease in the sheath potential² and thereby a reduction in the number of ions participating in the etch process. In effect, this decreases the energy of ion bombardment and consequently, the etch rate.

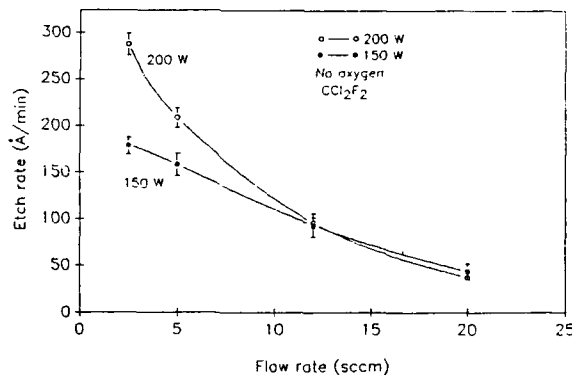


Figure 1: The etch rate of PZT thin films as a function of CCl_2F_2 gas flow rate.

The effect of RF power on the etch rate of PZT films is shown in Figure 2. In general, the etch rate increased with increasing RF power. It is well known that with an increase in the RF power, the sheath potential and the concentration of the reactive ions increase². The effect of gas pressure on the etch rate at different power values (Figure 1) does suggest that the increase in etch rate with RF power is due to the increase in sheath potential. The notable feature however is the actual value of the etch rate. At a gas pressure of 100 mTorr, O_2 content of 15 % and RF power as high as 200 W, an etch rate of the order of 30 nm/min was obtained. At lower gas pressures and higher power, however, the plasma was very unstable.

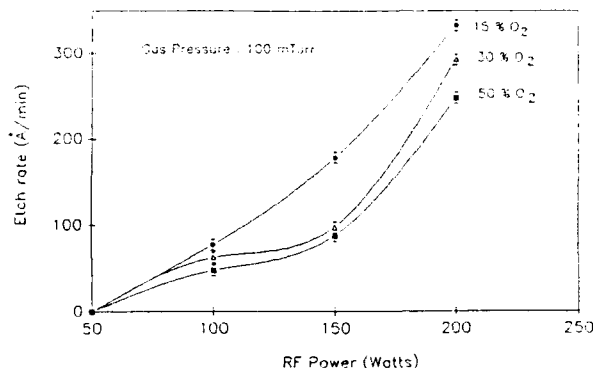


Figure 2: The effect of RF power on the etch rate of PZT thin films at constant gas pressure.

Figure 3 shows the effect of O_2 addition on the etch rate of PZT films at various gas pressures. In general, there is a peak in the etch rate with varying O_2 content at a particular gas pressure. At low gas pressures, it was found that the etch rate dropped significantly with increasing O_2 content in the chamber. O_2 addition in small amounts is known to enhance the etch rate in the case of SiO_2 etching. In our case, we can expect a mechanism of etching similar to that in SiO_2 . At lower gas pressures, the addition of small amounts of O_2 enhances the etch rate of the PZT films possibly by causing reduction in the recombination of the radicals. However, at higher O_2 content, the etch gas is diluted and therefore the etch rate is reduced. Addition of O_2 to the etch gas at high gas pressures, tends to reduce the number of radicals participating in the etch process near the sheath region. The effective impact energy of the ions participating in the sputtering is therefore increased as a result of reduced collisions.

The etch anisotropy under various etching conditions was studied using the SEM. Figure 4 is an SEM micrograph of a sample etched under conditions of low gas pressure and low RF power. Under these conditions we found the etch profile to be anisotropic. At high gas pressures and high RF power, the etch profile was more isotropic. Since the primary etch mechanism is by ion bombardment, one can expect high anisotropy at low gas pressures. However, at high RF power, the energy of the bombarding ions are very high, leading to significant damage of the etched surface.

The composition of the etched surface was determined as a function of etch time using XPS (Kratos XSAM 800) using a 13 kV Mg K α source and the standard-less ratio method was used for quantitative analysis. For this study, the etching was performed on a single sample (1 cm x 1 cm) without any overlying mask. The etching was done under the conditions of 150 W RF power, 100 mTorr gas pressure and 15 percent O_2 content in the chamber. An initial surface analysis was performed on the sample before the etching process and subsequent analyses were done at predetermined intervals during etching. Figure 5(a) is a comparison of the ESCA wide scan before and after the etch process. The components of the PZT solid solution clearly seem to be completely etched out at the end of the etch process. However, at the end of this process, Cl and F residues are present on the surface of the sample. These residues were removed easily by baking the sample at 100°C for 30 min. Figure 5(b) is a plot of the relative atomic concentration of Pb, Zr and Ti as a function of etch time. The concentrations of these elements were determined using the standard-less ratio method and more details regarding this method can be obtained from Ref 8. This plot is a clear indication of the relative etch rates of the three components in the PZT solid solution. Initially, the relative atomic concentration of Zr and Ti decreases quite rapidly. The narrow scan results show that after the first 30 seconds of etching under these conditions, there is a continuous decrease in the Zr concentration while the relative Ti concentration appears to be nearly constant. It is evident from Figure 5(b) that the etch rate of PbO is the limiting factor in the etching of PZT thin films and therefore any post etch residues are primarily due to the PbO.

The chlorides of Zr, Ti and Pb, have higher vapor pressures compared to the corresponding fluorides at the etching temperature (100°C) and therefore we expect the primary volatile by-products to consist of the chlorides. However, the actual presence of these compounds in the by-products have not yet been identified experimentally. The vapor pressure of the chlorides decreases in the order of $TiCl_4 > ZrCl_4 > PbCl_2$.

The etching of RuO_2 thin films were studied under similar reactor configuration and etching conditions. In the past, Saito et al.³ have investigated the reactive ion etching characteristics of MOD RuO_2 .

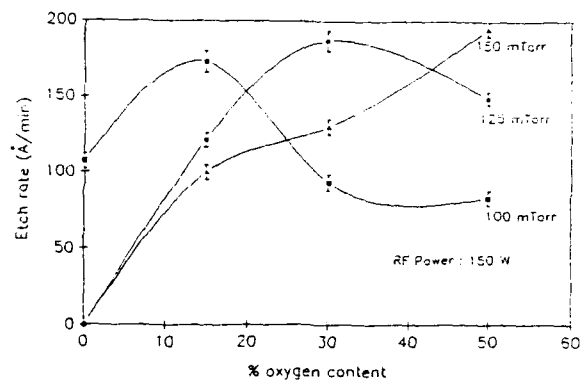


Figure 3: The etch rate of PZT films as a function of % O_2 in the etch gas.

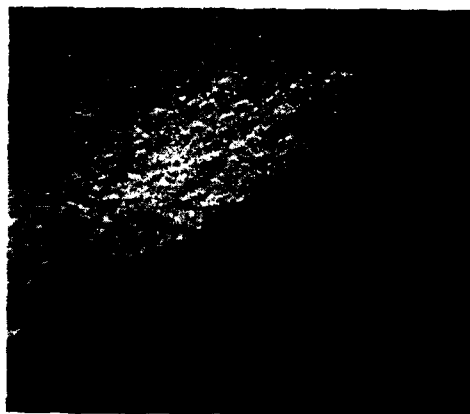


Figure 4: SEM micrograph of a PZT thin film sample showing the high etch anisotropy

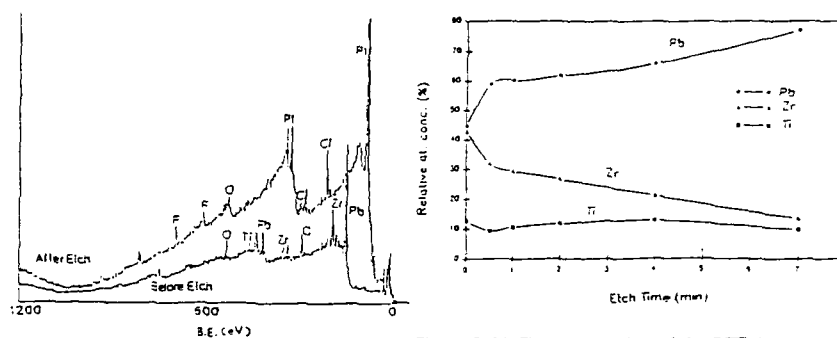


Figure 5 (a): The ESCA wide scan of the PZT film surface before and after the etch process.

Figure 5 (b): The composition of the PZT film surface as a function of etch time as determined from the ESCA studies

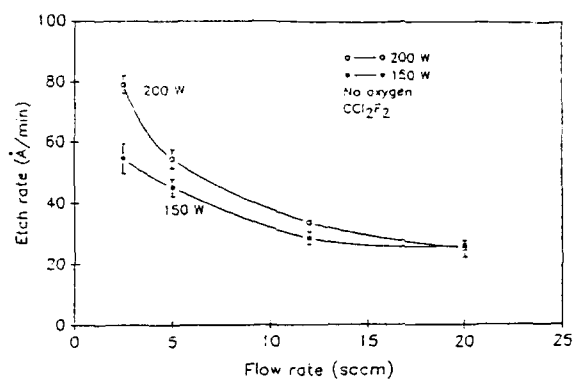


Figure 6: The etch rate of RuO_2 thin films as a function of flow rate of CCl_2F_2 gas.

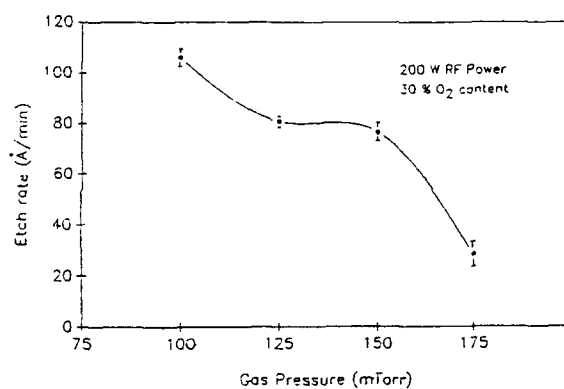


Figure 7: The effect of O_2 addition on the etch rate of RuO_2 thin films (compare to Fig. 6).

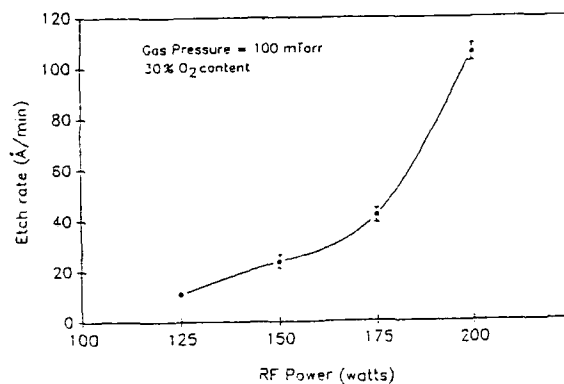


Figure 8: The effect of RF power on the etch rate of RuO_2 thin films.

thin films using CF_4/O_2 plasma. They have reported that RuO_4 and RuF_4 are volatile compounds that form as by-products during the etching of RuO_2 . Figure 6 shows the effect of increasing flow rate gas pressure on the etch rate of RuO_2 thin films at two different RF power values in pure CCl_2F_2 gas. As in the case of PZT films, the etch rate decreases with increasing gas pressure, indicating that ion-bombardment effects are responsible for the etching of these films. The actual values of the etch rates were however significantly lower than that of the PZT films. Typically, without any O_2 addition in the chamber, etch rates of the order of 7.5-8.0 nm/min were obtained at low gas pressures and high power. With the addition of O_2 (30%) to the etch gas, as shown in Figure 7, there was a considerable amount of increase in the etch rate at lower gas pressures. RuO_2 can react with oxygen ions in the plasma to produce volatile RuO_4 , RuO_3 .³ The ion derivatives of the CCl_2F_2 gas are responsible only for bombardment/sputtering of the reaction products. It is unlikely that fluoride and chloride derivatives of Ru will be removed as volatile by-products in significant amounts in comparison to $\text{RuO}_3/\text{RuO}_4$ because of the relatively higher boiling point of the former. In the absence of any O_2 in the etch gas, the etching process is an ion-induced phenomena (etching occurs by ion bombardment) as evident from the gas pressure effects. This is also confirmed by the RF power effects on the etch rate, as shown in Figure 8. Increasing the RF power increases the energy of the impacting ions thereby increasing the etch rate. When O_2 is added to the etch gas, the etching mechanism becomes an ion-enhanced phenomena i.e., the bombarding ions assist in the reaction of O_2 with RuO_2 films and in the removal of the by-products formed thereafter.

If the capacitor is to be etched in a single run, then the only concern regarding the selectivity in the etching process is between the bottom electrode and the substrate. High selectivity can be obtained by etching the RuO_2 bottom electrode in an O_2 enriched plasma. Since, ion bombardment effects are primarily responsible for the etching of PZT and RuO_2 films, it is favorable to use a low gas pressure and high RF power to obtain high rates. However, the RF power needs to be optimized to obtain high anisotropy without any mask damage.

SUMMARY

Thin films of PZT and RuO_2 have been successfully etched using CCl_2F_2 as the etch gas. The etch parameters, namely, gas pressure, % O_2 content and RF power, have been optimized to obtain high rates (~25-30 nm/min for PZT and 8-10 nm/min for RuO_2) and good anisotropy during etching. It was observed that low gas pressures favor high etch rates of PZT and RuO_2 films indicating that ion bombardment is the primary mechanism of etching in these films. Also, low RF power and low gas pressures favored anisotropic etching. The relative etch rates of the components of PZT films have been determined by studying the surface composition as a function of etch time using XPS. It has been determined that the etch rate of PbO is the limiting factor in the etching process. The XPS studies also revealed small amounts of fluorine and chlorine surface residues at the end of the etch process that were removed easily by low temperature baking. In the case of RuO_2 thin films, there is an increase in the etch rate with O_2 addition to the etch gas, possibly due to the formation of volatile $\text{RuO}_3/\text{RuO}_4$ compounds.

ACKNOWLEDGEMENTS

This study was partially supported by DARPA through a project from ONR. This work was also partially supported by Center for Advanced Ceramic Materials, the Virginia Center for Innovative Technology.

REFERENCES

- ¹ L. Parker and A. Tasch, *IEEE circuit and Device Mag.*, 17, January, 1990.
- ² S.M. Sze, *VLSI Electronics*, McGraw-Hill Publishing Company (1988).
- ³ C.K. Kwok, D.P. Vijay, and S. B. Desu, *Proceedings of the 4th International Symposium on Integrated Ferroelectrics*, Monterey, CA (1992). ⁴ M.R. Poor, A.M. Hurd, C.B. Fiedermann, and A.Y. Wu, *Mat. Res. Soc. Symp. Proc.*, 200, 211 (1990).
- ⁵ S. Saito and K. Kuramasu, *Jpn. J. Appl. Phys.*, 31, 135 (1992).
- ⁶ G. Yi and M. Sayer, *Ceram. Bull.*, 70(7), 1173 (1991).
- ⁷ C.J. Mogab, A.C. Adams, D.L. Flamm, *J. Appl. Phys.*, 49, 3796 (1978).
- ⁸ S.B. Desu and C.K. Kwok, *Mat. Res. Soc. Symp. Proc.*, 200, 267 (1990).
- ⁹ R.C. Weast and M.J. Astle, *CRC Handbook of Chemistry and Physics*, CRC Press Inc. (1980).

CHEMICALLY ASSISTED ION-BEAM ETCHING OF SOL-GEL DERIVED PZT, PLZT AND LiTaO₃ THIN FILMS FOR SILICON BASED DEVICE INTEGRATION

P. F. BAUDE, C. YE., AND D.L. POLLA
University of Minnesota, Microelectromechanical Systems Center
Department of Electrical Engineering
Minneapolis, MN 55455

ABSTRACT

Wet chemical, reactive ion etching and reactive ion-beam etching of sol-gel prepared PZT (54/46) [Pb(Zr,Ti)O₃], Lanthanum doped PZT [PLZT (9/65/35)] and LiTaO₃ have been investigated. Wet chemical etching using an HCl-HF solution, reactive-ion etching using a SF₆ plasma and chemically assisted ion-beam etching (CAIBE) using a xenon plasma and chlorine reactive gas were used. Etch rates for each method were determined and the ability to define small features in the thin film ferroelectric was investigated. It was found that for structures smaller than approximately 20 X 20 μm², chemically assisted ion beam etching provided by far the best results. 3 X 3 μm² capacitor and 2 μm wide optical waveguide structures in PZT, PLZT respectively, were successfully fabricated using a CAIBE system. An etch depth monitor enabled accurate *in-situ* etch rate monitoring of the PLZT and PZT thin films.

INTRODUCTION

Sol-gel prepared ferroelectric Pb(Zr_xTi_{1-x})O₃ thin films have been the object of much interest due to the relatively inexpensive and simple material preparation [1,2]. The use of thin film ferroelectrics in nonvolatile memory, sensing and optical devices has demanded the use of a variety of etching techniques such as RIE, wet chemical and ion-beam milling. The ability to integrate thin film PZT and PLZT on silicon or GaAs [3] with sophisticated signal processing circuitry requires the ability to define small feature structures such as capacitors, optical waveguides [2,4], and sensing devices that include micropressure sensors and pyroelectric detectors [1].

The rough edges and widely varying etch rates obtained using wet chemical etching inhibit device processing and performance. Reactive-ion etching of these films requires elevated temperatures that also complicate device processing. The use of chemically-assisted ion beam etching provides an anisotropic, low temperature, rapid etch technique that provides smooth edges and sidewalls and is an attractive candidate for thin ferroelectric device integration. The ability to stop the thin film etch is also important in optical waveguide fabrication. The modeling of ferroelectric optical planar, ridge and buried ridge guides indicates that in many cases the ferroelectric thin film does not have to be completely etched and is sometimes desirable to stop the etch before reaching the bottom cladding layer [5]. Fabrication of these strip-loaded optical waveguides designs requires the ability to monitor the etch rate and depth during the etch. The CAIBE system described in this paper incorporates an *in-situ* optical etch rate monitor that allows the etch to be stopped within 0.1 nm of the desired depth.

SAMPLE PREPARATION

Silicon (100) and (111) *p-type* 2" wafers of approximately 300 μm in thickness were used in this investigation. Several substrates were sputter deposited with 2500 Å of Pt for electrical characterization. Other samples were thermally oxidized with 1 μm of SiO₂ which served as a bottom cladding layer for optical waveguiding characterization. The platinum coated wafers were cleaned in an acetone-methanol, DI rinse followed by a soft bake at 200 °C for 10 minutes just prior to sol-gel deposition. The oxidized wafers were processed similarly with an initial HF dip and rinse. In the process of preparing the PLZT

films. Zr propoxide and Ti isopropoxide type were used in a reaction with lead and lanthanum acetate. LiTaO_3 precursors were lithium acetate and tantalum acetate. The synthesized solutions were then partially hydrolyzed in preparation for spin coating. The hydrolysis of the PLZT was found to be much quicker than that associated with PZT solutions also prepared in our laboratory [1]. Spin-coating was done at 2000 rpm for 60 seconds for each coat. The samples were subsequently dried and annealed at 200 °C for 20 minutes. Each layer contributed a film thickness of about 600 Å, measured after the final anneal. Thicker films were prepared by depositing multiple layers with an intermediate anneal at 450 °C for 15 minutes. A final anneal of the films at 650 °C for 10 minutes completed the deposition process. The PLZT thin films required an intermediate PLT buffer layer (10% Lanthanum) for crystallization and adhesion of the PLZT thin films [4].

WET CHEMICAL ETCHING

Wet chemical etching of the samples was first investigated as a means of defining the various geometries which included capacitor structures that ranged in size from $1 \times 10^{-3} \text{ cm}^2$ to $2.5 \times 10^{-5} \text{ cm}^2$. Successful etching of both the PLZT-PLT film using a HF-DI 1:50 solution in less than 60 seconds was achieved. The etch rate was measured to be 5 µm per minute for this solution. A smoky film was left on the surface after the etch and was easily removed with an HCl rinse. The etchant was stirred slowly during the etch and this seemed to provide better uniformity in the case of the optical waveguides. The resulting structures however were not promising for guides less than 500 µm in width because of the very rough sides. Additionally severe undercutting was observed. For 20 µm optical ridge waveguide structures the undercutting was observed to be more than 5 µm on each side. For the capacitor structures, inspection with an optical microscope revealed very rough edges resulting from either anisotropic etching of the polycrystalline films or some type of ionic etching of ferroelectric domains in the material. We were not able to detect any type of domain structure in the films when the etched sample was viewed with a optical microscope with a magnification of 1000X.

REACTIVE ION ETCHING

A number of groups have used reactive-ion etching (RIE) for the delineation of PZT and PLZT microstructures [6] (and more recently [7]). Similar work was done on PLZT capacitor and waveguide structures using a Technics™ PD IIA planar electrode low frequency RIE system. Several gases were used in the room temperature plasma etching experimentation including dichloro-difluoromethane (CCl_2F_2), Ar, SF_6 , and oxygen. The plasma power was varied between 100 W and 200 W and the chamber pressure was maintained at 150 mTorr. It was found that virtually no etching occurred for substrate temperatures less than 100 °C.

The substrate temperature was elevated with the addition of a resistive 700 W heater and monitored using a thermocouple that was read by an Omega™ thermometer via a feed-through at the base of the system. The etch rate for a PZT (54/46) thin film versus substrate temperature (in CCl_2F_2) is given below in Fig. 1. As shown the etch rate significantly increases with substrate temperature. The results for PLZT and PLT thin films were very similar and both materials required substrate heating. Masking structures to be etched at elevated temperatures required the use of a metal mask deposited using a lift-off procedure.

The maximum temperature used was 300 °C, yielding an etch rate of approximately 1 µm per hour. This is in good agreement with the bulk etch rates of Poor *et al* [6]. There were significant difficulties with masking the structures. Because the elevated temperatures make photoresist removal very difficult a variety of metals were patterned onto the sample using a standard liftoff procedure. The metal deposition is undesirable for waveguide fabrication because of optical absorption in the metal, however is appropriate for capacitors. The PLT thin films showed a higher etch rate for a given temperature than the

PLZT thin films in a SF_6 plasma. Although the need for metal mask complicates the processing

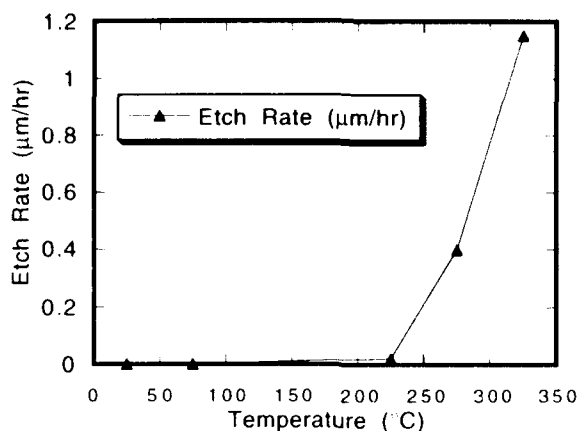


Figure 1. Etch rate versus substrate temperature of PLZT (54/46) thin film. Appreciable etching was not observed until the substrate temperature was increased to 275 °C.

somewhat it was not the motivation for finally using the ion-beam etching process, which does not require a metal mask. The structures etched in the RIE exhibited very rough side-walls, as observed by SEM, and proved unacceptable for any optical waveguiding due to scattering losses.

ION BEAM ETCHING

Chemically assisted ion-beam etching (CAIBE) was investigated as means of improving the smoothness of both the PLZT-PLT [4] and LiTaO_3 waveguides and the PZT capacitor structures. The system is illustrated in Fig. 2 showing the vacuum load-lock, sample position, discharge chamber and optical etch rate monitor apparatus.

The samples were loaded via a load lock into the chamber which was subsequently pumped down to 5×10^{-7} Torr. A 10 mW helium-neon laser operating at 633 nm was focused onto the sample through a window and the reflected beam was positioned on a silicon photodetector as shown in Fig. 2. The higher index of refraction of the PLZT layer relative to the underlying SiO_2 layer causes light to be reflected from both the top and bottom of the thin film PLZT. In the case of the capacitor structures the reflective platinum bottom electrode provided ample signal intensity for the photodetector. This provided an accurate *in situ* monitoring of the etch rate. The etch depth accuracy was confirmed by measuring the waveguide thickness with a profilometer after the etch. The optical etch rate monitor revealed information about the etch rate as a function of the various gas constituents' flow rates. The Xe flow rate was varied from 2 sccm to 15 sccm and it was observed that no significant increase occurred for flows greater than 10 sccm. The chlorine gas flow was 1 sccm and at that rate the etch rate increased by about 17% from the case of no chlorine present. There was also an improvement in the smoothness of the optical waveguide

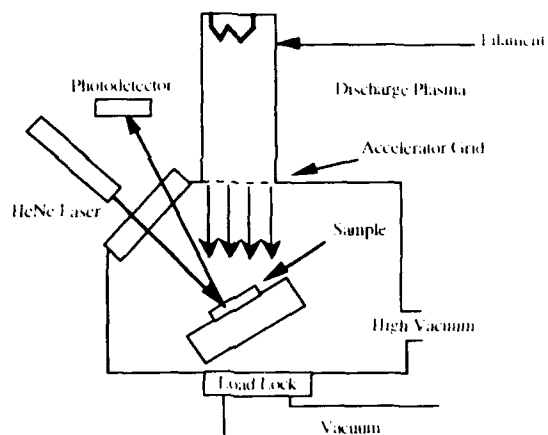


Figure 2. CAIBE experimental schematic illustrating Xenon plasma, sample position, optical etch rate monitor. The sample block can be rotated in the plane of the page to improve the smoothness of etched structures.

structures when chlorine was used. Table 1 below shows typical operating parameters for the CAIBE system. At these powers the etch rate of the PLZT (9/65/35), PZT (54/46) and LiTaO_3 were measured to be 847, 900, and 514 Å/min, respectively.

Table 1 *Ion-Beam Etching Parameters*

FILAMENT CURRENT	DISCHARGE POWER	BEAM POWER	ACCELERATOR POWER
6.73 A	1 A	25 mA	4 mA
	25 V	1000 V	250 V

In the case of the optical waveguides the SiO_2 layer beneath the PLT and PLZT layers etched at a different rate and thus acted as an etch stop indicator. The PLZT (9/65/35) and PZT (54/46) capacitor structures were on top of a Pt electrode which also acted as an etch stop indicator. For Pt films greater than 1000 Å the etch stop indicator provided a means to determine when the etch was complete and the ion beam was turned off. The resistivity of the lower Pt electrode was not effected when exposed to the ion beam for a short period of time. The reflectance signal versus time for PLZT(9/65/35) sample is shown in Fig. 3. The etch depth was derived from the HeNe wavelength (6328 Å) and the refractive index of the film. The calculated etch depth from the reflectance signal was 3578 Å and the measured etch depth was 3525 Å. The index of refraction value used in the former calculation was determined from optical reflectance measurements performed on the sample prior to its etch [8]. A 7 µm wide ridge waveguide is shown below in figure 4. The etching process used to fabricate this structure is discussed above. Optical waveguiding was observed in this type of structure and is discussed in detail in reference 4. The beam width is 5 cm and exhibits a gaussian distribution which presents a uniformity problem for large area etches. Interference patterns were observed on the sample after the etch indicating a macroscopic non uniformity in the etch depth. The total etch depth variance is about 300 Å from the

center to the perimeter on a 2 cm sample. The variance is not in agreement with the number of fringes observed which possibly indicates a stoichiometry variance although no chemical analysis was performed on the etched samples.

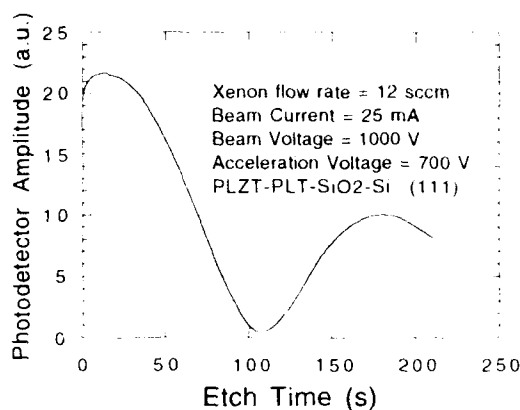


Figure 3. Reflectance signal of in-situ etch rate monitor in CAIBE system. The period of the reflected optical signal reveals the etch rate if the films refractive index is known.

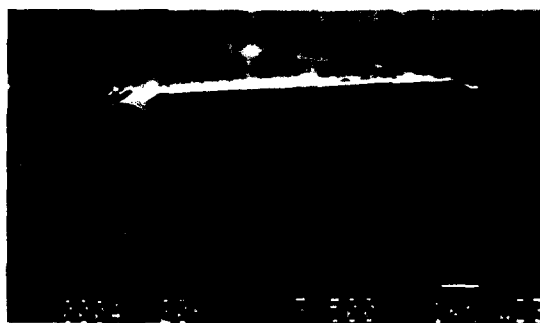


Figure 4. SEM photograph of 7 μm PLZT-PLT-SiO₂-Si optical ridge waveguide fabricated using the ion beam etching process.

CONCLUSION

Ion-beam etching of sol-gel derived ferroelectric PZT, PLZT and LiTaO₃ has been used to define capacitor and optical waveguide structures. The latter devices showed significant improvement when etched in the ion-beam system than when wet chemical etched or reactively ion etched with SF₆. Additionally the ion-beam etch is a low temperature process that simplifies the processing and increases the compatibility with silicon circuit fabrication for device integration. Wet chemical etching and reactive ion etching of the PZT and PLZT thin films resulted in structures with rough edges which proved prohibitive for optical waveguiding structures. The undercutting observed in the wet chemical etching

process can potentially complicate integrated processing for microsensor applications. Furthermore it is difficult to stop the etch of the ferroelectric etch at a desired depth. Reactive ion etching proved equally prohibitive for optical waveguide fabrication due to the metal masking and rough sidewalls. Recent results by Pan et al [7], however, have shown that room temperature RIE etches of PZT thin films are possible in a O_2 and $ClCl_2F_2$ gas mixture indicating that reactive ion etching remains a viable candidate for integrated processing of ferroelectric thin films. Chemically assisted ion beam etching and ion-beam etching provides a low-temperature controlled etch process for thin film ferroelectrics. CAIBE processing of PLZT, PZT and $LiTaO_3$ thin films provides the ability to define small feature capacitor and optical waveguide structures. The high etch rates of PLZT, PZT and $LiTaO_3$, low processing temperatures and compatibility with standard photolithographic masking steps make the CAIBE process an attractive method for integrating these ferroelectric thin films with silicon. Further work needs to be done on increasing large wafer uniformity and understanding the reactive etching mechanism.

ACKNOWLEDGMENTS

The authors would like to acknowledge the technical assistance of T. Nguyen, D. Glumac, P. Schiller, and T. Tamagawa.

REFERENCES

1. C. Ye, T. Tamagawa, and D.L. Polla, J. Appl. Phys. **70**, 5538, 1991
2. S.L. Swartz, S.J. Bright, P.J. Melling, and T.R. Shrout, Ferroelectrics, **108**, 71, (1990)
3. J. Choi, PhD Thesis, *GaAs Microsensors*, University of Minnesota, Dept. of EE, 1990
4. P.F. Baude, C. Ye, T. Tamagawa, and D.L. Polla, J. Appl. Phys., **73**, 7960 (1993)
5. P.F. Baude, MSEE Thesis, University of Minnesota, Dept. of EE, June 1993
6. M.R. Poor and C.B. Fleddermann, J. Appl. Phys. **70**, 3385 (1991)
7. W. Pan, D. P. Vijay and S.B. Desu, Presented at the 1993 Spring MRS Meeting, San Francisco, CA
8. P. Baude, C. Ye, T. Tamagawa, and D.L. Polla, Proceedings of the Fall 1992 MRS Meeting, 1992, Boston MA, (1993)

**EPITAXIAL FERROELECTRIC HETEROSTRUCTURES OF ISOTROPIC
METALLIC OXIDE (SrRuO_3) AND $\text{Pb}(\text{Zr}_{0.52}\text{Ti}_{0.48})\text{O}_3$**

C. B. EOM, R.B. VAN DOVER, JULIA M. PHILLIPS, R.M. FLEMING, R.J. CAVA,
J.H. MARSHALL, D.J. WERDER, C.H. CHEN, AND D.K. FORK*

AT&T Bell Laboratories, Murray Hill, NJ 07974

*Xerox Palo Alto Research Center, Palo Alto, CA 94304

ABSTRACT

We have fabricated epitaxial ferroelectric heterostructures of isotropic metallic oxide (SrRuO_3) and ferroelectric thin films [$\text{SrRuO}_3/\text{Pb}(\text{Zr}_{0.52}\text{Ti}_{0.48})\text{O}_3/\text{SrRuO}_3$] on (100) SrTiO_3 and YSZ buffer layered Si substrates by 90° off-axis sputtering. These heterostructures have high crystalline quality and coherent interfaces as revealed by X-ray diffraction, Rutherford backscattering spectroscopy and cross-sectional transmission electron microscopy. The ferroelectric layers exhibit superior fatigue characteristics over 10^{10} cycles with large remnant polarization.

Ferroelectrics hold potential for both dynamic and permanent data storage in digital memory systems[1]. Conventionally, to build these memory devices, polycrystalline ferroelectric thin films are grown on a Pt or Al base electrode. The high angle grain boundaries which occur in the ferroelectric thin film layer are detrimental to device performance because they cause aging and fatigue due to charge segregation and decay at the grain boundaries. Furthermore, the undesirable nature of the interfaces between ferroelectric layers and electrodes resulting from non-epitaxial growth leads to degraded performance characteristics [2]. Ramesh et al. reported that epitaxial thin film heterostructures of ferroelectric materials and certain cuprate superconductors grown by the laser ablation technique have outstanding fatigue properties[2, 3]. Unfortunately, the cuprate superconductors are not fully chemically and thermally stable, which puts some constraints on their processing and usage. Furthermore, the high T_c superconducting cuprates typically have relatively poor crystalline quality and rough surfaces. These drawbacks may limit the application of such device structures for non-volatile memory applications.

We recently reported the synthesis and properties of single crystal epitaxial thin films of the isotropic metallic oxide SrRuO_3 on miscut (100) SrTiO_3 substrates [4]. SrRuO_3 is a pseudo-cubic perovskite with pseudo-cubic lattice parameter of 3.93\AA [5, 6]. (Note: the a- and c-lattice parameters of PZT are 4.036\AA and 4.146\AA , respectively). The lattice mismatches of SrRuO_3 and ferroelectric $\text{Pb}(\text{Zr}_{0.52}\text{Ti}_{0.48})\text{O}_3$ (PZT) on the {001} surface is fairly small ($\sim 2.7\%$), which allows us to grow high quality epitaxial ferroelectric heterostructures with SrRuO_3 electrodes. Unlike most oxide superconductors, SrRuO_3 is stable up to 1200 K in oxidizing or inert gas atmospheres [7]. The resistivities of these films are isotropic and low ($\sim 340\ \mu\Omega\text{-cm}$ at room temperature), and the temperature dependence (dp/dT) shows good metallic behavior, which is important for electrode applications. All of these observations suggest that SrRuO_3 might be an ideal electrode material for epitaxial ferroelectric device structures.

The films have been grown *in situ* by the 90° off-axis sputtering technique in which almost the exact composition of the target is obtained over large areas (2" x 2" area from 2" diameter sputtering target) without a need for substrate block rotation [8, 9, 10]. This technique allows very good step coverage, which is important in fabricating ferroelectric devices. Two 2" magnetron sputter guns (US gun II) were mounted perpendicular to each other in an off-axis geometry for growth of these heterostructures: one for SrRuO₃ and the other for PZT. The substrate block is placed on a rotating arm to switch between guns. The details of multilayer growth by this technique were reported elsewhere[11].

A smooth surface is very important for the fabrication of multilayer ferroelectric devices. The surface morphology of SrRuO₃ films was investigated by scanning electron microscopy (SEM). The surface of the 2000Å thick SrRuO₃ film on SrTiO₃ substrate was featureless with a lateral resolution of 100Å. Using an atomic force microscope (AFM), Parks Scientific Instrument Model SFM-BD2, with UltraleversTM (tip radius ~ 100 Å), results from five scans over 4 μm x 4 μm area but over different spots on the same film reveal root mean square surface roughness of 6.9 ± 0.2 Å and peak-to-valley roughness of 53 ± 6 Å. We believe that the growth of SrRuO₃ films on SrTiO₃ is layer-by-layer, resulting in very smooth surfaces.

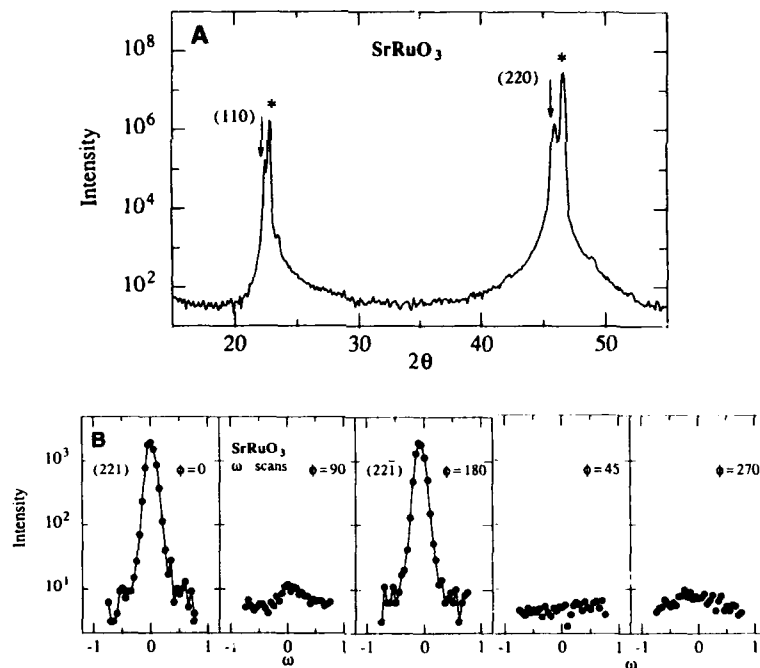


Figure 1. (a) XRD θ - 2θ scans on a SrRuO₃ thin film on (100) SrTiO₃ substrates.

The SrTiO₃ peaks are marked (*). (b) X-ray ω scans of the (221) reflection at $\phi=0^\circ$, $\phi=45^\circ$, $\phi=90^\circ$, $\phi=180^\circ$ and $\phi=270^\circ$ for a (110) oriented SrRuO₃ thin film on a (100) SrTiO₃ showing a single variant domain.

The film textures were investigated by x-ray diffraction (XRD) using a four-circle diffractometer with a $\text{CuK}\alpha$ source and a pyrolytic graphite monochromator and analyzer. The films were aligned so that the film normal was parallel to the ϕ axis of the diffractometer. This geometry allows full access to the reciprocal lattice (except for in-plane reflections) with $\omega = \phi$. Figure 1 (a) shows the θ - 2θ scan of SrRuO_3 thin films grown on (100) SrTiO_3 substrates. The only substantial peaks detected are from d-spacings corresponding to {110} or {002}. Because of the systematic absence of a (00 l) peak ($l=2n-1$) and the near-degeneracy of $d_{\{110\}}$ and $d_{\{002\}}$ in the pseudo-cubic SrRuO_3 structures, from the normal θ - 2θ scans alone it was not possible to distinguish whether the texture is {110} or {002} or a combination. We were able to establish that these films are purely {110} texture normal to the substrate by locating peaks that do not have a degenerate pair, e.g. the (113). The (113) peak was observed only at the position corresponding to {110} grains normal to the substrate and not at the position corresponding to {002} grains. Peaks with degenerate pairs cannot distinguish the texture, for example, (121) peak positions for {110} grains normal to the substrate are the same as those of the (103) peak positions for {002} grains normal to the substrate. After we established the pure {110} film texture we could assign unique indices to pairs of peaks with near-degenerate d-spacing and study in-plane texture. The ω scan rocking curve widths (FWHM) of the {220} reflections of SrRuO_3 are 0.16° , the instrument resolution.

The in-plane textures for these films were also investigated by scanning off-axis peaks. Figure 1 (b) shows ω -scans of the (221) reflection at $\phi=0^\circ$, $\phi=45^\circ$, $\phi=90^\circ$, $\phi=180^\circ$ and $\phi=270^\circ$ for a {110} SrRuO_3 thin film on (100) SrTiO_3 . (We have observed the same results with the non-degenerate (113) reflection.) The significant intensities only at $\phi=0^\circ$ and $\phi=180^\circ$, but no intensities at $\phi=45^\circ$, $\phi=90^\circ$ and $\phi=270^\circ$, clearly indicate that the grains are single domain with the in-plane epitaxial arrangement $\text{SrRuO}_3 [\bar{1}10]//\text{SrTiO}_3[010]$ and $\text{SrRuO}_3[001]//\text{SrTiO}_3[001]$. The high crystalline quality of the films has been confirmed by ion channeling using 1.8 MeV $^4\text{He}^+$ ions. The ratio of the backscattered yield (χ_{\min}) for a SrRuO_3 film along $\langle 100 \rangle$ to that in a random direction is 1.8%, which is very close to the value of Si single crystals.

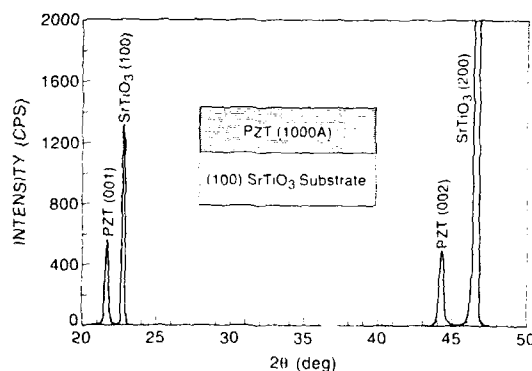


Figure 2 XRD θ - 2θ scan of a PZT thin film on (100) SrTiO_3 substrate showing (001) epitaxy.

Before growing the trilayer heterostructures, the optimum conditions for growing epitaxial PZT layers were determined. At this stage, the quality of the films was determined by means of XRD rocking curve measurements and RBS ion channeling. The composition of the film was measured on 1000Å thick PZT films on MgO substrates with RBS. The films were stoichiometric within experimental error. Figure 2 shows an XRD pattern of a 1000Å thick PZT film on (100) SrTiO₃ showing pure c-axis orientation. The rocking curve width (FWHM) of the {002} PZT was 0.2° and χ_{\min} along <100> is 15%. The AFM reveals the root mean square surface roughness of the films to be 7Å. We have also confirmed the epitaxial growth of PZT on top of a SrRuO₃ bottom electrode and vice versa. XRD exhibited only (00 ℓ) peaks of PZT and (*h**h*0) peaks of SrRuO₃, showing good epitaxy of both the SrRuO₃ electrodes (top and bottom) and ferroelectric layer [12].

Capacitor device structures were fabricated on (100) SrTiO₃ and YSZ buffer layered Si substrates to test the ferroelectric properties of the epitaxial PZT thin films between SrRuO₃ as shown in Figure 3. These Au-SrRuO₃-PZT-SrRuO₃ quaterlayers were patterned using standard photolithographic processing and ion milling to form a set of 200µm x 200µm square capacitors. A cross-sectional transmission electron microscopy (TEM) micrograph of the capacitor structure on (100) SrTiO₃ showed that the SrRuO₃ bottom electrode is single domain without domain boundaries, promoting the growth of high quality PZT on top [12]. However, the top electrode displays (110) epitaxy normal to the substrate with two in-plane orientations. In spite of the single domain bottom electrode, low angle domain boundaries can be seen in the PZT layer due to columnar growth.

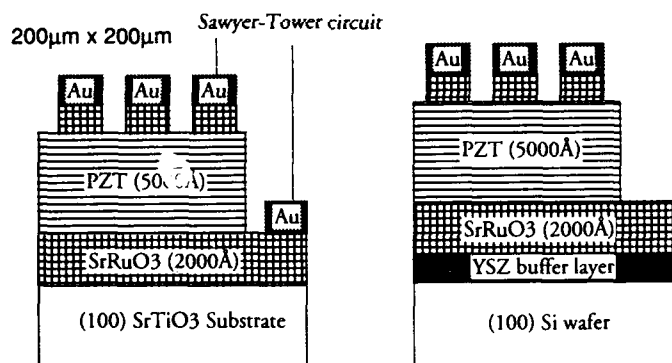


Figure 3. Schematic illustrations of capacitor test structures used to evaluate the ferroelectric properties of SrRuO₃/PZT/SrRuO₃ heterostructures.

The electrical properties of the capacitors were examined using a conventional Sawyer-Tower circuit [13]. For the devices on SrTiO₃ substrates, the remnant polarization obtained at 10V was 27 µC/cm², which is very close to the bulk value. The corresponding coercive field and coercive voltage were about 70 kV/cm and 3.5 V, respectively. The capacitors on the YSZ buffer layered Si substrates showed lower remnant polarization (10.5 µC/cm²) than those on SrTiO₃. We believe that this is mainly due to the (112) orientation of the SrRuO₃ layer and (110) orientation of the ferroelectric layer, which is not the favorable polarization direction

for PZT. We have recently been able to grow a (110) SrRuO_3 layer on both $\text{BaZrO}_3/\text{MgO}$ and CeO_2/YSZ double buffer layers on Si, which will allow us to grow c-axis oriented PZT on top of them [12].

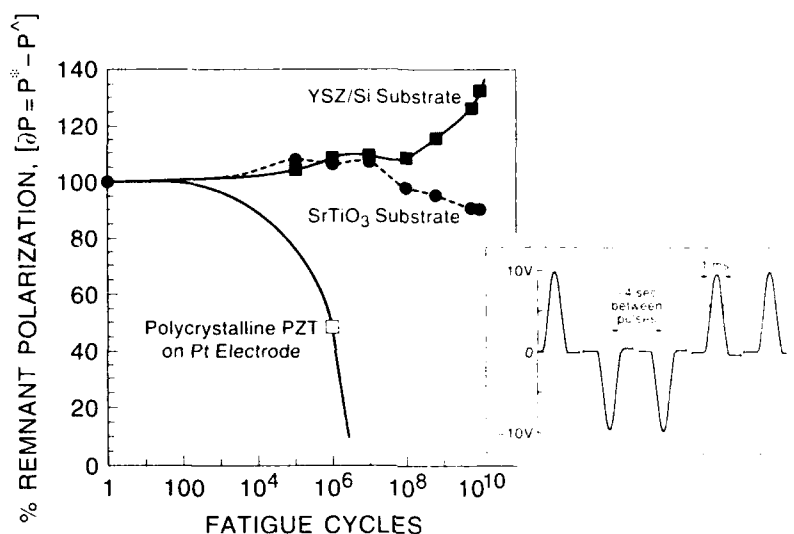


Figure 4. A plot of remnant polarization ΔP vs. fatigue cycles at 10 V for the $\text{SrRuO}_3/\text{PZT}/\text{SrRuO}_3$ structure, compared with data for a typical polycrystalline ferroelectric layers on Pt base electrode. Inset: the pulse train used to measure the effective read cycle discrimination ΔP .

Pulsed hysteresis measurements for fatigue tests were made using a Sawyer-Tower circuit with the waveform shown in the inset of Figure 4. A quiescent time of 4 sec was interposed between pulses to allow full relaxation of any transient effects in the ferroelectric layer [14]. The pulses were formed using an HP 8112A pulse generator under computer control and had a gaussian profile with 1.5 ms width and 1 ms transitions. The response was measured digitally with an HP 7090 digitizer and corrected for parasitic effects. The samples were stressed by bursts of 17.2 ms square wave using $V_{\text{max}} = 10 \text{ V}_{\text{p-p}}$ (200 $\text{kV}_{\text{p-p}}/\text{cm}$). This is comparable to the patterns commonly employed in simple fatigue tests [2]. Figure 4 shows the normalized remnant polarization, ΔP vs. fatigue cycles for $\text{SrRuO}_3/\text{PZT}/\text{SrRuO}_3$ capacitors on both SrTiO_3 and YSZ buffer layered Si substrates. The data of Figure 4 represent the effective read-cycle discrimination between a written "1" and "0" (sample pulsed to $-V_{\text{max}}$); in conventional notation $\Delta P = P^* - P^\wedge$.

In the case of a polycrystalline PZT layer on a Pt bottom electrode reported in the literature [1], the remnant polarization drops to 50% of its initial value after 10^6 cycles. But in the case of epitaxial PZT layers between SrRuO_3 electrodes the remnant polarization remains virtually unchanged. After 10^{10} cycles, the capacitors on SrTiO_3 substrates show only a 10% decay of remnant polarization. However, ΔP increases monotonically after 10^8 cycles in the capacitors on YSZ buffer layered Si substrates. This improvement in fatigue behavior is

attributed to improvement of electrode-ferroelectric interfaces as well as the absence of high angle grain boundaries in the PZT layers as observed in epitaxial ferroelectric layers between YBCO electrodes [2], and other metallic oxide electrodes such as RuO_x and $\text{La}_{0.5}\text{Sr}_{0.5}\text{CoO}_3$ [15, 16].

In conclusion, we have demonstrated that epitaxial ferroelectric heterostructures of $\text{SrRuO}_3/\text{Pb}(\text{Zr}_{0.52}\text{Ti}_{0.48})\text{O}_3$ (PZT)/ SrRuO_3 can be grown on (100) SrTiO_3 and buffer layered Si substrates *in situ* by 90° off-axis sputtering. This technique allow us to grow uniform stoichiometric films over a large area ($2" \times 2"$) with good step coverage, offering a promising technique for fabricating ferroelectric devices. The single crystal SrRuO_3 bottom electrode with high crystalline quality and smooth surface has allowed us to grow high quality ferroelectric layers. In addition, the thermal and chemical stability of the electrode material permits flexibility of device fabrication processes, as well as long term reliability of the devices at high temperature. Fatigue characteristics of the ferroelectric heterostructures with SrRuO_3 electrodes are far superior to those obtained with polycrystalline ferroelectric layers on Pt electrodes. These epitaxial heterostructures of ferroelectric/isotropic metallic oxide electrodes look promising for use as nonvolatile memory devices.

ACKNOWLEDGMENT

We would like to thank J.T. Evans(Radiant Technologies), E.S. Hellman, A. Kussmaul, E.H. Hardford, K. Short and D.W. Murphy for helpful discussions.

REFERENCES

1. J.F. Scott and C.A. Paz de Araujo, *Science*, **246**, 1400 (1989).
2. R. Ramesh, A. Inam, W.K. Chan, F. Tillerot, B. Wilkens, C.C. Chang, T. Sands, J.M. Tarascon and V.G. Keramidas, *Appl. Phys. Lett.* **59**, 3542 (1991).
3. R. Ramesh, A. Inam, W.K. Chan, B. Wilkens, K. Myers, K. Remschnig, D.L. Hart, J.M. Tarascon, *Science*, **252**, 944 (1991).
4. C. B. Eom et al, *Science*, **258**, 1766 (1993)
5. Paul R. Van Loan, *Ceramic Bulletin*, **51**, 231 (1972)
6. R.J. Bouchard and J.L. Gillson, *Mat. Res. Bull.*, **7**, 873 (1972)
7. W. Bensch, H.W. Schmalle, A. Reller, *Solid State Ionics, Diffusion & Reactions*, **43**, 171 (1990).
8. C.B. Eom et al., *Appl. Phys. Lett.*, **55**, 595 (1989).
9. C.B. Eom et al., *Physica C* **171**, 351 (1990).
10. Klein et al, *Materials Research Society Symposium Proceedings*, **243**, 167, (1992).
11. C. B. Eom, A. F. Marshall, J.-M. Triscone, B. Wilkens, S. S. Laderman, and T. H. Geballe, *Science*, **251**, 780 (1991)
12. C. B. Eom et al, in preparation
13. C.B. Sawyer and C.H. Tower, *Phy. Rev.* **35**, 269 (1930).
14. J.T. Evans, private communication
15. S.D. Bernstein, T.Y. Wong, Y. Kisler, and R.W. Tustison, *J. Mater. Res.*, **8**, 12 (1993)
16. J.T. Cheung et al., 1993 Materials Research Society Spring Meeting, San Francisco, CA. April (1993).

IMPACT OF BACKEND PROCESSING ON INTEGRATED FERROELECTRIC CAPACITOR CHARACTERISTICS

P.D. MANIAR, R. MOAZZAMI, R.E. JONES, A.C. CAMPBELL AND C.J. MOGAB
MOTOROLA, Semiconductor Products Sector, Advanced Products Research and Development
Laboratory, Austin, Texas 78721.

ABSTRACT

Integration of a ferroelectric capacitor module in a standard CMOS process subjects the ferroelectric to various ambients during backend processing, some of which can render the ferroelectric essentially non-operational for NVRAM applications. Post-crystallization processing of sol-gel deposited integrated ferroelectric PZT capacitors in the presence of hydrogen-containing, reducing ambients is observed to degrade the nonvolatile polarization. Low-pressure hydrogen anneals at temperatures as low as 200°C substantially degrade the nonvolatile polarization while the DRAM polarization remains roughly constant. Leakage current drops by one order of magnitude and fatigue is accelerated. A ferroelectric capacitor module can be integrated with minimal degradation with careful modifications in the backend processing.

INTRODUCTION

Ferroelectric PZT is of interest for both DRAM and NVRAM devices. PZT capacitors with Pt electrodes have demonstrated polarization and fatigue characteristics that could meet the requirements of gigabit-scale DRAM's [1] and NVRAM's operating at voltages as low as 1.5V [2]. However, integration of the ferroelectric capacitor module with a standard CMOS process requires considerable development due to materials and process incompatibilities with silicon technology, adhesion losses during processing, and limited patterning capabilities [3-7]. Integration requires depositing an interlevel dielectric (referred to as capacitor level dielectric [CLD] hereafter) over the ferroelectric capacitor prior to metallization [3-7]. Various dielectrics commonly used in silicon technology such as silicon dioxide, silicon nitride, PSG, BPSG or organic based dielectrics are CLD candidates, and can be deposited by CVD, sputtering or spin on techniques.

This paper describes the impact of backend CMOS processes on the PZT capacitor's electrical properties and specifically the effect of hydrogen-containing, reducing ambients. Polarization measurements were performed using high-speed single-shot pulse testing [8]. Polarization relaxation reduces the magnitude of the remanent polarization available for nonvolatile memory operation. The nonvolatile polarization reported here is the polarization remaining after all the relaxation processes are complete and is, therefore, the worst-case signal available for memory operation. The DRAM polarization is the nonremanent component of the ferroelectric hysteresis loop and includes both ferroelectric and nonferroelectric components [9]. The polarization relaxation is not included in the DRAM polarization.

Fine-grained polycrystalline $\text{PbZr}_{0.5}\text{Ti}_{0.5}\text{O}_3$ films were prepared by sol-gel deposition and subsequent crystallization at 700°C in an O_2 ambient. Film thickness was 1500Å and platinum was used for both top and bottom electrodes. The resultant films are in the perovskite phase and exhibit ferroelectric behavior with no non-ferroelectric pyrochlore-phase X-ray diffraction peaks. The grain size is typically less than 1000Å as observed by TEM. Atomic force microscopy reveals that the crystallized PZT surface has a texture of 100 to 250Å depending on the fabrication process.

POST-CRYSTALLIZATION ANNEAL OF PZT CAPACITORS IN HYDROGEN-CONTAINING, REDUCING AMBIENTS

Fully fabricated and electrically characterized PZT capacitors were subjected to low-pressure (< 5 torr) forming gas anneals, at temperatures from 100 to 400°C for less than a minute, which simulate typical CVD type conditions. These capacitors were then electrically characterized again, and changes in the ferroelectric properties were noted as shown in figures 1 through 4. The nonvolatile polarization degrades with increasing forming gas anneal temperature with nearly a 25% drop at temperatures as low as 200°C and more than an 80% drop at 400°C (see figure 1). The DRAM polarization does not degrade but rather undergoes a slight increase above 200°C (see figure 1).

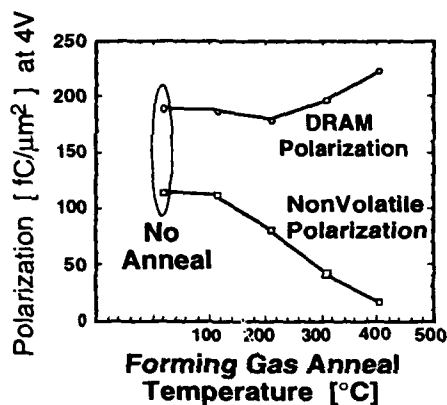


Figure 1. Impact of forming gas anneal on the nonvolatile and DRAM polarization of the PZT capacitor.

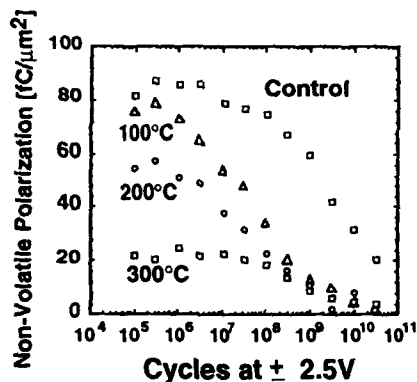


Figure 2. Accelerated nonvolatile fatigue of PZT capacitor from exposure to forming gas.

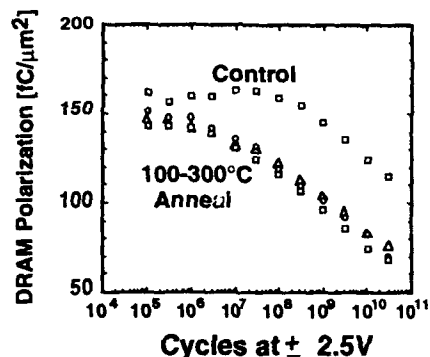


Figure 3. Accelerated DRAM fatigue of PZT capacitor from exposure to forming gas.

Fatigue of nonvolatile and DRAM polarization is accelerated after the forming gas anneals (see figure 2 and 3). Even though the starting nonvolatile polarization is different for different capacitors, all forming gas annealed capacitors show degradation and fatigue to the same value after 10^9 bipolar cycles. The nonvolatile polarization after 10^9 bipolar cycles is more than 80% lower than the capacitor not exposed to the forming gas anneal. The fatigue of the DRAM polarization is also accelerated by the forming gas anneals and is independent of the annealing temperature. This is a more severe DRAM fatigue test than the normal unipolar cycling. After 10^9 bipolar cycles the DRAM polarization is about 30% lower than the capacitor not exposed to the forming gas anneal.

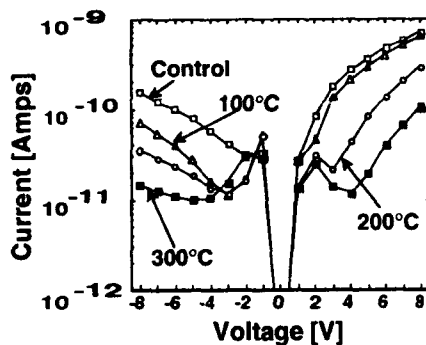


Figure 4. Leakage current in PZT capacitors at different temperatures of post crystallization anneals in forming gas. Film thickness is 1500Å and capacitor area is $1.04 \times 10^{-4} \text{ cm}^2$.

A surprising aspect of the post crystallization anneal in forming gas is that even though the degradation is observed for the nonvolatile polarization, and the fatigue is accelerated, the leakage current is actually lowered (see figure 4). With increasing temperature of the forming gas anneal, the leakage current gradually decreases until it is nearly an order of magnitude lower for the capacitor annealed at 300°C. (No leakage measurements were done on the capacitor annealed at 400°C in forming gas).

CAPACITOR LEVEL DIELECTRICS FOR INTEGRATION OF FERROELECTRICS

Integrating the ferroelectric capacitor with standard CMOS requires interconnect metallization which subjects the ferroelectric capacitor to pre-metal dielectric deposition. This capacitor level dielectric (CLD) can be silicon dioxide, silicon nitride, PSG, BPSG or polyimides and can be deposited by various techniques. Chemical vapor deposition (LPCVD or PECVD), sputtering or spin-on depositions are most commonly used. Here we present the results of our investigation of CVD and sputtering for CLD depositions. Figure 5 shows the DRAM polarization measured after the CLD depositions as compared to the control capacitor which received no CLD deposition. CLD-A and CLD-B refer to dielectrics deposited under different processing conditions. The DRAM polarization is influenced by the choice and processing of the CLD. At lower voltages CLD-A degrades the DRAM polarization by as much as 50% whereas, at higher voltages CLD-B degrades the DRAM polarization by about 25%. Therefore, the optimum processing conditions are not the same for all voltages and the CLD depositions must be tailored to the application.

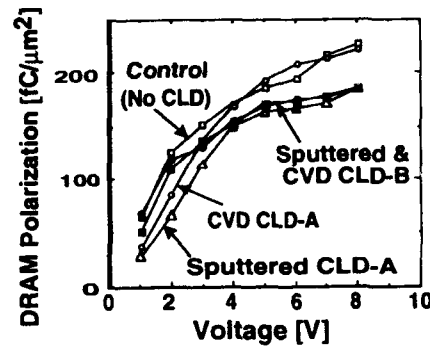


Figure 5. Comparison of different CVD and sputtered CLD's and their impact on the DRAM polarization during the integration of the PZT capacitor. CLD-A and CLD-B refer to different processing conditions.

In comparison to the dependence of DRAM polarization on the nature of the CLD, the nonvolatile polarization is even more sensitive, and inappropriate processing can lead to complete loss of the nonvolatile polarization. As shown in figure 6, the standard CMOS based CLD-A processing can severely degrade the nonvolatile polarization. As discussed in the earlier section, hydrogen containing reducing ambients, even at very low temperatures, can negatively impact the nonvolatile polarization and accelerate fatigue. Under appropriately selected processing, such as CLD-B, the ferroelectric capacitor can be integrated with minimal degradation.

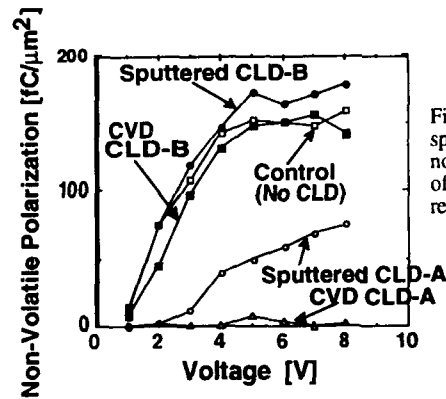


Figure 6. Comparison of different CVD and sputtered CLD's and their impact on the nonvolatile polarization during the integration of the PZT capacitor. CLD-A and CLD-B refer to different processing conditions.

These results suggest that the integration of ferroelectric capacitors for either DRAM or NVRAM applications requires careful selection and processing of the capacitor-level dielectrics. Further, there may not be a single CLD that can satisfy the requirements for both DRAM and NVRAM applications at all voltages. One must optimize the backend processing for a specific application.

SUMMARY AND CONCLUSIONS

Integration of PZT ferroelectrics with CMOS processing which subjects the PZT capacitor to the ambient of the CLD processing can severely degrade the nonvolatile polarization, reduce the DRAM polarization, and can accelerate the bipolar fatigue of either. Successful integration of ferroelectrics can be achieved by modifying CMOS processes to minimize degradation. As an example, figure 7 shows the nonvolatile and DRAM polarization characteristics for a PZT capacitor integrated through interconnect metallization using an optimized CLD process.

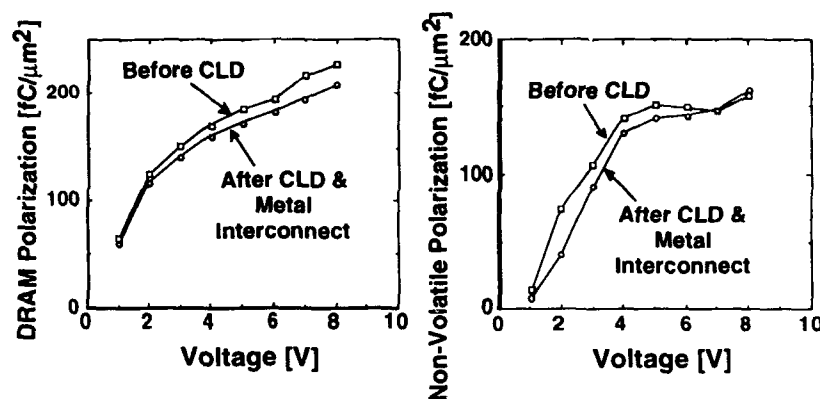


Figure 7. DRAM and nonvolatile polarization of integrated PZT capacitor after metallization using an optimized backend process.

ACKNOWLEDGMENTS

The authors gratefully acknowledge the technical assistance of Stacie Brown, Francisco DeLa Torre, Greg Etherington, Lee Howington, Brian Mowry, Ken Winters and Bob Wright.

REFERENCES

1. R. Moazzami, P.D. Maniar, R.E. Jones, A.C. Campbell, and C.J. Mogab, IEDM Technical Digest. 973, (1992).
2. R. Moazzami, P.D. Maniar, R.E. Jones, A.C. Campbell, and C.J. Mogab, 1993 Symposium on VLSI Technology. (1993).
3. Robertus A.M. Wolters, M.J.E. Ulenaers, U.S. Patent No. 5,122,477 (16 June 1992).
4. R. Cuppens, P.K. Larsen and G.A.C.M. Spierings, Microelectronic Engineering. **19**, 245, (1992).

5. William D. Miller, J.T. Evans, W.L. Kinney and W.H. Shepherd, U.S. Patent No. 5,046,045 (8 September 1991).
6. L.E. Sanchez, I.K. Naik, S.H. Watanabe, I.S. Leybivich, J.H. Madok and S.Y. Wu, ISIT-91 524, (1991).
7. M.P. Brassington, IEDMS, (November 1990).
8. R. Moazzami, N. Abt, Y. Nissan-Cohen, W.H. Shepherd, M.P. Brassington and C. Hu, Technical Digest Symposium on VLSI Technology, 61, (1991).
9. R. Moazzami, C. Hu, and W.H. Shepherd, IEEE Transactions Electron Devices, 39, 2044, (1992).

DEPOSITION, STRUCTURAL CHARACTERIZATION, AND BROADBAND (1KHz-40GHz) DIELECTRIC BEHAVIOR OF $\text{Ba}_x\text{Ti}_{2-x}\text{O}_y$ THIN FILMS

W.-T. LIU ^{a)}, S. COCHRANE ^{b)}, P. BECKAGE ^{c)}, D. B. KNORR ^{c)}, T.-M. LU ^{d)}, J. M. BORREGO ^{b)}, and E. J. RYMASZEWSKI ^{c)}

Center for Integrated Electronics, ^{a)} Also with Chemistry Department, ^{b)} Electrical, Computer, and Systems Engineering Department, ^{c)} Materials Engineering Department, ^{d)} Physics Department, Rensselaer Polytechnic Institute, Troy NY 12180-3590

ABSTRACT

An ion assisted deposition technique, called Reactive Partially Ionized Beam (RPIB) deposition, was used to prepare amorphous $\text{Ba}_x\text{Ti}_{2-x}\text{O}_y$ thin films at a low substrate temperature ($<60^\circ\text{C}$). The stoichiometry of the films varied from $x=1.0$ for BaTiO_3 to $x=0.2$ for Ti-rich films. The optical, thermal, and broadband electrical properties of this class of thin film dielectrics were systematically studied. A $1\mu\text{m}$ $\text{Ba}_x\text{Ti}_{2-x}\text{O}_y$ film is optically transparent with a band gap of 4.6eV. Both transmittance and bandgap decrease when the films are increasingly enriched with Ti. The Ti rich films remain amorphous at 600°C while the stoichiometric BaTiO_3 crystallizes into the perovskite structure. Annealed Ti rich films are thermally stable ($>700^\circ\text{C}$) with low leakage ($<0.1\mu\text{A}/\text{cm}^2$ at $0.5\text{MV}/\text{cm}$) and moderately high dielectric constant ($\epsilon_r = 15-35$). Polycrystalline BaTiO_3 deposited at 600°C on a $\text{Pt}/\text{Ta}/\text{SiO}_2/\text{Si}$ substrate has an $\epsilon_r = 400$. Capacitor structures with various metallizations were used to evaluate the dielectric properties, such as breakdown strength, leakage, ϵ_r and $\tan\delta$ from DC to 600MHz. A generic test vehicle was designed and fabricated to extend the frequency domain characterization of these dielectrics up to 40GHz. No dispersion of ϵ_r was observed in this frequency range for amorphous $\text{Ba}_x\text{Ti}_{2-x}\text{O}_y$.

INTRODUCTION

The use of high dielectric constant thin films in integrated circuit (IC) technology is of great interest because of the limiting performance that conventional SiO_2 thin films can offer. Amorphous ceramic materials, such as $\text{Ba}_x\text{Ti}_{2-x}\text{O}_y$ ($x = 0.2 - 1.0$) have attracted considerable attention recently because of their excellent characteristics of moderately high dielectric constant ($\epsilon_r = 15-40$), low $\tan\delta$, low leakage current, and high temperature stability. Deposition of device-quality amorphous $\text{Ba}_x\text{Ti}_{2-x}\text{O}_y$ at low temperature (from room temperature to 300°C) directly on metal, Si, and polymer substrates will make these films highly attractive for advanced IC technology. In addition, the growth of polycrystalline BaTiO_3 thin films on Si or on metal substrate at a temperature that is compatible with semiconductor processing technology could enable the fabrication of integrated ferroelectric devices.

The preparation of ferroelectric BaTiO_3 film by a variety of techniques has been reported by many researchers. A common difficulty is the inability to grow films that are very thin ($200\text{\AA}-5000\text{\AA}$), uniform, and defect free, at low substrate temperature over a large substrate area.¹ The work on $\text{Ba}_x\text{Ti}_{2-x}\text{O}_y$ reported in this paper utilizes a newly developed technique referred to as Reactive Partially Ionized Beam (RPIB) deposition. Using the technique, we have successfully fabricated very high quality amorphous $\text{Ba}_x\text{Ti}_{2-x}\text{O}_y$ thin films at or near room temperature.^{2,3} Further, the technique produces crystalline ferroelectric BaTiO_3 thin films if the substrate temperature is held above 500°C . This paper describes the deposition, microstructural characterization, and broadband dielectric behavior of this class of materials.

DEPOSITION OF $Ba_xTi_{2-x}O_y$ THIN FILMS

The details of the process technique have been published elsewhere.² The RPIB system is a dual-source evaporation and ionization system. TiO and Ba are source materials which are evaporated by electron bombardment heating and resistive heating of their crucibles, respectively. The base pressure of the system is 1×10^{-5} Pa. A 6×10^{-3} Pa O_2 ambient was established during deposition and monitored by a residual gas analyzer. Both TiO and O_2 are ionized at the outlet of the TiO crucible resulting in an ion current measured by a Faraday cup at the substrate which is 30cm above the crucibles. The total quantity of the ionized species is about 3%. The partially ionized beam was accelerated towards the substrate by a bias adjustable between 100-3000V. The substrate can be heated from 200°C-800°C by an array of tungsten halogen lamp heaters located above the substrate. The deposition process is monitored by an in-situ deposition controller which measures the evaporation rate of Ba and TiO separately.

Amorphous $Ba_xTi_{2-x}O_y$ is deposited on unheated substrates. The temperature of the substrate rises to less than 60°C during deposition due to radiation from the crucibles. The stoichiometry of the films is readily adjusted by changing the evaporation rate of Ba by the control of the power delivered to the Ba crucible while fixing the rate of TiO. The typical deposition rate is 350Å/min. The films are deposited on quartz, glasses, Si, and Si with various metallizations (Al, Ti/Cu/Ti, Pt/Ta, Au/Ti) for characterization. The variation of film thickness is less than $\pm 3\%$ and the variation of optical index is less than $\pm 1\%$ over a 3 inch substrate. Ferroelectric $BaTiO_3$ films are deposited on oxidized Si substrates metallized with 1000Å Ta/4000Å Pt. A three minute preheat of the substrate was used to stabilize the substrate temperature at $600 \pm 25^\circ\text{C}$ prior to the start of deposition. The substrate temperature was previously calibrated with two thermocouples attached to the substrate.

OPTICAL PROPERTIES

The Ba/Ti atomic ratio of amorphous $Ba_xTi_{2-x}O_y$ was determined for selected films by electron microprobe analysis and Rutherford backscattering. The refractive index, n , of the films were measured by ellipsometry at a wavelength of 6328Å as shown in Fig. 1. This continuous relationship established between n and Ba/Ti ratio of as-deposited films allows the value of n to characterize the stoichiometry of the films. The films enriched in Ti have higher n , ultimately approaching the value of TiO_2 . The stoichiometric $BaTiO_3$ ($x=1$) has an index of 1.90, in close agreement with the value for amorphous $BaTiO_3$ reported in literature.⁴ The optical transmittance ($T\%$) measured on a Perkin-Elmer spectro-photometer is also plotted in Fig. 1 against the refractive index for several $Ba_xTi_{2-x}O_y$ films 0.5µm in thickness deposited on a quartz substrate. The stoichiometric films are highly transparent with $T\% = 92\%$ referenced to air. This high $T\%$ is attributable to the amorphous structure of the films. It is also significant that an optically transparent film can be synthesized at nominally room temperature. We attribute this enhanced surface chemical reaction to the effect of ion bombardment in the RPIB technique.⁵ The $T\%$ decreases with increasing Ti content in the films. Non-stoichiometric films presumably have more defects in the amorphous network resulting in more scattering.

At short wavelengths the good transmission is terminated at the ultraviolet absorption edge which can be determined accurately by calculating the absorption coefficient, α , and plotting α^2 as a function of wavelength. The direct band edge appears as a linear portion of the data and the extrapolation to $\alpha = 0$ gives the value of the direct bandgap. The bandgap value calculated for the stoichiometric $BaTiO_3$ is $4.6 \pm 0.1\text{eV}$, which is 0.2eV higher than the value reported in literature for sputtered amorphous $BaTiO_3$ films.⁶ The band gap decreases to 4.3eV for the film with a Ba/Ti = 0.4.

THERMAL BEHAVIOR

The $\text{Ba}_x\text{Ti}_{2-x}\text{O}_y$ films deposited on unheated substrates are amorphous. Post deposition anneals of the films 3000Å in thickness deposited on Si wafers were carried out at temperatures from 100 - 900°C for 20 minutes in an ambient of flowing N_2 . The refractive index of the films of different stoichiometries as a function of the annealing temperature is shown in Fig. 2. In the temperature range of 20°C to 500°C, a gradual and incremental change in n is the result of densification. At a temperature between 500°C and 600°C, a large jump in n , from 1.95 to 2.23 was observed only for the films with stoichiometric composition. For off-stoichiometric films, the trend noted below 500°C continued to nearly 800°C. At 800°C, a sharp drop in index was noticed for all the samples.

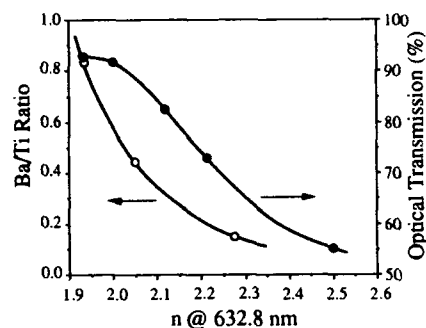


Fig. 1 Correlation curves between the Ba/Ti ratio, optical transmission, and refractive index of $\text{Ba}_x\text{Ti}_{2-x}\text{O}_y$ films.

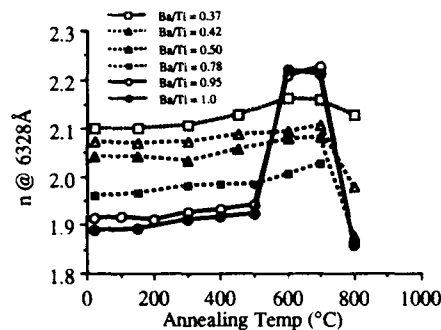


Fig. 2 Refractive index change of the films with different stoichiometries as a function of annealing temperature.

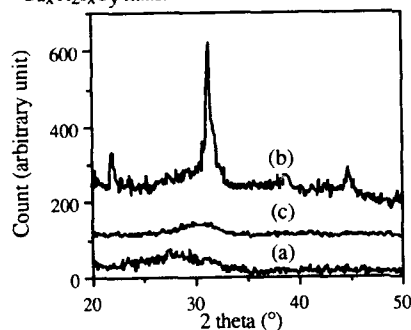


Fig. 3 X-ray diffraction patterns of a) stoichiometric film annealed at 500°C, b) the same film annealed at 600°C, c) off-stoichiometric film annealed at 700°C.

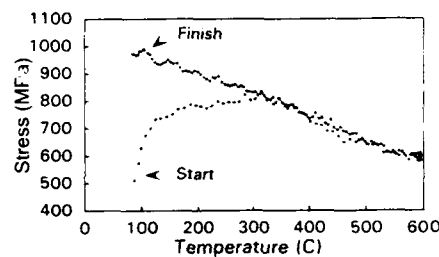


Fig. 4 The stress of 2500Å stoichiometric BaTiO_3 on Si substrate as a function of temperature.

The variation of the optical index with annealing temperature can be correlated to the crystallinity of the films. As-deposited films are amorphous as determined by x-ray diffraction regardless of the stoichiometry. Fig. 3 shows the x-ray diffraction patterns of the stoichiometric films annealed at 500°C (a) and 600°C (b). A 600°C anneal crystallizes the stoichiometric film into a perovskite crystal structure. An off-stoichiometric film ($\text{Ba/Ti} = 0.7$) annealed at 700°C is also shown (c). The off-stoichiometric film retains its amorphous structure even after a 700°C anneal resulting in a dielectric with $\epsilon_r = 30$ and $J_{\text{leak}} < 0.08 \mu\text{A}/\text{cm}^2$ at 0.5MV/cm. At temperatures above 800°C interdiffusion and reaction occurs between the Si and the film as detected by RBS.

A stoichiometric amorphous film on oxidized silicon was cycled from room temperature to 600°C, then cooled back to room temperature. The stress in the film as a function of temperature is calculated from the wafer deflection and is shown in Fig. 4. The intrinsic stress in the as-deposited film is 150 MPa tensile and increases substantially during heating to 300°C due to densification resulting in a very high stress upon returning to room temperature. The behavior becomes elastic representing the thermal expansion mismatch between the film and silicon. Subsequent thermal cycles, which are not shown, display entirely elastic behavior. The slope of 0.8 MPa/°C compares to the value of 0.65 MPa/°C calculated from the elastic modulus and coefficient of thermal expansion for crystalline BaTiO₃ indicating that the physical properties are similar for amorphous and crystalline BaTiO₃.

BROADBAND ELECTRICAL BEHAVIOR

In the frequency range of DC to 600MHz, simple parallel plate structures were used for the measurement of defect density, breakdown strength (E_{max}), leakage (J_{leak} @ 0.5MV/cm), ϵ_r and $\tan\delta$. Si wafers with Ti/Cu/Ti, Au/Ti, or Al metallization were used for the substrate and electrode. The area of the capacitors varied from 5×10^{-4} to 10 cm^2 to yield capacitance values of 20pf to 0.45 μf . Excellent breakdown strength, $E_{max} = 3.3 \text{ MV/cm}$, was obtained for 3000Å thick stoichiometric films, independent of the annealing temperature from 100 to 300°C. Fig. 5 shows the dielectric strength histogram of 200 capacitors measured across a 3 inch wafer for a film thickness of 1400Å. Because the voltage that causes catastrophic breakdown is greater than 50V, the voltage required to reach $10 \mu\text{A/cm}^2$ current density was used as the criterion instead. The distribution is centered around 14V and resembles a normal distribution indicating good uniformity and low defect density of the film. Fig. 6 represents the change of ϵ_r (at 1MHz) and J_{leak} with the stoichiometry of the dielectrics. All films received an anneal of 300°C under N₂ for 20 minutes prior to the measurement. The ϵ_r increases from 15 to 35 as the films become increasingly Ti rich. The J_{leak} also increases from 60nA/cm² to 100 $\mu\text{A/cm}^2$.

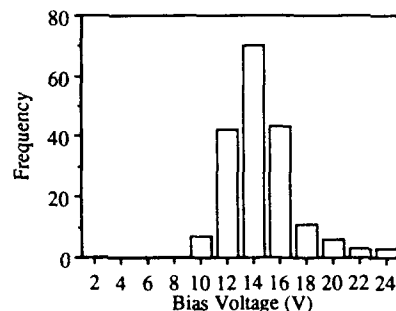


Fig. 5 A histogram of dielectric strength of 200 capacitors. The film thickness is 1400Å. The size of the capacitor is $2 \times 10^{-2} \text{ cm}^2$.

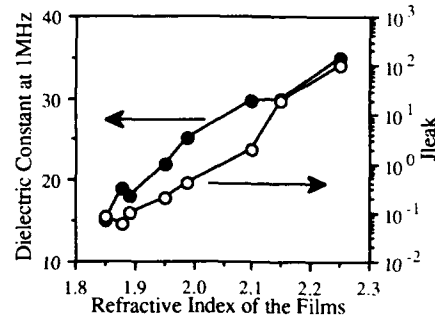


Fig. 6 ϵ_r (at 1MHz) and J_{leak} of 4500Å Ba_xTi_{2-x}O_y as a function of estimated Ba/Ti ratio of the films.

The ϵ_r and $\tan\delta$ of the dielectrics in the frequency range of 0.01-600MHz were determined through measurement of the capacitance and the shunt conductance on a 100pf and a 10pf capacitor, respectively, using a LCR meter (0.01-1MHz) and a RF impedance analyzer (1-600MHz). Parasitics associated with the setup were modeled as a standard transmission line. The values for the series and shunt element of the transmission line were determined by measuring a short and an open in place of the wafer sample at every measurement frequency and were used to correct the raw data. Fig. 7 plots ϵ_r and $\tan\delta$ of a film with a stoichiometric composition in the frequency range of 1KHz to 600MHz. The capacitors have virtually a constant ϵ_r of about 19. The $\tan\delta$ is as low as 0.005 for the film.

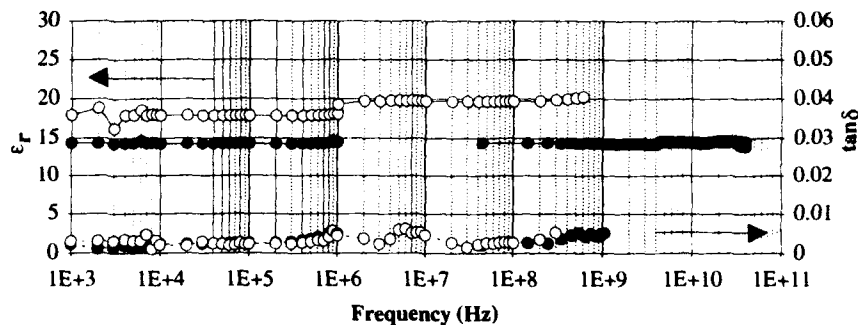


Fig. 7 Frequency domain (1KHz-40GHz) behavior of ϵ_r and $\tan\delta$ of amorphous $\text{Ba}_x\text{Ti}_{2-x}\text{O}_y$ thin films. No dispersion is seen in this range of frequencies.

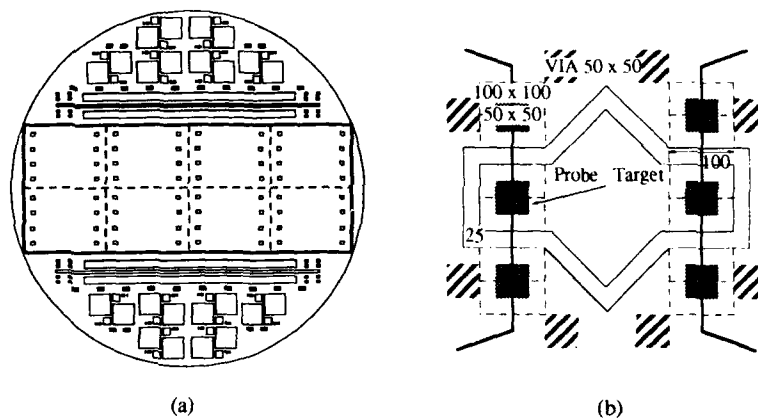


Fig. 8 a) the layout of the test vehicle, and b) a capacitor structure.

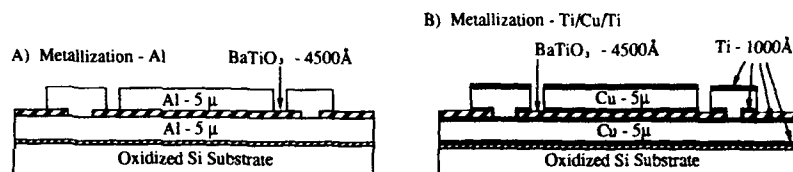


Fig. 9 Crosssections of the capacitors fabricated with a) Al metallization, b) Ti/Cu/Ti metallization.

To extend the measurement frequencies into the GHz realm, a generic test vehicle was designed and fabricated. The test vehicle consists of capacitors of various sizes, transmission lines, via chains, and other characterization structures configured to be probed by coplanar 50Ω microwave probes. The layout of the test vehicle is shown in Fig. 8 and it is fabricated by a two

mask process on 3 inch substrate that yields capacitor structure with cross-sections shown in Fig. 9. The metallization is either Al or Ti/Cu/Ti sandwich, Al and Cu being 5 μ m, and Ti being 1000Å, all deposited by electron beam evaporation. The Ba_xTi_{2-x}O_y dielectric of 4500Å was deposited and patterned by standard optical lithography. The etching of Ba_xTi_{2-x}O_y was carried out in buffered HF solution. The maximum temperature in the fabrication process is less than 100°C, and the structures were tested without an anneal.

S-parameters of the capacitors were measured on a HP8510 network analyzer. Excellent agreement between the simulated and the measured insertion loss (S_{21}) for capacitors with 1.5, 15, 150, and 1500pf capacitance was obtained. The effective ϵ_r calculated from the insertion loss measurement is plotted in Fig. 7 for frequencies from 50MHz to 40GHz along with the data obtained from a parallel plate structure measured from 1KHz to 600MHz. The film has a composition of Ba/Ti = 1. The data show that ϵ_r of amorphous Ba_xTi_{2-x}O_y thin films do not exhibit frequency dispersion associated with the relaxation of TiO₆ dipoles in the frequency range up to 40GHz. Other data, not shown in the figure, indicate that this excellent high frequency behavior is also maintained in off-stoichiometric films. The ϵ_r of ferroelectric BaTiO₃, however, is expected to exhibit severe dispersion starting at several hundred MHz due to the presence of ferroelectric domains.⁷ The frequency domain behavior of polycrystalline BaTiO₃ deposited at 600°C ($\epsilon_r = 400$ at 1MHz) is currently being characterized.

CONCLUSION

A self-ion assisted deposition technique referred as Reactive Partially Ionized Beam is used to deposit superior quality amorphous Ba_xTi_{2-x}O_y and polycrystalline BaTiO₃ at near room temperature and at 600°C, respectively. The amorphous Ba_xTi_{2-x}O_y films exhibit some highly desirable characteristics, such as high optical transmission, thermal stability, low defect density and leakage, high dielectric strength, moderately high ϵ_r and low tan δ . No dispersion of dielectric constant is seen for amorphous films in the frequency domain of 1KHz - 40GHz. A potential problem is the high stress resulting from deposition and annealing. These results show that amorphous Ba_xTi_{2-x}O_y films can be a very useful dielectric in advanced electronics, photonics, and optical applications.

ACKNOWLEDGEMENTS

The authors thank to B. Gittleman for his work in electron microprobe analysis. This work is supported in part by Digital Equipment Corporation and by DARPA under Contract No. ONR N00014-91J-4012 which is gratefully acknowledged.

REFERENCES

1. Ferroelectric Thin Films, edited by E. R. Myers and A. I. Kingon, (Mater. Res. Soc. Proc. **200**, 1990).
2. P. Li and T.-M. Lu, Appl. Phys. Lett., **57**, 2336 (1990).
3. W.-T. Lu, S. Cochrane, S. T. Lakshmikummar, D. B. Knorr, E. J. Rymaszewski, J. M. Borrego, and T.-M. Lu, IEEE Electron Device Letters, (to be published in July, 1993).
4. M. Wohlecke, V. Mareello, and A. Onton, J. Appl. Phys., **48**, 1748 (1977).
5. T. Takagi, Ionized-Cluster Beam Deposition and Epitaxy, (Noyes Publications, Park Ridge, New Jersey, 1988).
6. A. Onton and V. Mareello, in Structure and Excitation of A morphous Solids, (AIP Conf. Proc. **31**, New York, 1976), p.320.
7. C. Kittel, Phys. Rev., **83**, 458 (1951).

PART V

Degradation and Modelling

CORRELATIONS AMONG DEGRADATIONS IN LEAD ZIRCONATE TITANATE THIN FILM CAPACITORS

IN K. YOO, SESHU B. DESU, AND JIMMY XING
Virginia Polytechnic Institute and State University,
Department of Materials Science and Engineering,
Blacksburg, VA 24061

ABSTRACT

Many attempts have been made to reduce degradation properties of Lead Zirconate Titanate (PZT) thin film capacitors. Although each degradation property has been studied extensively for the sake of material improvement, it is desired that they be understood in a unified manner in order to reduce degradation properties simultaneously. This can be achieved if a common source(s) of degradations is identified and controlled. In the past it was noticed that oxygen vacancies play a key role in fatigue, leakage current, and electrical degradation/breakdown of PZT films. It is now known that space charges (oxygen vacancies, mainly) affect ageing, too. Therefore, a quantitative ageing mechanism is proposed based on oxygen vacancy migration under internal field generated by either remanent polarization or spontaneous polarization. Fatigue, leakage current, electrical degradation, and polarization reversal mechanisms are correlated with the ageing mechanism in order to establish guidelines for simultaneous degradation control of PZT thin film capacitors. In addition, the current pitfalls in the ferroelectric test circuit is discussed, which may cause false retention, imprint, and ageing.

INTRODUCTION

It is known that common degradation properties observed in ferroelectric thin films are fatigue, ageing, retention, imprint, and low voltage breakdown including electrical degradation. These properties have been studied extensively in order to improve reliability for industrial applications[1-10]. In general, each property has been improved separately. Unfortunately, however, there is a trade-off in the improvements of these properties. For example, when fatigue is reduced by using ceramic electrodes, leakage current increases[11]. Therefore, there is a need for guidelines to either develop a compromise among degradation rates or reduce these degradations simultaneously. For this purpose, it is important to understand degradations in a unified manner. Then, correlation(s) among degradations will provide clues for their simultaneous control. Correlations can be achieved if a common controlling parameter of each degradation is identified. In PZT films, it was reported that: (i) leakage current is controlled by Schottky emission at the interface[11], (ii) polarization reversal is determined by the coefficient of the dielectric viscosity[12] and interface state[13], and (iii) fatigue occurs due to defects in conjunction with interface state and the coefficient of the dielectric viscosity[1]. It was also reported that the source of electrical degradation and breakdown for ferroelectrics is oxygen vacancies[9-10]. A quantitative mechanism to describe the phenomena of ageing is yet to be developed; however, it is known that the source of ageing is primarily due to space charge[4,5]. Also the mechanisms involved in retention and imprint remain undeveloped. However, when taking the test conditions into consideration, it is easy to understand that they are related to the ageing mechanism.

CURRENT STATUS

Hysteretic property

Hysteretic properties of PZT thin films are described by the polarization reversal model which includes polarization due to domain nucleation, growth, merging, and shrinkage. The total electric displacement D , generated by external electric field E_A , consists of the linear dielectric polarization and the nonlinear polarization P_d caused by electric dipoles[14].

$$D = \epsilon_0 \epsilon E_A + P_d \quad (1)$$

where ϵ_0 is the permittivity of free space and ϵ is the linear dielectric constant of the ferroelectric. The rate of polarization as suggested by Rudyak[15] based on Barkhausen jumps at the domain wall is given as:

$$\frac{dP_d}{dt} = \text{Constant} \frac{(P_m - P_d)}{\tau} \quad (2)$$

where P_m is a constant and τ is the relaxation time which is associated with the coefficient of the dielectric viscosity β :

$$\tau = \frac{\beta}{E_L} \quad (3)$$

E_L is the macroscopic electric field related to the external field E_A and internal field E_i generated by polarization:

$$E_L = E_A - E_i = E_A - \frac{\eta}{\epsilon_0 \epsilon} P_i \quad (4)$$

Here η is the depolarization factor and P_i is the total polarization which includes both linear and nonlinear polarization. When external field increases linearly with time ($E_A = at$), polarization rate is expressed as:

$$\frac{dP_d}{dE_A} = \frac{\text{Constant}}{a\beta} (P_m - P_d) \quad (5)$$

where P_m is a constant.

In the domain growth stage, for the ferroelectric which has been preset by an electric field cycle, domain growth rate will be proportional to existing domain size because the larger the domain size is, the greater the chance of Barkhausen jumps at the domain walls. In addition, internal fields due to polarization are negligible in comparison to the external electric field because the polarization is low at this stage. Thus, domain growth rate can be expressed as:

$$\frac{dP_d}{dE_A} = \frac{\kappa E_A}{a\beta} (P_d + N_d) \quad (6)$$

where κ is an interface related constant and N_d is the critical size for domain nucleation.

At the domain merging stage, the chance of Barkhausen jump decreases because available area for the jump decreases due to domain merging. In addition, internal fields become

comparable with external field because of high polarization at this stage. Therefore, the polarization rate at merging stage is expressed as:

$$\frac{dP_d}{dE_A} = \xi \frac{E_L}{a\beta} (P_m - P_d) \quad (7)$$

where ξ is also an interface related constant.

Polarization process at the domain shrinkage stage is simply a relaxation type and it occurs spontaneously as the external field decreases. Thus, polarization rate can be described as:

$$\frac{dP_d}{dE_A} = \frac{\zeta}{a\beta} (P_m - P_d) \quad (8)$$

where ζ is another interface related constant.

When hysteresis loop is simulated based on the above polarization model, the linear dielectric constant can be calculated either at domain merging stage or domain shrinkage stage. Fig. 1 presents an example of hysteresis simulation with calculated linear dielectric constants where both linear constants show essentially the same value.

Fatigue

Fatigue is referred to as the decrease of switchable polarization with increasing switching cycle. Under alternating pulses, oxygen vacancies may move back and forth in the ferroelectric. When some vacancies arrive at the PZT-electrode interface, they are trapped

there because the chemical potential of vacancies is much lower at the interface than in the PZT body. Once they are trapped, it is difficult for vacancies to move back to the PZT body because of the chemical potential barrier.

Thus, vacancy entrapment occurs continuously even under alternating pulses. It is easy to understand that polarization at a certain test cycle n is different from that at the next cycle $n+1$ since polarization loss has occurred already at the test cycle n .

Since polarization induces internal fields, an internal field difference is expected between cycle n and cycle $n+1$. Therefore, effective movement is determined by internal field difference resulting in effective entrapment at a certain cycle

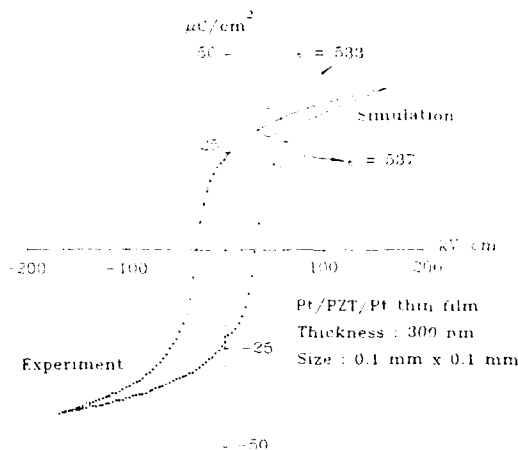


Fig. 1 Hysteresis loop simulation (Ref. 13)

n . When considering $\exp(-E_i) \approx 1 - E_i$, entrapment rate can be expressed as :

$$\frac{dN}{dn} = \lambda \Delta E_i \quad (9)$$

where N is total number of defects (oxygen vacancies, mainly) trapped at the interface.

As defects (oxygen vacancies) accumulate at the interface, this area undergoes microstructural damage resulting in polarization loss. Defect entrapment at a certain site affects adjacent sites because a certain atomic site is connected to other neighboring atomic sites. When another defect is entrapped at the site which has been already affected by the initial defect entrapment, the damage effect will be less in comparison to the previous one because the previous site has been damaged already. Therefore, polarization loss rate will decrease as defect entrapment increases and will then be proportional to the existing polarization.

$$\frac{dP}{dN} = -\nu P \quad (10)$$

where ν is a dimensionless constant which is related to the crystal lattice structure.

When the electric polarity is switched during the fatigue test, polarization reverses. Polarization is determined by the domain wall velocity v which can be expressed by electric field and domain wall mobility μ . Thus, internal field difference gives rise to domain wall velocity difference:

$$\Delta v = \mu \Delta E_i = \frac{\text{Constant}}{\beta} \Delta E_i \quad (11)$$

where β is the coefficient of the dielectric viscosity. When defects are trapped at the interface, internal field decreases due to polarization loss. This internal field reduction also gives rise to reduction of internal field difference and resultant reduction of domain wall velocity difference. It is assumed that domain wall velocity difference decreases in proportion to the defect entrapment :

$$\frac{d\Delta v}{dN} = -\gamma \frac{dN}{dn} \quad (12)$$

Eqs. (9), (10), (11), and (12), we obtain:

$$P = P_0 (An + 1)^{-m} \quad (13)$$

where P_0 is the initial polarization, A is the piling constant, and m is the decay constant. A controls steady state of polarization and m controls polarization decay rate.

Leakage Current

Non-ohmic leakage current is observed in PZT thin films with different current level for different polarities. Non-ohmic leakage current is controlled by several types of conduction mechanisms such as simple oxygen diffusion, grain boundary potential barrier height, space charge limiting, Poole-Frenkel emission, and Schottky emission. When leakage currents of

PZT thin films are plotted as a function of electric field, it is observed that they follow either Poole-Frenkel or Schottky emission. Schottky emission occurs at the interface between the ferroelectric and the electrode where a Schottky barrier is formed. If the top and bottom interfaces are asymmetric, leakage current levels will be different for positive and negative voltage biases. Poole-Frenkel emission occurs via trap levels in the bulk. Therefore, current conduction controlled by Poole-Frenkel emission gives symmetric current level at both positive and negative polarities regardless of asymmetric contacts. In our samples, a PZT film was deposited on the bottom electrode followed by annealing; an unannealed top electrode was deposited on the PZT film with no annealing. Therefore, top interface(contact) state is different from bottom interface. The asymmetric leakage current level for each polarity implies that it is controlled by interface, or in other words, by Schottky emission. As shown in Fig. 2, the asymmetric I/V characteristic follows Schottky relationships. However, it is noticed that I/V does not follow Schottky type at low electric field. This anomaly can be explained when internal field due to polarization is considered at low electric field. The Schottky emission is expressed as:

$$J = A^{**} T^2 \exp[(-\phi_B + c\sqrt{E})/kT] \quad (14)$$

where J is the current density, A^{**} is the effective Richardson constant, ϕ_B is the effective Schottky barrier height, c is a constant. If electric field E is replaced with macroscopic field E_L at low electric field, the I/V characteristics gives excellent curve fit as shown in Fig. 3.

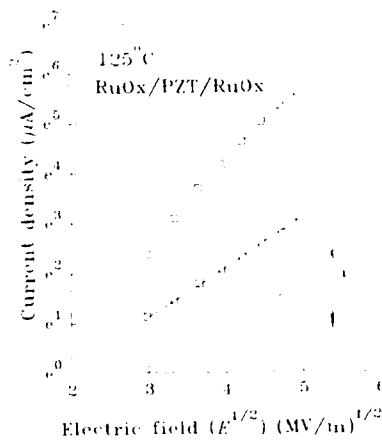


Fig. 2 Asymmetric leakage currents

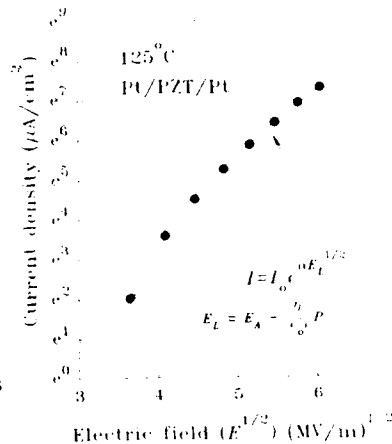


Fig. 3 Modified I/V

The evidence of Schottky emission becomes clearer when the temperature dependence of leakage current is studied. In Fig. 4, it is obvious that activation energies which are determined by Schottky barrier heights are different for each leakage current level at different polarities.

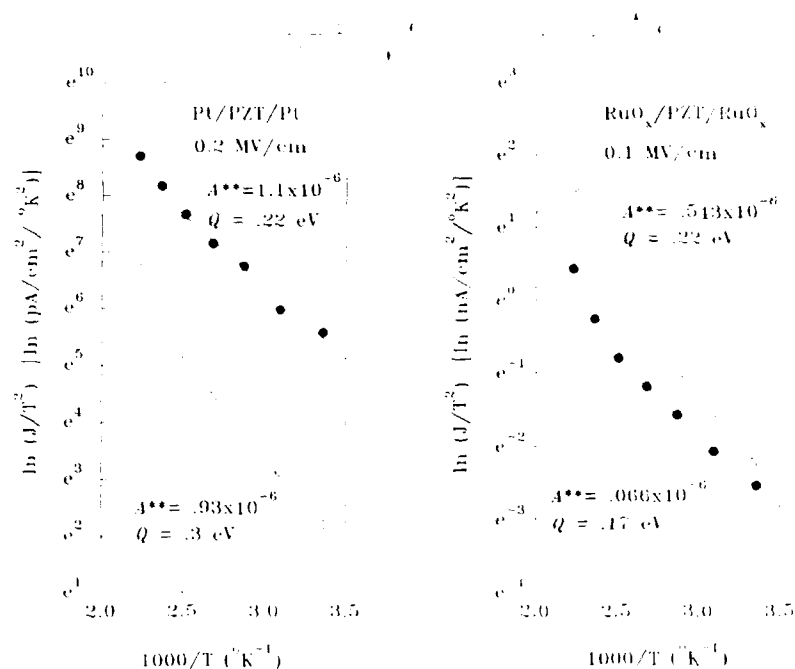


Fig. 4 Temperature dependence of leakage current (Ref. 11)

AGEING MECHANISM

Ageing is termed as switchable polarization loss in a poled ferroelectric capacitor. It is well known that one of the causes of ageing is space charge build up which gives rise to internal bias. Ageing has been expressed [6] by an experimental equation as:

$$K = K_0 (1 - \alpha T) \ln t / t_0 \quad (15)$$

where K is the dielectric constant at time t , α is the probability constant of domain motion, and T is temperature. In contrast to fatigue, internal field is formed by remanent polarization in ageing (internal field is generated by spontaneous polarization in fatigue). Space charges such as oxygen vacancies migrate to the interface under this internal field and build up there.

While the effective unidirectional defect movement caused by internal field difference was assumed in fatigue mechanism, continuous defect migration is expected under an internal field during ageing. The defect migration rate at a certain time t can be described as:

$$\frac{dN}{dt} = v\rho \exp\left[\frac{-\Delta G^* + zqbE_R/2}{kT}\right] \quad (16)$$

where
 v : Defect migration velocity
 ρ : Defect concentration
 ΔG^* : Potential barrier to jump
 z : Valence number
 q : Electronic charge
 b : Jump distance
 E_R : Internal field caused by remanent polarization ($= \frac{\eta}{\epsilon_0 \epsilon} P_R$)

As charged defects build up at the interface, they will balance the surface charges due to polarization. It is also possible for defects to become populated at the interface. The charge balance will give rise to temporary polarization reduction, and defect entrapment will give permanent polarization loss. Defect entrapment causes structural damage and affects neighboring atomic sites. The charge balance, however, does not affect neighboring sites. Thus, polarization reduction during ageing is expressed as:

$$\frac{dP_R}{dN} = -v \quad (17)$$

where P_R is the remanent polarization and v is a constant. Combining Eq.(16) with Eq.(17), we obtain:
 where C is a constant. The above equation is equivalent to the experimental equation Eq.(15).

$$P_R = P_{R0} - \epsilon_0 \epsilon \frac{2kT}{zqb\eta} \ln[Ct + 1]$$

$$\cong P_{R0} - \epsilon_0 \epsilon \frac{2kT}{zqb\eta} \ln Ct \quad \text{When } Ct \gg 1$$

AGEING RELATED TESTS

Retention is defined as retained charge for the period of time during which the polarized capacitor is electrically isolated or a constant bias voltage is maintained across the capacitor. In general, retention loss occurs temporarily when tested in a relatively short period of time. However, if the capacitor undergoes either repetitious retention test or prolonged retention period, ageing occurs. Fig. 5 presents a typical retention test for RuOx/PZT/RuOx in which retention and ageing are demonstrated.

In contrast to retention test, imprint test is carried out by applying alternating "write" pulses. So far there is no universally accepted definition for imprint yet. But one known effect of imprint is the reading failure of retained charge caused by preferred polarization

Tested by Harry Diamond Laboratories

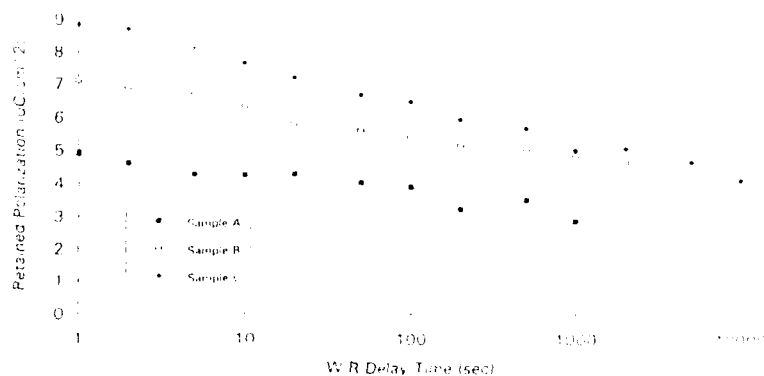


Fig. 5 Retention for PZT films on RuOx electrode: Sample A was polarized a day before the retention test was made. Sample B and C were polarized only minutes before these tests.

reading through a certain period of time during which the alternately polarized capacitor is left isolated or undergoes stress such as electric field, illumination, and heat. Regardless of test scheme, it is obvious that there exists a chance for the device to be aged if the polarized device is left at certain state for a long period of time during these tests. Both retention and imprint mechanisms should be developed in conjunction with ageing mechanism.

In addition, owing to their long period of test time, a careful test circuit system is required for these tests. False data can be collected during these tests if leaky sense capacitors are used in the Sawyer-Tower test circuit. Even virtual ground mode test can cause such false data when there is a leak in the circuit system. An example of this pitfall is illustrated in Fig. 6, where abrupt charge losses are observed at "open contact" when the device was polarized by negative "write". The device is connected to the high impedance ($10^{12} \Omega$) during retention period at open contact option. Since the impedance is leaky, charge loss is observed during both retention and imprint tests. When hysteresis loop is measured during this charge loss, the negative remanent polarization state appears to shift to the positive remanent polarization state during this period.

It is important to measure both switchable and non-switchable polarization to understand retention/imprint mechanism. It should be noticed in Fig. 7 that non-switchable polarization loss is higher than switchable polarization loss during accelerated retention test, while switchable polarization loss predominates non-switchable polarization loss during fatigue.

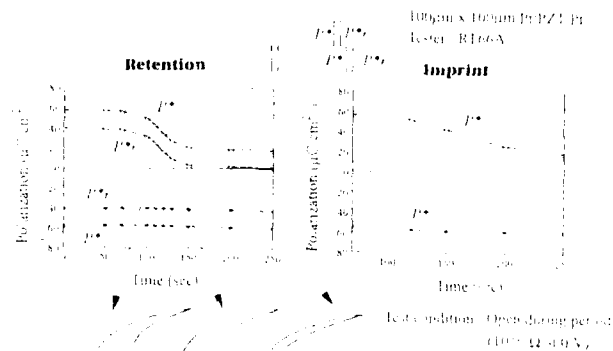


Fig. 6 False retention and imprint due to leaky circuit

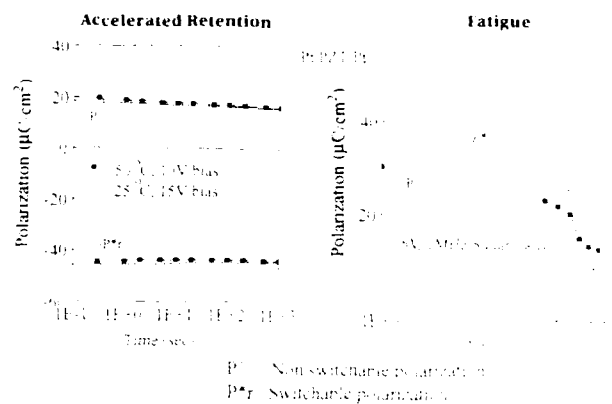


Fig. 7 Source of polarization loss during degradations

CORRELATIONS AND GUIDELINES FOR RELIABILITY IMPROVEMENT

From the studies conducted on the mechanisms involved in the degradation properties, it can be concluded that the key parameters which control degradation properties are defect concentration, interface state, and the dielectric viscosity of ferroelectrics. The degradation properties can be correlated to each other based on these parameters. Fig. 8 illustrates these correlations. Leakage current, electrical degradation, and breakdown form a sub-group from the viewpoint of test time. Semi-quantitative and qualitative studies on some ferroelectrics suggest that defects play a key role in electrical degradation breakdown. Ageing, retention, and imprint are also closely related in their test scheme. Dielectric viscosity plays an important role in fatigue; i.e., higher dielectric viscosity causes higher fatigue. In addition, according to the polarization reversal model, high dielectric viscosity causes high coercive

field and low remanent polarization. Therefore, ferroelectric materials with low coefficient of

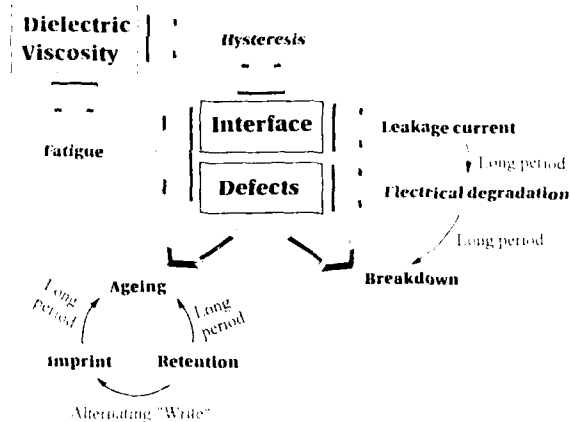


Fig. 8. Correlations based on key parameters

are provided on the basis of the above correlations. As mentioned before, a single parameter cannot be considered for reliability improvement. It is well known that conductive ceramic electrodes reduce fatigue property but increase leakage current. Thus, every parameter should be considered simultaneously for the simultaneous reduction of degradations. In our preliminary studies, we have chosen to use dopants (La and Nb) in order to control defect concentration and used a multilayer structure (Lead Titanate interlayer) along with ceramic electrode to control interface state. Leakage current, fatigue breakdown, and retention test results are shown from Fig. 10 through Fig. 12, respectively. It is noticed that 2% La dopant with Lead Titanate interlayer shows the lowest leakage current level and stable fatigue and retention. Even though polarization level is low for this multilayer, it still meets the minimum requirement for commercial memory application ($1\mu\text{C}/\text{cm}^2$).

the dielectric viscosity should be developed in order to reduce fatigue property and guarantee high remanent polarization. However, it does not follow that the ferroelectric with high remanent polarization shows low fatigue at all times because fatigue property is also related to interface state.

Therefore, the parameters should be compromised for minimization of degradation properties.

In Fig. 9, guidelines for reliability improvement

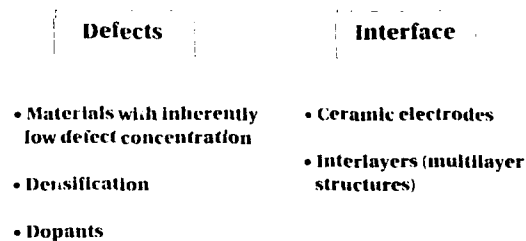


Fig. 9 Guidelines for reliability improvement based on correlations

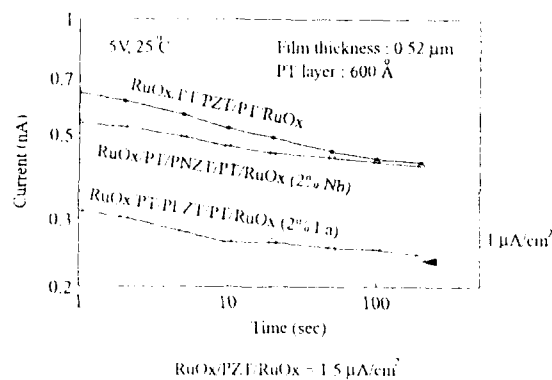


Fig. 10 Leakage currents of doped PZT films with multilayer structure.

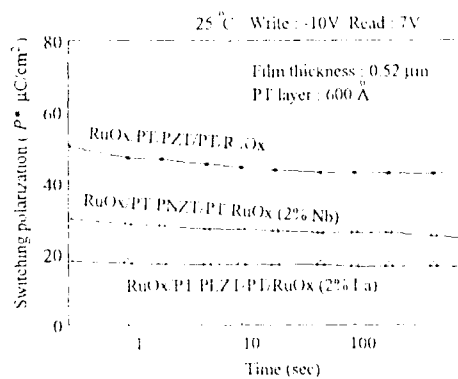


Fig. 11 Retention of doped PZT films with multilayer structure.

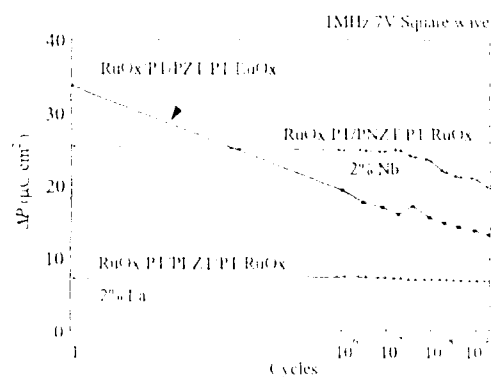


Fig. 12 Fatigue of doped PZT films with multilayer structure.

CONCLUSIONS

Correlations are not yet established completely because retention and imprint mechanisms are not fully understood. Electrical degradation/breakdown for PZT films should be studied more in order to understand defect behavior quantitatively during failure. However, preliminary guidelines for reliability improvement of PZT thin films were established and it was observed that La dopant with Lead Titanate interlayer (multilayer structure) along with RuOx electrode shows potential for reliable ferroelectric memory applications.

ACKNOWLEDGEMENT

The authors wish to acknowledge support from the Defence Advance Research Projects Agency and from Naval Weapons Support Center through the Office of the Naval Research.

REFERENCES

1. I.K. Yoo and S.B. Desu, *Phys. Stat. Sol. (a)* **133**, 565 (1992)
2. H.M. Duiker et al., *J. Appl. Phys.* **68**(11), 5783 (1990)
3. A. Yu. Kudzin, T.V. Panchenko, and S.P. Yudin, *Fiz. Tverd. Tela* **16**, 1589 (1975)
4. R. Lohkamper, H. Neuman, and G. Arlt, *J. Appl. Phys.* **68**(8), 4220 (1990)
5. K. Okazaki et al., *Ferroelectrics* **7**, 153 (1984)
6. C. Alemany et al., *J. Mater. Sci.* **19**, 2555 (1984)
7. B.S. Sarma et al., *Ferroelectrics* **5**, 69 (1973)
8. N. Ab: *3rd ISIF Proc.*, 404 (1991)
9. S.B. Desu and I.K. Yoo, *4th ISIF Proc.*, To be published, 1992
10. T. Baiatu, R. Waser, and K. Härdtl, *F. Am. Ceram. Soc.* **73**(6), 1663 (1990)
11. I.K. Yoo and S.B. Desu, *8th ISAF Proc.*, To be published, 1992
12. S. Zharov and V. Rudyak, *Fizika* (2), **9** (1989)
13. I.K. Yoo and S.B. Desu, *Phil. Mag.*, Submitted, 1993
14. S. Miller et al., *J. Appl. Phys.* **68**(12), 6463 (1990)
15. V. Rudyak, *Izvestiya Akademii Nauk SSSR. Seriya Fizicheskaya* **45**(9), 1586 (1981)

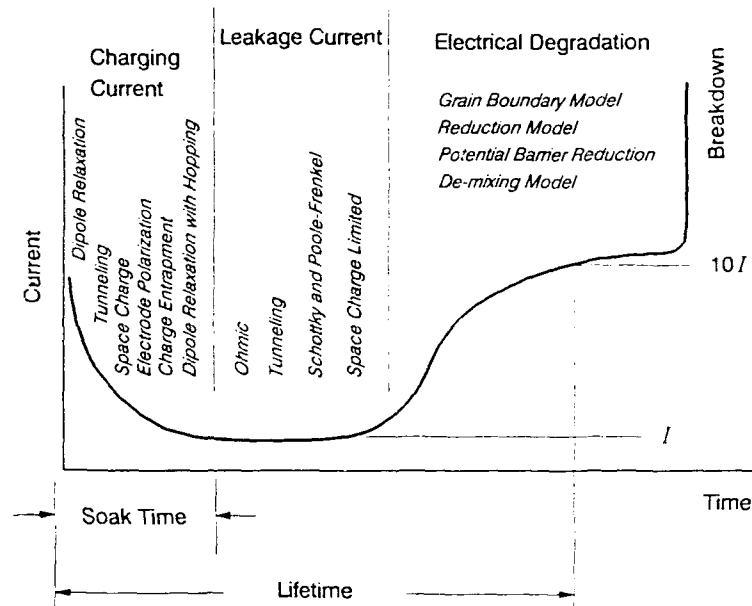
NOTE:

The term "degradation", as used in this paper, is in accordance with the definition as proposed in Ref. 9. The terms "degradation" and "electrical degradation" are distinct and different and are not to be confused.

The meanings are explained below:

In PZT, degradation is a generic term that means fatigue, ageing, imprint and electrical degradation / breakdown.

Electrical degradation, per se, is best explained by the following figure, which is reproduced here from Ref. 9 for the reader's convenience:



Time Dependent Dielectric Breakdown

ENERGY RELEASE DUE TO DOMAIN FORMATION IN THE STRAINED EPITAXY OF MULTIVARIANT FILMS

W. Pompe^{1,3}, X. Gong², Z. Suo², and J.S. Speck¹

College of Engineering, University of California, Santa Barbara, CA 93106

¹ Department of Materials

² Department of Mechanical and Environmental Engineering

³ Also: Max-Planck Research Group "Mechanics of Heterogeneous Solids", Dresden, Germany

ABSTRACT

Twin related domain formation is examined as a strain relaxation mechanism for a heteroepitaxial tetragonal film on a cubic substrate. Elastic relaxations are calculated for a single twin band in which the c-axis of the tetragonal domains is either related by a 90° rotation about an axis in the plane of the film or by a 90° rotation about the surface normal. In all cases, the strain energy change is evaluated for both the film and the substrate. A domain pattern map is developed that predicts single domain and multiple domain fields depending on the relative misfit strains and domain wall energy. The concept of a critical thickness, h_c , for domain formation is developed. For cases in which the c-axis is rotated 90° about an axis in the plane of the film, the critical thickness depends only on the relative coherency strain between the substrate and film and the ratio of the domain wall energy to the stored elastic energy. For the case of a pattern consisting of energetically equivalent domains with the c-axis in plane, the equilibrium distance of multiple domains is derived. For such multiple domains, a minimum wall separation distance exists which depends non-linearly on the film thickness.

INTRODUCTION

In this paper, the possibility of twin related domain formation is examined as a mechanism of strain energy release in the heteroepitaxial growth of thin films. For this to be possible, there must be at least two possible orientations (variants or twins) in which the strained film can align with respect to the substrate. The interest in this problem is motivated by current activity in the growth of thin film ferroelectrics [1, 2, 3] and thin film ferroelastics [4]. Domains must be considered as a mechanism of strain energy release in the heteroepitaxial growth of tetragonal ferroelectrics such as lead titanate or barium titanate on single crystal cubic substrates such as strontium titanate. The stability of monovariant films is a critical issue for ferroelectric applications such as sensors or memory. Therefore, not only the formation of periodic domain arrangements, but also single embedded domain segments require study.

Lattice-matched epitaxy provides a continuous elastic constraint for the thin film in two dimensions; the film may freely relax in the surface normal direction. The elastic constraint is achieved by matching the two-dimensional film periodicity to the two-dimensional periodic potential of the substrate. Therefore, elastic relaxations can only be concentrated in the film and substrate near discontinuities such as edges or domain boundaries, as demonstrated in extensive elasticity calculations by Hu [5] and by Freund and Hu [6].

RESULTS AND DISCUSSION

Definition of the Problem and Physical Model

The problem considered here involves the strained epitaxy of a thin tetragonal film on a cubic substrate. Domain formation is driven by minimizing the stored elastic energy and in ferroelectrics by additionally reducing the electrostatic energy. For the sake of simplicity of the elasticity analysis, we consider 90° boundaries which are normal to the film/substrate

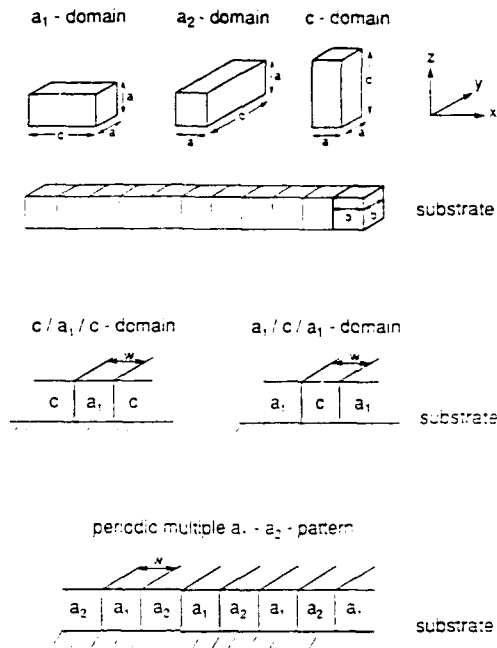


Figure 1 Characteristic configurations of multivariant tetragonal domains on an (001) cubic substrate.

interface and the domain boundary energy will be estimated by the twin boundary energy. We believe that the elastic effects of normal and inclined boundaries qualitatively show the same behavior. (In ferroelectric films the domain boundaries may be inclined to preserve the normal component of the polarization vector across the boundary, thus avoiding space charges.) The analysis is correct for ferroelastics or other non-polar multivariant materials.

We consider cases in which either the (001) plane (c-axis normal) or (100) plane of the film are parallel to the film/substrate interface. The substrate plane corresponds to (001) of a cubic crystal. The lattice parameter of the substrate square lattice is b and the lattice parameters of the film are a and c . The coordinate system used is shown in Fig. 1. For the present problem the interface is assumed to be fully coherent and thus free of misfit dislocations. It is important to note that generation of misfit dislocations represents a competitive process for strain relaxation for all misfitting films.

The film thickness is h and the x and y axes lie in the plane of the interface. We have to distinguish three different domain orientations. For one orientation, referred to as the c -domain in the following, the (001) plane of the tetragonal crystal is aligned along the interface with the substrate. Far from any lateral interfaces, the misfit strains of this domain are given as $\epsilon_{xx} = \epsilon_{yy} = \epsilon_u = \frac{(b-a)}{b}$. Additionally, the two variants of the film in which the (100) plane lies in the interface are relevant. Variant 1 of the a -domain has misfit strains $\epsilon_{xx} = \epsilon_c = \frac{(b-c)}{b}$, $\epsilon_{yy} = \epsilon_u$ and will be referred to as the a_1 domain. For the variant 2 of the a -domain, we select an orientation with misfit strains $\epsilon_{xx} = \epsilon_u$, $\epsilon_{yy} = \epsilon_c$ and refer to this domain as a_2 .

We begin by considering a thin misfitting film on a semi-infinite substrate. Initially, the film has infinite lateral extent. Two cases are considered. In Case I, the film is loaded in tension in the x-direction, in Case II the film is loaded in compression in the x-direction. Because the substrate is semi-infinite all stress and strain is concentrated in the film. Now consider the effect of finite size domains. Far from any boundaries, we anticipate that the film and substrate have the same stresses and elastic displacements as a laterally infinite film. At the boundaries however, the film can no longer sustain a normal stress σ_x , and there are resulting elastic relaxations in both the film and the substrate. There is a characteristic stress relaxation length in the film of the order of the film thickness h . If we bring islands together with different epitaxial misfits, then the net strain and displacement fields can be described by a superposition of the stress and displacement fields of isolated islands. When band-like domains with a large extension along the y-axis are considered, there will be a long-range stress relaxation with a logarithmic singularity in energy for a single boundary [7]. Thus, domain boundaries, and the material near the boundary, act as displacement "absorbers" in heteroepitaxial systems. This process of mutual elastic accommodation provides the basis for domain patterning as a mechanism of strain energy release in multivariant thin films.

Equilibrium Domain Structures

From this phenomenological description of stress relaxation along domain boundaries, some general results may be established concerning the stability of different misfitting thin film structures. The film forms three variants relative to the substrate: the c-axis is either normal to the film/substrate interface (c-variant), or parallel to the interface (a_1 and a_2 variants). The variants may coexist to form domains; a few patterns are shown in Fig. 1. Here we analyze the equilibrium domain patterns which result from the competition between the strain energy reduction and the domain wall energy. Thus, both the film thickness, h , and domain width, w , are regarded as variables in minimizing the combined strain and domain wall energy.

Our analysis indicates that a diagram of equilibrium domain patterns may be developed by using two non-dimensional variables: the relative coherency strain ϵ_r given by the ratio of one misfit strain, $\epsilon_a = \frac{b-a}{b}$, to the tetragonality strain, $\epsilon_T = \frac{c-a}{b}$, $\epsilon_r = \frac{b-a}{c-a}$, and the ratio of the strain energy over the domain wall energy, $hE\epsilon_T^2/\gamma$, where γ is the specific domain wall energy, and E is Young's modulus of the film. A calculated equilibrium diagram is presented in Fig. 2.

When $b < a$, or $\epsilon_r < 0$, all variants are under biaxial compression; the film tends to make an a -to- c switch to stabilize as a single c -domain. When $b > c$, or $\epsilon_r > 1$, all variants are under biaxial tension; the film tends to make a c -to- a switch to stabilize with alternating a_1 and a_2 domains. A value $\epsilon_r = \epsilon_c$ exists where the epitaxy causes the same strain energy in the a and c variants. This is the vertical line in Fig. 2; the c variant dominates on the left, and the a variants dominate on the right. A multi-domain region appears near $\epsilon_c - \Delta\epsilon \leq \epsilon_r \leq \epsilon_c + \Delta\epsilon$. For example, when $\epsilon_r < \epsilon_c$, the strain energy of a large c -domain may be diminished by embedding small a -domains. Similarly, when $\epsilon_r > \epsilon_c$, small c -domains may be stable within a large a -domain. The mechanism is efficient for thicker films, because the coexisting variants in the film add domain walls and deform the substrate. Thus the range of stable multiple domain structures increases with increasing film thickness.

Epitaxial, monovariant films of either type a or c provide the reference for the energy change to be considered in the later sections. Because the film is much thinner than the substrate, the substrate is undeformed and, to match the undeformed lattice of the substrate,

the film is strained by $\epsilon_a = \frac{b-a}{b}$, $\epsilon_c = \frac{b-c}{b}$. The stresses in the film for the c -variant and for the a -variants are determined by Hooke's law. The strain energy per unit volume can be readily computed for both the a -variants and the c -variant. Note that the a_1 and a_2 variants have the same strain energy. It follows by equating the energy densities of monovariant a and c domains that both variants are energetically equivalent when

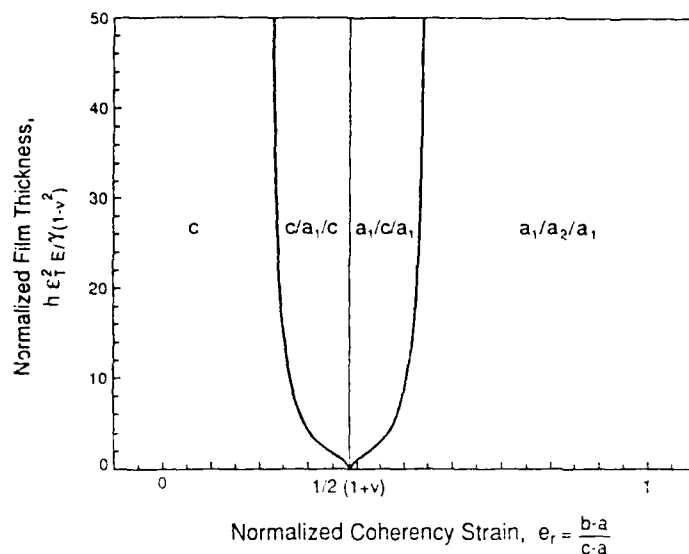


Figure 2 Equilibrium diagram of domain patterns. The domain pattern fields are computed on the basis of idealized configurations discussed in the text.

$e_r = e_c = \frac{\epsilon_a}{\epsilon_a - \epsilon_c} = \frac{1}{2(1+\nu)}$. This is the vertical line in Fig. 2. $e_c = 0.385$ (for $\nu = 0.3$).

The c -variant has the lower strain energy on the left of the line, and the a -variants have the lower strain energy on the right.

Further simplifications will be invoked to calculate the strain energy. The film and the substrate are taken to be elastically isotropic and homogeneous with Young's modulus E and Poisson's ratio ν . (A value $\nu = 0.3$ will be used in the plots.) Domain walls are assumed to be perpendicular to the film/substrate interface. Each domain is long in the y -direction compared to the film thickness, so that stresses everywhere are invariant with respect to y . To simplify some of the calculations, the film is sandwiched between two thick substrates, so that Green's functions for an infinite space under plane strain conditions can be used, as described elsewhere [8].

Formation of Domain Bands

When $e_r < e_c$, even though the c -variant has a lower strain energy than the a -variant, a small a -domain may emerge in a large c -domain to reduce the elastic energy in the film. This is done at the expense of adding the domain walls and deforming the substrate. Proper energy accounting requires that the elasticity problem be solved rigorously. In what follows a specific configuration, a long a_1 -band in a large c -domain (Fig. 3), is analyzed. We will determine (i) the equilibrium band width, and (ii) the stability range for domain formation. The a_1 -bands, disrupting a perfect c -variant film, bear much similarity with other strain-relaxing mechanisms in thin films. Familiar examples include misfit dislocations [9] and channeling cracks [10].

The lattice misfits among the variants and the substrate cause a complicated stress field. We solve the elasticity problem by linear superposition. Consider Problem A first, shown schematically in Fig. 3. Starting from the unbonded a_1 -band, c -domain and substrate, the a_1 -band is deformed to match the 3D lattice of the c -domain. Compared with the strain

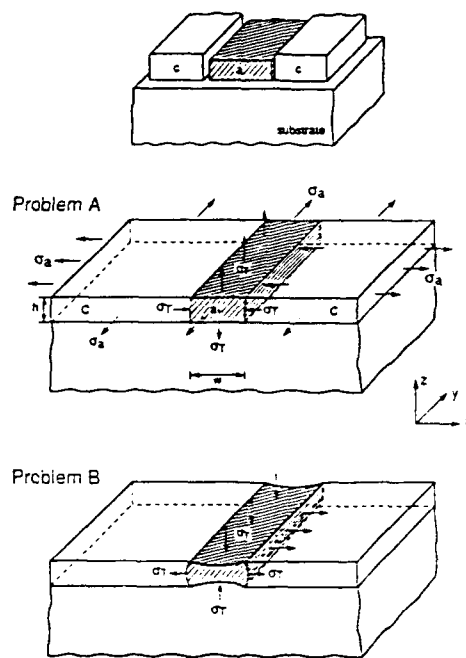


Figure 3 Micromechanical model of an embedded domain band. In Problem A clamping tractions are applied to match the variants and the substrate. In Problem B tractions σ_T in the opposite directions are applied to remove σ_T in Problem A.

energy per unit domain band length in an epitaxially bonded c -monovariant. Problem A increases the strain energy by $U_A = \frac{E}{1-\nu} \epsilon_T^2 h w \left(\frac{1-\nu}{1-\nu} - e_r \right)$.

Problem A differs from the problem of a c -monovariant one aspect: the clamping tractions σ_T that prevent relaxation. Upon removing the tractions, the lattice mismatches deform the system. On the basis of linear superposition, the displacement field, after removing σ_T from Problem A, is the same as that induced solely by the negative tractions without the lattice misfits, as illustrated by Problem B. The strain energy is reduced and the change in the strain energy scales as $U_B = -\epsilon_T^2 h^2 g\left(\frac{w}{h}\right)$, where g is a dimensionless function of w/h . The displacements in Problem B are obtained by integrating Green's functions; U_B is the work done per unit band length by tractions σ_T through the associated displacements. Both are described in elsewhere [8].

The difference in the strain energies in a large c -domain with and without the a_1 -band, $U_A + U_B$, is shown in Fig. 4, varying with both w and e_r . Two types of behaviors emerge. When $e_r < e_c - \Delta e = 0.2149$, embedding an a_1 -band of any w increases the strain energy, so that the c -monovariant is favored. When $e_c - L_c < e_r < e_c$, an a_1 -band over a limited range of width decreases the strain energy. The equilibrium band width w_{eq} minimizes the strain energy, which is indicated in Fig. 4 for one value of e_r . Also indicated is U_{eq} , the strain energy reduction due to embedding the a_1 -band.

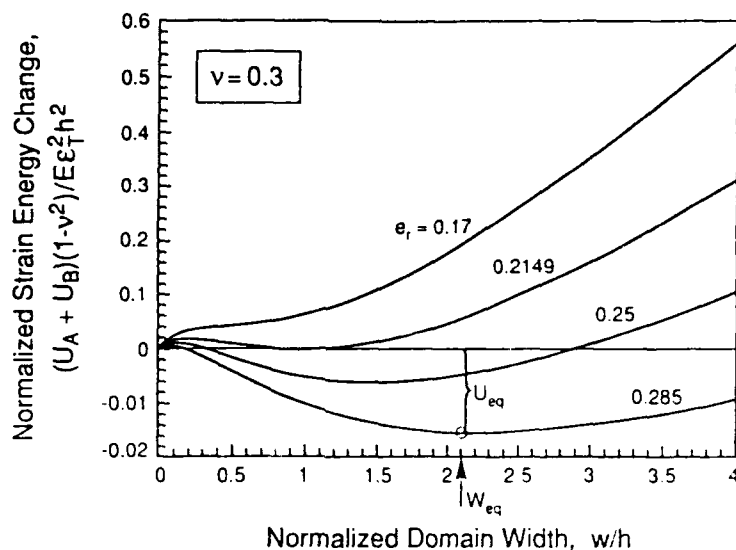


Figure 4 Calculated difference in the strain energies between a large c -domain with and without the a_1 -band for various relative coherency strains e_r . The equilibrium band width and the associated reduction in the strain energy are indicated for one curve.

Embedding an a_1 -band into a c -domain adds two domain walls. The a_1 -band forms when the strain energy reduction U_{eq} compensates the domain wall energy, i.e., $U_{eq} + 2\gamma h \leq 0$. Because U_{eq} scales as h^2 , this condition defines a critical film thickness, below which the a_1 -band is unstable, and the film stabilizes as a c -monovariant. The critical thickness, obtained from the calculated U_{eq} , is plotted in Fig. 2, separating two regions of equilibrium domain patterns: the c -monovariant prevails below the curve, and a_1 -bands form above the curve.

When $e_r > e_c$, an epitaxial a -monovariant has lower strain energy than c -monovariant. Similar calculations lead to the symmetric pattern in Fig. 2 which separates the region of coexisting a and c domains from the region of only a variants.

Patterning of Equivalent Variants

Now consider the region in the equilibrium diagram where the c -variant completely disappears. Epitaxial films of single a_1 or a_2 variant have the same strain energy. We will show that the film stabilizes with alternating a_1 and a_2 domains - that is, a monovariant film, say of a_1 -type, is unstable for any film thickness. Our conclusion thus differs from that of Roytburd [11].

The two variants are assumed to form alternating bands with the same width w (Fig. 1). The two variants accommodate each other, reducing the strain energy, causing a complicated stress distribution. The elasticity problem is solved by linear superposition described elsewhere [8].

Including both the change in the strain energy and the domain wall energy (with respect to a monovariant), the average energy change in the system, per unit length in both x and y

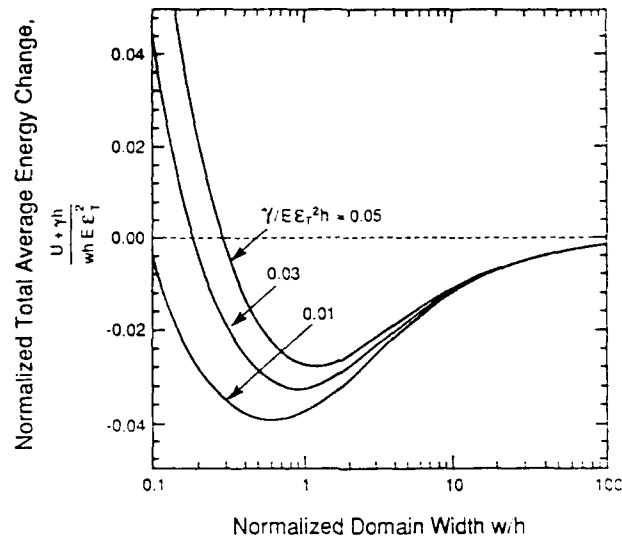


Figure 5 Total energy changes as a result of the competition between domain wall energy and strain energy reduction due to patterning (note the log-linear scales employed).

directions, is $\frac{(U + \gamma h)}{w}$. The computed results are plotted in Fig. 5, varying with the domain width and the domain wall energy. Note that the "energy change" is with respect to the strain energy in an a_1 -monovariant. When w/h is small, the domain wall energy dominates so that the energy change is positive. When w/h exceeds some finite value, the strain energy reduction dominates so that the energy change becomes negative. The average energy becomes indistinguishable from that of a monovariant film for large w/h . Consequently, an equilibrium domain width exists for any film thickness which minimizes the total energy below the strain energy of the a -monovariant. That is, the alternating pattern is always energetically favored over an a -monovariant.

CONCLUSIONS

By minimizing the combined strain energy and domain wall energy, we have developed a diagram of equilibrium domain patterns for a tetragonal film epitaxially grown on a cubic substrate (Fig. 2). The c and a variants dominate over the two sides of the diagram, separated by a critical value of the misfit parameter, $e_r = e_c$. When $e_c - \Delta e < e_r < e_c$, a critical film thickness exists below which the film stabilizes as a perfect c -variant. Above the critical thickness, bands of a_1 variant traverse the c -variant to reduce the strain energy. When $e_c < e_r < e_c + \Delta e$, a critical film thickness exists below which the c -variant disappears completely. In this region, the film can only stabilize with alternating a_1 and a_2 domains, but not a monovariant. The dependence of the stability ranges on the relative coherency strain of the film/substrate system opens a way for the engineering of domain configurations. Many parameters may be varied to control the domain structure, including choice of substrate, and alloying the substrate and film to control lattice parameters.

ACKNOWLEDGMENTS

We would like to thank Profs. F.F. Lange and A.G. Evans for encouragement and several enlightening discussions. The work of JS and WP was partially supported by the MRL Program of the National Science Foundation under Award No. DMR-9123048. The work of XG and ZS was supported by NSF through grant MSS-9258115, and by ONR through contract N00014-93-1-0110.

REFERENCES

1. J.T. Cheung, P.E.D. Morgan, D.H. Lowndes, X.-Y. Zheng, and J. Breen, *Appl. Phys. Lett.*, accepted for publication (1993).
2. J.T. Cheung, P.E.D. Morgan, and R. Neugaonkar, *Integrated Ferro.*, accepted for publication (1993).
3. R. Ramesh, W.K. Chan, B. Wilkens, H. Gilchrist, T. Sands, J.M. Tarascon, V.G. Keramidas, D.K. Fork, J. Lee, and A. Safari, *Appl. Phys. Lett.* **61** (1992) 1537.
4. A. Seifert, J.S. Speck, and F.F. Lange, *J. Am. Ceram. Soc.* **76** (1993) 443.
5. S.M. Hu, *J. Appl. Phys.* **50** (1979) 4661.
6. L.B. Freund, and Y. Hu, *Shear Stress at a Film-Substrate Interface due to Mismatch Strain*, (Office of Naval Research Contractor Report, 1988).
7. S.P. Timoshenko, and J.N. Goodier, *Theory of Elasticity* (McGraw-Hill, New York, 1951).
8. W. Pompe, X. Gong, Z. Suo, and J.S. Speck, *J. Appl. Phys.*, submitted for publication (1993).
9. L.B. Freund, *MRS Bulletin* **17** (1992) 52.
10. J.W. Hutchinson, and Z. Suo, *Adv. Appl. Mech.* **29** (1992) 63.
11. A.L. Roytburd, *Mat. Res. Soc. Symp. Proc.* **221** (1991) 256.

PART VI

**Characterization of Ferroelectric
Thin Film-Electrode Interfaces**

BOTTOM ELECTRODES FOR HIGH DIELECTRIC OXIDE COMPOUNDS: EFFECTS ON CRYSTALLIZATION OF LEAD CONTAINING FERROELECTRICS

A. GRILL, D. BEACH, C. SMART AND W. KANE

IBM-Research Division, T.J. Watson Research Center, Yorktown Heights, N.Y. 10598.

ABSTRACT

Several conductive structures, which appeared to be usable as base electrodes for integrated devices based on high dielectric materials, have been annealed for 30 minutes in oxygen at 650 °C. Similar structures coated with lead-based ferroelectrics deposited by the sol-gel method have been annealed for 1 min in oxygen at higher temperatures. The materials have been characterized by Rutherford backscattering (RBS) and scanning electron microscopy (SEM) and the crystallographic structure of the ferroelectrics films has been determined by X-ray diffractometry (XRD).

Only RuO₂/Ru has been found to be suitable as an electrode, at temperatures not exceeding 650 °C. It has also been found that the electrode materials can strongly affect the crystallization behavior of the sol-gel ferroelectric films and the formation of single-phase perovskite layers.

INTRODUCTION

Ferroelectric and paraelectric materials, characterized by special electrical, optical, and piezoelectric properties are good candidates for a large variety of applications, such as nonvolatile memories^{1, 2}, dynamic random access memory (DRAM)³, optical^{1, 2}, or piezoelectric devices.⁴ For device fabrication these films have to be deposited on suitable base electrodes. A variety of materials have been studied as such electrodes and the following is only a partial representative list: Pt, Pt/Ti, RuO₂, ReO₃, deposited on SiO₂/Si or MgO⁴⁻⁷, Pt/Ta on Si³, indium tin oxide, stannic oxide, Inconel,⁴ a nickel alloy similar to Inconel,⁸ palladium on sapphire.⁹

The high dielectric values of the ferroelectric/paraelectric materials makes them an important candidate for future generations of DRAM, where higher integration may require materials of high dielectric constants in order to be able to construct cells of sufficient capacitance in the reduced available area. Integration of ferroelectric or paraelectric materials in devices based on silicon technology requires the deposition of the high dielectric constant materials on suitable electrodes, in electrical contact with the Si. In order to obtain the ferroelectric or high dielectric properties the materials have to be generally annealed at elevated temperatures in an oxidizing environment and the electrodes must be compatible with such processing conditions. The oxide compounds cannot be deposited directly onto silicon because the interaction of the oxides with silicon at elevated temperatures will cause the formation of an interface layer of silicon oxide, which will significantly reduce the effective dielectric constant. Dielectric films useful for DRAM applications have, therefore, to be deposited on an intermediate base electrode which satisfies the following requirements:

1. it remains electrically conductive after exposure to an oxidizing environment at high temperatures to allow the connection of the memory capacitor to the transistor
2. it prevents diffusion of oxygen through it to the underlying silicon substrate and preserves the electrical properties of the transistor
3. it prevents diffusion of silicon to the surface of the electrode and the formation of an interfacial layer of low dielectric constant silicon dioxide
4. it does not interact with the high dielectric material at the high processing temperatures.

A previous paper¹⁰ discussed the behavior of several electrode structures upon annealing in oxygen at 650 °C for 30 min. This paper presents a continuation of that study. It describes the behavior of such structures in contact with lead based oxide materials in a variety of annealing conditions and their effect on the crystallization of sol-gel deposited films.

EXPERIMENTAL

Following the four requirements mentioned above, the following electrode structures have been investigated in the previous study¹⁰: Pt/Ta, Pt/TiN, Au/Ti/TiN, Ru/RuO₂/Ru. The RuO₂/Ru and TiN films have been prepared by sputtering, while the other layers have been prepared by electron beam evaporation. In spite of the fact that the Ta was found to oxidize when the Pt/Ta structure was annealed in oxygen at 650 °C for 30 min, this structure was used in the present study to investigate its behavior in contact with ferroelectric films for shorter annealing times. The structure was composed of 1000 Å Pt, over 500 Å Ta, over Si. Although it does not satisfy requirement (1) from above, the Pt/SiO₂ structure was also studied as an electrode in order to compare its effect on the crystallization of the oxide material.

Lead titanate (PT) and lead magnesium niobate with lead titanate, (PMN-PT 70-30) films have been deposited by the sol-gel method. The 1 molar stock solutions containing 10% excess lead of PT and PMN were prepared from lead acetate and titanium isopropoxide (PT), and lead acetate, magnesium and niobium ethoxide (PMN) using the method of Francis and Payne.¹¹ Hydrolyzed solutions containing 1 equivalent of water per mole of metal alkoxide were diluted with 2-methoxyethanol to a final concentration of 0.33 molar and aged overnight before deposition. Films were spun on to 1 inch substrates at a speed of 2,500 rpm and dried on a hot-plate at 350 °C for 30 s between coatings. Layers were approximately 1100 Å thick before annealing and 800 Å thick after annealing. Films were typically comprised of 3 to 5 layers. After deposition, the films were annealed in oxygen for 1 min at temperatures up to 800 °C.

The materials have been characterized by RBS, SEM, and XRD.

RESULTS AND DISCUSSION

It was shown elsewhere¹⁰ that, for a total thickness of about 1200 Å, after exposure to oxygen at 650 °C for 30 min., only the RuO₂/Ru structure satisfied the conditions enumerated in the Introduction. All other structures appeared to be unsuitable as bottom electrodes if exposed to oxygen at temperatures above 650 °C for prolonged

periods. As illustrated in Figure 1 for Pt/TiN (from Ref. 10), RBS showed that this annealing resulted in diffusion of oxygen through the Pt layer and oxidation of the underlying TiN film. Only the RBS spectrum of the RuO₂/Ru structure remained unchanged after annealing at 650 °C for 30 min., indicating that the structure prevented the diffusion of both oxygen and Si through it.¹⁰

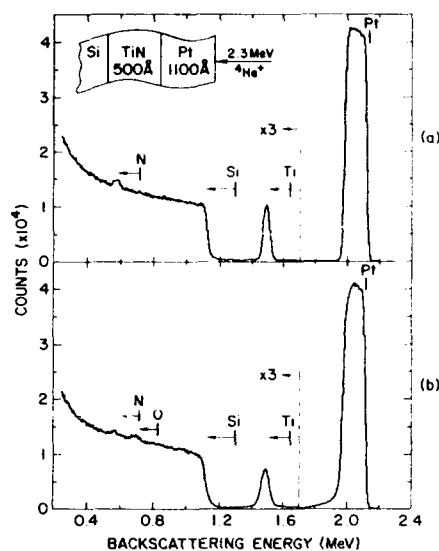


Figure 1. RBS spectra of Pt/TiN:
(a) - as deposited; (b) - after annealing.

adherent to the Si substrate, as shown in Figure 3. In this case the diffusion of oxygen through the Pt had, as expected, no effect on the electrode structure. However the Pt/SiO₂ structure cannot be used as an electrode providing electrical contact to the Si wafer.

A similar behavior was observed for the Pt/Ta structure, coated with a sol-gel layer about 2000 Å thick, and annealed in oxygen at 650 °C for only 1 min. The RBS spectrum of this sample showed the occurrence of oxygen inside the Ta layer, indicating that even such a short annealing time did not prevent oxygen from diffusing through the Pt layer, 1000 Å thick. The oxidation of the Ta layer had a disastrous effect on the annealed ferroelectric film, as illustrated in Figure 2. The figure shows SEM micrographs of PT films deposited on the Pt/Ta structure and annealed for 1 min at 700 °C in oxygen. The oxidation of the Ta resulted in its swelling and delamination from the substrate and caused blistering and cracking of the lead titanate film. In contrast to this, a continuous and uncracked film was obtained after identical annealing conditions, when a similar PT film was deposited on Pt/SiO₂. The Pt/SiO₂ structure remained uniform and well

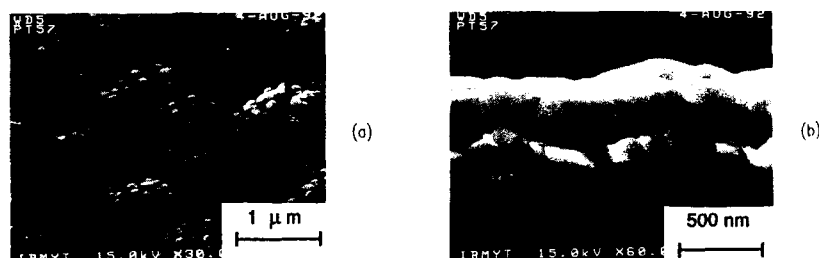


Figure 2. SEM micrograph of PbTiO₃ on Pt/Ta: annealed in oxygen for 1 min at 700 °C (a) - top view; (b) cross-section.



Figure 3. SEM micrograph of PbTiO_3 on Pt/SiO_2 : annealed in oxygen for 1 min at 700 °C (a) - top view; (b) cross-section.

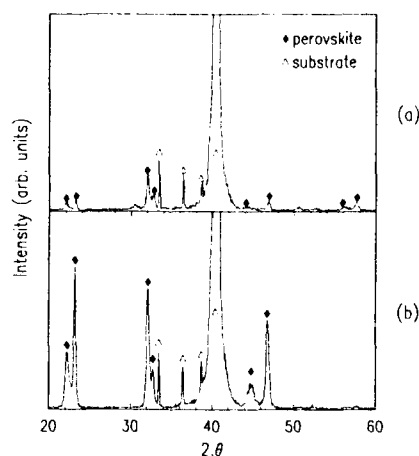


Figure 4. X-ray diffractogram of PbTiO_3 on Pt/SiO_2 : (a) - annealed in oxygen for 1 min at 600 °C; (b) - annealed in oxygen for 1 min at 800 °C.

crystallization of the pure perovskite phase (Figure 5a), however annealing at 800 °C causes the crystallization of both perovskite and pyrochlore phases (Figure 5b). (The volume fraction of perovskite to pyrochlore in these samples cannot be ascertained with any certainty from X-ray data because these thin films all show evidence of preferred orientation.)

Another example of the effect of the electrode material on the crystallization of sol-gel deposited lead based films is illustrated in Figure 6, which presents X-ray diffractograms of PMN-PT films annealed for 1 min at 650 °C. Identical films were deposited on two structures namely: (a) Pt/SiO_2 ; (b) a structure composed of 500 Å of Pt over 1000 Å of Pt-3%Ti alloy. The film deposited on Pt/SiO_2 crystallized in a highly (100) oriented perovskite phase, with a very small amount of pyrochlore (Figure 6a).

The composition of the electrode affected not only the uniformity of the annealed ferroelectric film but also its crystallization, as illustrated in the following X-ray diffractograms. Figure 4 compares the diffractograms of 2400 Å thick PT films deposited on Pt/SiO_2 and annealed for 1 min at 600 °C and 800 °C, respectively. Formation of the perovskite phase already occurs after annealing at 600 °C (Figure 4a) but the corresponding X-ray peaks are small. After annealing at 800 °C the X-ray diffractogram displays only strong and sharp peaks of the perovskite phase in addition to the peaks of the substrate (Figure 4b).

For comparison, Figure 5 shows the X-ray diffractograms of 4000 Å thick PT films deposited on Pt/Ta and annealed for 1 min at 600 °C and 800 °C, respectively. Annealing at 600 °C results in the

The film deposited on the Pt,Pt-3%Ti structure crystallized completely differently. The X-ray diffractogram shown in Figure 6b displays a strong pyrochlore peak and perovskite peaks of reduced intensities. The relative intensities of the perovskite peaks are also different from those in Figure 6a.

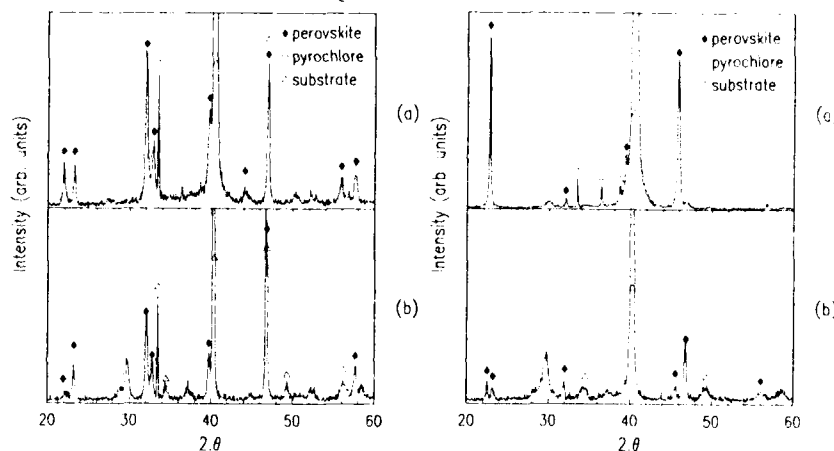


Figure 5. (left) X-ray diffractograms of PbTiO₃ on Pt/Ta: (a) - annealed in oxygen for 1 min at 600 °C (b) - annealed in oxygen for 1 min at 800 °C.

Figure 6. (right) X-ray diffractograms of PMN-PT annealed for 1 min at 650 °C: (a) - deposited on Pt/SiO₂ (b) - deposited on Pt-3%Ti-Ta.

CONCLUSIONS

The presented results showed that 1000 Å of Pt are insufficient to prevent diffusion of oxygen through it when annealed at temperatures as low as 600 °C for only 1 min. Using Pt as the oxidation resistant layer in a base electrode structure would result in oxidation of the underlying layer, disrupting the electrical conductivity path to the Si substrate. A conductive oxide film, such as RuO₂ seems to be the suitable choice for the bottom electrode material, at least for annealing temperatures lower than 650 °C. Even in applications where the diffusion of oxygen through the Pt may not be important, the barrier layer underneath the Pt has to be chosen carefully, because it can affect the crystallization of the film to the perovskite phase.

ACKNOWLEDGEMENTS

The authors wish to thank C. Cabral and D. Mikalsen for the deposition of the electrode layers and to T. Ross for the SEM measurements.

REFERENCES

- ¹ M. Okuyama and Y. Hamakawa, International Journal of Engineering Science **29** (1991) 391-400.

- ² G. H. Haertling, *J. Vac. Sci. Technol.* **A 9** (1991) 414.
- ³ K. Koyama, T. Sakuma, S. Yamamichi, H. Watanabe, H. Aoki, S. Ohya, Y. Miyasaka and T. Kikkawa, *IEEE IEDM 91* **91** (1991) 823.
- ⁴ M. Sayer, in *IEEE Ultrasonics '91 Symposium Lake Buena Vista, FL, Dec. 8-11, 1991*.
- ⁵ P. D. Hren, S. H. Rou, A. S. H., M. Ameen, O. Auciello and A. Kingon, *Ferroelectrics* **116** (1991).
- ⁶ R. Bruchhaus, D. Pitzer, O. Eibl, U. Scheithauer and W. Hoesler, in *Ferroelectric Thin Films II, 1991 Mat. Res. Soc. Symp. Proc.*, edited by A. I. Kingon, E. R. Myers, and B. Tuttle (Mat. Res. Soc., Pittsburg, PA, 1992), Vol. 243, p. 123.
- ⁷ S. B. Desu and I. K. Yoo, in *Proceedings ISIF-4, March 1992, Monterey, CA.*
- ⁸ T. Ogawa, *Integrated Ferroel.* **1** (1992) 1.
- ⁹ S. Yamamichi, T. Sakuma, K. Takemura and Y. Miyasaka, *Jap. J. Appl. Phys.* **30** (1991) 2193.
- ¹⁰ A. Grill, W. Kane, J. Viggiano, M. Brady and R. Laibowitz, *J. Mater. Res.* **7** (1992) 3260.
- ¹¹ L. E. Francis and D. A. Payne, *J. Am. Ceram. Soc.* **74** (1991) 3000.

FERROELECTRIC La-Sr-Co-O / Pb-Zr-Ti-O / La-Sr-Co-O HETEROSTRUCTURES ON SILICON : RELIABILITY TESTING

R. RAMESH*, T. SANDS*, V. G. KERAMIDAS* AND D.K.FORK**

*Bellcore, Red Bank, NJ 07701.

**Xerox Palo Alto Research Center
Palo Alto, CA 94304.

ABSTRACT

We report results of pulsed electrical testing of ferroelectric $\text{Pb}_{0.9}\text{La}_{0.1}\text{Zr}_{0.2}\text{Ti}_{0.8}\text{O}_3$ thin film capacitors with symmetrical La-Sr-Co-O top and bottom electrodes at room temperature and at 100°C. They have been grown on [001] Si with a Yttria stabilized zirconia (YSZ) buffer layer. A layered perovskite "template" layer (200-300Å thick), grown between the YSZ buffer layer and the bottom La-Sr-Co-O electrode, is critical for obtaining the required orientation of the subsequent layers. When compared to the capacitors grown with Y-Ba-Cu-O (YBCO) top and bottom electrodes, these structures possess two advantages : (i) the growth temperatures are lower by 60-150°C; (ii) the capacitors show a large remnant polarization, ΔP , (ΔP = switched polarization - non-switched polarization), 25-30 $\mu\text{C}/\text{cm}^2$, for an applied voltage of only 2V (applied field of 70kV/cm). The fatigue, retention and aging characteristics of these new structures are excellent at both room temperature and at 100°C.

INTRODUCTION

Ferroelectric thin film materials have had a strong resurgence in research and development recently, primarily because of their potential use as non-volatile, random access memories integrated with existing Si CMOS transistor circuitry [1-4]. Conventionally the ferroelectric thin films, such as lead zirconate titanate (PZT), are deposited onto Pt coated Si wafers with Pt top contact electrodes to form the capacitor structure. Thin film deposition techniques including sol-gel spin-on, sputtering, chemical vapor deposition, and pulsed laser deposition are being used to deposit the thin films. Solutions to reliability issues such as fatigue, aging, retention and imprinting are being explored concurrently with issues related to integration with CMOS drive circuitry [5-10]. Recent studies have shown that metal oxide electrodes yield capacitors with better fatigue properties compared to conventionally used Pt electrodes [11-13]. In the case of YBCO, the top and bottom electrodes are typically grown in the temperature regime of 700-800°C, which is higher than that conventionally used in Si process technology (about 550°C). In an effort to reduce the growth temperature, we have been studying a variety of other metallic perovskite compounds as potential candidates for the top and bottom electrodes. Among such oxides, the cubic perovskite La-Sr-Co-O (LSCO) has been shown to have desirable metallic properties in recent studies wherein the thin film heterostructures were grown on single crystalline oxide substrates (SrTiO_3) [11,12]. Even though LSCO is metallic and has good structural compatibility with the SrTiO_3 substrates used, in order to be useful in integrated ferroelectric memories, they have to be grown on Si wafers. We have taken the approach of finding methods to grow these epitaxial capacitor structures on Si using structural templates and chemical barrier layers to alleviate the problem of the chemical and structural incompatibility. In an earlier report, we addressed the issue of growth of high quality LSCO/PLZT/LSCO ferroelectric capacitor structures on YSZ-buffered-Si. This involved the use of a novel "template" approach to induce the preferred crystallographic orientation and crystallinity of the LSCO/PLZT/LSCO heterostructure. In this article, we elaborate on the ferroelectric properties of discrete capacitor structures fabricated from these heterostructures.

The heterostructures are grown by pulsed excimer laser deposition on to [001] Si which is buffered with yttria stabilized zirconia (YSZ) surface layer. The important feature of this approach is that it can be carried out at a substrate heater temperature of 640°C, (substrate temperature is approximately 50°C lower) which is substantially lower

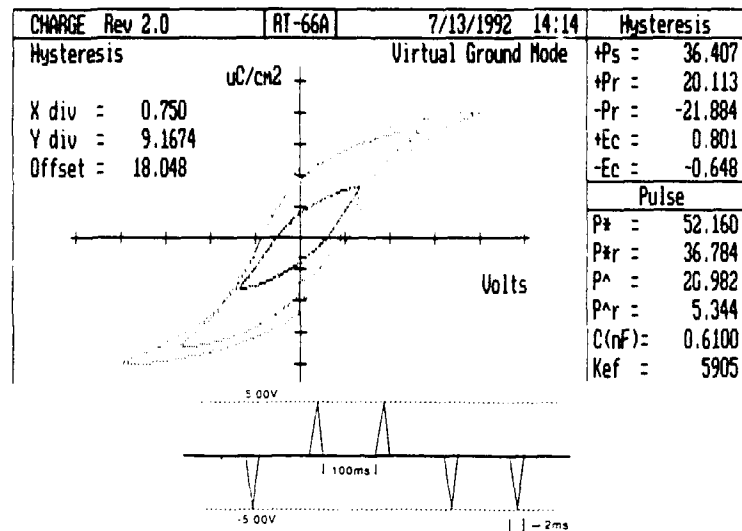


Figure 1: A typical family of hysteresis loops obtained from the LSCO / PLZT / LSCO ferroelectric capacitors. Also shown is the pulsed polarization values under saturation and remnant conditions. The inset shows the pulse train used to measure these values.

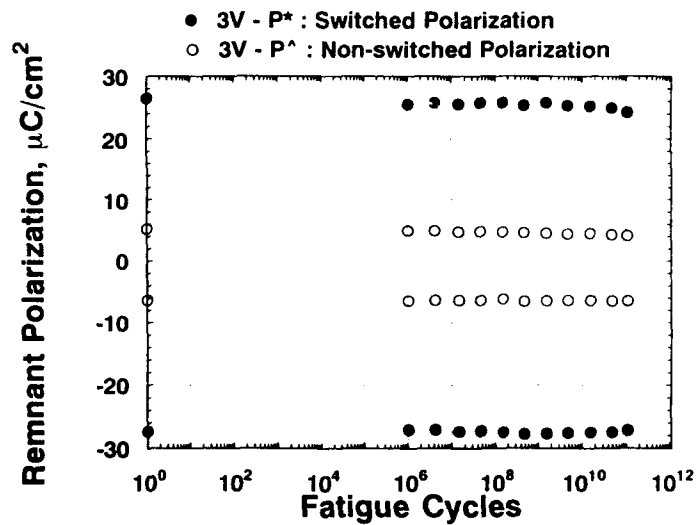


Figure 2: A plot of switched and non-switched remnant polarization as a function of fatigue cycles at a testing frequency of 1MHz and amplitude of $\pm 3\text{V}$ at room temperature.

than the previously reported range of 700-800°C for YBCO type top and bottom electrodes [13]. The YSZ layer is deposited at temperatures in the range of 750-800°C. The details of the deposition conditions are similar to that reported for the capacitors with YBCO top and bottom electrodes. Direct deposition of the LSCO/PLZT/LSCO layer onto the YSZ buffer layer yielded a weakly [110] oriented film. Capacitors fabricated from this heterostructure were only weakly ferroelectric. We attribute the [110] preferred orientation to the large difference in lattice parameters between YSZ (5.16Å) and LSCO (3.82Å), which is detrimental for a simple cube-on-cube orientation relationship. This problem was overcome through the use of a very thin (approximately 20-30nm) layer of c-axis oriented $\text{Bi}_4\text{Ti}_3\text{O}_{12}$, which acts as a perovskite "template" layer. This template layer is also grown at the same growth temperature. Another such perovskite "template" layer is Y-Ba-Cu-O, which preferentially grows with the c-axis orientation on YSZ-buffered Si. The LSCO top and bottom electrodes were 1000Å thick while the PLZT layer was 2700Å thick. With such a "template" layer, the LSCO/PLZT/LSCO heterostructure is also c-axis oriented. X-ray rocking curves about the [001] Bragg peak of the PLZT layer yielded a full width at half maximum of 0.7-0.8°. Rutherford backscattering analyses confirmed the composition of the various layers to be commensurate with that of the target and no measurable lead loss was observed as long as the substrate heater temperature was kept below 650°C. Test capacitors were fabricated using a shadow mask with areas in the range of 2×10^{-5} - 10^{-4} cm². Pt/Au dots were evaporated through shadow masks and were subsequently used as masks for the etching of the top LSCO layer, between the dots. Electrical measurements were made using the Radiant Technologies tester, RT66A, in conjunction with a pulse generator. For the bipolar fatigue experiments, internally generated 8.65µsec wide square pulses or externally generated square pulses were used. At the end of each fatigue period, the polarization characteristics of the capacitors were measured using the pulse sequence shown in the inset to Fig.1. High temperature testing was carried out using a temperature controlled hot stage attached to the probe station.

Fig.1 is a typical family of hysteresis loops measured with increasing voltage from 1-3V. The inset shows the pulse train used to measure the various relevant polarization values. We have measured a relatively large switched polarization at room temperature in the range of 25-30 µC/cm² at an applied voltage as low as 3V. The corresponding coercive voltage is typically in the range of 0.6-1.0V. The fatigue response of the test capacitors subjected to ±3V pulses at room temperature for a test frequency of 1MHz is shown in Fig.2. Under these test conditions, we have observed no serious degradation in the remnant polarization which typically decreases only by about 10% of the value at the beginning of the test and is completely recoverable by a 2 second poling treatment at 3V. Similar results have been obtained when tested at lower frequencies (which also ensures that the absence of significant fatigue is not due to incomplete switching resulting from the test frequency), as illustrated in Fig.3, in which the ΔP values for test frequencies of 1MHz and 50kHz at room temperature (RT) and 1MHz at 100°C are plotted. The behaviour at higher temperatures of up to 100°C is similar with the difference being that the remnant polarization is typically smaller by about 40-50% at 100°C compared to that at room temperature. The small increase of ΔP in the early stages of cycling is attributed to poling processes in the ferroelectric that effectively remove pinned domain walls and increase the ΔP value.

Concurrent with the high temperature fatigue studies, we are also testing the temperature dependent aging behaviour. Aging tests were carried out using a 8.6µsec write pulse of the desired amplitude (in this experiment -3V) followed by a set of read pulses after the set aging time. The read pulse train, of amplitude 2.5V, is the same as illustrated in the inset to Fig.1 and yields the switched and non-switched polarization values in the positive and negative directions. As in the case of the fatigue experiment, the capacitor would be considered to have failed if the difference between the switched and non-switched polarization is smaller than the detection criterion for the amplifier circuitry, i.e., for example 1µC/cm². Figs.4 and 5 show aging plots at room temperature and at 100°C respectively. We do not observe any significant loss of switched polarization under these aging conditions, when tested for the time scale shown. We are currently in the process of testing the aging behaviour for longer periods of time in order to explore longer term effects and study for drastic changes in aging behaviour.

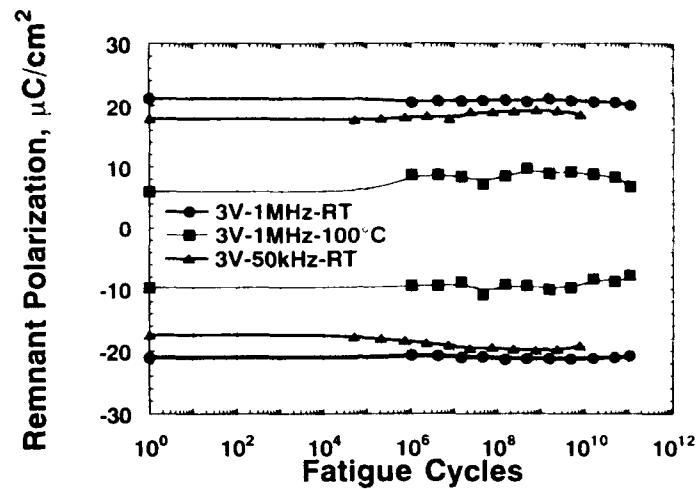


Figure 3: Comparison of the fatigue response (ΔP vs. fatigue cycles) at testing frequencies of 50kHz, 1MHz (both at room temperature) and at 100°C.

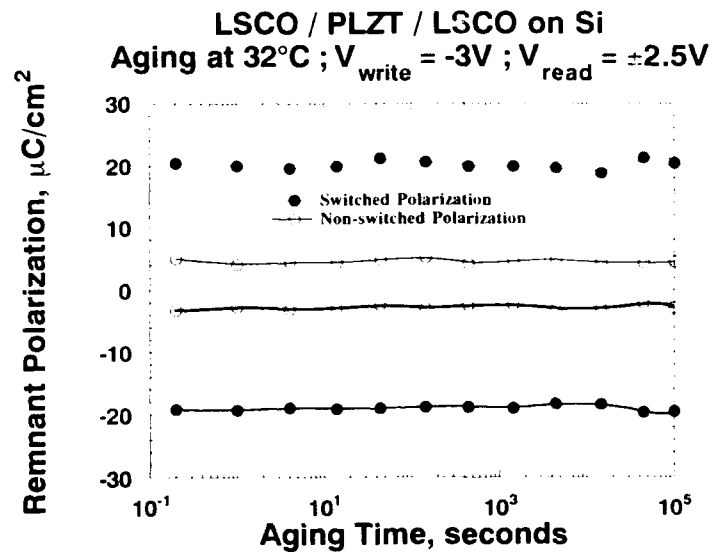


Figure 4: A plot of switched and non-switched remnant polarization as a function of aging time at room temperature. There is no significant loss in the ΔP value after aging for at least 10^5 seconds. Long term aging studies are underway.

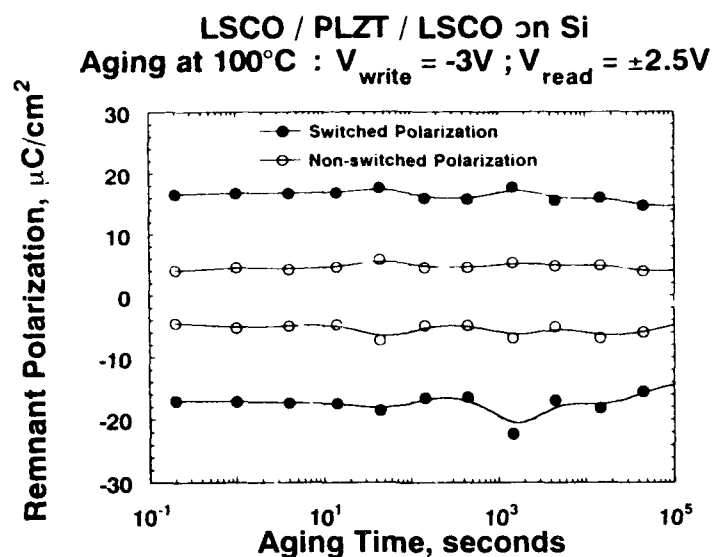


Figure 5: A plot of switched and non-switched remnant polarization as a function of aging time at 100°C. The behaviour is very similar to that at room temperature, although the ΔP value is smaller.

CONCLUSIONS : We have demonstrated the growth of highly oriented ferroelectric PLZT thin films capacitors with perovskite La-Sr-Co-O top and bottom electrodes on Silicon substrates. A novel template approach has been used to obtain the desired crystallographic orientation and quality in the LSCO/PLZT/LSCO heterostructure. The results of reliability testing, presented in brief in this paper, show that such capacitor structure are worthy of further detailed studies for integration with the Silicon based drive electronics.

REFERENCES

1. See for example, Proc. of Materials Research Society Fall Meeting Symposium on Ferroelectric Thin Films II, Eds. A.Kingon, E.R.Myers and B.Tuttle, Materials Research Society, Pittsburgh, PA, Dec., 1991; Proc. of Third Int. Symp. on Integrated Ferroelectrics, Ed. C.A. Paz de Araujo, University of Colorado, Colorado Springs, CO., April 1991; Proc. of Fourth Int. Symp. on Integrated Ferroelectrics, Monterey, CA, March 1992.
2. J.F.Scott and C.A.Paz de Araujo, Science, 246, 1400(1989); M.Sayer and K.Sreenivas, Science 247, 1056(1990); G.H.Haertling, JI. of Vacuum Science and Technology, 9, 414(1991).
3. S.Sinharoy, H.Buhay, D.R.Lampe and M.H.Francombe, JI. of Vac. Science and Technology, A10, 1554(1992).
4. J.T.Evans and R.D.Womack, IEEE JI. of Solid State Circuits, 23, 1171(1988).

5. H.M.Duiker, P.D.Beale, J.F.Scott, C.A.Paz de Araujo, B.M.Melnick, J.D.Cuchiaro and L.D.McMillan, *Jl. of Appl. Phys.*, **68**, 5783(1990).
6. S.K.Dey and R.Zuleeg, *Ferroelectrics*, **108**, 37(1990).
7. W.H.Shepherd, in *Proc. of Materials Research Society Fall Meeting Symposium on Ferroelectric Thin Films I*, Vol. 200, p207, Eds. A.Kingon and F.R.Myers, Materials Research Society, Pittsburgh, PA, Dec., 1990.
8. J.F.Scott, C.A.Paz de Araujo, B.M.Melnick, L.D.McMillan and R.Zuleeg, *Jl. of Appl. Phys.*, **70**, 382(1991); J.F.Scott, C.A.Paz de Araujo, H.B.Meadows, L.D.McMillan and A.Shawabkeh, *Jl. of Appl. Phys.*, **66**, 1444(1989).
9. G.A.C.M.Spierings, M.J.E.Ulenaers, G.L.M.Kampschoer, H.A.M.van Hal and P.K.Larsen, *Jl. of Appl. Phys.*, **70**, 2290(1991).
10. S.L.Miller, R.D.Nasby, J.R.Schwank, M.S.Rodgers and P.V.Dressendorfer, *Jl. of Appl. Phys.*, **68**, 6463(1990).
11. N.E.Abt, P.Misic, D.Zehngut and E.Regan, *Proc. of Fourth Int. Symp. on Integrated Ferroelectrics*, Monterey, CA, March 1992; S.D.Bernstein, T.Y.Wong, Y.Kisler and R.W.Tustison, *ibid*: S.B.Desu and I.K.Yoo, *ibid*.
12. R.M.Wolf, in *Materials Research Society Fall Meeting Symposium on Ferroelectric Thin Films II*, Boston, MA, Dec., 1991; J.T.Cheung, and R.R.Neurgaonkar, in *Proc. of Fourth Int. Symp. on Integrated Ferroelectrics*, Monterey, CA, March 1992.
13. R.Ramesh, W.K.Chan, B.Wilkins, H.Gilchrist, T.Sands, J.M.Tarascon, V.G.Keramidas, D.K.Fork, J.J.Lee and A.Safari, *Appl. Phys. Lett.*, **61**, 1537(1992).

EFFECTS OF PLATINUM ELECTRODE STRUCTURES ON CRYSTALLINITY AND ELECTRICAL PROPERTIES OF MOD-PREPARED PZT CAPACITORS

DENNIS J. EICHORST AND CYNTHIA J. BARON

Eastman Kodak Company, Research Laboratories, Rochester, NY 14650-2011

ABSTRACT

The most common electrode structure for lead zirconium titanate (PZT) integrated on Si is platinum with a Ti adhesion layer. However, platinum hillocks that can lead to sample shorting may form during annealing. Careful selection of the Pt/Ti electrode architecture and deposition conditions can give nearly hillock-free electrodes. The phase development and ferroelectric properties of PZT prepared by metallo-organic decomposition (MOD) were studied as a function of Pt electrode structure and PZT composition. In addition to evaporated or sputtered Pt/Ti electrodes, Pt electrode layers were also prepared by MOD. MOD Pt layers showed no hillock formation but generally resulted in greater pyrochlore content in PZT capacitors.

INTRODUCTION

The typical architecture for thin-film ferroelectric memories is lead zirconium titanate (PZT) deposited on Pt/Ti coated silicon substrates. In order to achieve a high remanent polarization, low coercive field, and minimal fatigue, various deposition methods and PZT compositions have been investigated.¹⁻⁷ For bulk samples, compositions near the morphotropic phase boundary (MPB: Zr/Ti = 53/47) give a maximum remanent polarization.⁸ However, in thin-films, the maximum remanent polarization may be shifted from the MPB.⁶ In addition to optimization of the ferroelectric processing, it has become evident that the underlying metallization can significantly influence the reliability of ferroelectric capacitors. Therefore, the influence of various platinum electrode structures on crystallinity and ferroelectric properties was studied for several PZT compositions. Solution deposition methods have met with good success, however, for this study sol-gel processing was considered overly susceptible to processing variations (i.e., solvent concentration, extent of distillation, moisture, etc.).^{9,10} Therefore, metallo-organic decomposition (MOD) was used, which is typically much less moisture sensitive and does not undergo significant polymerization.

EXPERIMENTAL

The types of substrates investigated included sputtered, e-beam evaporated and solution deposited Pt on 4" diam silicon (100) wafers with a thermal oxide. Table I describes the electrode structures and deposition methods. Sputter deposited Pt samples were obtained from Nova Electronic Materials.* The MOD Pt electrodes were prepared by depositing a commercial Pt solution (Engelhard-05X)[#] at 4000 rpm and heating to 650°C for 30 min in air using a 20°C/min heating rate. Two layers were deposited, giving a Pt thickness of 1000 Å. Prior to PZT deposition, the Pt electrodes were evaluated for potential hillock formation by annealing at 650°C for 1 hr in air. The annealing condition was selected to be in a temperature range typically used for crystallizing PZT films. A relatively long annealing time was selected in order to allow near complete hillock formation.

* Nova Electronic Materials, Tucson, AZ.

[#] Engelhard Corp., East Newark, NJ.

Table I
Si/SiO₂/Ti/Pt Deposition Conditions for Pt Coated Substrates

Substrate	Oxide (Å)	Ti Thickness (Å)	Pt Thickness (Å)	Temperature (°C)	Method
198	10000	2000	1000	25	Sputtered
163	8000	500	1000	200	Evaporated
207	4000	500	1000	25	Evaporated
202	8000	50	250	25	Evaporated
186	8000	—	1000	650	MOD

PZT solutions were formulated for Zr/Ti ratios of 60/40, 53/47, and 30/70 with 17.5% excess lead content. Metallo-organic precursors used were Pb(OOCC₉H₁₇)₂, Zr(OⁿPr)₂(OOCC₇H₁₅)₂, and Ti(OⁿPr)₂(OOCC₇H₁₅)₂. Pb(OOCC₉H₁₇)₂ was synthesized by reacting PbO with neodecanoic acid. The zirconium and titanium MOD precursors were prepared by reacting the respective n-propoxides with 2-ethylhexanoic acid. The constituent precursors were dissolved in 2-ethylhexanoic acid and 2 wt% abietic acid was added to promote film formation. Solutions were deposited on 1" x 1" substrates by spin-casting at 4000 rpm for 20 s. The films were decomposed at 300°C in a preheated furnace for 5 min. Crystallization was accomplished by inserting samples on a platinum boat into a 700°C preheated furnace for 5 min. The heat-treatment schedule was derived from optimization of perovskite content for films deposited on the sputter deposited Pt electrodes. The required crystallization temperature for optimum perovskite formation was slightly higher than the annealing temperature used for evaluation of Pt hillocks. A single deposition generally gave a 2000 Å crack-free film. Sample designations are given as substrate # followed by PZT composition (e.g., 207-60/40 corresponds to PZT 60/40 on the substrate having 500 Å Ti and 1000 Å Pt deposited by evaporation without substrate heating).

Gold top electrodes ranging in size from 2×10^{-4} to 1×10^{-2} cm² were sputtered through masks defined by standard photolithographic lift-off techniques. Hysteresis data were acquired with (i) Radiant Technologies RT66A* using a 20 V_{pp}, 6 Hz test signal, and (ii) an automated ferroelectric testing system (Eastman Kodak Company) with 20 V_{pp}, 10 Hz triangular waveform. Fatigue data were collected with the Kodak system using a 10 V_{pp}, 1.25 MHz signal.¹¹

RESULTS

Hillock formation was evaluated for the different electrode structures since this may be a contributing factor to ferroelectric degradations. Figure 1 compares the microstructures of platinum substrates annealed at 650°C for 1 h in air. The micrographs indicate similar hillock formation for the sputtered (substrate #198) and evaporated #207 (500 Å Ti/1000 Å Pt) electrodes. The MOD Pt (#186) and substrate #202 (50 Å Ti/250 Å Pt), on the other hand, were essentially hillock-free. Substrate #163 (200°C deposition) had large hillocks and considerable residual strain measured by X-ray diffraction (XRD) techniques. PZT films deposited on this substrate cracked, frequently with spalling of the Pt layer. Therefore, this substrate was not considered for further studies. However, Pt deposited under similar conditions as for #163 on 1" x 1" samples were hillock-free.¹² This may indicate a size effect not previously considered or difficulty in maintaining thermal equilibration in the current deposition system. Rapid thermal annealing at 650°C for 5 min (typical for RTA of PZT)

* Radiant Technologies, Albuquerque, NM.

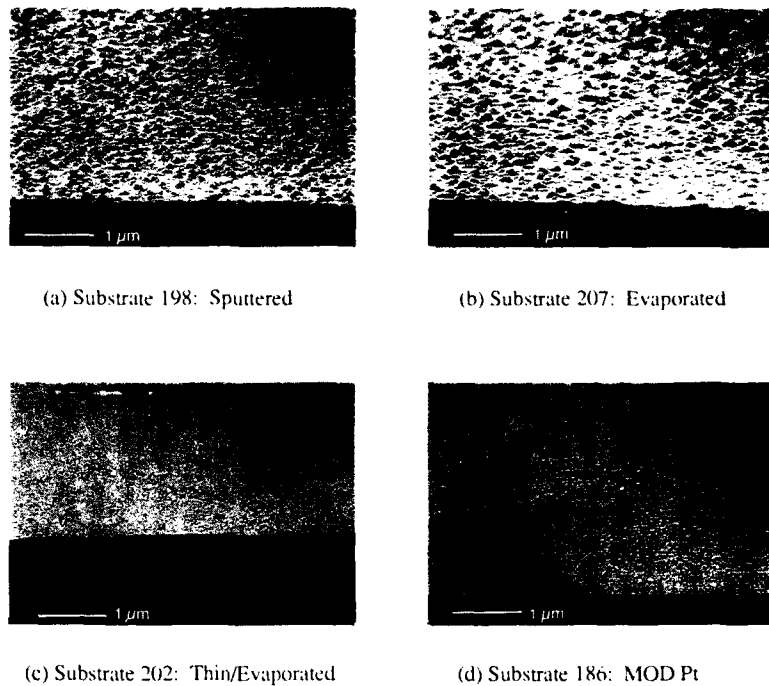


Figure 1. SEM photomicrographs of annealed Pt coated Si substrates.

produced fewer hillocks than conventional furnace annealing (650°C for 30 min).¹³ This difference may be due to decreased time at elevated temperatures, however, it indicates that altering the ferroelectric processing conditions may affect the electrode structures. XRD indicated all of the vapor deposited electrodes were preferentially (111) oriented, whereas the MOD Pt was random in nature.

XRD for the PZT films indicated only a broad pyrochlore peak with no perovskite phase for samples deposited on MOD Pt. Conversely, pure perovskite was (apparently) obtained for PZT on the evaporated and sputtered substrates. Perovskite orientation was evaluated based on relative peak intensities, $I(hkl)/[I(100)+I(110)+I(111)]$. Samples on substrate #202 (thin Ti/Pt) were preferentially (100) oriented with little dependence on composition. Samples on substrate #198 (sputtered Pt) were fairly random in orientation, the perovskite (111) peak was greatest (~40%) for PZT 53/47. Samples on substrate #207 had the greatest degree of (111) orientation (~40%), which decreased with increasing Ti content.

Figure 2 shows the microstructures for PZT 53/47 samples fired at 650°C on the different Pt substrates. The sample deposited on MOD Pt was highly cracked, however, SEM detected no grain structure (i.e., Figure 2d is nearly featureless). The sample on sputtered Pt (substrate #198) showed a dense microstructure with fairly uniform grain size. The samples on the evaporated Pt electrodes (substrates #202 and #207) showed the well-known "rosette"

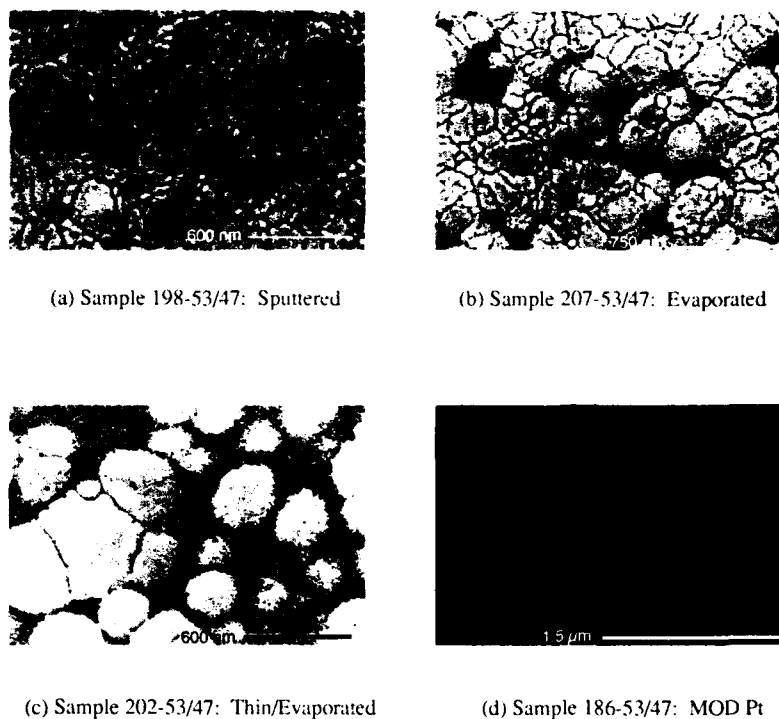


Figure 2. Microstructures of PZT 53/47 films with 17.5% excess Pb.

(perovskite) structure surrounded by a fine-grained pyrochlore (or amorphous) matrix.¹⁴ However, no pyrochlore was detected by XRD. Interestingly, the samples with the least hillock formation appeared to have the greatest pyrochlore or amorphous character.

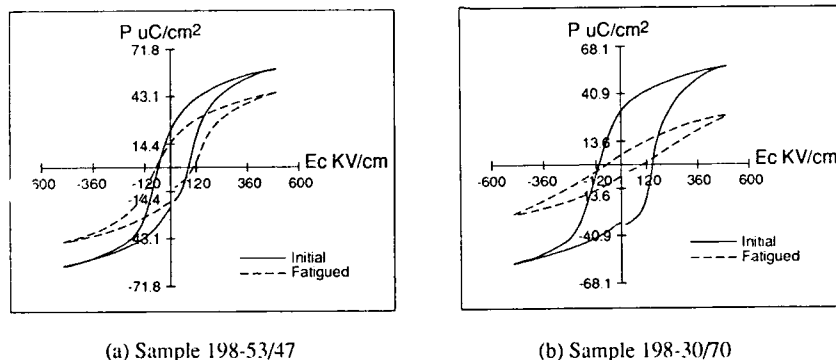
Table II lists the remanent polarization, coercive field, and fatigue behavior for the PZT films. Representative hysteresis loops and fatigue plots for PZT 53/47 and 30/70 on the sputtered Pt electrodes are shown in Figures 3 and 4. PZT films on vapor deposited Ti/Pt electrodes had remanent polarizations consistent with reported values. The low P_r values on MOD Pt are described below. P_r values depended on substrate type in a fashion consistent with the apparent pyrochlore content estimated from SEM. PZT on the sputtered electrode (#198) consistently had the highest polarization and most uniform microstructure. On the other hand, the coercive field showed very little dependence on substrate (Ti/Pt) type. Both P_r and E_c increased with Ti content as reported for similar samples.^{5,6} Fatigue behavior appeared rather similar for PZT on the various substrates. P_r decreased to 50% of the initial value between 5×10^7 and 5×10^8 cycles for most samples. An increase in the number of cycles prior to degradation may occur for greater zirconium contents. PZT 60/40 and 53/47 had an approximately constant P_r until a "roll-off" at $\sim 10^7$ cycles. PZT 30/70, on the other hand, had a continual decrease in P_r during cycling until the roll-off stage. Fatigue was accompanied by a decrease in resistivity from approximately $6 \times 10^{11} \Omega\text{-cm}$ to $8 \times 10^9 \Omega\text{-cm}$ (resistivities are

Table II
Ferroelectric Properties of PZT Films

Sample	RT66A		Kodak		
	+ P_r ($\mu\text{C}/\text{cm}^2$)	E_c (kV/cm)	+ P_r ($\mu\text{C}/\text{cm}^2$)	E_c (kV/cm)	50% $2P_r$
198 - 60/40	26.9	65	23.8	90	3×10^8
	53/47	67	23.1	80	3×10^8
	30/70	116	31.4	130	5×10^7
207 - 60/40	22.0	69	20.6	80	5×10^8
	53/47	78	19.9	90	1×10^8
	30/70	117	24.2	130	5×10^7
202 - 60/40	15.6	65	14.4	100	1×10^9
	53/47	80	19.7	110	5×10^7
	30/70	112	31.4	140	5×10^7
186 - 60/40	0.1	24	-	-	-
	53/47	38	-	-	-
	30/70	138	17.6	169	3×10^4

averaged for all substrates except MOD Pt) for PZT 60/40. PZT 53/47 samples also showed a slight decrease in resistivity (from approximately 4×10^{11} to $2 \times 10^{11} \Omega\text{-cm}$). PZT 30/70, on the other hand, had an initial resistivity of $6 \times 10^{11} \Omega\text{-cm}$ which did not decrease after fatigue cycling (1×10^9 cycles). PZT samples deposited on MOD Pt generally had lower resistivities (approximately $10^8 \Omega\text{-cm}$) than corresponding samples on Ti/Pt substrates.

Additional PZT samples deposited on MOD Pt were evaluated for ferroelectric behavior. PZT 60/40 (rhombohedral side of morphotropic phase boundary), PZT 53/47 (MPB) and PZT 47/53 showed no hysteresis. Furthermore, these films were highly cracked and XRD indicated only a broad pyrochlore peak. However, the Ti-rich compositions PZT 40/60, 30/70 and 20/80 exhibited hysteresis loops. Rutherford backscattering spectrometry (RBS) was carried out on samples of PZT 60/40 (non-ferroelectric) and PZT 40/60 (ferroelectric) in order to investigate the loss of ferroelectric behavior. PZT 40/60 was investigated since this composition had the minimum titanium content required for hysteresis. RBS scans (Figure 5) indicated diffusion of Pb through the MOD Pt layer for PZT 60/40. The Pb peak at ~ 1.4 MeV for the PZT 60/40 film



(a) Sample 198-53/47

(b) Sample 198-30/70

Figure 3. Hysteresis loops for (a) PZT 53/47 and (b) PZT 30/70 on sputter deposited Pt electrodes before and after fatigue.

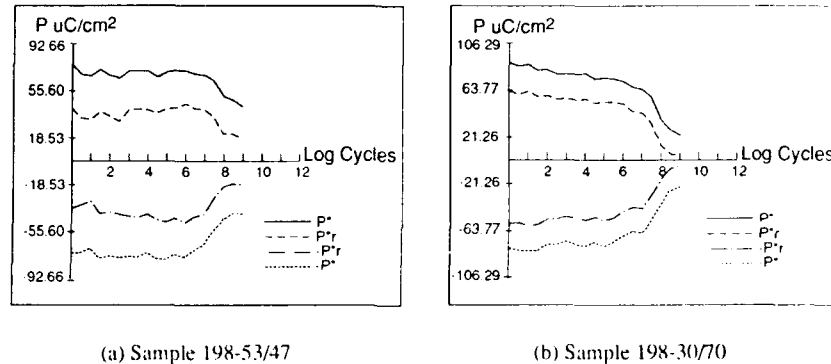


Figure 4. Fatigue data for (a) PZT 53/47 and (b) PZT 30/70 on sputter deposited Pt electrodes.

corresponds to a lead silicate layer. Furthermore, the peak at 1.8 MeV (Pb in PZT) is approximately 1/2 that observed in PZT 40/60. Therefore, Pb loss into the substrate accounts for loss of the ferroelectric properties of Zr-rich PZT deposited on MOD Pt. Sequential simplex optimization of PZT processing on MOD Pt indicated a decrease in the Pb excess (0–5%) and use of a slow heating rate ($\leq 10^\circ\text{C}/\text{min}$) in order to minimize Pb diffusion and obtain ferroelectric behavior.¹⁵ These results are in contrast to PZT deposited on Ti/Pt electrodes where a lead excess and rapid thermal annealing appear to give improved crystallinity and ferroelectric properties. Using the optimized method for multiple layer films (4 layers required for a 2000 Å film) the perovskite phase was developed and a remanent polarization of approximately $5 \mu\text{C}/\text{cm}^2$ obtained for PZT 53/47 on MOD Pt. However, this improvement in ferroelectric quality is not sufficient for memory applications. Use of a barrier layer (e.g., Ti) could greatly improve the ferroelectric properties while retaining the uniform surface of the MOD Pt electrodes. An alternative approach that appears promising is the incorporation of a lanthanum strontium cobalt oxide (LSCO) barrier layer.¹⁶ Use of the Pt/LSCO electrode has allowed remanent polarizations of approximately $25 \mu\text{C}/\text{cm}^2$ to be achieved for PZT 53/47 on MOD Pt.

SUMMARY

Sputtered (2000 Å Ti/1000 Å Pt) and e-beam evaporated (500 Å Ti/1000 Å Pt) electrodes had similar hillock formation. The substrate having thin metallization (50 Å Ti/250 Å Pt) and the MOD Pt layer were essentially hillock-free after annealing. The electrodes that underwent hillock formation appeared to nucleate the perovskite phase since these samples had a more uniform microstructure without the rosette structure. A decrease in remanent polarization occurred with increasing pyrochlore phase. Generally, remanent polarization increased with Ti content. Though MOD Pt was the most uniform electrode, suitable ferroelectric capacitors were difficult to prepare. Lead diffusion through the MOD Pt layer for samples with $\leq 60\%$ Ti gave non-ferroelectric films. Improved properties could be obtained for lower Pb contents and heating rates $\leq 10^\circ\text{C}$. Little dependence on substrate type was found for fatigue behavior for the Ti/Pt samples. Generally, the onset of degradation in fatigue occurred at a greater number of

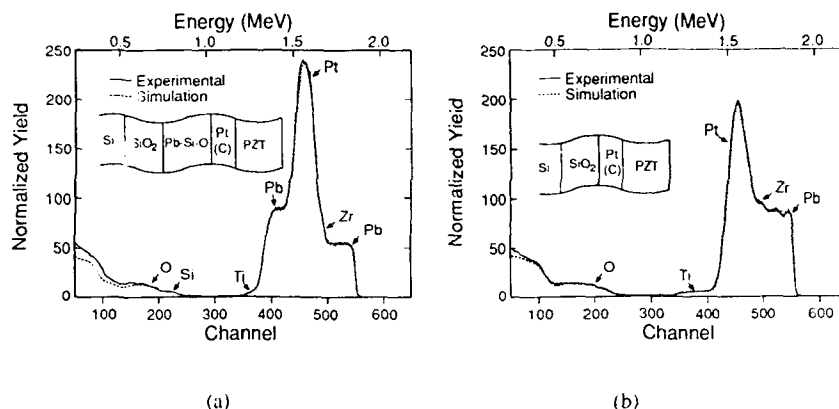


Figure 5. RBS scans of (a) PZT 60/40 and (b) 40/60 on MOD Pt substrates.

cycles for Zr rich compositions. The Ti rich compositions typically had a continual decrease in P_r whereas the other samples had the typical fatigue profile of a nearly constant P_r until roll-off, which occurred at approximately 10^8 cycles. Based on the different PZT microstructures obtained for identical processing on different substrates, it is apparent that processing should be optimized for each substrate architecture.

ACKNOWLEDGMENTS

The authors would like to thank G.R. Paz-Pujalt and L. Salter for helpful discussions and precursor synthesis. R.A. Nicholas and L.A. Bosworth III assisted in preparing Pt coated substrates. D.P. Stein, R.C. Bowen, and A.K. Mehrotra are gratefully acknowledged for SEM analysis. We are also thankful for RBS analyses by G.H. Braunstein.

REFERENCES

1. J.S. Horwitz, K.S. Grabowski, D.B. Chrisey, and R.E. Leuchtner, *Appl. Phys. Lett.* **59**(13), 1565-1567 (1991).
2. D. Roy, S.B. Krupanidhi, and J.P. Dougherty, *J. Appl. Phys.* **69**(11), 7930-7932 (1991).
3. K. Sreenivas and M. Sayer, *J. Appl. Phys.* **64**(3), 1484-1493 (1988).
4. Y. Sakashita, T. Ono, H. Segawa, K. Tominaga, and M. Okada, *J. Appl. Phys.* **69**(12), 8352-8357 (1991).
5. S.D. Bernstein, Y. Kisler, J.M. Wahl, S.E. Bernacki, and S.R. Collins, in *Ferroelectric Thin Films II*, edited by A.I. Kingon, E.R. Myers, and B. Tuttle (Mater. Res. Soc. Proc. **243**, Pittsburgh, PA, 1992), pp. 373-378.
6. H. Watanabe, T. Mihara, C.A. Paz de Araujo, in *Proceedings of the 3rd International Symposium on Integrated Ferroelectrics* (Colorado Springs, CO, 1991), pp. 139-150.

7. C.H. Peng, S.W. Park, and S.B. Desu, in *Ferroelectric Films*, edited by A.S. Bhalla and K.M. Nair (Ceramic Transactions **25**, 1992), pp. 169-186.
8. G. Haertling, *Ceram. Bull.* **43**(12), 875-879 (1964).
9. R.W. Schwartz, R.A. Assink, and T.J. Headley, in *Ferroelectric Thin Films II*, edited by A.I. Kingon, E.R. Myers, and B. Tuttle (Mater. Res. Soc. Proc. **243**, Pittsburgh, PA, 1992), pp. 245-254.
10. C.D.E. Lakeman and D.A. Payne, *J. Am. Ceram. Soc.* **75**, 3091-3096 (1992).
11. C.J. Baron, Eastman Kodak Company, unpublished results.
12. D.J. Eichorst, T.N. Blarton, C.L. Barnes, and L.A. Bosworth III, presented at the 5th International Symposium on Integrated Ferroelectrics (Colorado Springs, CO, 1993).
13. S.P. Barry, D.J. Eichorst and C.J. Baron, unpublished results.
14. M. Huffman, J.P. Goral, M.M. Al-Jassim, A.R. Mason, and K.M. Jones, *Thin Solid Films* **193/194**, 1017-1022 (1990).
15. D.J. Eichorst and C.J. Baron, unpublished results.
16. D.J. Eichorst and C.J. Baron, paper in preparation.

ELECTRON MICROSCOPY STUDY OF THE INFLUENCE OF THE ADHESION LAYER FOR Pt ELECTRODE ON THE MICROSTRUCTURE OF SOL-GEL CRYSTALLIZED PZT

Vidya Kaushik, Papu Maniar, Andrew Campbell, Robert Jones, Reza Moazzami, C. Joseph Mogab, Robert Hance and Ronald Pyle, Motorola Inc., Semiconductor Products Sector, Austin, Texas 78721

ABSTRACT

PZT ferroelectric capacitors are commonly fabricated using Pt electrodes. Crystallization in an oxygen ambient of sol-gel deposited PZT films is influenced by the nature of the adhesion layer used for the Pt electrode. Here we report results of the TEM investigation of the microstructures of PZT crystallized on Pt/Ti and Pt/TiO₂ substrates. PZT films on either substrate show a two-phase microstructure consisting of larger perovskite grains and fine-grained (<3nm) pyrochlore matrix. The perovskite grains are dense, free of any porosity and HRTEM shows the observed domains to be 90° <101> twins. EDS spectra detect a lower Pb/Ti ratio for the pyrochlore matrix compared to the perovskite grains. Differences between the two substrates consist of the perovskite to pyrochlore ratio and more importantly the perovskite grain size.

INTRODUCTION

Ferroelectric films are currently of interest to the semiconductor industry because of their potential applicability as dielectric films in high-density memory products. These materials have high dielectric constants and high charge-storage capacities. Much of the research at present focuses on issues related to the processing of thin films of such materials and on integrating these processes with existing silicon technology. PZT, or Lead Zirconium Titanate (Pb (Zr,Ti) O₃), appears to be a promising candidate in terms of process integrability. While the electrical properties of these films have been relatively well-studied, the material properties of PZT films have not been well characterized and correlated with its microstructure. Electron microscopy, in both scanning and transmission modes has been used in previous literature to study the microstructure of PZT films.¹⁻³ In this study, we have used transmission electron microscopy to examine the microstructure of PZT films crystallized using sol-gel techniques. In particular, the effect of substrate processing on the resultant structure of PZT films has been investigated.

EXPERIMENTAL

PZT films of the 0/50/50 type (i.e. 0% La/ 50% Zr/ 50% Ti) were deposited on silicon substrates after insulator and electrode deposition as shown schematically in Figure 1. Silicon dioxide serves as the insulator, titanium is used to overcome the problem of platinum adhesion to silicon dioxide and platinum is used as the bottom electrode. The titanium and platinum were sputter-deposited, and for the Pt/TiO_2 case, the titanium layer was annealed in oxygen at 650°C for 30 minutes prior to platinum deposition. PZT was deposited using a sol-gel technique and subsequently annealed in an oxygen ambient at 650°C for 30 minutes. Apart from annealing the titanium to form titanium dioxide, the wafers were identically processed. Samples for transmission electron microscopy were prepared for plan-view examination by standard techniques of mechanical polishing followed by ion-milling. The microscopy was performed on a commercial instrument operated at 200KV.

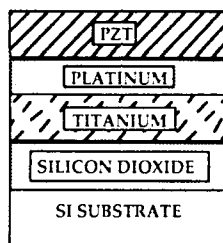


Figure 1: Schematic of the stack showing the silicon, insulator (oxide), titanium (or titania) layer, platinum electrode and PZT layer.

RESULTS AND DISCUSSION

Microstructure of PZT/ Pt/TiO_2

Figures 2 a-c show the microstructure observed on PZT films grown on platinum over titanium dioxide films. Figure 2a shows a two-phase structure, consisting of a large-grained structure within a small-grain matrix. Electron diffraction patterns from these phases show the large grains to be perovskite (tetragonal) phase PZT (Figure 2a), while the smaller grains were identified to be the pyrochlore (cubic) phase of PZT (Figure 2b). For ferroelectric applications, the perovskite structure is desirable since the cubic phase does not exhibit ferroelectric properties. The perovskite grain size is estimated to be in the range of 0.5-1.0 micron, while the pyrochlore grain size is $\sim 2\text{-}4\text{ nm}$.

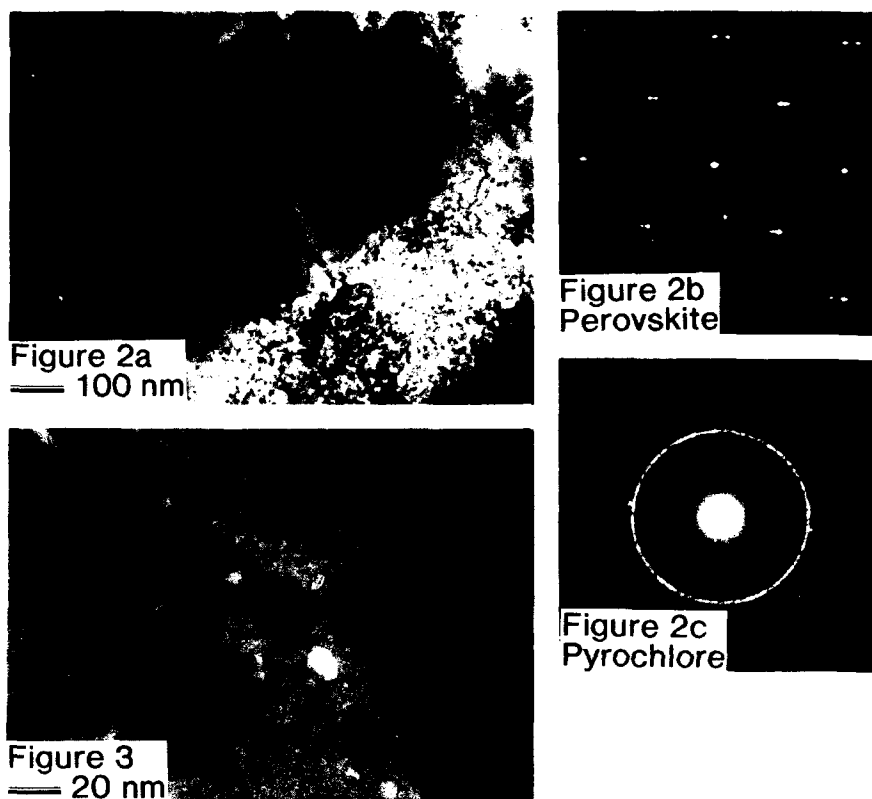


Figure 2: a) Microstructure of large perovskite PZT grains and pyrochlore matrix of PZT/Pt/TiO₂; b) Electron diffraction pattern (EDP) from large PZT perovskite-phase grains of Figure 2a in the [010] zone showing spot-splitting due to twinning along $\langle 101 \rangle$; c) EDP of small-grain matrix of Figure 2a which was indexed to be the pyrochlore phase of PZT.

Figure 3: Higher magnification of large grains showing inclusions of lighter contrast at grain boundaries.

The large PZT grains have within them a band structure, which was confirmed using electron diffraction and high-resolution electron microscopy to be due to $90^\circ \langle 101 \rangle$ twinning.⁴ It is widely believed that these twin regions correspond to ferroelectric domains although the link between the electrical properties and microstructure has not been clearly established. Figure 3 is a higher magnification image of the grain boundary between the large grains. Inclusions of lighter contrast are observed all along the grain boundaries, but not in the interior of these grains.

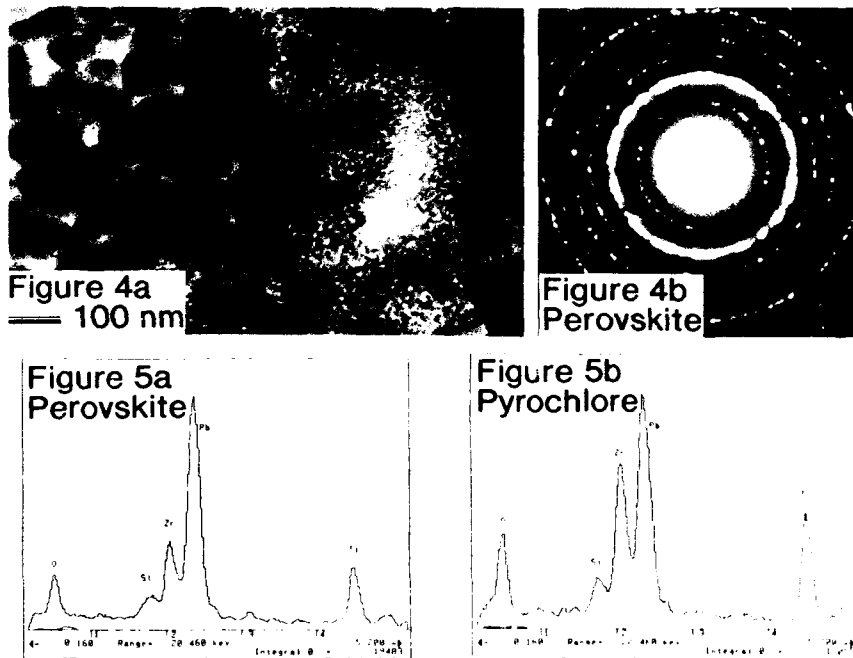


Figure 4: a) Microstructure of small perovskite PZT grains and pyrochlore matrix of PZT/Pt/Ti; b) EDP of small perovskite PZT grains of Figure 4a.

Figure 5: a) Energy dispersive spectrum (EDS) of large grains of perovskite PZT for PZT/Pt/TiO₂ showing titanium K_α, zirconium L_α and lead M_α peaks; b) EDS of pyrochlore matrix of PZT for PZT/Pt/TiO₂. The small silicon peak seen is an ion-milling artefact.

Microstructure of PZT/Pt/Ti

Figures 4a and b show the microstructure and electron diffraction pattern of the PZT layer deposited on platinum over titanium. There is a distinct difference in the observed film structure. Although a two-phase structure is still present, the larger-grains (relatively) are much smaller than in the case of platinum over titanium dioxide. Indexing of the diffraction pattern of Figure 4b shows the larger-grained phase to be perovskite PZT, while the smaller-grained matrix produced a diffraction pattern identical to that shown in Figure 2c, which was identified to be the pyrochlore phase. The grain size of the perovskite phase is estimated to be 0.1-0.2 micron. In contrast to the TiO₂ substrate case, the perovskite grains do not show the characteristic twinning or band structure. Inclusions were not observed at the grain boundaries in this case.

Compositional Analysis

Energy dispersive spectroscopy (EDS) was performed on these samples. Figures 5a and 5b show the spectra obtained from the sample with the TiO_2 substrate (spectra from the PZT/Pt/Ti sample were similar). Qualitative differences between the spectra of Figures 5a and b can be distinguished easily in terms of the relative heights of titanium $K\alpha$, zirconium $L\alpha$ and lead $M\alpha$ peaks. Spectral data were obtained from five different areas within each sample, from the perovskite grains and the small-grain matrix of each of the substrate cases studied. Areas chosen for EDS analyses were thin enough that Pt or Ti peaks from underlying layers were not present. Zr/Ti and Pb/Ti ratios from each sample were averaged and are shown in Table I. It should be noted that the ratio numbers shown in Table I are only integrated x-ray counts and cannot be correlated with concentrations in the material, in the absence of calibrating standards. However, since the spectra were all acquired under similar conditions, relative compositional differences between the perovskite grains and the pyrochlore matrix may be inferred. For both Ti and TiO_2 substrates, the data show that the perovskite PZT grains have a higher Pb/Ti ratio relative to the pyrochlore matrix. However, the Zr/Ti ratio is approximately the same between the grains and the matrix.

TABLE I

SAMPLE	(Zr/Ti) GRAINS (Zr/Ti) MATRIX	(Pb/Ti) GRAINS (Pb/Ti) MATRIX
PZT/Pt/ TiO_2	0.91	1.69
PZT/Pt/Ti	1.04	2.11

Table I: Integrated x-ray count intensity ratios for the two substrate samples studied. Numbers are average of five sets of spectra. Quantitation of the spectra was performed by considering the integrated counts under the Ti- $K\alpha$, Zr- $K\alpha$ and Pb- $L\alpha$ peaks. Prior to integration, background counts were removed by a thin-film routine within the commercial software.

CONCLUSIONS

The above results have enabled us to suggest the following hypothesis toward understanding the observations. It appears that when first deposited, the PZT layer is amorphous. During the subsequent heating cycle, it undergoes a phase transformation, firstly to the pyrochlore phase and then to the perovskite phase. This is consistent with other studies on sol-gel processed ferroelectric films.⁴ For PZT/Pt/ TiO_2 , we have larger perovskite grains with inclusions along grain boundaries, while for PZT/Pt/Ti, smaller perovskite grains without inclusions are observed. By examining the micrographs, the approximate volume per cent of the pyrochlore phase was estimated to be ~10-30% for the TiO_2 substrate and ~5-10% for the Ti substrate. Thus, a smaller fraction of the pyrochlore phase is observed for the small PZT grain case.

The distinctly different grain structures observed between the Ti and TiO₂ substrates suggests that the growth of the perovskite phase into either the large grain or small-grain morphologies is influenced by the underlying substrate. But since the layer immediately underlying the PZT film is platinum, it is possible that the Ti or TiO₂ substrate affects the platinum microstructure. This in turn affects the PZT microstructure by favoring a larger nucleation rate for PZT/Pt/Ti substrates. We know from a previous study⁵ that even for the Ti substrate case, the oxygen ambient annealing of the PZT film causes complete conversion of the Ti into TiO₂ and Pt₃Ti by consuming part of the platinum layer. The relative rates of PZT recrystallization compared to Ti conversion have yet to be studied. Attempts to perform TEM examinations on the platinum layer were unsuccessful because in plan-view, the PZT film obscures the imaging, while in cross-section, poor adhesion of the PZT film with the epoxy used caused samples to break during thinning. Further studies are in progress to understand the nucleation and growth of the perovskite phase from the pyrochlore phase.

Another interesting aspect of this study is the absence of twinned domains in the perovskite for the Ti substrate. While previous literature⁶ indicates a link between the twinned domains and ferroelectric properties, we have observed good ferroelectric properties even for the sample on Ti substrate which does not show the 90° twins. This may be indicative that other structures can equally well account for ferroelectric properties. It is possible that each of the small grains in the small-grain sample acts as an independent domain and participates in the polarization under applied electric field.

REFERENCES

1. S.A. Myers and L.N. Chapin, in "Ferroelectric Thin Films", Materials Research Society Symposia Proceedings Vol. **200**, 231, (1991).
2. B.A. Tuttle, T.J. Headley, B.C. Bunker, R.W. Schwartz, T.J. Zender, C.L. Hernandez, D.C. Goodnow, R.J. Tissot, J. Michael and A.H. Carim, in Journal of Mater. Res. Vol. **7**, (No. 7), 1876, (July 1992).
3. E.K.W. Goo, R.K. Mishra and G. Thomas, in J. App. Phys. **52** (4), 2940, (1981).
4. S.H. Rou, T.M. Graettinger, A.F. Chow, C.N. Soble, D.J. Lichtenwalner, O. Auciello and A.I. Kingon, in "Ferroelectric Thin Films II", Materials Research Society Symposia Proceedings, Vol. **243**, 81, (1992).
5. V.S. Kaushik, P. Maniar, J. Olowolafe, R. Jones, A. Campbell, R. Hance and C.J. Mogab, in Proceedings of Electron Microscopy Society of America (EMSA) 50th Annual Meeting, San Francisco Press 1364-65, (1992).
6. L.A. Bursill, Peng-Ju Lin and J.R. Sellar in Euro-Ceramics, 2,330, (1989).

TEXTURED $\text{Pb}(\text{Zr}_{0.54}\text{Ti}_{0.46})\text{O}_3$ THIN FILMS WITH $\text{YBa}_2\text{Cu}_3\text{O}_{7-\delta}$ AND YTTRIA-STABILIZED ZIRCONIA BUFFER LAYERS ON (001)Si

TSVETANKA ZHELEVA, P. TIWARI AND J. NARAYAN

Department of Materials Science and Engineering, North Carolina State University, Raleigh, NC 27695-7916

ABSTRACT

Characteristics of textured $\text{Pb}(\text{Zr}_{0.54}\text{Ti}_{0.46})\text{O}_3$ (PZT) thin films on (001)Si with $\text{YBa}_2\text{Cu}_3\text{O}_{7-\delta}$ (YBCO) and yttria-stabilized zirconia (YSZ) buffer layers have been studied using X-ray diffraction and high resolution electron microscopy techniques. Excimer KrF laser has been used for deposition of PZT, YBCO and YSZ thin films. The YBCO layer was utilized to provide a seed for PZT growth, while YSZ layer acted as a seed and a buffer layer for the growth of YBCO on (001)Si. High-resolution transmission electron microscopy (HRTEM) and X-ray diffraction were used to determine the texture and the nature of defects, interfaces and grain boundaries. Predominant orientation relationships were found to be $[001]\text{PZT}/[001]\text{YBCO}$; $[001]\text{YBCO}/[001]\text{YSZ}$; and $[001]\text{YSZ}/[001]\text{Si}$.

INTRODUCTION

Lead-zirconium titanates (PZT) are ferroelectric materials of considerable current interest because of their potential for various applications in electrooptics as infrared sensors and optical shutters and modulators [1-4], memory devices [5,6], etc. The performance of the PZT devices depends critically on the crystal structure of PZT and characteristics of ferroelectric domains and domain boundaries in the ferroelectric material [7,8]. PZT piezoceramics have a cubic perovskite structure above the Curie temperature. Depending on the compositional ratio (Zr:Ti), with the decrease of temperature PZT transforms into tetragonal or rhombohedral ferroelectric phases, which exist together in certain compositional range around the morphotropic phase boundary [9]. Thus, the ferroelectric domain structure in PZT is formed by twins which accommodate the stress in material during the paraelectric to ferroelectric transformation. Various techniques have been used to produce PZT films [10-13]. The advantages of pulsed laser deposition include low temperature processing, novel metastable crystal structures, reproduction of target stoichiometry, and in-situ processing of multistuctures in a single chamber.

The successful fabrication of $\text{Pb}(\text{Zr}_{0.54}\text{Ti}_{0.46})\text{O}_3$ (PZT)/ $\text{YBa}_2\text{Cu}_3\text{O}_{7-\delta}$ (YBCO)/yttria stabilized zirconia (YSZ)/Si multilayer structures, using laser physical vapor deposition method was previously reported by us [14]. The PZT films showed good ferroelectric properties with dielectric constant of 800-1000. The saturation and remanent polarization were determined to be 37.81 and 24.38 $\mu\text{C}/\text{cm}^2$, respectively, whereas the coercive field was 125 kV/cm. Superconducting YBCO phase was used as an electrode for the PZT films for electrical measurements. Yttria stabilized zirconia is used as a diffusion barrier as well as a seed for the growth of YBCO films on (001) Si. The present paper presents microstructural characterization of the above system by TEM and X-ray diffraction. The orientation relationships between the PZT film and underneath layers on Si (001) are determined for correlation with ferroelectric properties.

EXPERIMENTAL

Films were deposited using a single chamber LPVD technique [15], described previously. The target holder and processing chamber were modified to obtain in-situ processing. Laser deposition from YSZ, YBCO and PZT targets was carried out in an oxygen ambient. The processing parameters for the deposition of the above layers were optimized in a

separate series of experiments [16,17]. Excimer KrF laser ($\lambda=248$ nm, $\tau=20$ ns) at 5 Hz repetition rate was used to deposit PZT at 530°C and 0.4-0.6 torr oxygen; YBCO at 650°C, 0.2 torr oxygen; and YSZ at 775°C, 9×10^{-4} torr of oxygen ambient.

X-ray diffraction studies have been carried out on RIGACU X-ray diffractometer using Cu K α radiation. Transmission electron microscopy studies have been carried out on TOPCON EM-002B, operated at 200 kV ($C_s=0.5$ mm, resolution 0.18 nm).

RESULTS AND DISCUSSION

The crystallographic nature of the multilayer system of PZT/YBCO/YSZ/Si has been studied by X-ray diffraction and transmission electron microscopy. Figure 1 represents X-ray diffraction pattern of PZT film grown on YBCO and YSZ films on (001)Si by PLD. X-ray diffraction data showed that YBCO and the tetragonal phase PZT films are c-axis oriented along (001)Si. There is no evidence for the presence of the peaks associated with the lead deficient pyrochlore phase in the X-ray diffractogram.

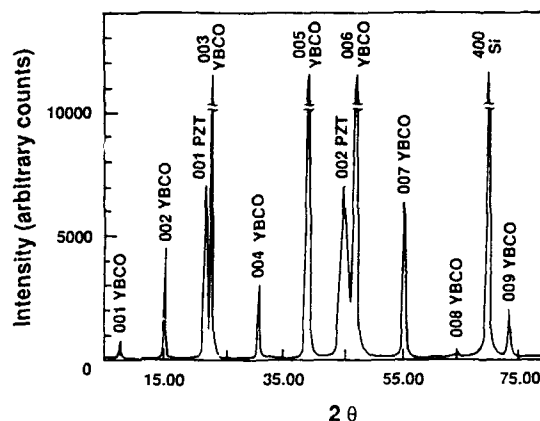


Fig.1 X-ray diffractogram of PZT/YBCO/YSZ/Si multilayer structure showing the presence of (00l) planes from YBCO and PZT films.

The narrow full width at half maximum of the diffraction lines of both PZT and YBCO films suggest growth of large grains with low density of defects. Since the characteristic feature of the PZT phase diagram is the existence of morphotropic phase boundary that separates the titanium rich tetragonal ferroelectric phase from the zirconium rich rhombohedral ferroelectric phase which exist together around $x=0.535$ in $\text{Pb}(\text{Zr}_x\text{Ti}_{1-x})\text{O}_3$ solid solution [18], the deposition conditions were optimized in separate series of experiments to achieve the tetragonal PZT ferroelectric phase only. Although the coexistence of the two ferroelectric phases as a result of internal stress relaxation process during paraelectric to ferroelectric transition was expected [19], the angular positions of PZT lines in Fig.1 correspond to the titanium rich tetragonal ferroelectric phase only.

The microstructure of this multilayer system - Figure 2, has been studied by transmission electron microscopy (TEM) in selected area electron diffraction (SAED) and high resolution modes. Ytria-stabilized zirconia layer of 0.3 μm thickness is grown on Si(001) to provide the buffer and the seed for the growth of YBCO film. The YBCO layer, 0.35 μm thick, provides a seed for PZT growth and also serves as an electrode for electrical measurements.

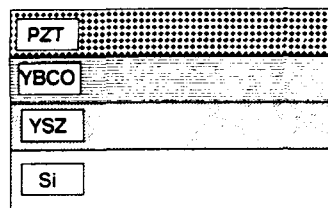


Fig.2 Schematic of PZT/YBCO/YSZ/Si multilayer.

SAED patterns and indexed spots of YSZ/Si and YBCO/YSZ interfaces, respectively, are presented on Fig 3(a-d). The relationships between Si(001) substrate and 0.3 μm thick YSZ buffer layer, showed cube-on-cube orientation relationships in local areas, with $[001]\text{YSZ} // [001]\text{Si}$, but as a whole the YSZ layer is textured. The interface between YBCO and YSZ buffer layers is smooth and unreacted with c-planes predominantly oriented parallel to (001) planes of YSZ and Si. Fig.4 (a) reveals large single crystal grains of YBCO with grain boundaries. High resolution TEM image of grain boundary between two YBCO grains in the YBCO film is shown in Figure 4(b). The c-planes in YBCO film are parallel to the YSZ/Si interface.

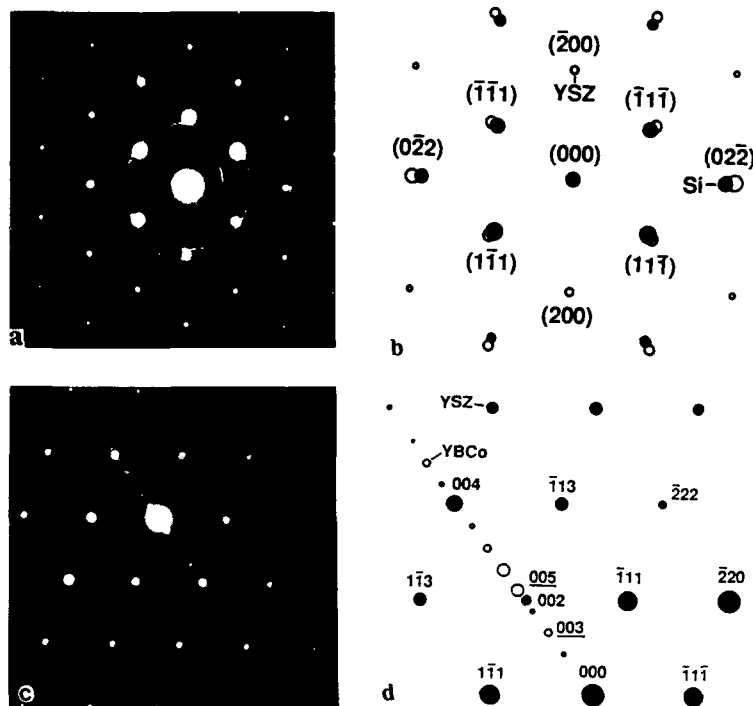


Fig.3 SAED patterns along with the indexed spots of YSZ/Si (a,b), and YBCO/YSZ (c,d) interfaces.

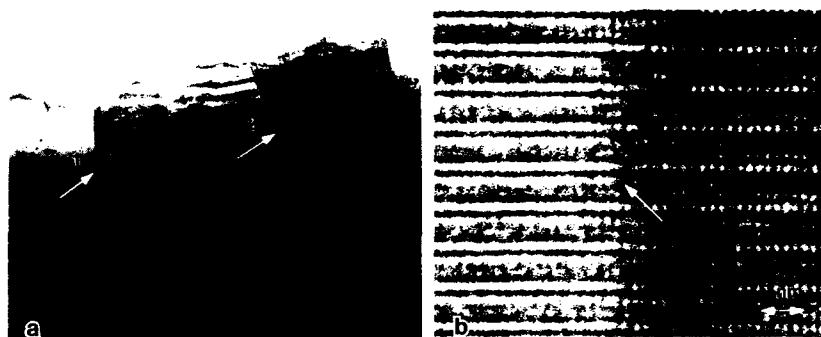


Fig.4 (a) Cross-sectional view of YBCO film with large single crystal grains with low angle (1) and high angle (2) grain boundaries pointed by arrows; (b) HRTEM image of interface between two grains.

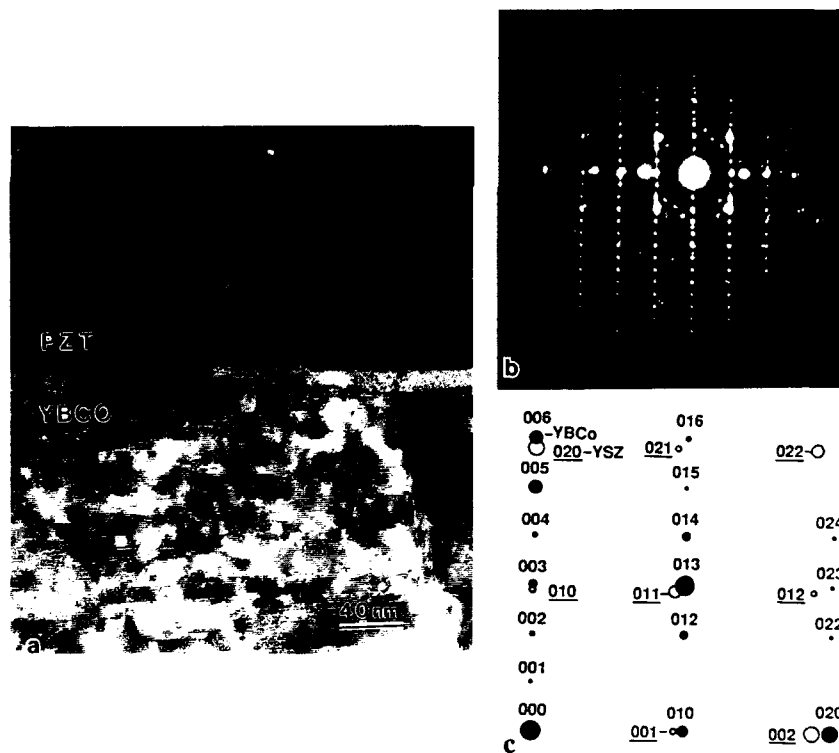


Fig.5 (a) Cross-section TEM micrograph of PZT/YBCO interface, along with the SAED (b) and indexed pattern (c).

Cross-section TEM micrograph of the interface between PZT and YBCO films is shown in Fig. 5(a). The orientation relationship of the two layers is $[100]_{\text{YBCO}}//[100]_{\text{PZT}}$. The interface is smooth with minimum or no interaction between PZT and YBCO layers. The selected area electron diffraction pattern from the interface is shown in Fig. 5(b). From the indexed pattern it is found that $(00l)$ and $(0k0)$ planes of YBCO are aligned with the $(00l)$ and $(0k0)$ planes, respectively, of PZT. The PZT film is also $[00l]$ textured. SAED pattern of the tetragonal PZT ferroelectric structure in $[100]$ and $[011]$ orientations along with the indexed spots are presented in Fig. 6(a-d). Note that there is a splitting of the spots along $[110]$, characteristic of 90° domain boundary in the tetragonal PZT phase. The angle of the tilt of the lattice planes along the domain boundary from here is less than 2° . A high resolution image in $[001]$ orientation reveals the lattice fringes of the tetragonal PZT phase as shown in Fig. 7. The region of dark diffuse contrast along the domain boundary, shown by arrow, is due to deviation of lattice plains from Bragg conditions because of a strain field existing around the domain boundaries. From that image there is no observable tilt in the lattice planes across the domain boundaries.

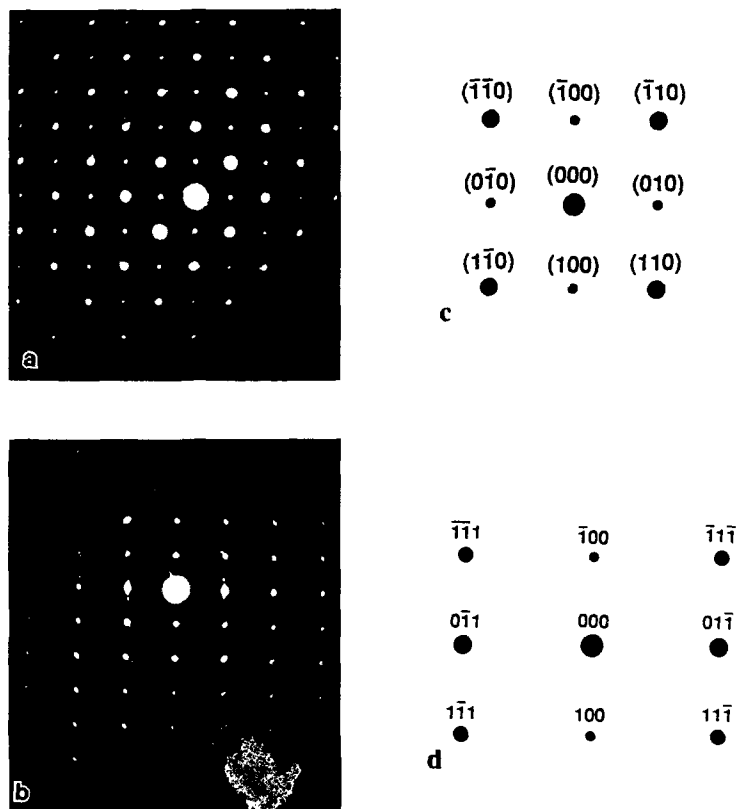


Fig. 6 SAED pattern of the tetragonal PZT ferroelectric phase in (a) $[001]$, and (b) $[011]$ orientations along with the indexed spots (c) and (d) respectively.



Fig.7 High-resolution image of the tetragonal PZT film in [010] orientation.

CONCLUSIONS

A successful deposition of the tetragonal ferroelectric PZT films on YBCO and YSZ buffer layers on Si(001) by PLD has been performed. YSZ films acted as a buffer layer and a seed for the growth of YBCO on Si(001). The utilization of the YBCO superconductor as a metallic bottom electrode for the growth of epitaxial PZT film has been shown to provide a very good (001) texture relationship with PZT. The nature of the interfaces between the films has been studied by TEM and smooth interfaces with minimal interfacial diffusion have been achieved. The predominant orientation relationships between the films and substrate were found to be $\text{PZT}[001]//\text{YBCO}[001]//\text{YSZ}[001]//\text{Si}[001]$. The properties of the above multilayer structure formed by PLD show promise for future applications of these materials.

REFERENCES

1. M. Okujama, Y. Matsui, H. Nakamo and Y. Hamakawa, *Ferroelectrics.*, **33**, 235 (1981).
2. R. Takayama, Y. Tomita, K. Iijima and I. Veda, *J. Appl. Phys.*, **61**, 411 (1987).
3. T. Kawaguchi, H. Adachi, K. Setsune and K. Wasa, *Appl. Opt.*, **23**, 2187 (1984).
4. M. Ishida, H. Matsunami and T. Tanaka, *Appl. Phys. Lett.*, **31**, 433 (1977).
5. J. F. Scott, L. Kammerdiner, M. Parris, S. Trayner, V. Ottenbacher, A. Shawabken and W. F. Olivier, *J. Appl. Phys.*, **64**, 787 (1988).
6. *Proc. Mat. Soc., Spring Meeting Symposium on Ferroelectric Thin Films*, ed. by F.R. Myers and A. Kingon (Mat. Res. Soc., Pittsburgh, PA, 1990).
7. F.K.W. Goo, R.K. Mishra and G. Thomas, *J. Appl. Phys. A*, **52**, 2940 (1981).
8. P.G. Lukuta, *J. Am. Ceram. Soc.*, **72**, 933 (1989).
9. P. Ari-Gur and L. Benguigui, *J. Phys. D: Appl. Phys.*, **8**, 1856 (1975).
10. A. Okada, *J. Appl. Phys.*, **49**, 4494 (1978).
11. M. Oikawa and K. Toda, *Appl. Phys. Lett.*, **29**, 491 (1976).
12. B.S. Kwak, E.P. Boyd and A. Erbil, *Appl. Phys. Lett.*, **53**, 1702 (1988).
13. K. Sreenivas, M. Sayer and P. Garret, *Thin Solid Films*, **172**, 251 (1989).
14. P. Tiwari, T. Zheleva, J. Narayan, *Appl. Phys. Lett.*, **63**, 30 (1993).
15. N. Biunno, J. Narayan, S. Sharan, *SPIE Proceedings*, 1190 (1989).
16. P. Tiwari, S. Kanetkar, S. Sharan, *Appl. Phys. Lett.*, **57**, 1578 (1990).
17. P. Tiwari, T. Zheleva, J. Narayan, *Proc. TMS*, Fall 1992, (accepted for publication).
18. K. Kakegawa, J. Mohri, T. Takahashi, H. Yamamura and S. Shirasaki, *Solid State Communications.*, **24**, 769 (1977).
19. T. Kala, *Phys. Stat. Sol.(a)*, **78** (1983).

PART VII

Chemical Vapor Deposition

ORGANOMETALLIC CHEMICAL VAPOR DEPOSITION OF LEAD ZIRCONATE-TITANATE THIN FILMS

M. DE KEIJSER, P.J. VAN VELDHoven, AND G.J.M. DORMANS

Philips Research Laboratories, Prof. Holstlaan 4, 5656 AA Eindhoven, The Netherlands

ABSTRACT

In this paper the growth of $\text{PbZr}_x\text{Ti}_{1-x}\text{O}_3$ on 10 cm platinized silicon wafers using the precursors tetra-ethyl-lead, titanium-tetra-isopropoxide, or titanium-tetra-tertiarybutoxide and zirconium-tetra-tertiarybutoxide will be discussed in some detail. The composition of the films as a function of growth parameters will be treated and the accompanying change in the ferroelectric properties will be discussed. For device manufacturing, the $\text{PbZr}_x\text{Ti}_{1-x}\text{O}_3$ films are subjected to a number of processing steps. Some results for partially processed wafers will be presented. Also, preliminary results of depositions on 15 cm wafers will be given.

INTRODUCTION

The integration of ferroelectric active layers in silicon technology demands for a deposition technique which is compatible with IC processing and yields lead zirconate-titanate, $\text{PbZr}_x\text{Ti}_{1-x}\text{O}_3$, films of sufficient quality to enable their application in, for example, ferroelectric non-volatile memories. Organometallic chemical vapor deposition (OMCVD) has already proven to be capable of yielding films of a high quality and, in combination with its relative ease of scaling-up, OMCVD is considered to be an important deposition technique for coming integrated ferroelectric devices.

OMCVD allows direct formation of oxidic thin films in the proper crystalline phase¹ and even epitaxial films for lattice matched substrates.²⁻⁵ It has the advantage over *in situ* vacuum techniques that a high oxygen partial pressure can be applied during the deposition. OMCVD can be easily scaled-up, both in wafer throughput as well as in wafer diameter. This makes the technique a promising candidate for deposition on an industrial scale. A characteristic of OMCVD, which is of importance in VLSI and ULSI technology, is that a very good step coverage can be achieved. With many other deposition techniques it is difficult to deposit films uniformly in, e.g., contact holes with large aspect ratios.

A real breakthrough of the use of ferroelectric thin films in electronic devices has not occurred, yet. It is expected, however, that with the availability of new and improved deposition techniques allowing for higher quality films deposited at lower temperatures, this will change. Recently, deposition techniques for ferroelectric thin films were reviewed by Roy et al.⁶

Among the ferroelectric materials the perovskite-type oxides attract the main attention with emphasis on the $\text{PbZr}_x\text{Ti}_{1-x}\text{O}_3$ system. In this paper the OMCVD of this material is described

in some detail. One should remember that other types of (ferroelectric) oxides can be deposited using OMCVD. In fact, the range of materials that can be deposited with this method is mainly limited by the availability of suitable precursors for the desired elements. The successful deposition of ferroelectric PbTiO_3 , $\text{PbZr}_x\text{Ti}_{1-x}\text{O}_3$ and $\text{Pb}_{1-3y/2}\text{La}_y(\text{Zr}_x\text{Ti}_{1-x})\text{O}_3$ has been reported.^{1,5,7-9} Also the deposition of $\text{PbZr}_x\text{Ti}_{1-x}\text{O}_3$ on 15 cm diameter wafers¹⁰ as well as on the conductive oxide RuO_x have been described.¹¹ In order to obtain sufficient control over the deposition process, knowledge of the influence of the deposition parameters on the film characteristics is essential. Using an OMCVD system which was specially designed for the deposition of oxides, deposition parameters were varied systematically and their influence on the film properties was studied.

EXPERIMENTAL

For a standard OMCVD process, no complicated hardware is necessary. But, as with many other techniques, also OMCVD systems can end-up as rather complicated pieces of equipment. Complications arise due to the fact that a number of the available precursors of essential elements of oxidic thin films have a rather low vapor pressure at room temperature. This implies that the temperature at which these precursors must be evaporated as well as the temperature of (parts of) the gas system have to be raised. In practice, this appears to be rather difficult since heating not only concerns stainless steel tubing but also components like valves and in some cases sensitive electronic equipment. *Several solutions have been used for this problem.*

In the custom-built system (Aixtron, Germany) that was used for this study, the gas lines and components for each particular precursor are heated to the desired temperature by making use of oil, which is also used to heat the bubbler in its thermostate-bath. This is done by making use of coaxial tubing; the inner tube is used for transport of the carrier gas containing the precursor. Through the outer tube flows the hot oil heating the inner tube. Uniform heating of transport lines in this set-up is relatively easily accomplished and it excludes the occurrence of hot-spots where the precursor might, prematurely, decompose. It is harder to heat components like valves. In practice this is done by mounting the components on metal blocks that are heated by the same oil that flows through the lines. The thermal isolation of the gas-system is of utmost importance to maintain the components at the desired temperature.

The set-up is equipped with a single-wafer horizontal rectangular reactor cell containing a rotating silicon carbide coated graphite susceptor supporting up to one 150 mm diameter wafer. This rectangular reactor cell is enclosed in a cylindrical tube in order to operate the system at reduced pressure. The outer cylindrical tube is continuously purged with a flow of inert gas. Heating of the susceptor is by IR lamps. The reactor cell is designed for use at pressures below 20 mbar and this pressure is obtained using an oil pump in combination with a mechanical booster. Each bubbler is equipped with a pressure control-system, enabling the bubbler pressure to be regulated independently of the carrier-gas flow. In Figure 1 a schematic of the reactor cell and the heating system of the gas lines is presented.

In order to ensure clean wafer handling and to prevent contamination of the reactor cell with e.g. moisture, the reactor outlet is placed in a N_2 flushed glove-box. Wafers are transported in and out of the reactor cell by means of a manually operated transport system. The sys-

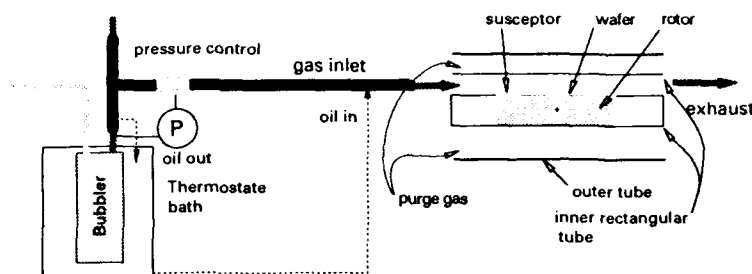


Figure 1. Schematic view of the reactor cell and the gas system. The susceptor enables a rotation of the wafer. The heating of a precursor line is done using the oil that is also used in the thermostat bath of the bubbler.

tem is completely computer-controlled enabling a reproducible run to run operation.

The substrates used were oxidized silicon wafers provided with a platinum electrode.¹² Wafers are loaded into the OMCVD deposition chamber without any pre-treatment. The system was pumped down to (for example) 6 mbar and this pressure was maintained during the run. A total gas flow of 3 standard litres per minute (SLM) consisting of 1.4 SLM oxygen and 1.6 SLM purified inert gas was used. In approximately 10 minutes the susceptor was ramped up to the desired temperature and the system was allowed to stabilize for another 5 minutes. The carrier gas flows through the bubblers and the pressures of the bubblers were set to the desired value. Two minutes before the deposition was started the bubblers containing the precursors were opened and switched to a vent line. For all elements commercially available precursors were used (Billiton Precursors, 99.999%); tetra-ethyl-lead, titanium-tetra-isopropoxide, or titanium-tetra-tertiarybutoxide and zirconium-tetra-tertiarybutoxide. The precursor partial pressures in the reactor cell are controlled by manipulating the pressure and temperatures of the bubblers as well as the carrier gas flow rates. Bubbler temperatures were in the range of 40-90°C and bubbler pressures were regulated between 100-300 mbar. Depositions were started by switching the precursors from vent to the reactor cell. The deposition time was typically 30 minutes and in this period a film thickness of 0.2-0.4 µm was obtained. Switching the precursors back to the vent line ends the deposition. The heater is switched off and the susceptor cools down to 400°C in about 20 minutes. The pressure is brought to one atmosphere and when the wafer has cooled down to room temperature it is taken out of the reactor cell.

Film morphology was examined using Nomarski optical microscopy and scanning electron microscopy (SEM). The chemical composition of the films was determined using x-ray fluorescence (XRF). This technique, combined with a dedicated thin film analysis software package, enabled the determination of the metals ratios within 2% accuracy. Uniformity both in composition and in thickness was estimated by XRF measurements at several positions over the wafer. The crystallinity of the $\text{PbZr}_x\text{Ti}_{1-x}\text{O}_3$ films was examined with x-ray diffraction (XRD) using $\text{CuK}\alpha$ radiation.

To electrically characterize the wafers three ways of processing were applied. The first is simply by sputtering on top gold contacts through a shadow mask with several well defined electrode areas. In this configuration the bottom electrode is shared by all the capacitors on the wafer. For convenience this way of processing the wafers will be denoted as Method A. In Method B a top blanket platinum layer is deposited and subsequently structured into well

defined electrodes with areas ranging from 9-50.000 μm^2 . Also the $\text{PbZr}_x\text{Ti}_{1-x}\text{O}_3$ and the platinum bottom electrode are structured. This way of processing allows a thorough electrical characterization, including fatigue and fast switching measurements. The third Method C, is an extension of Method B including an insulation and a metallization of the individual capacitors.

Small signal electrical properties of the capacitors are measured using an impedance analyzer at 100 kHz and an effective measuring voltage of 0.1 V. The ferroelectric properties are measured using a Sawyer-Tower circuit at 1 kHz.

In this work the chemical composition of the films as well as the uniformity in thickness and composition was studied as a function of the deposition parameters. Then the ferroelectric properties were studied as a function of the composition of the films. Preliminary results of the deposition over 150 mm diameter wafers will be presented.

RESULTS

The $\text{PbZr}_x\text{Ti}_{1-x}\text{O}_3$ films deposited at 700°C over a 10 cm platinized silicon wafers are shiny and have a homogeneous interference color over the wafer indicating that the film thickness is very uniform. Only very near the edge of the wafer (± 2 mm) a change in the interference color is observed. A Nomarski image taken with a magnification of 200 (not shown here) reveals that the surface morphology is slightly rough. This is caused by strong crystallization of the $\text{PbZr}_x\text{Ti}_{1-x}\text{O}_3$ film on the polycrystalline platinum electrode at the deposition temperature of 700°C. The SEM image with a magnification of 40.000 is presented in Figure 2. It shows the crystallites in more detail. On this microscopic level the film appears to have a rather rough surface morphology with well crystallized $\text{PbZr}_x\text{Ti}_{1-x}\text{O}_3$ grains in the order of 0.2 μm diameter.

The crystallinity of the films is confirmed by XRD measurements. In Figure 3 the XRD pattern of a $\text{PbZr}_x\text{Ti}_{1-x}\text{O}_3$ film with $x=0.6$ deposited at 700°C is presented showing high intensities for the (00 l) reflections. In this pattern no reflections due to the presence of other phases are observed.



Figure 2. Scanning electron microscopy image of a $\text{PbZr}_{0.6}\text{Ti}_{0.4}\text{O}_3$ film deposited at 700°C.

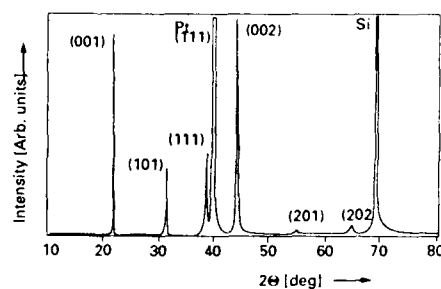


Figure 3. X-ray diffraction pattern of a $\text{PbZr}_x\text{Ti}_{1-x}\text{O}_3$ film with $x=0.60$ deposited at 700°C. No other phases are detected and the film shows a preferential (00 l) orientation.

Uniformity

For device fabrication it is necessary that the deposited film is very uniform over the wafer, both in composition and in thickness. Therefore, the deposition process was optimized with respect to compositional and thickness uniformity. In order to facilitate the treatment of the composition of the films, the following terms are introduced. In analogy with the general chemical formula for a perovskite-type compound, ABO_3 , the metals ratio is denoted by A/B and the ratio of the corresponding precursors in the gas phase by $(A/B)_g$. For $PbZr_xTi_{1-x}O_3$ this ratio corresponds to $Pb/(Zr+Ti)$. The ratio $Zr/(Zr+Ti)$ is denoted as x with the corresponding gas-phase ratio x_g .

In Figure 4 the A/B and x are plotted for films deposited at 700°C at three deposition pressures as a function of the position on 10 cm wafers. $(A/B)_g$ and x_g were kept constant at 0.45 and 0.65 respectively. The deposition pressure has an influence on both the value and the uniformity of A/B and x . An increase in the deposition pressure results in a decrease in both A/B and x . This decrease is attributed to depletion of the precursors in the gas phase; their average residence time in the high temperature region of the reactor cell increases when going to higher pressure (at a constant gas flux). This depletion can be suppressed most effectively by reducing this residence time by lowering the reactor pressure. At a pressure of 4 mbar stoichiometric films with a good uniformity over the 10 cm wafer can be obtained ($\pm 2\%$).

Also included in Figure 4 are preliminary results obtained on 15 cm wafers. The uniformity on these wafers is as good as that on 10 cm wafers.

Composition

The control of the composition is a matter of concern in the case of lead-based (ferroelectric) thin films. This is due to the relatively high vapor pressure of lead and lead oxide resulting in a relatively fast evaporation of these compounds from the growing surface. Many thin

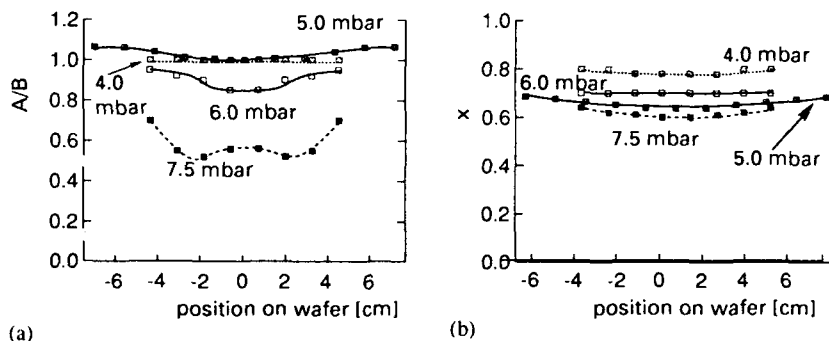


Figure 4. Composition of $PbZr_xTi_{1-x}O_3$ films deposited at 700°C using an $(A/B)_g$ of 0.45 and a x_g of 0.65 as a function of the position on 10 cm wafers for three reactor pressures. At a reactor pressure of 4 mbar uniform films are obtained both in A/B (a) and in x (b).

Preliminary results on 15 cm wafers are included in (a) and (b)

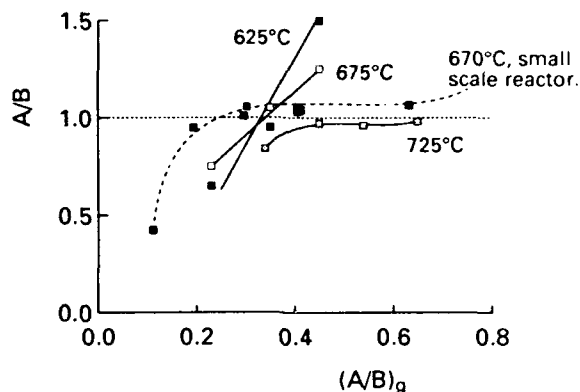


Figure 5. The composition of the film, given as A/B , as a function of the composition of the gas phase, $(A/B)_g$, at three temperatures.

films techniques yield $\text{PbZr}_x\text{Ti}_{1-x}\text{O}_3$ thin films only if compensation for lead-loss is provided. In the case of OMCVD the lead-loss can be compensated for by adjusting the lead precursor partial pressure. The high vapor pressures of both lead and lead oxide turn out to be a benefit as the composition of the film is not very sensitive to variations in both the deposition temperature and the precursor partial pressures within a certain range.^{5,13} In Figure 5 A/B is plotted against $(A/B)_g$ for $\text{PbZr}_x\text{Ti}_{1-x}\text{O}_3$ films deposited at three temperatures. Essentially the same behavior as has been observed before in a small scale vertical reactor (dashed curve) is seen.¹³ At the lowest temperature the composition of the solid is a reflection of the gas-phase composition. When the temperature is increased the A/B -ratio tends to become unity, i.e. stoichiometric $\text{PbZr}_x\text{Ti}_{1-x}\text{O}_3$ forms independent of $(A/B)_g$. A difference with results reported earlier,^{5,13} is that in this OMCVD system the temperatures at which the stoichiometric compound forms is higher; 725°C versus 670°C. This may indicate that the actual substrate temperature in the present OMCVD system is typically about 50°C lower than in the systems used in the earlier work. Also the geometries of the deposition cells may play a role (vertical versus the present horizontal reactor cell).

In the present system the composition of the films is insensitive for changes in gas phase composition, within a certain range, at a deposition temperature of 725°C and for $(A/B)_g > 0.45$. The occurrence of this process window is explained by the two competitive processes that take place on the growing surface. The first is the reaction of adsorbed PbO with TiO_2 and ZrO_2 to form $\text{PbZr}_x\text{Ti}_{1-x}\text{O}_3$. This reaction is hampered by the second process taking place on the surface: the desorption of PbO . If it is assumed that the rate of formation of $\text{PbZr}_x\text{Ti}_{1-x}\text{O}_3$ is much faster than the desorption rate of PbO , a stoichiometric $\text{PbZr}_x\text{Ti}_{1-x}\text{O}_3$ film forms and the excess PbO desorbs from the surface. At deposition temperatures below 700°C the desorption rate of PbO obviously is too slow and, unless $(A/B)_g$ is chosen accurately, off-stoichiometric films are formed.

In Figure 6 the value for x as measured with XRF is plotted against the gas phase ratio, x_g . The same non-ideal behavior as reported before¹³ is observed here. Such behavior can be described by the following equation where K is the so-called non-ideality factor.

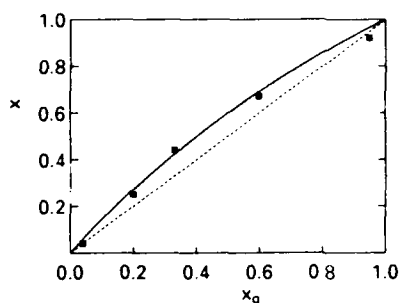


Figure 6. Film composition x versus x_g for $\text{PbZr}_x\text{Ti}_{1-x}\text{O}_3$ films deposited at 700°C using an $(\text{A/B})_g$ of 0.45. A non-ideal behavior is observed.

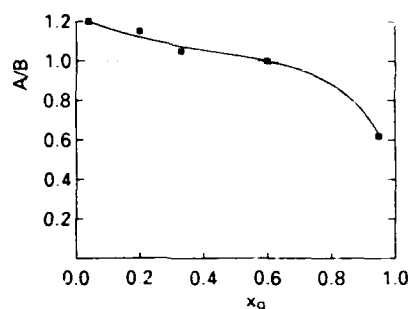


Figure 7. Film composition, A/B , for films deposited at 700°C with an $(\text{A/B})_g$ of 0.45 as a function of x_g . An increase in x_g causes a reduction in A/B .

$$\frac{x}{1-x} = K \frac{x_g}{1-x_g}$$

(1)

The value for K is calculated to be 1.49. The cause of this effect is probably the difference in adsorption efficiency between the zirconium and titanium precursor. Once this curve is known, one can deduce the necessary x_g for a certain value of x .

It turns out, however, that if x_g changes, also $(\text{A/B})_g$ has to be adjusted. This effect is illustrated in Figure 7 where, using at 700°C a fixed value for $(\text{A/B})_g$, A/B is plotted against x_g . It appears that when x_g increases, A/B decreases, i.e. the films deposited with a high zirconium content are found to be lead deficient when deposited at a fixed value of 0.45 for $(\text{A/B})_g$. This means that the necessary value for $(\text{A/B})_g$ moves out of the process window as given in Figure 5. This behavior is explained by the fact that the rate of formation of PbZrO_3 is slower than that of PbTiO_3 . Therefore the average residence time of the PbO on the surface is longer in the case of zirconium rich films and therefore also the desorption of PbO is larger in this case. This effect is compensated for by supplying a larger amount of PbO . In order to obtain stoichiometric films, the $(\text{A/B})_g$ has to be increased for higher values of x_g . So in order to deposit stoichiometric $\text{PbZr}_x\text{Ti}_{1-x}\text{O}_3$ with a certain value for x , one has to determine what value for x_g is necessary to obtain this, and then to adjust $(\text{A/B})_g$.

FERROELECTRIC PROPERTIES

Using optimized conditions, a set of stoichiometric films were deposited in which the x was varied. Wafers were processed according to the Methods A, B and C in order to determine the influence of processing on the ferroelectric performance of the films.

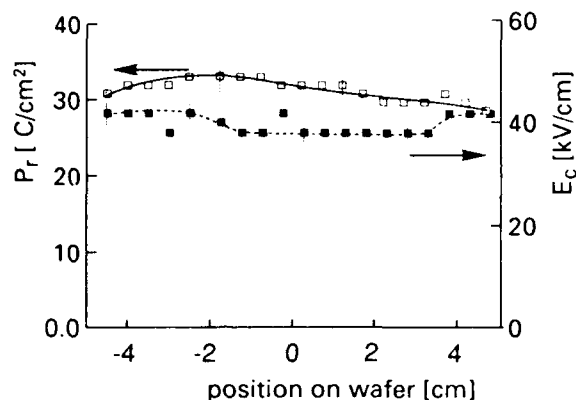


Figure 8. Values of the remanent polarization, P_r , and of the coercive field-strength E_c , of a representative $\text{PbZr}_x\text{Ti}_{1-x}\text{O}_3$ ($x=0.71$) film processed according to Method B, plotted versus the position on the 10 cm wafer.

Uniformity

In Figure 8 the values of the remanent polarization, P_r , and of the coercive field-strength, E_c , of a representative $\text{PbZr}_x\text{Ti}_{1-x}\text{O}_3$ ($x=0.71$) film processed according to Method B are plotted versus the position on the 10 cm wafer. The value for P_r is around $30 \mu\text{C}/\text{cm}^2$ and E_c is about 40 kV/cm. Within experimental error, the values for both P_r and E_c are constant over the 10 cm wafer. This is in line with the observed uniformity in composition and thickness of the $\text{PbZr}_x\text{Ti}_{1-x}\text{O}_3$ film implying that processing according to Method B does not cause a large inhomogeneity.

For the results presented next, the values for the (ferro)electric properties are averages of about 40 measurements taken over the full diameter of a 10 cm wafer when the wafers were processed according to Method B. In the case of Method A the values are averages over a few measurements.

Influence of the composition

Figure 9 presents the dependence of P_r and E_c on x . The value for P_r is more or less independent of x but shows a sudden drop at a composition near the morphotropic phase boundary ($x=0.53$). This behavior is observed for Methods A and B. A comparable behavior has been observed before.¹³

The value for E_c clearly decreases with increasing x . This observation is in line with literature data,^{8,13} and may be due to the increased number of poling directions present on material with a composition on the rhombohedral side of the morphotropic phase boundary.¹⁴ The

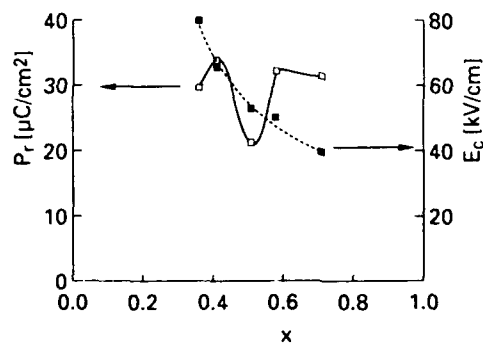


Figure 9. Dependency of P_r and E_c on the composition x of $\text{PbZr}_x\text{Ti}_{1-x}\text{O}_3$ films. The thickness of the films was around 200 nm.

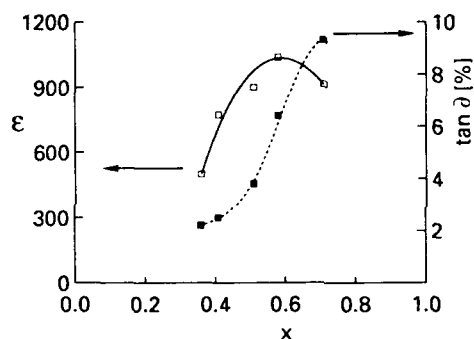


Figure 10. The dielectric constant, ϵ , and loss factor, $\tan \delta$, versus the composition x of $\text{PbZr}_x\text{Ti}_{1-x}\text{O}_3$ thin films. $A \approx 50,000 \mu\text{m}^2$, $f = 100 \text{ kHz}$.

dielectric constant, ϵ , and dissipation factor, $\tan \delta$, as a function of the composition of the films are plotted in Figure 10. The dielectric constant shows a maximum around a composition near the morphotropic phase boundary comparable to what has been reported for ceramic $\text{PbZr}_x\text{Ti}_{1-x}\text{O}_3$, although the maximum is less pronounced than for the ceramics.¹⁵

The dissipation factor shows an increase with x and is somewhat higher than reported for ceramic $\text{PbZr}_x\text{Ti}_{1-x}\text{O}_3$. Tentatively, this effect may be caused by a decrease in average grain size when going to higher values for x .

Influence of processing

For the fabrication of a device, the wafer, including the ferroelectric thin film, has to undergo a number of processing steps, like the deposition and etching of insulation and metal layers. Such a processing may have a pronounced effect on the performance of ferroelectric thin

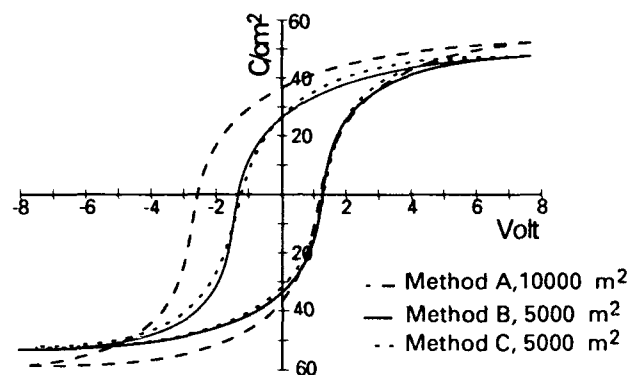


Figure 11. Hysteresis curves of films that were processed according to Methods A-C. It appears that the hysteresis curves of the three wafers are almost identical indicating that the processing has a negligible influence on these curves. Thickness = 200 nm, $x = 0.60$.

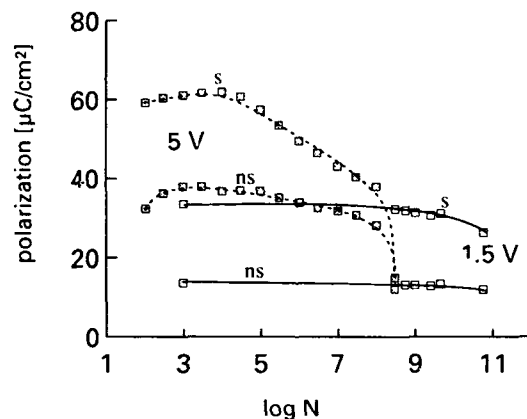


Figure 12. Endurance for a capacitor measured at two switching voltages. Thickness = 200 nm, $x = 0.60$.

film. Here some preliminary results are presented for $\text{PbZr}_x\text{Ti}_{1-x}\text{O}_3$ thin films that were processed into test devices.

In Figure 11 the hysteresis curves are presented of films that were processed according to the mentioned Methods A-C. It appears that the hysteresis curves of the three wafers are almost identical indicating that the processing has a negligible influence on the ferroelectric properties. Method A yields a hysteresis loop with a strong asymmetry and a higher value for the E_c of the capacitor. This effect is attributed to a rather poor quality of the sputtered gold top-electrode contact.

The endurance is a point of major importance for non-volatile memory applications. It is

determined by the degradation of ferroelectric properties caused by polarization reversals. This degradation, or fatigue, is a property of the complete capacitor structure, i.e. it is determined by the ferroelectric thin film properties, the electrodes and test conditions. It was demonstrated that for films deposited using OMCVD the difference in switched charge between a switching and a non-switching pulse still was sufficiently large after 10^{11} switching cycles.⁹ The present set of films, all deposited at the same conditions and processed in the three mentioned ways (but not giving the best endurance), show larger values for the switched charge but also a faster fatigue. The fatigue was measured using bipolar pulses of 100 ns width for Method B and C. At a switching amplitude of 5 V the films show a comparable degradation, starting at 10^7 cycles, indicating that processing does not influence the endurance. In Figure 2 the influence of pulse amplitude on the endurance for Method B is presented. Clearly, the use of a lower switching voltage leads to a better endurance. This effect has been observed before.¹⁶

CONCLUSION

The deposition of $\text{PbZr}_x\text{Ti}_{1-x}\text{O}_3$ using a dedicated OMCVD system is described. Uniform films over 15 cm wafers can be deposited, both in thickness and in composition, within an interval of optimized process conditions. On a microscopic level the films have a rather rough morphology. It appears that processing of the films has a negligible effect on the hysteresis loops of the films. The fatigue behavior is almost the same for the three ways of processing. Under optimal conditions the endurance exceeds 10^{11} cycles.

ACKNOWLEDGEMENT

The authors wish to thank P.K. Larsen and D.J. Taylor for the electrical characterization and stimulating discussions and M.J.E. Ulenaers for technical support.

REFERENCES

1. M. Okada and K. Tominaga, *J. Appl. Phys.* **71**, 1955 (1992).
2. T. Sugimoto, M. Yoshida, K. Yamaguchi, K. Sugawara, Y. Shiohara, and S. Tanaka, *Appl. Phys. Lett.* **57**, 928 (1990).
3. H. Funakubo, K. Imashita, N. Kieda, and N. Mizutani, *J. Ceram. Soc. Jpn.* **99**, 248 (1991).
4. M. de Keijser, G.J.M. Dormans, J.F.M. Cillessen, D.M. de Leeuw, and H.W. Zandbergen, *Appl. Phys. Lett.* **58**, 2636 (1991).
5. G.J.M. Dormans, P.J. van Veldhoven, and M. de Keijser, *J. Crystal Growth* **123**, 537 (1992).
6. R.A. Roy, K.F. Etzold, and J.J. Cuomo in *Ferroelectric Thin Films*, edited by E.R. Myers and A.I.

- Kingon (Mat. Res. Soc. Symp. Proc. **200**, Pittsburg, PA, 1990) pp. 141-152.
7. G.J.M. Dormans, M. de Keijser, and P.K. Larsen, *Integrated Ferroelectrics* **2**, 297 (1992).
 8. Y. Sakashita, T. Ono, H. Segawa, K. Tominaga, and M. Okada, *J. Appl. Phys.* **69**, 8352 (1991).
 9. G.J.M. Dormans, M. de Keijser, and P.J. van Veldhoven in *Ferroelectric Thin Films II* edited by A.I. Kingon, E.R. Myers, and B. Tuttle (Mat. Res. Soc. Proc. **243**, Pittsburg, PA, 1992) pp. 203-212.
 10. K. Kashiwara, H. Itoh, K. Tsukamoto, and Y. Akasaka, *Extended Abstracts of the 1991 International Conference on Solid State Devices and Materials*, Yokohama, 192 (1991).
 11. C.H. Peng, and S.B. Desu, *Appl. Phys. Lett.* **61**, 16 (1992).
 12. G.A.C.M. Spierings, J.B.A. van Zon, M. Klee, and P.K. Larsen, presented at the 4th International Symposium on Integrated Ferroelectrics, Monterey (1992). *Integrated Ferroelectrics* (in press).
 13. M. de Keijser, G.J.M. Dormans, P.J. van Veldhoven, and P.K. Larsen, presented at the 4th International Symposium on Integrated Ferroelectrics, Monterey (1992). *Integrated Ferroelectrics* (in press).
 14. G.H. Heartling, *Am. Ceram. Soc. Bull.* **43**, 875 (1964).
 15. B. Jaffe, R.S. Roth, and S. Marzullo, *J. Res. Nat. Bur. Stand.* **55** 239 (1955).
 16. P.K. Larsen, R. Cuppens, and G.A.C.M. Spierings, *Ferroelectrics* **128** 265 (1992).

MOCVD Growth and Structure of PbTiO₃ Thin Films

Y. Gao, G. Bai*, K. L. Merkle*, H. L. M. Chang*, and D. J. Lam*

Department of Materials and Metallurgical Engineering, New Mexico Institute of Mining and Technology, Socorro, NM 87801

* Materials Science Division, Argonne National Laboratory, Argonne, IL 60439

ABSTRACT

PbTiO₃ thin films grown on (001)MgO and (110)MgO by MOCVD have been characterized by x-ray diffraction and transmission electron microscopy. The PbTiO₃ films deposited on (001)MgO under the optimum conditions always show a bi-layer structure. The top layer of the films near the free surface is c-axis oriented with the orientation relationship (001)[100]PbTiO₃||((001)[100]MgO. The bottom layer of the films near the substrate is a-axis oriented with (100)[001]PbTiO₃||((001)[100]MgO. 90° domains were observed, but only in the c-axis oriented layers. The thickness of the a-axis oriented layers near the substrate decreases with decreasing the cooling rate. PbTiO₃ films deposited on (110) MgO, however, are single-layer, epitaxial films with (101)[001]PbTiO₃||((110)[001]MgO.

1. INTRODUCTION

Recently, technological applications of ferroelectric oxides in electronic and optical devices have drawn attention to study ferroelectric thin films. Ferroelectric oxides exhibit spontaneous electrical polarization, which can be switched from plus to minus by applying an external electric field. Switching between these two polarization states in ferroelectric thin films can be directly used for nonvolatile memories. In addition to the polarization switching of ferroelectric oxides, properties of interest include high dielectric constant, pyroelectricity, piezoelectricity, and electro-optic effects. These unique properties of ferroelectric oxides give them great potential for future applications in electronic and optical devices [1].

MOCVD is an economical and high-production-rate process, and can provide flexible control of deposition rate and film composition by adjusting the source temperature and carrier gas flow rate. In the last few years, ferroelectric thin films have been successfully prepared on various substrates by the MOCVD technique [2-6]. Epitaxial thin films on SrTiO₃ and LaAlO₃ were also reported for a number of ferroelectric oxides such as PbTiO₃ [2], Pb(Zr,Ti)O₃ [7], and BaTiO₃ [4, 6]. However, there is a lack of systematic study to correlate the processing parameters with the microstructure, which is essential for a basic understanding of the MOCVD growth of the ferroelectric thin films. Recently, such a study has been carried out for PbTiO₃ films grown on MgO by the present authors [8]. The most important result of that investigation was that the PbTiO₃ thin films on (001) MgO consist of two layers due to the substrate effect on the phase transformation. The one near the free surface is c-axis oriented with 90° domain structure, and the other near the substrate interface is a-axis oriented without the 90° domain structure. However, single-layer epitaxial films of PbTiO₃ were found on (001) SrTiO₃ [2]. Clearly, the final microstructure of epitaxial PbTiO₃ films will strongly depend on their substrates as well as other processing parameters. The purpose of this paper is to report the results of an extended study of the PbTiO₃ thin films grown on MgO. Primary emphasis is focused on the effects of the substrate orientation and cooling rate from the growth temperature to room temperature on the bi-layer structure.

2. EXPERIMENTAL

Thin films of PbTiO₃ were prepared in a horizontal, low-pressure, cold-wall reactor with a resistive substrate heater. Commercial extra-pure lead β-diketonate (Pb(thd)₄) and titanium isopropoxide (Ti(OC₃H₇)₄) from STREM Chemicals were used as the metal-organic precursors. The mixture of the precursor vapor was introduced into the reactor by high-purity nitrogen as a carrier gas. High-purity oxygen gas in a separate gas line was used as an oxidant. The flow rates of the carrier gas and evaporator temperature for each of the precursor chambers were controlled individually to adjust the film composition. Deposition parameters were used as follows: reactor chamber pressure, 10 torr; oxygen flow rate, 400 sccm; carrier gas flow rate for Pb, 100 sccm;

carrier gas flow rate for Ti, 10-25 sccm; Pb metal-organic source temperature, 116 °C-126 °C; Ti metal-organic source temperature, 32 °C. The PbTiO_3 thin films were grown on (001) MgO and (110) MgO at temperatures ranging from 550 °C to 700 °C.

The film structure and crystallinity were characterized by x-ray diffraction technique. The microstructure of the thin films was investigated by transmission electron microscopy (TEM) using both plan-view and cross-sectional specimens. TEM plan-view specimens were prepared by mechanical thinning, dimpling, and argon-ion milling at liquid-nitrogen temperature from the MgO side. TEM cross-sectional specimens were prepared using a standard technique as described in detail elsewhere [8].

3. RESULTS AND DISCUSSION

PbTiO_3 on (001) MgO

Fast cooling - When PbTiO_3 films deposited on (001) MgO at temperatures above 500 °C under optimum growth conditions were fast cooled down to room temperature by turning off the heater, x-ray diffraction spectra of the PbTiO_3 films show only two orientations, (001) and (100), parallel to the substrate surface. A representative x-ray diffraction spectrum is shown in Fig. 1(a). X-ray ϕ scans of appropriate crystallographic planes of the films and the substrates indicate that the films are likely to be single crystalline with two oriented regions: 1) the c-axis oriented region - (001)[100] PbTiO_3 || (001)[100]MgO; and 2) the a-axis oriented region - (100)[001] PbTiO_3 || (001)[100]MgO. The rocking curves (i.e. θ scan) of the (100) and (001) planes were performed to show the quality of each layer in the growth direction, for the a-axis and the c-axis oriented regions, respectively. The results show that the rocking curves of the (100) plane always consist of three peaks about 2° apart, while the rocking curves of the (001) plane show a single peak. A representative of the rocking curves is shown in Fig. 1(b) for the

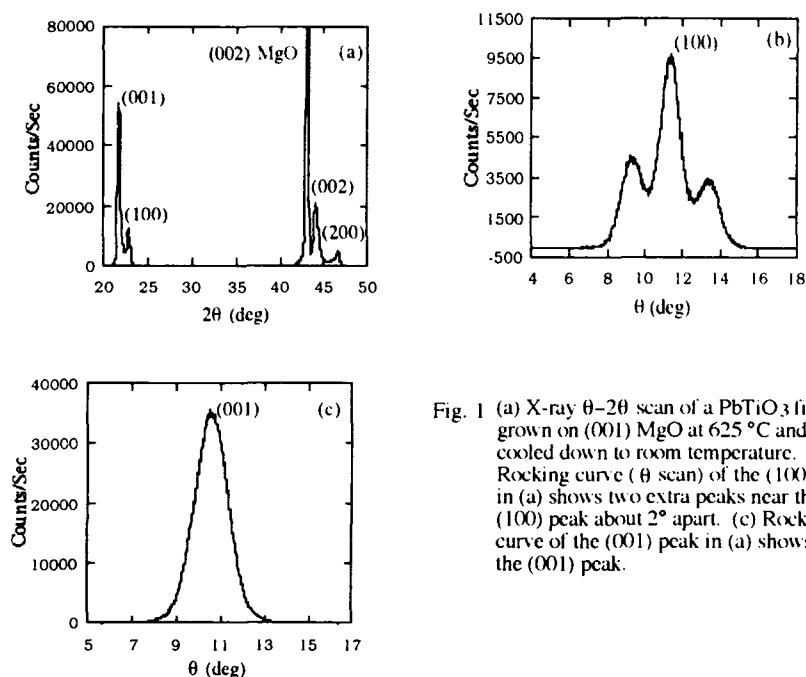


Fig. 1 (a) X-ray θ - 2θ scan of a PbTiO_3 film grown on (001) MgO at 625 °C and fast cooled down to room temperature. (b) Rocking curve (θ scan) of the (100) peak in (a) shows two extra peaks near the (100) peak about 2° apart. (c) Rocking curve of the (001) peak in (a) shows only the (001) peak.

(100) plane and in Fig. 1(c) for the (001) plane, respectively. The two extra peaks in Fig. 1(b) could come from 90° domains in the c-axis oriented region. The 90° domain walls in PbTiO_3 are the $\{101\}$ or $\{011\}$ twin boundaries, which were formed in the films through the phase transformation during cooling. Because of the slight difference between lattice constant a (0.391 nm) and c (0.409 nm), the a axis in the 90° domains of the c-axis oriented region will not be exactly parallel to the c axis in the matrix, but tilted slightly by an angle of about 2.6° calculated from the geometry of the domain structure. The calculated value is in agreement with the value measured from Fig. 1(b). For the same reason, the 90° domains in the a-axis oriented region of the film should be formed during cooling. Therefore, one should also see the two extra peaks in the (001) rocking curve of Fig. 1(c) as in the (100) rocking curve of Fig. 1(b). However, we did not see any trace of the extra peaks in the (001) rocking curves for all films. It is not clear from the x-ray diffraction analyses why the 90° domains were formed in the c-axis oriented region, but not in the a-axis oriented region due to a lack of information about the microstructure. Thus, the x-ray diffraction analyses have been supplemented by TEM studies.

Fig. 2(a) shows a TEM micrograph of a cross-sectional specimen for the film in Fig. 1. A bi-layer structure of the PbTiO_3 thin film is evident from the micrograph. Moreover, the 90° domains (or twins) are clearly observed in the top layer near the free surface, while the domains are not observed in the bottom layer near the substrate. A selected-area diffraction pattern (SADP) in Fig. 2(b) taken from a small area covering the bottom layer and the substrate shows that the bottom layer is the a-axis oriented region. The epitaxial orientation relationship between the a-axis oriented region and the substrate is $(100)[001]\text{PbTiO}_3\parallel(001)[100]\text{MgO}$. A SADP taken from an area covering both layers and the substrate is shown in Fig. 2(c), indicating that the top layer is the c-axis oriented region. Note that the diffraction spots from the bottom layer did not show up due to their weak intensity. Therefore, the epitaxial orientation relationship between the c-axis oriented region and the substrate is $(001)[100]\text{PbTiO}_3\parallel(001)[100]\text{MgO}$. The two sets of the 90° domains observed in Fig. 2(a) are the (101) and the $(\bar{1}01)$ domains inclined by about 45° . The tilt angle of the (010) orientations in the 90° domains from the (001) orientation in the matrix was measured from Fig. 2(c) to be about 2.8° , which is in agreement with the scale of 2° measured from the rocking curves and 2.6° calculated from the film lattice parameters. Note that a slightly large value of the tilt angle measured from the diffraction pattern could be due to the stress relaxation in the thin TEM specimen. It is now clear that the thin films consist of a bi-layer structure; the one near the free surface is c-axis oriented with the twins, and the other near the substrate is a-axis oriented without the twins. If a rocking scan of the (100) plane is performed, one will expect to see three peaks of about 2° apart, one from the bottom layer and two from the top layer. However, only one peak will be observed for a (001) rocking scan. This is consistent with the x-ray diffraction results discussed earlier. The formation of the bi-layer structure could be due to the competition between the phase transition and the substrate constraints. The mechanisms have been discussed in some detail elsewhere [8].

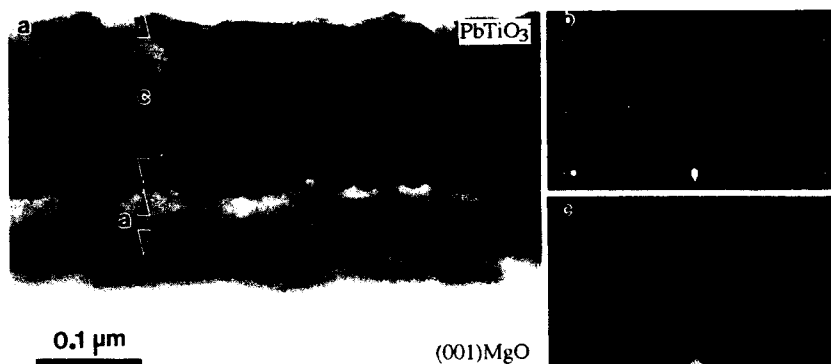


Fig. 2 (a) Cross-sectional TEM micrograph of the film in Fig. 1 shows a bi-layer structure. (b) SADP taken from interface region shows that the bottom layer is a-axis oriented. (c) SADP from a large area shows that the top layer near the free surface is c-axis oriented.

Slow cooling - When PbTiO_3 films were slowly cooled down to room temperature at a cooling rate of 20°C/hr after deposition, x-ray diffraction spectra of these PbTiO_3 films are similar to those of the fast-cooled films. The θ - 2θ scans show only (001) and (100) orientations; the (100) rocking curves show three peaks; and the (001) rocking curves show only one peak. However, the intensity of the (100) plane is relatively lower compared to the intensity in Fig. 1(a), indicating that the thickness of the a-axis oriented layer decreases with reducing the cooling rate.

A cross-sectional TEM micrograph of the slow-cooled thin films is shown in Fig. 3(a). The bi-layer structure is not visible in the micrograph. An electron diffraction pattern taken from the interface area shows that the film was grown epitaxially on the substrate with the c axis as the growth direction. The 90° domains are clearly observed in the film, and the domain boundaries appear to be continuous across the film thickness. In addition, some strain contrast can be seen near the interface, which could be associated with a thin, a-axis oriented layer. Such a thin layer near the interface has been observed using high resolution electron microscopy (HREM). A HREM image of the interfacial area is shown in Fig. 3(b). After measuring the lattice spacing of the thin layer, it was found that this layer is the a-axis oriented layer. The interface appears rough, which could be due to the rough surface of the MgO substrate. Large lattice distortion is likely associated with the lattice mismatch across the interface since no localized misfit dislocation has been observed at the interface.

It is found that the 90° domain size is similar in the two types of the thin films. Most of the domain boundary plane appears abrupt, but the segments near the ends of the domains consist of a number of small steps. Fig. 4(a) shows a HREM image of a flat segment of a (011) domain boundary near the free surface. It can be seen that this segment of the boundary is abrupt and structurally coherent. The boundary plane can be recognized by viewing the image under a shallow angle. The coherent lattice planes slightly, but abruptly, change their directions as they cross the boundary. The tilt of lattice planes across the domain boundary is found to be about 3.2° along [010] or [001] directions in Fig. 4(a). Note that the tilt angle across the boundary will be 6.4° if one measures it along the [011] direction of the matrix. The corresponding diffraction pattern in Fig. 4(b) shows that the tilt due to the twinning on the (011) plane of the tetragonal structure is about 3.3° , which is consistent with the value measured from the HREM image in Fig. 4(a). This value is close to the calculated value (3.3°) for PbTiO_3 single crystal, which indicates that the c/a ratio of the slow-cooled films is close to 1.06. In other words, the structure of the slow-cooled films is much closer to the bulk structure than that of the fast-cooled films. This can be understood if the large lattice stress due to the phase transformation is reduced during the slow cooling process.

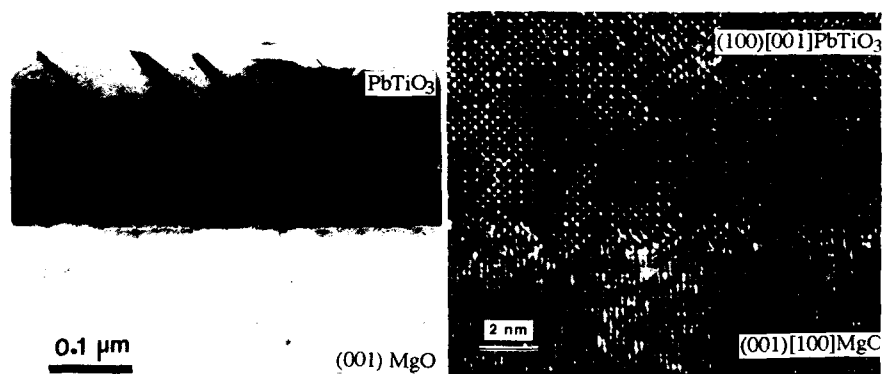


Fig. 3 (a) Cross-sectional TEM image of a film grown on (001)MgO slowly cooled down to room temperature. (b) HREM image shows that a thin layer near the interface is a-axis oriented.

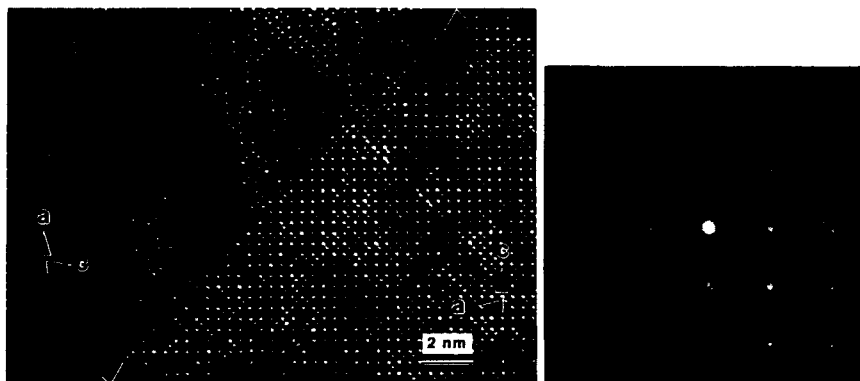


Fig. 4 (a) HREM image of a flat segment of the 90° domain boundaries near the free surface in the slow-cooled films. (b) SADP shows that the tilt angle across the boundary viewed along $\langle 100 \rangle$ is 3.2° , indicating that the ratio of c/a is about 1.06.

PbTiO₃ on (110) MgO

When PbTiO₃ films were grown on (110) MgO under optimum growth conditions, and then slowly cooled down to room temperature at a cooling rate of 20°C/hr , it was interesting to note that only two diffraction peaks in the θ - 2θ scans were observed from the films at $2\theta=31.56^\circ$ and $2\theta=32.2^\circ$, as shown in Fig. 5(a). The two peaks are (101) and (110), respectively. It appears that the two orientations could also be a result of the bi-layer structure of the films. The θ rocking scans of the (101) and (110) planes were performed to see whether the formation of the two orientations was due to the bi-layer structure. A representative of the rocking curves is shown in Fig. 5(b). It is seen that the rocking curve of the (101) plane shows a single peak, while the rocking curve of the (110) plane consist of two peaks about 2° apart. More importantly, there is no (110) peak at $2\theta=32.2^\circ$, indicating that only the (101) planes are parallel to the substrate surface. The intensity of the (110) planes observed in the θ - 2θ curve of Fig. 5(a) is contributed by the intensity overlapping of the two (110) peaks. The results indicate that the films consist of a single, (101) epitaxial layer with the $\{101\}$ twins or domains. Twinning will cause the (110) planes in the twin region to closely parallel to the (101) planes in the matrix. The tilt angle calculated from the domain geometry is about 2.8° , which is in agreement with the measured value of about 2° .

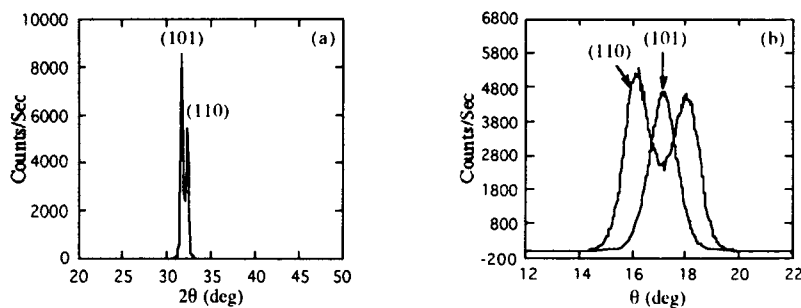


Fig. 5 (a) X-ray θ - 2θ scan of a PbTiO₃ film grown on (101)MgO at 625°C and slowly cooled down to room temperature. (b) Rocking curves of the (101) and (110) peaks in (a) shows one (101) peak and no (110) peak at the center, but two (110) peaks near the center about 2° apart, indicating that the (110) plane is not the growth plane.



Fig. 6 Plan-view TEM micrograph of a PbTiO₃ film on (110) MgO shows that the film is single crystalline with the {011} twins.

Cross-sectional TEM studies have confirmed the x-ray diffraction analyses that the PbTiO₃ films grown on (110) MgO are single-layer epitaxial films with the {101} domain structure. The epitaxial orientation relationship between the film and the substrate, obtained from electron diffraction patterns, is (101)[010]PbTiO₃|| (110)[001]MgO. Most of the 90° domain boundaries are (011) or (0 $\bar{1}$ 1) type inclined to the interface, while the others are (101) parallel to the interface, or (10 $\bar{1}$) perpendicular to the interface. The {011} 90° domains can be clearly seen in plan-view TEM micrographs as shown, for example, in Fig. 6. The angle between the two sets of the domains is about 74°, which is close to the calculated value (72°) of the angle between the projections of the (011) and (0 $\bar{1}$ 1) domain boundaries on the (101) plane.

4. CONCLUSIONS

The present studies have shown that the PbTiO₃ films grown on (001)MgO are single crystalline with a bi-layer structure at room temperature. The top layers near the free surface is c-axis oriented with the orientation relationship of (001)[100]PbTiO₃|| (001)[100]MgO. The bottom layer near the substrate is a-axis oriented with (100)[001]PbTiO₃|| (001)[100]MgO. The 90° domains were observed in the c-axis oriented layers of the PbTiO₃ films, but not in the a-axis oriented layers due to the substrate effect. HREM showed that the domain boundaries are abrupt and structural coherent. The formation of the bi-layer structure of the PbTiO₃ films appears to be the result of the combined effect of the cooling rate and the lattice mismatch across the interface on the phase transition of PbTiO₃ from the cubic to the tetragonal phase. The a-axis oriented layers decrease in thickness with decreasing cooling rate.

PbTiO₃ films deposited on (110) MgO are single-layer, epitaxial thin films with (101)[001]PbTiO₃|| (110)[001]MgO. Most of the 90° domain boundaries in the (101) films are (011) or (0 $\bar{1}$ 1) type inclined to the interface, while the others are (101) parallel to the interface, or (10 $\bar{1}$) perpendicular to the interface.

ACKNOWLEDGMENTS

This work was supported by the U. S. Department of Energy, Basic Energy Sciences - Materials Science under contract No. W-31-109-ENG-38.

REFERENCES

1. S. L. Swartz and V. E. Wood, *Condensed Matter News* **1**, 4 (1992).
2. M. de Keijser, G. J. M. Dormans, J. F. M. Cillessen, D. M. de Leeuw and H. W. Zandbergen, *Appl. Phys. Lett.* **58**, 2636 (1991).
3. K. Iijima, Y. Tomita, R. Takayama and I. Ueda, *J. Appl. Phys.* **60**, 361 (1986).
4. B. S. Kwak, K. Zhang, E. P. Boyd, A. Erbil and B. J. Wilkens, *J. Appl. Phys.* **69**, 767 (1991).
5. T. Ogawa, A. Senda and T. Kasanami, *Jpn. J. Appl. Phys.* **30**, 2145 (1991).
6. L. A. Wills, B. W. Wessels, D. S. Richeson and T. J. Marks, *Appl. Phys. Lett.* **60**, 41 (1991).
7. Y. Sakashita, T. Ono and H. Segawa, *J. of Appl. Phys.* **69**, 8352 (1991).
8. Y. Gao, G. Bai, K. L. Merkle, Y. Shi, H. L. M. Chang, Z. Shen and D. J. Lam, *J. Mater. Res.* **8**, 145 (1993).

METALLORGANIC CHEMICAL VAPOR DEPOSITION (MOCVD) OF TITANIUM-BASED FERROELECTRIC THIN FILMS

WARREN C. HENDRICKS, SESHU B. DESU*, JIE SI, CHIEN H. PENG

Virginia Polytechnic Institute & State University, Dept. of Materials Science and Engineering,
Blacksburg, Virginia 24061

ABSTRACT

Using hot-walled metallorganic chemical vapor deposition (MOCVD), thin films of lead zirconate titanate (PZT), lead titanate (PbTiO_3 or PT) and bismuth titanate ($\text{Bi}_4\text{Ti}_3\text{O}_{12}$ or BiT) were successfully prepared. For each material, titanium ethoxide ($\text{Ti}(\text{C}_2\text{H}_5\text{O})_4$) was used as the precursor for the titanium source, while lead bis-tetramethylheptadione ($\text{Pb}(\text{thd})_2$), zirconium tetrakis-tetramethylheptadione ($\text{Zr}(\text{thd})_4$) and triphenyl bismuth ($\text{Bi}(\text{C}_6\text{H}_5)_3$) were used as sources for lead, zirconium and bismuth, respectively. Dense, specular and highly transparent films were obtained for all three materials. Deposition conditions are given for each of the materials as well as the properties of the resulting films as determined by XRD, SEM and UV-VIS-NIR spectrophotometry. Ferroelectric properties are also given for the PZT and BiT films; for PZT (%Zr = 41; %Ti = 9) annealed at 600°C , the spontaneous polarization, P_s , was $23 \mu\text{C}/\text{cm}^2$ and the coercive field, E_c , was $65 \text{ kV}/\text{cm}$; for BiT annealed at 550°C , the spontaneous polarization, P_s , was $27 \mu\text{C}/\text{cm}^2$ and the coercive field, E_c , was $240 \text{ kV}/\text{cm}$.

INTRODUCTION

Many titanium-based ferroelectric materials, such as lead titanate, lead zirconate, and bismuth titanate, possess the perovskite crystal structure in their ferroelectric state. The presence of dual polarization states in these materials gives rise to interesting and useful properties such as ferroelectricity, pyroelectricity, piezoelectricity and optoelectronic properties. Interest in these materials has grown considerably in recent years, mostly for their application in nonvolatile ferroelectric random access memories (FRAM's) and high density dynamic RAM's (DRAM's) [1].

Many techniques are available for the deposition of ferroelectric thin films including metallorganic decomposition (MOD), sol-gel, sputtering and various evaporation processes. MOCVD offers the distinct advantages of flexible composition control and excellent step coverage along with amenability to large-scale processing [1]. In this paper, the deposition of lead titanate (PbTiO_3), lead zirconate titanate ($\text{Pb}(\text{Zr}_{1-x}\text{Ti}_x)\text{O}_3$) and bismuth titanate ($\text{Bi}_4\text{Ti}_3\text{O}_{12}$) using hot-wall MOCVD are discussed, including the structure and properties of the resulting films.

EXPERIMENTAL PROCEDURE

Three separate MOCVD reactors were used for each of the three materials but the essential structure and function of each system are identical. In each case, precursor vapors are produced from volatile sources which are contained in stainless steel bubblers and heated using customized mantle heaters. For each oxide component of the desired material, a separate bubbler and precursor source must be used. Table 1 lists the precursors used as well as their chemical formulas and common names. Except for titanium ethoxide, which is a nontoxic liquid at room temperature, each of the other precursors are stable, nontoxic powders; all are easy to handle. The powdered precursors must be replaced after each

* To whom all correspondence should be addressed

deposition but a sufficient quantity (approx. 40 cm³) of titanium ethoxide liquid may be stored under vacuum and used for more than 20 depositions [1].

TABLE 1: MOCVD Precursors and Chemical Formulas

Precursor	Formula	Common Name
lead bis-tetramethylheptadione	Pb(C ₁₁ H ₁₉ O ₂) ₂	lead-thd
zirconium tetrakis-tetramethylheptadione	Zr(C ₁₁ H ₁₉ O ₂) ₄	zirconium-thd
triphenyl bismuth	Bi(C ₆ H ₅) ₃	
titanium ethoxide	Ti(C ₂ H ₅ O) ₄	

Using nitrogen as a carrier gas, the heated vapors were delivered to the reactor; the carrier gas flow rates were monitored and controlled using mass flow controllers (MFC's). In each case, oxygen was also delivered using an MFC in order to provide an oxidizing atmosphere.

The actual reaction zone for each reactor consists of a stainless steel tube furnace heated along a portion of its length. All exposed tubing must be sufficiently heated using heating cords and tapes to prevent the precursors from condensing (~220 °C). The inside diameter for the PZT reactor is 80 mm while for the PT and BiT reactors the inside diameters are both 50 mm. Low pressure was achieved by means of mechanical pumps; liquid nitrogen cold traps are used in each case to condense byproducts and unreacted precursor that would otherwise enter the pump. Typical deposition conditions used for each of the three materials is given in Tables 2, 3, and 4.

TABLE 2: Deposition Conditions for PZT

Precursors	Pb(thd) ₂	Zr(thd) ₂	Ti(OEt) ₄
Precursor Temperature	145-165 °C	210-230 °C	90-115 °C
Carrier Gas (sccm, N ₂)	20-30	15-30	5
Substrate	sapphire	Pt/Ti/SiO ₂ /Si	RuO _x /SiO ₂ /Si
Substrate Temperature	550 °C		
Dilute Gas (sccm, O ₂)	500 - 1000		
Total Pressure	6 torr		
Deposition Rate (nm/min)	3 - 20		

TABLE 3: Deposition Conditions for PbTiO₃

Precursors	Pb(thd) ₂	Ti(OEt) ₄
Precursor Temperature	128 °C	83 °C
Carrier Gas (sccm, N ₂)	20-30	5
Substrate	sapphire, alumina	Pt/Ti/SiO ₂ /Si
Substrate Temperature	500 °C	
Dilute Gas (sccm, O ₂)	550	
Total Pressure	6 torr	
Deposition Rate (nm/min)	3 - 30	

TABLE 4: Deposition conditions for $\text{Bi}_4\text{Ti}_3\text{O}_{12}$

Precursors	$\text{Bi}(\text{C}_5\text{H}_9)_3$	$\text{Ti}(\text{OEt})_4$
Precursor Temperature	165-170 °C	75-127 °C
Carrier Gas (sccm, N_2)	30-50	0-8
Substrate	sapphire, Si	Pt/Ti/SiO ₂ /Si
Substrate Temperature	550 °C	
Dilute Gas (sccm, O_2)	500 - 1000	
Total Pressure	6 torr	
Deposition Rate (nm/min)	3 - 20	

The substrates used were of five types: 1" diameter sapphire disks (oriented within 30° of c-axis), polycrystalline alumina wafers, and multilayer substrates of Pt/Ti/SiO₂/Si and RuO_x/SiO₂/Si.

Prior to the deposition process, the substrates were placed in the reactor which was then sealed and pumped down to the base pressure, typically about 0.025 torr, using the mechanical pump. The furnace and bubblers were then heated up and allowed to stabilize at their respective set points. While flowing the dilute O_2 gas through the reactor to prevent backflow, the precursors were opened up to the bypass which leads directly to the cold trap avoiding the reactor; the carrier gas flow was also initiated at this time.

Using the pump valve, the pressure was adjusted to the desired deposition pressure. After several minutes, allowing for the system to reach steady state behavior, the precursor sources were opened to the reactor while the bypass was simultaneously closed. Deposition was allowed to continue for approximately thirty minutes in this manner.

RESULTS AND DISCUSSION

Specific results for each material are found in each of the following subsections.

LEAD TITANATE

The lead titanate films which were used for characterization purposes were found to be 50% PbO and 50% TiO₂ by EDS within experimental accuracy. Weight measurements were used to determine growth rates; the deposition in the uniform temperature zone of the reactor was found to be about 13 nm/min resulting in a 400 nm thick film after 30 minutes; the resulting crystal structure and morphology was also found to be good at this deposition rate. There was a noticeable substrate effect on the deposition rate in that the deposition rate tended to be several times higher on Pt substrates compared to adjacent sapphire or RuO_x samples. This may be a result of the ability of platinum to catalyze many chemical reactions. This effect was also noticed for PZT and has been reported in the literature by Swartz, et al. [3].

The lead titanate films were generally deposited at 500 °C; at temperatures of 525 °C and 550 °C blistering and peeling were found to occur on Pt as a result of residual stress. This may be a result of the phase transformation occurring as the film is cooled through the Curie temperature.

XRD using Cu-K α radiation was used to monitor phase constitution and reveal possible crystallographic orientation; a comparison of the typical XRD pattern for PbTiO₃ on each substrate is given in Fig. 1. Only the perovskite phase was observed in the as-deposited state; however, there was a noticeable increase in the peak intensities after annealing the films at 600 °C. This indicates that there may be some noncrystalline or microcrystalline material present prior to annealing.

Platinum substrates deposited with lead titanate showed the formation of a Pb-Pt intermetallic compound at the interface as inferred from XRD. The XRD patterns also demonstrate the tendency for [001] and [100] preferred orientation on Pt which has also been reported elsewhere [2,3]. There was no discernible orientation effect for the sapphire and alumina substrates.

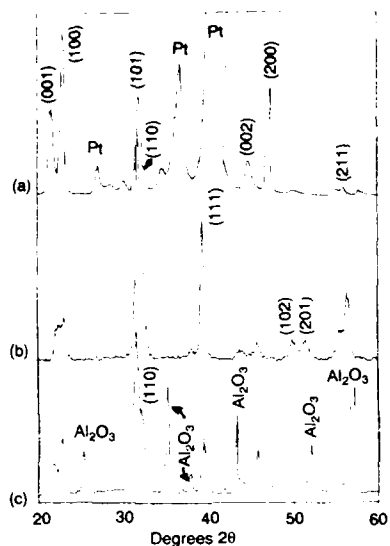


Figure 1: XRD of PbTiO_3 on (a) Pt/Si, (b) Sapphire, and (c) Polycrystalline alumina

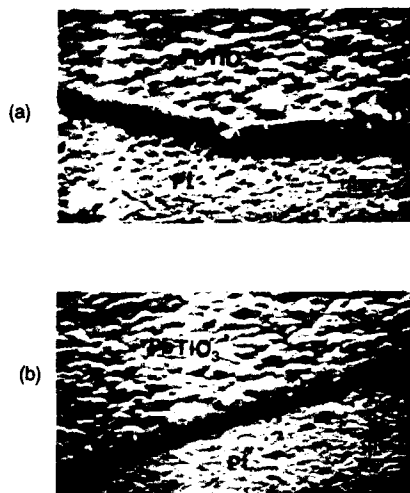
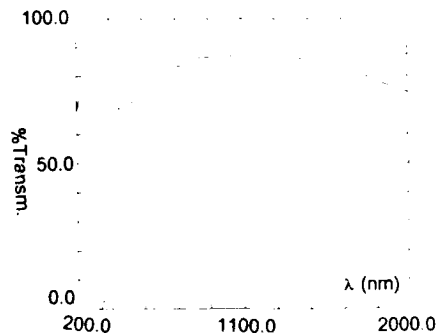


Figure 2: SEM micrographs of PbTiO_3 on Pt/Si for (a) As-deposited film and (b) After 600 °C, 1 hr anneal

Figure 3: UV-VIS-NIR transmission spectra for sapphire (upper curve) and PbTiO_3 on sapphire (lower curve)



SEM was used to show the film thickness uniformity and relatively smooth topography as may be seen in Fig. 2. This photograph was taken in profile along the cracked edge of the film on a platinum substrate. The cross-section of the film shows a dense, non-columnar structure although the surface is slightly rough.

UV-VIS-NIR spectrophotometry was used in both the transmission and reflectance (specular) modes on a 325 nm thick lead titanate film as shown in Fig. 3. The transmission properties of the film revealed a highly specular, nonabsorbing film as evidenced by the fact that the maxima in the interference fringes closely approach the transmitted intensity of the uncoated sapphire disk at higher wavelengths.

Using the envelope method, the optical properties of the film could be determined. The optical band gap was found to be 3.67 eV which compares to the literature value of 3.6 eV for the bulk solid [4]. For a wavelength of 632.8 nm (He-Ne laser), the refractive index was found to be 2.474, compared to the literature value of 2.668 [5]; the extinction coefficient was 0.0009. Using an effective medium approximation for the refractive index, the packing density was estimated to be about 89%.

LEAD ZIRCONATE TITANATE

PZT films were deposited over a range of compositions across the solid solution range from PbTiO_3 to PbZrO_3 corresponding to $\text{Pb}(\text{Zr}_x\text{Ti}_{1-x})\text{O}_3$ where x varies from zero to one. While the corresponding PZT phase, tetragonal or rhombohedral, was generally observed across the uniform temperature zone of the reactor, the Zr/Ti ratio tended to increase slightly as a function of position; however, this effect could be reduced substantially by increasing the dilute gas flow rate to 1000 sccm. XRD patterns were obtained on each of the three substrates across a range of compositions (Fig. 4). Highly [100] and [001] oriented PZT films were occasionally obtained on all of the substrates used as had been found for the case of PbTiO_3 on Pt but did not seem to correlate to the composition or processing parameters. A typical microstructure for a highly [100] oriented PZT film on sapphire is shown in Fig. 6 showing faceted grains, with an estimated average grain size of $0.5 \mu\text{m}$.

UV-VIS-NIR spectrophotometry was used to characterize the PZT films on sapphire as has been described previously for lead titanate (Fig. 5). Using the envelope method the film thickness was calculated to be 510 nm; the n and k values were 2.413 and 0.0008, respectively, at $\lambda = 633 \text{ nm}$ for the film with Zr/Ti = 60/40. The high refractive index and low extinction coefficient illustrate the fact that the films were highly dense and transparent.

Ferroelectric properties of the films were determined by first depositing the top electrodes. The top electrodes consisted of an array of circular disks of a suitable electrode material such as platinum, palladium or ruthenium oxide; each circular electrode has an area of $2.14 \times 10^{-4} \text{ cm}^2$. Hysteresis behavior was observed using an RT-66A ferroelectric tester; a typical hysteresis loop is shown in Fig. 7. The spontaneous polarization, P_s , was found to be $23 \mu\text{C}/\text{cm}^2$ while the coercive field, E_c , was found to be 70 kV/cm. AES depth profiling revealed a uniform composition through the thickness of this film.

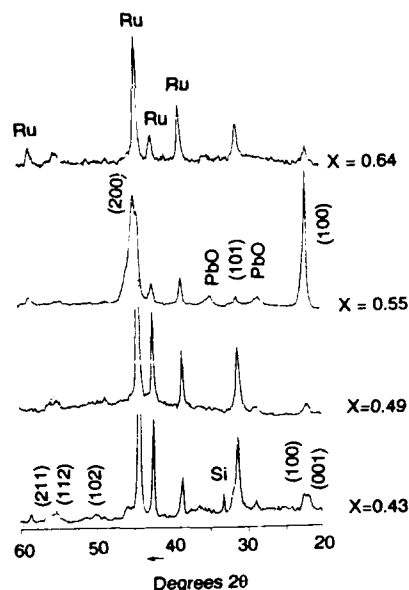


Figure 4: XRD of PZT on RuO_x for several PZT compositions

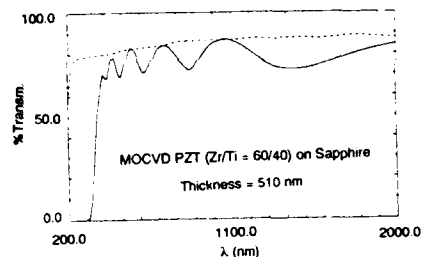


Figure 5: UV-VIS-NIR transmission spectra for PZT on sapphire

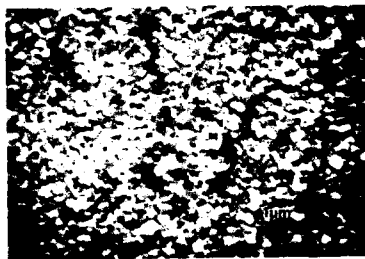


Figure 6: SEM micrograph of highly [100] oriented PZT film on sapphire substrate

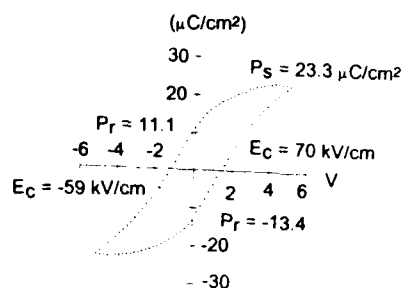


Figure 7: Ferroelectric hysteresis loop of 600 °C/30 min annealed PZT film for composition of (60/40)

BISMUTH TITANATE

The $\text{Bi}_4\text{Ti}_3\text{O}_{12}$ (BiT) films were specular, crack-free, well adhered and of uniform thickness in both the as-deposited and annealed states as shown in SEM micrographs of Fig. 10. The composition of the films (Bi/Ti) could be predictably controlled by altering the respective bubbler temperatures. The BiT phase was observed even in the as-deposited films but the crystallinity was observed to increase considerably upon annealing at temperatures from 500 °C to 600 °C as can be seen in the XRD spectra of Fig. 8. AES depth profile showed stoichiometric bismuth titanate through the film thickness.

Based on the UV-VIS-NIR transmission and reflectance spectra of the films on sapphire, the envelope method was used to determine the optical properties (Fig. 9). The film thickness was found to be 752 nm; n and k values were 2.507 and 0.003, respectively, at $\lambda = 633$ nm; for sol-gel BiT films, n was reported to be 2.33 [6]. These properties are indicative of relatively dense and transparent films.

Ferroelectric properties were determined for bismuth titanate as described previously for PZT. The film was deposited on Pt and annealed at 550 °C for one hour to optimize the properties. The hysteresis loop is shown in Fig. 11; spontaneous polarization, P_s , and coercive field, E_c , were 26 $\mu\text{C}/\text{cm}^2$ and 240 kV/cm, respectively, although it appears that film conductivity may be playing a role since the hysteresis loop does not appear fully saturated.

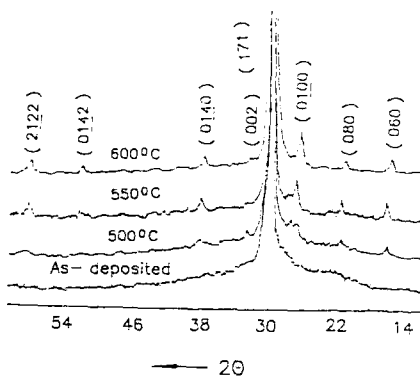


Figure 8: XRD of $\text{Bi}_4\text{Ti}_3\text{O}_{12}$ on Si for several annealing temperatures

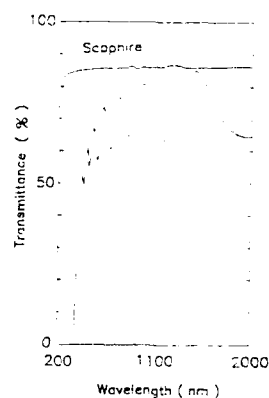
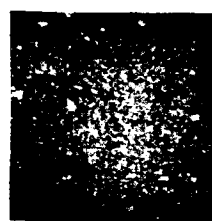


Figure 9: UV-VIS-NIR transmission spectra for BiT on sapphire



(a)



(b)

Figure 10: SEM micrographs of BiT on Si for (a) As-deposited film and (b) After 600 °C anneal

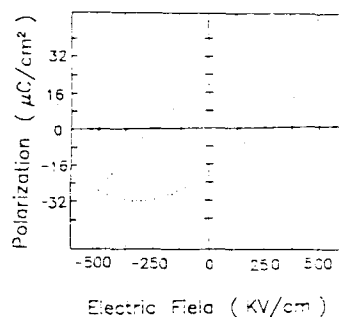


Figure 11: Ferroelectric hysteresis loop of 550 °C/1 hr annealed BiT film

SUMMARY

MOCVD was successfully used to deposit ferroelectric thin films of lead titanate, lead zirconate titanate (PZT), and bismuth titanate. Each process was individually optimized to provide good quality stoichiometric films. XRD and EDS revealed the proper crystalline phase and composition in each case and SEM showed the films to be smooth, dense, noncolumnar and of uniform thickness. The optical properties were determined for each of the films using UV-VIS-NIR spectrophotometry and revealed each of the films to be both highly dense and transparent. Using an RT-66A ferroelectric tester, ferroelectric properties are also given for PZT and bismuth titanate.

REFERENCES

1. C. H. Peng, Ph. D. Thesis, Virginia Polytechnic Institute & State University, Blacksburg, VA (1992).
2. T. Nakagawa, J. Yamaguchi, M. Okuyama, Y. Hamakawa, Jpn. J. Appl. Phys. **21**, L655 (1982).
3. S. L. Swartz, D. A. Seifert, G. T. Noel, Ferroelectrics, **93**, 37 (1989).
4. V.I. Zametin, Phys. Stat. Sol. (B), **124**, 625 (1984).
5. P. D. Thacher, Applied Optics, **16**, 3210 (1977).
6. P. C. Joshi and Abhai Mansingh, Appl. Phys. Lett., **59**, 2389 (1991).

PLASMA ENHANCED METALORGANIC CHEMICAL VAPOR DEPOSITION OF CONDUCTIVE OXIDE ELECTRODES FOR FERROELECTRIC BaTiO_3 CAPACITORS, Jiming Zhang, Guang-Ji Cui, Douglas Gordon, Peter Van Buskirk, and John Steinbeck, Advanced Technology Materials, Inc., 7 Commerce Drive, Danbury, CT 06810

ABSTRACT

Thin film heterostructures of $\text{BaTiO}_3/\text{YBa}_2\text{Cu}_3\text{O}_{7-x}$ (YBCO) and $\text{BaTiO}_3/\text{La}_x\text{Sr}_{1-x}\text{CoO}_3$ (LSCO) have been prepared by a novel single liquid source plasma-enhanced metalorganic chemical vapor deposition (PE-MOCVD) process. Both YBCO and LSCO are conductive oxides with perovskite structure and lattice parameters closely matched to BaTiO_3 . YBCO films were found to deteriorate after the deposition of BaTiO_3 under the PE-MOCVD conditions as revealed by X-ray diffraction and electrical characterization. LSCO thin films prepared by PE-MOCVD have a mirror-like surface, exhibit low electrical resistivity ($\rho = 200 \mu\Omega\text{-cm}$ at room temperature) and are robust to BaTiO_3 deposition. These characteristics make LSCO a promising electrode material for ferroelectric capacitors.

INTRODUCTION

The continuing drive toward increased circuit densities in DRAMs has spurred great interest in new dielectric materials that permit greater charge density in the storage capacitor. Ferroelectrics (FE) are particularly attractive for DRAM applications because of their intrinsically large dielectric constant, low leakage currents, and non-volatile radiation-hard memory capability[1-5].

Current applications of FE in microelectronics have been limited primarily by materials processing and compatibility problems[3-5]. In addition to using an appropriate growth technique, a suitable electrode material must be utilized[3-6]. Choice of the proper electrode materials is driven by materials compatibility issues as well as the electrical specifications for the memory element. In a FE capacitor memory, conducting electrodes must make intimate and ohmic contact to both sides of the FE thin film. The bottom electrode serves as the substrate during growth and the top electrode is deposited on top of the FE. FE capacitors have been plagued by switching fatigue which is normally associated with a gradual increase in E_c and a decrease in P_r after repeated polarization reversals[4,5]. To date, most electrode materials have been metals, such as Au, Al, and Pt. Incompatible electrode materials have been reported as one of the most significant causes for the failure of FE capacitors[4-8]. Switching fatigue has been extensively studied and is typically caused by electrode artifacts, microcracking and mobile space charge flow[4-7].

To solve the compatibility problem between the electrodes and FE capacitor, lattice/structure matched conductive oxides have recently been suggested as an alternative to metal electrodes[9-12]. Ramesh et al. at Bellcore recently reported the use of high temperature oxide superconductor (YBCO) as an electrode material for FE capacitors[9,10]. Epitaxial bismuth titanate and lead zirconium titanate (PZT) were grown on YBCO by laser ablation and ferroelectricity was observed. Recently, thin films of two other lattice matched conductive oxides, $\text{La}_x\text{Sr}_{1-x}\text{CoO}_3$ (LSCO) and $\text{Sr}_x\text{Ca}_{1-x}\text{RuO}_3$ (SCRO), have also

been successfully prepared by laser ablation and off-axis sputtering[11,12]. Both LSCO and SCRO exhibit isotropic, low electric resistivities and good compatibility with ferroelectric PZT films[11,12].

In this work, we report the results of the first plasma enhanced metal organic chemical vapor deposition (PE-MOCVD) of LSCO/BaTiO₃ and YBCO/BaTiO₃ heterostructures. For ULSI applications, CVD is preferred because of its compatibility with existing silicon semiconductor processes, high throughput, and ease of scale-up to manufacturing volumes. The usefulness of both LSCO and YBCO as electrode materials for FE capacitors will be discussed.

EXPERIMENTAL

All three materials (LSCO, YBCO, and BaTiO₃) were grown by a novel single liquid source plasma-enhanced metalorganic chemical vapor deposition (PE-MOCVD) process in an inverted vertical reactor configuration. Details of the reactor and the deposition conditions for YBCO and BaTiO₃ have been reported elsewhere[13,14]. Briefly, the requisite β -diketonate complexes ($M(\text{thd})_n$, $\text{thd} = 2,2,6,6$ -tetramethyl-3,5-heptanedionate) were dissolved in an organic solvent and the solution was injected by a liquid pump into a heated, stainless steel vaporizer[15] which was maintained at 200-230°C during deposition. The substrates used were (100) MgO, (100) LaAlO₃, and Pt metallized Si (Pt/Ta/ONO/Si, ONO stands for a SiO₂/Si₃N₄/SiO₂ trilayer). All films were deposited at 600-700°C. The film composition was controlled by varying the molar ratio of the organometallic complexes in the solution. The precursor vapor was carried upstream of the reactor inlet by nitrogen carrier gas (flow rate = 50-100 sccm) and the vaporization process took place on a continuous basis. The transport rate of the solution to the vaporizer was 5-10 mm³/min. and the typical film thickness was 0.3-0.5 μm . The reactor pressure was maintained at 1.5-2.0 Torr. The composition of the films was determined from energy dispersive X-ray analysis (EDX). Scanning electron microscopy (SEM) was used to study the surface morphology of the films. The microstructure of the films was characterized by X-ray diffraction (XRD) using a Rigaku D/Max-3HFX X-Ray Diffractometer. The thickness and surface topography of the films were measured with a Dektak IIA profilometer.

RESULTS AND DISCUSSION

YBCO and BaTiO₃ were first deposited on single crystal (100) LaAlO₃ and (100) MgO substrates. Fig. 1a shows the X-ray diffraction pattern for a typical YBCO film deposited at 680°C by PE-MOCVD on (100) LaAlO₃. Fig. 1b shows the X-ray diffraction pattern for a typical BaTiO₃ film deposited at 700°C by PE-MOCVD on (100) MgO. As can be seen from the figures, single phase, highly textured YBa₂Cu₃O_{7-x} and BaTiO₃ were formed in-situ by single liquid source PE-MOCVD. Pole figure measurements revealed that both the YBCO and BaTiO₃ films grew epitaxially on these single crystal substrates. Four probe electrical resistivity measurements indicated that the YBCO films were metallic at normal state until the film entered the superconducting state at $T_{c0} = 89$ K. The typical normal state resistivity at room temperature was 200 $\mu\Omega$ -cm. Details of the YBCO film and electrical properties have been reported elsewhere [13]. To examine the feasibility of YBCO films as electrodes for FE

capacitors under the PE-MOCVD conditions, BaTiO_3 films were deposited on top of the YBCO. Fig. 1c shows the X-ray diffraction pattern for a BaTiO_3 film deposited at 700°C by PE-MOCVD on YBCO/ LaAlO_3 . The deposition conditions were identical to those for the BaTiO_3 film shown in Fig. 1b. A single crystal LaAlO_3 substrate was placed side by side with the YBCO/ LaAlO_3 specimen as a monitor. As can be seen from Fig. 1c, both (100) and (110) BaTiO_3 peaks were observed. The crystallinity of the YBCO film was found to deteriorate compared to the YBCO film prior to BaTiO_3 deposition. In contrast, the BaTiO_3 film deposited on the monitor substrate was highly (100) oriented.

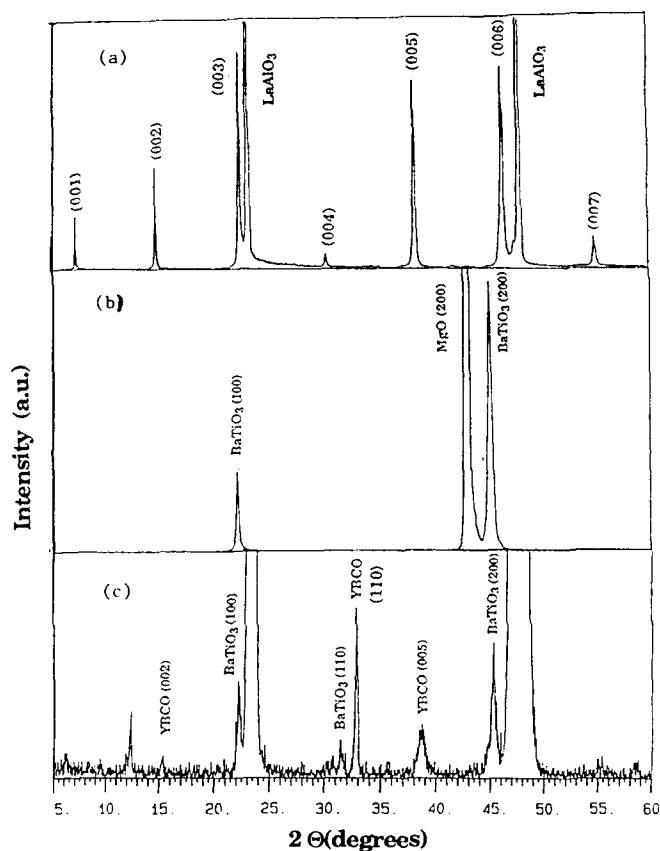


Fig. 1 (a) X-ray diffraction pattern for a YBCO film deposited on (100) LaAlO_3 at 680°C by single precursor PE-MOCVD. The film was epitaxial with the substrate as confirmed by pole figure measurement.

Fig. 1(b) X-ray diffraction pattern for a BaTiO_3 film deposited on (100) MgO at 700°C by single precursor PE-MOCVD.

Fig. 1(c) X-ray diffraction pattern for a $\text{BaTiO}_3/\text{YBCO}/\text{LaAlO}_3$ heterostructure.

YBCO and BaTiO_3 have also been deposited by single precursor PE-MOCVD on Pt/Ta/ONO/Si substrates. The composite buffer layer Pt/Ta/ONO has been extensively investigated as the bottom electrode for ferroelectric capacitors[16]; Pt is stable in the oxidizing growth atmosphere and the ONO stack prevents the formation of platinum silicide during growth. The intermediate Ta layer is needed to adhere the Pt to the ONO stack. Both YBCO and BaTiO_3 films grown on the stack were polycrystalline with somewhat preferred orientation (c-axis oriented for YBCO, a-axis oriented for BaTiO_3). Both YBCO/ BaTiO_3 /Pt/Ta/ONO/Si and BaTiO_3 /YBCO/Pt/Ta/ONO/Si heterostructures have been prepared by PE-MOCVD. In all the cases, the quality of YBCO films was poor.

The results discussed above indicate that YBCO is not a suitable electrode material for FE capacitors under the PE-MOCVD conditions. The intrinsic drawbacks of YBCO as an electrode for FE capacitors are its sensitivity to ambient environment, in particular water vapor, and the highly anisotropic electrical property along a- and c-axes. In this regard, LaSrCoO and SrCaRuO are two promising lattice matched, perovskite-type conductive oxides which exhibit isotropic, low electrical resistivities and good compatibility with ferroelectric PZT films[11,12]. Cheung et al. [11] recently demonstrated that LSCO films prepared by laser ablation exhibit crystallographically isotropic electrical conductivity and are much more stable than YBCO.

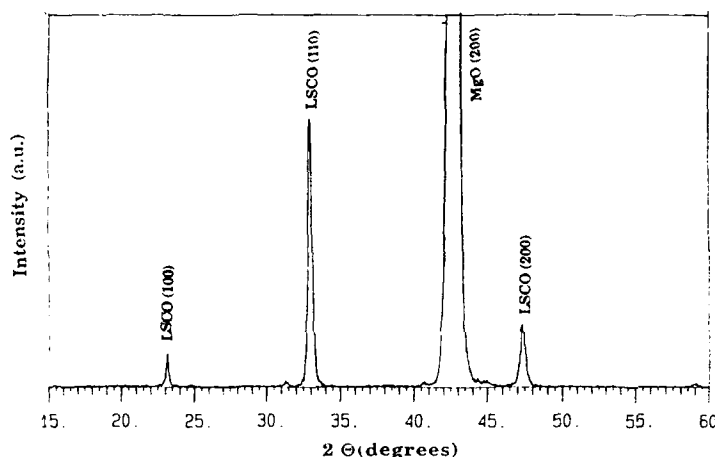


Fig. 2 X-ray diffraction pattern for a LSCO film deposited on (100) MgO at 700 °C by single precursor PE-MOCVD.

We have recently prepared LSCO films by single precursor PE-MOCVD. Figure 2 shows the θ - 2θ scan for a LSCO film deposited on (100) MgO substrate at 700 °C. As can be seen in Fig. 2, a phase pure LSCO was obtained. Only the (100) and (110) peaks were present in the CVD-derived films. To the best of our knowledge, this is the first report of growth of LSCO films by CVD. The as-deposited film was smooth and exhibited a mirror-like surface. Fig. 3 shows a scanning electron micrograph of the surface of a typical LSCO film on MgO (100). Fig. 3 indicates the formation of a dense, smooth film with no discernible grain boundaries. Fig. 4 shows a cross-sectional SEM micrograph of a LSCO

film on MgO (100) and indicates that a dense packed material was formed with a sharp interface. I-V measurements of patterned LSCO films using Au contact indicated that the contact between LSCO and Au electrode is ohmic. The resistivity of the LSCO film was $\sim 200 \mu\Omega\text{-cm}$ derived from the I-V curve. Fig. 5 shows an X-ray diffraction pattern for a $\text{BaTiO}_3/\text{LSCO}/\text{MgO}$ heterostructure. Only (100) and (110) peaks from BaTiO_3 and LSCO were observed. No noticeable deterioration of LSCO was observed following the BaTiO_3 deposition. We are currently optimizing the process to evaluate the electrical properties of the $\text{BaTiO}_3/\text{LSCO}$ and $\text{LSCO}/\text{BaTiO}_3$ heterostructures.



Fig. 3 Scanning electron micrograph of a typical LSCO film on (100) MgO. The film is deposited by single source PE-MOCVD.

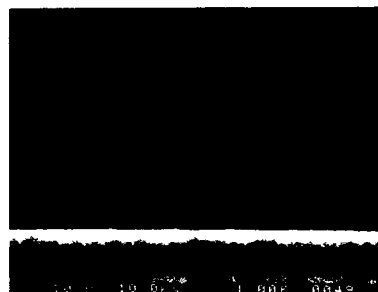


Fig. 4 Cross-sectional micrograph of a LSCO film on (100) MgO.

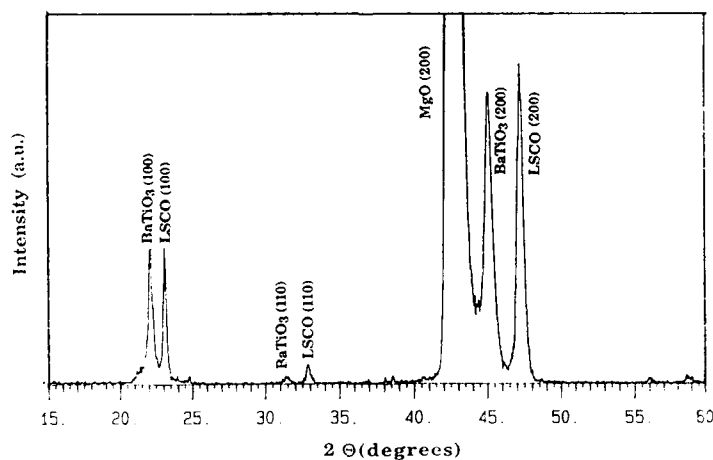


Fig. 5 X-ray diffraction pattern for a $\text{BaTiO}_3/\text{LSCO}/\text{MgO}$ heterostructure. Both BaTiO_3 and LSCO were deposited by single source PE-MOCVD.

SUMMARY

$\text{La}_x\text{Sr}_{1-x}\text{CoO}_3$ (LSCO) thin films have been prepared for the first time by a novel single liquid source plasma-enhanced metalorganic chemical vapor deposition (PE-MOCVD) process. LSCO thin films prepared by PE-MOCVD have a mirror-like surface and exhibit low electrical resistivity ($\rho \sim 200 \mu\Omega\text{-cm}$ at room temperature). Thin film heterostructures of $\text{BaTiO}_3/\text{YBCO}$ and $\text{BaTiO}_3/\text{LSCO}$ have been fabricated by PE-MOCVD. YBCO films were found to have deteriorated after the deposition of BaTiO_3 on them under the PE-MOCVD conditions. In contrast, LSCO thin films prepared by PE-MOCVD were smoother and more robust to the upper BaTiO_3 deposition as compared to YBCO. These characteristics render LSCO a promising electrode material for ferroelectric capacitors.

ACKNOWLEDGEMENT

The authors would like to thank Dr. Chuck Beetz for useful discussions. The authors would also like to thank Dr. Otmar Boser, Mr. Robert Borstler, and Dr. Galina Doubinana for assistance in electrical measurements. This research was supported by SDIO under contract NAS3-26709 managed by NASA and in part by NASA under contract NAS3-25932.

REFERENCES:

1. *VLSI Fabrication Principles*, S.K. Ghandhi, John Wiley & Sons, Inc., (1983).
2. *Silicon Processing for the VLSI Era*, S. Wolf., Lattice Press, (1990).
3. D. Bondurant and F. Gnadinger, *IEEE Spectrum*, **7**, 30 (1989).
4. J.F. Scott and C.A. Paz de Araujo, *Science*, **246**, 1400 (1989).
5. G.H. Haertling, *J. Vac. Sci. Technol.*, **A9**, 414 (1991).
6. W. Salaneck, *Ferroelectrics*, **4**, 97 (1972).
7. P.D. Hrenn, S.H. Rou, H.N. Al-Shareef, M.S. Ameen, O. Auciello, and A.I. Kingon, in *Proc. of 3rd International Symposium on Integrated Ferroelectrics*, p 612 (1991).
8. C.K. Kwok, D.P. Vijay, S.B. Desu, N.P. Parikh, and E.A. Hill, in *4th International Symposium on Integrated Ferroelectrics*, (1992).
9. R. Ramesh, A. Inam, B. Wilkens, W.K. Chan, T. Sands, J.M. Tarascon, D.K. Fork, T.H. Geballe, J. Evans, and J. Bullington, *Appl. Phys. Lett.*, **59**, 1783 (1991).
10. R. Ramesh, W.K. Chan, B. Wilkens, H. Gilchrist, T. Sands, J.M. Tarascon, V.G. Keramidas, D.K. Fork, J. Lee, and A. Safari, *Appl. Phys. Lett.*, **61**, 1537 (1992).
11. J.T. Cheung, P.E. Morgan, D.H. Lowndes, X.Y. Zhang, and J. Breen, *Appl. Phys. Lett.*, in press.
12. G.B. Eom, R.J. Cava, R.M. Fleming, J.M. Phillips, R.B. Van Dover, J.H. Marshall, J.W. P. Hsu, J.J. Krajewski, and W.F. Peck, *Science*, **258**, 1766 (1992).
13. Jiming Zhang, Robin A. Gardiner, Peter S. Kirlin, Robert W. Boerstler, and John Steinbeck, *Appl. Phys. Lett.* **61**, 2884 (1992).
14. P. Van Buskirk, R. P. Gardiner, P. S. Kirlin, *J. Vac. Sci. Technol.*, **A10**, 1578 (1992).
15. P.S. Kirlin, R.L. Binder, R.A. Gardiner, U.S. Patent No. 5,204,314 (20 April, 1993).
16. T. Sakuma, S. Yamamichi, S. Matsubara, H. Yamaguchi, and Y. Miyasaka, *Appl. Phys. Lett.* **57**, 2431 (1990).

GROWTH AND CHARACTERIZATION OF FERROELECTRIC $\text{Pb}(\text{Zr,Ti})\text{O}_3$ THIN FILMS BY MOCVD USING A 6 INCH SINGLE WAFER CVD SYSTEM

MASARU SHIMIZU, MASASHI FUJIMOTO, TAKUMA KATAYAMA, TADASHI SHIOSAKI, KENICHI NAKAYA*, MITSURU FUKAGAWA* AND EIKI TANIKAWA**
Department of Electronics, Faculty of Engineering, Kyoto University, Yoshida Honmachi, Sakyo-ku, Kyoto 606, Japan

* Amaya Co.Ltd., 3149-1 Kamite Nishikata, Koshigaya City, Saitama Prefecture 343, Japan

**CAT K.K., 2-14-7, Suido, Bunkyo-ku, Tokyo 112, Japan

ABSTRACT

Ferroelectric $\text{Pb}(\text{Zr,Ti})\text{O}_3$ (PZT) films with a perovskite phase were successfully grown by MOCVD using a 6 inch wafer CVD system. A two step growth process was proposed to obtain perovskite PZT films at high gas supplying ratios of $[\text{Zr}]/([\text{Zr}]+[\text{Ti}])$. The electrical properties of the PZT films obtained were measured. Large area growths of PZT films were carried out and the uniform films could be grown on the entire area of a 6 inch Si wafer. It was also found that the step coverage characteristic of the films grown by MOCVD was good.

INTRODUCTION

Recently ferroelectric $\text{Pb}(\text{Zr,Ti})\text{O}_3$ (PZT) thin films have been attracting much attention for a wide variety of electrical and optical applications, including memory devices, surface acoustic wave devices, optical modulator devices and integrated optic devices, because of their high dielectric constants, large spontaneous polarizations, and large pyroelectric, piezoelectric and electro optic effects.

Many thin film techniques to obtain PZT thin films, including physical and chemical methods, have been reported. Among the physical techniques, there are evaporation and sputtering methods. Among the chemical techniques, there are chemical vapor deposition (CVD), metalorganic chemical vapor deposition (MOCVD), metalloorganic decomposition (MOD) and sol-gel methods. Of all of these techniques, the sputtering methods (DC, RF, RF magnetron, ion beam etc.) have been the most widely used because of their convenience and the high melting point of the PZT materials. The sol-gel method is also a relatively new method for the preparation of PZT films and many studies have reported the ease of the composition control, a better homogeneity and a lower cost than other methods.

In the past several years, interest in the use of the MOCVD method has increased greatly because of its great usefulness, high potentiality and the recent development of new source materials. The MOCVD method has additional advantages such as a high controllability of film composition and crystalline structure, a high growth rate, good step coverage and the possibility of the scale-up of the process from the laboratory, to commercial based production. However there have been few reports on the large area growth and evaluation of PZT thin films for practical use using a productive MOCVD system [1]. Therefore, in order to confirm the advantages, as mentioned above, of the MOCVD method for the practical use of memory applications and to investigate the problems included in the MOCVD process, we developed a 6 inch wafer MOCVD system and performed experiments on the growth of PZT thin films.

In this paper we will describe the growth of PZT thin films using a 6 inch wafer MOCVD system. In particular, a two step growth which was performed to control the crystalline structure, the electrical properties and the large area growth of PZT thin films on a 6 inch wafer will also be described.

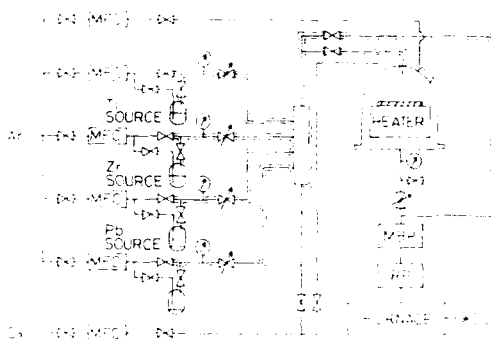


Fig.1. Schematic diagram of the MOCVD system.

EXPERIMENTAL PROCEDURE

In order to perform the large area growth of PZT thin films, an MOCVD system which could mount 6–8 inch Si wafers was developed. The MOCVD system used is schematically shown in Fig.1. This system consisted of a gas supplying system, a reaction chamber and an evacuation system. In the gas supplying system, there were temperature controlled ovens for the source precursor vessels. All stainless steel pipes connected from gas supplying system to the reaction chamber were heated by ribbon heaters to prevent the solidification of the source materials inside the pipes. The quartz reactor chamber was of a vertical type and had an inside diameter of 300mm. A 6–8 inch wafer could be loaded in this reactor. The pressure in the reactor could be kept constant using an automatic throttle valve. In the evacuation system, a mechanical booster pump and a rotary pump were used. The exhaust was released to the air through the thermal decomposition furnace.

In our experiments, $\text{Pb}(\text{DPM})_2$ (lead bisdipivaloylmethane, Nippon Sanso Co., purity: 99.9%), $\text{Zr}(\text{O}-t-\text{C}_4\text{H}_9)_4$ (zirconium tetratertiarybutoxide, Tri Chemical Lab. Ltd., purity: 99.999%), $\text{Ti}(\text{O}-i-\text{C}_3\text{H}_7)_4$ (titanium tetraisopropoxide, Tri Chemical Lab. Ltd., purity: 99.999%) and O_2 (purity: 99.995%) were used as the source materials. The carrier gas used was an Ar gas (purity: 99.9999%). The gas flow rates of the gases were controlled precisely using mass flow controllers.

$\text{Si}(100)$ and $\text{Pt}(111)/\text{SiO}_2/\text{Si}(100)$ were used as substrates. Pt films were coated by sputtering.

RESULTS AND DISCUSSION

Growth of PbO , ZrO_2 and TiO_2 thin films

In the first set of experiments, the growth behavior of PbO , ZrO_2 and TiO_2 films were investigated – in particular, the dependence of the deposition rate on the growth temperature, reactor pressure and oxygen concentration.

The deposition rates of PbO , ZrO_2 and TiO_2 films increased at growth temperatures lower than around 500°C, and at higher than around 500°C they decreased. This means the pyrolysis and oxidation of the source materials at the substrate surface determined the deposition rate.

Measuring the dependence of the deposition rate on the reactor pressure, it was found that the deposition rates of ZrO_2 and TiO_2 increased from 2 to 70 nm/min and from 7 to 50 nm/min, respectively, as the reactor pressures increased from 0.1 to 10 Torr. On the other hand, PbO films were not grown at reactor pressures lower than 1 Torr. PbO films showed a deposition rate increasing from 2 to 24 nm/min as the reactor pressure increased from 1 to 10 Torr.

The deposition rates of the ZrO_2 and TiO_2 films were independent of the oxygen concentration. This means that the main reaction is pyrolysis in Zr and Ti source materials [2]. On the other hand, the deposition rates of the PbO films increased as the oxygen concentration increased up to around 30%, an experimental result which indicates that the main reaction is the oxidation of the Pb source [3,4].

Growth $\text{Pb}(\text{Zr,Ti})\text{O}_3$ thin films

In the second set of experiments, PZT films were deposited at substrate temperatures of 550 and 600°C and at gas supplying ratios of $[\text{Zr}]/([\text{Zr}]+[\text{Ti}])$ ranging from 0 to 0.86. Perovskite PZT films with a tetragonal type were obtained at gas supplying ratios of $[\text{Zr}]/([\text{Zr}]+[\text{Ti}])$ lower than 0.6, as shown in Fig.2(a). Rhombohedral PZT films could be grown at a $[\text{Zr}]/([\text{Zr}]+[\text{Ti}])$ ratio of 0.74 and at 600°C. However when the films were prepared at gas supplying ratios of $[\text{Zr}]/([\text{Zr}]+[\text{Ti}])$ higher than 0.74, pyrochlore PZT films and ZrO_2 films were grown. At these higher $[\text{Zr}]/([\text{Zr}]+[\text{Ti}])$ ratios, substrate temperatures higher than 600°C were required to grow perovskite PZT. The formation of ZrO_2 at a higher Zr content region has been reported [5].

In order to avoid the formation of pyrochlore and ZrO_2 films and to obtain perovskite PZT films, a two step growth technique was proposed. In the two step growth process, PbTiO_3 layers with a perovskite phase were first introduced as an intermediate layer because they were easy to obtain in our growth process. In the succeeding process, PZT films were deposited on the PbTiO_3 layers. It was found that rhombohedral perovskite PZT films could be grown only on an intermediate PbTiO_3 layer at ratios of $[\text{Zr}]/([\text{Zr}]+[\text{Ti}])$ higher than 0.74 as shown in Fig.2(b), and when PZT films were deposited on the PbTiO_3 intermediate layers, the rhombohedral perovskite PZT films were obtained at lower substrate temperatures than when PZT films were directly deposited on $\text{Pt/SiO}_2/\text{Si}$. These experimental results means that an intermediate PbTiO_3 layer plays the very important role of forming the dense nuclei in the succeeding PZT growth process. The intermediate PbTiO_3 layer may also act as a buffer layer which relaxes the differences of the lattice constant between PZT and Pt.

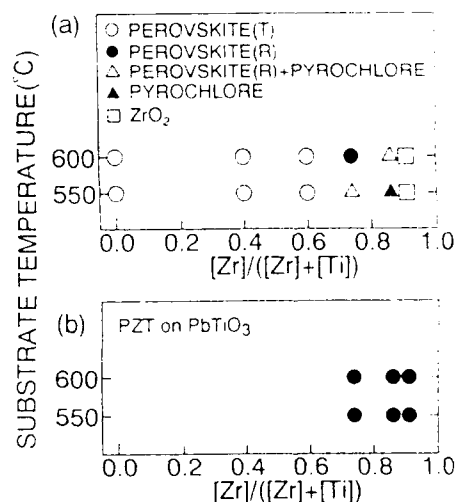


Fig.2. Crystalline phase diagram of films grown on ; (a) $\text{Pt/SiO}_2/\text{Si}$, (b) $\text{PbTiO}_3/\text{Pt/SiO}_2/\text{Si}$.

When PbO , ZrO_2 and TiO_2 layers were used as an intermediate layer instead of PbTiO_3 , only the TiO_2 layers were effective in the growth of the rhombohedral perovskite PZT films. The effectiveness of this use of the TiO_2 intermediate layer may have a close relationship to the deposition mechanism of PZT.

Film composition

The film composition was analyzed by the inductively coupled plasma (ICP) emission spectrometry method. In MOCVD, the film composition ($\text{Zr}/(\text{Zr}+\text{Ti})$) could be controlled by changing the Ar carrier gas flow rates of the Zr and Ti sources. The compositional ratio of films was not proportional to the gas supplying ratio $\text{Zr}/([\text{Zr}]+[\text{Ti}])$, which means the Zr content could not easily be contained in the films [5].

Electrical properties

The electrical properties of the films obtained were measured. The dependence of the relative dielectric constant of the films (100–160 nm) on the gas supplying ratio is shown in Fig. 3. The relative dielectric constants varied from 50 to 640 with the change in the film composition. The decrease of the relative dielectric constant at gas supplying ratios of $[\text{Zr}]/([\text{Zr}]+[\text{Ti}])$ higher than 0.6 was due to the formation of pyrochlore phase and ZrO_2 . The effect of intermediate layer in the two step growth on the dielectric constant was also investigated. The perovskite PZT films obtained on the PbTiO_3 intermediate layer had higher dielectric constants than those of non-perovskite films obtained on ZrO_2 and PbO intermediate layers. The perovskite PZT films grown using the two step growth process at high $[\text{Zr}]/([\text{Zr}]+[\text{Ti}])$ ratios also showed D-E hysteresis loops and these films were found to have ferroelectricity.

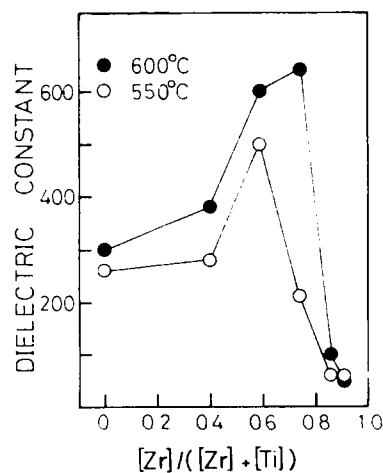


Fig. 3. Dependence of the relative dielectric constant of the films on the gas supplying ratio of $[\text{Zr}]/([\text{Zr}]+[\text{Ti}])$.

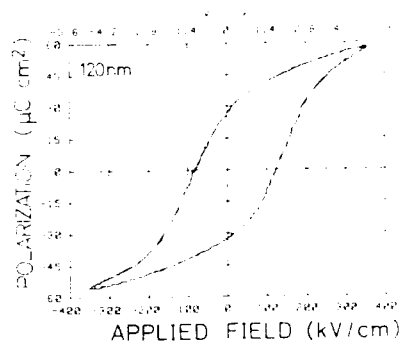


Fig. 4. D-E hysteresis loop of a 120 nm-thick PZT film.

Figure 4 illustrates a typical D-E hysteresis loop of a 120 nm-thick tetragonal PZT film grown at 600°C. The remanant polarization (P_r) and coercive field (E_c) of this film were 36 $\mu\text{C}/\text{cm}^2$ and 100 kV/cm. P_r and E_c of the films (100–160 nm) obtained were 9–38 $\mu\text{C}/\text{cm}^2$ and 70–220 kV/cm, respectively.

The switching characteristics were also investigated by applying double bipolar pulses with an amplitude of 5V. The typical switched charge density of a PZT film with a thickness of 100nm was 55 $\mu\text{C}/\text{cm}^2$ and the switching time was 25 μsec when the upper electrode with an area of $8 \times 10^{-3} \text{ cm}^2$ was used.

Large area growth of PZT

Corresponding with the requirements of a practical applications of the MOCVD process, large area growths of PZT films on a 6 inch Si wafer were performed. The film uniformity was affected by the gas flow rate, the substrate temperature, the distance between the gas nozzle and the substrate, and the shape of the gas nozzle. Prior to the large area growth of the PZT films, in order to investigate the optimum conditions for large area growth with good uniformity, depositions of PbO, ZrO₂, and TiO₂ films were carried out.

In the growth of the PbO films, PbO films with a good uniformity were grown using a funnel-shaped nozzle when the films were grown at substrate temperatures in a range from 400 to 600°C and at reactor pressures in a range from 3 to 5 Torr.

There was a marked difference in the optimum reactor pressure required to produce the PbO films, and that required for the TiO₂ and ZrO₂ films. TiO₂ and ZrO₂ films with a good uniformity could be grown at reactor pressures lower than 1 Torr. At reactor pressures lower than 1 Torr, the growth rate of PbO was very slow, as mentioned above. Therefore the optimum reactor pressure to produce PZT was determined to be 5 Torr.

When PZT films were prepared at 5 Torr and 600°C, the uniformity was very poor, although the PZT films were deposited entirely over the substrate.

In our next attempt, in order to improve the distribution of the gas flow for the growth of films with a good uniformity, a nozzle with a diameter of 28.5mm was used and a large amount of Ar carrier gas (10 l/min) was supplied. In this case, a slight improvement in uniformity was observed, but the thickness uniformity was still poor.

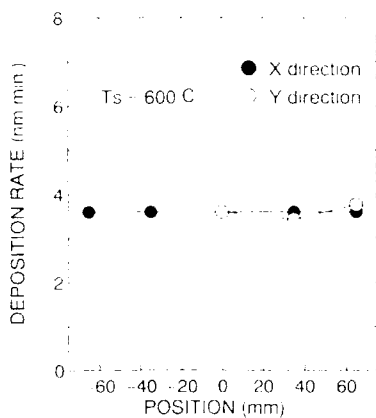


Fig.5. Measurement of the film thickness of a film on a 6 inch Si wafer (X:horizontal direction, Y:vertical direction).

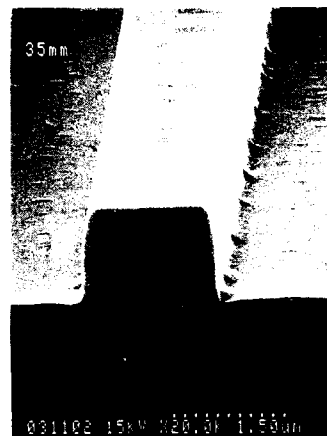


Fig.6. Cross sectional view of a PZT film obtained by MOCVD on a Si ridge pattern.

In the third attempt, a nozzle with a diameter of 20cm perforated with many small holes was used. Using this nozzle, good uniform films with a thickness varied by less than 5% were successfully obtained as shown in Fig.5. The good uniformity of the film composition was also observed.

Step coverage

As the functional device technology advances toward smaller device features, good step coverage becomes a more important requirement in thin film devices. To investigate the step coverage characteristics of films prepared by MOCVD, films were deposited on Si with ridge patterns of 1.1-10 μm in width. Figure 6 shows the cross sectional view of the PZT film deposited on the ridge pattern. This SEM photograph shows the good uniformity of both overall coverage and sidewall coverage, and we found the MOCVD process to be an effective method to get good step coverage characteristics.

CONCLUSIONS

Thin film growths of PZT were performed by MOCVD using a 6 inch single wafer CVD system. Tetragonal and rhombohedral PZT thin films with a perovskite phase could successfully be grown. The crystalline structure was changed by changing the gas supplying ratio of $[\text{Zr}]/([\text{Zr}]+[\text{Ti}])$. At ratios of $[\text{Zr}]/([\text{Zr}]+[\text{Ti}])$ higher than 0.7, perovskite PZT films could not be grown because of the formation of pyrochlore phase and ZrO_2 . However, when the two step growth process we proposed was carried out, perovskite PZT films could be grown and they showed ferroelectricity. The film composition could be controlled by changing the $[\text{Zr}]/([\text{Zr}]+[\text{Ti}])$ ratio.

The relative dielectric constants of the PZT films (100-160 nm in thickness) obtained at different gas flow rates of the Zr and Ti sources ranged from 260 to 640, and the remanent polarizations and coercive fields were 9-38 $\mu\text{C}/\text{cm}^2$ and 70-220 kV/cm, respectively.

Attempts at large area growths of PZT films with good uniformity were carried out, and uniform films could be obtained on a 6 inch wafer. Good step coverage characteristics were also obtained by our MOCVD process.

ACKNOWLEDGEMENTS

This work was partly supported by Grants-in-Aid for scientific research (B) (No.04452176) and for Scientific Research on Priority Areas (2)(No.04205075) from the Ministry of Education, Science and Culture, and by research grants from the Mazda Foundation's Research Grant and the Foundation for the Promotion of Material Science and Technology of Japan.

REFERENCES

1. P.C. Van Buskirk, R.Gardiner, P.S.Kirlin and S.B.Krupanidhi, Proc.8th IEEE Int.Sym. on Applications of Ferroelectrics (Greenville, SC, USA, 1992)pp.340-343.
2. M.Okada, K.Tominaga, T.Araki, S.Katayama and Y.Sakashita, Jpn.J.Appl.Phys. **29**, 718 (1990).
3. T.Nakai, T.Tabuchi, Y.Sawado, I.Kobayashi and Y.Sugimori, Jpn.J.Appl.Phys. **31**, 2992 (1992).
4. H.Yamazaki, T.Tsuyama, I.Kobayashi and Y.Sugimori, Jpn.J.Appl.Phys. **31**, 2995 (1992).
5. M.Shimizu, K.Hayashi, T.Katayama and T.Shiosaki, Proc. 8th IEEE Int.Sym. on Applications of Ferroelectrics (Greenville, SC, USA, 1992)pp.428-431.

PART VIII

Spin Pyrolysis of Thin Films

CRYSTALLIZATION BEHAVIOR AND ELECTRICAL PROPERTIES OF WET-CHEMICALLY DEPOSITED LEAD ZIRCONATE TITANATE THIN FILMS

S. MERKLEIN*, D. SPORN* and A. SCHONECKER**

* Fraunhofer-Institut für Silicidforschung, Neunerplatz 2, D - 97082 Würzburg, Germany

** Fraunhofer-Einrichtung für Keramische Technologien und Sinterwerkstoffe, Winterberg-str. 28, D - 01194 Dresden, Germany

ABSTRACT

A wet chemical deposition process for smooth and crackfree films in the system $\text{Pb}(\text{Zr}_{1-x}\text{Ti}_x)\text{O}_3$ (PZT) has been developed. Final film thicknesses, reached with one coating step, were in the region of 1 μm . Starting from lead acetate trihydrate, zirconium- and titanium-n-propoxide, high molarity (> 2M) coating sols have been prepared that could be handled in air and were stable for more than 170 days.

Films with compositions near the morphotropic phase boundary ($x=47$) and various lead contents were deposited on Pt-coated Si-wafers and Al_2O_3 -substrates by a spin-on method. Wet films could be pyrolyzed and densified with a fast heat treatment without cracking. The crystallization of films into the desired perovskite structure started at comparatively low temperatures (ca. 530 °C) and proceeded rapidly at temperatures above 650 °C. A slight molar excess of lead and a proper heating rate were found to produce films with the best electrical properties. The films on platinized Al_2O_3 substrates showed device-worthy dielectric and ferroelectric properties with typical values for P_r , E_c , and ϵ , of 24 $\mu\text{C}/\text{cm}^2$, 4.5 KV/mm and 650, respectively.

INTRODUCTION

Thin ferroelectric films in the system lead zirconate titanate $\text{Pb}(\text{Zr}_{1-x}\text{Ti}_x)\text{O}_3$ (PZT) are receiving increased attention due to their unique electrical and optical properties. In comparison with sputtered films, wet chemically derived PZT films can be produced less expensively and show superior ferroelectric properties, possibly because of their more uniform morphology and smaller crystallite sizes [1]. Potential applications for thin films include, amongst others, piezoelectric and pyroelectric sensors, actuators, electro-optic devices and non-volatile memories [2].

Up to now numerous wet chemical procedures for PZT thin film preparation have been reported, but the maximum film thickness reached with one coating step is often insufficient for application. Multiple deposition processes increase the thickness but reduce the reliability and increase the number of defects. We tried to work out a one step wet-chemical deposition procedure for PZT films with final thicknesses in the range of 1 μm .

EXPERIMENTAL PROCEDURE

Sol preparation:

At present methoxyethanol is the solvent most frequently used in PZT thin film preparation. Diols were proposed by Phillips [3] as solvents with possible cross-linking capabilities for Zr- and Ti-alkoxides. Commercially available lead acetate trihydrate, zirconium- and titanium-n-propoxide proved to be suitable as starting materials. 1,3-pro-

panediol was chosen as a solvent because of its high boiling point, high viscosity and good solubility for lead acetate. The general procedure of the coating sol preparation and film deposition is given in Figure 1.

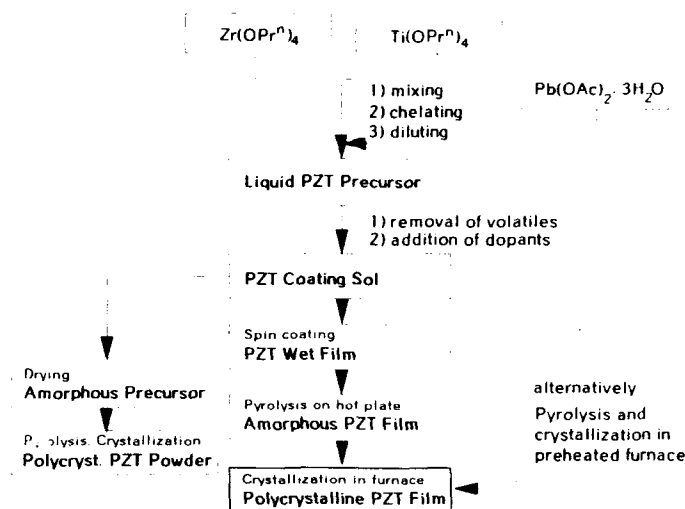


Fig. 1: General procedure of PZT powder and film preparation used in this work

The pure Zr/Ti-alkoxides are quite prone towards hydrolysis and condensation reactions followed by precipitation [4]. After reacting a mixture of the desired Zr/Ti ratio with one equivalent of the chelating agent acetylacetone it could be handled in air. The mixture was diluted with 1,3-propanediol before lead acetate trihydrate was added. The dehydration of the trihydrate could thus be avoided. On heating a clear solution was obtained from which low boiling reaction products as n-propanol and water were distilled off until the boiling point of the sol reached 190 °C. The resulting coating sol was a clear, viscous and gold-yellow liquid which had an exceptional high molarity of more than 2 M. This corresponds to a solid yield in the range of 40 mass%.

Spectroscopic analysis of the coating sol and the distillate revealed that all of the n-propoxide groups were substituted by 1,3-propanediol groups. A small proportion of acetylacetone is distilled off, but the main fraction remains bonded to the Zr- and Ti-alkoxides. This is demonstrated by a broad infrared absorption band at 1550 cm^{-1} . The closer analysis of the spectrum is difficult because of the overlapping absorption band from lead acetate (1530 cm^{-1}).

A certain amount of esters was formed from reactions between acetate, n-propanol and 1,3-propanediol as indicated by the infrared absorption bands at 1740 and 1720 cm^{-1} . Esterification reactions between lead acetate and the solvent alcohol or alkoxide groups have been reported previously [5], while some authors assume a reaction between lead- and Zr/Ti-compounds [6]. Heterometallic compounds, possibly resulting from such reactions, may increase the homogeneity in the PZT precursor [7].

The coating sols were remarkably stable according to dynamic light scattering experiments. A narrow distribution of particle sizes around 1.5 nm was found in a diluted coating sol, 10 d and even 170 d, after preparation. Measurements with a rotational rheometer revealed a newtonian flow behavior of the sols with dynamic viscosities in the range of

300 mPa.s which did not alter within the mentioned period. From these measurements the formation of polymers with high chain length can be excluded.

The thermal analysis of a PZT precursor powder reveals two exothermic events accompanied by weight losses at about 300 and 500 °C (Fig. 2). From FT-IR reflectance spectra of PZT precursor films (Fig. 3) which were heated to various temperatures it could be deduced that at temperatures below 250 °C esters and free solvent alcohol are removed. On further heating alkoxide and acetylacetonate groups are thermolyzed (ca 300 °C) and the absorption bands attributed to acetate are slightly shifted towards lower wavenumbers. They can be observed up to temperatures of 490 °C.

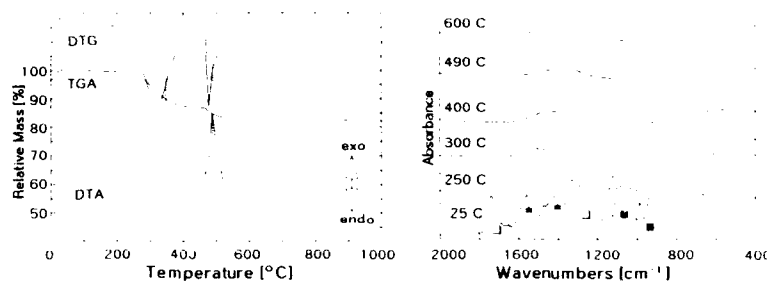


Fig. 2: Thermal analysis of a PZT precursor powder, predried at 200 °C (atmosphere: air; heating rate 10 K/min)

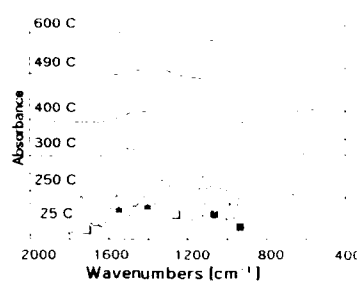


Fig. 3: FT-IR reflectance spectra of a PZT precursor film heated to various temperatures (□: Esters, ●: acetate, ■: 1,3-propanediol)

Film preparation:

A conventional spinner was used for film deposition on bare Al_2O_3 -substrates, platinum coated Si-wafers and platinized Al_2O_3 -substrates. Films dried at room temperature or with moderate heating cracked severely but we succeeded in producing crackfree, smooth and strongly adhering films up to a thickness of 1.1 μm by employing a special heat treatment. For that purpose the coated substrates had to be rapidly heated to temperatures exceeding 300 °C to evaporate solvent and to promote densification.

For the preparation of PZT-films suitable for electrical measurements, the freshly coated substrates were put on a hot plate at 300 °C and heated to 500 °C within 3 min. The final annealing was done in a furnace, raising the temperature at 100 K/h to 700 °C and keeping it for 2 h. In a separate one step procedure the films were directly put in a preheated furnace and kept at 700 °C for 10 minutes.

Film thicknesses were measured using a profilometer. For this, a step was created by etching a small area of the fired film.

Crystallization behavior:

Highly crystalline single phase PZT films were obtained from both procedures. The dependence of crystallization behavior of the films on temperature and time was investigated by normal and high temperature X-ray diffraction (XRD) measurements. Diffraction patterns of furnace-annealed films are given in Figure 4. In the temperature range between 500 and 600 °C a fine grained pyrochlore phase is found, indicated by two weak and broad peaks at 29.5 and 34 °2 θ . After heating to 530 °C small peaks at 22, 31 and 38.5 °2 θ indicate the initial formation of perovskite phase PZT. Single phase perovskite

without a trace of pyrochlore in the diffraction pattern is formed after a heat treatment at temperatures exceeding 650 °C.

Isothermal XRD measurements were performed on a high temperature diffractometer. Results are given in Figure 5. PZT(110) peak intensities were normalized with the Al_2O_3 (113) peak as internal standard with the requirement that all samples were of the same thickness. The crystallization was found to proceed very quickly (< 2 min) at temperatures above 600 °C. From the fact that no increase of the relative intensity occurred at higher temperatures, it could be assumed that crystallization was complete at approximately 700 °C.

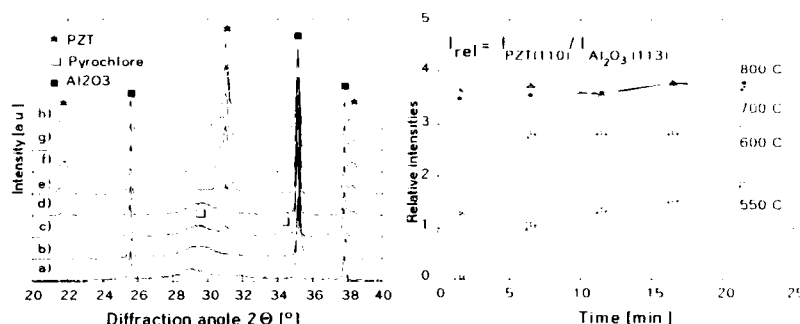


Fig. 4: X-ray diffraction patterns ($\text{Cu K}\alpha$ radiation) of PZT films on Al_2O_3 ; $\text{Pb}_{1.0}\text{Zr}_{0.53}\text{Ti}_{0.47}\text{O}_3$, heated for 10 min to a) 470 b) 500 c) 530 d) 570 e) 600 f) 650 g) 700 h) 800 °C

Fig. 5: Isothermal heating of PZT films on Al_2O_3 ; $\text{Pb}_{1.0}\text{Zr}_{0.53}\text{Ti}_{0.47}\text{O}_3$, normalized intensities of the PZT(110) X-ray diffraction peak

The heating rate also seemed to be an important factor in determining the fraction transformed to the perovskite phase in the film. A film heated with a high rate (estimated 200 K/sec) between room temperature and 500 °C developed a higher relative peak intensity on further heating with 5 K/min to 700 °C than a comparable film which was dried at 200 °C and then heated up to 700 °C with 5 K/min.

A very important factor affecting the crystallization behavior of PZT films is the lead content. In accordance with literature [8] it was found that a small molar excess of PbO in the range of 10 % significantly lowered the temperature of complete crystallization and reduced the quantity of undesired secondary phases.

Electrical characterization:

An array of circular gold electrodes 1 mm in diameter was sputtered on the surface to form capacitor-like structures. For measuring the dielectric and ferroelectric properties only those areas with an isolation resistance of > 10 MΩ were selected. Areas with defects were thus excluded. The electrical properties were measured at room temperature employing standard equipment and methods: impedance bridge for permittivity and loss factor measurement and integrating series capacitor circuit for recording the ferroelectric hysteresis loop, with cycle times ranging from 0.3 Hz to 20 KHz. In Figure 6 the spread of typical dielectric (relative permittivity ϵ_r) and ferroelectric data (remanent polarization P_r , coercive force E_c) are given. The ferroelectric behavior of a typical PZT film is demonstrated by the hysteresis loop in Figure 7.

The electrical characterization of the films revealed the following trends: excess lead improved the dielectric as well as the ferroelectric properties markedly, which is attributed to the better crystal structure and higher density. In comparison with the bulk properties of PZT the relative permittivity of the films is quite high, but values as high as 3000 were reported [8]. Annealing temperatures in the range of 700 °C were found to be sufficient for the development of good ferroelectric properties.

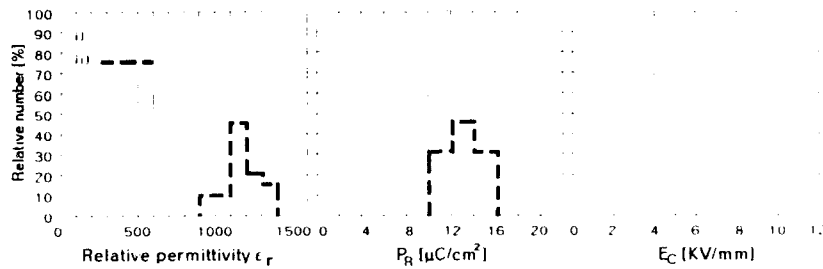


Fig. 6a: Distribution of ϵ_r , P_R and E_C of PZT films of the composition $\text{Pb}_{1-x}\text{Zr}_{0.53}\text{Ti}_{0.47}\text{O}_3$ on platinized Si-wafers, annealed at 700 °C for 10 min; i) 0.91 μm singly coated film ($\gamma=1.0$); ii) 0.67 μm singly coated film ($\gamma=1.1$)

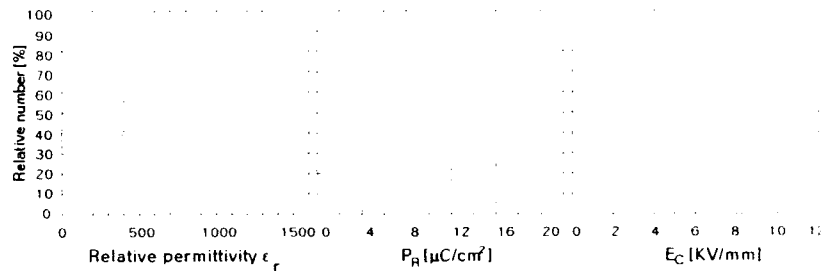


Fig. 6b: Distribution of ϵ_r , P_R and E_C of a PZT film of the composition $\text{Pb}_{1-x}\text{Zr}_{0.53}\text{Ti}_{0.47}\text{O}_3$, annealed at 700 °C for 10 min; 1.4 μm double coated film on platinized Al_2O_3 substrate ($\gamma=1.0$)

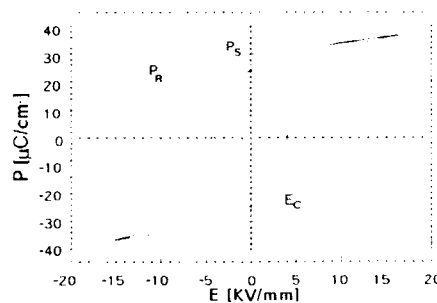


Fig. 7: Ferroelectric hysteresis loop of a 1.1 μm PZT film ($\text{Pb}_{1-x}\text{Zr}_{0.53}\text{Ti}_{0.47}\text{O}_3$) on Al_2O_3 ($U = 18 \text{ V}$, 50 Hz)

The heating conditions strongly influenced the electrical data of films prepared on platinized Si-wafers. Samples which were initially heated up to 500 °C on the hot plate showed much higher values for ϵ_r , P_r and a lower coercive force (Fig. 6a) than those prepared in the furnace ($\epsilon_r = 100-200$, $P_r = 4-12 \mu\text{C}/\text{cm}^2$, $E_c = 7-11 \text{ KV}/\text{mm}$). On platinized Al_2O_3 these values were independent of the conditions, but the coercive force was higher for films prepared on the hot plate. Systematic experiments with varying heating rates have to be performed, however preliminary results seem to indicate that the heating rate in the temperature range up to ca. 600 °C affects the phase composition and microstructure of the fired film. A fast heating rate below 500 °C helps to avoid the formation of the pyrochlore intermediate phase. In the temperature region around 500 °C the nucleation of the perovskite phase starts. It is assumed that the number of the nuclei can be influenced by the heating rate. Thus the further development of the microstructure is affected. The knowledge of these factors is important for the tailoring of ferroelectric properties.

CONCLUSIONS

Coating sols with long term stability have been developed that are used to produce crackfree PZT films with thicknesses up to 1 μm in one coating step. It was found that with a fast heating rate the fraction of perovskite phase was increased and cracking could be avoided. The crystallization behavior indicated that a homogenous distribution of the elements was maintained throughout the whole preparation process. A slight excess of PbO and proper annealing conditions helped to avoid the intermediate formation of an undesired pyrochlore phase. The crystallization of PZT started at 530 °C, complete transformation in the perovskite phase was reached at temperatures above 650 °C within minutes. A 1.1 μm thick film on Al_2O_3 -substrate annealed at 700 °C showed device worthy ferroelectric properties with typical values for P_r , E_c , and ϵ_r of 24 $\mu\text{C}/\text{cm}^2$, 4.5 KV/mm and 650. Values for ϵ_r exceeding 1000 were measured for films on platinized Si-wafers. The ferroelectric properties strongly depend on the heating conditions. Further studies will include the tailoring of the poling behavior for special applications.

REFERENCES

- [1] D.R. Uhlmann, G. Teowee, J.M. Boulton, S. Motakef and S.C. Lee, *J. Non-Cryst. Solids* 147&148 409 (1992).
- [2] G.H. Haertling in *Ferroelectric Films*, edited by A.S. Bhalla and K.M. Nair (Am. Ceram. Soc. 25, 1992) pp. 1-18.
- [3] N.J. Phillips and S.J. Milne, *J. Mater. Chem.* 1 893 (1991).
- [4] R.C. Mehotra, *J. Non-Cryst. Solids* 121 1 (1990).
- [5] R.W. Schwartz, R.A. Assink and T.J. Headly in *Ferroelectric Thin Films II*, edited by A.I. Kingon, E.R. Myers and B. Tuttle (Mater. Res. Soc. Proc. 243, Pittsburgh, PA, 1992) pp. 245-254.
- [6] C.D. Lakeman, J.F. Campion and D.A. Payne in *Ferroelectric Films*, edited by A.S. Bhalla and K.M. Nair (Am. Ceram. Soc. 25, 1992) pp. 413-439.
- [7] R. Papiernik, L.G. Hubert-Pfalzgraf and F. Chaput, *J. Non-Cryst. Solids* 147&148 36 (1992).
- [8] G. Teowee, J.M. Boulton and D.R. Uhlmann in *Better Ceramics Through Chemistry V*, edited by M.J. Hampden-Smith, W.G. Klemperer and C.J. Brinker (Mater. Res. Soc. Proc. 271, Pittsburgh, PA, 1992) pp. 345-350.

PREFERRED ORIENTATIONS FOR SOL-GEL DERIVED PLZT THIN LAYERS

TOSHIHIKO TANI, ZHENGKUI XU and DAVID A. PAYNE

Department of Materials Science and Engineering, Materials Research Laboratory and Beckman Institute, University of Illinois at Urbana-Champaign, Urbana, IL 61801

ABSTRACT

PLZT thin layers were deposited onto various substrates by sol-gel methods, and crystallized under different conditions and substrate treatments. Relationships are given for the chemical characteristics of the substrate's surface and the preferred orientations which develop on heat treatment. A preferred (111) orientation always developed for perovskite crystallized on Pt layers which contained Ti on the surface. This was attributed to the formation of Pt_3Ti and the role of heteroepitaxial nucleation and growth sites. In addition, a preferred (100) orientation was also obtained on unannealed $\text{Pt/Ti/SiO}_2/\text{Si}$ substrates which were free of Ti on the surface. This was attributed to self-textured growth with flat faces striving for minimum surface energy conditions. The results are discussed in terms of the importance of interfacial chemistry on the control of texture for crystallization of PLZT thin layers on coated substrates.

INTRODUCTION

Thin layers of lead zirconium titanate (i.e., PZT), and lanthanum-modified PZT (i.e., PLZT) in the perovskite structure, have potential applications in non-volatile memory elements, infrared sensors, microactuators and positioners, and electro-optic devices. Processing methods, include: RF sputtering, chemical vapor deposition, laser ablation and sol-gel processing. In this paper, we report on sol-gel processing which has the distinct advantage of precise compositional control, structural and chemical uniformity, and the use of inexpensive equipment. We extend the method to the development of textured microstructures with controlled orientations.

Materials with preferred orientation and epitaxy have unique and often better properties than those which are randomly oriented. Furthermore, thin layers with preferred orientation are preferred for basic studies on phase transformations when large single crystals are not available, as is the case for PZT and PLZT crystalline solutions. Epitaxy has been reported for PbTiO_3 and PZT thin layers deposited on single crystals, and on Pt films, by vapor phase methods.^{1,2} However, for sol-gel processing, epitaxial growth is thought to occur less likely due to the low mobility of nuclei in the solid matrix and competitive processes between homogeneous and heterogeneous nucleation and growth reactions. Preferred orientations have been reported for the sol-gel method on lattice matched SrTiO_3 and MgO single crystal substrates^{3,4} and some were confirmed to be epitaxial by TEM.⁵ In addition, preferred orientations were reported for perovskite thin layers deposited on polycrystalline Pt.^{6,7,8} (111) and (100) orientations can develop on a commonly used multilayer substrate, $\text{Pt/Ti/SiO}_2/\text{Si}$, where the face-centered Pt layer has a self-textured (111) orientation. Okuwada et al.⁶ reported a strong dependence of preferred orientation on heating rate for lead magnesium niobate (PMN), i.e., (111) at slow heating rates and (100) at faster heating rates. Spierings et al.⁸ reported that PZT layers could develop with preferred (100) orientation on as-prepared $\text{Pt/Ti/SiO}_2/\text{Si}$ substrates whereas (100) and (111) orientations developed on annealed substrates. However, no reasonable explanations have been proposed to-date which relate the processing parameters with the observed orientation results, and few studies have been carried out on the mechanism by which texture develops in sol-gel derived layers. This makes the study of heterogeneous nucleation an important issue.

In this paper, we report relationships between the chemical characteristics of different types of substrates and the preferred orientations which develop on crystallization of PLZT. The results indicate the types of mechanism by which texture develops for perovskite thin layers.

EXPERIMENTAL PROCEDURE

Preparation of Substrates

Pt sheet, (00.1)sapphire slices, and four types of platinumized silicon wafers were used as base substrate materials. Two types of (100)Si substrates (referred to as A and B) were supplied with the following thicknesses for Pt/Ti/SiO_2 : A; 300/20/500 nm and B; 150/20/500 nm. Additional

Table I Substrates for PLZT deposition

Substrate	Coating	Anneal (650 °C, 30 min, air)
Pt	No	No
(00.1)Al ₂ O ₃	No	No
(00.1)Al ₂ O ₃	Pt (300 nm)	Yes and No
(00.1)Al ₂ O ₃	Pt/Ti (300/100 nm)	Yes and No
A [Pt/Ti/SiO ₂ /(100)Si]	No	Yes and No
B [Pt/Ti/SiO ₂ /(100)Si]	No	Yes and No
B [Pt/Ti/SiO ₂ /(100)Si]	TiO ₂ (~10 nm)	Yes
C [Pt/Ti/SiO ₂ /(111)Si]	No	Yes and No
C [Pt/Ti/SiO ₂ /(111)Si]	Ti (~10 nm)	No
C [Pt/Ti/SiO ₂ /(111)Si]	TiO ₂ (~10 nm)	No
D [Pt/Ti/(111)Si]	No	Yes and No

substrates, Pt/Ti/SiO₂/(111)Si and Pt/Ti/(111)Si (referred to as C and D, respectively) were obtained with thicknesses of 300/100/300 nm for C and 300/100 nm for D. Additional coatings of Pt, Ti, Pt/Ti or TiO₂ were also deposited onto the surfaces of the substrates as indicated in Table I. Pt and Ti layers were deposited by electron-beam evaporation; and TiO₂ by a metallo-organic decomposition method, i.e., by spin-coating a 0.05 M solution of titanium isopropoxide in isopropanol, followed by heat-treatment at 300 °C. Since Ti has a hexagonal close-packed structure and Pt a face-centered cubic structure, Ti should develop with a preferred (00.1) orientation and Pt layers with a preferred (111) orientation. However, the substrates were not heated during initial deposition, and epitaxy would not develop (even on sapphire). Annealing of the configured substrates was investigated prior to sol-gel deposition. The substrates were characterized by X-ray diffraction (XRD), Auger electron spectroscopy (AES), scanning electron microscopy (SEM) and transmission electron microscopy (TEM).

Preparation of PLZT Thin Layers

PLZT compositions (7.5-8.0/70/30) near the morphotropic phase boundary were prepared according to Budd's method,⁹ with the exception that lead acetate trihydrate was previously dehydrated in vacuum at 100 °C for 20 hours before preparation of the lead precursor solution. The elimination of water was confirmed by FTIR analysis. Lead acetate was dissolved in methoxyethanol, refluxed for one hour, and distilled under vacuum. Titanium isopropoxide, zirconium n-propoxide and lanthanum isopropoxide were dissolved in methoxyethanol and the solution was refluxed and thermally distilled. The two precursor solutions were combined, refluxed and distilled. Partially hydrolyzed solutions were aged for one day prior to spin-casting onto substrates at 3000 rpm for 50 s. After each deposition, the coated substrates were placed on a hot plate at 300 °C. Specimens with five to ten deposited layers were later heat-treated in a box furnace between 500-800 °C for 1-30 min in air or oxygen. The typical thickness for a PLZT layer was 0.3 µm. PLZT layers deposited on annealed substrates were compared with those deposited on unannealed substrates. Two types of heating rates were used, i.e., fast (> 1000 °C/min) and slow (20 °C/min). The thermal processing conditions were varied and related to microstructure development and texture. The latter were characterized by XRD, SEM and TEM methods.

RESULTS

Characterization of Substrates

Observations in the SEM indicated the grain size and surface roughness increased with annealing temperature for Pt on A-type substrates, i.e., Pt/Ti/SiO₂/Si. Figure 1 gives XRD data obtained for (111)Pt, which shows the diffraction angle sharpened and shifted to a higher value with increasing annealing temperature. The shift in peak angle started at 400 °C, and saturated above 550 °C, for 30 minute anneals. The d-spacing for (111)Pt shifted from 2.266-9 Å to 2.252-4 Å, which is similar to 2.254 Å, the d-spacing for (00.4)Pt₃Ti (in the Ni₃Ti structure). Figure 2 gives AES data which indicates Ti transport through the Pt layer, and oxidation at the surface, after heat treatment at 650 °C for 30 min in air. The results agree with the observations of Bruchhaus et al.¹⁰ and Olowolafe et al.¹¹ Figure 3 gives TEM photographs of the platinized layer, before and after annealing. The grain size increased from 20-60 nm to 50-100 nm, and became more uniform with equiaxed shape. EDAX verified the Pt grains did not contain any Ti before annealing. Small

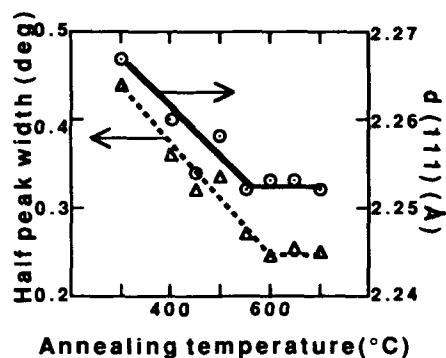


Fig.1 XRD data for the (111) Pt electrode.

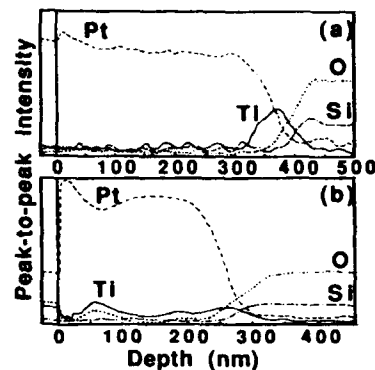


Fig.2 AES of A substrates (a) before and (b) after annealing at 650 °C for 30 min.

light grains, 10-20 nm in size, appeared at triple points after annealing, and were found to contain a significant amount of Ti as well as Pt. Electron diffraction analysis in the TEM was consistent with one set of diffraction rings for pure Pt on unannealed specimens. After annealing, the diffraction pattern consisted of a set of rings which were slightly shifted from that of Pt, with the inclusion of an additional set of rings. The d-spacings for the shifted set of rings correspond to Ni_3Ti -type Pt_3Ti and Cu_3Au -type Pt_3Ti , though only one type of weak superlattice spot was detected. The additional set of rings was attributed to rutile.

Examination of the B-type substrate, with the thinner Pt layer (150 nm), unexpectedly detected Ti present in the layer prior to annealing. The d-spacing for Pt (111) was 2.243-4 Å by XRD, which corresponds to 2.244 Å for (111) in the Cu_3Au -type structure. This suggests the B-type substrate was prepared at a higher temperature than the A-type substrate, with Ti diffusion into Pt. After annealing at 650°C for 30 min the peak also shifted to 2.253 Å for the B-type substrate.

Characterization of PLZT Thin Layers

XRD confirmed PLZT layers crystallized into the perovskite structure when heat-treated above 650 °C, regardless of the type of substrate used, except when deposited onto D-type substrates (Pt/Ti/Si) — where poor crystallinity and random orientations occurred. Table II lists preferred orientations in terms of XRD peak height ratios, (100)/(110)/(111). Layers crystallized on Pt sheet had a random orientation, with a XRD pattern close to perovskite powder. XRD patterns for fast-fired PLZT on unannealed and annealed A-type substrates are given in Fig. 4. The layers exhibit a strong preferred orientation, with (100) growth on unannealed substrates, and with (111) growth on annealed substrates. Layers fired at a slow rate (20°C/min) had a preferred (111) orientation, even on unannealed substrates. TEM examination determined that the layers were comprised of columnar-type perovskite grains, with a diameter of 0.1-0.2 micron at the base, and with a surface coating of nanocrystalline pyrochlore grains on the top. The surface layer was Zr-rich and Pb-deficient, in agreement with the results of Tuttle et al.¹² Microcrystallites containing Pb and Ti



Fig.3 TEM of Pt on A-type substrates (a) before and (b) after annealing at 650 °C for 30 min.

Table II Relative peak intensity data for PLZT layers crystallized by fast-firing at 700°C for 30 min.

Substrate	(100)/(110)/(111)
Pt	12/84/4
(00.1)Al ₂ O ₃	6/6/88
Pt/(00.1)Al ₂ O ₃	13/55/33
Pt/(00.1)Al ₂ O ₃ , annealed	5/68/27
Pt/Ti/(00.1)Al ₂ O ₃	6/11/83
Pt/Ti/(00.1)Al ₂ O ₃ , annealed	3/5/92
A[Pt/Ti/SiO ₂ /Si]	83/1/16
A[Pt/Ti/SiO ₂ /Si], annealed	10/1/89
B[Pt/Ti/SiO ₂ /Si]	4/5/91
B[Pt/Ti/SiO ₂ /Si], annealed	1/1/98
TiO ₂ /B[Pt/Ti/SiO ₂ /Si]	59/23/18
C[Pt/Ti/SiO ₂ /Si]	80/1/20
C[Pt/Ti/SiO ₂ /Si], annealed	13/10/77
Ti/C[Pt/Ti/SiO ₂ /Si]	8/28/64
TiO ₂ /C[Pt/Ti/SiO ₂ /Si]	45/10/45

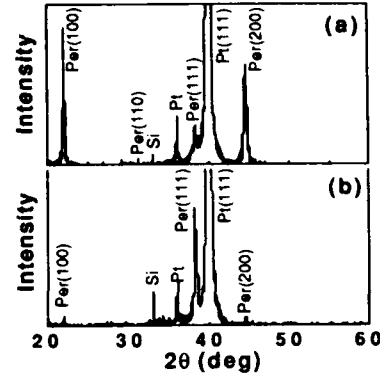


Fig.4 XRD for PLZT layers on (a) unannealed and (b) heat-treated A-type substrates.

were detected under the Pt electrode layer, and the lattice parameters were similar to PbTi₃O₇. PLZT layers on C-type substrates showed the same type of preferred orientation previously observed on A-type substrates (i.e., (100) before annealing and (111) after heat-treatment). B-type substrates had a strong tendency for (111) preferred orientation even without annealing. Previous characterization data indicated Ti present in the as-supplied Pt layers.

Figure 5 gives XRD data for PLZT on unannealed C-type substrates, with and without, a thin Ti layer (10 nm) on the top of the Pt electrode. PLZT layers on unannealed Ti/C-type substrates had a preferred (111) orientation, whereas layers on conventional C-type substrates had a strong (100) orientation. PLZT layers on TiO₂/C-type substrates showed both (100) and (111) orientations, and had a minor phase of PbTiO₃. A TiO₂ coating on top of unannealed B-type substrates was found to change the preferred orientation direction from (111) to (100).

XRD data for PLZT on Pt/Ti/Al₂O₃ indicated a strong preferred (111) orientation whereas layers crystallized on Pt/Al₂O₃ did not show any substantial effect, as shown in Fig. 6 and Table II. Annealing of Pt/Ti/Al₂O₃ substrates increased the preferred (111) orientation. XRD of PLZT thin layers crystallized directly on a (00.1) sapphire indicate a sharp perovskite (111) peak. This was attributed to epitaxial growth on the single crystal. The dimensional mismatch was 4.5 %.

DISCUSSION

The results indicate PLZT always crystallized with a preferred (111) orientation whenever Ti was present on the Pt surface. However, for a pure Pt surface, PLZT crystallized in a preferred (100) orientation or with random orientation. The effect were strikingly demonstrated for

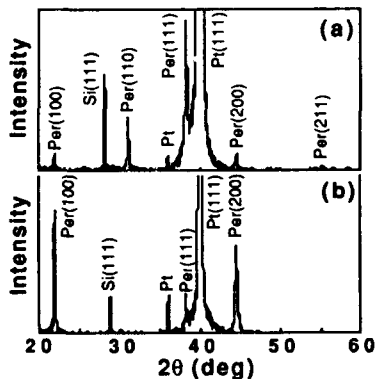


Fig.5 XRD for PLZT on unannealed C-type substrates (a) with, and (b) without, Ti on Pt.

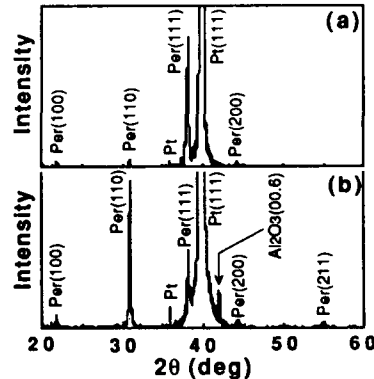


Fig.6 XRD for PLZT layers on heat-treated (a) Pt/Ti/Al₂O₃ and (b) Pt/Al₂O₃ substrates.

annealing studies on A- and C-type substrates where the preferred orientation could be changed from (100) to (111) by heat-treatment. Diffusion of Ti to the Pt surface is thought to be important for preferred (111) orientation. Figure 7 illustrates atomic configurations for Pt and Ti atoms in the Pt_3Ti structure (for the (111) plane in the Cu_3Au -type structure, or the (00.1) plane in the Ni_3Ti -type structure). By comparison with the (111) plane in the perovskite structure, the Ti locations are within 4 % lattice match. Formation of intermetallic Pt_3Ti compounds would reduce the interfacial energy between the electrode and the perovskite layer, thus favoring the epitaxial nucleation and growth of (111) perovskite planes parallel to the substrate. Preferred (111) orientations can therefore be attributed to epitaxial nucleation and growth. Preferred (111) orientation was also dominant for PLZT layers crystallized on $\text{Pt/Ti/Al}_2\text{O}_3$ substrate. However, random orientation occurred on pure Pt on Al_2O_3 . This is attributed to the relatively inert surface of Pt to oxides and the lack of epitaxial nucleation and growth sites. Thus, random orientations develop by competitive heterogeneous and homogeneous mechanisms.

Another type of preferred orientation can occur for a flat-face growing in a certain direction with a minimum surface energy.¹³ The preferred orientation, where the plane with the lowest surface energy grows parallel to the substrate, is termed a self-structure.¹⁴ An F-face, or a flat face, is the crystallographic face which contains two or more Periodic Bond Chains (PBC) — which are defined as an uninterrupted array of the strongest bonds between the building blocks in the structure.¹⁵ The Ti(Zr)-O bond array is a PBC for the perovskite structure. The (100) plane contains two PBCs so it is an F-face for growth. We have made calculations based upon the broken-bond model, using dissociation energies for PbO , TiO_2 and ZrO_2 as reference data for bonding energies, and determined the lowest surface energy to be for the (100) face. A supportive consideration is that perovskite single crystals can be grown in cubic form with (100) facets — because the (100) planes are the slowest growing planes, i.e., F-faces. Therefore, a (100) plane is preferred in non-epitaxial textured growth, and was observed in the present work whenever PLZT thin layers were crystallized on unannealed A- and C-type substrates. Wu et al.¹⁶ reported highly (100) oriented sputter-deposited PLZT thin layers on amorphous SiO_2 . This type of growth — off a featureless amorphous surface — can be attributed to the minimum energy F-face model. (100) self-textured growth can also occur when randomly-oriented heterogeneous nuclei form on a substrate and the (100) plane overgrows all others. Kushida et al.¹⁷ sputter-deposited PbTiO_3 on a (100) SrTiO_3 single crystal patterned with Pt and observed the overgrowth of epitaxial (100) PbTiO_3 layer over randomly oriented polycrystalline grains of Pt. Another important feature of the (100) plane in the perovskite structure is that the planes containing A^{+2} and B^{+4} ions construct an alternate layered structure with A^{+2} and B^{+4} ions on different planes. Layered structures are favored when one of the ionic species is deficient, e.g., for Pb loss to the atmosphere or by interfacial reaction with the substrate. TEM examination identified PbTi_3O_7 under the Pt electrode, giving rise to Pb deficient conditions at the interface for heterogeneous nucleation sites. This could be induced for PLZT thin layers crystallized on TiO_2/B -type substrates, where Pb deficiency would lead to the preferred (100) orientation. This type of self texture was reported for sputter-deposited LiNbO_3 on R-cut sapphire by Fujimura et al.¹⁸ In their work, Li-deficient conditions resulted in (01.2) LiNbO_3 epitaxial film formation rather than (10.0) LiNbO_3 growth, which has a better lattice match with the substrate and should exclusively form under Li-sufficient conditions. Li and Nb ions form an alternating layered structure in the direction normal to the (01.2) plane in

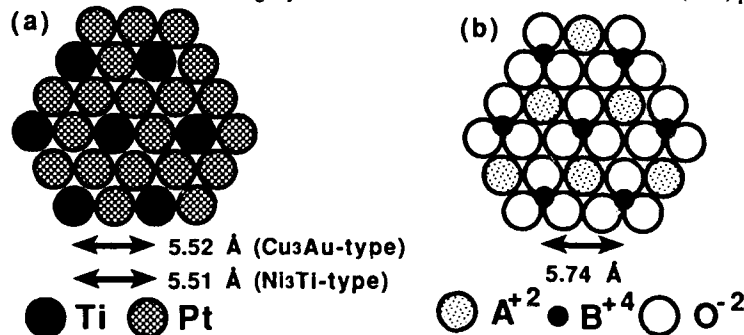


Fig. 7 Configurations for (a) the (111) plane for Cu_3Au -type Pt_3Ti and the (00.1) plane for Ni_3Ti -type Pt_3Ti , and (b) the (111) plane for perovskite PLZT.

LiNbO₃, which is favored under Li-deficient conditions.

The heating rate dependence for orientation effects reported by Okuwada et al. for PMN, and also observed in the present work for PLZT, can be attributed to competitive processes between epitaxial and self-textured growth and is related to Ti diffusion through the Pt layer. For slow heating rates, Ti diffuses through and forms Pt₃Ti at the interface for epitaxial crystallization of perovskite. The diffusion temperature for Ti is lower than the crystallization temperature for perovskite. Thus, we can attribute the formation of preferred (111) orientations due to the coexistence of Ti at the interface between Pt and PLZT. However, a preferred (100) orientation, on the other hand, can be attributed to self-textured F-face growth of the lowest surface-energy face and is favored under lead-deficient conditions.

CONCLUSIONS

PLZT was crystallized in the perovskite structure with, either a preferred (100) orientation or, a (111) orientation, through control of the surface chemistry between the Pt and the PLZT layer. A preferred (111) orientation was always obtained when the Pt layer had Ti on the surface. PLZT crystallized in the (111) direction by heteroepitaxial nucleation and growth off Pt₃Ti crystallites. In addition, a preferred (100) orientation could be obtained off Ti-free surfaces for unannealed Pt/Ti/SiO₂/Si substrates. This is considered to be self-textured growth, in accordance with minimum surface energy conditions, for flat-faced surfaces. The results for TiO₂/Pt/Ti/SiO₂/Si substrates indicate Pb-deficient conditions favor self-textured (100) growth.

ACKNOWLEDGMENTS

The authors are grateful to Mr. M. Toyoda of Murata Manufacturing Company and Mr. P. Schuele of Ramtron Corporation for supplying some of the substrates used and the metal layer combinations. The research was supported by DOE DMR-FG02-91ER45439 and by a grant from Toyota CRDL. The use of facilities in the Center for Microanalysis of Materials in the Materials Research Laboratory at the University of Illinois is gratefully acknowledged.

REFERENCES

- ¹K. Iijima, Y. Tomita and R. Takayama and I. Ueda, *J. Appl. Phys.*, **60**, 361 (1986)
- ²M. Adachi, T. Matsuzaki, T. Yamada, T. Shiosaki and A. Kawabata, *Jpn. J. Appl. Phys.*, **26**, 550 (1987)
- ³C. Chen, D. F. Ryder, Jr. and W. A. Spurgeon, *J. Am. Ceram. Soc.*, **72**, 1495 (1989)
- ⁴Y. Wang, P. Zhang, B. Qu and W. Zhong, *J. Appl. Phys.*, **71**, 6121 (1992)
- ⁵K. Okuwada, S. Nakamura, M. Imai and K. Kakuno, *Jpn. J. Appl. Phys.*, **30**, L1052 (1991)
- ⁶K. Okuwada, M. Imai and K. Kakuno, *Jpn. J. Appl. Phys.*, **28**, L1271 (1989)
- ⁷S. Hirano, T. Yogo, K. Kikuta, Y. Araki, M. Saito and S. Ogasahara, *J. Am. Ceram. Soc.*, **75**, 2785 (1992)
- ⁸G. A. C. M. Spierings, J. B. A. van Zon, M. Klee and P. K. Larsen, *Proceedings of the 4th International Symposium on Integrated Ferroelectrics*, 280 (1993)
- ⁹K. D. Budd, S. K. Dey and D. A. Payne, *Brit. Ceram. Soc. Proc.*, **36**, 107 (1985)
- ¹⁰R. Bruchhaus, D. Pitzer, O. Eibl, U. Scheithauer and W. Hoesler, *Mat. Res. Soc. Symp. Proc.*, **243**, 123 (1992)
- ¹¹J. O. Olowolafe, R. E. Jones, A. C. Campbell, P. D. Maniar, R. I. Hegde and C. J. Mogab, *Mat. Res. Soc. Symp. Proc.*, **243**, 355 (1992)
- ¹²B. A. Tuttle, R. W. Schwartz, D. H. Doughty and J. A. Voigt, *Mat. Res. Soc. Symp. Proc.*, **200**, 159 (1990)
- ¹³L. Ickert and H. G. Schneider, "Growth of Monocrystalline Layers", in *Advances in Epitaxy and Endotaxy*, edited by H. G. Schneider, V. Ruth and T. Kormány, Elsevier (1990)
- ¹⁴S. Goto, N. Fujimura, T. Nishimura and T. Ito, *J. Crystal Growth*, **115**, 816 (1991)
- ¹⁵P. Hartman, "Structure and Morphology", in *Crystal Growth*, edited by P. Hartman, North-Holland Publishing, Amsterdam (1973)
- ¹⁶A. Y. Wu, D. M. Hwang and L. M. Wang, *Proceedings of 8th International Symposium on Applications of Ferroelectrics*, 301 (1992)
- ¹⁷K. Kushida and H. Takeuchi, *Ferroelectrics*, **108**, 3 (1990)
- ¹⁸N. Fujimura, M. Kakinoki and T. Ito, *Mat. Res. Soc. Symp. Proc.*, **243** (1992) 545

SOLUTION CHEMISTRY OPTIMIZATION OF SOL-GEL PROCESSED PZT THIN FILMS

STEVEN J. LOCKWOOD, R. W. SCHWARTZ, B. A. TUTTLE, AND E. V. THOMAS
Sandia National Laboratories, Albuquerque, NM 87185

ABSTRACT

We have optimized the ferroelectric properties and microstructural characteristics of sol-gel PZT thin films used in a CMOS-integrated, 256 bit ferroelectric non-volatile memory. The sol-gel process utilized in our work involved the reaction of Zr *n*-butoxide, Ti isopropoxide, and Pb (IV) acetate in a methanol/acetic acid solvent system. A 10-factor screening experiment identified solution concentration, acetic acid addition, and water volume as the solution chemistry factors having the most significant effects on the remanent polarization, coercive field, ferroelectric loop quality, and microstructural quality. The optimal values for these factors were determined by running a 3-factor uniform shell design, modelling the responses, and testing the models at the predicted optimal conditions. The optimized solution chemistry generated 3-layer, 300-400 nm thick films on RuO₂ coated silicon substrates with coercive fields of less than 25 kV/cm (a 40-50 % improvement over the original solution chemistry), a remanent polarization of 25-30 $\mu\text{C}/\text{cm}$, and a reduction in the pyrochlore phase content below observable levels.

INTRODUCTION

PZT thin films are being investigated for an increasing number of diverse applications, including non-volatile memories, decoupling capacitors, optical storage devices, and DRAMs [1-4]. Sol-gel processing is proving to be a powerful technique for generating these films with the required tailored properties. However, there is still a very large gap in our understanding of the cause and effect relationships between the solution chemistry and the resulting ferroelectric properties. This is due, in large part, to the complexity of the sol-gel chemistry as well as the complexity of the physical transformation of the sol to the crystalline film. Studies of the solution chemistry effects in our system utilizing alkoxide/acetate precursors in methanol/acetic acid have provided a better understanding of what reactions are occurring and how reaction byproducts are an important factor in controlling reaction equilibria and rates [5,6]. Yet even with this information, we are not yet able to accurately predict how to manipulate the processing factors or chemical reactions to produce desired ferroelectric properties.

One approach to building this understanding is to systematically evaluate the solution chemistry factors and develop models relating ferroelectric properties to these factors. The work described below is in support of a program to build a 256 bit ferroelectric non-volatile memory. The sol-gel process employed in this work utilized Zr and Ti alkoxides and Pb(IV) acetate in a methanol/acetic acid solvent system. An improvement in coercive field (to meet voltage operating requirements) and in PZT microstructure (to achieve the required yield for $5\mu\text{m} \times 5\mu\text{m}$ capacitors) was the goal of this study.

The initial phase of the study involved screening a number of solution chemistry and processing factors to identify those having the greatest impact on properties. This was followed by a statistical experimental design which generated data for modelling the various responses. The models were then tested and an optimized solution chemistry was identified.

EXPERIMENTAL

Solution Synthesis, Film Fabrication, and Electrical Property Characterization

The Inverted Mixing Order process, employed in this study, is a modification of the process of Yi, Wu, and Sayer [7] in which the order of precursor addition has been reversed. All films were 53:47 compositions with 10% excess Pb. The process flow diagram is shown in Figure 1. PZT films were deposited on silicon substrates with RuO₂ bottom electrodes by spin coating for 30 sec. Film thicknesses varied from 0.1 to 0.8 μm , depending on the number of layers, the solution concentration, and the spinner speed. Individual layers were heat treated at 310°C for 3 min to decompose the residual organics. The films were crystallized at 675°C for 30 min (50°C/min ramp rate) in ambient air. Ferroelectric properties were measured on a Radiant Technologies RT66A operated in virtual ground mode with an applied field of 250 kV/cm.

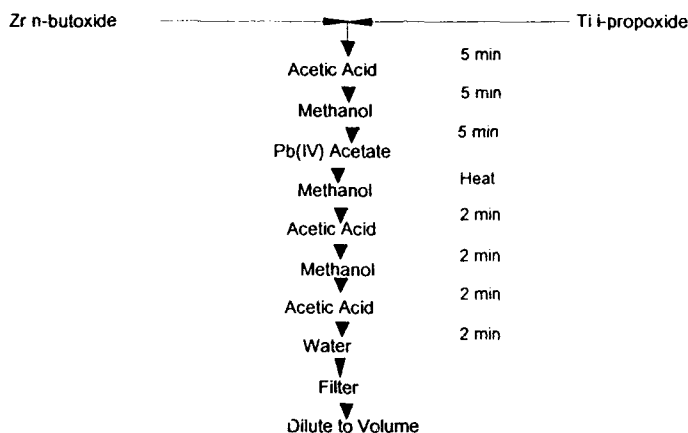


Figure 1. The IMO Process

Plackett-Burman Screening Study

Ten factors (eight solution chemistry, two film deposition) were initially identified as potentially having significant effects on material properties. To fully model this number of factors would require well over 100 experiments. To reduce this task to a manageable level it was necessary to screen the factors to identify those having the greatest impact on the desired responses. A modified Plackett-Burman screening design, requiring only 15 experiments, was employed [8]. Table I lists the factors, the range of factor levels, and for comparison, the nominal values. The range of design values was chosen to be as wide as technically reasonable, and if possible, to bracket the nominal values.

Response Surface Modelling

From the screening study three factors were identified as having significant effects on several of the measured responses. A three-factor uniform shell design was chosen (see Figure 2 for a graphical representation) [9]. This allowed for either a Main Effects + Interactions (ME+I) model or a Quadratic model to be fitted to the data. The center point of the design was run in triplicate. All other factors were set to their nominal values.

Table 1. Plackett-Burman Screening Design Factors

Variable	Screening Values (Low or High)	Nominal Value
Zr/Ti Reaction Time	0 or 15 min	5 min
Acetic Acid Amount	¼ or 2 times nominal	4:1 HOAc to Zr+Ti
Acetic Acid Reaction Time	0 or 15 min	5 min
Solution Concentration	0.4 or 0.8 M	0.4 M
Pb Dissolution Temperature	75 or 100°C	75°C
Refluxing	No or Yes	No
Post-dissolution Acetic Acid	0 or 10 mL	10 mL
Water Volume	0.5 or 5 mL	2 mL
Number of Film Layers	2 or 4	4
Spinner Speed	1000 or 6000 rpm	3000 rpm

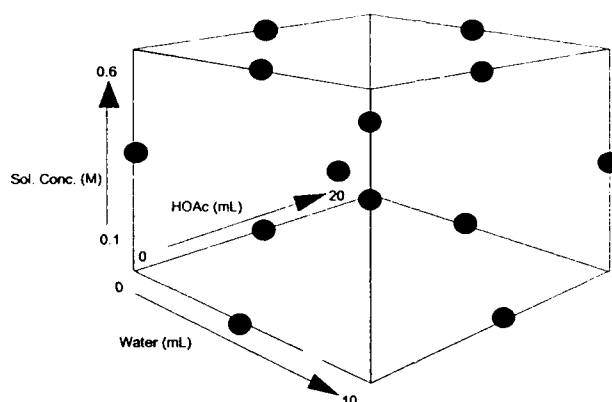


Figure 2. Uniform Shell Design for 3 Factors

RESULTS AND DISCUSSION

Plackett-Burman Screening Study

The value of a screening design is that the effects of a large number of factors can be evaluated with relatively few experiments. However, there is a trade-off. The results from the screening design are confounded; that is, the main effect (the effect of a single factor) and interactions (effects produced by the synergism or antagonism of two or more factors) are combined. The simplifying assumption invoked (and it is generally valid) is that main effects will dominate.

Table II summarizes the results of the screening study. Six of the ten factors had statistically significant effects on one or more of the responses. Several of the responses showed no measurable dependence on any of the factors. However, several factors exhibited strong effects on coercive field, the ferroelectric response we were most interested in improving. Three factors (post-dissolution acetic acid, solution concentration, and water volume) were chosen for further study. These factors also exhibited statistically significant effects on several of the other responses. Looking at the direction of effects for the three major factors it can be seen that the desired direction of change is antagonistic among the responses. For example, to improve coercive field (i.e., lowering the value) the model requires increasing the solution concentration. However, the models for loop quality (higher values are associated with higher quality), P_r , and capacitor yield all require decreasing solution concentration to improve those properties. Clearly the optimized

conditions will be a compromise and therefore are not readily predictable without a more detailed examination of their effects and possible interactions.

Table II. Summary of the Plackett-Burman Screening Study

Decreasing Importance of Factor ↓	Decreasing Fit to the Model →			
	Coercive Field	Loop Quality	Remanent Polar.	Capacitor Yield
	Post HOAc (-)	Post HOAc (-)	Post HOAc (-)	Sol'n Conc. (-)
	Sol'n Conc. (-)	Sol'n Conc. (-)	# of Layers (+)	
	Water Vol. (-)	Spinner Speed (+)	Sol'n Conc. (-)	
	Initial HOAc (+)	Water Vol. (-)		
	Spinner Speed (+)	Initial HOAc(-)		

Note: The sign associated with the factor indicates the direction of the effect from the low level to the high level (e.g., a "Sol'n Conc. (-)" indicates that the numerical value of the response decreases from 0.4 M to 0.8 M).

Response Surface Modelling

A three-factor uniform shell design was performed to study the effects of solution concentration, the post-dissolution acetic acid amount, and the water volume in more detail. Table III lists the range of values measured for the responses. The bottom row of the table gives the values for the nominal composition. No individual design run had the best value for all responses, but several compositions yielded responses that were each individually superior to those of the nominal composition.

Table III. Summary of the 3-Factor Uniform Shell Design Results

	P_r ($\mu\text{C}/\text{cm}^2$)	P_s ($\mu\text{C}/\text{cm}^2$)	E_c (kV/cm)	V_c (V)	Capacitor Yield (%)	Microstruc. Quality (0-5)*	Loop Quality**
Design Runs	0 - 47.2	0 - 78.9	26.1 - 200+	0.96 - 4.97	0 - 100	0 - 5	0 - 105
Nominal	23 - 30	45 - 50	40 - 45	1.5 - 2.0	90 - 100	3	40

* 0 (poorly defined) to 5 (fully dense microstructure with 1-5 μm rosettes)

** A figure of merit to quantify hysteresis loop quality using P_r , P_s , and E_c .

Two models were fitted to the data. An ME+I model allows for simple response surfaces. The quadratic model allows for more complex response surfaces, including curvature. As an illustrative example, the coercive field models are presented below. All the other models had similar shaped response surfaces.

Main Effects + Interactions Model

$$E_c = 102.1 + 35.6 \cdot X_1 - 86.0 \cdot X_2 + 4.4 \cdot X_3 + 9.6 \cdot X_1 \cdot X_2 + 0.8 \cdot X_1 \cdot X_3 - 9.7 \cdot X_2 \cdot X_3 \quad (1)$$

Quadratic Model

$$E_c = 31.7 + 35.6 \cdot X_1 - 86.0 \cdot X_2 + 4.4 \cdot X_3 + 9.6 \cdot X_1 \cdot X_2 + 0.8 \cdot X_1 \cdot X_3 - 9.7 \cdot X_2 \cdot X_3 + 36.1 \cdot X_1^2 + 42.9 \cdot X_2^2 + 44.1 \cdot X_3^2 \quad (2)$$

Where X_1 = Acetic Acid; X_2 = Solution Concentration; X_3 = Water Volume in normalized design units (-1 to +1).

From inspection of the models it can be seen that solution concentration is the dominant factor in determining E_c . Solution concentration is the dominant term in all of the other response models.

as well. To determine the optimal composition a grid search program was run with criteria set for each response. A "sweet spot", a composition or compositions meeting all criteria, was identified from each model (see Table IV).

Table IV. Criteria and "Sweet Spots" for Each Model

Criteria for selecting "sweet spots":

$P_f \geq 25 \mu\text{C}/\text{cm}^2$ $P_s \geq 40 \mu\text{C}/\text{cm}^2$ V_c 0.5 to 1.5 V E_c 10 to 40 kV/cm
Capacitor Yield $\geq 99\%$ Microstructural Quality ≥ 4 Loop Quality ≥ 50

	Main Effects + Interactions	Quadratic
Post Dissolution Acetic Acid	0 - 4 mL	5 - 10 mL
Solution Concentration	0.50 - 0.54 M	0.56 M
Water Volume	0 - 6 mL	9 - 10 mL

Common between the models is the higher solution concentration, but as might be expected, it is not at the maximum value of the modelled space. Acetic acid ranged from zero up to the nominal composition volume. The water volume covered the entire design space, but both "sweet spot" regions favored water volumes greater than nominal. To test the models three compositions were run; one from the ME+I model and two from the Quadratic model. The compositions and property results are presented in Table V along with the nominal composition for comparison.

Table V. Comparison of the Nominal Composition with the "Sweet Spots"

	Acetic Acid (mL)	Sol'n Conc. (M)	Water Vol. (mL)	P_f ($\mu\text{C}/\text{cm}^2$)	E_c (kV/cm)	V_c (V)	Micro. Quality	Loop Quality
Nominal	10	0.40	2	27	43	1.7	3	40
ME+I	0	0.50	5	26.9	23.9	1.0	4	105.2
Quad. 1	10	0.56	10	25.0	33.2	1.2	4	50.0
Quad. 2	5	0.56	10	29.6	33.0	1.2	3	41.4

All three "sweet spot" runs met the predicted criteria and were an improvement over the nominal composition, particularly with respect to E_c . The ME+I "Sweet Spot" was the superior composition, showing improvements over the nominal composition in every measured response except for P_f where it maintained the nominal value. Comparison of actual values to the model is of limited value. Several of the samples in the original design had extremely poor properties and the measured values for polarization and coercive field were quantitatively meaningless. However, these values qualitatively represented the responses. Therefore, the models generated were successfully used to predict compositional areas to investigate, rather than to quantitatively predict actual film properties.

As for using the information from this study to develop a more fundamental understanding of the solution chemistry, some cautious conclusions can be drawn. The compositions that represented improved properties were consistent with a solution chemistry that generates a denser, perhaps more highly crosslinked structure. Increasing the water volume would be expected to increase hydrolysis, generating more species for condensation. However, water is a byproduct of some of the condensation reactions, and therefore excess water could inhibit condensation. Similar effects have been noted in the PbTiO_3 system [10]. With solution concentration, a higher concentration should promote condensation and aid film densification by reducing the amount of organic removal required. But too high of a concentration leads to film cracking and organic removal problems. The role of acetic acid following the Pb dissolution is not well understood. Sufficient acetic acid is added prior to the lead acetate to completely chelate the Zr/Ti alkoxides. However, the post-dissolution acetic acid may be more than a simple solvent. It may be acting as a

weak acid catalyst. Acid catalysis leads to linear polymerization rather than crosslinkages in many sol-gel systems, whereas base catalysis generally promotes crosslinking [11].

Some preliminary work has been done to test these ideas. If crosslinking is important, substituting a base for the acetic acid at the back end of the process would be expected to yield improved films. When ammonium hydroxide was used in place of the post-dissolution acetic acid, a dense film microstructure with no observable pyrochlore was generated. However, the ferroelectric properties were only comparable to the nominal composition. The role of solution concentration remains to be resolved. It may be a physical effect; a denser gel/film as a result of less solvent/organics. Or the sol may have a different polymeric structure due to concentration effects on reaction equilibria. Additional experimentation will be required to resolve this, possibly by studying dilution and viscosity effects.

CONCLUSION

A sol-gel process utilizing alkoxide and acetate precursors in an acetic acid/methanol solvent system was optimized to generate 53/47 PZT thin films with improved microstructure and ferroelectric properties. Ten solution chemistry and film processing factors were screened for their ability to measurably impact a variety of responses. The three most statistically significant factors with respect to coercive field (post-dissolution acetic acid, solution concentration, and water volume) were evaluated in greater detail using 3-factor uniform shell design. Models generated from the data identified several compositions predicted to be superior to the nominal composition. Testing of these models confirmed these compositions as superior. Coercive field was reduced from over 40 kV/cm to less than 25 kV/cm. Pyrochlore phase clearly visible in the nominal composition films was no longer observable in the optimized composition films.

ACKNOWLEDGMENTS

This work was supported by the U.S. Department of Energy under contract DE-AC04-76DP00789. We would like to thank Christine Roth for her efforts in preparing the sol-gel solutions and performing the film depositions.

REFERENCES

1. S. L. Swartz, S. J. Bright, and J. R. Busch in *Ceramic Transactions*, **14**, 159-178 (1990).
2. J. Fukushima, K. Kodaira, and T. Matsushita, *J. Mater. Sci.*, **19**, 595 (1984).
3. R. W. Vest and J. Xu, *Ferroelectrics*, **93**, 21 (1989).
4. G. H. Heartling, *Ferroelectrics*, **116**, 51 (1991).
5. R. W. Schwartz, B. C. Bunker, D. B. Dimos, R. A. Assink, B. A. Tuttle, D. R. Tallant, and I. A. Weinstock, *Integrated Ferroelectrics*, **2**, 243-254 (1992).
6. R. W. Schwartz, R. A. Assink, and T. J. Headley in *Ferroelectric Thin Films II*, edited by A. I. Kingon, E. R. Meyers, and B. A. Tuttle (Mater. Res. Soc. Proc. **243**, Pittsburgh, PA, 1992) pp. 245-254.
7. G. Yi, Z. Wu, and M. Sayer, *J. Appl. Phys.*, **64** (5), 2717 (1988).
8. R. L. Plackett and J. P. Burman, *Biometrika*, **33**, 305-325 (1946).
9. D. H. Doehlert, *Appl. Stat.*, *JRSS-C* (1970).
10. K. D. Koefor in *Better Ceramics Through Chemistry*, edited by C. J. Brinker, D. E. Clark, and D. R. Ulrich (Mater. Res. Soc. Proc. **32**, New York, NY, 1984) pp. 15-24.
11. K. D. Budd, S. K. Dey, and D. A. Payne, *Brit. Ceram. Soc. Proc.*, **36**, 107 (1985).

MICROSTRUCTURAL CHARACTERIZATION OF SOL-GEL DERIVED LEAD TITANATE DEPOSITED ON SILICA

JOSEPH M. SCHWARTZ, LORRAINE FALTER FRANCIS, AND LANNY D. SCHMIDT
University of Minnesota, Department of Chemical Engineering and Materials Science,
Minneapolis, MN 55455

ABSTRACT

The microstructural evolution of lead titanate prepared by a sol-gel method was examined using transmission electron microscopy (TEM) following treatments in air at progressively higher temperatures. TEM specimens were prepared by spin coating a film or dispersing particles onto specimen grids coated with SiO_2 or SiO_2 with a barrier layer. The effects of different barrier materials, thermal treatment conditions, and the addition of platinum particles were examined. Lead titanate formed crystalline perovskite at ~ 550 - 600°C on all support materials examined. On SiO_2 supports, the pyrochlore phase formed at lower temperatures and converted partially to perovskite at higher temperatures. Barrier layers of TiO_2 , Al_2O_3 and polyimide prevented pyrochlore formation.

INTRODUCTION

Lead titanate, PbTiO_3 (PT), is a well-known ferroelectric that is under investigation for pyroelectric, memory, and micromechanical applications. For many devices, the ferroelectric thin layer must be integrated with a Si semiconductor by depositing and heating the layer on Si, SiO_2 , or a platinum layer which is integrated with Si. Under some conditions, interdiffusion between the substrate and film can degrade film properties and result in the formation of nonferroelectric phases [1-3]. The ability to follow the microstructural changes and possible reactions with the substrate that accompany thermal treatments of PT thin layers is of great interest for improving process compatibility and properties.

TEM is an excellent method for the study of microstructure development, especially when combined with energy dispersive spectroscopy (EDS) and electron energy loss spectroscopy (EELS) for analysis of crystal structure and chemical composition. For a study of microstructure evolution, a useful specimen preparation method would involve depositing a coating directly onto a special TEM grid that acts as an electron transparent substrate capable of being heated to processing temperatures. In a previous study of model catalyst systems, TEM samples were prepared by evaporating the metal catalyst particles onto SiO_2 and Al_2O_3 support layers on TEM grids [4]. The microstructural evolution of the *same areas* of the sample was observed following sequential heat-treatments in different atmospheres. We now report on the use of a similar technique to study the evolution of sol-gel derived thin layers and particles of lead titanate following heat-treatments in air at different temperatures.

EXPERIMENTAL

Figure 1 outlines the methods used to prepare TEM specimens and study microstructure development. The procedure involved three stages: (i) preparation of a silica coated TEM grid to act as a support, (ii) deposition of an alkoxide-based solution or dispersion of sol-gel derived particles onto the TEM support grid, and (iii) investigation of the microstructure by alternating between heat-treatments in a furnace and TEM examinations.

The TEM support grids were prepared by a series of vacuum depositions and thermal treatments. First, a Si film ($300 \pm 50 \text{ \AA}$) was vacuum evaporated onto a Formvar coated gold microscope grid (400 mesh, tabbed pinpointer grid; Pelco Co.). The Si coated grid was heated in oxygen at 800°C for 20 hours to burn off the Formvar and oxidize the Si into a uniform film of amorphous SiO_2 ($\sim 600 \text{ \AA}$). A thin film of platinum ($\sim 20 \text{ \AA}$) was then deposited onto half of the support grid by vacuum evaporation. To disperse the film into small Pt particles, the grid was heated in hydrogen at 650°C for 6 hours. The SiO_2 coating provides an electron transparent support for a sol-gel layer and is also capable of being heated to high temperatures without a change in structure. Titania and alumina coatings were prepared on the SiO_2 covered TEM grids by similar methods; however, these layers were crystalline after oxidation.

A PT methoxyethoxide solution was synthesized according to the procedure described by Budd *et al.* [5]. A precursor solution (0.1 M PT, 0.1 M H_2O , 0.01 M NH_4OH) suitable for

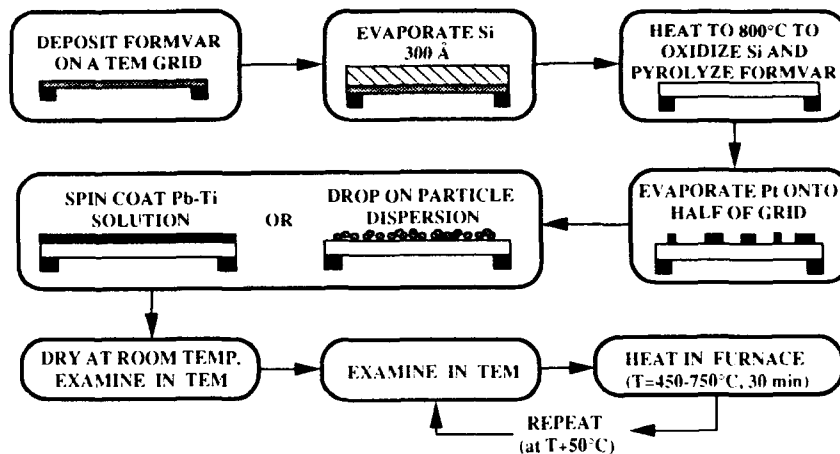


Figure 1. Outline of sample preparation and procedure.

coating was prepared and deposited onto the TEM support grid by a spin coating method (60 sec, 2000 rpm). Particle dispersions were prepared by controlled reaction of the alkoxide solution with water. The grid was dried at room temperature and then studied in the TEM.

TEM was performed in a Philips CM30 microscope. EDS was carried out in the microscope using an EDAX PV9900 spectrometer to measure quantitative chemical composition. EELS was performed in the microscope using a Gatan model 666 spectrometer. To follow microstructure changes with thermal treatment, the specimens were alternately heated and examined in the TEM. Heat-treatments were carried out in a tube furnace in air. The specimens were heated in stages at successively higher temperatures from 450°C to 700°C, in steps of 50-100°C; each stage was 30 minutes at temperature.

RESULTS AND DISCUSSION

1) Development of Thin Layer Amorphous Structure

Figure 2 shows the TEM photomicrographs of a thin sol-gel PT layer on a SiO₂ support grid heat-treated in stages up to 500°C. The microstructures shown were from a region of the support that did not have Pt particles. In this analysis, the same area of the specimen was examined after each heating as indicated by the arrows, which point to the same places in each micrograph. At temperatures below 500°C, electron diffraction showed that the PT layer remained amorphous. On a fine level, microstructures appeared to have a slightly grainy texture that became more coarse as the temperature increased. The most interesting features present in the layer were circular areas of low contrast that appear in the dried state (Fig. 2A). These areas decrease in size upon heating to 450°C (Fig. 2B) and completely disappear after heating at 500°C (Fig. 2C). For amorphous materials, contrast in TEM can come from two possible sources, thickness, and atomic number. The low contrast areas in our TEM specimens are either thinner or have a higher concentration of lower atomic number species (e.g., Ti) than the darker areas.

EELS was used to qualitatively determine the composition of low and high contrast features, and to measure the specimen thickness. EELS spectra from both the low and high contrast areas showed the presence of both Pb and Ti. A strong carbon edge was visible in all areas of the sample before heating and disappeared after the 450°C heat-treatment. The ceramic layer was on average 400 Å thick at the completion of heating as determined by analysis of the EELS data. Thickness measurements on selected areas using EELS showed that the low contrast areas were about 150-200 Å thinner than the high contrast areas.

EDS was used to determine the elemental composition of the low contrast areas compared to the entire sample. Since the TEM samples are thin, the lateral spatial resolution of EDS is only

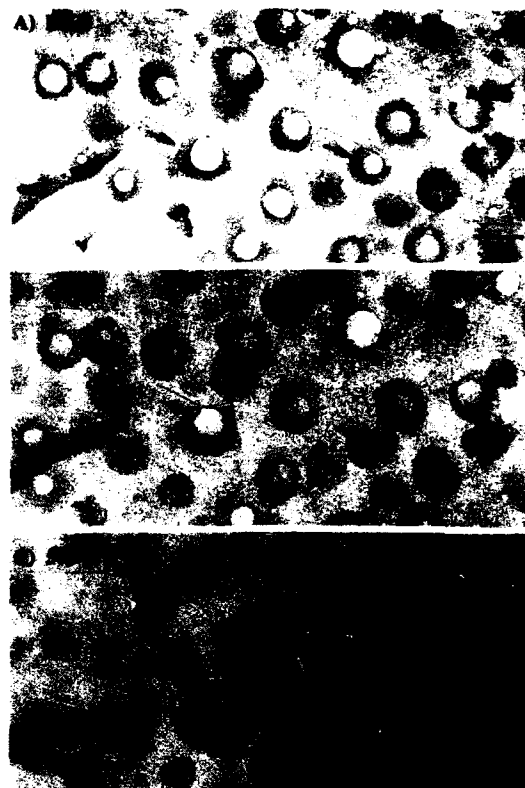


Figure 2. TEM micrographs of a PT layer on a SiO_2 support with no Pt after thermal treatment stages of (a) drying, (b) 450°C for 30 min., and (c) 500°C for 30 min. All micrographs are from one specimen showing the same area.

slightly larger than the probe size used. Probe sizes as small as $\sim 50 \text{ \AA}$ were used, and the measured Pb:Ti ratio changed by less than 5% from the low to high contrast areas. This is below the level of significance due to uncertainties in background subtraction. Thinner areas could form during drying from localized solvent evaporation or formation of discontinuities due to poor wetting. These drying induced artifacts could also result in a build up of PT coating in surrounding areas, accounting for the dark rings around the low contrast areas. Based on observations of sol-gel derived PT particles dispersed on SiO_2 supports, the disappearance of these features after the 500°C heat-treatment may be due to interdiffusion between the film and the SiO_2 support. The addition of Pt particles has little or no effect on the amorphous structure of the lead titanate film under the conditions we examined.

2) Crystalline Phase Development of Thin Films

Figure 3 shows a continuation of the microstructure evolution shown in Fig. 2 for heat-treatment, up to 650°C . Heating the sample to 550°C resulted in the formation of a crystalline

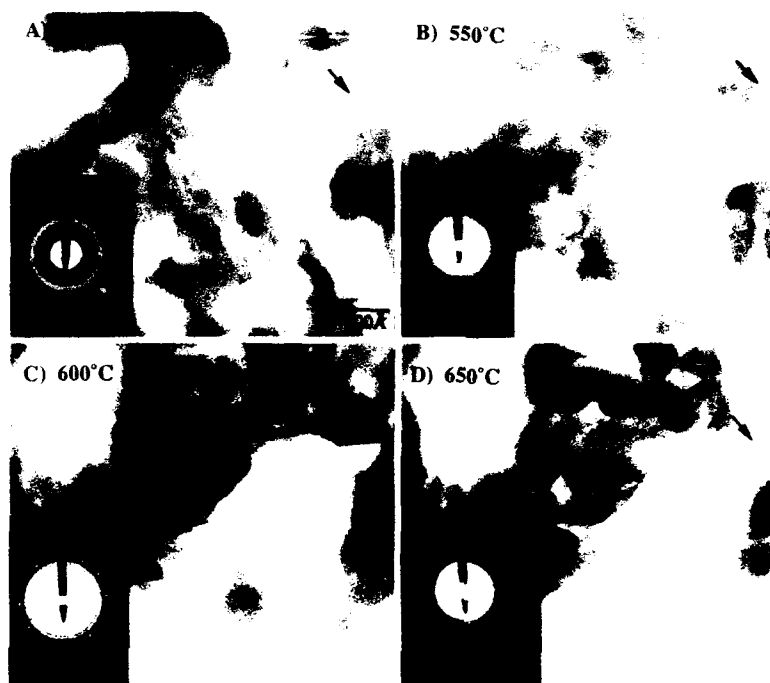


Figure 3. TEM micrographs and electron diffraction patterns of a PT layer on a SiO_2 support with no Pt after thermal treatment stages of (a) 500°C for 30 min., (b) 550°C for 30 min., (c) 600°C for 30 min., and (d) 650°C for 30 min. All micrographs are from the same specimen as shown in Fig. 2.

phase which has a cubic structure ($a = 10.5 \text{ \AA}$). The electron diffraction data is consistent with the pyrochlore form of lead titanate, $\text{Pb}_2\text{Ti}_2\text{O}_6$. This form of PT was first described by Martin [6] for glass ceramic samples and later found in many sol-gel derived lead-based perovskites. Pyrochlore does not possess the desired dielectric and ferroelectric properties of perovskite, but the pyrochlore form is metastable and will transform to perovskite with higher temperature heating in many cases. The microstructure of the pyrochlore in the thin layer specimen is not clearly defined, but the ring formation in the electron diffraction pattern indicates that the grain size is small. The perovskite phase begins to form upon heating to 600°C , as determined by electron diffraction (Fig. 3C). However, the pyrochlore phase is also present with perovskite. When the specimen was heated further at 650°C for 30 minutes (Fig. 3D), the pyrochlore did not transform completely to perovskite. Both phases are still present after heating to 700°C and 750°C (not shown). No other crystalline phases were found by electron diffraction; amorphous phases such as lead silicates cannot be identified in the TEM. The lack of crystalline TiO_2 or PbO at any temperature supports the earlier conclusion that chemical heterogeneities do not form on drying.

The formation and persistence of pyrochlore in the TEM specimen can be explained by considering the effects of Si contamination and layer thickness. Pyrochlore formation is observed most often when films are deposited onto quartz, glass or silicon substrates. The diffusion of Si from the substrate into the film or Pb diffusion into the substrate has been cited as the cause for pyrochlore formation on Si containing substrates. The effect of Si addition to

sol-gel derived PT powders has been studied in detail by Wright and Francis [7]. They found that unmodified PT powders crystallized directly into the perovskite phase at 500°C, but PT gels modified with even small additions of Si (<2 mole%) formed first into pyrochlore and then transformed either partially or completely to the perovskite phase at a higher temperature (e.g., 650°C for 10 mole % Si addition). The higher than expected formation temperature for perovskite in the TEM specimens is probably related to Si contamination. Very thin layers will have an increased effect of interdiffusion. Yamaguchi also reported that the formation of pyrochlore occurs most easily in thinner films prepared from very dilute alkoxide solutions [2]. Tensile stresses resulting from drying and crystallization could also cause the less dense pyrochlore phase to be favored in thin films.

Several methods have been developed for avoiding or inhibiting pyrochlore formation in PT-based sol-gel thin films. Rapid thermal processing is often an effective method to avoid formation of low temperature metastable phases, and also to minimize diffusion effects [8]. In a separate experiment, we heated a TEM specimen directly to 700°C after heating at 400°C to pyrolyze organics. Both pyrochlore and perovskite were formed in this case; thus, for very thin PT layers on SiO₂, the formation of the pyrochlore phase could not be avoided by rapid heating. Platinum has also been used to promote perovskite formation. In our study, Pt particles did not affect the crystallization vs. temperature behavior of lead titanate within the 50°C resolution of our experiments, but they did promote perovskite formation by epitaxial growth [9].

Barrier layers are an effective means of preventing interdiffusion and pyrochlore formation [10,11]. No pyrochlore formed when there was a barrier layer of Al₂O₃ or TiO₂ between the lead titanate and the SiO₂. Perovskite formed on these supports after the 550°C treatment. However, an intervening oxide barrier layer may affect the final ferroelectric properties of the layer (e.g., dielectric constant). We have investigated an alternative barrier layer technology in which a polymer layer prevents diffusion during crystallization and is then pyrolyzed.

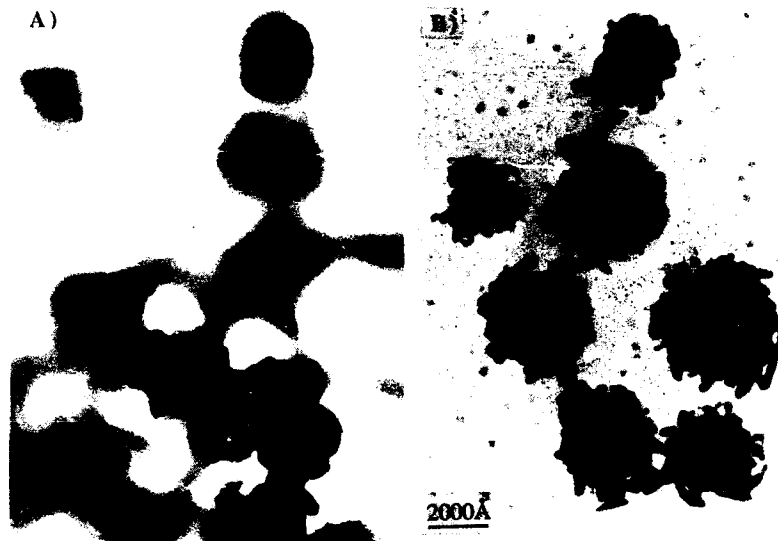


Figure 4. TEM micrographs of sol-gel derived PT particles on a SiO₂ support after thermal treatments of (a) 550°C for 30 min., (b) 600°C for 60 min. (a) is from a sample with no polyimide and (b) had a polyimide diffusion barrier layer.

Figure 4 shows the effects of a polyimide layer on the crystallization of small particles of lead titanate on a SiO_2 support. Small particles were used instead of thin films in order to clearly demonstrate the effects of reactions with the support. The polyimide layer inhibited reaction between lead titanate and SiO_2 . When no barrier layer is used (Fig. 4A), the interaction results in the formation of holes in the SiO_2 support adjacent to every particle. When this sample (without polyimide) was heated to 600°C , the TEM specimen was completely destroyed. When a polyimide diffusion barrier was present (Fig. 4B), particles crystallize without interaction with the SiO_2 support. Another advantage of a barrier layer was that no pyrochlore is formed. After lead titanate crystallizes into perovskite, it will not transform into pyrochlore and appears to have less reactivity with SiO_2 . EELS showed that there was no carbon or nitrogen remaining on the sample, indicating that the polyimide layer was completely pyrolyzed, leaving only perovskite lead titanate. The polyimide diffusion barrier will be discussed in more detail elsewhere [9].

SUMMARY

A new technique has been developed to study microstructural evolution and substrate interactions in thin ceramic films and applied to lead titanate. Thin films crystallized into pyrochlore, $\text{Pb}_2\text{Ti}_2\text{O}_6$, at about 500°C on amorphous SiO_2 supports due to interactions between PT and SiO_2 . Crystalline perovskite, PbTiO_3 , the desired phase, formed at higher temperatures ($\sim 550^\circ\text{C}$), but the pyrochlore phase persisted. Platinum particles did not affect the crystallization temperature of PT on SiO_2 supports under the conditions investigated. Pyrochlore did not form on crystalline Al_2O_3 or TiO_2 supports at any temperature; perovskite was the sole crystalline phase forming at $\sim 550^\circ\text{C}$. The use of a fugitive polyimide barrier layer holds promise for preparation of Pb-based ferroelectrics on Si-containing substrates because it successfully prevented pyrochlore formation in particles on SiO_2 .

ACKNOWLEDGEMENTS

The assistance of John Wright in solution preparation is appreciated.

REFERENCES

1. S. H. Rou, T. M. Graettinger, A. F. Chow, S. N. Soble, D. J. Lichtenwalner, O. Auciello, and A. I. Kingon in *Ferroelectric Thin Films II*, edited by A. I. Kingon, E. R. Myers, and B. A. Tuttle (Mater. Res. Soc. Proc. **243**, Pittsburgh, PA, 1992) pp. 31-91.
2. Y. Takahashi, Y. Matsuo, K. Yamaguchi, M. Matsuki, and K. Kobayashi, *J. Mater. Sci.*, **25**, 3960 (1990).
3. M. T. Goosey, A. Patel, R. W. Whatmore, and F. W. Ainger, *Brit. Ceram. Proc.*, **41**, 49 (1989).
4. J. M. Schwartz and L. D. Schmidt, *J. Catal.*, **138**, 283 (1992).
5. K. D. Budd, S. K. Dey, and D. A. Payne, *Brit. Ceram. Proc.*, **36**, 107 (1985).
6. F. W. Martin, *Phys. and Chem. of Glasses*, **6** (4), 143 (1965).
7. J. S. Wright and L. F. Francis, *J. Mater. Res.*, in press.
8. J. Chen, K. R. Udayakumar, K. G. Brooks, and L. E. Cross, *J. Appl. Phys.*, **71** (9), 4465 (1992).
9. J. M. Schwartz, J. S. Wright, L. F. Francis, L. D. Schmidt, in preparation.
10. N. R. Parikh, J. T. Stephen, M. L. Swanson, and E. R. Myers in *Ferroelectric Thin Films*, edited by E. R. Myers and A. I. Kingon (Mater. Res. Soc. Proc. **200**, Pittsburgh, PA, 1990) pp. 193-198.
11. L. D. Madsen and L. Weaver, *J. Elec. Mater.*, **21** (1), 93 (1992).

SUBSTRATE INFLUENCED NUCLEATION AND CRYSTALLIZATION OF LiNbO_3 THIN FILMS MADE BY SOL-GEL

VIKRAM JOSHI*, DEBASIS ROY**, AND MARTHA L. MECARTNEY**

*Department of Chemical Engineering and Materials Science, University of Minnesota, Minneapolis, MN 55455.

**Materials Science and Engineering Program, University of California, Irvine, CA 92717

ABSTRACT

Lithium niobate films were deposited on amorphous carbon, silicate glass, (0001) sapphire, and (100) silicon by spin or dip coating double metal ethoxide sols. The crystallinity and microstructure of the deposited films were examined by XRD and TEM. Crystallization behavior and resulting microstructure were strongly influenced by the type of substrate. The formation of crystalline LiNbO_3 on amorphous carbon was detected at room temperature. Randomly oriented polycrystalline films were obtained on glass at 400°C. Choice of one mole of water per mole of ethoxide generated heteroepitaxial growth of LiNbO_3 thin films on (0001) sapphire. Oriented but polycrystalline films were obtained on silicon. The electrical behavior of film on silicon was evaluated in metal-ferroelectric-semiconductor configuration. A dielectric constant of 35 and a dissipation factor of 0.004 was measured at 100 KHz.

INTRODUCTION

LiNbO_3 is an important ferroelectric material with many attractive properties such as a large spontaneous polarization ($70 \mu\text{C}/\text{cm}^2$), a very high Curie temperature (1210 °C), and a large negative birefringence (-0.08) [1]. Sol-gel processing has been successfully employed for synthesizing thin films of LiNbO_3 [2,3,4]. In addition to being simple and inexpensive, the sol-gel technique has demonstrated the possibility of low temperature crystallization of LiNbO_3 films, critical for integrated optics applications. Hirano and Kato [5] observed the onset of crystallization in LiNbO_3 thin films at 250°C when annealed in wet O_2 . In our studies on bulk LiNbO_3 gels, crystallization was initiated at temperatures as low as 200°C [6].

The purpose of this work is to investigate the effect of various substrates on nucleation, crystallization, and microstructure of LiNbO_3 thin films. The different substrates can be divided into two categories: amorphous and crystalline. The difference between the two amorphous substrates (carbon and glass) was in the wetting behavior of the sol. The wetting of the amorphous carbon substrates was a problem as the deposited sol coalesced into thick regions leaving behind very thin regions of the film. In contrast, the films on glass were very uniform, indicating good wetting behavior. LiNbO_3 and sapphire are isostructural materials belonging to the space group $R\bar{3}c$. Highly oriented and even epitaxial films of LiNbO_3 have been obtained on single crystal sapphire [4,5], even though the lattice mismatch between the two is 7.5%. Silicon

was chosen as a substrate from the point of incorporating LiNbO_3 films in integrated optics applications.

EXPERIMENTAL

Details of the thin film synthesis procedure have been described elsewhere [7]. 0.25 molar sols of partially hydrolyzed lithium niobium double ethoxide, $\text{LiNb}(\text{OC}_2\text{H}_5)_6$, were used for dip and spin coating. For this work the ratio of ethoxide to water was kept at 1:1. The films on amorphous carbon substrates were deposited in a controlled environmental chamber. The chamber atmosphere was saturated with the solvent (ethanol). This allowed for slow drying due to reduced evaporation rate of the solvent. No heat treatment was given to these films. Films on glass substrates were dip coated whereas spin coating was employed on sapphire and silicon substrates. Films on glass and sapphire substrates were annealed at 400°C for 1 hour in air. Heat treatment in air did not produce crystalline films on silicon at 400°C . Crystalline films on silicon were obtained when annealed in $\text{H}_2\text{O}/\text{O}_2$ at 400°C for 100 min.. All the films, except for those on amorphous carbon substrates, were annealed at a ramping rate of $10^\circ\text{C}/\text{min}$. followed by furnace cooling.

Crystallographic and microstructural characterization was done by transmission electron microscopy (TEM) with a Philips CM20. All samples in the microscope were looked in a stage cooled with liquid N_2 in order to minimize electron beam heating effects. Film texture (i.e. preferred orientation) was studied by X-ray diffraction (XRD) utilizing $\text{Cu K}\alpha$ radiation in a Siemens D5000 diffractometer. Thickness and refractive indices of the films were measured using a Rudolph type 436 ellipsometer. Circular gold electrodes of $2.83 \times 10^{-3} \text{ cm}^2$ area were sputtered on the surface of the annealed film on silicon substrates using a shadow mask to study electrical properties in the metal-ferroelectric-semiconductor (MFS) configuration. The relative dielectric constant, ϵ_r , and dissipation factor, $\tan \delta$, were measured as a function of frequency using an impedance analyzer (model 4192A, Hewlett Packard Inc.). The ferroelectricity in the films was investigated in terms of hysteresis behavior by determining the remanent polarization and coercive field in a computer controlled standardized ferroelectric test system, RT-66A (Radiant Technologies).

RESULTS

Crystallization and Microstructure

Figure 1 shows the TEM micrograph of partially hydrolyzed lithium niobium ethoxide sol on amorphous carbon substrate. As mentioned earlier, the sol did not wet these substrates well and thin regions of the film were left behind during shrinkage of the sol. These thin sections were less than 50 nm thick and were crystalline. The rings in the selected area diffraction (SAD) pattern of this film indexed to LiNbO_3 d spacings. There are few d spacings missing from this SAD pattern which indicates some degree of texturing in the film. Also, one of the d spacings (3rd ring)



Figure 1: LiNbO_3 thin film (< 50 nm) on amorphous carbon substrate. No heat treatment.

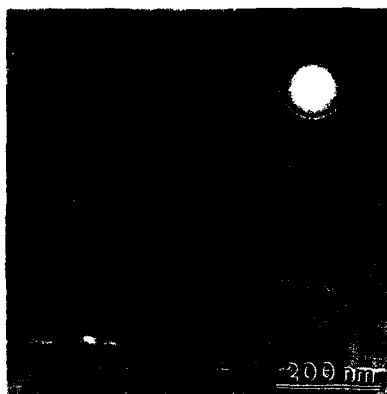


Figure 2: 120 nm thick LiNbO_3 film on glass substrate, annealed at 400°C for 1 hour in air.

is off by 4% from its theoretical position in LiNbO_3 crystal structure. The grain size varies from 40 to 80 nm, most grains on the order of 75 nm.

The microstructure of the films on glass, annealed at 400°C for 1 hour (Fig. 2), is similar to the films on carbon substrates. The grains in the LiNbO_3 on glass are smaller and their size varies from 30-50 nm. The SAD pattern of this film is also similar to the film on carbon substrate. XRD spectrum of this film indicated a strong orientation of $(10\bar{1}4)$ planes parallel to the substrate. The same $(10\bar{1}4)$ d spacing is also one of the missing rings in the SAD pattern. Information from the XRD and electron diffraction strongly suggests texturing of the film along the $[10\bar{1}4]$ direction.

Epitaxial films were obtained on (0001) sapphire substrates. Figure 3 shows microstructure of one such film. The prominent features of this film are its single crystalline nature and absence of porosity. The zone axis in the SAD pattern is (0001) indicating very well oriented growth with the substrate. From this particular area, substrate has been completely milled during ion milling of the specimen but in the other regions of the film which were still attached to the substrate, Moiré fringes were observed and the corresponding SAD patterns confirmed the

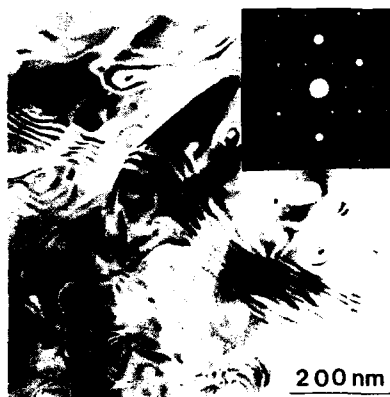


Figure 3: 175 nm thick LiNbO_3 film on (0001) sapphire. 400°C for 1 hour in air.

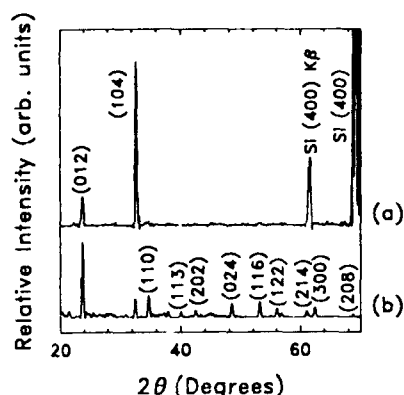


Figure 4: XRD of LiNbO_3 on (100) Si
(a) θ - 2θ scan and (b) glancing angle scan.

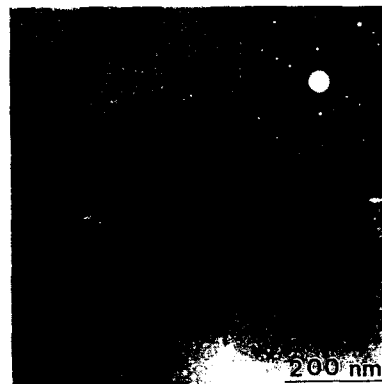


Figure 5: 175 nm thick LiNbO_3 film on silicon. 400°C for 100 min. in $\text{H}_2\text{O}/\text{O}_2$.

epitaxy of LiNbO_3 on sapphire with the following orientation relationship:

$$(0001) \text{LiNbO}_3 // (0001) \text{sapphire and } [11\bar{2}0] \text{LiNbO}_3 // [11\bar{2}0] \text{sapphire}$$

XRD profiles of the film on (100) silicon are shown in Figure 4. Normal coupled scan shows a strong orientation of $(10\bar{1}4)$ planes of LiNbO_3 parallel to the substrate surface. Randomly oriented polycrystalline LiNbO_3 would have a peak intensity ratio of 100:40 between the $(01\bar{1}2)$ and $(10\bar{1}4)$ peaks whereas the intensity ratio of these peaks in Figure 4a shows a ratio of 20:100. From this data one can determine that about 92% of the film is oriented with $(10\bar{1}4)$ planes parallel to (100) Si. However, the glancing angle XRD scan at 2° (Fig. 4b) reveals misorientation in the plane of the film and the polycrystalline nature of the films.

Figure 5 is a plan view TEM image of the same film showing the microstructure. The selected area diffraction (SAD) pattern insert shows evidence for a random alignment of the grains in the plane of the film. The grains are irregularly shaped but estimates of the grain size obtained from dark field images indicated a grain size of about $0.5 \mu\text{m}$. Tiny pores of less than 10 nm in size are present within the grains and along the grain boundaries. Refractive index measurements of this film indicated a value of 2.14. The refractive indices values for the bulk LiNbO_3 are $n_o=2.296$ and $n_e=2.208$ [1]. Combining this information and the Lorentz Lorentz relationship [8], we obtained a value of 5% for the residual porosity present in the film.

Electrical properties

The resistance compensated loop shown in Figure 6 indicates ferroelectricity in the films with a remanent polarization of $2.1 \mu\text{C}/\text{cm}^2$ and a coercive field of about 18 KV/cm. The length of the hysteresis profile was about 282 ms and the maximum applied voltage was 1 V.

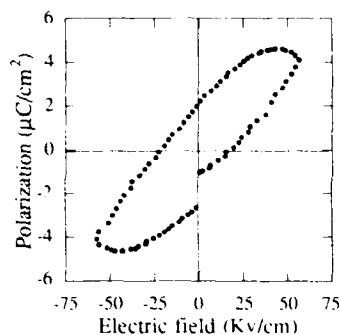


Figure 6: Hysteresis loop from a 400°C annealed LiNbO_3 film in MFS configuration.

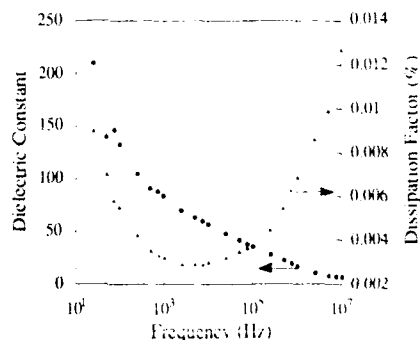


Figure 7: Dielectric constant and dissipation factor as a function of frequency.

Figure 7 shows the variation in dielectric constant and dissipation factor as a function of frequency measured at 10 mV on lithium niobate films in MFS configuration. The dielectric constant of the films annealed at 400°C shows a value of 35 and a dissipation factor of 0.004 at a measuring frequency of 100 KHz.

DISCUSSION

The most surprising result of the present work is the observation of room temperature crystallization in LiNbO_3 thin films on amorphous carbon substrates. It is relevant to mention here our work on thin gel films [6] and room temperature dried films on glass substrates. These films were amorphous and stable in electron beam and even intentional beam heating did not initiate nucleation of crystalline LiNbO_3 . We believe that the crystallization of LiNbO_3 on amorphous carbon substrates under no heat treatment conditions is not an electron beam artifact. Though the exact mechanism behind this phenomenon is still unknown, some of the possible factors could be (a) influence of interfacial energy, (b) slow drying which allows more time for the polymeric species (building blocks) to attain equilibrium sites, and (c) very thin films (less than 50 nm) which facilitate transportation of polymeric species.

It is also very interesting to note that the films on glass attain a similar microstructure and texture only after being annealed at 400°C for 1 hour. Lower temperatures and lesser soaking times failed to crystallize LiNbO_3 films on glass substrates. Also, a slight shift in one of the d spacings in the SAD patterns of the films on both carbon and glass substrates implies that on amorphous substrates, LiNbO_3 does not nucleate as an equilibrium ferroelectric crystalline phase.

On crystalline substrates (sapphire and silicon), all the d spacings indexed to ferroelectric LiNbO_3 crystal structure and ferroelectricity was detected in the films on silicon. The value of

spontaneous polarization is much lower in the present thin films (about $5 \mu\text{C}/\text{cm}^2$) in comparison with bulk single crystal lithium niobate ($70 \mu\text{C}/\text{cm}^2$). This could be due to the fact that the loop presented in Figure 6 is essentially from a smaller signal and not saturated. It was not possible to go beyond a maximum applied voltage of 1.5 V without seriously distorting the shape of the loop due to charge injection across the film-substrate interface. The value of dielectric constant at higher frequencies (35 at 100 KHz) is very close to the calculated value of 36 based on orientation information obtained from XRD, i.e. 92% (10 $\bar{1}$ 4) and 8% (01 $\bar{1}$ 2), and the contributions from the corresponding dielectric constants towards the overall dielectric constant of the films [9]. However, the strong dispersion observed at low frequencies is probably associated with factors such as electrode polarization and lossy nature of the films.

CONCLUSIONS

1. Evidence of room temperature crystallization in LiNbO_3 thin films on amorphous carbon substrates. The films were polycrystalline with some d spacings missing in the SAD patterns.
2. Heat treatment of 400°C for 1 hour yielded polycrystalline LiNbO_3 films on glass.
3. Dense, epitaxial films were obtained on (0001) sapphire substrates at 400°C .
4. Films on silicon were oriented but polycrystalline. Ferroelectricity was measured and experimental dielectric constant values matched with bulk LiNbO_3 data.
5. The observed microstructures and properties are a strong function of various processing parameters including choice of substrate.

ACKNOWLEDGMENTS

This work has been supported through a grant from the AFOSR under contract no. 49620-89-C-0050 and Packard fellowship for science and engineering.

REFERENCES

1. R.S. Weis and T.K. Gaylord, *Appl. Phys. A* **37**, 191 (1985).
2. S. Hirano and K. Kato, *J. Non-Cryst. Solids* **100** 538 (1988).
3. D.P. Partlow and J. Gregg, *J. Mater. Res.* **2** 595 (1987).
4. K. Nashimoto and M.J. Cima, *Materials Letters* **10** 348 (1991).
5. S. Hirano and K. Kato, *Advanced Ceramic Materials* **3** 503 (1988).
6. V. Joshi and M.L. Mecartney, *J. Mater. Res.*, submitted.
7. V. Joshi, G.K. Goo, and M.L. Mecartney, *Mater. Res. Soc. Symp. Proc.* **243** 459 (1992).
8. M. Born and E. Wolf in *Principles of Optics*, (Pergamon, New York, 1975).
9. V. Joshi, D. Roy, and M.L. Mecartney, to be published in *Appl. Phys. Lett.* (1993).

PREPARATION AND CHARACTERIZATION OF SOL-GEL DERIVED HETEROEPITAXIAL LiNbO_3 AND LiTaO_3 THIN FILMS

Keiichi Nashimoto
Materials Research Laboratory, Fuji Xerox Co., Ltd.,
1600 Takematsu, Minamiashigara, Kanagawa, 250-1, Japan.

ABSTRACT

Dense epitaxial LiNbO_3 thin films without any misoriented plane on sapphire substrates were obtained with a sol-gel process utilizing 2-methoxyethanol based metal alkoxide precursors without pre-hydrolysis and rapid thermal annealing. Epitaxial LiNbO_3 films annealed at 700°C were transparent and showed refractive indices close to bulk single crystal values. Epitaxial and transparent LiTaO_3 films crystallized successfully on sapphire substrates with single orientations with the present process. X-ray rocking curve full widths at half maximum of epitaxial LiNbO_3 and LiTaO_3 films on sapphire (110) substrates and annealed at 700°C were less than 0.4° .

INTRODUCTION

Recent progress in ferroelectric thin film technology has produced a number of processes to prepare epitaxial ferroelectric thin films to fabricate optical waveguides, for instance. Most epitaxial methods include dry processes which are generally costly and complicated to prepare stoichiometric epitaxial ferroelectric thin films. Typical dry deposition processes, such as rf-magnetron sputtering [1], pulsed laser deposition [2], metalorganic chemical vapor deposition [3], require manipulation of target composition and/or precise control of deposition conditions in order to obtain stoichiometric ferroelectric thin films.

The sol-gel process is advantageous in processing cost, large area fabrication, and stoichiometric composition control although it has been believed as a process to prepare randomly oriented polycrystalline ferroelectric thin films until recently. Partlow and Gregg observed a partial homoepitaxy when they prepared LiNbO_3 thin films on LiNbO_3 single crystals by a sol-gel process using hydrolyzed metal ethoxides [4]. Afterwards, LiNbO_3 thin films with preferred orientation on sapphire substrates were prepared from partially hydrolyzed metal ethoxide precursors [5].

Oriented or epitaxial ferroelectric thin films other than LiNbO_3 prepared by a sol-gel process include PbTiO_3 [6], $\text{Pb}(\text{Zr}_{1-x}\text{Ti}_x)\text{O}_3$ (PZT) [7], $\text{Pb}(\text{Mn}_{1/3}\text{Nb}_{2/3})\text{O}_3$ (PMN) [8] up to now. We reported the solid state heteroepitaxial crystallization of LiNbO_3 thin films with single orientations on sapphire substrates from non-hydrolyzed metal ethoxide precursors [9]. We observed a change in orientation of LiNbO_3 from epitaxial to random with an increase in amount of water added to hydrolyze metal ethoxide precursors. Epitaxial LiNbO_3 thin films annealed at 400°C looked dense and smooth although they apparently had microporosity of 10

nm in diameter when they were observed by transmission electron microscope [10]. Development of pore sizes up to 100 nm in diameter was observable by scanning electron microscopy when epitaxial LiNbO_3 thin films were annealed at 700°C although they still showed better quality than oriented or polycrystalline LiNbO_3 thin films in terms of density and refractive index. Finally, an ideal epitaxial LiNbO_3 thin film is a fully dense defect free single crystal.

In the present study, we examined precursor chemistry and annealing conditions in order to improve the quality of sol-gel derived epitaxial LiNbO_3 thin films. The feasibility of the process presented in this study to prepare other materials such as LiTaO_3 was also examined.

EXPERIMENTAL

Likewise the previous process [9, 10], 0.5 M ethanol based precursor solutions for LiNbO_3 thin films were prepared from lithium ethoxide (LiOC_2H_5) and niobium ethoxide ($\text{Nb}(\text{OC}_2\text{H}_5)_5$) in absolute ethanol ($\text{C}_2\text{H}_5\text{OH}$). In the present report, we prepared methoxyethanol based precursors from LiOC_2H_5 and $\text{Nb}(\text{OC}_2\text{H}_5)_5$ by alcohol exchange reactions in 2-methoxyethanol ($\text{CH}_3\text{OC}_2\text{H}_4\text{OH}$) in a dry nitrogen atmosphere. Equal molar amounts of each ethoxide were dissolved in absolute 2-methoxyethanol to form 0.6 M solutions. The solutions were stirred and distilled for 2 hours. Within one hour, the boiling point of the solutions increased to 125°C indicating progress of the alcohol exchange reaction. The distillation was followed by refluxing for 22 hours at 125°C for completion of the alcohol exchange reaction. The formation of lithium methoxyethoxide ($\text{LiOC}_2\text{H}_4\text{OCH}_3$) and niobium methoxyethoxide ($\text{Nb}(\text{OC}_2\text{H}_4\text{OCH}_3)_5$) was confirmed by ^1H NMR spectroscopy of dried precursors.

Optically polished sapphire substrates with (110) or (001) orientation were cleaned in organic solvents, an aqueous 20 vol% HCl solution, and deionized water. Conductive indium tin oxide coated Pyrex glass (ITO glass) was also utilized as a substrate after organic solvent cleaning in order to examine electrical properties of polycrystalline thin films prepared by the present process. The cleaned substrates were ethanol spin-dried followed by spin-coating with the non-hydrolyzed precursors at 2000 rpm in a dry nitrogen environment. The coated substrates were heated in wet oxygen at 300°C for 2 min in order to pyrolyze the coating films. The pyrolyzed amorphous films were further heated at a specified temperature to crystallize them epitaxially. Heating was performed at a conventional heating rate of $10^\circ\text{C}/\text{min}$ or at a rapid heating rate of $10^\circ\text{C}/\text{sec}$ (that is RTA: rapid thermal annealing).

Texture and quality of the prepared epitaxial films were analyzed by $\text{Cu K}\alpha$ θ - 2θ X-ray diffraction (XRD) and XRD pole figures. Morphology of obtained films were observed by scanning electron microscopy (SEM). Refractive indices and thicknesses of the films were measured by ellipsometry with He-Ne laser. P-E hysteresis loops of polycrystalline thin films on ITO glass were measured by Sawyer-Tower circuit.

RESULTS AND DISCUSSION

Figure 1(a) shows a SEM image of an epitaxial LiNbO_3 thin film prepared on sapphire (110) from an ethanol based precursor and annealed at 700°C at a heating rate of $10^\circ\text{C}/\text{min}$. The thin film is porous because of development of pores, as reported before [9, 10]. Whereas, epitaxial LiNbO_3 thin films prepared on sapphire (110) from a methoxyethanol based precursor and annealed in the same condition as the above were fully transparent and denser than the above LiNbO_3 . Number density and size of pores are greatly reduced although no obvious change in grain size was observed. In differential scanning calorimetry of dried precursors, the peak intensity of the exotherm around 270°C , due to pyrolysis of organic groups of the methoxyethanol based precursor, was weaker than that of the ethanol based precursor. This fact suggests the formation of pores may be suppressed by the easier pyrolysis of precursors. In addition to the precursor chemistry, the rapid heating rate, as fast as $10^\circ\text{C}/\text{sec}$, reduced porosity as shown in Figure 1(b). This behavior of LiNbO_3 in terms of porosity is in agreement with the report by Eichorst and Payne when they prepared polycrystalline LiNbO_3 on silicon although they reported change in grain size in addition to change in pore size [11].



Figure 1. SEM of epitaxial LiNbO_3 thin films on sapphire (110) substrates prepared from (a) an ethanol based precursor with a slow heating rate and (b) a methoxyethanol based precursor with RTA.

Epitaxy of these thin films on sapphire (110) was confirmed by XRD θ - 2θ patterns and XRD pole figures as reported before [9, 10]. XRD θ - 2θ patterns of these thin films indicated no Li-deficient phase and single plane orientation of LiNbO_3 (110) // Al_2O_3 (110). XRD pole figures of these thin films on sapphire (110) for the (012) plane showed symmetric patterns of four spots indicating in-plane orientation of LiNbO_3 [001] // Al_2O_3 [001].

XRD data and refractive indices of epitaxial LiNbO_3 thin films prepared on sapphire substrates are summarized in Table I. As suggested by the SEM of LiNbO_3 thin films, LiNbO_3 prepared from the ethanol based precursor showed lower refractive indices than LiNbO_3 prepared from the methoxyethanol based

precursor. RTA processed LiNbO_3 had relatively higher refractive indices than LiNbO_3 annealed at a conventional slow heating rate. The slightly higher refractive indices of the RTA processed LiNbO_3 than single crystal values could be caused by residual stress in LiNbO_3 due to RTA process. In contrast, RTA processed LiNbO_3 had relatively larger XRD rocking curve full width at half maxima (FWHM) than those of LiNbO_3 annealed at a slow heating rate. All LiNbO_3 thin films derived from the methoxyethanol based precursors and annealed at 700°C had rocking curve FWHMs less than 0.4° . LiNbO_3 grown on sapphire (001) showed larger rocking curve FWHMs than those of LiNbO_3 on sapphire (110). RTA processed LiNbO_3 derived from the methoxyethanol based precursor started to crystallize epitaxially at 400°C and showed almost similar refractive indices above 600°C . These LiNbO_3 were epitaxial even with a short annealing time of 1 min at 700°C although LiNbO_3 required more than 5 min to show high refractive indices close to single crystal values.

With a similar process using methoxyethanol based precursors and RTA, transparent epitaxial LiTaO_3 thin films were successfully crystallized on sapphire (110) and (001) at 700°C as shown in Figure 2. No misoriented plane was observed in XRD patterns. The films looked smooth and crack-free when they were observed by SEM. There was no granular structure as observed in the previous paper reporting the preparation of LiTaO_3 thin films on sapphire substrates from partially hydrolyzed ethoxide precursors [12]. LiTaO_3 thin films, which have higher melting temperature by about 400°C than LiNbO_3 , showed relatively lower refractive indices than that of single crystals compared with LiNbO_3 thin films, as shown in Table I. Rocking curve FWHMs of LiTaO_3 thin films on sapphire (110) and annealed at 700°C were also less than 0.4° .

Table I. XRD data and refractive indices of LiNbO_3 and LiTaO_3 thin films on sapphire substrates.

Precursor	Substrate	Heating Rate ($^\circ\text{C}/\text{sec}$)	Annealing		FWHM (deg) ¹⁾	Refractive Index ²⁾
			Temp ($^\circ\text{C}$)	Time (min)		
$\text{LiNb}(\text{OC}_2\text{H}_5)_6$	(110)	0.17	700	90	0.19	2.103
$\text{LiNb}(\text{OC}_2\text{H}_4\text{OCH}_3)_6$	(110)	0.17	700	90	0.22	2.280
$\text{LiNb}(\text{OC}_2\text{H}_4\text{OCH}_3)_6$	(110)	10	700	90	0.40	2.295
$\text{LiNb}(\text{OC}_2\text{H}_4\text{OCH}_3)_6$	(110)	10	700	30	0.39	2.294
$\text{LiNb}(\text{OC}_2\text{H}_4\text{OCH}_3)_6$	(110)	10	600	30	0.46	2.267
$\text{LiNb}(\text{OC}_2\text{H}_4\text{OCH}_3)_6$	(001)	10	700	30	1.57	2.264
$\text{LiTa}(\text{OC}_2\text{H}_4\text{OCH}_3)_6$	(110)	10	700	30	0.34	2.098
$\text{LiTa}(\text{OC}_2\text{H}_4\text{OCH}_3)_6$	(001)	10	700	30	1.12	1.982

1) FWHM on Sapphire (110) = 0.072° .

2) Bulk LiNbO_3 = 2.201~2.289, Bulk LiTaO_3 = 2.176~2.180.

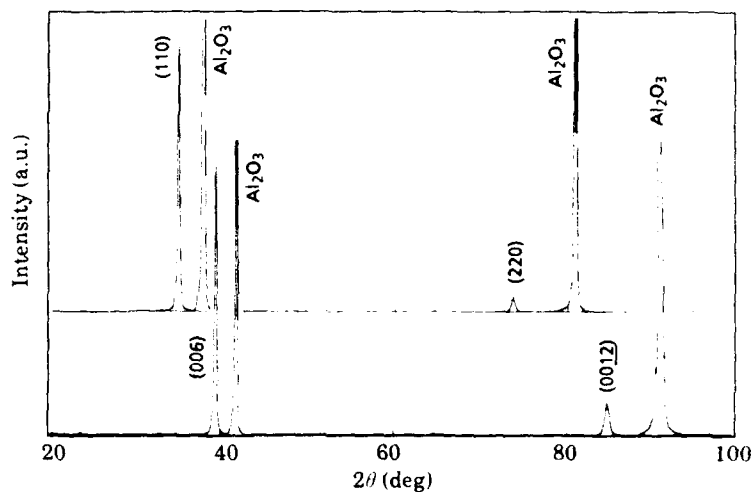


Figure 2. XRD patterns of epitaxial LiTaO_3 thin films on (a) a sapphire (110) substrate and on (b) a sapphire (001) substrate.

The present process employing non-hydrolyzed precursors was also applicable to preparing multi-layer polycrystalline LiNbO_3 thin films. For electrical measurement, the $0.3 \mu\text{m}$ thick LiNbO_3 layer was prepared on ITO glass from the methoxyethanol based precursor and by RTA at 600°C . For obtaining this film, spin-coating and pyrolysis were repeated three times prior to crystallization. The obtained LiNbO_3 was a transparent and crack-free polycrystalline thin film. Figure 3 shows P-E hysteresis loops from $\text{Pt/LiNbO}_3/\text{ITO}$ structure measured at 75 Hz. The leakage current through the LiNbO_3 layer was subtracted from the loops. The leakage current was $4 \times 10^{-5} \text{ A/cm}$ at 2.0 Volts. It was difficult to saturate the polarization of the LiNbO_3 film before dielectric breakdown. The remanent polarization of the LiNbO_3 film was $0.4 \mu\text{C/cm}^2$ and the coercive field was 30 kV/cm at an applied voltage of 2.0.

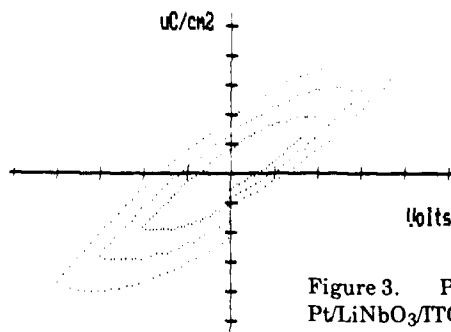


Figure 3. P-E hysteresis loops of $\text{Pt/LiNbO}_3/\text{ITO}$ structure (X div = 0.5 Volt, Y div = $0.2 \mu\text{C/cm}^2$.)

CONCLUSIONS

The effect of precursor chemistry and annealing condition on the quality of sol-gel derived epitaxial LiNbO_3 thin films on sapphire substrates was examined. Process utilizing the combination of methoxyethanol based precursors and rapid thermal annealing dramatically improved the quality of LiNbO_3 in terms of density and morphology. Obtained LiNbO_3 thin films had similar refractive indices to bulk single crystals when they were annealed over 600 °C. The application of the present process to preparation of the other material was successful. The present process gave crack free epitaxial LiTaO_3 thin films on sapphire. This may be the first demonstration of epitaxial LiTaO_3 on sapphire by a sol-gel method to our knowledge. LiTaO_3 had relatively lower refractive indices than bulk single crystals. Remanet polarization of polycrystalline LiNbO_3 on ITO glass as large as 0.4 $\mu\text{C}/\text{cm}^2$ was observed.

ACKNOWLEDGMENT

The author would like to thank Dr. A. Inoue of Fuji Xerox Co., Ltd. for helpful comments and encouragement.

REFERENCES

1. H. Adachi, T. Kawaguchi, M. Kitabatake, and K. Wasa, *Jpn. J. Appl. Phys.* **22**, suppl. 22-2, 11 (1983).
2. K. Nashimoto, D. K. Fork, and T. H. Geballe, *Appl. Phys. Lett.* **60**, 1199 (1992).
3. M. de Keijser, G. J. Dormans, J. F. Cillessen, D. M. de Leeuw, and H. W. Zandbergen, *Appl. Phys. Lett.* **58**, 2636 (1991).
4. D. P. Partlow and J. Gregg, *J. Mat. Res.*, **2**, 595 (1987).
5. S. Hirano and K. Kato, *Adv. Ceram. Mat.* **3**, 503 (1988).
6. C. Chen, D. F. Ryder, Jr., and W. A. Spurgeon, *J. Am. Ceram. Soc.* **72**, 1495 (1989).
7. S. L. Swartz, P. J. Melling, and C. S. Grant in *Optical Materials*, edited by D. B. Pocker and C. Ortiz (Mater. Res. Soc. Proc. **152**, Pittsburgh, PA, 1989) pp. 227-232.
8. K. Okuwada, S. Nakamura, M. Imai, and K. Kakuno, *Jpn. J. Appl. Phys.* **30**, L1052 (1991).
9. K. Nashimoto and M. J. Cima, *Mater. Lett.* **10**, 348 (1991).
10. K. Nashimoto, M. J. Cima, and W. E. Rhine in *Ferroelectric Thin Films*, edited by A. S. Bhalla and K. M. Nair (Am. Ceram. Soc. Ceram. Trans. **25**, Westerville, OH, 1992) pp. 371-383.
11. D. J. Eichost and D. A. Payne in *Sol-Gel Optics*, edited by J. D. Mackenzie and D. R. Ulrich (SPIE Proc. **1328**, Bellingham, WA, 1990) pp. 456-465.
12. S. Hirano and K. Kato in *Processing Science of Advanced Ceramics*, edited by I. A. Aksay, G. L. McVay, and D. R. Ulrich (Mater. Res. Soc. Proc. **155**, Pittsburgh, PA, 1989) pp. 181-190.

PART IX

Niobium and Barium Based Ferroelectrics

GROWTH, MICROSTRUCTURES AND OPTICAL PROPERTIES OF KNbO_3 THIN FILMS

THOMAS M. GRAETTINGER*, P. A. MORRIS**, R. R. WOOLCOTT*,
F. C. ZUMSTEG**, A. F. CHOW*, AND A. I. KINGON*

*North Carolina State University, 1001 Capability Dr., Raleigh, NC 27695-7919

**DuPont Company, Experimental Station, Wilmington, DE 19880-0356

ABSTRACT

Potassium niobate, KNbO_3 , possesses high nonlinear optical coefficients making it a promising material for frequency conversion into the visible wavelength range. While epitaxial thin films of KNbO_3 have been reported [1,2], only limited data exists concerning the optical loss mechanisms and nonlinear optical properties of these films. In this study, epitaxial thin films of KNbO_3 have been grown using ion beam sputter deposition and evaluated in terms of their microstructures and optical properties. Characterization of the microstructures of these films includes the in-plane epitaxial relationship to the substrate. The relationships between the growth parameters and microstructures developed to the indices of refraction and the optical losses (absorption and scattering) are discussed.

INTRODUCTION

The next generation of laser writing and optical storage devices will require a high resolution coherent light source. The resolution necessary can be achieved by using a blue light source where high resolution is achieved because of the short wavelength. Currently no compact blue laser source is commercially available, but the production of blue laser radiation through second harmonic generation (SHG) in a nonlinear optical material presents the most promising approach demonstrated thus far. Achieving the necessary second harmonic power (1-5 mW) from a relatively low power semiconductor laser diode requires high conversion efficiency in the nonlinear material.

Many factors influence the SHG efficiency including the nonlinear susceptibility of the material (d_{ijk}), the refractive index (n), the optical pathlength (L), and the waveguide width and thickness (w, t) as shown in the following equation.

$$\frac{P^{(2\omega)}}{P^{(\omega)}} \propto \frac{d_{ijk}^2}{n^3} L^2 \frac{P^{(\omega)}}{w \cdot t} \quad (1)$$

This relationship makes clear the advantages of using the nonlinear material in a resonator system where L becomes large enough to produce efficient SHG output. Such systems have been demonstrated for several materials including KNbO_3 . [3,4] Also clear from the above relationship is the increased efficiency resulting from confining the fundamental beam, $P(\omega)$, in a waveguide structure, thereby decreasing the parameter t .

The nonlinear optical material used determines the device design. Many of the commonly used nonlinear materials including KTP, LiTaO_3 , and LiNbO_3 require complex phase matching schemes in order to produce efficient SHG. [5,6,7] KNbO_3 , however, can be used to produce light in the blue region of the optical spectrum by Type I phase matching. [8] This is an attractive attribute for a thin film device where producing complex phase matching structures within the material may be difficult. In addition, KNbO_3 possesses large nonlinear optical susceptibilities, comparable to the other materials mentioned. KNbO_3 thin films have been fabricated by several growth methods including ion beam sputtering [1], rf-diode sputtering [2], the sol-gel process [9], and liquid phase epitaxy, LPE [10]. To date, the films produced by the sputtering methods have exhibited the best optical properties with optical propagation losses as low as 1.1 dB/cm reported [2].

Low optical propagation losses are paramount to fabricating a viable SHG device. Two primary loss mechanisms exist for transmission through waveguides, absorption and scattering. Absorption can result from impurities, carriers, and interband transitions. Absorption decreases SHG efficiency by the following,

$$\frac{P^{(2\omega)}}{P^{(\omega)}} \propto \frac{d_{ijk}^2}{n^2} \frac{1}{\kappa} P^{(\omega)} \quad (2)$$

where κ is the absorption coefficient of the nonlinear optical material. While absorption processes have been shown to limit the properties of several optical materials, scattering is the major component of the propagation loss in most thin film waveguides. Scattering is typically caused by inhomogeneities in the film, microstructural defects, and imperfections at the film-substrate and film-surface interfaces. The loss produced by interface roughness is a good example to illustrate the interface control necessary to produce a low-loss thin film. The radiation loss factor, α , is related to the interface roughness by [11]

$$2\alpha \propto \frac{(n_f^2 - n_s^2)b^2}{t^3} \quad (3)$$

where n_f is the refractive index of the film, n_s is the index of the substrate, b is the amplitude of the interface roughness, and t is the film thickness as shown in Fig. 1. Loss due to interface roughness is especially difficult to control for nonlinear optical materials which have high indices of refraction, $n > 2.00$. The large index difference between the light guiding film layer and the substrate

scales the radiation loss factor by the difference of the squares of the indices, making even small interface roughness result in large optical propagation loss for thin films.

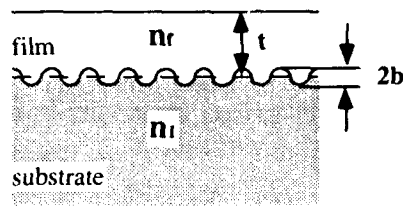


Fig. 1. Model used to calculate the radiation loss caused by interface roughness.

The microstructural requirements for low-loss light-guiding thin films are not well defined. Microstructural features such as high and low angle grain boundaries, grain size, and domain walls may contribute to large propagation loss through scattering. The detriment to film quality of each feature is expected to be related to the material-substrate system chosen. Control of film microstructure is possible by proper choice of growth technique and deposition parameters.

KNbO₃ FILM GROWTH

KNbO₃ films have been grown by rf-diode sputtering, LPE, sol-gel, and ion beam sputtering as stated previously. In this investigation, KNbO₃ films were grown using two ion beam sputter deposition processes. The first, shown in Fig. 2, was developed at N. C. State [1]. This process uses a single primary ion source to sputter material from multiple, elemental and elemental oxide targets which are sequentially rotated in front of the ion beam. Thus, thin layers of the target materials, niobium and potassium superoxide (KO₂), are deposited on the substrate. At the deposition temperature, these layers are continuously interdiffusing and the proper structure is formed in situ. Control of film stoichiometry is achieved by adjusting the relative thickness of the layers. The thickness of each layer is computer-controlled through feedback from a quartz crystal resonator.

A second ion beam sputter deposition system, shown in Fig. 3, has recently been set up at DuPont. This system uses two primary ion sources to cosputter the Nb and KO₂ targets. Stoichiometric control is attained by adjusting the relative sputtering rates of the two targets. The sputtering rates are primarily controlled by adjusting the ion beam energy and ion beam current incident on each target. In addition, the deposition rate from each target is monitored by a quartz crystal resonator.

Many process parameters were kept constant in both deposition systems so that changes in nucleation and growth mechanisms resulting from cosputtering versus layer by layer growth could be investigated. Table I summarizes the most important common processing conditions. Single crystal, (001) oriented magnesium oxide, MgO, was used as the substrate for all films in this study. The substrate temperature during deposition was between 600 and 650°C with the higher temperatures used during the growth of thick films for optical characterization. The ion beam energy was kept in the range of 500 to 1000 eV to minimize damage to the growing film from high energy backscattered primary ions. Films from 500 to 5000 Å were deposited using both deposition techniques.

Table I. Process parameters for ion beam sputter deposited KNbO₃ thin films.

Targets	Nb, KO ₂
Substrate	MgO (001)
Growth Temp.	600-650°C
Ion beam energy	500-1000 eV
Ion beam current	0.025-0.100 mA/cm ²
Growth rate	500 Å/hr.
Oxygen background pressure	1×10^{-5} - 1×10^{-4} torr
Cooling rate	5°C/min.

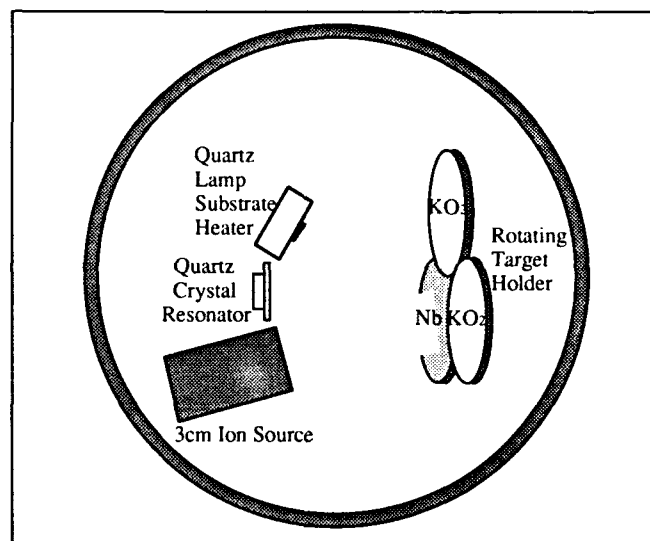


Fig. 2. Ion beam sputter deposition system used for layer-by layer growth.

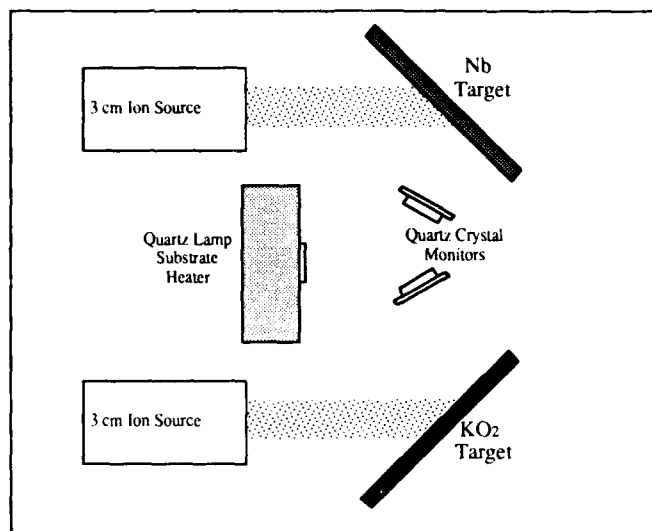


Fig. 3. Ion beam sputter deposition system used for cosputtering.

Rutherford Backscattering Spectrometry (RBS) was used to determine film composition. A 2 MeV $^4\text{He}^+$ ion beam normally incident on the samples was used for the measurements. Fig. 4 shows the result of a typical RBS measurement. The experimental spectrum shown is in excellent agreement with the simulated spectrum of a stoichiometric KNbO_3 film also shown in the figure. Simulated RBS spectra were also used to determine the thickness of films which supported only single guided modes. DekTak measurements were used to verify the thickness determined by RBS. The thickness determined was then used to calculate the refractive index of such films.

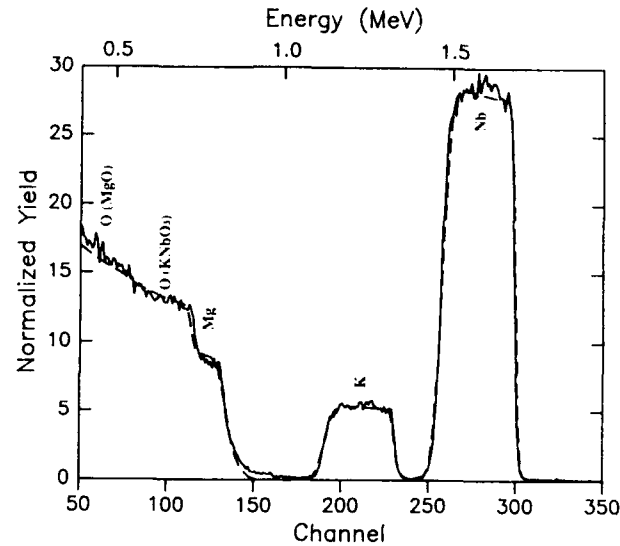


Fig. 4. RBS spectrum of a KNbO_3 thin film grown on MgO . The dashed line represents the simulated spectrum of a stoichiometric KNbO_3 film.

EPITAXY STUDY

Crystal orientation is critically important to SHG performance. Phase matching of the fundamental and second harmonic waves can normally be accomplished only in certain crystallographic directions in a crystal. Therefore, it is desirable to produce a thin film that is a single crystal, requiring epitaxy in both planar directions of the thin film and no microstructural defects. In practice it is very difficult to grow a true heteroepitaxial film. Lattice mismatch between film and substrate is often accommodated by the formation of microstructural defects such as high and low-angle grain boundaries and the formation of domain walls in ferroelectric thin films. For these reasons, neighboring grains or domains may not have the same crystallographic orientation across the boundary or wall, ruining the phase matching conditions as the fundamental and second harmonic waves cross these boundaries.

The standard x-ray diffractometer theta-two theta scan is a powerful technique for determining the crystalline structure of thin films and for determining if any preferential orientation exists. The resulting pattern is also useful in identifying the crystalline phases present. Fig. 5 shows a typical x-ray diffraction pattern for a KNbO_3 thin film deposited on MgO . From this diffraction pattern it is clear that the film is single phase KNbO_3 and highly

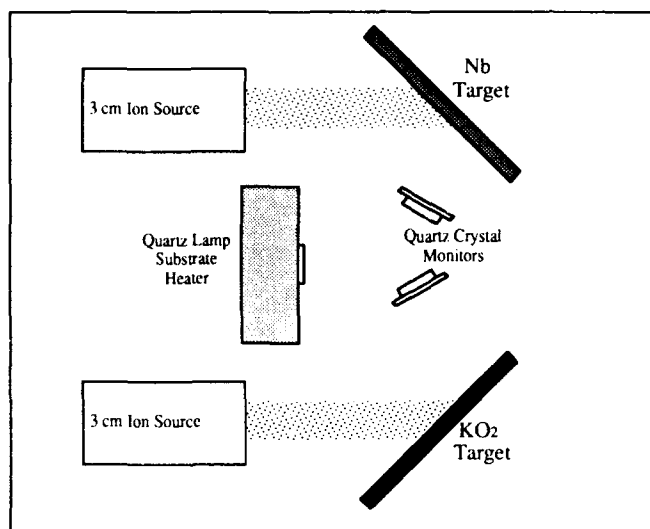


Fig. 3. Ion beam sputter deposition system used for cosputtering.

Rutherford Backscattering Spectrometry (RBS) was used to determine film composition. A 2 MeV $^4\text{He}^+$ ion beam normally incident on the samples was used for the measurements. Fig. 4 shows the result of a typical RBS measurement. The experimental spectrum shown is in excellent agreement with the simulated spectrum of a stoichiometric KNbO_3 film also shown in the figure. Simulated RBS spectra were also used to determine the thickness of films which supported only single guided modes. DekTak measurements were used to verify the thickness determined by RBS. The thickness determined was then used to calculate the refractive index of such films.

oriented with $(110)\text{KNbO}_3\parallel(001)\text{MgO}$ where the indices given for KNbO_3 are for the orthorhombic phase. This orientation of the orthorhombic unit cell is pictured in Fig. 6. As shown in the figure, the $[001]\text{KNbO}_3$ is in the plane of the film. However, it can not be determined from the standard diffraction pattern if the $[001]\text{KNbO}_3$ is parallel to the $[100]\text{MgO}$ or the $[010]\text{MgO}$. The in-plane orientation of the film, is necessary for phase matching considerations as discussed earlier.

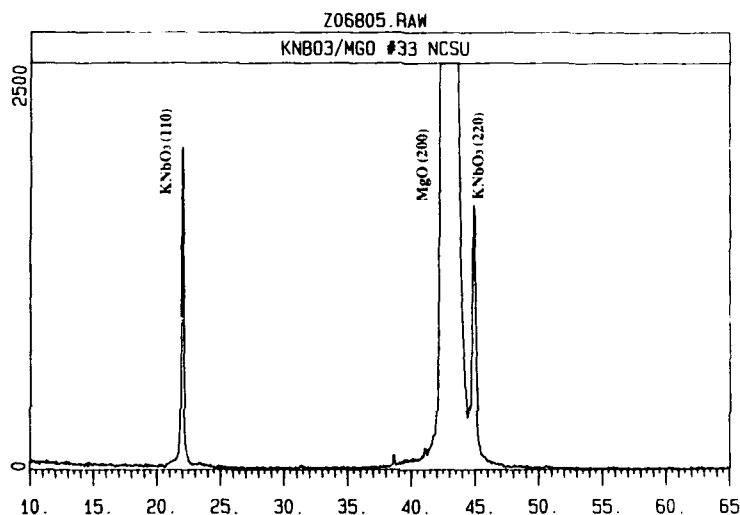


Fig. 5. X-ray diffraction pattern of a KNbO_3 thin film deposited on $\text{MgO}(001)$.

In order to investigate the in-plane orientation of the KNbO_3 thin films, a pole figure rotation stage in combination with an x-ray diffractometer was used. This apparatus has the ability to probe crystal planes which are not parallel to the substrate surface. First, (110) pole figures were constructed for the KNbO_3 thin films and a representative figure is shown in Fig. 7. This figure makes it clear that the film is tilted along the MgO $[100]$, $[010]$, $[\bar{1}00]$, and $[0\bar{1}0]$ directions. Samples deposited by both ion beam sputtering methods exhibited this behavior, suggesting that the tilt is a substrate influenced characteristic and is not related to deposition method. Lattice tilt is a well known mechanism for accommodating lattice mismatch between film and substrate. The lattice mismatch between the $(001)\text{KNbO}_3$ and $\{100\}\text{MgO}$ planes is 6.0%. This mismatch is relatively large for achieving high quality heteroepitaxial growth. In addition to tilt, low angle grain boundaries twinning, and inversion domain

boundaries have been observed previously in KNbO_3 thin films grown by ion beam sputtering.[12]

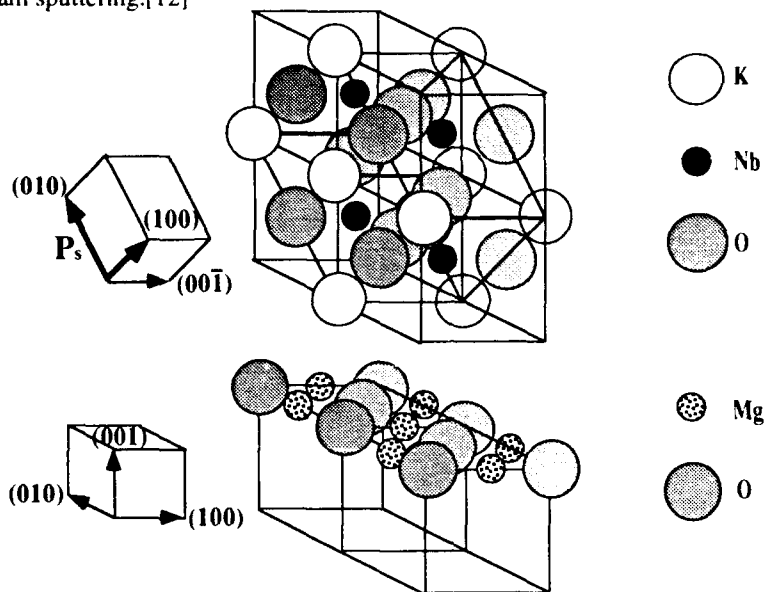


Fig. 6. The orientation of the orthorhombic unit cell of KNbO_3 on $\text{MgO}(001)$.

With this knowledge it is probable that complete in-plane epitaxy has not been achieved. The films may be best described as textured with in-plane rotation.

Due to the large lattice mismatch between KNbO_3 and MgO the films may be highly strained. Others have reported the growth of tetragonal KNbO_3 films[2] which may be a result of strain in those films. The (110) and (220) reflections of orthorhombic KNbO_3 match closely the peaks observed for the ion beam sputtered films grown in this study. To confirm that the films grown by ion beam sputtering were indeed orthorhombic, the pole figure rotation stage was used to rotate the samples so that planes which are not parallel to the substrate surface would reflect in the standard diffractometer geometry. In this manner, the (131) and (311) planes, among others, were identified and their d-spacings are consistent with orthorhombic KNbO_3 . Further, these planes also exhibited tilt about the expected positions which were based on alignment of the $[110]\text{KNbO}_3$ and $[001]\text{MgO}$ directions.

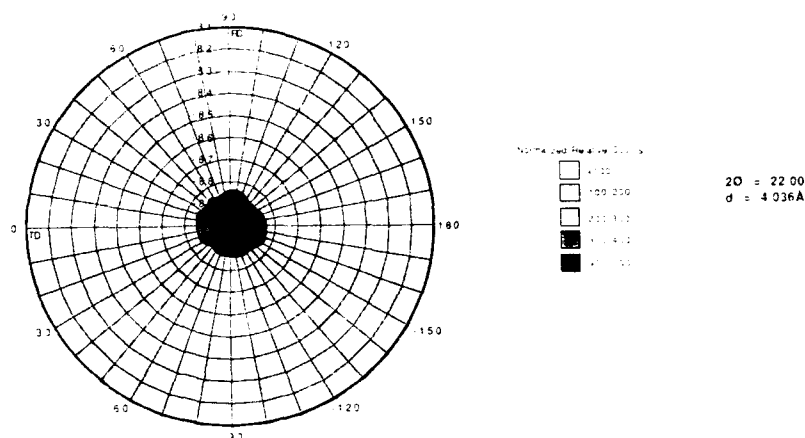


Fig. 7. (110) pole figure for a KNbO₃ thin film deposited on MgO.

OPTICAL PROPERTIES

The indices of refraction of layer-by-layer deposited and cosputtered KNbO₃ thin films were measured using the prism coupling m-line technique. The mode lines appeared relatively sharp as shown in Fig. 8 which shows the measurement of a layer-by-layer deposited film. Both types of films supported TE and TM guided modes. The results of these measurements are presented in Table II along with the indices of bulk KNbO₃ for orientations which correspond to the guided modes. The film indices for TE modes should be compared to the (001) and (1 $\bar{1}$ 0) indices of bulk KNbO₃, 2.3291 and 2.2242, respectively, since these are the major and minor axes of the index ellipsoid in the plane of the film. If the films were single crystal, both values should have been observed as the films were rotated 90 degrees during the measurements. This birefringence was not observed, however. Instead, the measured TE indices match closely with the average of the bulk (001) and (1 $\bar{1}$ 0) indices. The fact that birefringence was not seen in the TE measurements supports the conclusion that the films are textured with in-plane rotation as stated above. However, strain effects and twinning could also account for the lack of birefringence in the TE index. The TM indices of both types of ion beam sputtered films, on the other hand, are in good agreement with the expected (110) bulk index.

```

ID=                                     09:52
Prism= 4329                          Substrate N= 1.74   Data= 2499 to -1
Wavelength= 632.8                    Prism N= 2.8659
+1477 (2.2226)                       +339 (2.0287)
Index= 2.2658
Thickness= 0.4739

```

Table II. Refractive indices of thin films and bulk KNbO_3 .

Film	Substrate	Mode/Orientation	Refractive Index
Layer-by-layer	MgO	TE	2.2856±.0003
		TM	2.2021±.0012
Cosputtered	MgO	TE	2.2207±.0041
		TM	2.1975±.0046
Bulk KNbO ₃		(001)	2.3291
		(110), (1 $\bar{1}$ 0)	2.2242

A fiber probe was used to measure the optical propagation loss in the KNbO₃ films. A large degree of scattering prevented the measurement of propagation loss in the films using the fiber probe. As discussed earlier, microstructural features such as grain boundaries and interface roughness can be major contributors to scattering loss. These features are found in the sputtered films and must be controlled in the future to yield low-loss waveguides.

SUMMARY

Thin films of KNbO_3 were fabricated by ion beam sputtering using both layer-by-layer and cosputtering ion beam deposition methods. Both methods have demonstrated good compositional control and stoichiometric KNbO_3 thin films have been produced. However, in-plane epitaxy is necessary to achieve efficient SHG in a thin film. To investigate the in-plane epitaxy of the films a pole figure rotation stage in combination with a standard x-ray diffractometer was used. The results of this study show that the KNbO_3 films are tilted $1\text{--}1.5^\circ$ about the substrate normal along the MgO cubic directions. This is an indication that the films are textured with in-plane rotation. The refractive indices of the thin films were measured using the prism coupling m-line technique and compare favorably with bulk values. Birefringence was observed between TE and TM modes, but was not observed in TE measurements at 90° supporting the conclusion that the films are textured and true in-plane epitaxy has not been achieved. Further work to understand the relationships between growth, microstructure, and loss mechanisms is needed to achieve a thin film material suitable for an efficient SHG device.

ACKNOWLEDGMENTS

The authors would like to acknowledge; the Office of Naval Research for partial support of this work under contract N00014-91-J-1307, and Bruce Rothman and the Laboratory for Research on the Structure of Matter at the University of Pennsylvania for assistance and use of their equipment in making the RBS measurements under NSF #DMR91-20668.

- ¹T. M. Graettinger, S. H. Rou, M. S. Ameen, O. Auciello, and A. I. Kingon, Appl. Phys. Lett. **58**, 1964 (1991).
- ²S. Schwyn Thöny and H. W. Lehmann, and P. Günter, Appl. Phys. Lett. **61**, 373 (1992).
- ³W. J. Kozlovsky, W. Lenth, E. E. Latta, A. Moser, and G. L. Bona, Appl. Phys. Lett. **56**, 2291 (1990).
- ⁴C. Zimmermann, T. W. Hänsch, R. Byer, S. O'Brien, and D. Welch, Appl. Phys. Lett. **61**, 2741 (1992).
- ⁵C. J. van der Poel, J. D. Bierlein, J. B. Brown, and S. Colak, Appl. Phys. Lett. **57**, 2074 (1990).
- ⁶K. Yamamoto, K. Mizuuchi, and T. Taniuchi, Optics Lett. **16**, 1156 (1991).
- ⁷M. Fujimura, T. Suhara, and H. Nishihara, Electronics Lett. **27**, 1207 (1991).
- ⁸P. Günter, Appl. Phys. Lett. **34**, 650 (1979).
- ⁹M. Amini and M. D. Sacks in Better Ceramics through Chemistry IV, (Mater. Res. Soc. Proc. **180**, Pittsburgh, PA, 1990) p. 675.
- ¹⁰R. Gutmann and J. Hulliger, Cryst. Prop. Prep. **32-34**, 117 (1991).
- ¹¹D. Marcuse, Theory of Dielectric Optical Waveguides, (Academic Press, New York, 1974), p. 138.
- ¹²A. I. Kingon, S. H. Rou, M. S. Ameen, T. M. Graettinger, K. Gifford, and O. Auciello in Electro-Optics and Non-linear Optic Materials, edited by A. S. Bhalla, E. M. Vogel, and K. M. Nair (Ceramic Transactions **14**, Westerville, OH, 1990) pp. 179-196.

FORMATION OF BaMgF_4 FILMS ON Pt/MgO , Si AND GaAs SUBSTRATES

KOUJI AIZAWA, TATSUYA ICHIKI AND HIROSHI ISHIWARA

Precision & Intelligence Laboratory, Tokyo Institute of Technology, 4259 Nagatsuta, Midori-ku, Yokohama 227, Japan

ABSTRACT

Crystalline quality of BaMgF_4 films grown on Pt/MgO , Si , and GaAs substrates either by solid phase crystallization (SPC) or by molecular beam epitaxy (MBE) has been investigated. In the SPC method, the films are deposited typically at 300°C in amorphous state and subsequently crystallized at temperatures higher than 500°C . It has been found from X-ray diffraction analysis that (010)-oriented films are grown on the three substrates by the SPC method, while that (011)- and (120)-oriented films are grown on respective (100)- and (111)-oriented substrates of Si and GaAs , when the MBE method is used at substrate temperatures around 500°C . These results show that the spontaneous polarization which is generated along a-axis of a BaMgF_4 crystal, is not parallel to the film surface, only when the films are grown on (111) substrates by MBE.

INTRODUCTION

Recently, it has become important to form ferroelectric thin films directly on semiconductor substrates from a viewpoint of fabrication of novel electron devices such as nonvolatile memory FETs (field effect transistors) [1]-[6] or adaptive-learning FETs [7]. Actually, ferroelectric/Si FETs have been fabricated using such oxide films as $\text{Bi}_2\text{Ti}_2\text{O}_7$ [1]-[3], $\text{PLZT}(\text{Pb}, \text{La}, \text{Zr}, \text{Ti}, \text{O}_2)$ [4], and LiNbO_3 [6]. However, electrical properties of the devices are still insufficient for practical uses, mainly due to existence of the interface states between the films and Si substrates, and due to interdiffusion of constitution elements. On the other hand, it has been reported that the interface electrical properties between fluoride insulator films and semiconductor substrates are excellent in such structures as $\text{CaF}_2/\text{Si}(111)$ [8], $(\text{Ca}, \text{Sr})\text{F}_2/\text{GaAs}(111)$ [9], and $\text{GaF}_3/\text{sulfur-treated GaAs}(100)$ [10]. We speculate from these results that use of ferroelectric fluorides such as BaMgF_4 [11] is effective to avoid the interface state problem and to realize the electron devices with excellent ferroelectric/semiconductor structures.

BaMgF_4 is an orthorhombic crystal with lattice parameters of $a=0.581\text{nm}$, $b=1.451\text{nm}$, and $c=0.413\text{nm}$. Some pioneering studies on the formation of BaMgF_4 films have been done by S. Sinharoy et al [12], [13]. The crystal has the spontaneous polarization P_s along a-axis and its value is reported to be $8.5\mu\text{C}/\text{cm}^2$ [12]. However, it has been reported that the P_s value for polycrystalline films which were deposited at 250°C and subsequently annealed at 600°C is only $1.6\mu\text{C}/\text{cm}^2$ along a direction perpendicular to the film surface [12]. The origin of the small P_s value is considered due to a fact such that the films are composed of the randomly oriented crystallites and consequently, only a part of crystallites contribute to the polarization perpendicular to the film surface. In this paper, we investigate the crystalline quality of BaMgF_4 films formed on Pt/MgO , Si and GaAs substrates by changing the substrate orientations and the growth conditions.

EXPERIMENTAL PROCEDURE

Preparation of substrates

In the experiment, BaMgF_4 films were deposited on Pt/MgO , Si , and GaAs substrates. Pt/MgO substrate was prepared by depositing (100)-oriented Pt films on $\text{MgO}(100)$ wafers at 640°C using an electron beam evaporation method. The pressure during deposition of Pt films

was kept in the range from 0.4 to 2×10^{-4} Pa, and their thickness was about 120 nm. In case of Si substrates, n-type (100)- and (111)-oriented single crystal wafers were used. They were boiled in organic solvents, cleaned using Shiraki method[14], and loaded in a vacuum chamber. GaAs wafers with (100) and (111) orientations were also used. They were chemically etched with $3\text{H}_2\text{SO}_4\text{:H}_2\text{O}_2\text{:H}_2\text{O}$ solution and immersed in $(\text{NH}_4)_2\text{S}_x$ solution for 15 min to passivate the surfaces by sulfur atoms. Since it has been reported that oxidation of GaAs surfaces is prevented by the sulfur passivation process[15], this process is considered to be effective for epitaxial growth of fluoride films.

Formation of the fluoride films

BaMgF_4 films were formed on Pt/MgO, Si, and GaAs substrates either by solid phase crystallization (SPC) or by molecular beam epitaxy (MBE). The source material for evaporation was polycrystalline BaMgF_4 grains. They were prepared by mixing BaF_2 and MgF_2 powders with 99.99% purity and by heating at 1000°C for 1h in N_2 atmosphere. In the SPC method, the films were deposited typically at 300°C in amorphous state, and annealed at temperatures higher than 500°C for 15min for crystallization. A base pressure of the deposition chamber was less than 5×10^{-5} Pa. In the MBE method, the films were grown at temperatures higher than 400°C . A base pressure of the MBE chamber was less than 1×10^{-5} Pa.

The fluoride films on Pt/MgO(100) substrates were formed only by the SPC method. Their thicknesses were from 140 to 160 nm. Whereas, the films on Si and GaAs substrates were formed by both SPC and MBE methods. In case of Si substrates, the wafers were first heated in vacuum at 850°C for 40min to evaporate surface oxide layers. Then, fluoride films 35 to 120 nm thick were deposited with deposition rates ranging from 0.5 to 2 nm/min. In case of GaAs substrates, the substrate temperature was simply increased to a deposition temperature.

Characterization of crystalline quality

Crystalline quality of the films and the epitaxial relation with the substrates were analyzed by X-ray diffraction (XRD) analysis, X-ray pole figure measurement, and the channeling measurement in Rutherford backscattering spectrometry (RBS) with 1.5 MeV He ions.

RESULTS AND DISCUSSION

Solid phase crystallization

Figures 1(a) and 1(b) show XRD patterns of the films formed on Pt/MgO(100) and Si(100) substrates. The thicknesses of the fluoride films on Pt/MgO and Si substrates are 160 nm and 106 nm, respectively. The fluoride films were deposited at 300°C on both substrates and annealed at 600°C on Pt/MgO or at 500°C on Si. We can see from these figures that the diffraction peaks in both samples are only from (010)-oriented BaMgF_4 crystallites in the films, except for those of the substrates. Figures 2(a) and 2(b) show the 2θ rocking curve of BaMgF_4 (040) peaks in these samples. The FWHM (full width at half maximum) value is 0.7° in the film on Pt/MgO(100), while it is about 3.2° in the film on Si(100). We can see from these results that the preferred orientation of crystallites is much stronger on Pt/MgO(100) substrates. It has also been found that crystallites in the films on Si(111), GaAs(100), and GaAs(111) substrates are also oriented along the $\langle 010 \rangle$ direction and their FWHM values in the rocking curve measurement are as large as that on Si(100).

Figure 3 shows the annealing time dependence of the FWHM values of BaMgF_4 (040) peaks in the films formed on GaAs(100) substrates by the SPC method. In this figure, "in-situ" means that the samples were annealed at 600°C in the deposition chamber without breaking vacuum, while "ex-situ" means that the vacuum annealing was done in the same

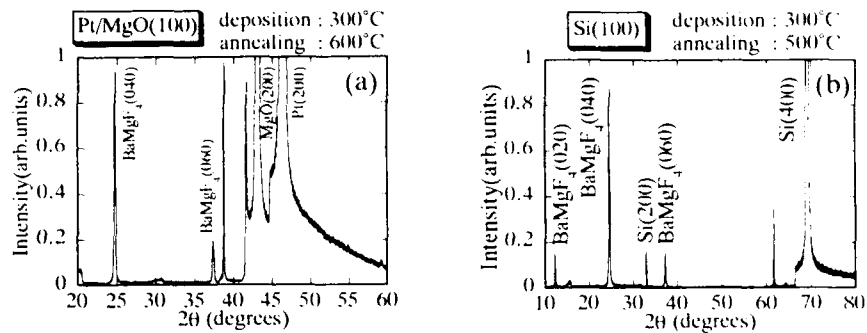


Fig.1 X-ray diffraction patterns of the fluoride films formed on (a) Pt/MgO(100) and (b) Si(100) substrates. The samples shown in (a) and (b) were prepared by depositing at 300°C and annealing at 600°C, respectively. The film thicknesses were (a) 160nm and (b) 106nm.

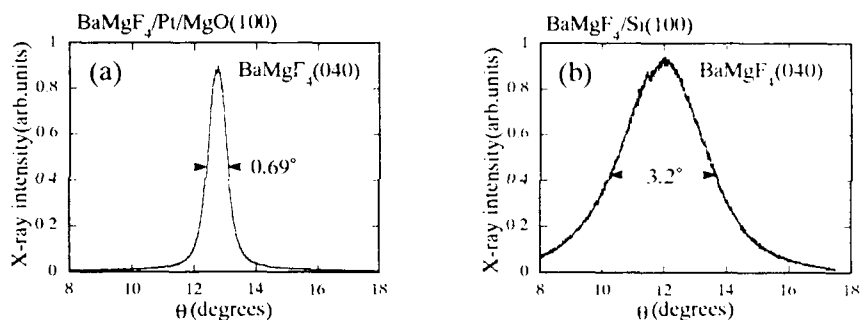


Fig.2 2θ rocking curves of the BaMgF₄(040) diffraction peak. The samples shown in (a) and (b) are the same as those in Fig.1(a) and 1(b), respectively.

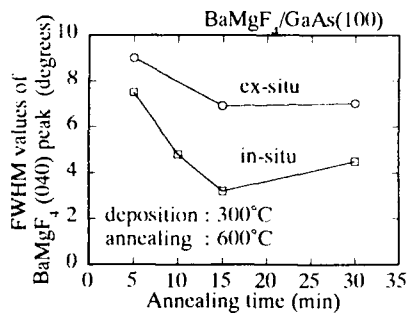


Fig.3 Annealing time dependence of FWHM values of BaMgF₄(040) diffraction peak, which were determined by 2θ rocking curve. The films were deposited at 300°C on GaAs (100) substrates and annealed at 600°C.

chamber after the samples were exposed to air. We can see from this figure that the FWHM values vary from 3° to 9° with the annealing time and annealing conditions, and that the in-situ annealing is more effective in the preferred orientation of crystallites. We can also see from this figure as well as the result on X-ray intensity [16] that an annealing time of 15min is long enough to complete crystallization of the film in the SPC process at 600°C . We have to note, however, that strongly (010)-oriented BaMgF_4 films do not show the spontaneous polarization in the surface normal direction.

Molecular beam epitaxy

Figures 4(a) and 4(b) show XRD patterns for BaMgF_4 films grown on Si(111) and GaAs(111) substrates, respectively. Growth temperatures on the respective substrates were 510°C and 400°C , and the film thicknesses were about 60nm and 200nm. We can see from these figures that the diffraction peaks are only from (120)-oriented BaMgF_4 crystallites except for those of Si and GaAs substrates. It was also found that the preferred orientation of the films on Si(100) and GaAs(100) substrates was (011). These results clearly show that the crystallite orientations in the films are strongly affected by the substrate orientation in case of MBE.

Crystalline quality of the films on Si substrates was further investigated using XRD analysis and RBS. It was found from the X-ray intensity measurement that the optimum growth temperature of the films was about 500°C for both (111) and (100) substrates. The X-ray rocking curve measurements were also done for these samples, which revealed that the FWHM value for the BaMgF_4 (120) peak in a film on Si(111) substrate was about 0.6° , while the value for the BaMgF_4 (011) peak on Si(100) was about 0.67° . We estimate from these values and the resolution of the diffractometer that the spreads of crystallite orientations in the films are about 0.5° .

Figure 5(a) and 5(b) show RBS random and aligned spectra for the fluoride films grown on both Si(100) and (111) substrates, respectively. We can see from Fig. 5 that the channeling minimum yields (χ_{\min}), which is defined as the ratio of the aligned yield for a Ba peak to random yield, is about 0.75 in a film grown on a Si(100) substrate, while it is about 0.55 in a film on a Si(111) substrate. These results show that the $\langle 011 \rangle$ and $\langle 120 \rangle$ axes in the films are well aligned to the surface normal $\langle 100 \rangle$ and $\langle 111 \rangle$ axes of the substrates, respectively. It is interesting to note that relatively good epitaxial alignment holds between two materials with completely dissimilar crystal structures.

Finally, X-ray pole figure measurements were conducted in order to determine the epitaxial relation around the surface normal axis. The figures for the $\langle 040 \rangle$ axes in the films on Si(100) and (111) substrates showed four-fold and six-fold patterns, respectively, which means that the azimuthal directions of crystallites are determined according to the substrate symmetry. The obtained epitaxial relations were $\text{BaMgF}_4[100]/\text{Si}[011]$, $\text{Si}[01\bar{1}]$, $\text{Si}[0\bar{1}1]$, and $\text{Si}[0\bar{1}\bar{1}]$ for a film on Si(100) and $\text{BaMgF}_4[100]/\text{Si}[01\bar{1}]$, $\text{Si}[0\bar{1}1]$, $\text{Si}[0\bar{1}\bar{1}]$, $\text{Si}[\bar{1}01]$, and $\text{Si}[\bar{1}0\bar{1}]$ for a film on Si(111). These relations are schematically shown in Fig. 6.

CONCLUSION

Epitaxial growth of BaMgF_4 films on Pt/MgO, Si, and GaAs substrates was attempted using solid phase crystallization (SPC) and molecular beam epitaxy (MBE) methods. The main results obtained through characterization by XRD analysis, X-ray pole figure measurement, and RBS are as follows.

- (1) BaMgF_4 films formed on Pt/MgO, Si, and GaAs substrates by low temperature deposition followed by high temperature annealing (SPC) showed the strong (010) preferred orientation along the surface normal direction. The strongest preferred orientation was observed in a film on Pt/MgO(100) substrate.

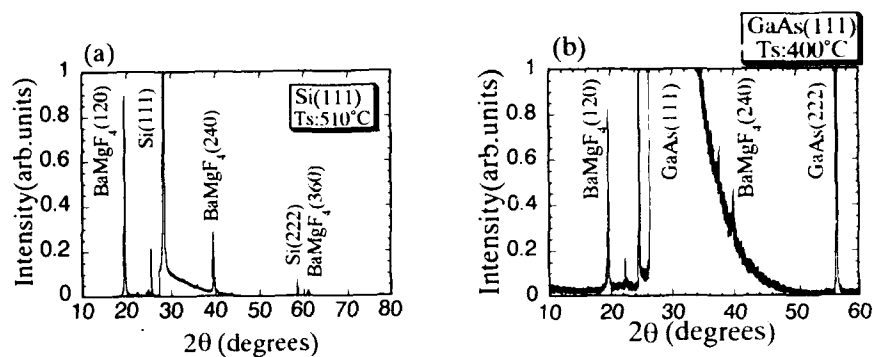


Fig.4 X-ray diffraction patterns of the fluoride films grown on (a) Si(111) and (b) GaAs(111) substrates.

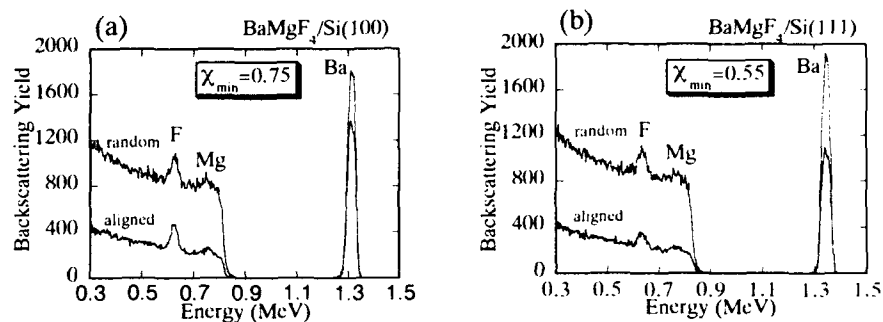


Fig.5 RBS random and aligned spectra for BaMgF_4 films on (a) Si(100) and (b) Si(111) substrates. The samples shown in (a) and (b) are the same as those in Fig.4(a) and 4(b), respectively.

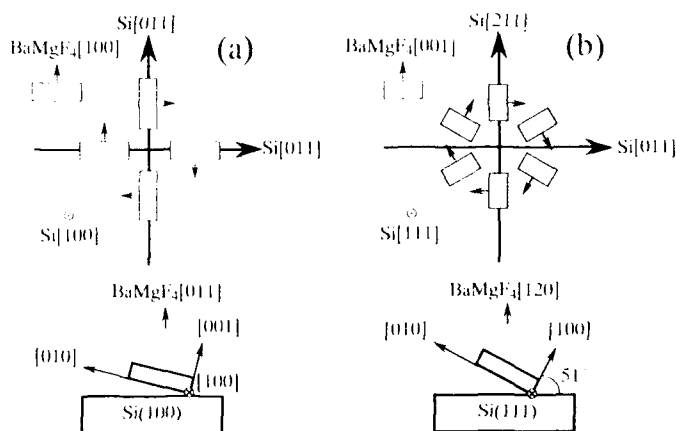


Fig.6 Schematic illustration of the epitaxial relation between BaMgF_4 crystallites and Si substrate. The orientations of Si substrates are (a) (100) and (b) (111). The size of the boxes is proportional to the projection of the unit cell length.

- (2) The spread of crystallite orientations in BaMgF_4 films on GaAs (100) substrates changed by the annealing time and annealing conditions in the range from 3° to 9° .
- (3) (011)-oriented epitaxial films were grown on (100) substrates of Si and GaAs, while (120)-oriented films were grown on (111) substrates of Si and GaAs. The optimum temperature for the growth on Si substrates was about 500°C .
- (4) The channeling minimum yields in RBS for BaMgF_4 (100) films on Si(100) and (120) films on Si(111) were 0.75 and 0.55, respectively. The epitaxial relations around the surface normal axis were also determined by X-ray pole figure measurement.
- (5) In case of a BaMgF_4 (120) film on Si(111), a-axis in a crystallite is 51° -off from the film surface and the spontaneous polarization along the surface normal direction of the film ($P_s \sin 51^\circ$) is expected to be about $6.6 \mu\text{C}/\text{cm}^2$, if the P_s value for a bulk crystal is assumed.

ACKNOWLEDGMENTS

The authors gratefully acknowledge the help of Dr. A.Saiki of Tokyo Institute of Technology for X-ray pole figure measurements and useful discussion. They are also grateful to Mr. M.Kumagai of Kanagawa High Technology Foundation for his RBS measurements. This work was supported by a 1992 Grant-in-Aid for Scientific Research (A) (No. 04402035) from Ministry of Education, Science and Culture.

REFERENCES

1. S.Y.Wu, IEEE Trans. Electron Devices **ED-21**, 499(1974).
2. S.Y.Wu, Ferroelectrics **11**, 379(1976).
3. K.Sugibuchi, Y.Kurogi, and N.Endo, J. Appl. Phys. **40**, 2871(1975).
4. Y.Higuma, Y.Matsui, M.Okuyama, T.Nakagawa, and Y.Hamakawa, Jpn. J. Appl. Phys. **17-1**, 209(1977).
5. S.V.Tolstousov, V.Mukhortov, V.Mukhortov, V.Dudkevich, and E.Fesenko, Ferroelectrics Lett. **1**, 51(1983).
6. T.A.Rost, H.Lin, and T.A.Rabsom, Appl. Phys. Lett. **59**, 3654(1991).
7. H.Ishiwara, Jpn. J. Appl. Phys. **32**, 442(1993).
8. C.-C.Cho, T.S.Kim, B.E.Gnade, H.Y.Liu, and Y.Nishioka, Appl. Phys. Lett. **60**, 338(1992).
9. T.Waho and H.Sacki, Jpn. J. Appl. Phys. **30**, 221(1991).
10. H.Ricard, K.Aizawa, and H.Ishiwara, Appl. Surf. Sci. **56-58**, 888(1992).
11. M.Eibschutz, H.J.Guggenheim, S.H.Wemple, I.Camlibel, and M.DiDomenico Jr., Phys. Lett. **29A**, 409(1969).
12. S.Sinharoy, H.Buhay, M.H.Francombe, W.J. Takei, N.J. Doyle, and J.H.Rieger, J. Vac. Soc. Technol. **A9**, 409(1991).
13. S.Sinharoy, H.Buhay, M.G.Burke, D.R.Lampe, and T.M.Pollak, IEEE Trans. Ultrason. Ferroelectr. & Freq. Control **38**, 663(1991).
14. A.Ishizaka and Y.Shiraki, J. Electrochem. Soc. **133**, 666(1986).
15. J.Fan, H.Oigawa, and Y.Nannichi, Jpn. J. Appl. Phys. **27**, L1331(1988).
16. K.Aizawa and H.Ishiwara, Jpn. J. Appl. Phys. **31**, 3232(1992).

FERROELECTRIC PROPERTIES OF *a*-AXIS TEXTURED BaTiO₃ THIN FILMS

H. A. LU*, L. A. WILLS*, B. W. WESSELS*, X. ZHAN**, J. A. HELFRICH***, J. B. KETTERSON***

*Dept. of Materials Science and Engineering, Northwestern University, Evanston, IL 60208

**Basic Industrial Research Laboratory, Northwestern University, Evanston, IL 60201

***Dept. of Physics, Northwestern University, Evanston, IL 60208

ABSTRACT

Ferroelectric and dielectric properties were measured for BaTiO₃ thin films prepared by metalorganic chemical vapor deposition which were highly *a*-axis textured. No ferroelectric hysteresis was observed from the as-deposited BaTiO₃ films on Pt coated MgO. Upon applying an electric field exceeding a threshold electric field, $E_t \sim 50 - 100$ kV/cm, a ferroelectric hysteresis was observed. A spontaneous polarization $P_s \geq 15$ $\mu\text{C}/\text{cm}^2$ was measured for the textured films.

INTRODUCTION

The realization of ferroelectric thin films for electronic applications such as nonvolatile memories and dielectric thin films relies on the growth of high quality films on conducting substrates. While epitaxial growth of BaTiO₃ thin films on insulating substrates such as LaAlO₃ and SrTiO₃ has been reported[1,2], the film deposition on metallic substrates has been generally less successful. To date, only deposition of randomly oriented BaTiO₃ films on metallic substrates were reported using metalorganic chemical vapor deposition (MOCVD). In this paper, we report the successful growth of highly *a*-axis textured BaTiO₃ thin films on Pt coated MgO, and their measured ferroelectric and dielectric properties.

EXPERIMENTAL PROCEDURE

The BaTiO₃ thin film deposition process was similar to that reported earlier[1]. A Pt layer of ~ 1 μm thick was sputtered on (100) MgO substrates. A BaTiO₃ thin film was subsequently deposited on Pt via MOCVD. Both *a*-axis textured and randomly oriented BaTiO₃ films were obtained. The textured films were obtained only on the highly (100) textured Pt layer. The film thickness is in the range of 0.3 - 1.0 μm . For electrical characterization, Al dots of 350 μm diameter were evaporated on to the film which served as the top electrical contacts. Part of the film was etched away to expose the Pt bottom electrode. Fig. 1 shows the sample configuration for the electrical properties measurement. The ferroelectric hysteresis of the film was measured using a modified Sawyer-Tower circuit[3] with a 600 Hz sinusoidal applied field. The dielectric properties were measured using a computer interfaced Hewlett-Packard impedance analyzer. A DC bias voltage was applied across the film through a voltage source also controlled by the computer. The amplitude of the AC signal used for the impedance measurement was 20 mV.

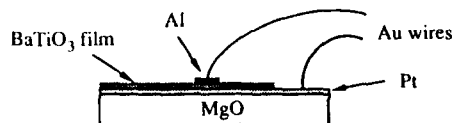


Fig. 1. Sample configuration for electrical measurements on BaTiO_3 thin films.

RESULTS AND DISCUSSIONS

Fig. 2 is a x-ray diffraction $\theta / 2\theta$ scan of a highly a -axis textured BaTiO_3 film. The strongest diffraction peaks were from (100) and (200) BaTiO_3 reflections. The (110) or (101) reflections were very weak, indicating a highly preferred orientation of the film with the a -axis aligned parallel to the film normal. The average grain size of the film is $\sim 0.2 \mu\text{m}$ as determined from the surface morphology using scanning electron microscopy and atomic force microscopy. Fig. 3 shows the measured frequency dependence of the film's dielectric constant and dissipation factor in the frequency range of 200 Hz to 1 MHz. The dielectric constant, $\epsilon \sim 10$, measured for the as-deposited films was low compared to the values for bulk BaTiO_3 single crystals ($\epsilon_c \sim 200$ and $\epsilon_a \sim 4000$) [4] and that reported for BaTiO_3 thin films ($\epsilon \sim 100 - 550$) [5,6,7]. The measured dissipation factor, $D \sim 0.03$, showed little dispersion over the measured frequency range. The as-deposited film generally exhibited no observable ferroelectric hysteresis.

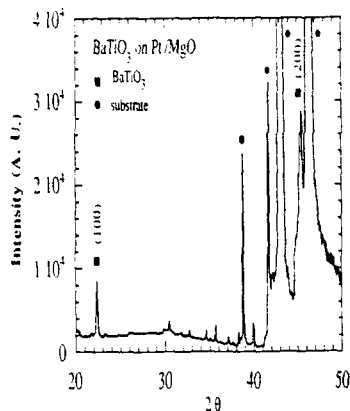


Fig. 2. X-ray diffraction $\theta / 2\theta$ scan of a BaTiO_3 thin film deposited on Pt coated MgO substrate.

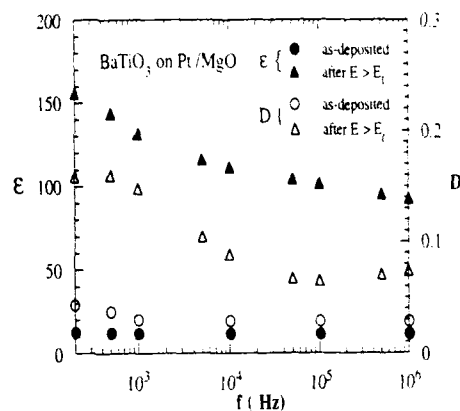
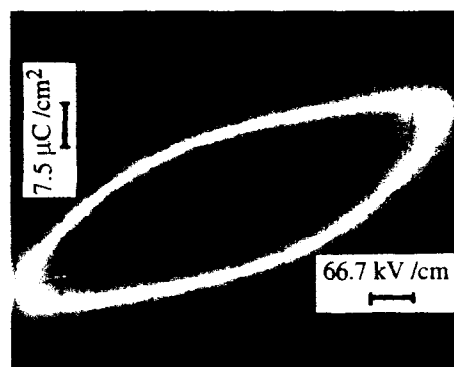


Fig. 3. Dielectric constants measured from the as-deposited film, and after $E > E_t$ was applied across the film.

After a DC electric field exceeding a threshold electric field, E_t , was applied across the film, the dielectric constant increased substantially, usually by one order of magnitude to $\epsilon \sim 100$ (Fig. 3). Concurrently the dissipation factor increased to $D \sim 0.1$. Nevertheless the film remained highly resistive. The increased dissipation factor corresponded to a resistivity of $300 \text{ M}\Omega \text{ cm}$ across the film. This was in agreement with the directly measured film resistance. The dielectric constant remained at this value after withdrawing of the applied DC field. E_t measured for different films and contacts ranged from $\sim 50 - 100 \text{ kV/cm}$. Also plotted in Fig. 3 is the film's dielectric constant and dissipation factor measured at zero bias voltage after $E > E_t$ was applied.

A ferroelectric hysteresis was observed after the threshold field was exceeded. Fig. 4 shows the measured uncompensated hysteresis loop for an *a*-axis textured film after an electric field, $E > E_c$, was applied. The hysteresis was obtained at the maximum amplitude of the sinusoidal voltage source. Due to the extremely high coercive electric field of the film, saturation of the hysteresis was not observed as indicated by the slightly rounded shape of the hysteresis loop. The rounding of the hysteresis before saturation was also observed in the randomly oriented film where the coercive field was much lower and saturation can be reached. From the hysteresis after $E > E_c$ was applied, the values of spontaneous polarization $P_s \geq 15 \mu\text{C}/\text{cm}^2$, remanent polarization $P_r \sim 13 \mu\text{C}/\text{cm}^2$, and coercive electric field $E_c \sim 220 \text{ kV}/\text{cm}$ were determined. (For comparison, the reported values for bulk single crystal BaTiO_3 are $P_s \sim 26 \mu\text{C}/\text{cm}^2$ and $E_c \sim 5 \text{ kV}/\text{cm}$)[4].

Fig. 4. Ferroelectric hysteresis measured after an electric field $E > E_c$ was applied across an *a*-axis textured BaTiO_3 thin film.



The measured electrical properties can be related to the crystalline structure of the BaTiO_3 thin film. For the *a*-axis textured film, the *c*-axis lies in the film plane. The depolarization energy arising from the lattice dipole interaction favors the *c*-axis of the different grains being "randomly" oriented in the film plane. This *c*-axis orientation configuration, combined with the strain and the fine-grain structure of the film, may contribute to the low dielectric constant and the lack of ferroelectric hysteresis observed from the as-deposited BaTiO_3 thin films[8].

Upon poling with an external electric field, the lattice dipoles in the ferroelectric crystals are aligned to the field direction. For bulk BaTiO_3 , poling was achieved with moderate electric fields ($0.5 - 2 \text{ kV}/\text{cm}$) near the Curie temperature[9]. The change of the dielectric constants of BaTiO_3 films as illustrated in Fig. 3 can be attributed to the poling of the film. Due to the small film thickness, very high electric field (orders of magnitude higher than the poling field of the bulk BaTiO_3) could be applied across the film, thus enabling the film to be poled at room temperature. At the threshold field, the lattice dipoles were aligned by the electric field, resulting in the *c*-axis being oriented to the film normal. As a result of this lattice dipole alignment, relatively high dielectric constants and ferroelectric hysteresis loops were observed after the threshold field was exceeded.

The ferroelectric and dielectric properties measured from the BaTiO_3 thin films depended on the film's crystalline structure. Table 1. lists the properties measured for the *a*-axis textured and the predominantly randomly oriented BaTiO_3 thin films derived from MOCVD. Also listed are the electrical properties of the BaTiO_3 thin films reported by other research groups. In

comparison, the charge storage parameters (P_s , P_r) presented in this work were the highest among the reported values for BaTiO₃ thin films so far.

Table 1. The electrical properties of the MOCVD derived BaTiO₃ thin films and those reported by other research groups.

Method	substrate	Crystal Quality	Properties	Reference
MOCVD	Pt	a-axis textured	$P_s \geq 15 \mu\text{C}/\text{cm}^2$ $P_r \sim 13 \mu\text{C}/\text{cm}^2$ $E_c \sim 220 \text{ kV}/\text{cm}$ $\epsilon \sim 100$, $D \sim 0.03 - 0.1$	This work
MOCVD	Pt	random	$P_s \sim 16 \mu\text{C}/\text{cm}^2$ $P_r \sim 10 \mu\text{C}/\text{cm}^2$ $E_c \sim 70 \text{ kV}/\text{cm}$ $\epsilon \sim 100$, $D \sim 0.03 - 0.1$	This work
Reactive evaporation	(100)Pt	(100) epitaxy	$P_s \sim 11 \mu\text{C}/\text{cm}^2$ $P_r \sim 4.7 \mu\text{C}/\text{cm}^2$ $\epsilon \sim 550$ (1 kHz), $D \sim 0.01-0.05$	Iijima et. al, 1990[5]
r.f. magnetron sputtering	Pd	random	$\epsilon \sim 160$, 330	Shi et. al, 1991[6]
MOCVD	NiCr/BaTiO ₃	random	$\epsilon \sim 250$	Kwak et. al, 1991[7]

For bulk single crystal BaTiO₃: $P_s \sim 26 \mu\text{C}/\text{cm}^2$, $E_c \sim 1.5 \text{ kV}/\text{cm}$, $\epsilon_c \sim 200$, $\epsilon_a \sim 4000$, from Merz et. al, 1953[4].

SUMMARY

Highly a-axis textured BaTiO₃ thin films were deposited on the Pt coated MgO substrates using MOCVD. Dielectric and ferroelectric properties were measured for the films. Upon poling of the film, spontaneous polarization of $\geq 15 \mu\text{C}/\text{cm}^2$ was achieved. The poled films exhibited polarization parameters comparable to that of the bulk single crystal BaTiO₃.

ACKNOWLEDGEMENT

This work was supported by the Materials Research Laboratories Program of the National Science Foundation, at the Materials Research Center of the Northwestern University (Award No. DMR-9120521) and the Department of Energy (grant DE-FG02-85-ER-45209), partial support of H. A. Lu was provided by a private funding from D. Zeng, and partial support of L. A. Wills was provided by a fellowship from IBM.

REFERENCE

1. L. A. Wills, B. W. Wessels, D. S. Richeson, T. J. Marks, *Appl. Phys. Lett.* **60**, 41 (1992).
2. C. S. Chern, J. Zhao, L. Luo, Y. Q. Li, P. Norris, B. Kear, F. Cosandey, C. J. Maggiore, B. Gallois, and B. J. Wilkens, *Appl. Phys. Lett.*, **60**, 1144 (1992).
3. H. Diamant, K. Dreuck, and R. Pepinsky, *Rev. of Sci. Instr.*, **28**, 30 (1957).
4. W. J. Merz, *Phys. Rev.* **91**, 513 (1953).
5. K. Iijima, T. Terashima, K. Yamamoto, K. Hirata, and Y. Bando, *Appl. Phys. Lett.*, **56**, 527 (1990).
6. Z. Q. Shi, Q. X. Jia, and W. A. Anderson, *J. Vac. Sci. Tech. A*, **10**, 733 (1992).
7. B. S. Kwak, K. Zhang, E. P. Boyd, A. Erbil, and B. J. Wilkens, *J. Appl. Phys.* **69**, 767 (1991).
8. G. Arlt, D. Hennings, and G. de With, *J. Appl. Phys.* **58**, 15 (1985).
9. B. A. Wechsler, M. B. Klein, and D. Rytz, *SPIE*, **681**, 91 (1986).

PREPARATION AND CHARACTERIZATION OF EPITAXIAL KNbO_3 THIN FILMS BY A SOL-GEL METHOD

HIDEHIRO ENDO* AND M. J. CIMA**

*Advanced Materials & Technology Research Laboratories, Nippon Steel Corp., 1618 Ida, Nakahara-ku, Kawasaki 211, JAPAN

**Department of Materials Science & Engineering, Massachusetts Institute of Technology, 77 Massachusetts Ave., Cambridge, MA 02139

ABSTRACT

Epitaxial formation of KNbO_3 films on several substrates was examined. The films were prepared by a sol-gel process using potassium ethoxide and niobium pentaethoxide. Hetero-epitaxial KNbO_3 films with (100) orientation were successfully obtained both on MgO (100) and SrTiO_3 (100) substrates by heat treatments above 700°C , while polycrystalline KNbO_3 were formed on Si (111) substrates. Higher temperatures and extended soaking time promoted the grain growth of KNbO_3 and KNbO_3 films with improved surface morphologies (smoother surfaces) could be obtained by controlling heat treatment parameters.

INTRODUCTION

Ferroelectric materials are of great interest for their wide dielectric, piezoelectric, pyroelectric and electro-optic applications. Among these materials, due to its high electro-optic and non-linear optical coefficients and good photorefractive properties, potassium niobate (KNbO_3) has recently received attention for a variety of applications, such as optical waveguides, frequency doublers, holographic storage devices and so on. [1]

Conventionally, solid-state reactions between potassium carbonate and niobium oxide powders were used for preparing potassium niobate. By these methods, however, it is difficult to obtain a stoichiometric, chemically homogeneous, single phase product due to inhomogeneity in mixing of the reactants and preferential volatilization of K_2O under higher processing temperatures. In addition, thin films of KNbO_3 can not be obtained by these solid-state reactions.

The sol-gel method is a promising chemical technique for preparing ferroelectric films since it allows for excellent homogeneity, precise compositional control, lower temperature process, reproducible coating thickness, preparation of large area films by spin coating or dip coating, and simple and inexpensive equipment. In recent years, investigations have been widely done for sol-gel derived ferroelectric thin films, such as BaTiO_3 [2,3], PbTiO_3 [4-6], PZT [4,7,8], PLZT [4], $\text{Li}_2\text{B}_4\text{O}_7$ [9] and LiNbO_3 [10-14].

Only a few studies have been reported for sol-gel processing of KNbO_3 . Wu *et al.* [15] prepared KNbO_3 powders through a sol-gel technique using potassium ethoxide and niobium ethoxide as precursors, but they did not succeed in obtaining single phase KNbO_3 . They observed Nb-rich (potassium deficient) precipitates. Swartz *et al.* [16] used potassium methoxyethoxide and niobium ethoxide for the deposition of KNbO_3 thin films on silicon, alumina and single crystal SrTiO_3 substrates. Although highly oriented KNbO_3 (221) films were formed on SrTiO_3 (210), they observed unidentified second phases in the all films, even on SrTiO_3 substrates. Amini *et al.* [17] fabricated polycrystalline single-phase KNbO_3 films on KBr substrates by using bimetallic alkoxides (potassium niobium ethoxide and propoxide), while potassium deficient hydrate phase ($\text{K}_4\text{Nb}_6\text{O}_{17} \cdot 3\text{H}_2\text{O}$) was formed on fused SiO_2 substrates. Cheng *et al.* [18] prepared KNbO_3 thin films on several substrates via sol-gel process. Single crystal like KNbO_3 was obtained on SrTiO_3 substrate, while polycrystalline KNbO_3 was formed on MgO and ZrO_2 .

In this study, epitaxial formation and microstructural evolution of KNbO_3 films by a sol gel method were investigated in order to understand the effects of heat treatments (temperature, time and heating rate) and substrates.

EXPERIMENTAL PROCEDURE

For the preparation of KNbO_3 films, potassium niobate precursor was obtained from potassium

ethoxide ($\text{K}(\text{OEt})$ or $\text{K}(\text{C}_2\text{H}_5\text{O})$) and niobium pentaethoxide ($\text{Nb}(\text{OEt})_5$ or $\text{Nb}(\text{C}_2\text{H}_5\text{O})_5$) (Kojundo Chem. Lab., Japan) in a dry nitrogen atmosphere. Since these alkoxides are extremely sensitive to moisture and carbon dioxide [13], the whole procedure was conducted in the pure dry N_2 ambient. Equal molar amounts of each alkoxide were dissolved and mixed in absolute ethanol for 24h at room temperature to form a 0.05M double alkoxide ($\text{KNb}(\text{OEt})_6$) solution. After an additional 24h stirring, the solution was concentrated to 0.5M at room temperature by using vacuum distillation method. Dry gel powder was also prepared from portion of the solution by removing solvent under vacuum at room temperature.

Optically polished MgO with (100) orientation (Tateho/ACMC, SC), SrTiO_3 (100) (Commercial Crystal Inc., FL) and Si with (111) (Virginia Semiconductor, VA) were used as substrates. In a dry N_2 environment the precursor was spin-coated onto $6.3 \times 6.3 \times 0.5$ mm substrates at 2000 rpm and dried for 0.5h at room temperature. These substrates were cleaned in an acetone ultrasonic bath before the spin coating procedure.

The coated substrates were then heat-treated for 0.5h at 500 to 800°C in a flowing mixture of water vapor and oxygen and heated further for 0.5 to 10h in a dry oxygen atmosphere. Two kinds of heating schedules were adopted to examine the effect of the heating rates on the morphologies of the films.

Weight losses of the dry gel powders were measured by thermal gravimetric analysis (TGA). Characterization of the prepared films was performed using X-ray diffraction method (XRD), scanning electron microscopy (SEM) and transmission electron microscopy (TEM).

RESULTS AND DISCUSSION

Effects of Heating Parameters

TGA analysis was conducted for the dry gel powder of the precursor between room temperature and 800°C in a dry oxygen ambient at the ramp of 10°C/m. Weight loss below 300°C occurred slowly with two maximum rates around 100 and 230°C. A large weight loss occurred abruptly at 300°C, while only a small weight loss was observed above 350°C. The total weight loss up to 800°C was 53.4% which is very close to the theoretical weight loss which occurs going from $\text{KNb}(\text{OEt})_6$ to KNbO_3 (55.3% loss). Each weight loss around 100, 230, 300°C and above 350°C may attribute to volatilization of water and/or alcohol, to decomposition of alkoxy groups, to decomposition of carbonates and hydroxides, and to crystallization of the powders, respectively. [14]

Crystallization temperature was determined for the films on MgO (100) substrates by using a X-ray diffraction method. Heat treatments were conducted in the temperature ranges between 400 and 800°C for 1 to 10h with the heating and cooling rates of 10°C/m ("Rapid" Heating Schedule: HS-1). No peak other than MgO (200) reflection ($2\theta=42.9^\circ$) was found up to 500°C, indicating that the films consist of amorphous carbonates or hydroxides. By the heat treatment at

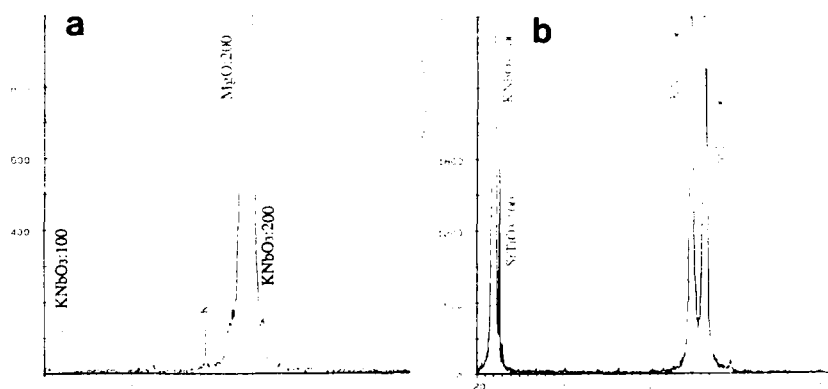


Fig.1. X-ray diffraction patterns of KNbO_3 films on (a) MgO (100) and (b) SrTiO_3 (100) substrates heat treated at 700°C for 1h

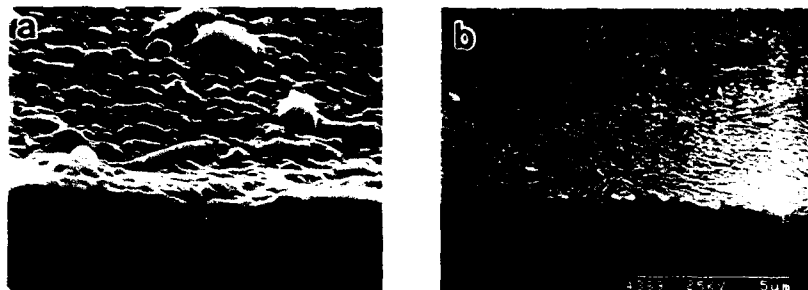


Fig. 2. Scanning electron micrographs of KNbO_3 films on MgO (100) substrates heat treated at 700°C for 1h by (a) HS-1 and (b) HS-2

600°C , a very weak and broad peak of KNbO_3 (100) ($2\theta=22.15^\circ$) was firstly observed from the film. Although this film is still amorphous-like, a preferential growth of epitaxial KNbO_3 (100) on MgO (100) substrate is suggested to occur during crystallization. Except for MgO (200) reflection, only the sharp peaks of KNbO_3 (100) and (200) were detected from the films heat treated at the temperatures above 700°C . In the figure 1(a), the X-ray powder diffraction pattern is indicated for the KNbO_3 films on MgO (100) fired at 700°C for 1h. Because both KNbO_3 and MgO have the same crystalline system, cubic (NaCl structure for MgO and Perovskite for KNbO_3 at higher temperatures), and lattice parameter mismatching between them is relatively small (within 4.7%) [18], epitaxial formation of KNbO_3 (100) has been performed on the MgO (100) substrate.

Although epitaxial formation of KNbO_3 was obtained on MgO by the heat treatments above 700°C , the surfaces of these films were very rough with a lot of defects, such as nodules and craters. Scanning electron micrograph of the crystalline KNbO_3 films (30° tilted surfaces) heat treated at 700°C for 1h (by HS-1) is shown in the figure 2(a). The film is covered with huge amounts of defects. The effect of the heating rates on the morphological changes of the films were examined for the aim of obtaining the films with smoother surfaces. As clarified from the TGA analysis, large weight losses accompanying a large amount of gas generation occurred mostly from the room temperature to 300°C and there was a very small weight loss (little gas generation) above 300°C . Thus, a modified heating schedule ("Slow" Heating Schedule: HS-2) in which heating rates were $2^\circ\text{C}/\text{m}$ from R.T. to 300°C , $5^\circ\text{C}/\text{m}$ from 300 to 500°C and $25^\circ\text{C}/\text{m}$ from 500°C to the final temperatures, was adopted. Scanning electron micrograph of the KNbO_3 film on MgO substrate heat treated at 700°C for 1h by HS-2 is compared in the figure 2(b). It is obvious from the figure that a defect-free KNbO_3 film with improved surface was successfully obtained by changing heating schedule. Slower heating rate, especially at the lower temperatures up to 300°C , drastically prevented the defect formation on the films by decreasing gas generating speed within the films.

By fixing the heating schedule (HS-2) and soaking time (1h), the effect of heat treatment temperatures on the microstructural evolution of KNbO_3 films was investigated. In the figure 3, scanning electron micrographs of KNbO_3 films on MgO (100) substrates heat treated at (a) 600°C , (b) 700°C and (c) 750°C for 1h by HS-2, are shown. The film fired at 600°C (figure 3(a)) exhibits a relatively smooth surface with a thickness of $0.1\text{--}0.2\mu\text{m}$. With increasing heat treatment temperature, the surface roughness of the film becomes larger due to the grain growth with a direction perpendicular to the substrate surface. Only [100] reflections appear in the X-ray diffraction pattern even after these grain growth.

Under the fixed heat treatment conditions of 700°C by HS-2, soaking time was varied in the range of 1 to 10h. No phase was detected other than KNbO_3 [100] and MgO (200) reflections by changing soaking time from the films on MgO (100) substrates heat treated at 700°C . Nevertheless, grain growth was also observed in the KNbO_3 films as soaking time increases. In the figure 4, morphological changes (SEM photographs) are indicated for the KNbO_3 films on MgO heat treated at 700°C for (a) 1, (b) 5 and (c) 10h. It is clear from the figures that the extended soaking time promoted the grain growth of KNbO_3 .

Cross section TEM images and electron diffraction patterns of KNbO_3 films on MgO (100) heat treated at 750°C for (a) 1h and (b) 5h are compared in the figure 5. In the film fired for 1h, an

amorphous like grain (Fig.5(a), B) was still observed on MgO substrate (C) along with crystalline grain (A) of cubic KNbO_3 . A lot of bubbles were found in the amorphous like grain, which may indicate that the final stage of pyrolysis (gas generation), crystallization (hetero-epitaxial growth) and densification occur in the film simultaneously. Extended soaking time promoted crystallization and densification of the films and a dense KNbO_3 film was obtained on MgO substrate (Fig.5(b)).

Effect of Substrate

KNbO_3 films were prepared on Si (111) and SrTiO_3 (100) substrates in addition to MgO (100)

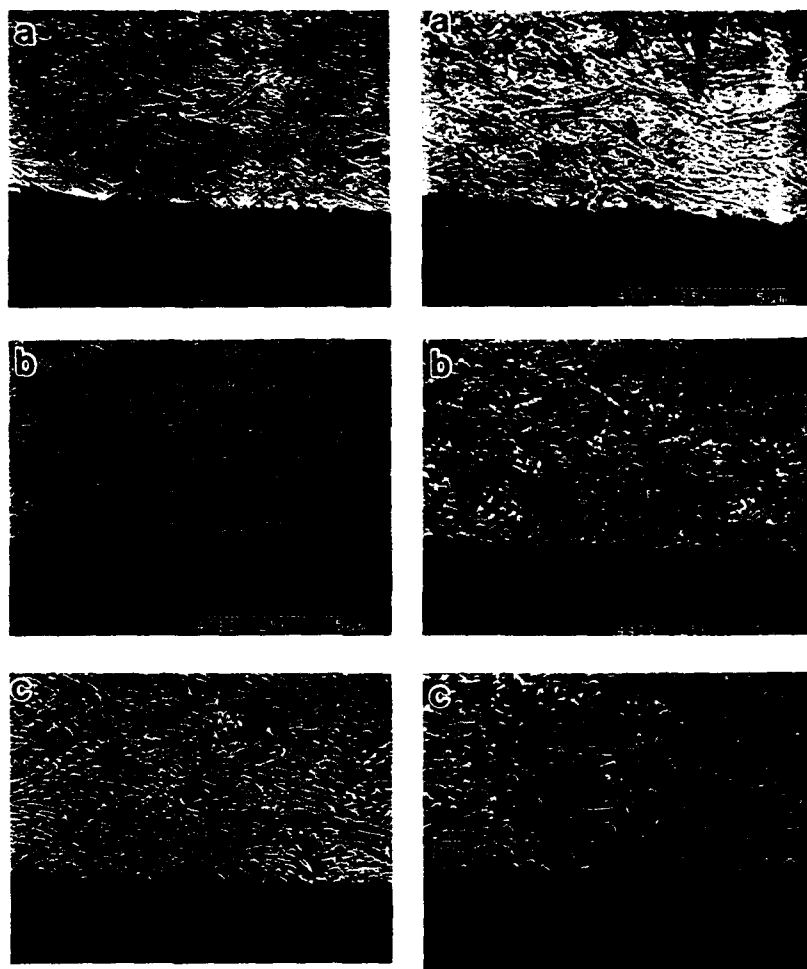


Fig.3. Scanning electron micrographs of KNbO_3 films on MgO (100) substrates heat treated at (a) 600, (b) 700 and (c) 750°C for 1h by HS-2

Fig.4. Scanning electron micrographs of KNbO_3 films on MgO (100) substrates heat treated at 700 °C for (a) 1h, (b) 5h and (c) 10h by HS-2

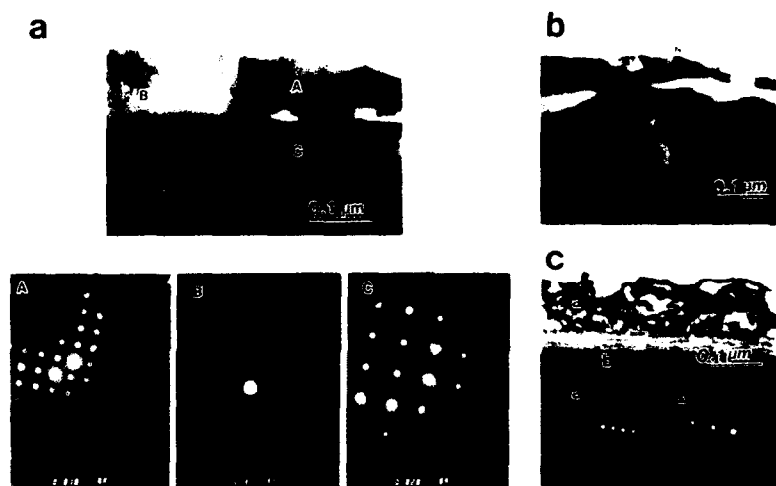


Fig.5. Cross section transmission electron micrographs and electron diffraction patterns of KNbO_3 films on MgO (100) substrates heat treated at 750°C for (a) 1h and (b) 5h, and (c) on SrTiO_3 (100) substrate at 700°C for 1h by HS-2

by the heat treatment of 700°C for 1h by HS-2 in order to examine the effect of the substrate on the microstructural development of the films. X-ray powder diffraction pattern is shown for the KNbO_3 film on SrTiO_3 (100) in the figure 1(b). While the epitaxial formation of KNbO_3 was observed both on MgO (100) and SrTiO_3 (100) substrates, a series of peaks corresponding to KNbO_3 reflections along with Si (111) and (222) were detected from the film on Si (111). Silicon (crystalline form : cubic) has a much larger lattice parameter (5.430\AA) than KNbO_3 (4.015\AA) to lead the polycrystalline KNbO_3 formation due to the huge lattice parameter mismatching between them. The surface morphologies of KNbO_3 films heat treated at 700°C for 1h (HS-2) on (a) Si (111) and (b) SrTiO_3 (100) substrates are compared in the figure 6. In the film on Si (111) substrate, innumerable number of KNbO_3 powders (grains) in size of $0.1\text{--}0.2\text{ }\mu\text{m}$ were dispersed, which resulted in creating the rough surface, while the film with very smooth surface was obtained on SrTiO_3 (100). Because lattice parameter mismatching between KNbO_3 ($a=4.015\text{\AA}$) and SrTiO_3 (Perovskite structure, $a=3.905\text{\AA}$) is very small, epitaxial formation of KNbO_3 has been more preferred on SrTiO_3 substrate to lead a smoother surface of the film. It is concluded that phase development in KNbO_3 films is highly dependent upon the nature of the substrate and that,

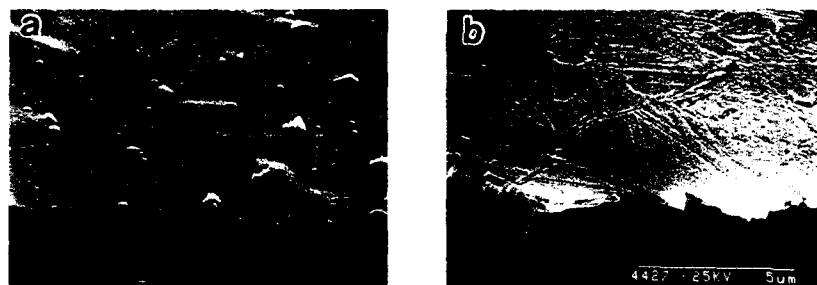


Fig.6. Scanning electron micrographs of KNbO_3 films on (a) Si (111) and (b) SrTiO_3 (100) substrates heat treated at 700°C for 1h by HS-2

for the purpose of epitaxial formation, the substrate with smaller lattice parameter mismatching should be preferable.

CONCLUSIONS

Hetero-epitaxial KNbO_3 films with (100) orientation were successfully obtained both on MgO (100) and SrTiO_3 (100) substrates by a sol-gel method using potassium ethoxide and niobium pentaethoxide.

(1) Crystallization of KNbO_3 began around 600°C and epitaxial films were formed on MgO by heat treatments above 700°C .

(2) KNbO_3 films with defect-free, smoother surfaces could be obtained by controlling heat treatment conditions. Especially, a controlled heating schedule was very effective to improve the surface morphologies of the films by minimizing gas generating speed during heat treatments.

(3) Higher temperatures and extended soaking time promoted the grain growth of KNbO_3 . By controlling heat treatment parameters, KNbO_3 films with smooth surface could be obtained.

(4) Phase development and microstructural evolution of KNbO_3 films was dependent on the substrate. Polycrystalline KNbO_3 were formed on Si (111) substrates with KNbO_3 powders (grains) dispersed in the films.

REFERENCES

- [1] L.M. Sheppard, *Am. Ceram. Soc. Bull.*, **71** 85-95 (1992)
- [2] J. Fukushima, K. Kodaira and T. Matsushita, *ibid.*, **55** 1064-65 (1976)
- [3] T. Tsuchiya, T. Kawano, T. Sei and J. Hatano, *J. Jap. Ceram. Soc.*, **98** 743-48 (1990)
- [4] K.D. Budd, S.K. Dey and D.A. Payne, *Brit. Ceram. Soc. Proc.*, **36** 107-21 (1985)
- [5] *Idem*, Better Ceramics Through Chemistry II, Mater. Res. Soc., Pittsburgh, PA (1986) pp. 711-15
- [6] C. Chen, D.F. Ryder, Jr. and W.A. Spurgeon, *J. Am. Ceram. Soc.*, **72** 1495-98 (1989)
- [7] T. Suzuki, M. Matsuki, Y. Matsuda, K. Kobayashi and Y. Takahashi, *J. Jap. Ceram. Soc.*, **98** 754-58 (1990)
- [8] S.K. Dey, K.D. Budd and D.A. Payne, *IEEE Trans. Ultrason. Ferroelect. Freq. Contr.*, **35** 80-81 (1988)
- [9] H. Yamashita, T. Yoko and S. Sakka, *J. Am. Ceram. Soc.*, **74** 1668-74 (1991)
- [10] D.J. Eichorst and D.A. Payne, Better Ceramics Through Chemistry III, Mater. Res. Soc., Pittsburgh, PA (1988) pp. 773-78
- [11] M.I. Yanovskaya, E.P. Turevskaya, A.P. Leonov, S.A. Ivanov, N.V. Kolganova, S.Y. Stefanovich, N.Y. Turova and Y.N. Venevtsev, *J. Mater. Sci.*, **23** 395-99 (1988)
- [12] D.P. Partlow and J. Gregg, *J. Mater. Res.*, **2** 595-605 (1987)
- [13] S. Hirano and K. Kato, *Adv. Ceram. Mater.*, **3** 503-506 (1988)
- [14] *Idem*, Processing Science of Advanced Ceramics, Mater. Res. Soc., Pittsburgh, PA (1989) pp. 181-90
- [15] E.T. Wu, A.X. Kuang and J.D. MacKenzie, Proc. of the Sixth IEEE International Symposium on Applications of Ferroelectrics, 388-90 (1986)
- [16] S.L. Swartz, P.J. Melling and C.S. Grant, Optical Materials: Processing and Science, Mater. Res. Soc. Proc., **152**, Pittsburgh, PA (1989) pp. 227-32
- [17] M.M. Amini and M.D. Sachs, Mater. Res. Soc. Symp. Proc. **180** 675-83 (1990)
- [18] C.H. Cheng, Y. Xu and J.D. Mackenzie, Mater. Res. Soc. Symp. Proc. **271** 383-88 (1992)

PART X

Materials and Processes

LOW TEMPERATURE PREPARATION OF BaTiO₃ FILMS ON SILICON

M.E. Pilleux* and V.M. Fuenzalida† *

*Universidad de Chile, Facultad de Ciencias Físicas y Matemáticas, Departamento de Física, Casilla 487-3, Santiago, Chile.

† To whom correspondence should be addressed.

ABSTRACT

Insulating BaTiO₃ thin films were obtained on titanium coated silicon wafers using a novel low temperature technique. They were produced hydrothermally by introducing the substrate in a 0.25M Ba(OH)₂ solution inside an autoclave and heating in the 200–250°C range for 8 hours. This treatment delivered smooth pinhole-free films on the Ti with thicknesses ranging from 35nm (200°C) to 45nm (250°C), with grains in the 100–300nm diameter range in all films. The films exhibited a dielectric constant up to 227, a breakdown field of 70MV/m, and a dc resistivity of $1 \cdot 10^9 \Omega\text{m}$.

INTRODUCTION

Because of its large dielectric constant and ferroelectric properties, barium titanate is an important and promising material for the future development of hybrid devices for microelectronics and integrated optoelectronics. For the construction of dynamic random access memories (DRAMs) a low temperature film deposition procedure is desired. This is because of strict materials processing conditions and compatibility with standard silicon technology. High temperatures (above 700°C) trigger undesirable chemical reactions between the film and the silicon substrate. Moreover, they may smear out existing doping profiles from earlier processing stages.

Most chemical processes, like chemical vapor deposition, sol-gel, and metalorganic deposition, need an *in situ* or postdeposition treatment of at least 600°C [1]. This is also true for vacuum evaporation and sputtering, which require at least 500°C for the development of a crystalline microstructure. An important variation is the laser ablation method, which in principle does not require heating of the silicon substrate at all. Good results, however, require a substrate temperature of 600°C [2].

A completely different approach was developed by Yoshimura *et. al.*, who were able to grow polycrystalline BaTiO₃ on titanium or titanium covered glass and plastic substrates using the hydrothermal method, without need of a postdeposition treatment [3]. The hydrothermal procedure, which can be electrochemically assisted, consists of the reaction between titanium and a Ba(OH)₂ solution at temperatures below 300°C [3,4]. To our knowledge, this is the only method of growing polycrystalline BaTiO₃ films at such low temperatures. A further advantage of the technique is its possibility of coating objects with an irregular geometry.

Here we present an extension of this method for the deposition of BaTiO₃ films on titanium coated silicon substrates. The films were characterized using x-ray photoelectron spectroscopy (XPS), Auger electron spectroscopy (AES), and electrical measurements.

FILM FABRICATION

Substrates

A 0.5 μ m titanium film was deposited using rf sputtering onto 2 inch n-type degenerate (100) silicon wafers. The sputtering conditions were the following: rf power 800W, Ar partial pressure 1 Pa, and rf frequency 13.6MHz. Ti was deposited on both sides in order to prevent the reaction of silicon in the alkaline solution [5].

Hydrothermal procedure

The substrates were hydrothermally reacted in a stainless steel autoclave. They were submerged in a 0.25M Ba(OH)₂ solution prepared with boiling deionized water. The solution was contained in a Teflon beaker. The sealed autoclave was maintained at the temperatures of 200 and 250°C for 8 hours, in different experiments. This treatment time should provide a highly crystalline film [6]. After the treatment the samples were rinsed in boiling deionized water.

CHARACTERIZATION

Thickness

The Ti coated silicon substrates displayed a metallic mirror like color. The hydrothermally treated samples exhibited homogeneous colors that ranged from violet to gold in different samples. Film thickness and surface roughness were measured with a profilometer, and corroborated with the Tolansky method, by measuring the step height of the BaTiO₃ film on Ti. The step was produced by chemical etching.

The roughness of the Ti substrate without hydrothermal treatment was 2nm rms. After the hydrothermal treatment the BaTiO₃ film exhibited an rms roughness of 4nm (200°C sample) and 5nm (250°C sample). The thickness was 34 \pm 3nm in the 200°C sample and 49 \pm 5nm in the 250°C sample. These values are much lower than those reported in the literature [6,7]. The calibrated AES in depth measurements yielded a similar film thickness estimation. Notice that this is the first time in which the thickness of hydrothermal films is directly measured by standard techniques. Previous estimations, based only on the mass change of the substrate, may have systematic errors due to etching of the substrate in the aggressive alkaline solution.

Microstructure

The film morphology was characterized using scanning electron microscopy (SEM). Cross sectional views of the titanium layer revealed that the 500nm film on the polished side of the wafer had a columnar microstructure. We do not know how this substrate microstructure influenced the final film thickness and microstructure.

The hydrothermal films displayed a homogeneous crack free appearance in all scanned areas of all samples. The surface showed grains with a mean diameter of 100nm, and places where grain agglomeration occurred, leading to a coliflower structure (see Fig.1). This type of microstructure may indicate that the grain growth mechanism is dominated by nucleation and growth through a diffusion process of ionic species from the solution. The films exhibited very strong adherence to the substrate, and did not crack or peel when scratched with a metal object.

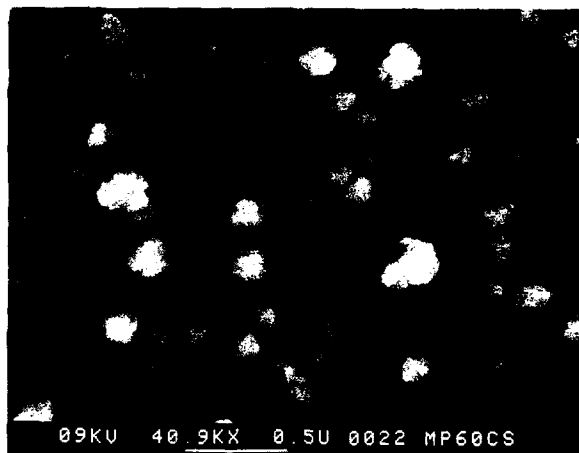


Figure 1. SEM micrograph of the surface of a BaTiO_3 film made at 250°C . The bar indicates $0.5\mu\text{m}$.

Photoemission analysis

The XPS measurements were acquired with a hemispherical analyzer using $\text{MgK}\alpha$ unfiltered radiation. The Ar ion sputtering for the depth analysis was performed using 4keV ions.

The surface oxygen peak displayed a high binding energy shoulder, probably due to adsorbed water [8]. It also exhibited a high strontium contamination, with a concentration very close to that of barium. Strontium was probably incorporated from the $\text{Ba}(\text{OH})_2$ reagent, where it is present as an impurity ($< 1.5\%$). Small quantities were detected in the film up to the BaTiO_3/Ti interface. The amount of strontium and its distribution throughout the film were unexpected. Because of its smaller ionic radius, it should diffuse easier than barium into the film and therefore it would be expected to be more abundant in the bulk. We do not have yet an explanation for these observations.

A semiquantitative concentration analysis was made with the main film constituents at each stage of the erosion process, concluding that the Ba/Ti ratio and the oxygen content correspond to that of BaTiO_3 .

AES analysis

An AES depth profile of Ba, Ti, O, and C in the 200°C BaTiO_3 film was collected from the surface up to the titanium layer with a double pass cylindrical mirror analyzer. The primary electron energy was 3keV , and the ion beam was operated at 3.5keV .

Fig.2 shows that the barium and oxygen signals follow each other throughout the film, and that they go from an initial surface value where they appear depleted (probably

due to surface contamination), then rise together as the film is penetrated, and finally decrease on reaching the Ti metal. Similar results were obtained in the 250°C sample [5].

The carbon signal in Fig.2 has been scaled in order to observe its in-depth variation. Initially the carbon signal is very high due to the presence of adsorbed graphite-like carbon. The carbon signal disappeared after eroding the surface, and reappeared when reaching the titanium layer, due to TiC present in the titanium film.

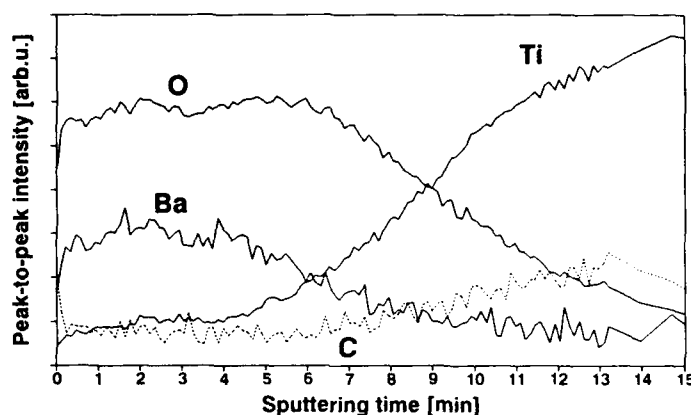


Figure 2 AES depth profile of a BaTiO₃ film grown at 250°C. The dielectric was sputtered up to the titanium substrate. Notice the correlation between barium and oxygen, and that carbon was absent in the film. The curves were scaled for legibility.

Electrical measurements

Aluminium dots 0.5mm in diameter were vacuum evaporated onto the film. Electrical contact was provided by two tungsten needles, one perforating the film and touching the underlying unreacted titanium film, and the other touching the aluminium dot. This provides a metal-insulator-metal (MIM) structure.

The I-V curve is linear up to 80mV ($\approx 2\text{MV/m}$), where a leakage current of $0.106\mu\text{A}$ was measured. This lead to a low signal dc conductivity of $0.25\mu\text{mho/m}$ (resistivity $4 \cdot 10^6\Omega\text{m}$). The I-V curves up to an applied voltage of 1.7V (leakage $200\mu\text{A}$) did not show dielectric breakdown, providing a lower estimate of the breakdown field of 50MV/m. The dielectric breakdown was further studied by low frequency capacitance-conductance-voltage (C-G-V) measurements, using an ac signal of 50mV rms. A sudden permanent change in the ac conductance with increasing bias was detected at a field of 70MV/m in all samples. This is consistent with the dc behavior.

The conductivity σ , measured with an ac modulation of 50mV rms, is shown as a function of the frequency f in Fig.3a. A good fit is found in the log-log plot with the model:

$$\sigma(f) - A = K \cdot f^\alpha, \quad (1)$$

where $A=20\mu\text{mho/m}$, $\alpha = 0.83$, and K is a constant (see Fig.3b). Notice that the constant A, corresponding to the extrapolated conductivity at zero frequency, is two orders of magnitude larger than the actual dc conductivity, which was measured at a similar signal level. This suggests that the conduction mechanisms are different for dc

and ac currents.

The permittivity ϵ was measured as a function of the frequency between 100Hz and 100kHz and is depicted in Fig.3c. The highest value, at 100Hz, is 227 in the 200°C sample, while in the 250°C sample it was 141. These values are comparable to those obtained by the laser ablation technique [2].

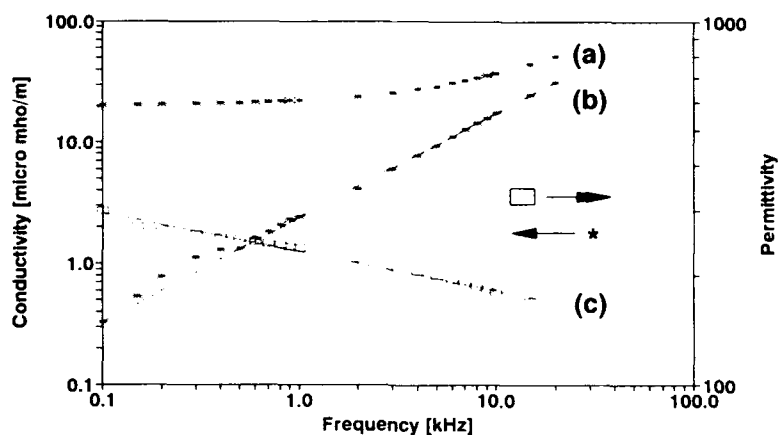


Figure 3. Frequency (f) dependence of (a) conductivity σ of a film grown at 200°C; (b) Dependence of $(\sigma(f) - A)/A$, where A is the extrapolated low frequency conductivity; and (c) Permittivity $\epsilon(f)$. The modulation was 50mV rms.

The temperature dependence of the permittivity was measured from room temperature up to 140°C. When increasing the temperature, a broad maximum was found between 110°C and 120°C, but no maximum is observed on decreasing the temperature. This behavior has been attributed to adsorbed water in experiments carried out with unsintered BaTiO₃ fine powders. This is consistent with our XPS observations.

CONCLUSIONS

Carbon-free BaTiO₃ films were grown on titanium coated silicon substrates using the hydrothermal method below 250°C.

High permittivity films were obtained at temperatures as low as 200°C. The hydrothermal technique is a promising method for thin film production that might be compatibilized with conventional silicon processing, since the low formation temperatures inherent to the method may facilitate the use of BaTiO₃ ceramics with semiconductor devices. This is because the method considerably reduces the film/substrate interactions, as well as the possibility of smearing out of preexisting doping profiles and structures, provided that they stand the somewhat hostile chemical environment during the film fabrication.

ACKNOWLEDGEMENTS

This research was funded by grants from FONDECYT 92906, Fundación Andes C10810-2, C10003, and C52228, and Universidad de Chile PG04192. We wish to thank Dr. J. Santiago Aviles, Dr. I. Eisele, and Dr. R. Avila for allowing us the use of their facilities, and Mr. K. wa Gachigi for the SEM observations.

REFERENCES

1. P.C. Van Buskirk, R. Gardiner, and P.S. Kirlik, *J. Vac. Sci. Technol. A*, **10** [1] 1578 (1992).
2. D. Roy and S.B. Krupanidhi, *Appl. Phys. Lett.*, **61** [17] 2057 (1992).
3. M. Yoshimura, S.E. Yoo, M. Hayashi and N. Ishizawa, *Jpn. J. Appl. Phys.*, **28** [11] L2007 (1989); *J. Ceram. Soc. Jpn.*, **98** [8] 930 (1990).
4. M.E. Pilleux, C.R. Grahmann, V.M. Fuenzalida, and R. Avila, *Appl. Surf. Sci.*, **65/66**, 283 (1993).
5. M.E. Pilleux and V.M. Fuenzalida, unpublished results.
6. R. Bacsá, P. Ravindranathan, and J.P. Dougherty, *J. Mater. Res.*, **7** [2] 123 (1992).
7. N. Ishizawa, H. Banno, M. Hayashi, S.E. Yoo, and M. Yoshimura, *Jpn. J. Appl. Phys.*, **29** [11] 2467 (1990).
8. M.E. Pilleux and V.M. Fuenzalida, *J. Appl. Phys.*, **74** [7] (1993), to be published.
9. A.K. Goswami, *J. Appl. Phys.*, **40** [2] 619 (1969).

MICROSTRUCTURAL CHANGES DUE TO PROCESS CONDITIONS IN SOL-GEL DERIVED KNbO_3 THIN FILMS

G.J. Derderian*[‡], J.D. Barrie*, K.A. Aitchison*, P.M. Adams*, and M.L. McCartney[‡]

*Mechanics and Materials Technology Center, The Aerospace Corporation, M2/248, P.O. Box 92957, Los Angeles, CA 90009.

[‡]Materials Science and Engineering / Department of Mechanical and Aerospace Engineering, University of California at Irvine, Irvine CA 92717.

ABSTRACT

KNbO_3 thin films have been deposited from $\text{K}(\text{OMe})/\text{Nb}(\text{OMe})_5$ sols onto (100) MgO substrates. Microstructural changes were observed relative to stoichiometry, aging, and the hydrolysis temperature. The production of single phase, oriented films has been demonstrated, and was found to be strongly dependent on process conditions. The films were characterized by XRD, TEM, SEM, EDS, and Raman spectroscopy.

INTRODUCTION

Thin film KNbO_3 ferroelectrics show promise for use as high speed electrooptic devices, optical waveguides, and frequency doublers [1-3]. Fabrication methods for KNbO_3 include various techniques such as ion beam sputtering [4] and sol-gel [5-9]. Sol-gel is a relatively simple technique that offers the advantage of a low temperature, low cost method to produce crystalline KNbO_3 thin films [10]. However, the synthesis of multicomponent crystalline oxides by the sol-gel process is often complicated by precipitation and phase separation resulting from different hydrolysis rates of the individual component alkoxides used as sources. The best single phase sol-gel films to date appear to be derived from methanolic solutions [5,6]. Very little work to date has focussed on the influence of process parameters and stoichiometry on the development of microstructure in the films, although it is known that the microstructure can significantly affect electrical and optical properties [11].

In this work we fabricated stoichiometric and slightly non-stoichiometric films in order to study the effects of processing conditions on the nucleation and crystal growth in KNbO_3 sol-gel derived thin films made from methanolic sols. The non-stoichiometric films provided an opportunity to easily measure nucleation densities and relative KNbO_3 crystallization.

EXPERIMENTAL

All reactions and manipulations were carried out under dry nitrogen using standard Schlenk techniques. Methanol and ethanol were dried by distillation over molecular sieves. Benzene was dried by distillation over calcium hydride.

Potassium ethoxide (KOEt) and potassium methoxide (KOMe) were prepared from the metal. The potassium content was determined by hydrolysis followed by titration of KOH against 0.1N HCl . Niobium ethoxide [$\text{Nb}(\text{OEt})_5$] (Alfa Products) was distilled (142°C , 0.1 mm Hg) prior to use. The distilled niobium ethoxide was diluted with ethanol to form a 1M stock solution.

$\text{K}(\text{OEt})$ and $\text{Nb}(\text{OEt})_5$ were combined in ethanol and refluxed for 24 hours to promote the formation of the double ethoxide [5]. Ethanol was removed by evaporation resulting in crystallization of the double ethoxide. This solid was dissolved in methanol to form a solution which was 0.26M in K . This will be referred to as a "methoxide solution". It is expected that there was a small amount ($\sim 1\%$) of residual ethanol and/or ethoxide in the solution. Three stoichiometric ratios of Nb/K were used in the methoxide solutions, niobium

rich (52% niobium, 48% potassium), potassium rich (52% potassium, 48% niobium), and equimolar (50% niobium, 50% potassium). The solutions were analyzed for K and Nb by flame atomic absorption. The solutions were hydrolyzed by the addition of a 2.5M solution of deionized water in methanol in a ratio of 0.2 moles of water per mole of alkoxide (designated 0.2/1). Hydrolysis was performed on sols which were either at room temperature or cooled in an ice bath.

Single crystal (100) MgO substrates, (Commercial Crystal Labs or Harrick Scientific Corp), were ultrasonically cleaned in acetone followed by vapor degreasing with trichloroethylene immediately prior to spin coating.

Spin coated films were prepared by placing a few drops of the sols prepared above onto the substrates followed by spinning at 3000rpm for 30 seconds in air. The coated substrates were immediately inserted into a hot tube furnace and held for 1 hour at 320°C under flowing oxygen. These steps were repeated three times to achieve the desired thickness of approximately 2000Å. The films were crystallized by insertion into a hot tube furnace and held for 4 hours at 800°C under flowing oxygen.

X-ray diffraction (XRD) was performed using a Siemens D5000 diffractometer and a Philips Electronics Inst. APD 3720 vertical powder diffractometer. Scanning electron microscopy (SEM) analysis was performed on a JEOL JSM-840 in both the backscattered and secondary electron modes. Semiquantitative energy dispersive X-ray analysis (EDS), was done using an EDAX EDS. Microstructural features were studied with an analytical Phillips CM20 transmission electron microscope (TEM) equipped with an EDAX EDS. TEM samples were prepared using standard dimpling and ion milling techniques, as well as a chemical etch technique [4]. Raman spectra were measured on an Instruments S.A. Ramanor U-1000 spectrometer coupled to an Olympus research grade microscope.

RESULTS

Three different stoichiometric ratios of potassium to niobium solutions were all hydrolyzed 0.2/1 at 0°C and spun 1 hour after hydrolysis to compare the effects of composition. The equimolar, niobium rich, and potassium rich solutions all produced orthorhombic KNbO_3 films on (100) MgO which were highly (110) oriented (approximately 88%, 95%, and 86% respectively), as seen in Figure 1. The films derived from the equimolar

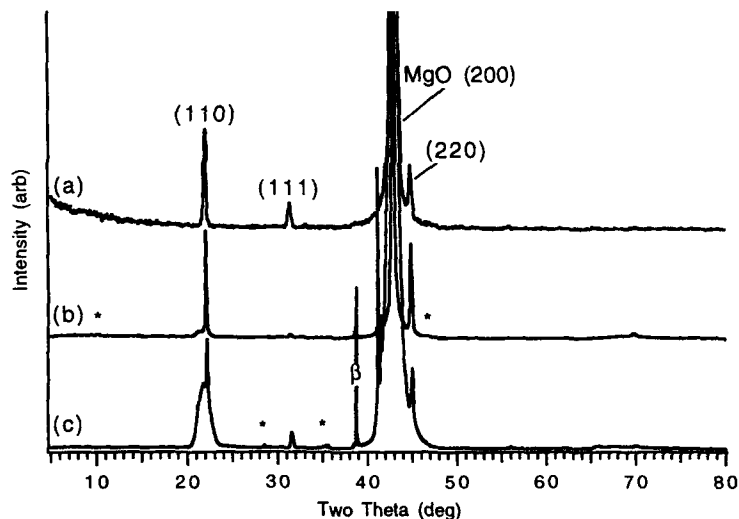


Figure 1. Comparison of XRD for methoxide films with different compositions: a) equimolar, b) niobium rich, c) potassium rich.

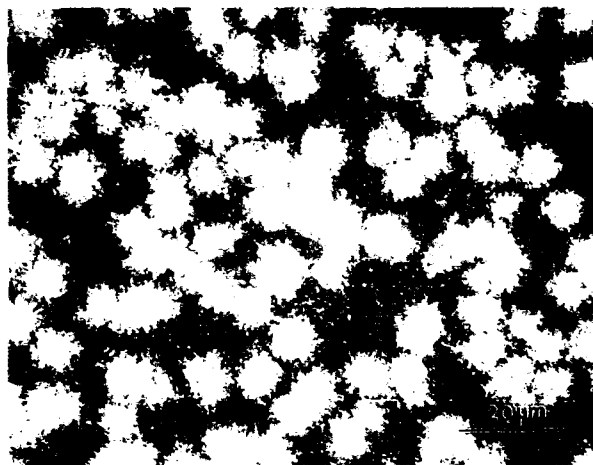


Figure 2. Typical microstructure with rosettes and matrix (optical micrograph). Each rosette represents a nucleating site.

solution were single phase while both of the non-stoichiometric solutions had one or more unidentified second phases. The single phase films exhibited low optical scatter, while the niobium rich films scattered non-uniformly due to multiple phases, and the potassium rich films also scattered non-uniformly due to cracking and grain boundary effects. When full crystallization of the film to KNbO_3 did not occur, the film microstructure is characterized by rosette-like growths surrounded by a matrix (Figure 2). Raman spectra of these films confirmed that the rosettes are orthorhombic KNbO_3 while the matrix exhibited no appreciable Raman scatter. TEM micrographs show that the rosettes are single crystal epitaxial KNbO_3 with (110) orientation (Figure 3a). Ferroelectric domains can be seen in the rosette. The matrix in this example consists of niobium rich polycrystalline phases which grow with a needle-like morphology (Figure 3b). The amount of the KNbO_3 rosettes in the



Figure 3. TEM micrographs of rosette and matrix: a) epitaxial orthorhombic KNbO_3 rosette, b) needle-like niobium rich second phase.

films was strongly dependent on process conditions. These changes were most easily observed in the niobium rich solutions.

Hydrolysis of the niobium rich solutions with 0.2 moles of water per mole of alkoxide prior to spinning resulted in rosette coverage of 81% with 5 μm rosettes when the solution was held at 0°C during hydrolysis. Hydrolysis at room temperature (rather than 0°C) decreased the amount of KNbO_3 formed to 52% with 6 μm rosettes. Films which were spin coated one day after the hydrolysis of the niobium rich solutions (rather than one hour, as above) had increased amounts of second phases and the number of KNbO_3 rosettes was decreased. Furthermore, the concentration of KNbO_3 rosettes in the films decreased when the time between dissolution of the double ethoxide in methanol and hydrolysis of the solution increased (Figure 4). Further details on this aging effect will be presented in a future publication.

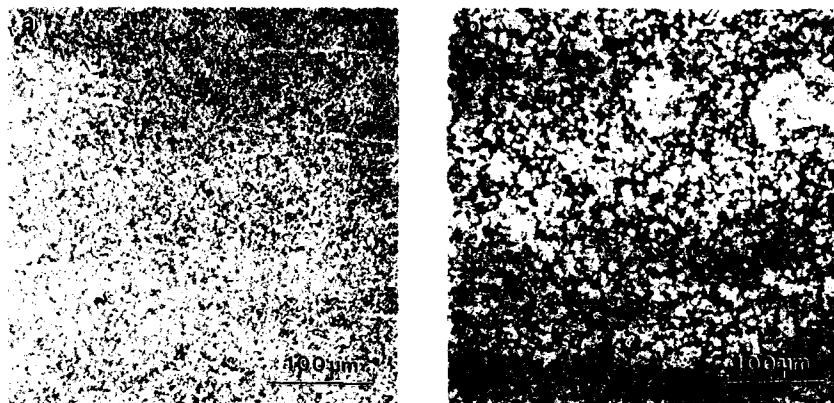


Figure 4. Aging of niobium rich sol: a) unaged b) aged with decreasing amount of KNbO_3 rosettes (optical micrographs).

DISCUSSION

Single phase oriented KNbO_3 thin films with low optical scatter can be formed on (100) MgO substrates by the sol-gel technique using methoxide solutions under certain conditions. An equimolar ratio of potassium and niobium in the solution is necessary to avoid the formation of second phases. Hydrolysis of this equimolar solution at 0°C prior to spinning enhances the formation of orthorhombic KNbO_3 provided that the films are prepared immediately after the hydrolysis step. It is not surprising that solutions which are not equimolar in potassium and niobium do not produce single phase films, however, the nature of the nucleation and growth of these mixed phase films helps explain the changes in microstructure observed. Films crystallize by formation of KNbO_3 nuclei which grow laterally throughout the film. For the equimolar solutions, this leads to single phase films in which the KNbO_3 grains have coalesced. This process occurs rapidly at 800°C. In films derived from the niobium rich solutions, the growth of KNbO_3 grains is arrested at the stage where insufficient potassium remains in the matrix. Each of the rosettes which are observed in the optical and electron micrographs represents an individual nucleation site. The evaluation of the nucleation density in films prepared under various processing conditions allows us to monitor the effects of each condition on crystallization of KNbO_3 films. These observations were especially valuable in the interpretation of hydrolysis and aging behavior.

When slightly niobium rich methoxide solutions were hydrolyzed at reduced temperatures immediately prior to spinning, films with small amounts of second phases were produced. When hydrolysis was done at room temperature or the hydrolyzed sol was allowed to age, the concentration of orthorhombic KNbO_3 rosettes formed in the films decreased and the amount of second phases increased. These results indicate that the nucleation of KNbO_3 rosettes in the crystallizing films depends upon a homogeneous distribution of potassium and niobium in the hydrolyzed sol. When the temperature of the hydrolysis reaction is increased there is a reduced homogeneity of the solution with the double alkoxide species becoming less stable, and the hydrolysis rates of all the alkoxide species in solution increasing. Both of these processes are likely to lead to a reduced association between potassium and niobium in the solution.

Similarly, when the sol is allowed to age at room temperature for one or more days, the distribution of potassium and niobium in the sol may be disturbed by reactions such as those discussed above. The deterioration of film quality may be an effect which may be related to this aging. Clearly, the double alkoxide sol-gel synthesis route to produce single phase KNbO_3 films is a highly sensitive process.

CONCLUSIONS

Single phase (110) oriented thin films of KNbO_3 can be made on (100) MgO substrates by the sol-gel technique under certain conditions. Solutions must have an exactly 1:1 niobium to potassium ratio to avoid extensive second phase formation. Non-stoichiometric sols allow for nucleation and growth studies and related to process conditions. Rosette type growth of KNbO_3 is observed. Hydrolysis at low temperatures aids in the crystallization of the KNbO_3 phase through formation of homogeneous solutions which result in a high nucleation density of orthorhombic KNbO_3 . Aging the solution decreases the concentration of KNbO_3 formed. The sensitivity of the final microstructure to variations in process conditions such as temperature and aging may make it difficult to employ methanolic alkoxide solutions in the routine fabrication of device quality KNbO_3 thin films.

ACKNOWLEDGMENTS

The authors wish to thank E. Fletcher, and J. Ciofalo for their assistance. The work was supported by the Aerospace Sponsored Research program and a Packard Fellowship in Science and Engineering.

REFERENCES

1. R.L. Holman, L.M. Althouse Johnson, D.P. Skinner, Proceedings of the Sixth IEEE Int. Symp. on Appl. of Ferroelectrics, 1986, 32-41.
2. P. Gunter, Phys. Rep., **93** (4), 199-299, (1982).
3. B.A. Tuttle, Mat. Res. Soc. Bull., **12** (7), 40-45, (1987).
4. A.I. Kingon, O.H. Auciello, M.S. Auciello, M.S. Ameen, S.H. Rou, and A.R. Krauss, Appl. Phys. Lett., **55**, 301, (1989).
5. M.M. Amini and M.D. Sacks, J. Am. Ceram. Soc., **74** (1), 53-59, (1991).
6. B.A. Tuttle, B.D. Bunker, D.L. Lamppa, R.G. Tissot, and J.L. Yio, Ceram. Trans., **11**, 329-41, (1990).
7. S.L. Swartz, P.J. Melling, and C.S. Grant, Mat. Res. Soc. Proc., **152**, (1989).
8. I.A. Fathi and D.E. Clark, Mat. Res. Soc. Symp. Proc., **180**, 401-06, (1990).
9. Y. Xu and J.D. Mackenzie, Integrated Ferroelectrics, **1**, 17-42, (1992).
10. D.R. Ulrich, J. of Non-Crystalline Solids, **100**, 174-193, (1988).
11. T.M. Graettinger, S.H. Rou, M.S. Ameen, O. Auciello, and A.I. Kingon, Appl. Phys. Lett., **58** (18), 1964-1966, (1991).

EPITAXIAL GROWTH OF Pt(001) THIN FILMS ON MgO(001) UNDER OXIDIZING CONDITIONS

G. Cui, P. C. Van Buskirk, J. Zhang, C. P. Beetz, Jr. and J. Steinbeck
Advanced Technology Materials, Inc., 7 Commerce Drive, Danbury, CT 06810

Z. L. Wang and J. Bentley
Metals and Ceramics Division, Oak Ridge National Laboratory, Oak Ridge,
TN 37831-6376

ABSTRACT

Epitaxial Pt(001) thin films have been grown on MgO(001) substrates using dc magnetron sputtering with an Ar/O₂ mixture at 700°C. The width (FWHM) of the rocking curve of the Pt(002) peak is between 0.16° and 0.20°, which is only 0.05° wider than that of the MgO (002) peak of the cleaved substrate. The film surface roughness is about 1 nm (rms) for a 240 nm thick Pt film. No grain structure could be observed using SEM. In contrast, the films deposited at 700 °C with pure Ar, have both Pt(111) and Pt(001) oriented growth, as shown by XRD $\Theta - 2\Theta$ scans, with the Pt(111) peak having the largest intensity. BaTiO₃ epitaxial films have also been deposited on Pt(001)/MgO(001). The width (FWHM) of the rocking curve of the BaTiO₃(200) peak is 0.4°. The surface morphology of the epitaxial BaTiO₃(100) thin films on Pt(001)/MgO(001) is featureless. XRD pole figure measurements on Pt/BaTiO₃/Pt trilayer shown a very good in-plane alignment of all layers. The epitaxial growth relationship was also confirmed by TEM electron diffraction and cross-section imaging. The Pt/BaTiO₃/Pt epitaxial trilayer could serve as a prototype for ferroelectric capacitors and may be able to improve the electrical properties of the capacitors.

INTRODUCTION

In multilayer systems, epitaxial growth has been an important issue for high quality multilayer structures and of great interest for applications. Epitaxial growth of metallic films is also important in oxidizing environments employed in the deposition of ferroelectric, magnetic oxides and HTSC films. Recently, Lairson et al. [1] reported epitaxial growth of Pt films on MgO(001), MgO(110), MgO(111), and Al₂O₃(0001) substrates using a sputtering technique. In a pure argon atmosphere of 3.0 mTorr, the relative intensity of Pt(111) to the total Pt(111) and Pt(200) peak intensity varied from nearly 100% for temperatures below 550°C to 0.1% at a deposition temperature of 680°C when MgO(001) substrates were used. In a mixture of 10 mTorr Ar and 5 mTorr oxygen, epitaxial growth of Pt(001) on MgO(001) at 680°C was demonstrated. In this report, we present data showing the epitaxial growth of Pt(001) on MgO(001) at 700°C with a mixture of 6 mTorr Ar and 5 mTorr O₂. Pt(111) and Pt(200) oriented growth was observed when Pt was deposited in pure Ar at the same temperature. The epitaxial Pt(001) films grown under oxidizing conditions have mirror-like surfaces with a surface roughness of 1 nm (rms), single crystal-like structure and rocking curve widths as low as 0.2°. These films have been shown to be suitable for subsequent growth of epitaxial films and multilayers of ferroelectric materials.

DEPOSITION PROCESS

A vacuum chamber was equipped with a 2" magnetron sputtering gun which can be operated in a dc or rf mode, and with a 2" resistance heater (US

GUIN II). A turbo pump was used to reach a base pressure of $1-3 \times 10^{-6}$ Torr. A Pt metal target was used with a purity of 99.95%. Ultra high purity oxygen gas (minimum purity 99.99%) and zero grade argon gas (THC less than 0.5 ppm) were used as working gases. The distance between the target and substrates was 10 cm. MgO substrates were used in this work. The substrates were cleaned with dichloromethane (methylene chloride CH_2Cl_2), acetone and methanol in an ultrasonic bath, then blown dry with nitrogen before loading into the chamber.

The experimental parameters used are shown in table I.

Table I Experimental parameters

Run	Samp. Substrate	Ts °C	Ar/O2 mTorr	Thick nm	Orientation Pt(###)	FWHM ω
I	PT03A MgO(100)	695	4.2/0	100	(111)+(200)	$0.33^\circ/0.7^\circ$
	PT03B MgO(100)	695	4.2/0	100	(111)+(200)	$0.33^\circ/0.63^\circ$
II	PT04A MgO(100)	695	6.4/4.6	170	(200)	0.23°
III	PT05A MgO(100)	700	5.6/4.8	240	(200)	0.20°
	PT05B MgO(100)	700	5.6/4.8	240	(200)	0.18°
	PT05C MgO(100)	700	5.6/4.8	240	(200)	0.16°
	PT05D MgO(100)	700	5.6/4.8	240	(200)	0.18°

CRYSTAL STRUCTURES

A Rigaku VS - DXR3000 diffractometer was used for the film structure characterization. $\text{Cu K}\alpha$ monochromatic radiation was used in these experiments with a graphite 224R monochromator to avoid any $\text{K}\beta$ line from appearing the diffraction patterns. The instrumental resolution for the rocking curve is 0.08° . A pole figure camera was used to determine the quality of the in-plane alignment between the film and substrate and between multilayers.

A typical $\Theta - 2\Theta$ Scan of an epitaxial Pt(001) film on MgO(001) is shown in Fig. 1a. Only the MgO(002), Pt(002), MgO(004) and Pt(004) peaks could be observed.

Expanding the intensity scale by 1000x as shown in Fig. 1b did not reveal any additional features. The rocking curve width (HWHM) is 0.20° for Pt(002) and 0.15° for MgO(002) as shown in Fig. 1c. These data indicate the epitaxial growth of Pt(001) on MgO(001), which was reproducible.

In contrast to the oxidizing sputtering condition, Pt(111)/Pt(002) oriented growth on MgO(001) substrates was observed at the same substrate temperature when sputtered in pure Ar. Surprisingly, no Pt(220), Pt(311) peaks appeared in the XRD at $2\Theta=67.5^\circ$ and 81.3° , respectively. The rocking curve width (FWHM)

was 0.33° for Pt(111) and 0.7° for Pt(002) as shown in Fig. 2c.

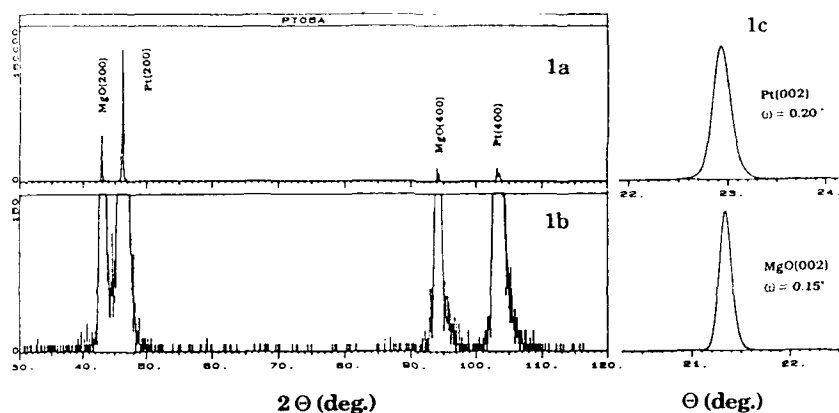


Fig. 1a and 1b A typical $\Theta - 2\Theta$ Scan of epitaxial Pt(001) film on MgO(100).
1c Rocking curve of Pt(002) peak and MgO(002) peak.

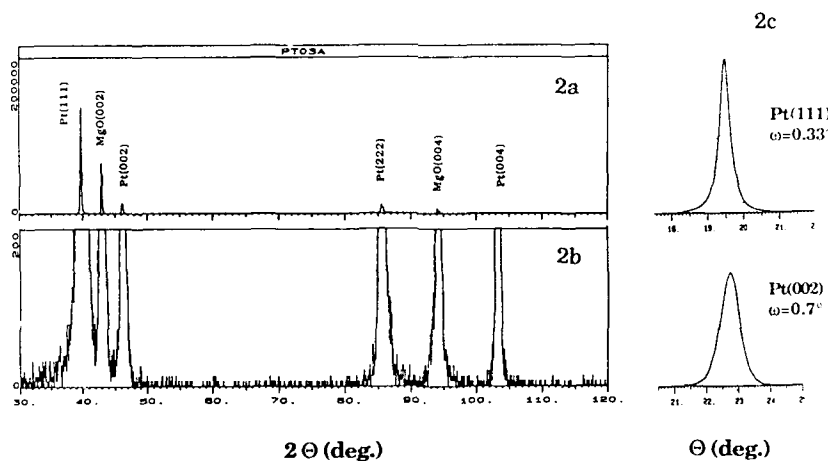


Fig. 2a and 2b A $\Theta - 2\Theta$ Scan of Pt(111)/Pt(002) oriented growth on MgO(100).
2c Rocking curve of Pt(111) peak and Pt(002) peak.

Pole figure measurements of a trilayer sample of Pt/BaTiO₃/Pt/MgO are shown in Fig. 3. A schematic cross-section view of the trilayer is shown in Fig. 3d. The x-ray measurement probes all three films, so that the in-plane orientation of each can be determined. The MgO(202) peak was chosen for MgO substrate pole figure measurement as shown in Fig. 3a. The intensity of MgO(202) was not very strong because of attenuation due to the trilayer of

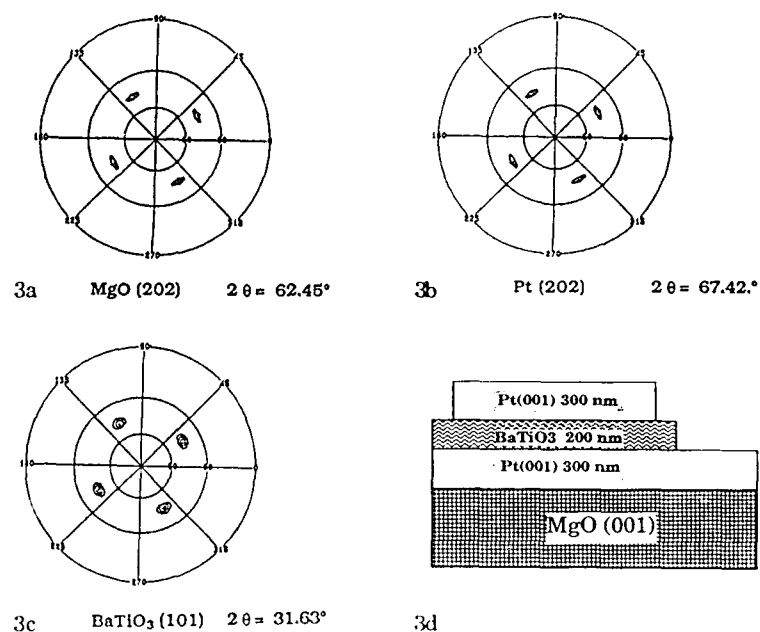


Fig. 3 Pole figure measurement on Pt(001)/BaTiO₃(001)/Pt(001) trilayer

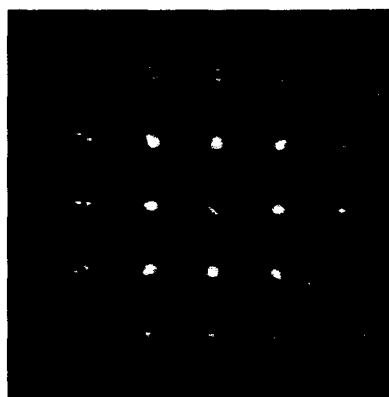


Fig. 4 Electron diffraction pattern of the epitaxial Pt film on MgO substrate. It indicates Pt[001] // MgO[001] and Pt[100] // MgO[100].

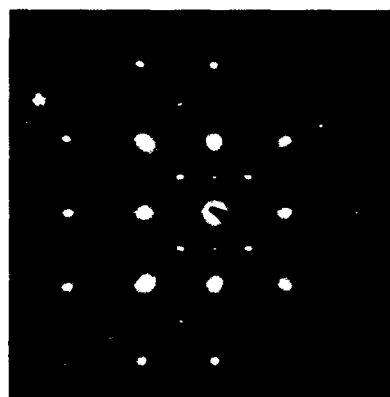


Fig. 5 Electron diffraction pattern of the Pt(001)/BaTiO₃(001)/Pt(001) trilayer. It indicates : Pt[001] // BaTiO₃[001] // Pt[001] and Pt[100] // BaTiO₃[100] // Pt[100].

Pt/BaTiO₃/Pt on the top of the MgO substrate. The Pt(202) was chosen for both top and bottom Pt films pole figure measurements, which are shown in Fig. 3b. The sharpness and good symmetry of the diffraction peaks indicate good in-plane alignment between the bottom Pt film and the substrate and between the bottom and the top Pt layers. The pole figure measurement of the BaTiO₃ (101) peak in Fig. 3c shows a very good peak distribution, which indicates a good epitaxial heterostructure of the trilayer. The peak width of BaTiO₃ (101) is wider than the Pt (202) peak, which is consistent with the rocking curve measurement.

MICROSTRUCTURE

Transmission electron microscopy (TEM) was used to identify the quality of the epitaxial growth relationship. TEM studies were performed at 300 kV using a Philips CM30 analytical electron microscope with image resolution of 0.23 nm. Selected area and convergent beam electron diffraction patterns were recorded successfully from the substrate and the film in order to determine the relative orientation of the two adjacent layers. An accuracy of better than 0.2° was achieved. In Fig. 4 the electron diffraction pattern of the Pt film on MgO substrate shows Pt[001]/MgO[001] and Pt[100]/MgO[100], which indicates an excellent epitaxial growth relationship between the Pt film and the MgO substrate. The electron diffraction pattern of the trilayer of Pt/BaTiO₃/Pt indicates an epitaxial growth relationship between the Pt and the films (Fig. 5), revealing the epitaxial relationships of Pt[001]/BaTiO₃[001]/Pt[001] and Pt[100]/BaTiO₃[100]/Pt[100]. Fig. 5 is fully consistent with the pole figure measurements on the trilayer of Pt/BaTiO₃/Pt as shown in Fig. 3.

DISCUSSION AND SUMMARY

Molecular beam epitaxy (MBE) is most often used to fabricate epitaxial films and epitaxial multilayers. However, other film growth techniques can also be used, for instance laser ablation, sputtering deposition, and chemical vapor deposition. In this work we have shown the feasibility of making epitaxial films and multilayers using the sputtering technique.

The epitaxial growth of Pt films in an oxidizing environment is compatible with epitaxial growth conditions of ferroelectric and magnetic oxides. The role of oxygen in the epitaxial growth is not yet clear, but it is speculated to be associated with mobile PtO species on the surface.

There are numerous published papers, concerning the effect of bottom electrodes on the electrical properties of ferroelectric films [2]. While fatigue and failure mechanism of ferroelectric capacitors are not completely understood, film orientation is known to be an important determinant of degradation in the remanent polarization [3]. Polycrystalline Pt bottom electrodes may induce early failure during fatigue testing. TEM images of our epitaxial trilayer of Pt(001)/BaTiO₃(001)/Pt(001) show an abrupt interface (to be published later) between BaTiO₃ and Pt bottom electrode. The grain boundary-free nature of the epitaxial trilayer may provide a method for solving the problem.

In conclusion, we have demonstrated the epitaxial growth of Pt(001) on MgO(001) substrates in an oxidizing environment. We have also demonstrated the growth of epitaxial trilayers of Pt(001)/BaTiO₃(001)/Pt(001) on MgO(001) substrates. TEM images reveal a sharp interface between the BaTiO₃(001) and bottom Pt(001) electrode, which might be helpful for improving the performance of epitaxial ferroelectric capacitors.

ACKNOWLEDGMENT

The authors would like to thank Dr. P. S. Kirlin for helpful discussion. This work was supported by Navy N66001-92-C-7008 and DARPA N00014-90-C-020. ZLW and JB were sponsored by the Division of Materials Science U.S. Department of Energy, under contract DE-AC05-84OR21400 with Martin Marietta Energy Systems, Inc.

REFERENCES

1. B.M. Lairson, M.R. Visokay, R. Sinclair, and B.M. Clemens, Appl. Phys. Lett. **61**(12), 1390 (1992)
2. P.D. Hren, S.H. Rou, H.N. Al-Shareef, M.S. Ameen, O. Auciello, and A.I. Kingon, Proceedings 3rd International Symposium on Integrated Ferroelectrics (ISIF-91), p. 612, Colorado Springs, April 3-5, 1991
3. B.A. Tuttle, J.A. Voigt, T.J. Garino, D.C. Goodnow, R.W. Schwartz, D.L. Headley, M.O. Eatough, Proc. 8th Int. Symp. on Appl. Ferroelectrics, Greenville, S.C., USA 8/30-9/2, 1993 pp 344-348

AEROSOL ROUTES TO PEROVSKITE PHASE MIXED METAL OXIDES

C.D. CHANDLER[†], Q. POWELL[‡], M.J. HAMPDEN-SMITH^{†*} and T.T. KODAS^{‡*}

[†]Department of Chemistry and Center For Micro-Engineered Ceramics, University of New Mexico, Albuquerque, NM 87131

[‡]Department of Chemical and Nuclear Engineering and Center For Micro-Engineered Ceramics, University of New Mexico, Albuquerque, NM 87131

*Authors to whom correspondence should be addressed

ABSTRACT

Sub-micron sized metal oxide particles were formed via aerosol decomposition using single-source mixed metal-organic precursors specifically designed to decompose at low temperatures. The advantage of these single-source precursors over mixtures of individual precursors is that each particle contains a fixed stoichiometry and molecular level homogeneity. Furthermore, the loss of volatile intermediates (such as PbO) may be avoided. Aerosol processing routes can produce uniform sub-micron sized powder that can be sintered at low temperatures for various thin film and membrane applications. The single-source precursors were prepared in pyridine by reaction of divalent metal α -hydroxycarboxylates of general empirical formula $A(O_2CCMe_2OH)_2$ (where A = Pb, Ca, Sr, Ba; Me = methyl) with metal alkoxides (for example, $Ti(O-i-Pr)_4$) with the elimination of two equivalents of alcohol. These species were then hydrolyzed in solution and yellow powders were isolated by removal of the pyridine solvent *in vacuo*. These powders were dissolved in water and used to prepare mixed metal oxide powders via spray pyrolysis. Phase-pure submicron-sized particles of $PbTiO_3$ and $BaTiO_3$ were produced at temperatures of 600-900 °C. The particles were hollow, ranged in size from 0.1 to 1 μm and consisted of 30-50 nm crystallites.

INTRODUCTION

Spray pyrolysis can be used to produce multi-source, high-purity powders that consist of non-agglomerated submicron-sized particles.¹ Usual aerosol techniques involve the use of several precursors, each containing a single-component of the final material, which are mixed in a suitable solvent and sprayed into a furnace. The reaction proceeds by removal of solvent from the droplets, then the precursors decompose and solid state diffusion within each particle leads to the final ceramic. This approach, although simple, has several fundamental problems which either increase the processing temperature required to form the ceramic or degrade the properties of the final material. For example, as the solvent evaporates from the droplet, the precursors may segregate because of different solute precipitation rates and nucleation behavior of the precursors within the particles (see Figure 1). Reaction between the precursors can then occur to form intermediates with incorrect stoichiometry and which are also segregated to produce a conglomerated product. These compositional inhomogeneities must be eliminated

by solid-state diffusion and complete reaction may not occur if the temperature and diffusion rates are not sufficiently high. Also, the loss of volatile intermediates such as MoO_3 , V_2O_5 and PbO can result in the production of powders with the incorrect stoichiometry or an undesired phase.^{2,3} This is the case for the formation of perovskite phase PbTiO_3 , where lead loss generally leads to crystallization of the pyrochlore phase.

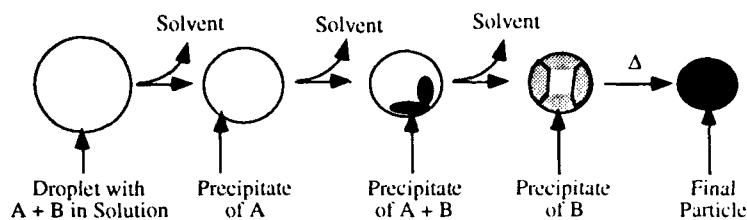


Figure 1. Schematic representation of particle formation by aerosol decomposition using multiple precursors.

Single-source precursors have a fixed stoichiometry of the metal atoms within the molecule and this can overcome the problems of segregation and the need for solid state diffusion. As shown in Figure 2, the use of a single-source precursor results in a precipitate which retains the homogeneity achieved during precursor preparation. This lowers the time and temperature required for the formation of ceramic particles and avoids the problem of phase segregation. In addition, if volatile species are confined in phases above which their vapor pressure is negligible, this approach has the potential to minimize or eliminate losses of volatile species such as PbO . Thus, these aerosol-derived powders with uniform sub-micron sized particles can be sintered at low temperatures for various thin film and membrane applications.

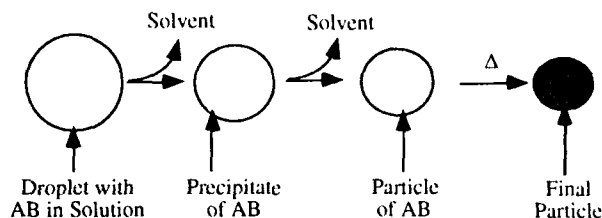


Figure 2. Particle formation by aerosol decomposition using single-source precursors.

In this work, we have investigated the use of single-source precursors for the formation of perovskite phase metal oxides with empirical formula ABO_3 . The preparation of the single-source precursors to these materials has been described previously.^{4,5} By using this method, phase-pure PbTiO_3 and BaTiO_3 powders were produced from the precursors $\text{Pb}(\text{O}_2\text{CCMe}_2\text{O})_2\text{Ti}(\text{O}-i\text{-Pr})_2$ and $\text{Ba}(\text{O}_2\text{CCMe}_2\text{O})_2\text{Ti}(\text{O}-i\text{-Pr})_2$ respectively, in an aerosol reactor.

EXPERIMENTAL

The reactor design has been described elsewhere.⁶ Water solution concentrations were on the order of 1-2 wt.% for all of the precursors. All solutions were placed in a modified Collision Nebulizer which generated the droplets in an oxygen carrier gas. The droplets were transported into a hot-wall reactor consisting of a mullite tube (3.25 inch I.D. X 60 inch length) contained in a three-zone furnace with a heated zone of 36 inches. Pure oxygen was supplied to the Collision at 35 psig. The carrier gas flow rate of 19.4 lpm (ambient conditions) was monitored with a rotameter. Reactor residence times varied according to the reaction temperature and ranged from 5.5 to 3.8 seconds at 550 °C and 900 °C respectively. The powders were collected on a 147 mm nylon filter that was contained within a stainless steel filter holder.

Particle compositions and morphologies were examined using X-ray diffraction (XRD), transmission electron microscopy (TEM), and scanning electron microscopy (SEM). The extent of reaction was determined by thermal gravimetric analysis (TGA) in air. The Pb to Ti ratio of the PbTiO_3 powder made at 650 °C was measured using flame atomic absorption (AA) spectroscopy.

RESULTS AND DISCUSSION

PbTiO_3

Phase-pure PbTiO_3 was prepared at reaction temperatures of 600, 650, 700 and 750 °C. The powder obtained at 550 °C was not fully reacted and gave a weight loss of 6.5% at 500 °C, as determined by TGA. X-ray powder diffraction data revealed that the material was either amorphous or the crystallite size was very small, as indicated by the broad peaks obtained in the XRD pattern. Powders produced at 600 to 750 °C exhibited about a 2% weight loss by TGA (Figure 3). X-ray powder diffraction showed that the powders made at 600 to 750 °C were phase-pure PbTiO_3 . The XRD results indicate that the formation of pyrochlore was avoided and perovskite was the favored product under the conditions used. This eliminated the need for sintering at higher temperatures, which is common in sol-gel routes to convert pyrochlore to the perovskite phase.⁶

Scanning electron microscopy data for the PbTiO_3 powder produced at 550 °C, showed that it consisted primarily of collapsed shells with diameters of about 0.4 μm . Powders made at 600 °C and 650 °C consisted of 0.3 μm and 0.4 μm particles exhibiting both hollow and collapsed shell morphologies. At 750 °C, the particles were spherical and about 0.4 μm in diameter. Transmission electron microscopy data for the 750 °C powder (Figure 4) showed that the particles were hollow, with a crystallite size of approximately 50 nm. Decreasing XRD peak broadening with increased temperatures indicated that the crystallite size increased along with increasing furnace temperatures.⁶

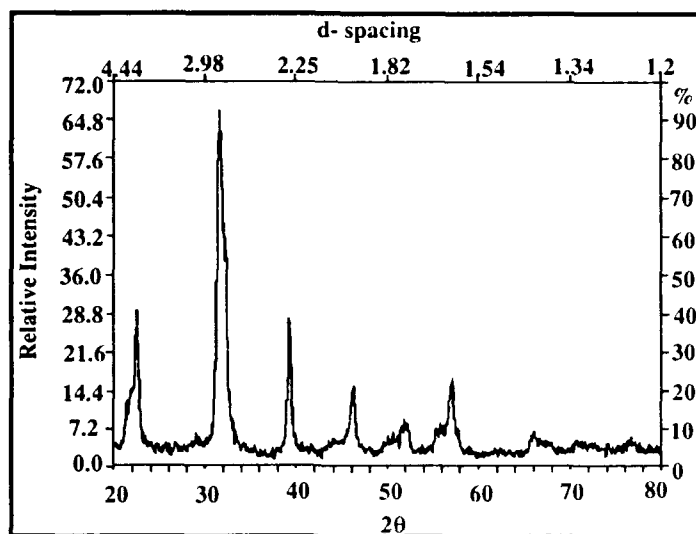


Figure 3. XRD of PbTiO_3 powder produced at 750°C .

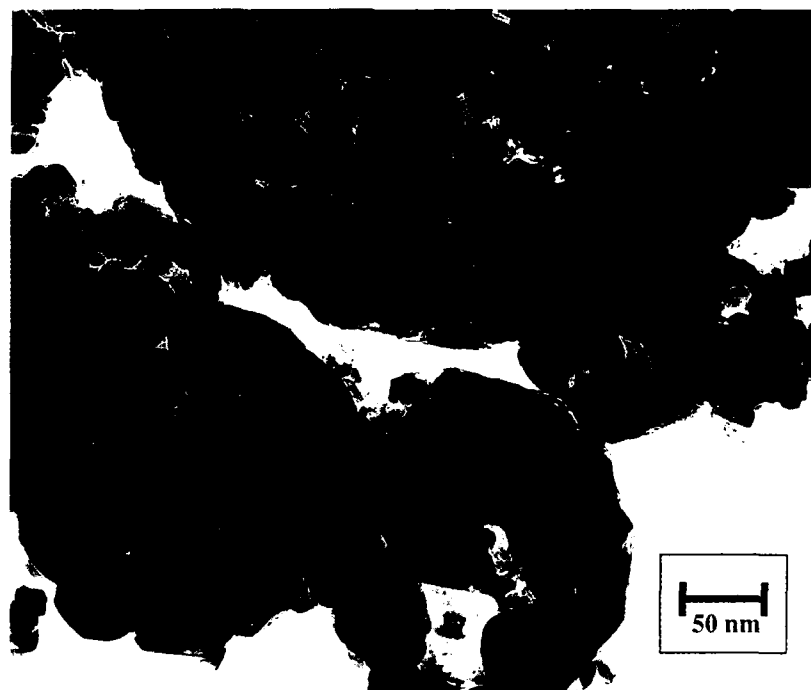


Figure 4. TEM photograph of PbTiO_3 particles formed at 750°C .

BaTiO₃

Phase-pure BaTiO₃ was prepared at 900 °C, as indicated by XRD and TGA. At 750 °C, the precursor was partially decomposed and the product was contaminated by carbonate as indicated by the TGA decomposition pattern. The powder produced at 750 °C had a weight loss of 14% by TGA; of this, 2% was due to the presence of carbon while the remaining weight loss (12%) occurred at 700 °C, which corresponds to the decomposition temperature of barium titanium carbonate.⁶ Elemental analysis of the sample confirmed the assignment of carbon and carbonate, since no hydrogen was detected and 4% carbon was found. Scanning electron microscopy data showed that all of the powders were made up of spherical unagglomerated particles with an average diameter of about 0.4 μm. The 900 °C powder consisted of hollow particles with crystallites on the order of 30 nanometers, as determined by TEM. The XRD powder pattern of the material produced at 750 °C could not be identified; however the infrared spectrum and TGA decomposition pattern of the powder correspond to the reported values for Ba₂Ti₂O₅(CO₃).⁷ The 900 °C XRD pattern showed phase-pure BaTiO₃.

SUMMARY AND CONCLUSIONS

The production of submicron-sized, non agglomerated, phase-pure PbTiO₃ and BaTiO₃ particles from single-source precursors was demonstrated. The minimum reaction temperatures were 600 °C for PbTiO₃ and 900 °C for BaTiO₃. These temperatures are high relative to those required to produce crystalline, perovskite phase metal oxide powders from these precursors in the solid state.⁵ This is probably the result of the short residence time in the aerosol reactor.

The use of single-source precursors provides a method for avoiding the problem of phase segregation within particles that contain more than one metallic component. This approach also provides a method for avoiding the problem of the formation of unwanted volatile intermediates, such as PbO, that can result in a change of stoichiometry during reaction. However, hollow particles were formed which may be difficult to densify into a ceramic compact. These powders should be suitable for the formation of ceramic films at low sintering temperatures.

ACKNOWLEDGMENTS

We thank Leo Archer for obtaining the X-ray Powder diffraction data, the Center for Micro-Engineered Ceramics for funding and ONR for Analytical Facilities

REFERENCES

1. T.T. Kodas, *Advanced Materials* **6** (1989) p. 180.
2. S.W. Lyons, J. Ortega, L. Wang, and T.T. Kodas, *Mat. Rev. Soc. Symp. Proc.* **271** (1992) p. 907.
3. S.W. Lyons, T. Ward, T.T. Kodas, and S. Pratsinis, *J. Mater. Res.* **7** (1992) p. 3333.
4. C.D. Chandler, M.J. Hampden-Smith, and C.J. Brinker, *Mater. Res. Soc. Symp. Proc.* **271** (1992) p. 89.
5. C.D. Chandler, and M.J. Hampden-Smith, *Chem.Mater.* **4** (1992) p. 1137.
6. C.D. Chandler, C. Roger, and M.J. Hampden-Smith, *Chem. Rev.* **93** (1993) p. 1205

FERROELECTRIC THIN FILMS VIA SOL-GEL PROCESSING OF SINGLE-SOURCE PRECURSORS

C.D. CHANDLER[†], M.J. HAMPDEN-SMITH[†], AND R.W. SCHWARTZ^{††}

[†]Dept. of Chemistry and Center for Micro Engineered Ceramics, U.N.M., Albuquerque, NM 87131

^{††}Sandia National Laboratory, Albuquerque, NM, 87185.

ABSTRACT

The use of single-source mixed metal-organic precursors specifically designed for the formation of crystalline perovskite phase mixed metal oxide powders has been investigated. Pyridine solutions of divalent metal α -hydroxycarboxylates of general empirical formula $A(O_2CCMe_2OH)_2$ where $A = Pb, Ca, Sr, Ba$; $Me = methyl$, were designed to react with metal alkoxides, for example, $Ti(O-i-Pr)_4$, with the elimination of two equivalents of alcohol to form species with fixed A:B stoichiometry of 1:1 according to the equation: $A(O_2CCMe_2OH)_2 + B(OR)_4 \rightarrow A(O_2CCMe_2O)_2B(OR)_2 + 2HOR$. Hydrolysis of these compounds in pyridine produces clear solutions which on removal of the solvent *in vacuo*, yield yellow powders. These powders readily dissolve in ethanol to give solutions from which thin films can be formed either by dip-coating or spin coating. The crystallization behavior, composition and ferroelectric properties of these films is discussed. The crystallization of the films generally required substantially higher temperatures compared to powders obtained from the same precursor solutions.

INTRODUCTION

The potential use of perovskite phase ABO_3 ferroelectric thin films in high density DRAM's, nonvolatile memories, electro-optic shutters and spatial light modulators has lead to an increased research effort to obtain these ceramics with a uniform composition and phase with a view to the integration of ferroelectrics into silicon device technology. With these aims comes the conflict between high processing temperatures required to crystallize the film and the low thermal stability of the device architecture, in particular, aluminum interconnects.¹ As a solution to this problem, the sol-gel process offers the possibility of crystallizing the film at temperatures which are far lower than conventional solid state techniques. This process is used extensively to obtain thin films either by spin or dip coating a substrate wafer multiple times to increase film thickness. This method of producing thin films also has the potential to provide good homogeneity, good compositional control and high purity. However, due to the thermal constraints of silicon devices in which Al metallization is incorporated, it is desirable that the maximum processing temperature for crystallization of ferroelectric films is below 400 °C.

The ferroelectric properties of these ABO_3 materials are derived from the crystal chemistry of the perovskite phase. However, in Pb based systems the formation of pyrochlore, initially as the low temperature phase has required that higher temperatures (650 °C) be used² to transform the pyrochlore to the perovskite phase. The control of the formation of the perovskite phase over the pyrochlore polymorph in lead titanate systems is being investigated by seeding these films with small perovskite crystallites from which it is hoped that growth of perovskite will occur at low temperatures in preference to pyrochlore. Work with seeding thin films of PZT has been reported and lowering of the crystallization temperature of the perovskite phase was observed.³

EXPERIMENTAL

Preparation of the precursors for PbTiO_3 and $\text{Pb}(\text{Zr}_{0.52}\text{Ti}_{0.48})\text{O}_3$ has been described elsewhere.^{4,5} The precursors were dissolved in an ethanol (95%) and ethanolamine (5%) solution to give a 10 wt.% concentration of PbTiO_3 . The solution was filtered through a 0.2 micron filter prior to use. Silicon wafers onto which have been deposited layers of SiO_2 , Ti (500Å) and Pt (2000Å) were used as substrates in these experiments. The oxide films were deposited by spin coating the precursor onto the substrate at 3500 RPM for 20 sec, then baking at 400 °C for 5 min. in an oxygen atmosphere. The ferroelectric properties and resistivities were measured on a Radiant Technologies RT66A ferroelectric tester operated in the virtual ground mode. The films were also characterized by SEM and XRD. Further annealing of the films was carried out in air at 500 °C.

The 60 nm crystallites of PbTiO_3 that were used as "seeds" were obtained by ultrasonic disruption of PbTiO_3 particles formed by spray pyrolysis of the same precursors which has been described elsewhere.⁶ A series of parallel experiments were carried out with either the presence or absence of seeds.

RESULTS AND DISCUSSION

PbTiO_3

Seeded and unseeded films were produced at 400 °C and these were found to be largely amorphous by XRD. However, two broad peaks at $2\theta = 29^\circ$ and 31° which correspond to pyrochlore and perovskite, respectively, were observed. Analysis of the peak broadening by the Scherrer formula yields a calculated crystallite size of ~3 nm. The films annealed at 400 °C for 5 minutes displayed linear dielectric behavior. Further heating at 400 °C for 2-3 hours sharpened the perovskite peak observed by XRD but even after annealing for 36 hours the film was still primarily amorphous or micro-crystalline. Continued heating of the seeded film at 400 °C for 144 hours produced films with a well developed crystalline morphology as seen in the SEM photograph (Figure 1).

These crystallites were ~0.2 μm in length with well developed facets. Heating at 500 °C for 2 hours produced further crystallization of the perovskite phase in both the seeded (Figure 2) and unseeded (Figure 3) films. However, SEM observation revealed the presence of a diphasic microstructure, indicating that transformation to the perovskite phase was still incomplete. The effect of seeding the films at this stage could be distinguished with increased perovskite transformation occurring in the seeded film. This difference was also evident in the XRD of the films which showed different amounts of crystalline development relative to the amorphous peak (Figures 4 and 5). The crystallite size of both the films was found to be 17 nm by XRD and this is in agreement with the crystallite size observed in the SEM. The SEM photographs of the films at this stage showed that the crystallized region had contracted from the surrounding material which may be limiting the amount of growth that can occur on the surface of the crystallized regions. The ferroelectric properties of the films were poor due to the presence of the amorphous material and the small crystallite size. Further heating at 500 °C continued to crystallize the films with growth in the crystallite size of both the seeded and unseeded films. After 6 hours at this temperature most of the film had crystallized but some amorphous material remained in areas between the large crystalline regions (Figure 7).

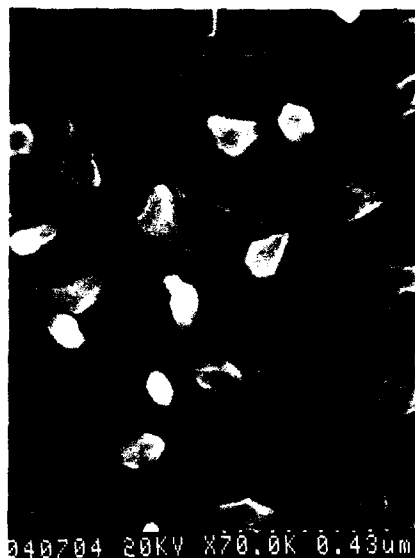


Figure 1. SEM photograph of PbTiO_3 (seeded) film after heating for 144 hours at 400°C .



Figure 2. SEM photograph of crystal growth of PbTiO_3 (seeded) after annealing at 500°C for 2 hours.



Figure 3 SEM photograph of crystallite growth in the unseeded film of PbTiO_3 heated at 500°C for 2 hours.

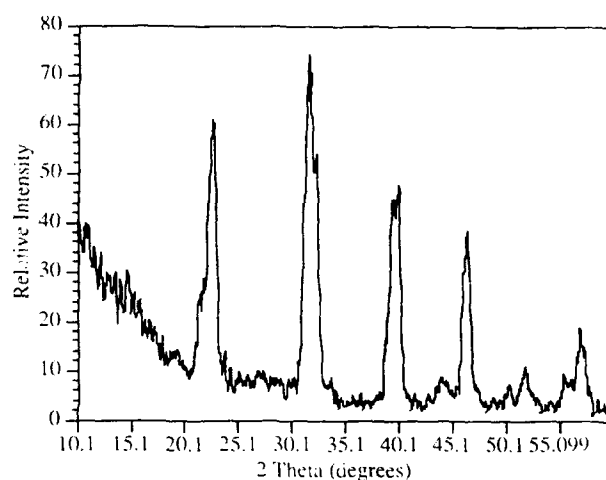


Figure 5. XRD Pattern of PbTiO₃ seeded thin film after annealing for 2 hours at 500°C.

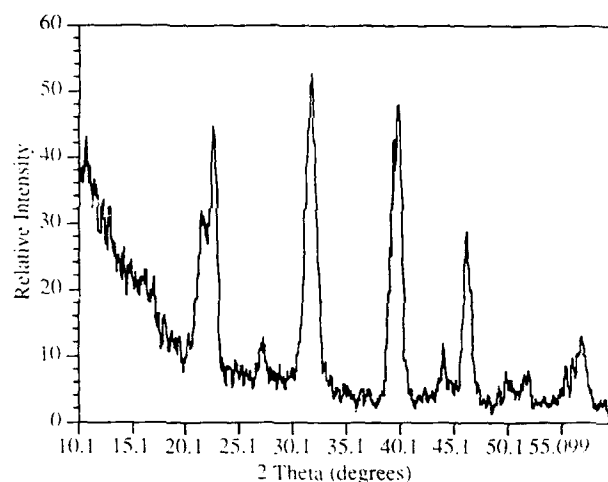


Figure 6. XRD Pattern of PbTiO₃ unseeded thin film after annealing for 2 hours at 500°C.

Ferroelectric properties for lead titanate films are displayed in Figure 8. Films fired at 400 °C for 2 hours may be characterized as linear dielectrics, due to the absence of ferroelectric hysteresis, indicating that they are most likely amorphous or pyrochlore in nature. Resistivities for the samples prepared under these conditions were relatively high with $R = 2E+10\Omega$ and $R_y = 3E+12\Omega$ which is expected for an amorphous phase. Further heat treatment at 500 °C for two hours resulted in very lossy hysteresis loops and a significant decrease in thin film resistivity $R = 1E+7\Omega$ and $R_y = 1E+9\Omega$. This is consistent with the crystallographic data which shows the presence of small perovskite crystallites. Further heat treatment at 500 °C resulted in some improvement in the hysteretic

characteristics and an increase in resistivity. However, the general shape of the loops would seem to indicate that a large volume fraction of amorphous material remains.



Figure 7 SEM photograph of PbTiO_3 (seeded) heated to 500°C for 6 hours.

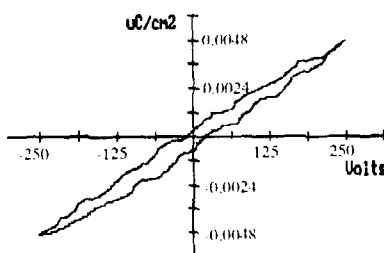


Figure 8a : Polarization behavior for film as deposited after heating to 400°C .

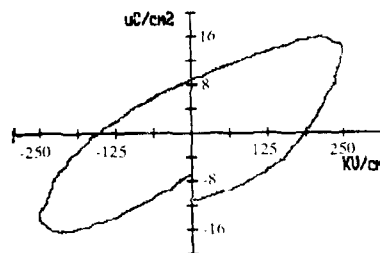


Figure 8b: Polarization behavior for film after annealing at 500°C for 6 hr..

$\text{Pb}(\text{Zr}_{0.52}\text{Ti}_{0.48})\text{O}_3$

The preparation of thin films of $\text{Pb}(\text{Zr}_{0.52}\text{Ti}_{0.48})\text{O}_3$, PZT, at 400°C which were not seeded with nano-sized crystallites was also investigated. The films were found to be amorphous by XRD. The SEM photographs indicated that the films were featureless, consistent with their amorphous nature. Annealing the films at 550°C for two hours induced

crystallization of the pyrochlore phase as indicated by the XRD pattern. Continued annealing at 650 °C increased the degree of crystallization of the pyrochlore phase in the film and perovskite was observed for the first time. The largest peak in the XRD pattern was due to pyrochlore which indicates that this phase was still the preferred phase at this temperature or that the conversion of the pyrochlore to perovskite was slow at this temperature. The ferroelectric properties of these films were poor due to the amount of amorphous material and pyrochlore present in the films. These films were more difficult to crystallize than the PbTiO_3 films and this is under investigation.

SUMMARY AND CONCLUSIONS

PbTiO_3 and PZT films were prepared from single-source precursors and were found to be amorphous as deposited and required further annealing to crystallize them. The PZT films crystallized in the pyrochlore phase at 550 °C but on further heating to 650 °C the perovskite phase was formed. The PbTiO_3 films crystallized as the perovskite phase at 400 °C but only on extensive heating >36 hours or by heating at 500 °C for ~4 hours. Seeding the films with 60 nm perovskite phase crystallites increased the degree of crystallization but did not lower the crystallization temperature under the conditions employed.

In contrast to the crystallization behavior of the films, the crystallization of ceramic powders from these precursors occurred at 350 °C. The cause of the different crystallization behavior in the films is currently under further investigation.

ACKNOWLEDGMENTS:

We thank Leo Archer for obtaining the X-ray powder diffraction data, the Center for Micro-Engineered Ceramics for funding and ONR for Analytical Facilities

REFERENCES

- (1) Chandler, C. D.; Roger, C.; Hampden-Smith, M. J. *Chem. Rev.* **1993**, *93*, 1205.
- (2) Kwok, C. K.; Desu, S. B. *Appl. Phys. Lett.* **1992**, *60*, 1430.
- (3) Kwok, C. K.; Desu, S. B. *J. Mater. Res.* **1993**, *8*, 339.
- (4) Chandler, C. D.; Hampden-Smith, M. J.; Brinker, C. J. *Mater. Res. Soc. Symp. Proc.* **1992**, *271*, 89.
- (5) Chandler, C. D.; Hampden-Smith, M. J. *Chem. Mater.* **1992**, *4*, 1137.
- (6) Chandler, C.D.; Powell, Q.; Hampden-Smith, M. J.; Kodas, T.T. *Mater. Res. Soc. Symp. Proc.* **1993**, *310*, in Press.

DRY ETCHING OF PZT FILMS IN AN ECR PLASMA

Barbara Charlet and Kerrie E. Davies*¹; CEA, DTA, LETI, CEN-Grenoble 85 X- F 38041, Grenoble Cedex, France.

ABSTRACT

PZT films were etched in an ECR microwave reactor with RF polarization. The etch rate was evaluated using various gas mixtures including combinations of two of the following: Cl₂, NF₃, SF₆ and HBr. The etch rate was measured as a function of the percentage of one gas in the mixture. Other parameters investigated included gas pressure, bias voltage on the electrode and substrate temperature. Results of the effect of temperature show that etch rates are higher on high temperature substrates than on low temperature substrates. A mixture of Cl₂ and SF₆ provided a PZT etch rate of 750 Å / min on a substrate, at approximately 100 °C. We evaluated the resultant etch profile and surface roughness.

1. INTRODUCTION

Lead Zirconate Titanate, PZT, is a ferroelectric ceramic currently of great interest for a wide range of electronic, sensor and optical applications (1;2). As device feature sizes decrease in the interests of higher performance, the use of PZT and other ferroelectric materials has gained increased interest. This is due to their high dielectric constants which allow greater charge storage in a small area. Other proprieties including low dielectric loss, temperature insensitivity and high breakdown strength make the PZT film suitable for fabrication of thin film capacitors.

High rate etching of PZT has been obtained by wet etching (3), but for achieving small feature size dry etching techniques are necessary. However, the classical dry etching reactors like RIE (reactive ion etching) have the disadvantage of relatively low etch rates (4) and depending on the chemistry can involve residues remaining on the etched surface or sidewalls. Also chemically assisted ion beam etching (CAIBE) (5) and dc hollow cathode plasma etching (6) gave interesting results at relatively low etch rate.

Intensive studies have been in progress for many years on dry etching development for Integrated Circuit (IC) technology. Different types of reactors were evaluated for silicon, others semiconductors, different dielectrics and metals. However the etching performance approach for the ferroelectric material is avaricious.

This paper reports the results of PZT and Pt thin film dry etching process development in a new generation Elecron Cyclotron Resonnance (ECR) reactor.

¹*Present address University of New South Wales, Sydney, Australia

II. EXPERIMENTAL SET UP

Dry etching of PZT and Pt layers was investigated in an industrial prototype machine, RCE 160, built by Alcatel. This machine can be used in either an ECR configuration or in a RIE configuration. Substrate polarisation in an ECR plasma is supplied by RF (radio frequency) biasing. In the ECR configuration the plasma is generated by a multi-antenna microwave source at 2.45 GHz and uses a multi-polar magnetic field of 875 Gauss to create the electron cyclotron resonance. The plasma diffuses down to the substrate area. In the RIE case, the plasma is generated by an applied radio frequency voltage at 13.56 MHz. Fig.1. shows a schematic of the basic electrical and vacuum equipment. The substrate holder is 100 mm in diameter. It is cooled by a recycled mixture of water and alcohol and with helium flow for the wafer-backside cooling. The minimum temperature can be set to 0°C. It is connected on the RF power. The bias voltage applied to the substrate can be selected and the appropriate RF voltage is putted on automatically by the machine. The stainless steel chamber is grounded. Gases which could be fed into the reactor included: Ar, SF₆, Cl₂, HBr and NF₃, or any combination of these.

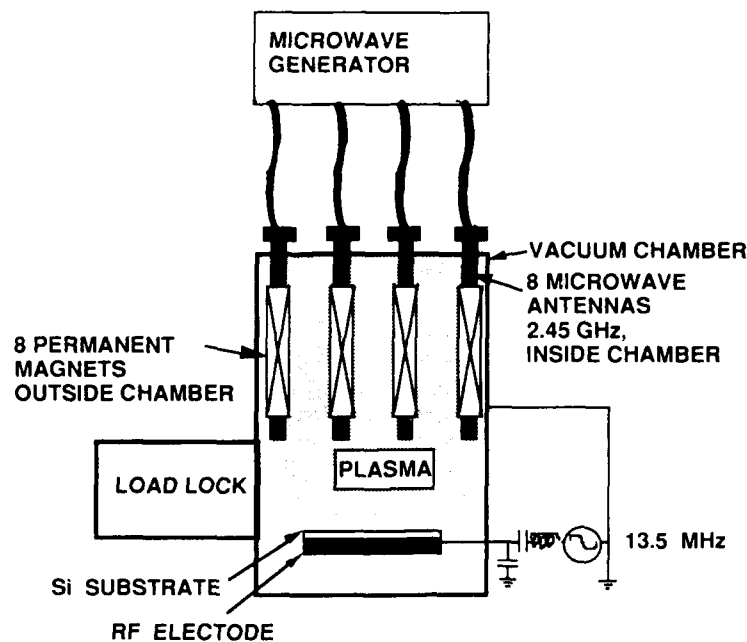


Fig.1. Schematic of the experimental reactor

The samples consisted of PZT (450 nm) layers prepared by the sol-gel method on the sputtered Pt (70 nm) layer deposited on the oxidized 4" Si substrate. The first experiments were done using a polyimide adhesive mask. Later the

photolithographical process was applied for the positive photoresist (Shipley 1400-31) and SiO₂ mask elaboration. The sample temperature was evaluated by temperature stickers placed on the etched layer surface. Etch rates were determined by an Alphastep surface profilometer and SEM photographs.

Diagnostic tools included: laser interferometry for end-point detection and real-time etch rate measurement of the PZT or SiO₂ film and emission spectroscopy for end-point detection.

II. EXPERIMENTAL RESULTS AND DISCUSSION

Our study consisted, at first, to compare the etch rate of PZT and platinum to the etch rate of silicon and SiO₂ for one given chemistry. Figure 2 shows the etch rate for the different materials exposed to a plasma of SF₆ and Cl₂ (50/50) at a pressure of 3 μ bar for 3 minutes. The silicon and SiO₂ etch rate variations as a function of bias voltage are not as significant as the etch rate for PZT and Pt, where we can observe a very strong increase with bias voltage. At 200 V the etch rate is 14 times greater than at 50 Volts. By comparison the SiO₂ etch rate only increases by a factor of about 2.5. The PZT etch rate is very dependent on the ion energy and is proportional to the bias voltage squared at high value end of the curve. There appears to be no selectivity between PZT and Pt etching. Under the same conditions a curve is also shown of thermal SiO₂ etch rate in Argon plasma, which gives an indication of the physical sputtering rate.

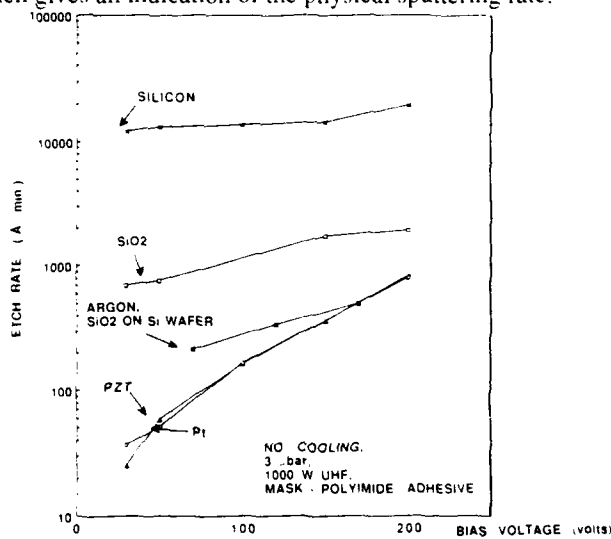


Fig.2. Etch rates vs.bias voltage in SF₆ and Cl₂ (50/50%) plasma

The energetical impact of plasma was investigated separately in ECR and in RF plasma condition. There seems to play a crucial role, because the etch rate of PZT obtained with plasma ECR was negligible and the same effect was

observed for the RF plasma. Adding RF assistance to the microwave ECR discharge resulted in a reasonable etch rate.

Substrate temperature is another important parameter in the evaluation of the etching performance. The substrate and etched layer temperature was measured for two different RF biases as a function of etch time for SF₆ and Cl₂ plasma chemistries. The substrate temperature was also measured for an Ar plasma at 50V RF bias. The measurements were performed with and without backside wafer cooling. As the etch time increases from 1 minute to 5 minutes at 200V bias voltage, the substrate temperature rises from 245°C to over 290°C for an uncooled substrate. This compares with only 80°C to 95°C for a cooled substrate, at 200 V bias voltage (see Fig. 3). A similar trend is seen at 50 V bias voltage. An argon discharge heats the substrate by about 150 to 250°C during four minutes in uncooled conditions at 50V RF bias. Fig. 4 shows the etch rate of PZT and SiO₂ as a function of bias voltage for both cooled and uncooled substrates. At low values of bias voltage the cooling effect has an significant influence on the etching performances of both PZT and Pt layers. Although at 200 V the SiO₂ etch rate is the same with and without wafer cooling. However, for uncooled PZT, the etch rate is 825 Å/min compared with 340 Å/min for the substrate cooling condition. This indicates that the PZT etch rate is more dependent on substrate temperature than the SiO₂ etch rate. The uncooled PZT etch rate curve is parallel to the cooled etch rate curve on this logarithmic scale, for applied voltages. Uncooled substrates provide higher PZT etch rates with a factor of 2 to 3. However, cooled substrates are preferable when a more constant temperature is required for the etching elaboration.

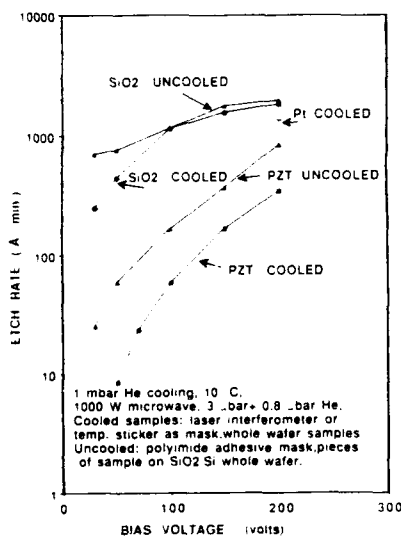


Fig.3. Substrate temperature as a function of etch time

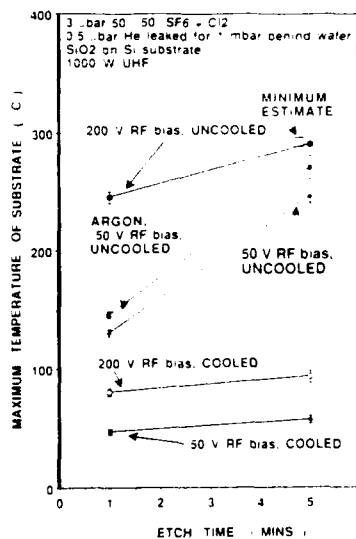


Fig.4. Etch rate of SiO₂ and PZT in SF₆ and Cl₂ (50/50%) plasma

The PZT etch rate was plotted as a function of % Cl₂ in SF₆. It is shown in Fig. 5. for 1 μ bar and 3 μ bar plasma conditions. A peak at 80% Cl₂ and a minimum value at 100 % Cl₂ for 1 μ bar pressure was observed. A mixture of Cl₂ and SF₆ at this pressure can increase the etch rate by 35% over pure SF₆ and by 120 % over pure Cl₂ etching. At 3 μ bar the etch rates are lower than at 1 μ bar. This result is probably due to the ECR plasma enhancement contribution at low operating pressure. The etch rate for 100 % argon is 60 $\text{\AA}/\text{min}$ indicating that there is a large chemical effect in the etch rate of PZT.

The etch rate curve for % HBr in SF₆ is shown in Fig. 6. It indicates that Cl₂ chemistry is more performant than HBr in the low pressure etching condition.

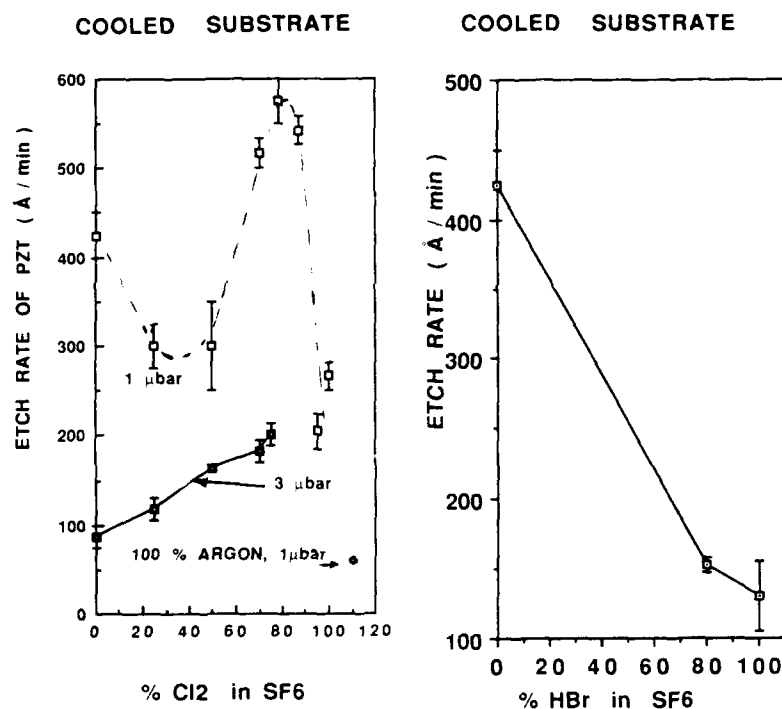


Fig.5. Etch rate of PZT as a function of % Cl₂ in SF₆ at 1000W microwave power and 150V bias

Fig.6. Etch rate of PZT as a function of % HBr in SF₆ at 1 μ bar.

Preliminary experiments on the profile of etched PZT with a SiO₂ sloped mask profile in 50% SF₆ and 50% Cl₂ indicates that the SiO₂ mask profile is reproduced in to the PZT wall. The photoresist mask had a vertical definition before etching and the etching profile obtained with this mask, in the case of cooled substrate, was almost vertical.

CONCLUSIONS

We have studied the etching of PZT and Pt thin films in a plasma reactor combining a RF and ECR discharge. The etching performance of the ferroelectric layers was compared with the classical IC materials like bulk Si and thermal SiO₂. We observe a very important influence of substrate temperature and bias voltage in the PZT and Pt etching rate evolution. Relatively high etching rate (850 Å/mn) were obtained for the uncooled substrate condition (T=280°C). The lower etching rate was observed in the substrate cooling condition. In the optimised pressure and gas composition it is possible to have an etching rate of about 600 Å/mn at substrate temperature T=100°C. This temperature condition permits the use of a photoresist mask during etching process.

ACKNOWLEDGMENTS

The authors would like to thank L. Peccoud, H. Achard and H. Macé for their contribution to this work.

REFERENCES

1. S.L. Swarz and V.E. Wood, Condensed Matter News vol.1 N°5 (1992)
2. Abhai Mansingh, Ferroelectrics vol.102 pp.69-84 (1990)
3. D. Asselanis, D. Mancha, US Patent N°4,759,823 Jul (1988)
4. K. Saito, J.H. Choi, T. Fukuda and M. Ohue, Jap. J. Appl. Phys. vol.31 pp.L1260-L1262 (1992)
5. S.H. Lee, S.C. Esener, M.A. Title and T.J. Drabik, Optical Engineering, vol.25, N°2, (1986)
6. M.R. Poor, A.M. Hurd, C.B. Fleddermann and A.Y. Wu, MRS Proc., Ferroelectric Thin Films, vol.200, (1991)

TRANSMISSION ELECTRON MICROSCOPY OF PZT THIN-FILMS PREPARED BY A SOL-GEL TECHNIQUE

Supapan Seraphin, Dan Zhou, G. Teowee*, J.M. Boulton, and D.R. Uhlmann
Department of Materials Science and Engineering, University of Arizona,
Tucson, Arizona 85721

*Donnelly Corporation, 4545 Fort Lowell Road, Tucson, Arizona 85721

ABSTRACT

The microstructure of lead zirconate titanate (PZT) thin films prepared by a sol-gel technique was investigated using transmission electron microscopy (TEM) and transmission electron diffraction. We investigated the microstructure of three sets of thin films with different chemical compositions: PZT 53/47 films with no excess PbO; with excess PbO; and PZT 65/35 with no excess PbO. All samples were fired for 30 minutes at temperatures ranging from 400C to 700C. Incorporation of excess PbO in the 53/47 film fired at 450C resulted in polycrystalline perovskite grains with an average grain size of less than 0.1 μm . Grain boundaries are decorated by 5-10 nm diameter precipitates possibly caused by the segregation of remnant pyrochlore or excess PbO. The films have high values of dielectric constant (up to 2500) when fired at 700C. PZT 65/35 fired at 700C consists of two distinct phases: a fine-grained matrix of pyrochlore, and 10- μm diameter rosettes of perovskite. The correlations between the compositions, the microstructure of the films, and their processing conditions on the one hand, and ferroelectric properties on the other are discussed.

INTRODUCTION

Lead zirconate titanate (PZT) is one of the best known perovskites used in ferroelectric applications in both bulk and thin film form [1]. PZT is a solid solution containing lead titanate (PT) and lead zirconate (PZ) in various stoichiometric ratios. PZT x/y refers to $\text{Pb}(\text{Zr}_x/100\text{Ti}_y/100)\text{O}_3$ where x, y are equal or less than 100 and $x+y = 100$. PZ is antiferroelectric while PT is ferroelectric. Solid solutions of these two end members produce mostly ferroelectric materials whose properties strongly depend on the Zr/Ti ratio. PT-rich and PZ-rich compositions belong to the tetragonal and rhombohedral modifications, respectively, of the perovskite crystal structure. The composition of 53 atom% Zr and 47 atom% Ti (PZT 53/47) at the rhombohedral-tetrahedral boundary in the PZ-PT phase diagram is the most important one since the material exhibits maximum values of dielectric constant, electromechanical coupling factor, and piezoelectric coefficients [1]. Among various techniques used to prepare PZT films, the sol-gel technique offers possibilities to control the properties of a material through the processing conditions used and the chemistry employed [2]. Several investigations indicate that the microstructure of PZT thin films depends strongly on the composition and processing conditions [3-5]. For example, it has been reported that with an increasing Zr/Ti stoichiometry ratio in sol-gel derived PZT thin films the grain size of the rosettes increases [6]. In this paper, we report on the microstructure as characterized by transmission electron microscopy (TEM) of PZT thin films prepared by a sol-gel technique. We examined PZT 53/47, with and without excess PbO, and PZT 65/35 films. The annealing temperature ranged from 400 to 700C. The annealing duration at a given temperature was 30 minutes.

EXPERIMENTAL PROCEDURE

To prepare PZT precursor solutions, Pb acetate trihydrate ($\text{Pb}(\text{OAc})_2 \cdot 3\text{H}_2\text{O}$) was dissolved in methanol. Freshly distilled Ti iso-propoxide and Zr n-propoxide in n-propanol, in the appropriate molar quantities, were added to the methanolic Pb acetate solution with vigorous stirring to give the desired stoichiometries of PZT 53/47 and 65/35. After refluxing for 3 hours, the solutions were concentrated to 1.0 M. The effect of excess PbO was also investigated by incorporating 15 mole% PbO into the PZT 53/47 precursor. Spincoating the precursor solution on a clean substrate was performed in a Class 100 clean room. The substrates were Si(100) wafers which had previously been thermally oxidized before being sputtered with Pt to form a 2000Å thick Pt film on the 1500Å thick silicon dioxide layer. The green films were fired at 500C to burn off residual organics, yielding films about 1700Å thick per coating. In order to obtain thicker films, multiple coatings were performed. Typically three coatings were required to obtain films about 0.5 µm thick. Finally, these films were fired at crystallization temperatures of 400, 450, and 700C, for 30 min. The structure and phase of the films were determined by a Scintag X-ray diffractometer. The x-ray diffraction results are correlated with the microstructure observed in a Hitachi 8100 transmission electron microscope at 200 keV.

TEM samples of both cross-sectional and plan view specimens were prepared by ion milling with 6 kV argon ions. For cross-sectional samples, four slices of 2 mm x 6 mm wafers were glued together, mechanically thinned to 100 µm, dimpled to about 25 µm, and then ion milled at an angle of 15° on a liquid nitrogen cold stage.

RESULTS AND DISCUSSION

The microstructures of PZT 53/47 films containing no excess PbO, fired at 450, and 700C are shown in Fig. 1. The image of the film fired at 450C is featureless with faint dark regions of 100 nm in size (which is approximately the same size of the polycrystalline grains in PZT 53/47 films with excess PbO fired at the same temperature, shown in Fig. 3(b)). The electron diffraction pattern (not shown here) indicates the presence of an amorphous phase. In contrast, the film fired at 700C consists of two phases. The phase of higher density, which appears darker in the micrograph, has a spherical morphology and comprises roughly 80 volume% of the film. The selected area electron diffraction pattern in the inset of Fig. 1(b) is a ring pattern corresponding to polycrystalline perovskite PZT mixed with the pyrochlore phase (PbTi_3O_7 , cubic). The innermost ring has the highest intensity indicating that the majority of the grains prefer the <100> orientation. This is likely to happen since the underlying Pt layer has <200> orientation. The result is in good agreement with the x-ray diffraction data which shows the presence of perovskite and minor traces of pyrochlore.

Fig. 2(a) shows a portion of the TEM cross-sectional view of the PZT 53/47 film of Fig. 1(b). The film consists of polycrystalline grains of 50 nm diameter and over 200 nm long. The grains grow along the direction perpendicular to the interface. The corresponding electron diffraction pattern shown in Fig. 2(b) represents a perovskite single crystalline pattern viewing along the <110> direction. The splitting and/or elongation of most diffraction spots are due to the misalignment of the grains along the viewing direction.

PZT 53/47 films with excess PbO, giving a stoichiometry of $\text{Pb}_{1.15}\text{Zr}_{0.53}\text{Ti}_{0.47}\text{O}_{4.5}$, have significantly different microstructures. Fig. 3 shows a series of TEM images and corresponding electron diffraction patterns of the PZT 53/47 films with excess PbO, fired at 400, 450, and 700C, respectively. At 400C, the films have a small compact grain size ranging from 30 to 100 nm. Grain boundaries are decorated by 5-10 nm diameter precipitates possibly caused by the segregation of the remnant pyrochlore phase or excess PbO. The corresponding electron diffraction shown in Fig. 4(a) indicates the presence of mainly polycrystalline pyrochlore mixed with some perovskite phase. When fired at 450C, the films still have a

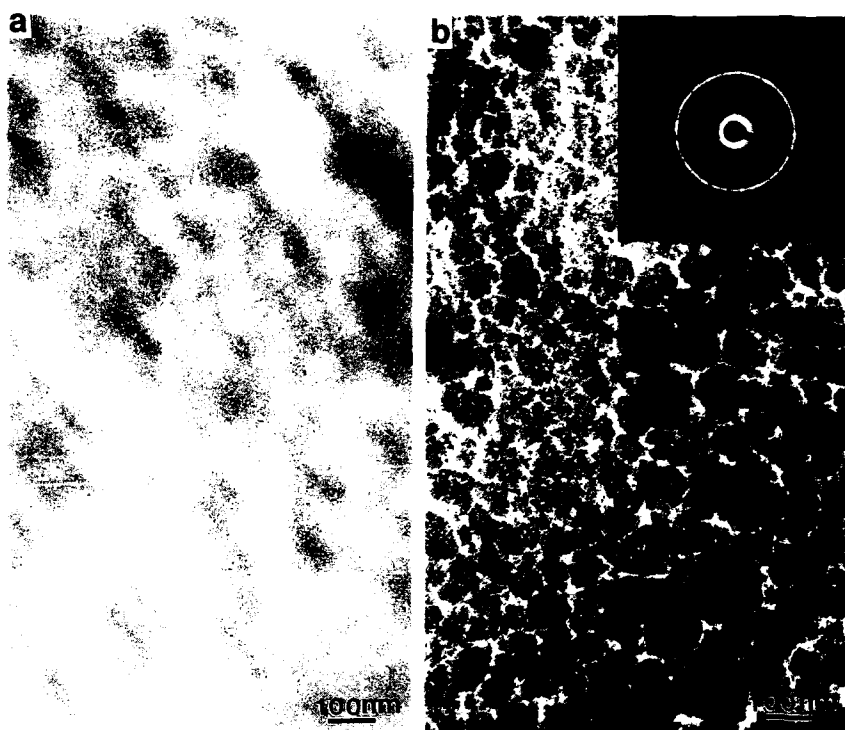


Fig. 1. Plan view TEM images of PZT 53/47 fired at (a) 450C, and (b) 700C.



Fig. 2. Cross-sectional TEM image (a) and electron diffraction pattern (b) of PZT 53/47 fired at 700C for 30 min.

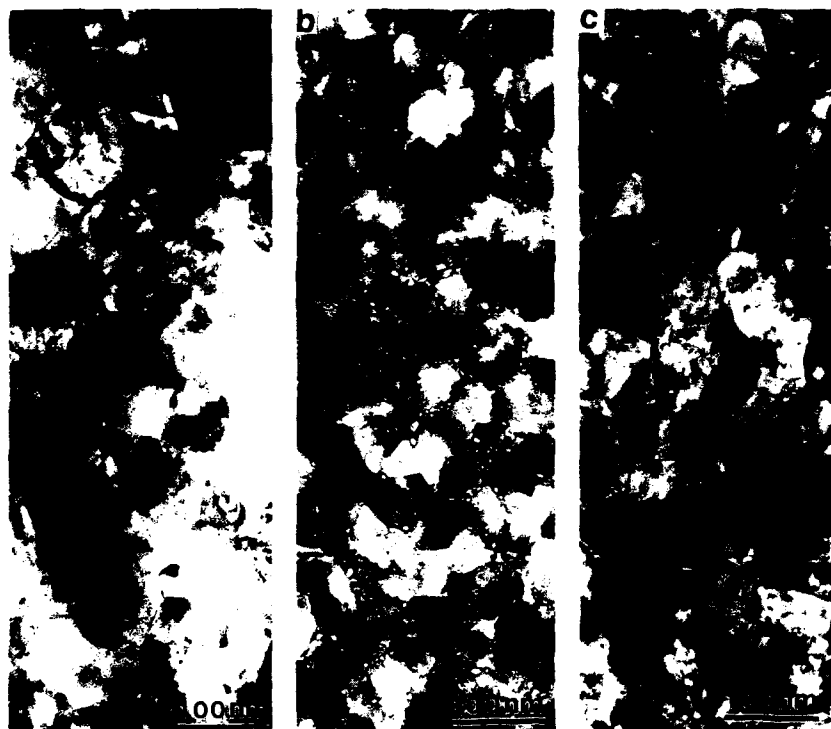


Fig. 3. Plan view image of PZT 53/47 films with excess PbO, fired at (a) 400C, (b) 450C, and (c) 700C.

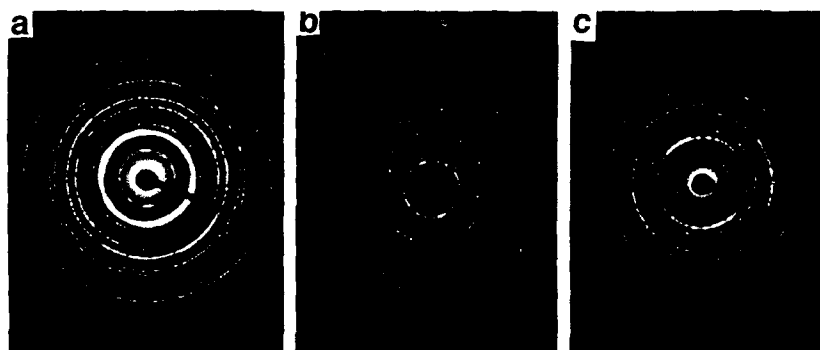


Fig. 4. Selected area electron diffraction patterns of PZT 53/47 films with excess PbO, fired at (a) 400C, (b) 450C, and (c) 700C.

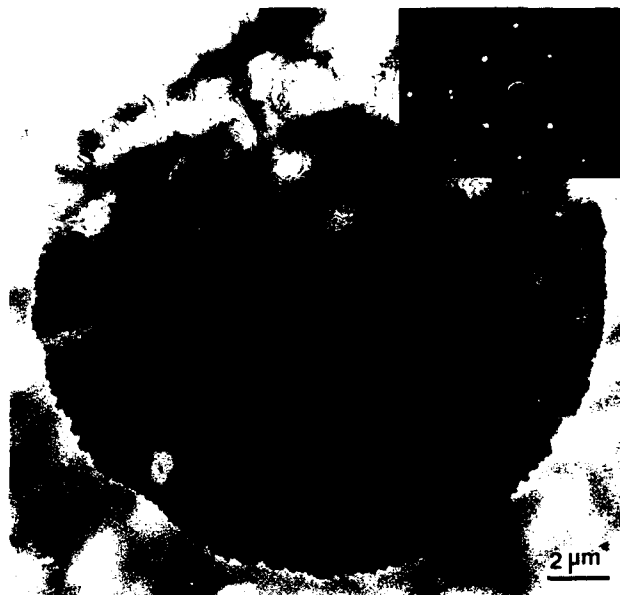


Fig. 5. TEM image and the electron diffraction pattern of perovskite "rosette" in PZT 65/35 fired at 700C.

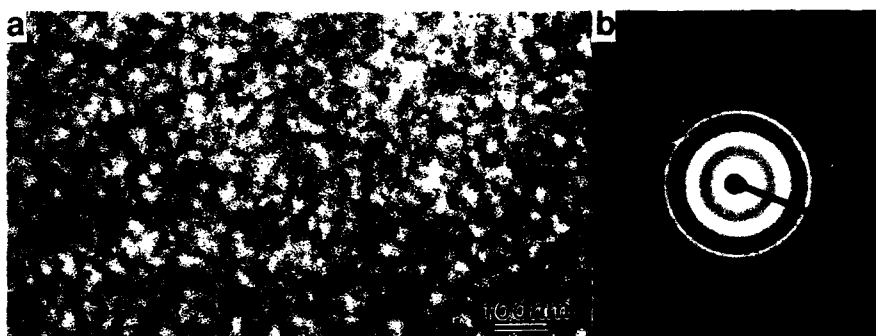


Fig. 6. TEM image (a) and electron diffraction pattern (b) of the pyrochlore-containing matrix of PZT 65/36 film fired at 700C.

polycrystalline structure with a slightly larger grain size. Note that this sample contains a higher density of decorated precipitates at the grain boundaries than the films fired at 400°C. The diffraction pattern in Fig. 4(b) shows that the sample consists mainly of perovskite and some pyrochlore. At a firing temperature of 700°C, the grains grew larger with a noticeable decrease in the number of precipitates at the grain boundaries. The electron diffraction pattern shows a pure perovskite phase. Twinnings are observed occasionally in these films, however well-ordered domains are not observed in any of the samples.

The effect of excess PbO on the microstructure is illustrated by comparing the microstructures of Fig. 1(b) and Fig. 3(b). The excess PbO enhances grain growth and hence results in higher domain wall mobility. It also promotes the formation of single phase perovskite which is reflected in the improvement in the dielectric constant from 1000 in the films without excess PbO to a value of 2500 for films with excess PbO for films fired at 700°C.

The PZT 65/35 film with no excess PbO, fired at 700°C have a drastically different structure compared to the other films. They contain numerous perovskite PZT rosettes embedded in a pyrochlore matrix. Fig. 5 depicts the general morphology of a rosette of about 1.5 µm in diameter, much larger than the values of 3-4 µm diameter observed in other work [4,7]. The electron diffraction of the rosette, shown in the inset, corresponds to a single crystal of the perovskite viewing along the $\langle 100 \rangle$ direction. The splitting of the diffraction spots indicates a slight misalignment of the rosette. Fig. 6(a) shows that the matrix of the film is a mixture of the two interpenetrating phases with higher and lower density materials of approximately 50 nm in size. The electron diffraction pattern, Fig. 6(b), indicates that the matrix contains small grains of pyrochlore phase. Due to the preponderance of the pyrochlore phase over perovskite, the film exhibits a low dielectric constant of only 600.

CONCLUSIONS

1. PZT 53/47 films without excess PbO fired at 400°C and 450°C are amorphous. When fired at 700°C, the films contain perovskite phase with spherical structure. They exhibit a preferred orientation in the $\langle 100 \rangle$ direction.
2. In contrast, all PZT 53/47 films with excess PbO fired at 400, 450, and 700°C are polycrystalline. When fired at 400°C, the films are a biphasic mixture of mainly pyrochlore and some perovskite. The fraction of the perovskite phase increases for 450°C firing. At 700°C, the films are pure perovskite, and hence have a high dielectric constant.
3. PZT 65/35 films consist of two distinct phases with perovskite rosettes embedded in a pyrochlore-containing matrix.

ACKNOWLEDGEMENT

We gratefully acknowledge the support of the Air Force Office of Scientific Research.

REFERENCES

1. B. Jaffe, R. Cook, and H. Jaffe, *Piezoelectric Ceramics*, Academic Press, 1971.
2. G. Teowee, J.M. Boulton, and D.R. Uhlmann, *Mat. Rev. Soc. Proc.* **243** (1992), 255.
3. C.C. Hsueh and M.L. McCartney, *Mat. Rev. Soc. Proc.* **200** (1990), 219.
4. S.A. Myers and L.N. Chapin, *ibid.*, 231.
5. J.P. Goral, M. Haffman, and M.M. Al-Jassam, *ibid.*, 225.
6. G. Teowee, J.M. Boulton, E.A. Kuzer, M.N. Orr, D.P. Birnie III, D.R. Uhlmann, S.C. Lee, K.F. Galloway, and R.D. Schrimpt, *Proc. 5th ISAF* (1992), in the press.
7. B.A. Tuttle, T.J. Headley, B.C. Bunker, R.W. Schwartz, L.L. Zender, C.L. Hernandez, D.C. Goodnow, R.J. Eissot, J. Michael, and A.H. Carim, *J. Mater. Res.* **7** (1992), 1876.

CURRENT STATUS OF AND RECENT RESULTS ON GROUP 2 SOURCE COMPOUNDS FOR VAPOR PHASE EPITAXY OF FERROELECTRIC THIN FILMS

WILLIAM S. REES, JR.*, HENRY A. LUTEN, MICHAEL W. CARRIS, CELIA R. CABALLERO, WERNER HESSE, AND VIRGIL L. GOEDKEN†

Department of Chemistry and Materials Research and Technology Center, MS: B-164, The Florida State University, Tallahassee, FL, USA, 32306-3006

† Deceased 22 December 1992

ABSTRACT

Much interest in the area of ferroelectric thin films has been generated by the recent developments in unique property observation for these materials. As deposition methods move toward potential commercialization, the importance of chemically and thermally stable at use temperature, high vapor pressure and purity, readily available and economically competitive sources for the requisite group 2 elements will emerge. This presentation entails an initial overview of the presently utilized compounds, their advantages and disadvantages. New group 2 CVD precursors have been developed based both on inter- and intramolecular stabilization of cyclopentadienides, alkoxides and β -diketonates. Recent results on the coordination environment around the central metal atom have offered insight into the next generation of polydentate, monoanionic ligand design. Specific details are discussed for the metal complexes of "scorpion-tail" β -diketoethers. Results of comparison studies between these new precursors and earlier compounds are presented as a model for designing future sources.

Introduction

There is an interest in the preparation of some ferroelectric materials in thin film form by chemical vapor deposition (CVD).^{1,2} One composition presently attracting attention is BaTiO_3 . In order to achieve reasonable epitaxial growth rates at usable substrate temperatures, precursor molecules containing the elements of interest should transport in the vapor phase at processing conditions of less than 200°C and greater than 5 Torr.³ This presents a significant problem for the case of barium. Most researchers have utilized the *bis*(β -diketonate) complexes of this group 2 element as the source of the metal. Although $\text{Ba}(\text{fod})_2$ ⁴ and $\text{Ba}(\text{hfac})_2 \cdot \text{tetraglyme}$ ⁵ each possess the requisite vapor pressure characteristics demanded for employment in CVD, they also each suffer from the primary deposition of BaF_2 , and the requirement for a subsequent, hydrolytic conversion into the desired oxide form of the ferroelectric perovskite material.⁶ To date, research on non-fluorine containing, high vapor pressure barium-containing compounds has focused on intramolecular coordination of alkoxides⁷ and cyclopentadienides.⁸ In the absence of Lewis bases, hydrocarbon-based *bis*(β -diketonates) are oligomeric (Fig. 1).⁹ Substantial progress has been made in the utilization of these compounds in the CVD growth of superconducting metal oxides.¹⁰

Experimental

Ba(tmhd)₂·2 *o*-phen. In a 250 ml Schlenk flask were combined 1.00 g (7.3 mmol) of barium, 2.82 g (15.3 mmol) of Htmhd, 5.25 g (29.1 mmol) of *o*-phen and 100 ml of THF (distilled from Na/benzophenone). With rapid stirring, anhydrous NH₃(g) (passed over KOH) was bubbled through the mixture. The solution was warmed to 40°C and the reaction was allowed to proceed for 5 h. The solution was transferred under N₂(g) to another flask leaving unreacted barium behind. The solution flask was sealed and cooled to -20°C. A pale, beige precipitate formed. This precipitate was recrystallized from a minimum amount of hot toluene (distilled from Na) to give 4.67 g (5.4 mmol) of Ba(tmhd)₂·2 *o*-phen, 74% based on barium. **Characterization:** mp: 216°C. ¹H NMR: (300 MHz, positive δ downfield referenced to Si(CH₃)₄ = 0 ppm utilizing residual C₆D₅H = 7.15 ppm in solvent C₆D₆) 9.38 [d, 2H, *o*-phen], 7.41 [d, 2H, *o*-phen], 7.11 [s, 2H, *o*-phen], 6.93 [d, 2H, *o*-phen], 5.81 [s, 1H, tmhd], 1.25 [s, 18H, tmhd]. ¹³C{¹H} NMR: (75 MHz, positive δ downfield referenced to Si(CH₃)₄ = 0 ppm utilizing CDCl₃ = 77.0 ppm) 199 [tmhd], 151 [*o*-phen], 146 [*o*-phen], 136 [*o*-phen], 129 [*o*-phen], 123 [*o*-phen], 77 [tmhd], 41 [tmhd], 28 [tmhd]. IR (Nujol): 2847(vs), 1612(w), 1583(s), 1522(w), 1501(m), 1489(m), 1417(vs), 1349(m), 1261(w), 1221(m), 1173(w), 1168(w), 1134(w), 1119(w), 857(m, sh), 841(m, sh), 785(w, sh), 769(w, sh), 762(w, sh), 730(m, sh), 712(w, sh). UV/VIS: c = 1.44 × 10⁻⁶ M, λ_{max} = 263 nm, ε = 5.87 × 10⁴ M⁻¹cm⁻¹, λ_{max} = 231 nm, ε = 10.98 × 10⁴ M⁻¹cm⁻¹. TGA: (Fig. 4). **Sublimation:** A sublimator equipped with a dry-ice/acetone cooled cold finger was charged with 0.50 g (0.579 mmol) of Ba(tmhd)₂·2 *o*-phen. The sublimator was evacuated to 10⁻⁵ Torr and warmed slowly. Sublimation occurred at 220 - 260°C. After 1 h, 0.48 g of sublimed material was recovered from the cold finger leaving a residue of 0.02 g. The ¹H-NMR of the sublimate showed it to be *o*-phenanthroline enriched, indicating decomposition of the compound in the solid state and unequal sublimation rates of the decomposition products.

Ba(tmhd)₂·bipy. Under a N₂ atmosphere, 1.32 g (9.6 mmol) of barium was combined with 80 cc of anhydrous Cabosil™ (dried at 100°C / 0.01 Torr for 48 h) in a 250 ml flask equipped with a magnetic stirring bar and a dry-ice/acetone cooled condenser. Into this mixture was condensed 125 ml of anhydrous NH₃(l) (passed over KOH), completely dissolving the barium. The NH₃(l) then was allowed to evaporate slowly with stirring, leaving a barium coating on the Cabosil. The flask was evacuated to remove any residual NH₃. To the resulting gray solid was added 80 ml of hexane (distilled from LiAlH₄) followed by 2.68 g (14.5 mmol) of Htmhd and 5.68 g (36.4 mmol) of bipy in 20 ml of toluene (distilled from Na). Rapid gas evolution was evident. The reaction mixture was stirred for 3 h and then filtered through a Schlenk frit. The frit was washed with 20 ml of toluene and 20 ml of hexane. The solvents were removed under vacuum to give a white solid. The solid was recrystallized from a minimum amount of hot hexane to give 4.26 g (4.93 mmol) of Ba(tmhd)₂·bipy, 89% based on Htmhd. **Characterization:** mp: 157°C. ¹H NMR: (see above) 8.66 [d, 1H, bipy], 8.15 [d, 1H, bipy], 7.11 [td, 1H, bipy], 6.71 [td, 1H, bipy], 5.84 [s, 1H, tmhd], 1.28 [s, 18H, tmhd]. ¹³C{¹H} NMR: (75 MHz, positive δ downfield referenced to Si(CH₃)₄ = 0 ppm utilizing CD₃C₆D₅ = 20.4 ppm) 200 [tmhd], 157 [bipy], 150 [bipy], 137 [bipy], 124 [bipy], 121 [bipy], 90 [tmhd], 42 [tmhd], 29 [tmhd]. IR (Nujol): 2847(vs), 1581(s), 1564(s), 1523(w), 1480(m), 1435(w), 1416(vs), 1352(m), 1217(w), 1169(w), 1148(w), 1121(m), 1057(w), 1037(w, sh), 1022(w, br), 1001(m, sh), 949(w), 929(w), 862(w), 790(w), 757(m), 739(w, sh). UV/VIS: c = 1.30 × 10⁻⁶ M, λ_{max} = 236 nm, ε = 13.17 × 10⁴ M⁻¹cm⁻¹, λ_{max} = 284 nm, ε = 29.55 × 10⁴ M⁻¹cm⁻¹. TGA: (Fig. 4). MW: (benzene cryoscopy) obs. 748 g/mol (calc. monomer: 660 g/mol). **Sublimation:** A sublimator equipped with a dry-ice/acetone cooled cold finger was charged with 0.75 g (1.4 mmol) of Ba(tmhd)₂·bipy. The sublimator was evacuated to 10⁻⁴ Torr and heated slowly. At approximately 70°C a white solid, identified as bipy (mp), sublimed onto the cold finger. This solid was allowed to migrate to the top of the cold finger before the finger was cooled. The remainder of the solid in the bottom of the sublimator sublimed at 160 - 220°C over a period of 1 h and was identified as pure [Ba(tmhd)₂]_{3,4} by ¹H-NMR and mp.

Ba₆(tmhd)₁₀(Me₂SiO₂) • H₂O. In a 500 ml 3-necked flask, equipped with a reflux condenser (with a N₂(g) inlet), addition funnel, and a mechanical stirrer (all ground glass joints were sealed with silicone stopcock grease), 13.2 g (0.096 mol) of barium was reacted with 32.0 g (0.17 mol) of Htmhd. After one half of the Htmhd was added, 20 ml of distilled toluene was added and the resulting mixture was heated at reflux for 2 d. The solution was cooled to room temperature and 30 ml of diethyl ether was added to dissolve the solid. The solution was filtered through a Schlenk frit to remove the unreacted barium. An aliquot of the filtrate was allowed to stand at room temperature for 2 d to grow crystals. Attempts to synthesize this compound with stoichiometric quantities of reagents currently are in progress. **Crystallographic data:** Formula, C₁₁₂H₉₈O₂₃Ba₆Si; Mol Weight, 2764.85; Crystal System, triclinic; Space Group, P1; a = 1473.1(4) pm, b = 1860.5(4) pm, c = 2850.7(4) pm; α = 73.98(2)°, β = 83.31(2)°, γ = 75.72(2)°; V(10⁶) = 7268(2) pm³; Z = 2; ρ = 1.381 g/cm³; Abs. Coeff. = 16.586 cm⁻¹; 2θ Scan range, 2° < 2θ < 50°; Scan mode, ω/2θ; No. of measured reflections, 18179; No. of independent reflections, 11926; No. of reflections with F_o > 4σ(F_o), 7175; No. of refined parameters, 712; R = 7.5%; R_w = 9.2%; Maximum unassigned electron density, 1.207 e/Å³. Selected distances (pm) and angles (°): Ba1-Ba2, 410.2; Ba1-Ba4, 402.9; Ba1-Ba6, 403.8; Ba2-Ba3, 406.6; Ba2-Ba5, 403.8; Ba3-Ba4, 413.2; Ba3-Ba5, 402.5; Ba4-Ba6, 407.7; O23-Ba1, 313.0; O23-Ba2, 317.9; O23-Ba3, 329.5; O23-Ba4, 311.7; Ba2-Ba1-Ba4, 89.4; Ba1-Ba2-Ba3, 91.0; Ba2-Ba3-Ba4, 88.5; Ba1-Ba4-Ba3, 91.1; Ba4-Ba1-Ba6, 60.7; Ba1-Ba4-Ba6, 59.8; Ba1-Ba6-Ba4, 59.5; Ba3-Ba2-Ba5, 59.6; Ba2-Ba3-Ba5, 59.9; Ba2-Ba5-Ba3, 60.6; Ba2-Ba1-Ba6, 115.2; Ba3-Ba4-Ba6, 114.8; Ba1-Ba2-Ba5, 115.7; Ba4-Ba3-Ba5, 115.3.

Results and Discussion

Intermolecular Lewis Base Stabilization

Previous workers have added neutral β-diketone to the carrier gas stream in efforts to augment the vapor pressure of "Ba(tmhd)₂".¹¹ Other research groups have chosen H₂O,¹² THF,¹³ or NH₃¹⁴ as the additive. The compound also has been crystallized with MeOH¹⁵ and Et₂O¹⁶ of solvation. Although the vapor pressure of Ba(hfac)₂ was enhanced substantially upon complexation with tetraglyme, the comparable Ba(tmhd)₂ adduct proved to be unstable toward vapor phase dissociation (Fig. 2).^{6f} Likewise, the nitrogen-based adducts [Ba(tmhd)₂•2 NH₃]₂^{9b} (Fig. 3) and [Ba(tmhd)₂•2 tmeda]₂¹⁷ dissociated the neutral amine in the gas phase, even though it was tightly bound both in the solid state and in solution.

A recent report¹⁸ of Ba(tmhd)₂•*o*-phen prompted us to explore several difunctional nitrogen-centered aromatic Lewis bases. The details of the preparation and characterization of Ba(tmhd)₂•L_x were presented above, in the experimental section of this contribution.¹⁹ The TGA data for these compounds has been summarized (Fig. 4). The least volatile

example given is Ba₅(tmhd)₉OH • 3 H₂O, followed by [Ba(tmhd)₂ • 2 NH₃]₂. In the intermediate vapor pressure regime, [Ba(tmhd)₂]_{3,4} is the next least volatile, closely

followed by Ba(tmhd)₂ • 2 *o*-phen. The most volatile example shown here is Ba(tmhd)₂ • bipy; however, note that decomposition accompanies volatilization. Thus, this composition is rendered a curiosity for CVD utilization purposes. Stoichiometric mixtures of [Ba(tmhd)₂]_{3,4} and L_x^{19a} yielded comparable results (c, e; d, f) to those observed for the complexed molecular species. Indications of some solid state reactivity are presented by comparison of the data for a mixture containing uncomplexed *o*-phen (e) and that of *o*-phen alone (g). Thus, the role of added Lewis base in influencing the vapor pressure of [Ba(tmhd)₂]_{3,4}, and chemical derivatives of this oligomer, is rendered less simple to interpret. The likely implication of these results is an impeding of the degree of oligomerization, and the resultant concomitant enhancement in vapor pressure, due to the predisposition of "Ba(tmhd)₂" toward decreased self-catenating interactions triggered by the presence of the added Lewis base.

Cluster Formation

In the absence of any external Lewis base, "Ba(tmhd)₂" exists as a trimeric/tetrameric cluster.⁹ A commercially available composition, labeled "anhydrous Ba(tmhd)₂", proved to be "Ba₅(tmhd)₉(OH)·3 H₂O" (Fig. 5).²⁰ We have isolated a derivatized cluster, by reaction with polydimethylsiloxane,²¹ of the formula Ba₆(tmhd)₁₀(Me₂SiO₂)·H₂O (Fig. 6). Presumably, this comes from either the primary cluster species Ba₆(tmhd)₁₀(OH)₂ or Ba₆(tmhd)₁₀(O₂⁻²). Credence is lent to the peroxy option by the recent independent synthesis and structural identification of Ba₆(tmhd)₁₀(O₂)·3 H₂O.²²

Intramolecular Stabilization

Due to the prevalence of cluster formation when Lewis bases are not added to "Ba(tmhd)₂" formulations, and the demonstrated vapor phase lability of intermolecular addition compounds, we have explored intramolecular stabilization of these species. These investigations began with Ba(dmmd)₂ (Fig. 7).²³ Recently, this theme has been emulated for a ketoimide.²⁴ In neither example was a panacea discovered. Both compounds are substantially more volatile than previous "Ba(tmhd)₂"-based derivatives, yet neither is as volatile as Ba(hfac)₂·tetraglyme.

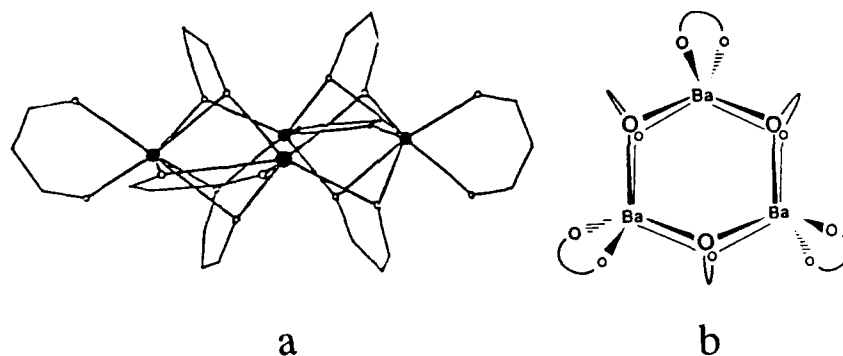


Figure 1: (a) Molecular representation of [Ba(tmhd)₂]₄. The *t*-butyl groups have been omitted for clarity (* ≡ Ba, o ≡ O, vertex ≡ C). (b) Proposed structure of [Ba(tmhd)₂]₃ (O-O ≡ tmhd).

Summary

The rather large ionic radius for barium (161 pm),²⁵ combined with its propensity to adopt coordination numbers of 8 - 12,²⁶ presents a significant challenge to the synthetic chemist. The ionic charge (+2) demands the utilization of low valent, multidentate anionic ligands (intramolecular stabilization) and/or the incorporation of additional neutral ligands (intermolecular stabilization) to inhibit cluster formation. The employment of fluorine-containing ligands reduces the presence of solid state hydrogen bonding, through the lone electron pairs on oxygen atoms of the β-diketonate ligand, yet introduces the incompatibility of primary BaF₂ deposition on the route to a ferroelectric thin film. Proper advantage of steric bulk can be important to limit the intermolecular contacts in the solid state, both by providing metal atom "coverage", and by blocking access to the above-

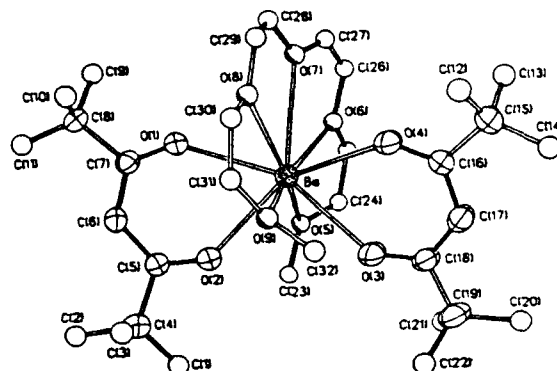


Figure 2: ORTEP plot of $\text{Ba}(\text{tmhd})_2 \cdot \text{tetraglyme}$. Hydrogen atoms have been omitted for clarity.

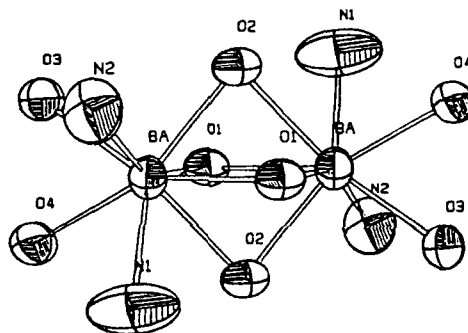


Figure 3: ORTEP plot of the core atoms of $[\text{Ba}(\text{tmhd})_2 \cdot 2 \text{NH}_3]_2$.

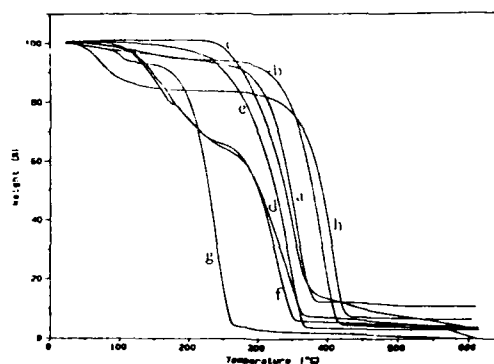


Figure 4: TGA ($10^\circ\text{C}/\text{min.}$, $\text{N}_2(\text{g})$ atm.). (a) $[\text{Ba}(\text{tmhd})_2]_{3,4}$; (b) $[\text{Ba}(\text{tmhd})_2 \cdot 2 \text{NH}_3]_2$; (c) $\text{Ba}(\text{tmhd})_2 \cdot 2 o\text{-phen}$; (d) $\text{Ba}(\text{tmhd})_2 \cdot \text{bipy}$; (e) stoichiometric mixture of (a) and $o\text{-phen}$; (f) stoichiometric mixture of (a) and bipy ; (g) $o\text{-phen}$ alone; (h) $\text{Ba}_5(\text{tmhd})_9(\text{OH}) \cdot 3 \text{H}_2\text{O}$.

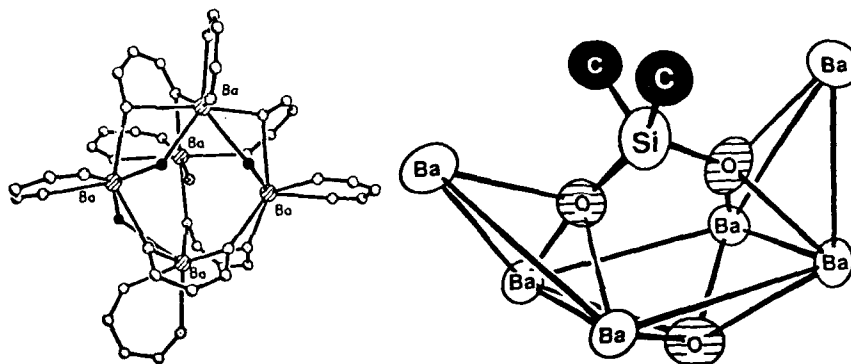


Figure 5: ORTEP plot of $\text{Ba}_5(\text{tmhd})_9(\text{OH}) \cdot 3 \text{H}_2\text{O}$. Hydrogen atoms and *t*-Bu groups have been omitted for clarity.

Figure 6: ORTEP plot of the core atoms of $\text{Ba}_6(\text{tmhd})_{10}(\text{Me}_2\text{SiO}_2) \cdot \text{H}_2\text{O}$.

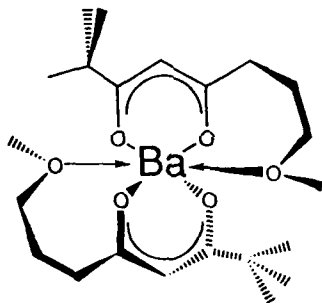


Figure 7: Proposed structure of $\text{Ba}(\text{dmmod})_2$.

mentioned lone electron pairs. The role of ligand symmetry has not yet been explored fully for these systems. In other examples, it has been a major factor in CVD precursor development.^{27, 28} Likewise, thermal decomposition by-products often lend insight into the necessary criteria for design of the next generation of CVD source compounds.^{27, 29} Such challenges also are being met in the case of the group 2 compounds, however, development is proceeding at a more modest pace, primarily due to the charge/size ratio for barium, one specific element of interest for ferroelectric thin film CVD.

Acknowledgments

We gratefully appreciate Professors Hubert-Pfalzgraf (Niece, ref. 17(b)) and Barefield (Georgia Tech, ref. 22) for willingly sharing data from unpublished experiments. The initiation of this project was under DARPA contract number MDA 972-88-J-1066. The Deutsche Forschungsgemeinschaft (W. H.) provided a postdoctoral fellowship. MARTECH permitted access to the TGA.

References

1. L.A. Wills, B.W. Wessels, D.S. Richeson, and T.J. Marks, *Appl. Phys. Lett.* **60**, 41 (1992).
2. P.C. Buskirk, R. Gardiner, and P.S. Kirlin, *J. Mater. Res.* **7**, 542 (1992).
3. G.B. Stringfellow, *Organometallic Vapor-Phase Epitaxy: Theory and Practice* (Academic, New York, 1989).
4. fod (7, 7 - dimethyl - 1, 1, 1, 2, 2, 3, 3 - heptafluorooctane - 4, 6 - dionato) = $(\text{CH}_3)_3\text{CCOCHCOCF}_2\text{CF}_2\text{CF}_3^-$.
5. (a) hfac (1, 1, 1, 5, 5, 5 - hexafluoropentane - 2, 4 - dionato) = $\text{CF}_3\text{COCHCOCF}_3^-$; (b) tetraglyme (tetraethyleneglycol dimethylether) = $\text{CH}_3(\text{OCH}_2\text{CH}_2)_4\text{OCH}_3$.
6. (a) K. Timmer, K. Spee, A. Mackor, H.A. Meinema, A.L. Spek, and P. van der Sluis, *Inorg. Chim. Acta* **190**, 190 (1991); (b) C.I.M.A. Spee, E.A. van der Zouwen-Assink, K. Timmer, A. Mackor, and H.A. Meinema, *J. Phys. IV* **1**, C2, 295 (1991); (c) G. Malandrino, D.S. Richeson, T.J. Marks, D.C. DeGroot, J.L. Schindler, and C.R. Kannewurf, *Appl. Phys. Lett.* **58**, 182 (1991); (d) J.M. Zhange, B.W. Wessels, D.S. Richeson, T.J. Marks, E.C. Degroot, and C.R. Kannewurf, *J. Appl. Phys.* **69**, 2743 (1991); (e) S.J. Duray, D.B. Buchholz, S.N. Song, D.S. Richeson, J.B. Ketterson, T.J. Marks, and R.P.H. Chang, *Appl. Phys. Lett.* **59**, 1503 (1991); (f) R. Gardiner, D.W. Brown, P.S. Kirlin, and A.L. Rheingold, *Chem. Mater.* **3**, 1503 (1991); (g) A.L. Spek, P. van der Sluis, K. Timmer, and H.A. Meinema, *Acta Cryst. C* **64**, 1741 (1990).
7. (a) W.S. Rees, Jr. and D.A. Moreno, *J. Chem. Soc., Chem. Commun.* **1991**, 1759; (b) W.S. Rees, Jr. and D.A. Moreno, in *Spectroscopy and Structure of Molecules and Nuclei*, edited by N.R. Johnson, W.N. Shelton, and M.A. El-Sayed (World Scientific, 1992) pp. 367-374.
8. (a) W.S. Rees, Jr. and K.A. Dippel, in *Proceedings of the International Conference on the Ultrastructure Processing of Ceramics, Glasses, Composites, Ordered Polymers, and Advanced Optical Materials* (Wiley, New York, 1992) pp. 327-332; (b) W.S. Rees, Jr. and K.A. Dippel, *Organic Preparations and Procedures International* **24**, 531 (1991).
9. (a) A. Gréizes, S. Sans-Lenain, and D. Médus, *C. R. Acad. Sci. Paris* **313II**, 761 (1991); (b) W.S. Rees, Jr., M.W. Carris, and W. Hesse, *Inorg. Chem.* **30**, 1164 (1991).
10. (a) W.S. Rees, Jr., Y.S. Hascicek, and L.R. Testardi, in *Better Ceramics Through Chemistry V*, edited by M.J. Hampden-Smith, W.G. Klemperer, and C.J. Brinker (Mater. Res. Soc. Proc. **271**, San Francisco, CA, 1992) pp. 925-931; (b) W.S. Rees, Jr., in *Proceedings of the Fourth Florida Microelectronics and Materials Conference*, edited by R. Rasmussen (University of South Florida Press, 1992) p. 83; (c) W.S. Rees, Jr. and A.R. Barron, *NASA Review Series*, edited by A. Hepp **1993**, in press; (d) W.S. Rees, Jr. and A.R. Barron, *Adv. Mater. Opt. and Elect.* **1993**, accepted for publication; (e) W.S. Rees, Jr., *Ceramics Ind. Intl.* **1993**, April, pp. 22-26; (f) K. Watanabe, H. Yamane, N. Kobayashi, T. Hirai, and Y. Muto, in *Studies of High Temperature Superconductors: Advances in Research and Applications*, Vol. 8, edited by A. Narlikar (Nova Science Publishers, New York, 1992) pp. 107-144; (g) L.M. Tonge, D.S. Richeson, T.J. Marks, J. Zhao, J. Zhang, B.W. Wessels, H.O. Marcy, and C.R. Kannewurf, in *Electron Transfer in Biology and the Solid State: Inorganic Compounds with Unusual Properties, Part III*, edited by R.M. Johnson, R.B. King, D.M. Kurtz, Jr., C. Kutal, M.L. Norton, and R.A. Scott (Amer. Chem. Soc. Adv. Chem. Series **226**, Washington, D. C., 1990) pp. 351-368.
11. (a) tmhd (2, 2, 6, 6 - tetramethylheptane - 3, 5 - dionato) = $(\text{CH}_3)_3\text{CCOCHCOC}(\text{CH}_3)_3^-$; (b) P.H. Dickinson, T.H. Geballe, A. Sanjurjo, D. Hildenbrand, G. Craig, M. Zisk, J. Collman, S.A. Banning, and R.E. Sievers, *J. Appl. Phys.* **66**, 444 (1989).
12. S. Matsuno, F. Uchikawa, and K. Yoshizaki, *Jpn. J. Appl. Phys.* **29L**, 947 (1990).
13. (a) J. Zhao, K.-H. Dahman, H.O. Marcy, L.M. Tonge, T.J. Marks, B.W. Wessels, and C.R. Kannewurf, *Appl. Phys. Lett.* **53**, 1750 (1988); (b) J. Zhao, H.O. Marcy, L.M. Tonge, T.J. Marks, B.W. Wessels, and C.R. Kannewurf, *Physica C* **159**, 710 (1989).
14. A.R. Barron, J.M. Buriak, L. Chetham, and R. Gordon, *Abstract 343 HTS, 177th Meeting of the Electrochemical Society*, Montreal, Canada, 1990.

15. A. Gléizes, S. Sans-Lenain, D. Médus, and R. Morancho, *C. R. Acad. Sci. Paris* **312II**, 983 (1991).
16. P. Zanella, G. Rossetto, A. Polo, F. Benetollo, and M. Porchia, *Polyhedron* **11**, 979 (1992).
17. (a) tmeda (N, N, N', N' - tetramethylethylenediamine) = $(\text{CH}_3)_2\text{NCH}_2\text{CH}_2\text{N}(\text{CH}_3)_2$; (b) L.G. Hubert-Pfalzgraf (personal communication).
18. (a) o-phen = 1, 10-phenanthroline; (b) H. Zama, K. Sakai, and S. Oda, *Jpn. J. Appl. Phys.* **31L**, 1243 (1992).
19. (a) L = o-phen, bipy; (b) bipy = 2, 2'-bipyridine
20. S.B. Tumipseed, R.M. Barkley, and R.E. Sievers, *Inorg. Chem.* **30**, 1164 (1991).
21. A.W. Apblett and A.R. Barron, *Organomet.* **9**, 2137 (1990).
22. E.K. Barefield (personal communication).
23. (a) dmmod (2, 2 - dimethyl - 8 - methoxyoctane - 3, 5 - dionato) = $(\text{CH}_3)_3\text{CCOCHCOCH}_2\text{CH}_2\text{CH}_2\text{OCH}_3^-$; (b) W.S. Rees, Jr., C.R. Caballero, and W. Hesse, *Angew. Chem., Int. Ed. Engl.* **31**, 735 (1992).
24. D.L. Schulz, B.J. Hinds, C.L. Stern, and T.J. Marks, *Inorg. Chem.* **32**, 249 (1993).
25. R.D. Shannon, *Acta Cryst.* **A32**, 751 (1976).
26. W.S. Rees, Jr., *Encyclo. Inorg. Chem.*, Vol. 2, section editor R.L. Wells, editor R.B. King (Wiley, New York, 1993) accepted for publication.
27. W.S. Rees, Jr., H.A. Luten, M.W. Carris, E.J. Doskocil, and V.L. Goedken, in *Better Ceramics Through Chemistry V*, edited by M.J. Hampden-Smith, W.G. Klemperer, and C.J. Brinker (Mater. Res. Soc. Proc. **271**, San Francisco, CA, 1992) pp. 141-147.
28. (a) W.S. Rees, Jr., D.M. Green, and W. Hesse, *Polyhedron* **11**, 1667 (1992); (b) W.S. Rees, Jr., D.M. Green, T.J. Anderson, E. Bretschneider, B. Pathangey, and J. Kim, *J. Electronic Mater.* **21**, 361 (1992); (c) W.S. Rees, Jr., T.J. Anderson, D.M. Green, and E. Bretschneider, in *Wide Band-Gap Semiconductors*, edited by J.I. Pankove and Y. Hamakawa (Mater. Res. Soc. Proc. **242**, Pittsburgh, PA, 1992) pp. 281-286; (d) W.S. Rees, Jr., D.M. Green, T.J. Anderson, and B. Pathangey, in *Chem. Persp. of Microelectr. Mater. III*, edited by C.R. Abernathy, C.W. Bates, Jr., D.A. Bohling, and W.S. Hobson (Mater. Res. Soc. Proc. **282**, Pittsburgh, PA, 1993) pp. 63-67.
29. (a) W.S. Rees, Jr. and C.R. Caballero, in *Chemical Vapor Deposition of Refractory Metals and Ceramics*, edited by T.M. Besmann, B.M. Gallois, and J. Warren (Mater. Res. Soc. Proc. **250**, Pittsburgh, PA, 1992) pp. 297-301; (b) W.S. Rees, Jr. and C.R. Caballero, *Adv. Mater. for Optics and Electron.* **1**, 59 (1992).

PART XI

Characterization

EXAMINATION OF TITANIUM OXIDES, LEAD OXIDES AND LEAD TITANATES USING X-RAY DIFFRACTION AND RAMAN SPECTROSCOPY

LYNNETTE D. MADSEN and LOUISE WEAVER*

McMaster University, Hamilton, Ontario L8S 4L7 and *Northern Telecom Electronics Limited (NTEL), P.O. Box 3511, Station C, Ottawa, Ontario, Canada K1Y 4H7.

ABSTRACT

Single oxides (with titanium or lead) deposited as thin films by low pressure metalorganic chemical vapour deposition were investigated by x-ray diffraction and Raman spectroscopy. Examination of mixed oxides (titanates) and silicates were also carried out using these techniques. The crystallographic nature of these thin films were examined and comparisons made to their bulk counterparts. The deposition and anneal conditions for producing cubic PbTiO_3 films are discussed briefly.

INTRODUCTION

The motivation for this work comes from the current interest in $\text{Pb}(\text{Zr},\text{Ti})\text{O}_3$ (or PZT) thin films for application in dynamic or non-volatile random access memory cells [1-2]. Understanding of these less complex oxides may prove to be important in understanding degradation effects (fatigue) apparent with device operation. There has also been some indication of enhancement in growth characteristics of PZT through the use of seed layers of PbTiO_3 [3].

The structural characterization of the less complex oxides, namely, lead and titanium oxides and lead titanate (PbTiO_3) are examined using Raman spectroscopy and glancing angle (GA) x-ray diffraction (XRD). Additional characterization of these films was carried out using scanning and transmission electron microscopy (SEM and TEM).

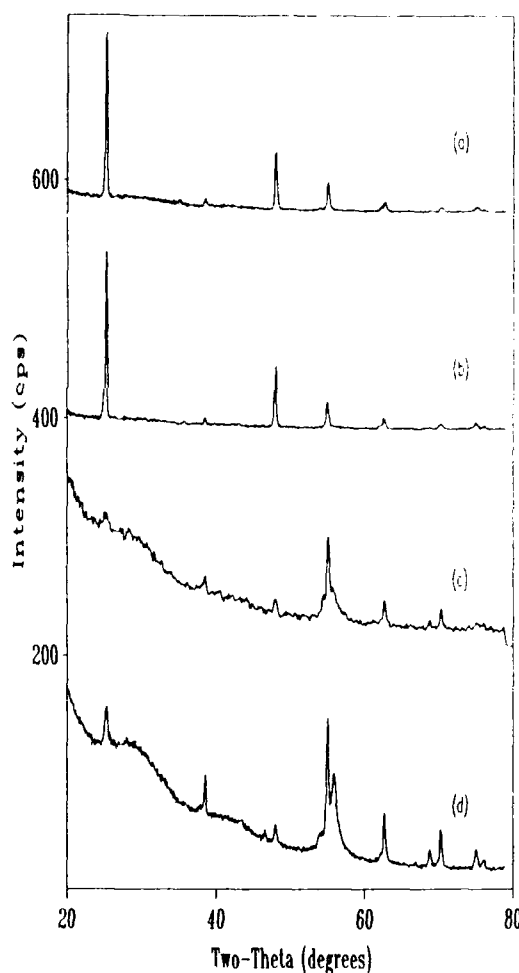


Figure 1: XRD spectra obtained from (a) low temperature TiO_2 deposition and (b) after annealing, (c) high temperature TiO_2 deposition and (d) after annealing

EXPERIMENTAL

Films of binary or tertiary oxides were deposited at temperatures ranging from 400 to 515°C using metal organic chemical vapour deposition (MOCVD) with standard Ti and Pb precursors and O₂ gas. Nitrogen was used as a balance and purge gas. The deposition temperature refers to the wafer chuck temperature and not the actual wafer temperature which was correspondingly lower by some 20 to 30°C. Pressure in the deposition chamber was monitored using a baratron gauge and was throttle-valve controlled to values ranging from 0.6 to 3 Torr in accordance with the selected deposition parameters. Film thicknesses varied from 200 nm to 6 µm (as measured using SEM and/or TEM cross-sections) for deposition durations of 20 to 240 min. 100 mm substrates of Si <100> or same coated with 100 nm of SiO₂ were used. Interactions between the films and underlying layers appeared independent of the presence or absence of an oxide coating. Analysis of the films was carried out on the films as-deposited and after a rapid thermal anneal (RTA) of 615°C for 40s.

Powder samples were obtained from Johnson Matthey [4]: PbO (litharge and massicot samples), PbO₂, Pb₃O₄, PbSiO₃, and PbTiO₃. Powders of bulk materials served as standards for Raman spectroscopy where references did not otherwise exist. Raman spectra were collected using an ISA MOLE S3000 Raman microprobe system. The Raman spectra were excited with the 457.9 nm line from a 5 kW Ar⁺ laser. Powder samples were put into precision optical cells to avoid possible vapourization of the lead powder by the laser. The power at the sample was attenuated to ~200 mW and an acquisition scanning time of 50 s covering the wavenumber range from 105 to 2758 cm⁻¹ was used.

X-ray diffraction data was collected on a Siemens D500 (Cu Kα source) diffractometer in the θ -2 θ and grazing incidence configuration. The θ -2 θ mode was used for the powder samples described above, while the thin films were examined in GA mode. The grazing incidence attachment was equipped with 0.1° divergence soller slits and a LiF (100) monochromator crystal and was used in parallel mode configuration. Operating parameters of 45 kV and 40 mA were used and acquisitions were carried out using a 1 to 4s dwell time and a step size of 0.05°. A fixed GA of 2° was used except where other GA's are specified. The samples analyzed were approximately 15 by 51 mm in size and were mounted in a customized jig for holding silicon samples from 100 mm diameter wafers. Phase identification was aided through the use of the Siemens system and μ PDSM software packages in conjunction with ICDD's Joint Committee

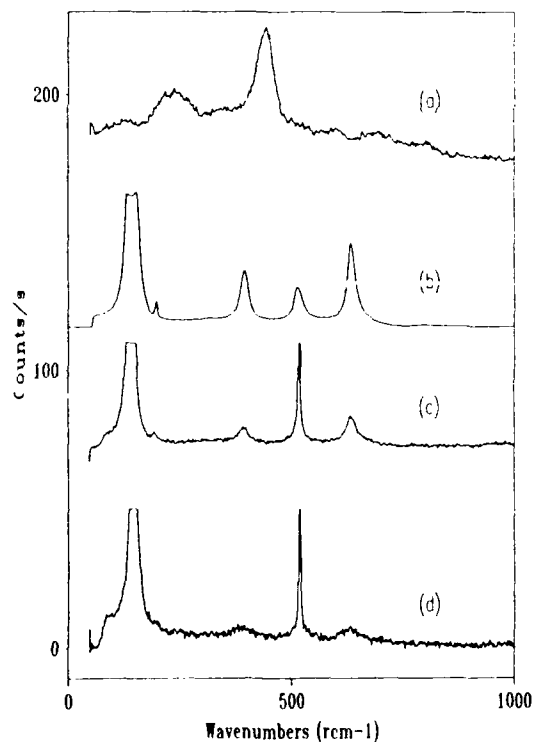


Figure 2: Raman Spectra of TiO₂ standard for rutile (a), anatase (b), and low temperature (c) and high temperature (d) TiO₂ thin films.

Table I. Crystallographic variation through a litharge and PbO_2 film.

Glancing Angle		2° (2θ values)	5° (2θ values)	10° (2θ values)
Overlapping Reflections		28.7	28.7 , 59.3	28.7 , 75.6
Defining Reflections	PbO (litharge)	31.8 , 45.7, 48.6 , 54.8 , 78.1	31.8 , 45.7, 54.8, 77.9	17.8, 31.9 , 45.8, 54.9
	PbO_2	34.2	34.3	32.4 , 34.2

Major reflections ($>20\%$ maximum intensity for standards) are indicated with **bold type**

Powder Diffraction Standards (JCPDS).

Electron microprobe analysis (EMPA) was carried out with an accelerating voltage of 15kV using a large spot size. Data was averaged over ten locations and corrected using $\phi\rho Z$.

RESULTS AND DISCUSSION

All the titanium oxide films deposited gave the expected TiO_2 low temperature phase anatase. As anticipated, the anneals were insufficient to cause the phase transformation to rutile. A wide variation in deposition rates and film texture was observed.

Samples deposited at 400°C had a low deposition rate of 280 nm/min and no obvious preferred orientation (fig. 1) when compared to the JCPDS anatase standard (21-1272), while the high temperature deposition at 515°C resulted in almost twice the deposition rate, 520 nm/min, and films with a strong 211 reflection indicating a preferred orientation (fig. 1). Raman spectra were similar for both cases and were indicative of anatase phase (fig. 2).

Primarily four types of lead oxide were deposited either singly or in combination with each other [5]. Litharge, the low temperature, tetragonal form which is red in appearance exists in equilibrium at $491 \pm 3^\circ\text{C}$ [6] with massicot, the high temperature, yellow, orthorhombic form. An early study [7] showed a complex phase relationship between massicot and litharge in terms of pressure, temperature and stability, however researchers have shown massicot can be

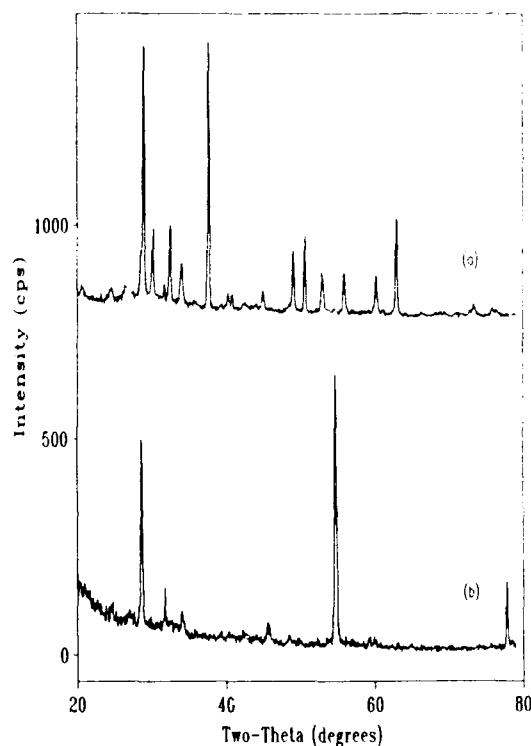


Figure 3: XRD spectra of one sample of litharge- PbO_2 (a) and a sample of massicot- PbO_2 (b) acquired using 2° GA.

Table II: Types of lead titanate compounds in the JCPDS database

Compound	Crystal System	JCPDS reference number	Common Name
PbTiO_3	cubic	40-99	
PbTiO_3	tetragonal	6-452	macedonite
PbTiO_3	tetragonal	42-4	
$\text{Pb}_2\text{Ti}_2\text{O}_6$	cubic	26-142	pyrochlore (structure type)
PbTi_2O_7	cubic	20-601	
PbTi_3O_7	monoclinic	21-949	

stable at ambient temperatures [6]. The deposition parameters used in this work bridged the pressure-temperature region where either form could be produced. As well, the composition where oxygen is greater than lead resulted in the presence of PbO_2 (scrutinyite) with litharge or massicot (fig. 3). One sample examined by XRD was identified as $\alpha\text{-PbO}$ rather than PbO litharge (as the former matched with the standard for 33 reflections and the latter only matched on 14).

Depth profiling from 0.5 to 10^3 GA was undertaken for one litharge/ PbO_2 sample producing a very complex array of reflections (Fig. 4). Due to overlapping peaks at one or more 2θ values (Table I) and strong preferred orientation, it is difficult to identify the phase changes throughout the film. However, conventional θ - 2θ XRD indicates a predominance of litharge and calculations from EMPA results suggest less than 15% PbO_2 .

XRD analyses showed some powder samples, such as litharge to contain massicot impurities, however it was still possible to obtain defining Raman signatures for comparison purposes. Other researchers have reported difficulties securing pure samples and have used specially grown crystals instead [6]. However the differences in the spectral region of 289cm^{-1} between the massicot and litharge is sufficient to make a positive

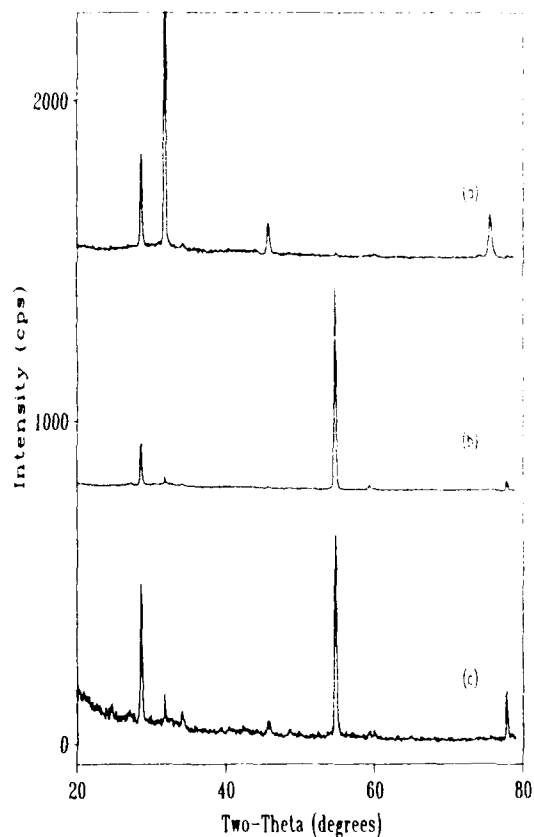


Figure 4: XRD spectra for GA of 2° (a), 5° (b) and 10° (c) GA in all cases indicating a mixture of litharge and PbO_2 .

Table III: Comparison of residual d-spacing values (nm) of lead titanate films to standard patterns.

Thin Films	Standard for Massicot	Standard for $\text{Pb}_2\text{Ti}_2\text{O}_6$
.29758, .29749	.29459	.302
.3078, .3079	.3068	.315

identification. The differences in excitation in this region was used to confirm the XRD thin film results with Raman spectroscopy.

In the creation of PbTiO_3 films it is necessary to balance the Pb and Ti deposition. The composition of the films was easily manipulated through changes in deposition temperature and pressure and source flow rates and temperatures. At low deposition temperatures (400°C), the Pb deposition rate was reduced such that a pure anatase film was created. The otherwise identical conditions for a 515°C PbTiO_3 were used with N_2 substituted for the Ti source. In the absence of the Ti precursor, just Pb, in its pure non-oxidized form was deposited.

At least six types of Pb-Ti-O compounds are known to exist (Table II) and two PbTiO_3 forms were positively identified in terms of the thin films examined here. As deposited the films were macedonite as the transition temperature for the phase change is 490°C [8]. Due to the interaction with the underlying layers, silicates were formed at the oxide or Si interface during the deposition process (fig.5). Commonly a pyrochlore phase is observed with PbTiO_3 or PZT-type compounds [9], but it is not clear from the XRD analyses that this compound is present (Table III). Massicot seems more likely as a secondary phase than pyrochlore as calculations from EMPA results indicate excess Pb is present.

Upon annealing films close to a 1:1 Pb:Ti ratio transformed to the high temperature PbTiO_3 phase (40-99) (fig.6), while those films off stoichiometry by too great a factor remained as macedonite.

CONCLUSIONS

MOCVD films of anatase TiO_2 were deposited regardless of the deposition and anneal temperatures used within the limits of this study. Lead oxide depositions produced various compounds: litharge, massicot, $\alpha\text{-PbO}$, scrutinyite, and pure lead. PbTiO_3 thin films must be close to stoichiometry or excessive amounts of lead oxide will prevent the tetragonal to cubic conversion with high temperature anneals of 615°C .

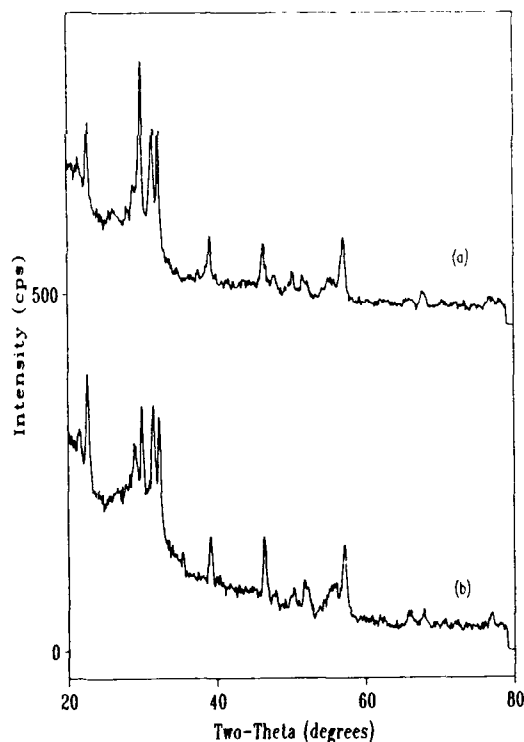


Figure 5: XRD spectra of two macedonite samples with impurities as indicated.

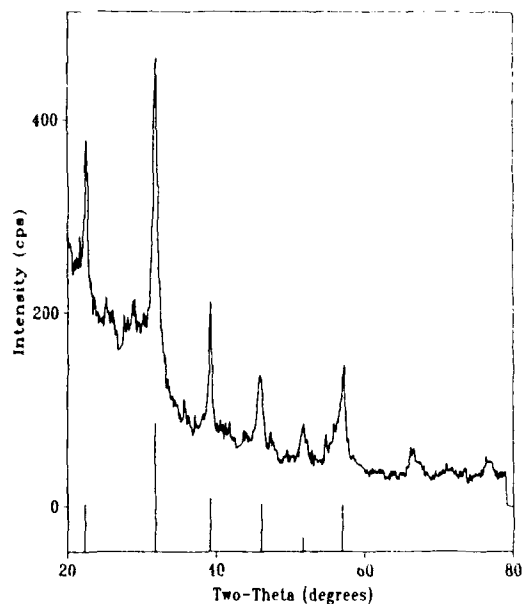


Figure 6: XRD spectra of annealed film showing match to cubic PbTiO_3 , 40-99 standard (vertical lines).

ACKNOWLEDGEMENTS

This project has been funded by NTEL, the Ontario Centre for Materials Research (OCMR) and the Natural Science and Engineering Research Council of Canada (NSERC). Additionally, support of L. Madsen's supervisors: Drs. G. Weatherly of McMaster University and I. Emesh at NTEL is acknowledged. Thanks are extended to J.P. Charland for useful discussions on XRD, and to Energy, Mines and Resources Canada (CANMET) for use of their diffractometer. D. Mayer assisted with the TEM sample preparation. Dr. M. Simard-Normandin and her students were responsible for the Raman spectroscopy acquisitions. EMPA was provided by the Surface Science Laboratory at the University of Western Ontario.

REFERENCES

1. L.H. Parker and A.F. Tasch, *IEEE Cts. and Dev. Mag.*, 17-26 (Jan. 1990).
2. D. Bondurant and F. Gnadinger, *IEEE Spectrum*, 30-33 (July 1989).
3. M. Shimizu, M. Fujimoto, T. Katayama, T. Shiosaki, K. Nakaya, and M. Fukagawa, presentation at Spr. Mater. Res. Soc. Mtg. (1993).
4. Johnson Matthey Alfa Products, P.O. Box 8247, Ward Hill, MA, USA 01835-0747
5. M.F. Abadir, A.M. Gadalla and Y.M. El-Agamawi, *Trans. & J. Brit. Cer. Soc.* **75**, 68 (1976).
6. D.M. Adams and D.C. Stevens, *J. Chem. Soc.*, 1096 (1977).
7. W.B. White, F. Dachille and R. Roy, *J. Am. Cer. Soc.* **44**(4), 170 (1961).
8. B. Jaffe, W.R. Cook and H. Jaffe, *Piezoelectric Ceramics*, Academic, New York (1971).
9. W. Wong-Ng, T.C. Huang, L.P. Cook, P.K. Schenck, M.D. Vaudin, C.K. Chiang and P.S. Brody, *Mater. Res. Soc. Proc.* **243**, 423 (1992).

OPTICALLY INDUCED PARAMAGNETIC DEFECTS IN PbTiO_3 SINGLE CRYSTALS

W.L. WARREN*, B.A. TUTTLE*, B.N. SUN**, Y. HUANG**, AND D.A. PAYNE**

*Glass and Electronic Ceramics Department, Sandia National Laboratories
Albuquerque, NM 87185

**Department of Materials Science and Engineering, Materials Research Laboratory, and
Beckman Institute, University of Illinois at Urbana-Champaign, Urbana, IL 61801

ABSTRACT

Optical excitations for trivalent platinum ($5d^7, t_{6e}$) and trivalent Pb ($6s^1$) ions in lead titanate single crystals have been observed for the first time by electron paramagnetic resonance (EPR). The g and hyperfine coupling, A , tensors of Pt^{+3} defects were found to be axial: $g_{\parallel} = 1.938$, $g_{\perp} = 2.478$, $A_{\parallel} = 0.0164 \text{ cm}^{-1}$, and $A_{\perp} = 0.0324 \text{ cm}^{-1}$. Analysis of the EPR spectra by crystal field theory indicates that the Pt^{+3} ions are in tetragonally distorted (elongated) octahedral sites, strongly suggesting that they substitute for the central Ti^{+4} ions in the perovskite lattice. Axially symmetric Fe^{+3} impurities were also observed in the crystals, and they also appear to substitute for the Ti^{+4} cation. Identification of Pb^{+3} in these single crystals further shows that holes trapped at Pb^{+2} ions are an inherent feature of Pb-based perovskite ferroelectrics.

INTRODUCTION

Transition metal ions in type ABO_3 perovskite compounds have been widely studied by electron paramagnetic resonance (EPR) and optical spectroscopy methods [1-4]. In most cases it is believed that they behave as deep centers and significantly affect the electronic and optical properties of the ceramic involved. In recent years, PbTiO_3 , and lead zirconate titanate (PZT), ceramics have attracted much attention for use in non-volatile semiconductor and optical memories. However, unlike BaTiO_3 , and SrTiO_3 , very little is known about the nature or identity of paramagnetic centers in PbTiO_3 [5,6]. In this study, we have used EPR to obtain such information for PbTiO_3 crystals; we find for the first time that optical illumination activates Pt^{+3} and Pb^{+3} ions in these crystals. Fe^{+3} ions were also observed in the as-received crystals. The observation of Pt in the PbTiO_3 crystals may be of considerable interest since it is widely used as the interface electrode in semiconductor ferroelectric memories. The observation of Pb^{+3} centers in these crystals, coupled with our earlier observations of Pb^{+3} in polycrystalline PZT ceramics [7], shows that these centers are not located at grain boundaries, and are thus, germane to Pb-based perovskite ferroelectrics.

EXPERIMENTAL DETAILS

The PbTiO_3 crystals were grown by a self-flux method. The starting material was comprised of 78-82 mol% PbO (>99.9%) and 18-22 mol% TiO_2 (>99.9%). The mixture was placed in a pure platinum crucible (most likely the source of Pt observed in this work) of 50 ml capacity and heated to 1100°C for over 15 hrs, slowly cooled to 930°C at a constant rate of approximately $0.3\text{--}1.5^\circ\text{C/hr}$, and then cooled to room temperature in approximately 72 hrs. Greater experimental details are provided in Ref. 8. Two crystals types were investigated: black and yellow. The original purpose of this study was to determine if EPR could aid in

understanding the difference. It was found that the black crystal had significantly more Fe and Pt transition metal impurities than the yellow crystal.

The EPR measurements were made at 77K using an X-band Bruker ESP-300E spectrometer. An optical access EPR cavity was used to UV-illuminate the sample *in situ* with 2.8 eV monochromatic light. An Oriel 100 W Hg arc lamp in conjunction with a 2.8 eV narrow-band interference filter was used as the monochromatic light source. The light power density was 1 mW/cm².

RESULTS AND DISCUSSION

A. Fe³⁺

The black as-received PbTiO₃ crystal exhibited a fairly large axially symmetric Fe³⁺ EPR signal. Figure 1 shows the angular dependence of the three resonance lines of Fe³⁺ by rotating the magnetic field around one of the symmetry axes. The resonance could be fit by the following spin Hamiltonian for an S = 1/2 system,

$$H_S = g_{\parallel} \beta H_z S_z + g_{\perp} \beta (H_x S_x + H_y S_y) \quad (1)$$

where β is the Bohr magneton, H is the magnetic field and g_{\parallel} (g_{\perp}) is the g -value parallel (perpendicular) to the symmetry axis ($g_{\parallel} = 2.071$ and $g_{\perp} = 5.927$). It was determined that Fe³⁺ was the source of the paramagnetism since its spin Hamiltonian parameters are very close to that observed earlier in PbTiO₃ [2], BaTiO₃ [1], and SrTiO₃ [4]. The solid lines are fit by solving the spin Hamiltonian in eqn. (1). The zero field crystal splitting for this ion is very large ($D > hv$), which is attributed to a large tetragonal field. It has been suggested that an adjacent oxygen vacancy is the origin of the large tetragonal field; hence, this defect is sometimes denoted as an Fe³⁺-oxygen vacancy center [1,4]. The identification of g_{\perp} was determined by the rotation of the magnetic field around one of the crystal axes, i. e., rotation within the (100) plane yielded an orientation independent resonance line (Fig. 1) which results from paramagnets whose z axes always remain perpendicular to the external magnetic field. Since the g -tensors exhibit axial symmetry, and it is well known that PbTiO₃ has a tetragonal crystal structure, we expect that Fe³⁺ has substituted for Ti⁴⁺ as was also found by other investigators [1,2,4].

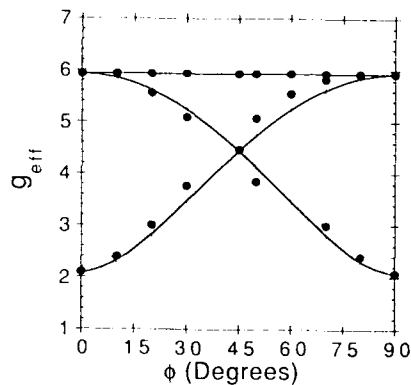
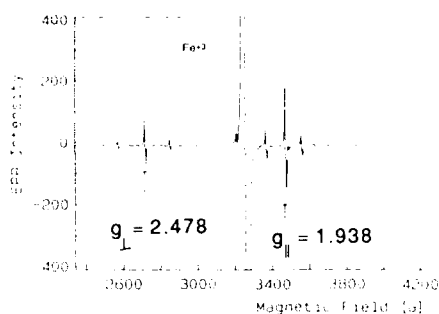


Fig. 1. Angular variation of the effective g -value of the Fe³⁺ resonance. There are three lines associated with Fe³⁺. ϕ is the angle in degrees from the [001] direction in the (100) plane.

B. Pt^{+3}

Following 2.8 eV illumination at 77 K, a new EPR signal was activated in the PbTiO_3 crystals, with clearly resolved hyperfine structure, as illustrated in Fig. 2. (This activated resonance was generated to a much larger degree in the black crystal.) In EPR, the chemical signature of the paramagnetic defect is uniquely characterized by its hyperfine structure, where the number of spectral lines is given by $2I + 1$, where I is the nuclear spin. For an element with several isotopes having different nuclear moments and spin, the EPR spectrum will be a superposition of the electronic Zeeman and nuclear hyperfine spectrum of each isotope weighted by its natural abundance.

Fig. 2 EPR spectrum showing the Pt^{+3} resonance following 2.8 eV illumination at 77K. H is parallel to the $[001]$ direction.



We attribute the observed spectra in Fig. 2 to an impurity with several possible isotopes having $I = 0$ or $I = 1/2$. The central lines (marked by the arrows) are due to the $I = 0$ isotopes whereas the two satellite lines about each central line are due to the $I = 1/2$ isotopes. We find that the experimental ratio of the doubly integrated intensity of the central line to the satellite lines is 1.96, in excellent agreement with that expected value for platinum ions (1.9586). Platinum has four stable isotopes of which ^{194}Pt , ^{196}Pt , and ^{198}Pt are 66.2 % abundant and have $I = 0$, while ^{195}Pt is 33.8 % abundant and has $I = 1/2$. Platinum is the only element in the periodic table that can explain the EPR spectrum of Fig. 2.

Having determined that the EPR signal is due to a Pt impurity, we rotated the PbTiO_3 crystal within the (100) plane to determine the magnetic anisotropy. The observed anisotropy of the effective g -value is illustrated in Fig. 3. The observed $S = 1/2$, $I = 1/2$ spectra can be fit by the following Spin Hamiltonian,

$$H_S = g_{\parallel}\beta H_z S_z + g_{\perp}\beta(H_x S_x + H_y S_y) + A_{\parallel}S_z I_z + A_{\perp}(S_x I_x + S_y I_y) \quad (2)$$

where A_{\parallel} (A_{\perp}) is the nuclear hyperfine coupling constant parallel (perpendicular) to the symmetry axis, S (I) is the electron (nuclear) spin, and the other terms are the same as in eqn. (1). The fit is illustrated by the bold lines in Fig. 3. The axial spin Hamiltonian parameters are $g_{\parallel} = 1.938 \pm 0.001$, $g_{\perp} = 2.478 \pm 0.001$, $A_{\parallel} = 0.0164 \pm 0.0002 \text{ cm}^{-1}$, and $A_{\perp} = 0.0324 \pm 0.0002 \text{ cm}^{-1}$. Again, as discussed earlier, g_{\perp} was determined by the orientation independent resonance line. It is reasonable to assume that the Pt substitutes for the Ti^{+4} since (1) it exhibits axial symmetry and (2) the ionic radii of the Pt^{+4} (0.77 Å) and Ti^{+4} (0.75 Å) ions are similar [9].

From crystal field theory it is possible to determine the structure, and oxidation state, of the optically generated Pt ion in the perovskite lattice. Since the ground state of the Pt resonance can be fit using an $S = 1/2$, $L = 1/2$ system, two oxidation states are possible for the Pt ion, Pt^{+3} (d^7) and Pt^{+4} (d^6) as long as the Pt ion is in a tetragonally distorted, strong octahedral field as schematically illustrated in Fig. 4 [10]. Under the strong field limit, the octahedral crystal field must be greater than the spin pairing energy; 5d ions are almost always under the strong field approximation [11,12]. Since the Pt substitutes for the Ti^{+4} ion in the lattice, it is more reasonable from charge considerations to assume that the oxidation state of the Pt is +3 rather than +1, as was assumed for $BaTiO_3$ crystals doped with Pt [13].

Fig. 3. Angular dependence of the Pt^{+3} g-tensor. The defect exhibits axial symmetry. There are three resonance lines associated with Pt^{+3} . ϕ has the same meaning as in Fig. 1.

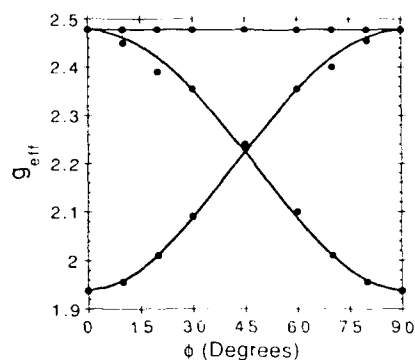
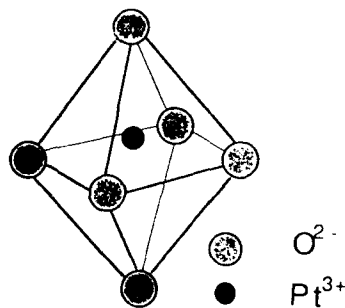


Fig. 4. Schematic illustration of the environment around the Pt^{+3} ion in $PbTiO_3$.



For d^7 (t^6e) ions, i.e., Pt^{+3} , in tetragonally elongated, strong octahedral fields, the g-tensors are predicted to be [14]

$$g_{\parallel} = g_e - 3\lambda^2/\Delta^2 \quad (3)$$

$$g_{\perp} = g_e(1 - 3\lambda/\Delta) - 6\lambda^2/\Delta^2 \quad (4)$$

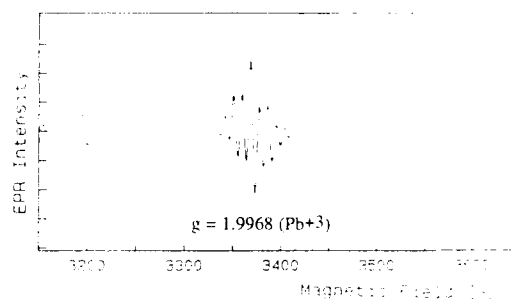
where λ is the spin-orbit coupling constant ($\lambda < 0$), and Δ is the crystal field splitting. From eqns. (3) and (4) it is easy to see that $g_{\perp} > g_{\parallel}$, $g_{\parallel} < g_e$, and $g_{\perp} > g_e$, which are all experimentally observed, and consistent with our assignment of Pt^{+3} [14].

At this juncture, it should be mentioned that these results also indicate that the oxidation state of the *diamagnetic* Pt ions in the virgin, unilluminated, PbTiO_3 crystals is +4. Since the greatest density of optically generated Pt^{+3} ions was observed with photon energies around 2.8 eV (a photon energy of 2.8 eV roughly corresponds to the optical band-gap of these crystals), it is reasonable to assume that it is the capture of the photo-generated electrons at diamagnetic Pt^{+4} ions that makes them paramagnetic.

C. Pb^{+3}

Figure 5 shows that optical illumination of the yellow crystal leads to the generation of another EPR-active center centered at $g = 1.9968$. This center was not observed in any appreciable concentration in the black crystal, probably since the light is only absorbed at the surface. Evidently, in the yellow crystal, a greater density of these EPR-centers is created since the 2.8 eV light can penetrate further into the sample. In a separate work on polycrystalline PZT ceramics [7], we demonstrated that the EPR-signal around $g \approx 1.995$ is due to Pb^{+3} by observing the very large nuclear hyperfine interactions of the 21.1% $I = 1/2$ ^{207}Pb nuclei. To confirm that the resonance at $g = 1.9968$ is also due to Pb^{+3} in these PbTiO_3 crystals, we have been able to observe the core ^{207}Pb hyperfine interactions located at 5522 G and 11,223 G (not shown). Analysis of this resonance by exactly diagonalizing the spin Hamiltonian indicates that the hyperfine interaction is extremely large (1.110 cm^{-1}). (Recall that the largest Pt^{+3} hyperfine interaction was only 0.0324 cm^{-1} .) These observations in part demonstrate that the paramagnetism in Fig. 5 is due to Pb^{+3} centers.

Fig. 5. EPR spectrum of Pb^{+3} following 2.8 eV illumination at 77K.



The additional features associated with the Pb^{+3} signal in Fig. 5 most likely arise from ^{207}Pb superhyperfine interactions from nearest neighbor Pb sites in the crystal. Because of space limitations, the spin resonance features associated with the Pb^{+3} center in these PbTiO_3 crystals will be discussed in greater detail elsewhere [16].

We believe that the observation of Pb^{+3} in these single crystals is of considerable importance in our understanding of this center in this class of ferroelectric materials. In another paper within these proceedings [17], it was shown that the Pb^{+3} centers could only be optically generated in the perovskite structure of polycrystalline PZT, i.e., the amorphous and pyrochlore phases did not show the optical activation of Pb^{+3} . Observation of these centers in single crystals enables us to also show that Pb^{+3} centers are not an artifact of the polycrystalline ceramics. For example, we now know that the defects are not located primarily at grain boundaries. These results, coupled with our earlier observations, provide a fundamental understanding of the Pb^{+3} center. It is simply a hole trapped at the corner Pb^{+2} site, and that these centers appear to be an intrinsic part of Pb-based perovskite ferroelectrics.

CONCLUSIONS

In conclusion, we have been able to observe the optical generation of Pr^{3+} and Pb^{3+} ions in PbTiO_3 crystals. Since the Pr^{3+} EPR spectrum is axially symmetric, and can be described by an $S = 1/2$, $I = 1/2$ system, it has been argued that the Pr^{3+} ions are in a tetragonally distorted strong octahedral field, and have substituted for the central Ti^{4+} ions in this perovskite lattice. The observation of Pb^{3+} centers in these single crystals provides additional evidence that these defects are an intimate feature of Pb-based perovskite ferroelectrics.

REFERENCES

- 1) E. Possenriede, O.F. Schirmer, H.J. Donnerberg, G. Godefroy, and A. Maillard, *Ferroelectrics*, 92, 245 (1989).
- 2) D.J. A. Gainon, *Phys. Rev.*, 134, A1300 (1964).
- 3) E. Possenriede, O.F. Schirmer, J. Albers, and G. Godefroy, *Ferroelectrics*, 107, 313 (1990).
- 4) E.S. Kirkpatrick, K.A. Muller, and R.S. Rubins, *Phys. Rev.*, 135 A86 (1964).
- 5) A. Molak, and K. Wojcik, *Ferroelectrics*, 125, 349 (1992).
- 6) D. Hennings, and H. Pomplun, *J. Am. Ceram. Soc.*, 57, 527 (1974).
- 7) W.L. Warren, B.A. Tuttle, P.J. McWhorter, F.C. Rong, and E.H. Poindexter, *Appl. Phys. Lett.*, 63 (1993).
- 8) B.N. Sun, Y. Huang, and D.A. Payne, *J. Crystal Growth*, submitted.
- 9) F.A. Cotton and G. Wilkinson, "Advanced Inorganic Chemistry," (John Wiley and Sons, NY, 1988) p. 1387.
- 10) The tetragonal distortion may arise from the Jahn-Teller effect.
- 11) A. Abragam, and B. Bleaney, *Electron Paramagnetic Resonance of Transition Ions* (Dover Publications, New York, 1970).
- 12) J.E. Wertz, and J.R. Bolton, *Electron Spin Resonance* (Chapman and Hall, New York, 1986).
- 13) Z. Sroubek, K. Zdansky, and E. Simanek, *Phys. Status Solidi*, 3, K1 (1963).
- 14) H.H. Tippins, *Phys. Rev.* 160, 343 (1967). Equations (2) and (3) ignore the effects of covalency.
- 15) These g-tensor relationships do not uniquely support the d^7 assignment; they are consistent with it.
- 16) W.L. Warren, B.A. Tuttle, B.N. Sun, Y. Huang, and D.A. Payne, to be submitted.
- 17) W.L. Warren, B.A. Tuttle, R.W. Schwartz, W.F. Hammetter, D.C. Goodnow, J.T. Evans, and J.A. Bullington, these proceedings.

DEPOSITION OF DIELECTRIC THIN FILMS BY ATOMIC LAYER EPITAXY AND THEIR APPLICATION FOR ELECTROLUMINESCENCE DISPLAYS

Dong Heon Lee, Yong Soo Cho, Jeon Kook Lee and Hyung Jin Jung
Division of Advanced Materials, Electro-optic Ceramics Lab,
Korea Institute of Science and Technology, Seoul 130-650, Korea.

ABSTRACT

Various dielectric thin films have been studied for electroluminescence display (ELD) application to improve dielectric constant and breakdown voltage. In this work, amorphous BaTiO_3 thin films were deposited on indium tin oxide (ITO) - coated glass substrates by atomic layer epitaxy (ALE) using metalorganic precursors. Influences of deposition conditions on microstructure, interface characteristics and dielectric properties are investigated. It was possible to obtain dielectric films with good dielectric properties and textured, flat surface microstructure without defects due to the improvement of qualities of the grown films. These results were examined by XRD, SEM and AES analysis.

INTRODUCTION

Various studies have been performed to choose a proper dielectric layer for use in a.c.-thin film electroluminescence (ACTFEL) displays [1-3]. Performance and reliability of the EL device depend on the quality of the dielectrics used. The dielectric thin films prevent active phosphor layer from breakdown, which is sandwiched by the dielectric layers as shown in Fig.1. Therefore, the dielectric strength must be as high as possible, and high enough dielectric constant is needed so that low driving voltage is possible. There are other requirements for good dielectrics. Because the metal electrode and conducting oxide are contacted on them, they must be chemically and mechanically resistant. Although good dielectrics are appropriately chosen, it is difficult to operate the device if defects such as pinholes and cracks, or any improper interface reactions occurring in the processing of thin film deposition. Thus, proper processing conditions are very important as well as the selection of good dielectric materials.

Perovskite BaTiO_3 thin film can be a good candidate for dielectric layers compared with other dielectric layers such as Al_2O_3 , Y_2O_3 , Ta_2O_5 , etc. [4]. High temperature processing must be avoided due to an interface reaction between the dielectrics and ITO coated substrate, for example sodium diffusion from glass substrate. Therefore, crystalline BaTiO_3 thin film with excellent dielectric properties cannot be used. However, because amorphous barium titanate (α - BaTiO_3) has relatively high dielectric constant and breakdown voltage, many works on α - BaTiO_3 as an insulating layer have been reported [5,6].

Many methods to prepare BaTiO_3 thin films, such as r.f. sputtering [7], metalorganic chemical vapor deposition (MOCVD) [8], molecular beam epitaxy (MBE) [9] and excimer laser ablation [10] were reported. The ALE is a deposition method with which obtaining abrupt interfaces with monolayer abruptness over a large area can be obtained [11,12]. The ALE system consists of alternatively exposing the substrate to the one species and the other one, with only one monolayer of each species remaining on the surface after each exposure. This allowed to control composition by monolayer binary growth. Thickness of thin film depends on the number of deposition cycles.

In this work, we report the deposition of BaTiO_3 thin film on ITO coated soda lime glass substrate by the ALE. The ALE system used for perovskite structure is introduced. Microstructure, interface reaction and dielectric properties are discussed, and the possibility of the insulating layer in ACTFEL is investigated.

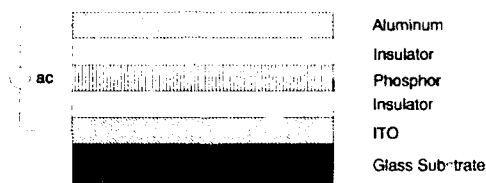


Fig. 1. Sandwiched structure of ELD.

EXPERIMENTAL

A schematic diagram of the ALE system used for this study is shown in Fig. 2. All conditions for varying the experimental parameters were controlled by a computer. Metal organic sources of β -diketonate complex ($\text{Ba}(\text{tmhd})_2$, $\text{tmhd} = 2,2,6,6$ -tetramethyl-3,5-heptanedione: $\text{Ba}(\text{C}_{11}\text{H}_{19}\text{O}_2)_2$) and titanium tetra-isopropoxide were used. N_2O gas was used as an oxygen source. N_2 gas was used as the carrier gas for the metalorganic sources. Substrate was ITO coated soda lime glass. Flow rate of carrier gas and source gas was controlled by commercial mass flow controller. Working pressure of 1 to 2 torr was maintained during film deposition. Substrate temperature was varied from 400°C to 500°C .

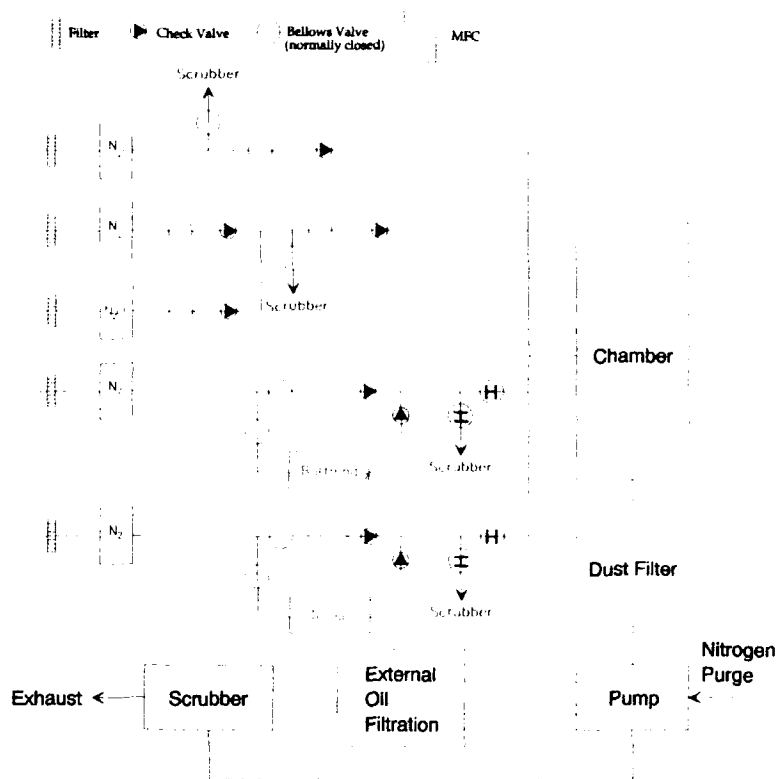


Fig. 2. Schematic diagram of the ALE system

Samples were characterized by X-ray diffraction (XRD) and scanning electron microscopy (SEM) to investigate the crystalline nature and microstructure, respectively. Auger electron spectroscopy (AES) was employed to determine the composition of the films. The dielectric properties and I-V characteristics were measured to investigate whether the requirements as an insulating layer for TFELD are satisfied.

RESULTS AND DISCUSSION

Fig.3 shows XRD patterns of $BaTiO_3$ thin films grown at a deposition temperature of 450°C . Peaks of ITO thin layer represented polycrystalline nature without any

preferred orientation. However, BaTiO_3 thin films were amorphous at 450°C . Any diffraction pattern indicating crystallinity was not observed even at 500°C .

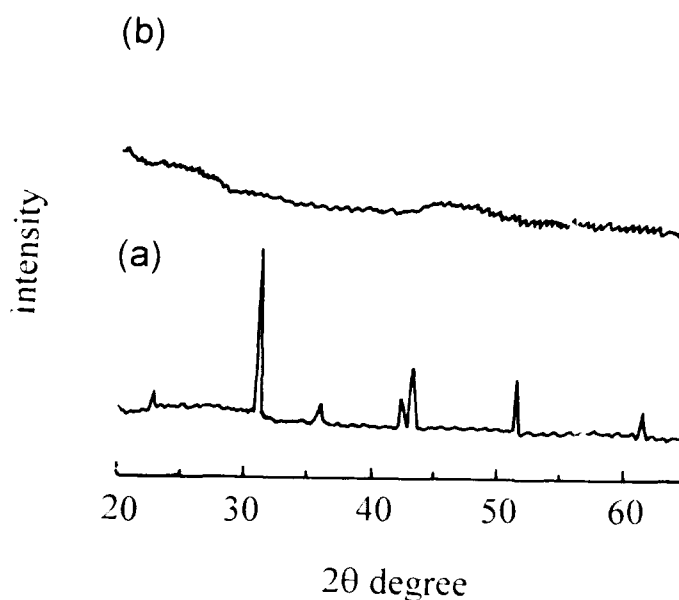


Fig. 3. XRD patterns of (a) ITO coated glass substrate and (b) BaTiO_3 thin film deposited at 450°C .

The thickness of the as-deposited film was found to be proportional to the total number of deposition cycles and independent on the working pressure and flow rate of the source vapors. Also, the variations of substrate temperature from 400°C to 500°C did not bring significant effects on the film thickness and crystalline nature. This agreed well with general results by the ALE, which has been studied in II-VI compounds such as ZnS [13]. By the ALE, in general, film thickness are independent of normal growth variables such as substrate temperature, reactant partial pressure, exposure times, etc., over some wide range of the variables.

It is important to have clean and flat surface microstructure throughout films in the EL application because a rough surface causes diffuse scattering of light and pinholes in the dielectric layer leads to breakthrough. The surface morphology of a 300 nm thick BaTiO_3 films is shown in Fig.4. The microstructure shows flat and smooth surface without any defects. Textured surface was observed in micrographs with higher magnification.

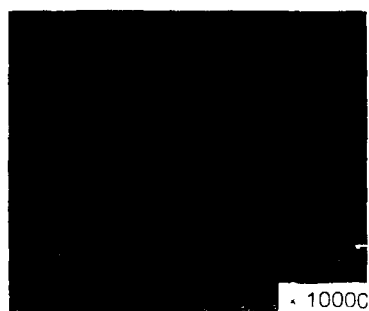


Fig. 4. SEM photograph of a BaTiO_3 thin film deposited at 450°C .

The ALE-prepared BaTiO_3 film was also investigated by AES. Fig 5 shows the spectrum taken on the surface of the film deposited on ITO coated glass substrate held at 450°C . Results of the films indicated that Ba, Ti and O were the primary elements present and any contamination such as carbon was not detectable. Also no interdiffusion between BaTiO_3 and ITO glass was observed as confirmed by depth profile analysis of AES.

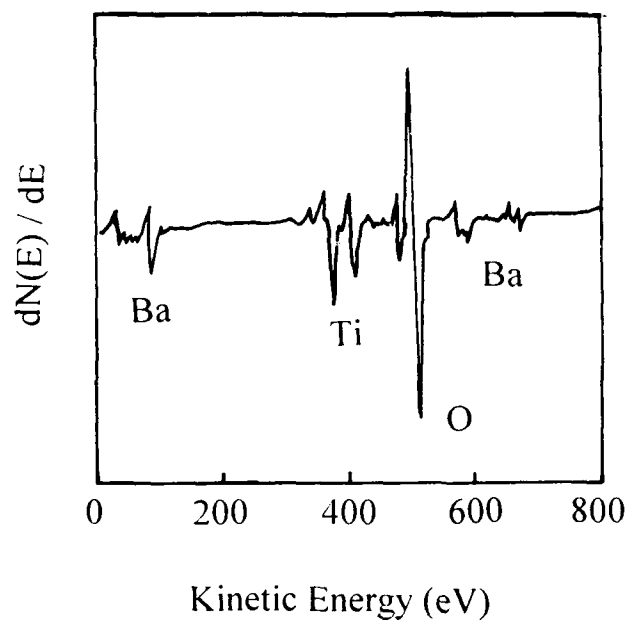


Fig. 5. Auger electron spectroscopy of BaTiO_3 film grown by ALE.

I-V characteristics for the α -BaTiO₃ thin film was examined. The dielectric constant of the films was 19 at room temperature. Films deposited at 450°C had a higher charge storage capacity ($Q_{BD} = \epsilon' V_{BD}$) equal to 4.2 $\mu\text{C}/\text{cm}^2$ than the values obtained in BaTiO₃ films grown by r.f. sputtering [5,6]. This indicates that films of high quality can be obtained by ALE technique, resulting in an increase in dielectric properties.

In summary, ALE grown α -BaTiO₃ thin films are adequate for EL application due to the excellent dielectric properties and low temperature processing.

CONCLUSION

Deposition of BaTiO₃ thin film was studied for the first time using metalorganic sources for the ALE technique. It was possible to prepare amorphous BaTiO₃ thin layer on ITO coated soda lime glass substrate at the substrate temperature of 450°C. A microstructure with flat and smooth surface without pinholes or cracks was observed. The dielectric properties meet well the requirements for a dielectric layer for TFEL applications. Further studies about self-limiting growth mechanism and interface reaction during the deposition of films with perovskite structure by the ALE technique are needed.

REFERENCES

- [1] P. M. Alt, D. B. Dove and W. E. Howard, *J. Appl. Phys.*, **53**, 5186 (1982).
- [2] W. E. Howard, *IEEE Trans. Electron Devices*, **24**, 903 (1977).
- [3] H. Kozawaguchi, B. Tsjigama and K. Murase, *Jpn. J. Appl. Phys.*, **21**, 1028 (1982).
- [4] S. K. Tiku and G. C. Smith, *IEEE Trans. Electron Devices*, **31**, 105 (1984).
- [5] K. Sreenivas, A. Mansingh and M. Sayer, *J. Appl. Phys.*, **62**, 4475 (1987).
- [6] D. J. McClure and J. R. Crowe, *J. Vac. Sci. Technol.*, **16**, 311 (1979).
- [7] V. S. Dharmadhikari and W. W. Grannemann, *J. Appl. Phys.*, **53**, 8988 (1982).
- [8] B. S. Kwak, K. Zhang, E. P. Boyd, A. Erbil and B. J. Wilkens, *J. Appl. Phys.*, **69**, 767 (1991).
- [9] R. A. McKee, F. J. Walker, J. R. Conner and E.D. Specht, *Appl. Phys. Lett.*, **59**, 782 (1991).
- [10] G. M. Davis and M. C. Gower, *Appl. Phys. Lett.*, **55**, 112 (1989).
- [11] T. Suntola, J. Antson, A. Pakkala and S. Lindfors, *SID 80 Digest*, 109 (1980).
- [12] J. Nishizawa, H. Abe and T. Kurabayashi, *J. Electrochem. Soc.*, **132**, 1197, (1985).
- [13] J. Hyvarinen, M. Sonninen and R. Tornqvist, *J. Cryst. Growth*, **86**, 695 (1988).

PRISM-FILM COUPLING IN ANISOTROPIC PLANAR WAVEGUIDES OF EPITAXIAL (101) RUTILE THIN FILMS

C. M. Foster, S.-K. Chan, H.L.M. Chang, R. P. Chiarello, and D. J. Lam
Materials Science Division, Argonne National Laboratory, 9700 S. Cass Avenue, Argonne, IL 60439

ABSTRACT

We report optical waveguiding in single-crystal, epitaxial (101) oriented rutile (TiO_2) thin films grown on (1120) sapphire ($\alpha\text{-Al}_2\text{O}_3$) substrates using the MOCVD technique. The propagation constants for asymmetric planar waveguides composed of an anisotropic dielectric media applicable to these films are derived. Modifications to the prism-film coupling theory for this anisotropic case are also discussed. By application of this model to (101) oriented rutile thin films, we directly obtain values of the ordinary and extraordinary refractive indexes, n_o and n_e , of the rutile thin films as well as film thicknesses. We obtain typical values of the refractive indexes ($n_o=2.5701\pm0.0005$; $n_e=2.934\pm0.001$) near to those for bulk rutile single crystals indicating the exceptional quality of these films.

INTRODUCTION

The tremendous benefits derived from optical communications and the great promise of high-speed optical computers has stimulated interest in the guidance of light by dielectric waveguides. Many aspects of light propagation in waveguides structures, such as optical fibers and the thin-film guides of integrated optics, have been investigated in great detail. Moreover, the fundamental propagation characteristics, such as the propagation constants and field distributions of guided modes, have been comprehensively reviewed in the literature [1].

Due to its high refractive index, rutile (TiO_2) is an ideal material for passive optical waveguides. The reduced defect size and enhanced dielectric properties of single-crystal, epitaxial thin films should significantly reduce optical loss due to grain-boundary scattering in planar waveguides as compared to structures produced from polycrystalline material. Recently, we have studied in detail the crystal structure of rutile thin films on sapphire (1120) by high resolution electron microscopy (HREM) and four-circle x-ray diffraction [2-3]. These studies have indicated that epitaxial (101) oriented rutile thin films grown on (1120) sapphire substrates by the MOCVD process possess a highly anisotropic single-crystal nature. Consequently, an understanding of the optical waveguiding in these films must necessarily take into account the anisotropy of the rutile dielectric tensor. For optical waveguide applications, the main parameters of interest which characterize thin films are the ordinary and extraordinary refractive indexes, n_o and n_e , and the film thickness. One method that has been particularly well adapted to this problem in the case of isotropic films, is the prism-coupling technique. This technique was first described by Tien, Ulrich, and Martin [4] and more recently by others [5-6]. Waveguide propagation in arbitrarily oriented, anisotropic, dielectric media has been treated to some degree of generality [7]. The electromagnetic field distributions and propagation constants have been calculated in closed form only in specific cases [9]. However, none of these treatments are directly applicable to (101) oriented rutile films. In this paper, we report optical waveguiding in single-crystal, epitaxial (101) oriented rutile thin films grown on (1120) sapphire substrates using the MOCVD technique. By application of these results, we directly obtain values of the ordinary and extraordinary refractive indexes, n_o and n_e , as well as film thickness for (101) oriented rutile thin films.

THEORY

We calculate the electromagnetic field distributions and propagation constants for a waveguide by solving Maxwell's equations subject to the appropriate boundary conditions. We endeavor to model a system which is simple enough so that the refractive indexes and film thickness of an anisotropic, (101) oriented orthorhombic thin film can easily be obtained using prism-film waveguide coupling. Therefore, we consider asymmetric planar waveguides composed

of anisotropic dielectric media, e.g. absorptionless, non-magnetic medium with a dielectric matrix \mathbf{K} [8]. For this medium, Maxwell's curl equations are

$$\bar{\nabla} \times \mathbf{E} = -\mu_0 \dot{\mathbf{H}} \text{ and } \bar{\nabla} \times \mathbf{H} = \epsilon_0 \mathbf{K} \dot{\mathbf{E}} \quad (1), (2)$$

where $\dot{\mathbf{E}}$ and $\dot{\mathbf{H}}$ are time derivatives of the fields. Combined, these equations yield

$$\nabla(\nabla \cdot \mathbf{E}) - (\nabla \cdot \nabla) \mathbf{E} = -\mu_0 \epsilon_0 \mathbf{K} \ddot{\mathbf{E}} \text{ and } \nabla \times [\mathbf{K}^{-1} \nabla \times \mathbf{H}] = -\mu_0 \epsilon_0 \ddot{\mathbf{H}} \quad (3), (4)$$

where we use the symbols ϵ_0 and μ_0 for the permittivity and the permeability of free space. Solutions of Eq. (3) or (4) yield either the electric field, \mathbf{E} , or the magnetic field, \mathbf{H} , respectively, and then either Eq. (1) or (2) can be used to obtain the other field.

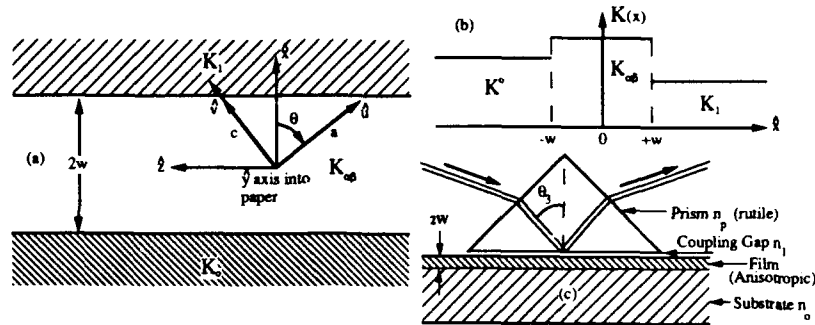


Fig. 1. (a) The coordinate system (u, y, v) in which the dielectric tensor of the rutile film is diagonal, and the coordinate system (x, y, z) , which is used to express the spatial dependence of the fields, are shown. (b) The assumed dielectric constant dependence on the coordinate x is shown for an asymmetric rutile thin film. (c) Schematic of a prism-film coupler.

We consider crystalline thin films of at least orthorhombic symmetry with a (101) growth plane. As shown in Fig. 1a, the \bar{a} crystallographic axis of the film is rotated by an angle θ about the \bar{b} -axis with respect to the vector normal to the film surface which we define as the \bar{x} -axis. This angle is determined by $\theta = \tan^{-1}(a/c)$, where a and c are the unit cell parameters of the material which we will consider to be orthorhombic. This anisotropic medium has a dielectric matrix \mathbf{K} , thickness $2w$, and is located between two semi-infinite isotropic media (i. e. air and a substrate). The \bar{x}' coordinate system (u, y, v) , in which the dielectric tensor of the rutile film is diagonal, is rotated by an angle θ with respect to the \bar{x} coordinate system (x, y, z) , which is aligned with respect to the dielectric boundaries. It is advantageous to resolve the gradient operator and field vectors along the principal (u, y, v) axes while expressing the spatial dependence of the fields in terms of (x, y, z) coordinates. We will denote components of the diagonal dielectric tensor $K_{\alpha\beta}$ in the (u, y, v) coordinate system as $K_u = n_u^2$, $K_y = n_y^2$, $K_v = n_v^2$, and assume that the substrate indexes K_0 and K_1 are isotropic.

We search for a solution of Eq. 3 or 4 of the forms $\bar{\mathbf{E}} = \bar{\mathbf{e}}(x) \exp(i(\omega t - \beta z))$ and $\bar{\mathbf{H}} = \bar{\mathbf{h}}(x) \exp(i(\omega t - \beta z))$ corresponding to waves traveling in the $+z$ direction. Here ω is the angular frequency of the light and t is the time. As shown in Fig. 1b, the dielectric tensors depend only upon the variable x ; therefore, $\bar{\mathbf{e}}$ and $\bar{\mathbf{h}}$ need only be functions of x . The lack of y dependence and the diagonal nature of the dielectric tensors in the (u, y, v) coordinate system leads to the decoupling of $\bar{e}_y(x)$ from the $\bar{e}_u(x)$ and $\bar{e}_v(x)$ components of Eq. (3). A similar decoupling occurs for the $\bar{h}_y(x)$ component of Eq. (4). Therefore, transverse electric (TE) and transverse magnetic (TM) modes exist in this case. The explicit forms for the resulting plane wave differential equations for the TE and TM cases are given in Ref. [10]. These differential equations have constant coefficients in the different regions of the waveguide as shown in Fig. 1a and can be readily solved. For the following analysis, it is convenient to define the following

$$K'_x = K_u K_v / K_y, \quad (10)$$

$$K_x = \{K_v \sin^2 \theta + K_u \cos^2 \theta\}; K_z = \{K_u \sin^2 \theta + K_v \cos^2 \theta\}, \quad (11); (12)$$

and

$$K_{xz} = \{K_v - K_u\} \sin \theta \cos \theta, \quad (13)$$

where $\kappa_0^2 = \epsilon_0 \mu_0 \omega^2$. By application of the usual continuity condition on the electric and magnetic fields at the boundaries, the spatial dependence of the fields can be obtained and are shown in Ref. [10]. For TE modes, the fields depend on the real parameters, δ , γ , β , and b , which are determined by the following four eigenvalue equations

$$\beta^2 = \kappa_0^2 K_0 + \delta^2; \beta^2 = \kappa_0^2 K_1 + \gamma^2; \beta^2 = \kappa_0^2 K_y - b^2 \quad (14); (15); (16)$$

$$\tan(2bw) = \frac{(\gamma/b) + (\delta/b)}{1 - (\gamma\delta/b^2)}. \quad (17)$$

Explicit forms for $e(x)$ and $h(x)$ for the TE modes are given in Ref. [10]. This results from the alignment of the transverse E field with the principal axis of the dielectric tensor and from the non-magnetic nature of the media. For the TM modes, the fields depend on the real parameters, δ , γ , β , b_1 and b_2 , which are determined by Eqs. (14) and (15), and the following

$$b_1 = \beta K_{xz}/K_x; b_2^2 = \kappa_0^2 K'_x - \beta^2 \{K'_x/K_x\} \quad (18); (19)$$

and

$$\tan(2b_2 w) = \frac{(K'_x \gamma/K_1 b_2) + (K'_x \delta/K_0 b_2)}{1 - (K'_x \gamma/K_1 b_2)(K'_x \delta/K_0 b_2)} \quad (20)$$

Explicit forms for $e(x)$ and $h(x)$ for the TM modes are given in Ref. [10]. From these results, if we assume a (101) oriented tetragonal film with properties corresponding to bulk rutile on (1120) sapphire substrate ($2w=0.5332 \mu\text{m}$, $n_1=1.0003$, $n_1=1.766$, $n_{\text{film}}^o=2.5839$, $n_{\text{film}}^e=2.8659$ [11] and a laser wavelength of $0.6328 \mu\text{m}$), we find that $|h_x(x)/h_z(x)| < 0.01$ for the TE modes; while $|e_x(x)/e_z(x)| < 0.01$ for the TM modes. Therefore, the waveguide modes in these films are essentially TEM (transverse electromagnetic) in character. In addition, For the TE₀ and TM₀ modes, we find that the peak intensities inside the film differ by only ~11%; while the field intensity at the film-substrate boundary is reduced from the peak intensity by $>3.7 \times 10^5$ and $>4.5 \times 10^6$ for the zero order TE and TM modes, respectively.

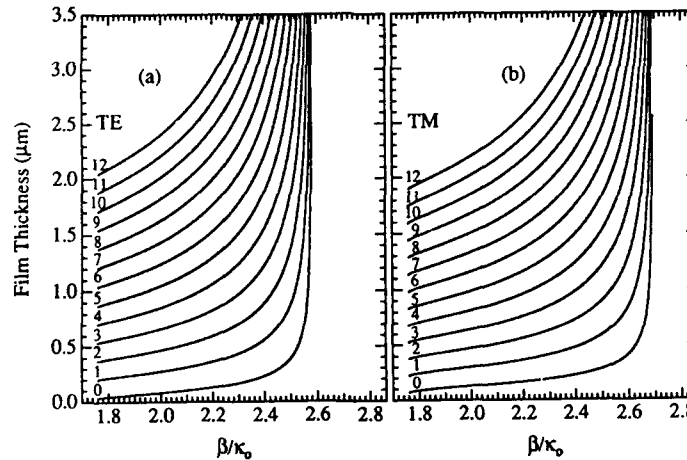


Fig. 2. The film thickness $2w$ vs. β/κ_0 for the first twelve modes (the mode orders are indicated by number) using $n_1=1.000$, $n_0=1.758$, $n_{\text{film}}^o=2.5839$, $n_{\text{film}}^e=2.8659$, $\theta=57.215^\circ$ and a laser wavelength of $0.6328 \mu\text{m}$; (a) corresponds to TE modes and (b) corresponds to TM modes.

As shown in the description of the prism-film coupler by Tien and Ulrich [5], efficient waveguide coupling occurs when the component parallel to the film surface of the wave vector of the evanescent fields in the air gap (associated with the light which is totally reflected from the prism base) matches that of one of the characteristic waveguide modes in the film. This component is $\beta = \kappa_0 n_p \sin \theta_3$, where n_p is the refractive index of the prism and θ_3 is the angle with respect to the normal of the light incident upon the prism base (see Fig. 1c). As shown in Ref. [5], propagation will only occur if the total phase shift of all waves which are multiply reflected between the film-substrate and film-air surfaces is equal to a multiple of 2π . This leads to the expression for the waveguide modes in the very weak coupling limit [5],

$$2bw - 2\phi_{01} - 2\phi_{12} = 2m\pi \quad (21)$$

where b is the propagation constant, m is the mode order, and ϕ_{01} and ϕ_{12} are the half-angle reflection phase shifts at the film-substrate and film-air interfaces, respectively. We can generalize Eq. (21) for the case for (101)-oriented crystalline thin films. The expressions for b in this case are given by Eq. (16) for TE modes and Eq. (19) for TM modes. Furthermore, for both TE and TM modes, a single equation for the thickness, w , can be obtained by eliminating δ , γ , and β between the appropriate four eigenvalue equations. From the resulting expressions, the appropriate half-angle phase shifts for TE modes can be extracted [10]. Explicit forms for ϕ_{01} and ϕ_{12} for both TE and TM modes are given in Ref. [10]. For TE and TM modes, combining Eq. (21) with the appropriate expressions for ϕ_{01} and ϕ_{12} yield single equations for the film thickness as a function of the propagation constant β . In Fig. 2, we plot for orders, $m = 0$ to 12, the thickness of the film required for a TE mode (a) or a TM mode (b) to propagate with a propagation constant β/κ_0 for a tetragonal film with optical properties corresponding to bulk rutile on (1120) sapphire substrate (parameters given above).

RESULTS AND DISCUSSION

Details of the x-ray, Four-circle x-ray, and prism-film wave guide coupler have been reported previously [10]. To determine the orientation and the degree of crystallinity of the films quantitatively, we performed x-ray scattering measurements, these data are presented elsewhere [3]. The specular and off-specular x-ray diffraction spectrum indicated that the film consisted of a single growth plane corresponding closely to the (101) plane of rutile single crystals [3] ($2\theta = 36.12^\circ$). The rocking curve for the growth plane (θ -scan) indicated an intensity full width at half maximum (FWHM) of 0.30° . The azimuthal ϕ -scan data detected no in-plane misorientation of the film with respect to the substrate, and showed a FWHM of 0.83° indicating the very high degree of in-plane epitaxy for this film. A least squares refinement of the 4-circle x-ray diffraction results for 13 off-specular reflections was used to determine the lattice parameters for the film of $a = 4.59\text{\AA}$, $b = 4.54\text{\AA}$, and $c = 2.96\text{\AA}$, with $\alpha = 89.8^\circ$, $\beta = 88.9^\circ$, and $\gamma = 89.9^\circ$ as compared to bulk tetragonal TiO_2 with $a = b = 4.5937\text{\AA}$, $c = 2.9587\text{\AA}$, and $\alpha = \beta = \gamma = 90.0^\circ$. Thus, according to the x-ray measurements, the film has a highly-crystalline, distorted rutile structure, particularly with respect to the b -axis.

As discussed in Ref. [3], the film-substrate interface along TiO_2 $[\bar{1}01]$ direction is sharp at the atomic level and structurally coherent, due to the small lattice mismatch ($\sim 0.5\%$) along this direction; whereas, the film-substrate interface along the TiO_2 $[010]$ direction is also atomically sharp, but is structurally semi-coherent, with a periodic array of misfit dislocations at the interface. These misfit dislocations are attributed to the compressive strain resulting from the $\sim 5.9\%$ lattice mismatch along the TiO_2 $[010]$ direction. It is reasonable to associate the distorted b -axis lattice constant of the film observed by x-ray with the semi-coherent nature of the interface along this direction observed by HREM. However, to the resolution level of the HREM studies ($\sim 0.2\text{\AA}$), the majority of the strain associated with the dislocations was localized to within only a few lattice constants from the interface in contrast to the bulk distortion observed by x-ray. For the purpose of the waveguide analysis, necessary rotation angle for the dielectric tensor determined from the a and c lattice parameters yields a value of $\theta = 57.16^\circ$, which compares with $\theta = 57.215^\circ$ for single crystal rutile.

In order to characterize the waveguide properties of our epitaxial (101) oriented rutile thin films grown on sapphire (1120), we performed prism-film coupling experiments. In Fig. 3, we show the reflected intensity of $0.6328\text{ }\mu\text{m}$ HeNe laser light from the base of 45° and 60° rutile

prisms as a function of effective propagation constant, $\beta = \kappa_0 n_p \sin \theta_3$ (the data from the two different prisms was combined). Three TE and one TM modes are clearly observed. In addition, two features with distorted line shapes were observed very near the substrate cutoff which seem to correspond to a possible fourth TE and second TM mode. The observed β/κ_0 values for these features are given in Table I.

Polarization	m	β/κ_0		
		Observed	Theory	Diff.
TE	0	2.5206	2.5207	-0.0001
	1	2.3682	2.3682	+0.0000
	2	2.1011	2.1009	+0.0002
	3	<1.75	----	----
TM	0	*	2.6362	----
	1	*	2.4635	----
	2	2.1787	2.1605	-0.0131
	3	<1.7771	1.7815	>0.0044

Table I. Waveguide Results

*These modes were predicted to be outside the available β/κ_0 range of either a 45° or 60° rutile prism and were not observed.

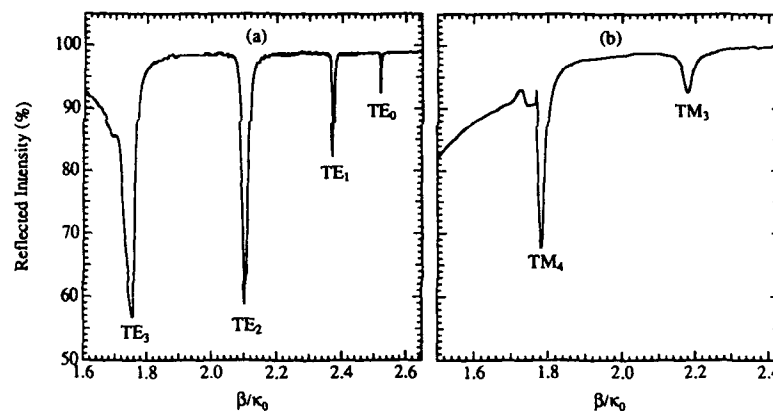


Fig. 3. Results of prism coupling experiments on epitaxial rutile (101) films on sapphire (1120). Three TE modes are shown in (a) and one TM mode is shown in (b). The modes designated TE₃ and TM₃ are very close to the substrate cut-off and were not used in subsequent analysis.

As shown in Ref. [10], a single equation can be obtained (for either TE or TM modes) for the film thickness as a function of the propagation constant β , with the refractive indexes of the substrate, n_0 , the air gap, n_1 , and the dielectric properties of the film, K_u , K_y and K_v , the film thickness $2w$, and the rotation angle θ as parameters. The equation for the TE modes is independent of K_u , K_v and θ ; therefore, the values of K_y and $2w$ may be determined independently. Since none of the films measured were of such a thickness to allow more than one TM mode to be clearly observed, K_u and K_v could not be determined separately. Due to a distorted line shape, the TM₃ mode observed in Fig. 3b was not considered in the analysis where $K_u = K_y$ was assumed. By fitting the β/κ_0 values observed in Fig. 3, the best assignment of mode orders were obtained along with the following properties for the film: $n_{film}^0 = 2.5701 \pm 0.0005$; $n_{film}^E = 2.934 \pm 0.0015$ at $\lambda = 0.6328 \mu\text{m}$ and a film thickness of $2w = 0.5332 \pm 0.0015 \mu\text{m}$. These values of the film refractive indexes are typical of all films measured.

The measured refractive indexes of the films are near to the properties of bulk TiO_2 single crystals, indicating the high quality of these films. However, two structure features of the films should result in deviations of the dielectric properties of the films relative to bulk. First, from the x-ray data, the films have a slightly mosaic structure both parallel and perpendicular to the growth plane ($\sim 0.3^\circ$ and $\sim 0.8^\circ$, respectively) which should result in an small averaging of the anisotropic dielectric properties of the films. Secondly, the x-ray refinement indicated a substantial contraction of the film b -axis lattice constant and a small extension of the film c -axis lattice constant relative to that of bulk rutile. Such a distorted crystal structure should be optically biaxial. To investigate this, the measured film parameters were used to determine theoretical values for β/κ_0 (assuming $\kappa_x = \kappa_y$) for the TE and TM modes following the analysis given above [10]. For the TE modes, the predicted β/κ_0 values for the assigned mode orders compared well with the measured results. For the TM modes, the predicted β/κ_0 values for the TM_0 and TM_1 modes were outside of the measurable range for our rutile prisms. An accurate measurement of the deviation of the TM_3 mode β/κ_0 value from theory could not be obtained due to a distorted line shape. The theoretical TM_2 mode β/κ_0 value, showed a larger deviation from experimental results than was observed for any of the TE modes. It is reasonable to conclude that the deviation of the TM_2 mode angle could be attributed to strain induced biaxial characteristics associated with the observed structural distortion along the film b -axis. This is currently being investigated.

In conclusion, we report optical waveguiding experiments using a prism-film coupler on TiO_2 (rutile) thin films deposited using the MOCVD technique. The propagation constants for asymmetric planar waveguides composed of an anisotropic dielectric medium applicable to (101) oriented rutile thin films grown on (11 $\bar{2}$ 0) sapphire substrates are derived. By application of this model to (101) oriented rutile thin films, we directly obtain values of the ordinary and extraordinary refractive indexes, n_o and n_e , as well as film thickness. We obtain values of the refractive indexes ($n_o = 2.5701 \pm 0.0015$; $n_e = 2.934 \pm 0.001$) near to that for bulk TiO_2 single crystals indicating the exceptional quality of these films. The authors would like to thank Anthony Marturano for his assistance in the calculation. This work has been supported by the U.S. Department of Energy, Basic Energy Sciences-Materials Sciences under Contract #W-31-109-ENG-38.

REFERENCES

1. D. Marcuse, Theory of Dielectric Optical Waveguides (Academic Press, New York, 1974); N. S. Kapany and J. J. Burke, Optical Waveguides (Academic Press, New York, 1972).
2. Y. Gao, K. L. Merkle, H. L. M. Chang, T. J. Zhang, and D. J. Lam, *J. Mater. Res.* **6**, 2417 (1991); Y. Gao, K. L. Merkle, H. L. M. Chang, T. J. Zhang, and D. J. Lam, *Phil. Mag. A* **65**, 1103 (1992).
3. H. L. M. Chang, H. You, Y. Gao, J. Guo, C. M. Foster, R. P. Chiarello, T. J. Zhang, and D. J. Lam, *J. Mater. Res.* **7**, 2495 (1992).
4. P. K. Tien, R. Ulrich, and R. J. Martin, *Appl. Phys. Lett.* **17**, 447 (1970); K. Tanaka and A. Odajima, *Appl. Phys. Lett.* **38**, 481 (1981); C. Liao and G. I. Stegeman, *Appl. Phys. Lett.* **44**, 164 (1984); S. S. Thöny and H. W. Lehmann, *Appl. Phys. Lett.* **61**, 373 (1992).
5. P. K. Tien and R. Ulrich, *J. Opt. Soc. Am.* **60**, 1325 (1970).
6. J. E. Midwinter, *IEEE J. Quant. Elec.* **QE-6**, 583 (1970); R. Ulrich, *J. Opt. Soc. Am.* **60**, 1337 (1970); P. K. Tien, *Appl. Opt.* **10**, 2395 (1971); R. Ulrich and R. Torge, *Appl. Opt.* **12**, 2901 (1973); H. Kogelnik and H. P. Weber, *J. Opt. Soc. Am.* **64**, 174 (1974).
7. D. P. Gia Russo and J. H. Harris, *J. Opt. Soc. Amer.* **63**, 138 (1973); M. O. Vassell, *J. Opt. Soc. Am.* **64**, 166 (1974).
8. D. F. Nelson and J. McKenna, *J. Appl. Phys.* **38**, 4057 (1967).
9. G. Leclerc and A. Yelon, *Appl. Opt.* **23**, 2760 (1984); S. Yamamoto, K. Shibata and T. Makimoto, *Opt. Comm.* **31**, 139 (1979); R. A. Andrews, *IEEE J. Quant. Elec.* **QE-7**, 523 (1971); *IEEE J. Quant. Elec.* **QE-8**, 27 (1972).
10. C. M. Foster, S.-K. Chan, H. L. M. Chang, R. P. Chiarello, T. J. Zhang, J. Guo, and D. J. Lam, *J. Appl. Phys.* **73** (10), 1 (1993).
11. J. M. Bennett and A. T. Glassman, in Handbook of Laser Science and Technology Vol. 4, Optical Materials: Part 2, Ed. by M. J. Weber, (CRC Press, Inc., Boca Raton, FL, 1988).

THE DEFECT STRUCTURE OF BaTiO₃ THIN FILMS

L.A. WILLS AND B.W. WESSELS

Department of Materials Science and Engineering and Materials Research Center, Northwestern University, Evanston, Illinois 60208

ABSTRACT

The defect structure of BaTiO₃ thin films grown on (100) Si was examined using transient photocapacitance spectroscopy. The concentration, optical cross section and associated energy levels of both native and impurity defects in as-grown and annealed BaTiO₃ films were evaluated. Deep level defects with peak energies of $E_v + 1.8$, $E_v + 2.4$, $E_v + 2.7$, $E_v + 3.0-3.1$ and $E_v + 3.2-3.3$ eV were observed in the as-grown films. Upon vacuum annealing, the concentration of the traps at $E_v + 3.0$ and $E_v + 3.2$ eV increased while the concentration of the traps at $E_v + 1.8$ and $E_v + 2.4$ eV decreased. The levels at $E_v + 3.0-3.1$ and $E_v + 3.2-3.3$ eV are attributed to oxygen vacancies. The other levels are tentatively ascribed to Fe and Fe related defects.

INTRODUCTION

Considerable interest in BaTiO₃ ferroelectric thin films has emerged due to its dielectric and non-linear optical properties [1]. These properties are strongly influenced by point and extended defect structures. While the point defect structure of BaTiO₃ ceramics has been extensively studied [2-4], much less is known about the defect structure of thin films. Recently, both textured and epitaxial BaTiO₃ thin films were prepared by metalorganic chemical vapor deposition (MOCVD) at temperatures of 800°C [5,6]. The extended defect structure of the films deposited on LaAlO₃ was evaluated using high resolution transmission electron microscopy [7,8]. However, determining the point defects is much more difficult due to their low concentration in thin films. In this paper, the point defect structure of BaTiO₃ thin films is determined using transient photocapacitance spectroscopy. The associated energy level, concentration, and optical capture cross section of the defects present in the BaTiO₃ thin films are reported. Initial measurements indicate the presence of oxygen vacancies in as-grown and annealed films.

EXPERIMENTAL

Sample Preparation

BaTiO₃ thin films were grown by low pressure metalorganic chemical vapor deposition (MOCVD) at 800°C. Barium hexafluoroacetylacetonate tetraglyme (Ba(hfa)₂(tetraglyme)) and titanium tetraisopropoxide (99.999%) were chosen as the metalorganic precursors. Two grades of Ba(hfa)₂(tetraglyme) (low purity (99+ %) and high purity (99.999%)) were used for growth to examine their effect on the resulting electrical properties of the thin films. The substrates consisted of thermally oxidized p-type Si ($\rho = 1-2 \Omega\text{-cm}$), where the SiO₂ layer was 100-300 Å. The growth conditions are described in detail, elsewhere [5,6]. X-ray diffraction showed that the BaTiO₃ thin films grown on SiO₂/Si were polycrystalline with a random orientation.

Metal-insulator-semiconductor (MIS) BaTiO₃/SiO₂/Si diodes were fabricated for transient photocapacitance measurements. Semi-transparent Au electrodes (100 Å) with an area of 0.118 cm² were evaporated onto the BaTiO₃ surface. To insure the integrity of the electrical contact, a thicker (350-500 Å) Au dot ($1.88 \times 10^{-3} \text{ cm}^2$) was evaporated on top of the transparent electrode. Evaporated aluminum formed an ohmic contact to the backside of the Si substrate. For vacuum annealing, the metal contacts were removed and the samples were heated to 950°C at 10^{-4} Torr for time intervals ranging from 4-20 hours.

The resistivity of the BaTiO₃ films was calculated using the linear region of the current-voltage curves from the MIS diode. The as-deposited films had resistivities ranging from 10⁸-10⁹ Ω-cm. However, the highly textured BaTiO₃ films grown on LaAlO₃ with a low purity and high purity Ba precursor were semi-insulating ($\rho = 200$ -1000 Ω-cm) [8] and insulating ($\rho = 10^6$ -10⁷ Ω-cm), respectively [9].

Transient Capacitance Spectroscopy Measurements

Transient photocapacitance spectroscopy of the MIS structures was measured using a technique initially described by Chantre et al. for the study of semiconductors [10]. Recently, this technique has been extended to evaluate MIS structures [11,12]. For this measurement, chopped light from a 250W Oriel quartz-halogen lamp dispersed through a Zeiss monochromator was focussed onto the diode cooled to 80K. Photocapacitance was measured with a capacitance meter at 1MHz. Spectra were recorded while negatively biasing the MIS diodes in the accumulation region with a field of 10⁴ V/cm. The transient photocapacitance was measured for time intervals of 10-100 msec. Following illumination, the sample was equilibrated in the dark for 5 to 7 sec. The time derivative of the photocapacitance was plotted as a function of photon energy.

Upon illumination of an MIS diode, a photocapacitance signal can arise from emptying or filling of traps in (1) the semiconductor, (2) the semiconductor-insulator interface, (3) the SiO₂/BaTiO₃ interface, (4) the insulator, or (5) the BaTiO₃/metal interface. However, the contributions from different traps can be spectrally and temporally resolved. The time derivative of the photocapacitance is a direct measure of the trap concentration. Provided the charge is only trapped at defects uniformly distributed throughout the insulator and retrapping is negligible, the time derivative of the photocapacitance is given by [11]:

$$dC/dt|_{t=0} = d(Q/V)/dt|_{t=0} = (qAd/V) dn_t/dt|_{t=0} \quad (1)$$

where Q is the total trapped charge, q is unit charge per electron, A is the diode area, d is the insulator thickness and V is the effective bias. Since short illumination times are used, only a fraction of the traps in the insulator layer are populated. The total concentration of traps, N_t , is related to the concentration of trapped electrons, n_t , by the expression [10,12]:

$$dn_t/dt|_{t=0} = \sigma\Phi N_t \quad (2)$$

where σ is the optical cross section of the trap and Φ is the intensity of the light. Combining Eq. 1 and 2, the total trap concentration is given by

$$N_t = (1/\sigma\Phi) (V/qdA) dC/dt|_{t=0} \quad (3)$$

The optical cross section is obtained by measuring the capture rate of an electron, c_n , by the trap, given by

$$c_n = \sigma_n\Phi \quad (4)$$

The capture rate of an electron is determined from the fit of a semi-log plot of the photocapacitance as a function of time [13]. Substituting the intensity of light and measured capture rate, c_n , into Eq. 4, the optical cross section of the trap is obtained.

RESULTS AND DISCUSSION

As-Deposited BaTiO₃ Films

The photocapacitance response of a typical BaTiO₃/SiO₂/Si MIS diode is plotted as a function of the illumination time in Figure 1. For a photon energy of 2.7 eV (Fig. 1 curve a), the photocapacitance increases rapidly up to 10 msec and then begins to saturate. For an excitation energy of 3.17 eV, the photocapacitance increases at a slower rate (Fig. 1 curve b).

The time derivative of the photocapacitance signal is shown as a function of energy for the above sample deposited with a high purity Ba source (Fig. 2a). Transient photocapacitance peaks were present at $E_v + 1.2$, $E_v + 1.4$, and $E_v + 3.1$ eV. A shoulder was also observed in the spectrum at $E_v + 3.2$ eV (Fig. 2a). For comparison, the transient photocapacitance spectrum of a typical BaTiO₃ film grown with a low purity precursor obtained for a 20-40 msec time interval is shown in Fig. 2b. In addition to the peaks at $E_v + 1.2$, $E_v + 1.4$, and $E_v + 3.1$ eV, a broad transition with a peak at $E_v + 1.8$ eV and a shoulder at $E_v + 2.4$ eV is observed in the lower purity film.

To determine the origin of the transitions observed in the BaTiO₃ MIS diodes, the transient photocapacitance of a control sample, SiO₂/Si MIS diode was examined. The transient photocapacitance spectrum of a SiO₂/Si control sample measured using a 20-40 msec time interval has peaks at 1.2-1.3, 1.4 and 2.4 eV (Fig. 3). The 1.25 eV peak with a threshold energy of 1.1 eV arises from the photoexcitation of intrinsic carriers in Si. The possible identity of the levels at 1.4 and 2.4 eV are only suggested here by comparing to other work. The level at 1.4 eV was previously observed as a shoulder in transient photocapacitance spectroscopy of MIS structures with thermally grown SiO₂ on Si and attributed to a defect in the SiO₂ layer [12]. Additionally, the peak at 2.4 eV was previously observed with photo-depopulation/injection measurements on similar structures and was attributed to Na in the SiO₂ [14]. The Na in the SiO₂ layer is presumably a contaminant in the deionized water used during oxidation. The peaks at 1.2 and 1.4 eV have the same energy and shape in both the BaTiO₃/SiO₂/Si (Fig. 2) and SiO₂/Si (Fig. 3) spectra. This indicates that these peaks are of common origin and involve transitions in the SiO₂/Si. However, the broad transition in Fig. 2(b) with a shoulder at 2.4 eV is not attributed to defects in the SiO₂/Si layer.

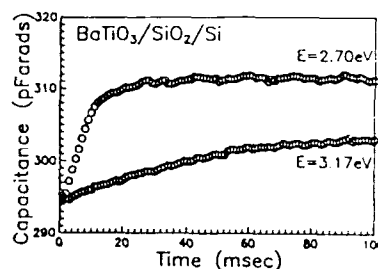


Fig. 1. The time dependent photocapacitance response of a typical BaTiO₃ MIS diode at two excitation energies.

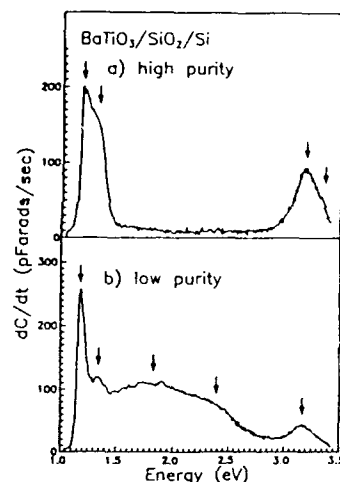


Fig. 2. Transient photocapacitance obtained at a 20-40 msec time interval for a BaTiO₃ film grown with a) a high and b) a low purity precursor.

From the comparison of the BaTiO₃ and SiO₂/Si MIS diode spectra, the transient photocapacitance peaks at $E_v+1.85$, $E_v+2.4$, $E_v+3.0-3.1$ and $E_v+3.2-3.3$ eV are attributed to transitions in the BaTiO₃ film. The optical capture cross section of these defects is related to the time dependence of the photocapacitance (Eq. 4). The measured optical cross section, σ , for the defects with energy less than 2.9 eV is 10^{-14} cm²; whereas, 10^{-13} cm² is obtained for traps at higher energies. Upon substitution of the appropriate values for σ into Eq. 3, a trap concentration of $10^{13}-10^{14}$ cm⁻³ was estimated for the various defect levels. The measured levels, their concentration and optical capture cross section for several BaTiO₃ films are listed in Table I.

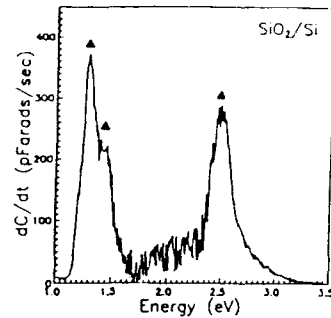


Fig. 3. Transient photocapacitance spectrum at a 20-40 msec time interval for a SiO₂/Si MIS diode.

Table I. The associated energy level, light intensity, optical cross section and concentration of the defects in several as-grown BaTiO₃ films measured with transient photocapacitance. Peak energies are referenced from the valence band. Samples 297, 298, and 302 were prepared using a high purity Ba precursor.

Energy (eV)	Φ (cm ⁻² .sec ⁻¹)	σ (cm ²)	Trap Concentration (cm ⁻³)			
			256	279	297	298 302
1.7-1.9	1.6×10^{14}	10^{-14}	10^{13}	3×10^{13}	--	-- --
2.4	7×10^{14}	10^{-14}	2×10^{13}	1×10^{14}	--	-- --
2.7-2.8	8×10^{12}	5×10^{-14}	6×10^{13}	--	--	-- --
3.0-3.1	4×10^{12}	10^{-13}	7×10^{13}	8×10^{13}	10^{14}	10^{13} 3×10^{13}
3.2-3.3	2×10^{12}	10^{-13}	3×10^{13}	9×10^{13}	7×10^{13}	10^{13} 8×10^{13}

Since the defect levels at $E_v+3.0-3.1$ and $E_v+3.2-3.3$ eV were observed in both low and high purity films, they are likely to be related to native defects (Table I). On the other hand, the defect levels at $E_v+1.8$ and 2.4 eV are tentatively attributed to the residual impurities since they are only seen in the lower purity films (Table I).

Vacuum Reduction Experiments

To identify the traps with levels at $E_v+3.0-3.1$ and $E_v+3.2-3.3$ eV in BaTiO₃, the samples were reduced in a vacuum ($P_{O_2} \sim 10^{-5}$ Torr) at 950°C and the transient photocapacitance was subsequently measured (Fig. 4). The peak intensity of the levels at $E_v+3.0-3.1$ eV and $E_v+3.2-3.3$ eV increased following vacuum reduction, which suggests that these defects are related to oxygen vacancies. This observation is

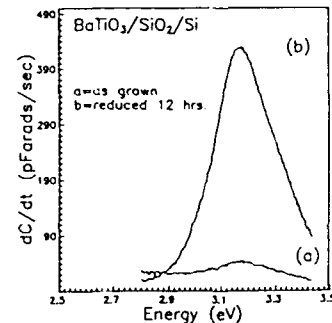


Fig. 4. Transient photocapacitance at a 20-40 msec time interval for an a) as-grown and b) 12 hour vacuum reduced film.

consistent with previous optical absorption measurements of vacuum reduced single crystal BaTiO_3 , where the absorption peak at $E_v + 3.0\text{eV}$ was attributed to oxygen vacancies [15]. Furthermore, theory predicts that the energy levels associated with oxygen vacancies in BaTiO_3 will lie near the conduction band [16,17] of BaTiO_3 , 3.5 eV [18,19].

Further analysis of the vacuum annealed samples derived from the 99+% pure Ba precursor showed that the measured photocapacitance peak intensity of the levels at $E_v + 1.8$ and $E_v + 2.4\text{eV}$ decreased (Fig. 5a), while a new peak at $E_v + 2.65\text{eV}$ (Fig. 5b) developed. In contrast, vacuum reduction of films derived from the high purity precursor did not show these transitions that lie deeper within the bandgap. Therefore, these trapping levels are believed to be impurity related. Since Fe is one of the most abundant impurities in undoped bulk BaTiO_3 [20], these defects most likely involve iron. This is consistent with photoconductivity measurements which identified an Fe related trap at $E_v + 2.6\text{eV}$ in $\text{Fe}:\text{BaTiO}_3$ [21]. In addition, electron paramagnetic resonance and optical absorption measurements of single crystal $\text{Fe}:\text{BaTiO}_3$ showed that Fe^{4+} yielded an absorption peak at 2.69 eV, which correlates well with the peak at $E_v + 2.65\text{eV}$ in the BaTiO_3 films [22]. Other optical absorption studies have shown Fe related defects with peaks at $E_v + 2.34$ and $E_v + 2.48\text{eV}$ [23]. We propose that the changes in the peak intensities for the mid-gap levels, after vacuum reduction may result from the reduction of Fe^{3+} to Fe^{4+} . Therefore, the levels in the as-deposited films at $E_v + 1.85\text{eV}$ and $E_v + 2.4\text{eV}$ may be Fe related.

CONCLUSIONS

In summary, transient photocapacitance spectroscopy has been used to determine the energy levels, optical cross section, and concentration of deep level defects in BaTiO_3 thin films. The defect levels at $E_v + 3.0\text{--}3.1\text{eV}$ and $E_v + 3.2\text{--}3.3\text{eV}$ in the BaTiO_3 films are attributed to native oxygen vacancies with a concentration of ($\sim 10^{14}\text{cm}^{-3}$) and $\sigma = 10^{13}\text{cm}^2$. In addition, the transient photocapacitance of BaTiO_3 films indicated the presence of residual impurity related defects, tentatively ascribed to Fe impurities. These traps had energies of $E_v + 1.8\text{eV}$, $E_v + 2.4\text{eV}$ and $E_v + 2.7\text{--}2.8\text{eV}$ with $\sigma = 10^{14}\text{cm}^2$. A detailed model for the defect structure of BaTiO_3 thin films based on resistivity and transient capacitance will follow in future papers.

ACKNOWLEDGEMENTS

The Division of Basic Energy Sciences of the Department of Energy funded this work under Grant Number DE FG02 85 ER 45209. Partial support of L. Wills by an IBM fellowship is gratefully acknowledged. The Optical Facility and Materials Preparation Facility in the Materials Research Center at Northwestern University were used throughout this project.

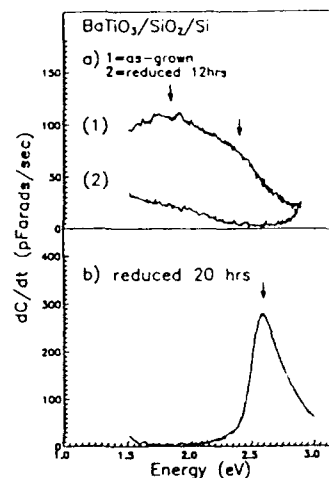


Fig. 5. Transient photocapacitance spectra at a 20-40 msec time interval for a) as-grown and 12 hour reduced and b) 20 hour reduced BaTiO_3 film.

REFERENCES

1. See for example, Ferroelectric Thin Films II edited at A.I. Kingon, E.R. Myers and B. Tuttle (Mat. Res. Soc. Symp. Proc. **243**, Boston, MA, 1992).
2. N.H.Chan and D.M.Smyth, J.Electrochem.Soc., **123**, 1584 (1976).
3. D.M. Smyth, M.P. Harmer and P. Peng, J.Am. Ceram. Soc. **72** (12), 2276 (1989).
4. J. Nowotny and M. Rekas, Solid State Ionics **49**, 135 (1991)
5. L.A. Wills, B.W. Wessels, D.L. Schulz and T.J. Marks, Ferroelectric Thin Films II, edited by A.I. Kingon, E.R. Myers and B. Tuttle, (Mater. Res. Soc. Symp. Proc. **243**, Boston, MA, 1992) pp. 217.
6. L.A. Wills, B.W. Wessels, D.S. Richeson and T.J. Marks, Appl. Phys. Lett., **60** (1), 41 (1991).
7. V.P. Dravid, H. Zhang, L.A.Wills, and B.W. Wessels, J. of Mater. Research (in press).
8. J. Chen, L.A. Wills and B.W. Wessels, J. Elec. Mat., **22**, 701 (1993).
9. L.A. Wills, B.W. Wessels, J.L. Schindler, C.R. Kannewurf, D.L. Schulz and T.J. Marks, presented at TMS: Elec. Mat. Conf. (1992).
10. A. Chantre, G. Vincent and D. Bois, Phys. Rev.B, **23** (10), 5335 (1981).
11. W.A. Feil and B.W. Wessels, Presented at Mat. Res. Soc. Spring Meeting (1992).
12. W.A. Feil and B.W. Wessels, J. Appl. Phys. (in press).
13. H.G. Grimmeiss, Proc. of the Conf. of Metal-Semiconductor Contacts, Inst. of Phys. London, Conf. Ser.# 22, 187 (1974).
14. V.J.Kapoor, F.J. Feigel and S.R. Bulter, J. App. Phys., **48**, 739, (1977).
15. S. Ikegami and I. Ueda, J. Phys. Soc. Japan, **19**,159 (1964).
16. V.V Prisedski and Y.D. Tret'yakov, Inorg. Mater., **21**, 1217 (1986).
17. S.M. Maksimov, O.I Prokopalo, I.P. Raevskii, S.A. Prosandeev, A.B. Fisenko and V.P. Sachenko, Sov. Phys. Sol. State, **27**, 562 (1985).
18. G.M. Davis and M.C. Gower, Appl. Phys. Lett., **55**, 112 (1989).
19. M.N. Kamalasanan, S. Chandra, P.C. Joshi and A. Mansingh, Appl. Phys. Lett. **59** (27), 3547 (1992).
20. E. Possenriede, P. Jacobs, and O.F. Schirmer, J. of Phys. Condens. Matter **4** [19], 4719 (1992).
21. G.Godefroy, P.Jullien and L.Cai, Ferroelectrics, **13**, 309 (1976).
22. E.Possenriede, H. Krose, O.F. Schirmer and G. Godefroy, Ferroelectrics, **125**, 343 (1992).
23. M. Aguilar,C.Gonzalo and G. Godefroy, Ferroelectrics, **25**, 467 (1980).

A MODEL OF THE METAL-FERROELECTRIC-METAL CAPACITOR

G. TEOWEE^{*a}, and D.R. UHLMANN^a

^{*}Donnelly Corp., Tucson, AZ 85712

^aArizona Materials Laboratories, Department of Materials Science and Engineering, University of Arizona, Tucson, AZ 85721

ABSTRACT

Ferroelectric (FE) films, especially PZT films, have received increasing attention for microelectronic applications such as ferroelectric memory and high density DRAM. There has been significant progress in the preparation of high quality PZT films involving wet chemical and physical vapor deposition techniques. Metal-FE-metal structures, typified by Pt-PZT-Pt capacitors, are the basic building blocks for the ferroelectric devices. The leakage currents of the capacitors are known to be non-ohmic and exhibit an exponential dependence on applied voltage.

The present paper presents a model based on totally depleted back-to-back Schottky barriers. Predictions based on the model can provide significant new understanding of the FE behavior of thin films. For example, the assumption of total depletion leads to the presence of a built-in field within the film which can explain the ubiquitously higher values of coercive field in FE films than found in bulk ceramics. It will be shown that the agreement between model predictions and actual device I-V characteristics of Pt-PZT-Pt capacitors is very close. Further, the model can also explain the observed hysteresis loop asymmetry and low dielectric constants of films of relaxor FE's, whose dielectric constants are much smaller than those of bulk materials.

I. INTRODUCTION

Ferroelectric (FE) films, especially lead zirconate titanate (PZT) films, have received increasing attention for microelectronic applications, namely in the areas of non-volatile ferroelectric memory and high dielectric constant materials in high density DRAM. PZT is a widely explored FE material utilized for its FE, dielectric, electro-optic, acousto-optic, pyroelectric and piezoelectric properties in both bulk and thin film forms [1]. There has been significant progress in the preparation of high quality PZT films involving wet chemical methods [e.g., 2] and physical vapor deposition techniques such as sputtering [e.g., 3], laser ablation [e.g., 4] and MOCVD [e.g., 5]. For comparison with the predictions of the model presented in this paper, actual device characteristics, namely the I-V leakage currents, were obtained on sol-gel derived PZT 53/47 films prepared in our laboratories. The details of film preparation and leakage characterization have been published elsewhere [e.g., 6].

II. MODEL OF THE PT-PZT-PT CAPACITOR

Metal-FE-metal structures, typified by Pt-PZT-Pt capacitors, are the basic building blocks for active and passive FE devices. It is recognized that the capacitors are not simple metal-insulator-metal devices with ohmic contacts, but rather back-to-back

Schottky barriers. These Schottky barriers are themselves fairly complicated due to the presence of surface states at the interfaces, the polycrystallinity of the PZT films which can significantly affect surface states at the Pt-PZT interfaces, and domain structures which affect the states of polarization in the PZT films. Additionally, the depletion width may be comparable to or even larger than the film thickness resulting in wholly depleted films between the electrodes.

Previous modeling of PZT capacitors was based on the assumption of partially depleted PZT films, i.e., depletion widths smaller than the film thickness, resulting in back-to-back Schottky barriers [7]. Adsorbed oxygen at the surfaces of titanate ceramics has often been suggested to give rise to trapping surface states [8]. The presence of such surface states and polarization states at the interfaces can lead to band bending, which in turn affects the type of contact formed, viz., ohmic or rectifying. Rectifying contacts result in uneven field and potential distributions in the PZT films, which affect the final device characteristics.

The work function of Pt metal, ϕ_{Pt} is 5.5 eV. The typical band gap, E_g , and electron affinity, X_{PZT} , for a PZT film are about 3.5 eV and 1.75 eV respectively. For a p-type PZT film (the conductivity in PZT ceramics [1] has been determined to be p-type), the Fermi level, E_f , lies closer to the valence band, E_v , than to the conduction band, E_c . Since the work function of Pt is higher than that of PZT, the contact should be ohmic. I-V leakage characteristics of these capacitors indicate, however, that the contact is not ohmic (or linear); rather, the current depends logarithmically on the applied voltage. The only case where the contacts can be rectifying is in the presence of surface states (arising, e.g., from absorbed oxygen at the PZT surface and/or termination of the PZT crystalline lattice at the metal contacts). These surface states with a density of D_0 and a neutral energy level at E_0 result in band bending near the contacts and barrier heights of ϕ_b at the interfaces. It is further assumed that these barrier heights are similar at both interfaces, i.e., the capacitor should behave electrically symmetrically independent of the polarity of the applied voltage.

Equilibrium

At equilibrium (no applied bias), it is assumed that the width of the depletion region, w , is larger than the thickness, t , of the PZT film, i.e., the film is totally depleted. Poisson's equation may be used to calculate the field and potential distribution in the totally depleted film, i.e.,

$$\frac{-d^2\phi}{dx^2} = \frac{dE}{dx} = \frac{\rho(x)}{\epsilon_{PZT}} \quad (1)$$

where ϕ = potential
 E = electric field
 ρ = charge density
 ϵ_{PZT} = dielectric constant of PZT

The solutions to Poisson's equation are shown in Fig. 1. Note that t and the acceptor concentration, N_a , are constant throughout the film. By applying Gauss Law at the Pt-PZT interface, the maximum field E_0 is:

$$E_o = \frac{qN_a t}{2\epsilon_{PZT}} \quad (2)$$

The built-in potential, ϕ_i , at the center of the film is obtained by the negative of the area under the field:

$$\phi_i = \frac{1}{2} \left(\frac{qN_a t}{2\epsilon_{PZT}} \right) \cdot \frac{t}{2} = \frac{qN_a t^2}{8\epsilon_{PZT}} \quad (3)$$

The density of electrons, n_s , at the center of the film (with the highest barrier height of $\phi_b + \phi_i$) is:

$$n_s = N_c e^{\frac{-q(\phi_b + \phi_i)}{kT}} \quad (4)$$

where N_c is the effective density of states at the conduction band. The currents are proportional to the electron density; and at equilibrium with no external bias,

$$J_I = J_{II} = KN_c e^{\frac{-q(\phi_b + \phi_i)}{kT}} \quad (5)$$

where J_I and J_{II} are the thermally induced current densities at Interfaces I and II respectively; and K is a proportionality constant. Since $J_I = J_{II}$, there is no net current flow, as expected.

There exists a built-in field within the film (see Fig. 1) whose magnitude depends on the distance inside the film. The field is zero at the center of the film and is of different signs at the contacts. The maximum fields are found at the interfaces. The

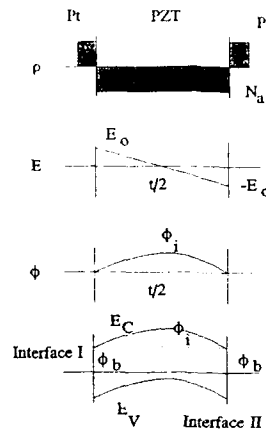


Figure 1. The solutions to Poisson's equation for a wholly depleted PZT film, showing the charge distribution (ρ), electric field (E), potential (ϕ) and energy band diagram at equilibrium

presence of this field can affect significantly the FE properties of the film. For example, assuming $N_a = 10^{18}/\text{cm}^3$, film thickness, $t = 0.5 \mu\text{m}$ and $E_{\text{PZT}} = 1000$, it is calculated that $E_o = 45.2 \text{ kV/cm}$ according to Eqn. (2). The magnitude of this field is comparable to the E_c values ($\sim 20\text{--}60 \text{ kV/cm}$) measured on PZT films prepared in our laboratories [e.g., 2]. The E_c for similar bulk ceramics is about 1 kV/cm . Thus the higher values of E_c found in FE films can likely be attributed to the built-in field which needs to be overcome to switch the domains. Since E_o is linearly dependent on N_a , a high purity PZT film with a low value of N_a is expected to yield a low value of E_c . Note, too, that if the acceptor concentration, N_a , is not uniform throughout the film (resulting perhaps from variations in Pb content), the uneven field distribution can lead to asymmetric values of E_c , as are frequently encountered in FE films.

The uneven built-in field can give rise to different regions within the film with different T_c 's, which in turn can lead to a transition in the FE properties over a range of temperature, as documented for the dielectric constants of FE thin films as a function of temperature. Additionally, the presence of such a built-in field can smear out the FE properties of films of relaxor FE's (e.g., PMN) which are much more sensitive to electric fields than are normal FE films (e.g., PZT). As a result of this built-in field, the dielectric constant is much lower in relaxor thin films (~ 1000) than found in similar relaxor bulk ceramics ($\sim 10,000$).

Current-Voltage Characteristics

Upon application of an external voltage, V_a (or field, V_a/t), the charge remains essentially constant since N_a and t are fixed. However, the field is now shifted by V_a/t as indicated in Fig. 2. The distance, y (denoting zero field or maximum potential) is given by:

$$y = \frac{1}{2} \left[t - \frac{V_a}{E_o} \right] \quad (6)$$

(where $V_a < E_o t$)

The new built-in voltage $\phi'_i(V_a)$ as a function of applied bias, V_a , is now:

$$\phi'_i(V_a) = \frac{E_o t}{4} - V_a \left[\frac{1}{2} - \frac{V_a}{4E_o t} \right] \quad (7)$$

From Fig. 1:

$$\phi_i = \frac{E_o t}{4} \quad (\text{at } V_a = 0) \quad (8)$$

$$\therefore \phi'_i(V_a) = \phi_i - V_a \left[\frac{1}{2} - \frac{V_a}{4E_o t} \right] \quad (9)$$

The current consists predominantly of a net electron flow across the depleted film even though the film was initially assumed to be p-type. Note, however, that by the depletion approximation, no majority free carriers are present throughout the wholly

depleted films. The current results from injection of electrons at the interfaces. The effective barrier heights seen at interface I and II are $\phi_b + \phi_i (V_a) + V_a$ and:

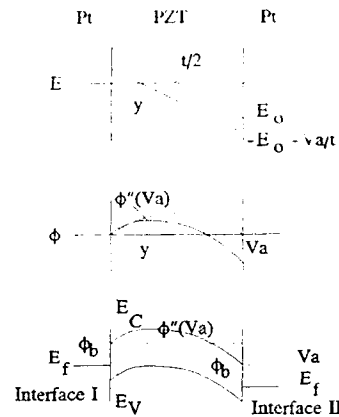


Figure 2. The solutions to Poisson's equation for a wholly depleted PZT film showing the electric field (E), potential (ϕ) and energy band diagram at an applied bias $V_a < E_{ot}$

$$\phi_b + \phi_i'(V_a) = \phi_b + \phi_i - V_a \left[\frac{1}{2} - \frac{V_a}{4E_{ot}} \right] \quad (10)$$

and

$$\phi_b + \phi_i'(V_a) + V_a = \phi_b + \phi_i + V_a \left[\frac{1}{2} + \frac{V_a}{4E_{ot}} \right] \quad (11)$$

The current flows at both interfaces due to the applied voltage, V_a , are then:

$$J_I = KN_c e^{-q \left[\phi_b + \phi_i - V_a \left(\frac{1}{2} - \frac{V_a}{4E_{ot}} \right) \right] / kT} \quad (12)$$

$$J_{II} = KN_c e^{-q \left[\phi_b + \phi_i - V_a \left(\frac{1}{2} + \frac{V_a}{4E_{ot}} \right) \right] / kT} \quad (13)$$

The net current due to electron flow is:

$$\begin{aligned} J_T &= J_I - J_{II} \\ &= 2KN_c e^{-q(\phi_b + \phi_i)/kT} e^{-\frac{qV_a^2}{16\phi_i kT}} \left[\sinh \frac{qV_a}{2kT} \right] \end{aligned} \quad (14)$$

Consider now an applied bias, $V_a > E_{ot}$. The effective barrier heights at interfaces I and II are ϕ_b and $\phi_b + V_a$, respectively. Hence the current flow is

$$\begin{aligned}
 J_T &= J_I - J_{II} \\
 &= KN_c e^{-\phi_b/kT} (1 - e^{-qV_A/kT})
 \end{aligned} \tag{15}$$

Since $V_A > E_{ot}$ (or $4\phi_i$), the term in the bracket ~ 1 , and

$$J_T = KN_c e^{-\phi_b/kT} \tag{16}$$

The current is limited strictly by Interface I; and for constant ϕ_b (assumed independent of applied voltage), the current is then constant with increasing voltage above E_{ot} . A general plot of the I-V behavior of the back-to-back Schottky barrier according to the proposed model is shown in Fig. 3a and agrees quite well with observed I-V characteristics (Fig. 3b). Also shown in Fig. 3a are the I-V characteristics expected for a conventional, partially depleted Pt-PZT-Pt capacitor which is dominated by the reverse bias current (Eq. 16) of a Schottky barrier and is fairly independent of applied bias.

By considering the dependency on t in Eqn. (14), it is predicted that in thinner films, the current and saturation voltage should increase and decrease, respectively with decreasing thickness. Since the saturation current is determined by the current at Interface I (Eqn. (16)), the magnitude of the saturation current is expected to be independent of film thickness, assuming other parameters are constant, namely N_a and ϵ_{PZT} .

III. CONCLUSIONS

A successful model of the Pt-PZT-Pt capacitor has been proposed which is based on totally depleted back-to-back Schottky barriers rather than partially depleted Schottky barriers. Predictions of the model agree closely with measured device characteristics obtained in our laboratories (particularly I-V leakage currents).

The model appears to have far-reaching consequences for understanding PZT (or any general FE) films. It predicts that there exists a large built-in field (about 50 kV/cm) within the films. The presence of such built-in fields can explain the elevated values of E_c compared to those of corresponding bulk ceramics, the asymmetry of hysteresis loops found in some FE films (due to uneven field distributions), the diffuse transition of ϵ_r values with temperature near T_c and the much lower values of ϵ_r in relaxor films (about 1000-2000) compared with values for bulk ceramics (up to 25,000). Aging behaviors of the films can be influenced by the fields. The deleterious effects of aging (viz., the monotonic decrease of ϵ_r with time due to gradual domain reorientation) can perhaps be mitigated by tailoring the N_a profile across the film to achieve a constant field along the polarization direction.

ACKNOWLEDGMENTS

The financial support of the Air Force Office of Scientific Research is gratefully acknowledged, as are stimulating discussions with Professors D. Birnie and R. Schrimf of the University of Arizona.

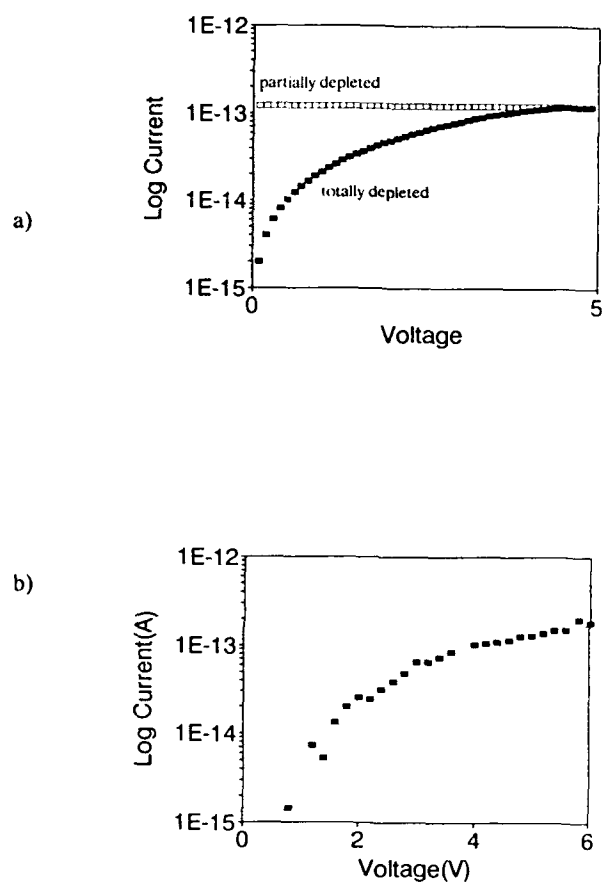


Figure 3. The a) predicted totally depleted and partially depleted and b) measured I-V characteristics of a Pt-PZT-Pt capacitor with similar barrier heights at both interfaces

REFERENCES

- [1] B. Jaffe, W.R. Cook and M. Jaffe, Piezoelectric Ceramics, Academic Press, 1971.
- [2] G. Teowee, J.M. Boulton and D.R. Uhlmann, Mat. Res. Soc. Symp. Proc., Vol. 243, 255 (1992).
- [3] K. Hirata, N. Hosokawa, T. Hase, T. Sakuma and Y. Miyasaku, Jpn. J. Appl. Physics, 31, 3021 (1992).

- [4] D. Roy and S.B. Krupanidhi, *J. Mater. Res.*, 7, 2521 (1992).
- [5] T. Tomonari, T. Ishiu, R. Sakata and T. Takenaka, *Jpn. J. Appl. Phys.*, 31, 2998 (1992).
- [6] G. Teowee, J.M. Boulton, E.A. Kneer, M.N. Orr, D.P. Birnie II, D.R. Uhlmann, S.C. Lee, K.F. Galloway and R.D. Schrimpf, to be published in *Proc. 8th ISAF* (1992).
- [7] C.J. Brennan, *Proc. of 3rd Intl. Symp. Integ. Ferroelectrics* (1991), 354.
- [8] H.A. Sauer and S.S. Flaschen, *Bulletin of the Amer. Ceram. Soc.* 39, 304 (1960).

EFFECT OF Zr/Ti RATIO ON THE FATIGUE AND RETENTION BEHAVIOR OF SOL-GEL DERIVED PZT FILMS

G. TEOWEE^{*a}, J.M. BOULTON^a, M.N. ORR^a, C.D. BAERTLEIN^a, R.K. WADE^a,
D.P. BIRNIE III^a and D.R. UHLMANN^a

^{*}Donnelly Corp., 4545 E. Ft. Lowell Rd., Tucson, AZ 85712

^aArizona Materials Laboratories, Department of Materials Science and Engineering,
University of Arizona, Tucson, AZ 85721

ABSTRACT

A series of sol-gel derived PZT films with various Zr/Ti ratios - namely PT, 0/100 - 20/80, 35/65, 53/47, 65/35, 80/20, 94/6 and PZ, 100/0 - were prepared on platinized Si wafers. Excess PbO was added to the precursor chemistries to compensate for eventual PbO loss and also to aid in obtaining the desired perovskite phase.

It was found that the phase assembly, namely the presence of tetragonal or rhombohedral perovskite phases, plays an important role in determining the fatigue and retention behavior. PT-rich (or tetragonal) films offer better retention characteristics than those observed in PZ-rich (or rhombohedral) or PZT 53/47 films. Films with PZ-rich compositions tend to exhibit superior fatigue behavior compared with PT-rich films.

INTRODUCTION

Lead zirconate titanate (PZT) is a widely studied ferroelectric (FE) material utilized for its FE, dielectric, electro-optic, acousto-optic, pyroelectric and piezoelectric properties in both bulk and thin film forms [1]. PZT is a solid solution containing lead titanate (PT) and lead zirconate (PZ) in various stoichiometric ratios. PZT x/y refers to $\text{Pb}(\text{Zr}_{x/100}\text{Ti}_{y/100})\text{O}_3$ where $x, y \leq 100$ and $x + y = 100$. PZ is antiferroelectric (AF), while PT is ferroelectric; and solid solutions of these two end numbers produce mostly FE materials with material properties which are highly dependent on the Zr/Ti ratio. Examples of the effect of this stoichiometry ratio on material properties include dielectric constant, planar coupling constant and T_c , the Curie point. PT-rich and PZ-rich compositions belong to the tetragonal and rhombohedral modifications respectively of the perovskite crystal structure. In the PZ-PT phase diagram, the rhombohedral-tetragonal boundary is the most important feature, termed the morphotropic phase boundary (MPB). It is located at about 53 atom % Zr, 47 atom % Ti (PZT 53/47). Not only is the dielectric constant highest at this boundary, but also the electromechanical coupling factor and piezoelectric coefficients achieve their maximum values here [1].

Recently PZT films have attracted considerable attention for applications in non-volatile ferroelectric memory since such films exhibit switchable polarization, fast switching times and excellent fatigue and retention behaviors [e.g., 2]. Most of the attention has been focused on the MPB composition, namely PZT 53/47. The numerous techniques used to prepare PZT films include magnetron sputtering [3], diode sputtering [4], e-beam evaporation [5], laser ablation [6], MOCVD [7], and sol-gel methods [8]. There is, unfortunately, scant attention in the literature directed to exploring the effect of Zr/Ti ratio on the FE properties of PZT films. The film properties are expected to vary since the crystal structure and FE nature (whether FE or AF) change with Zr/Ti ratio.

EXPERIMENTAL

The precursor solutions were prepared using Pb acetate and Ti/Zr alkoxides. The desired stoichiometries were achieved in these precursor solutions by adding the appropriate molar ratios of Pb, Zr and Ti (where applicable). Mole % excess PbO was also incorporated as shown by the chemical formulae $\text{Pb}_{1.1}\text{Zr}_x/100\text{Ti}_y/100\text{O}_{3.1}$ where $x, y \leq 100$ and $x + y = 100$. The specific compositions chosen cover the range of tetragonal, orthorhombic and rhombohedral modifications of PZT, namely PZT 0/100, PZT 20/80, PZT 35/65, PZT 53/47, PZT 65/35, PZT 80/20, PZT 94/6 and PZT 100/0. After refluxing for 3 hours, the solutions were concentrated to 1.0 M.

Substrates chosen were Si(100) wafers which had previously been thermally oxidized before being sputtered with Pt to yield Pt(2000Å)/SiO₂(1500Å)/Si. Spincoating was performed in a Class 100 clean room using a Headway Spinner at 2000 rpm for 30s. The precursor solutions were filtered using a syringe filter (0.2 µm) to minimize particle contamination. The green films were fired at 500°C to burn off the organics, yielding films ~1700Å thick per coating. In order to achieve thicker films, multiple coatings were performed. Typically three coatings were required to obtain films about 0.5 µm thick. Finally, the films were fired at 700°C to crystallize them fully into single-phase perovskite.

Microlithography was used to define 130 µm x 130 µm Pt top electrode pads using the lift-off technique. The monolithic Pt-PZT-Pt capacitors were completed by obtaining back-contact through acid-etching one portion of the film. Prior to characterization, the capacitors were post-metallization annealed at 100°C or 350°C for 30 mins to consolidate the top electrodes.

The phase assembly in the films was monitored by X-ray diffraction (XRD) using a Scintag XRD Diffractometer. The FE properties, namely the fatigue and retention behavior, were measured using a Radiant Technologies RT-66A Ferroelectric Tester. To determine the fatigue behavior of the PZT films, 100 kHz bipolar square pulses with amplitudes of 8V were applied from an external HP 3314A Function Generator and the polarization changes as monitored in the hysteresis loops using the virtual ground method were recorded up to 10⁸ cycles. For retention behavior, a single bipolar pulse of 8V was applied to each capacitor under test and the polarization was monitored up to 10³ s.

RESULTS AND DISCUSSION

The fatigue and retention behavior of the PZT films were analyzed based on P^* , namely the difference between the maximum polarization in one polarity and the remanent polarization, P_r , in the reverse polarity as a function of cycling or time respectively. Note that P^* is a strong function of the applied voltage (or field) since the voltage determines the maximum polarization achieved. The voltage applied to the films was preset to 8 V.

The values of P^* measured for the films as a function of Zr content and processing temperature, namely 700 and 750°C, are shown in Fig. 1.

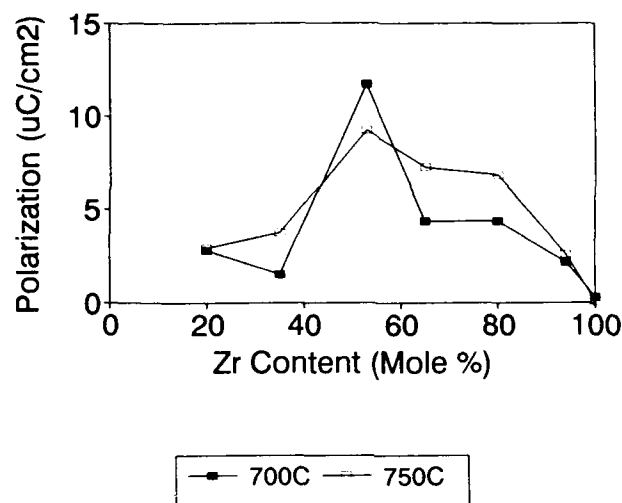


Fig. 1 Value of polarization (P^*) of PZT thin films as a function of Zr content and firing temperature.

The polarization P^* reaches a maximum value at the MPB composition, namely PZT 53/47. As expected, the polarization values are higher for films fired at (i.e., 750C) than for those fired at (i.e., 700C), likely due to enhanced crystallinity and larger grain sizes after firing at the higher temperature. It has been reported that PZT films with larger grain sizes obtained from higher annealing temperature and/or the presence of judiciously controlled excess PbO lead to FE films exhibiting large values of polarization and dielectric constant due to enhanced domain wall mobility [9].

Figs. 2a and b show the effects of cycling using 8 V amplitude 100 kHz square waves on the values of P^* for a series of PZT films with different stoichiometries. The polarizations after fatiguing have been normalized with respect to the polarization values in the virgin capacitors. It can be observed that films fired to higher temperatures are less susceptible to the deleterious effects of fatigue, namely the monotonically decreasing polarization with continuous cycling. In both sets of films fired to 700C and 750C, films with compositions removed from the MPB tend to display superior fatigue resistance; among the films, PZT 53/47 films exhibit the fastest decrease in polarization with cycling. The fatigue behavior was superior in the PZT 53/47 films fired to higher temperatures, i.e. 750C, compared to similar PZT 53/47 films fired to 700C.

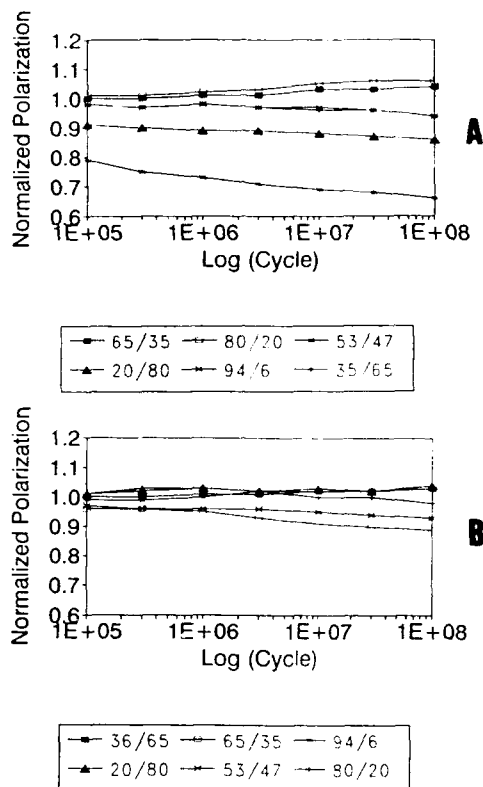


Fig. 2 The effect of fatigue on values of normalized P^* in various PZT thin films fired to a) 700C and b) 750C for 30 min.

For films fired at 700C, rhombohedral PZT films (with high Zr/Ti content) tend to be superior in fatigue behavior compared with tetragonal films. In contrast, for films fired at 750C, the observations are reversed, i.e., tetragonal films exhibit better fatigue resistances than rhombohedral films. It has been documented [10] that in PZT films, the partial pressure or activity of PbO increases with Zr content, e.g., and hence leads to more significant PbO loss (arising from PbO volatility and/or diffusion into substrates) in PZT films fired at higher temperatures.

The retention behaviors of the PZT films fired to 700C and 750C are shown in Figs. 3a and b respectively, where the polarizations are also normalized with respect to the initial values of polarization.

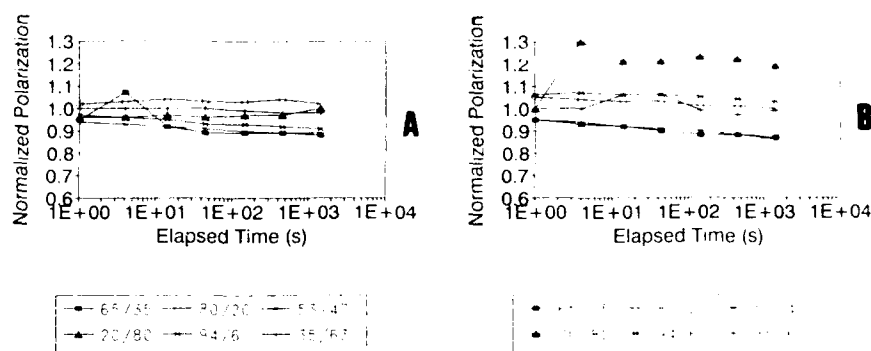


Fig. 3 Retention behavior of various PZT thin films fired to a) 700°C and b) 750°C.

Films near the MPB composition exhibited the least desirable retention behaviors, i.e., the fastest decrease of P^* with time; while films away from the MPB composition (i.e., with highly tetragonal or rhombohedral crystal structures) exhibited superior retention capability, i.e., virtually time-independent polarization values.

One important aspect of processing PZT films is the effect of post-metallization annealing after the deposition of top Pt electrodes. For PZT 53/47 films, post-metallization annealing seems to be deleterious to the overall fatigue behavior: for an unannealed film, the polarization decreased to only 0.93 of its virgin value after 10^8 cycles, whereas for an annealed 53/47 film, the polarization dropped to 0.67 of its virgin value after the same number of polarization reversals. Other PZT films with stoichiometries different from PZT 53/47 appear less affected by such post-metallization annealing with respect to their fatigue behavior. However, the present authors have reported that the leakage current increases with post-metallization annealing temperature ranging from 100°C to 450°C even for such films which have been fired to 700°C [8]. Preliminary ED studies of the Pt substrates where the top PZT films were etched off indicated an appreciable amount of Pb interdiffusion into Pt.

CONCLUSIONS

The fatigue and retention behaviors have been measured for PZT thin films with various stoichiometries fired to 700°C and 750°C. These FE properties are dependent not only on the Zr/Ti stoichiometry, but also the phase assemblage, firing temperature and post-metallization annealing. Films of the MPB composition, PZT 53/47, exhibited the worst fatigue and retention behaviors, i.e., the largest change in polarization values with cycling and time. Regardless of the stoichiometries, PZT films fired to higher temperatures show superior fatigue behavior than those fired at lower temperatures. Rhombohedral PZT films tend to be superior in fatigue resistance; however, at elevated firing temperatures (e.g., 750°C), these rhombohedral films are less desirable in terms of fatigue behavior due to excessive PbO loss.

Post-metallization annealing results in not only poorer fatigue behavior, but also increased leakage currents, probably attributed to PbO diffusion into both the substrates and top Pt electrodes. However, based on judicious choice of composition and firing temperature, it is possible to obtain entirely fatigue-free PZT films up to 10^8 cycles, e.g., in PZT 35/65 films fired to 700°C, which are highly attractive for ferroelectric memory applications.

ACKNOWLEDGMENT

The financial support of the Air Force Office of Scientific Research is gratefully acknowledged.

REFERENCES

- [1] B. Jaffe, W.R. Cook and H. Jaffe, Piezoelectric Ceramics, Acad. Press, NY 1971.
- [2] J.F. Scott, L.D. McMillan and C.A. Araujo, Ferroelectrics 116, 147 (1991).
- [3] K. Hirata, N. Hosokawa, T. Hase, T. Sakuma and Y. Miyasaka, Jpn. J. Appl. Phys. 31, 3021 (1992).
- [4] A. Okada, J. Appl. Phys. 48 (7), pp. 2905-2909 (1977).
- [5] M. Oikawa and K. Toda, Appl. Phys. Lett. 29 (8), pp. 491-492 (1976).
- [6] D. Roy and S.B. Krupanidhi, J. Mater. Res. 7, 2521 (1992).
- [7] H. Tomonani, T. Ishiu, K. Sakata, and T. Takenaka, Jpn. J. Appl. Phys. 31, 2998 (1992).
- [8] G. Teowee, J.M. Boulton, E.A. Kneer, M.N. Orr, D.P. Birnie III, D.R. Uhlmann, S.C. Lee, K.F. Galloway and R.D. Schrimpf, to be published in Proc. 8th ISAF (1992).
- [9] G. Teowee, J.M. Boulton and D.R. Uhlmann, Mat. Res. Soc. Symp. Proc., Vol. 243, 255 (1992).
- [10] G. Teowee, J.M. Boulton, S. Motakef, D.R. Uhlmann, B.J.J. Zelinski, R. Zannoni and M. Moon, Proc. SPIE 1758, 236.

A Novel Method for Determining the Curie Temperature of Ferroelectric Films

*Chi Kong Kwok and Seshu B. Desu**

Department of Materials Science and Engineering, Virginia Polytechnic Institute and State University, Blacksburg, VA 24061.

ABSTRACT

A novel technique to measure the Curie temperature of ferroelectric thin films has been developed. The method is based on identifying changes in slope of film stress vs temperature plot. At the Curie temperature, ferroelectric films undergo a phase transition from ferroelectric phase to paraelectric phase. Due to this phase transformation, physical properties of films such as elastic constants and coefficients of thermal expansion also change at the Curie temperature. Consequently, at this temperature the temperature coefficient of film stress changes since it is related to elastic constants and thermal expansion coefficient. Thus, by measuring the film stress as a function of temperature, the Curie temperature can be determined. The Curie temperatures measured by this method are in good agreement with the literature values. Small discrepancies that were observed can be attributed to the intrinsic stresses present in the films.

A Novel Method for Determining the Curie Temperature of Ferroelectric Films

The high values of switchable spontaneous polarization, dielectric constant, pyroelectric coefficient, piezoelectric coefficient and electro-optic coefficient of ferroelectric films have been exploited for several applications including nonvolatile electronic memories, dynamic random access memories, infrared detectors, acoustic transducers, waveguide devices and optical memories [1]. The upper operating temperature of these devices is limited by the Curie temperature (T_c) of the ferroelectric film because above the Curie temperature the material becomes paraelectric and loses all its interesting ferroelectric properties. Therefore, for a given application the Curie temperature limits the choice of material. For example, because of its low T_c BaTiO₃ is not a preferred material for nonvolatile memory applications when compared to Pb(Zr_{1-x}Ti_x)O₃ (PZT), although the ferroelectric properties are comparable. In addition to limiting the material choice, T_c also limit the amount of dopants used to improve certain characteristics of a material since the dopants can reduce the Curie temperature. For example, La-doping of Pb(Zr_{1-x}Ti_x)O₃, despite its advantages, is limited to around 2 atom% because La additions reduce T_c in a linear manner at the rate of approximately 37°C per atom% La [2].

The nature of ferroelectric to paraelectric transition (i.e. sharp vs broad transition) and T_c are, in general, sensitive functions of microstructure, dopant concentration, and more importantly, state and amount of mechanical stress [3]. For thin films, mechanical stresses are very important since stresses are always present in the film, unless they are free standing. For example, it is shown that compressive stresses of the order of 400 MPa increased T_c of BaTiO₃ thin films by about 29°C [4].

It is apparent from the above discussion that an accurate determination of T_c of ferroelectric films is crucial. Although several standard techniques are available, most of these require the deposition of electrodes because they depend on changes in the

temperature dependence of electrical properties (e.g., polarization, dielectric constant). In this letter, a simple method is reported for determining the Curie temperature of ferroelectric films, which does not require any electrodes. In this technique, T_c of a ferroelectric film is obtained from the slope changes in film stress vs temperature plots. Concomitantly, the effect of film stress on the Curie temperature can also be evaluated. In addition, using this method the elastic stiffness and thermal expansion coefficient of the film can also be obtained [4].

The contribution of the thermoelastic component (thermal stress component), σ_{th} , arising because of the difference in the linear thermal expansion coefficients of the substrate and the film materials, to the total film stress, σ_{tot} , is defined by the expression

$$\sigma_{th} = [E_f/(1-\nu_f)] T_1 \int_{T_1}^{T_2} (\alpha_s - \alpha_f) dT \quad (1)$$

where E_f and ν_f are, respectively, the Young's modulus and Poisson's ratio for the film material; α_s and α_f are the linear thermal expansion coefficients of the substrate and film, respectively and T_1 and T_2 is the temperature interval. From equation 1, the slope of a stress vs temperature plot can be related to the thermal expansion coefficient by:

$$(d\sigma/dT) = [E_f/(1-\nu_f)](\alpha_s - \alpha_f) \quad (2)$$

For obtaining equation 2, the values of E , α , and ν are assumed to be independent of temperature, which is valid within the uncertainty of the experimental techniques employed.

For a given substrate, the slope of the stress-temperature curve is determined by the film properties E_f , ν_f and α_f (equation 2). A change in the slope of the stress-temperature curve is expected at the Curie Point because ferroelectric and paraelectric phases have different properties. Thus, by measuring the film stress as a function of temperature T_c can be obtained, in principle, for a ferroelectric film. Similarly, other characteristic phase transition temperatures of the films can also be obtained. It should be pointed out that other components of total film stress such as extrinsic and intrinsic stresses may have an influence on the nature of changes in the slope of the stress-temperature curve.

The stress of the films was measured using an optically leveraged laser-beam apparatus (Flexus F2400). This tester is capable of running *in-situ* stress measurements at temperatures up to 900°C. It uses a laser as the probing source and a position-sensitive detector to measure the displacement of the laser reflection from the wafer surface. These displacements are converted to radii of curvature. The sensitivity of this tester is limited to a radius of curvature of 4000 m, which corresponds to about 1.3 MPa for a 0.3 μm film on a 525 μm thick Si substrate. For the case of a homogeneous, isotropic thin film deposited on a thick substrate where the film-substrate bond is strong enough to suppress slippage, the total film stress is related to the radius of curvature (R) of the substrate by Stoney's equation [5]

$$\sigma_{tot} = [E_s/(1-\nu_s)](t_s^2/6t_f)(1/R) \quad (3)$$

where t_s and t_f are thicknesses of substrate and film, respectively and $E_s/(1-\nu_s)$ is the biaxial modulus of the substrate.

PZT films with three compositions, Zr/Ti ratios of 0/100, 53/47, and 75/25 were deposited on 100 mm diameter Pt coated Si wafers by a sol-gel process [6]. Film preparation by sol-gel process involves precursor (sol) preparation, hydrolysis, polycondensation, film formation, and sintering. In this study, PZT films were fabricated from sol-gel precursors (0.4M) of lead acetate, titanium isopropoxide, and zirconium n-propoxide dissolved in glacial acetic acid and n-propanol. The proper amounts of Zr and Ti alkoxides were premixed in the presence of propanol and acetic acid before the addition of lead acetate. These solutions were hydrolyzed with appropriate amounts of water and were further diluted with propanol and acetic acid to form the final precursors. Thin films were deposited by spin coating on Pt coated Si substrates using spin speed of 3000 rpm. After spin coating, each film was dried at 150°C for 5 minutes on a hot plate. Film thicknesses were around 0.3 μm after two coatings. The configuration of the PZT film on Pt wafers is as follows: PZT (0.3 μm)/Pt (400 nm)/Ti (30 nm)/SiO₂ (200 nm)/(100) Si substrate. Detailed description of the PZT film deposition can be found in Reference [7].

For each sample, two identical heating-cooling cycles were run sequentially. The samples were heated in two identical annealing cycles from room temperature to 650°C and cooled down to room temperature twice in ambient condition. The heating rate was 5°C/min and the cooling rate was 2.5°C/min. The main reason for annealing the samples in two cycles is that all irreversible transitions are presumably completed in the first cycle and the second heating-cooling cycle only involves the reversible Curie transition.

The stress-temperature plots of PZT films with Zr/Ti ratios of 75/25, 53/47, and 0/100 during the second heating-cooling cycles are shown in Figures 1, 2, and 3, respectively. The square symbols indicate measurements during heating while inverted triangles symbols indicate measurements during cooling. All three plots exhibit similar stress response as a function of annealing temperature. However, the pure PbTiO₃ film has a more abrupt change in stress at temperatures around 450°C. The film stresses of these PZT films decrease from initial stresses ranging from 800 to 1300 MPa in tension after the first annealing cycle. The decrease in stress is relatively linear with the annealing temperature until a break of linearity is observed at a higher temperature. Evidently, the variation of film stress as a function of annealing temperature is a reversible process. The stress-temperature profiles during heating matched very well to those during cooling. This indicates that the irreversible transitions and reactions are presumably completed after the first annealing cycle. As expected, changes in slope for the stress-temperature curves were observed at the Curie transition due to the changes in physical properties. When the samples underwent paraelectric (cubic) to ferroelectric (noncubic) transformations, the elastic constant and the coefficient of thermal expansion (α_f) of these samples also underwent a change. Consequently, these changes of elastic constant and α_f resulted in the discontinuity found in the stress-temperature profiles at the Curie temperature. Hence, Curie temperatures can be determined from these stress-temperature plots and their values are tabulated in Table I. It should be noted that the experimental Curie temperature values presented in table I are the averages of at least four measurements.

The Curie temperatures of PZT films measured by the film stress method are in qualitative agreement with those obtained from the bulk PZT ceramics [8], but Table I shows they are 17°C to 28°C higher than in these corresponding bulk ceramics. This can be attributed to the large intrinsic stresses present in the films. The ferroelectric to paraelectric transition (at the Curie point) results in a volume decrease, the intrinsic

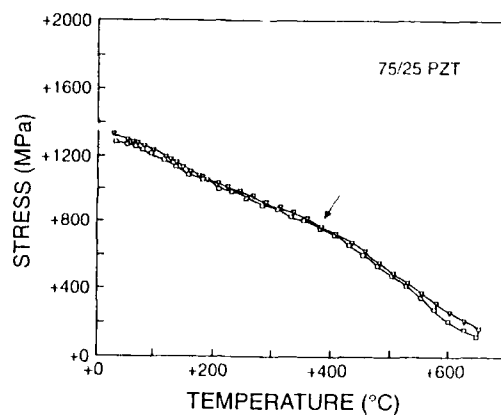


Figure 1. Film stress of the 75/25 PZT film as a function of annealing temperature. The square symbols indicate measurements during heating, inverted triangles symbols indicate measurements during cooling.

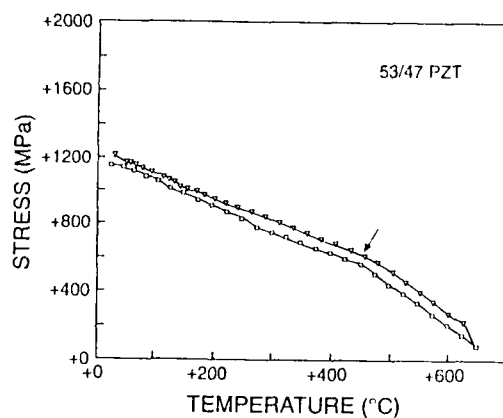


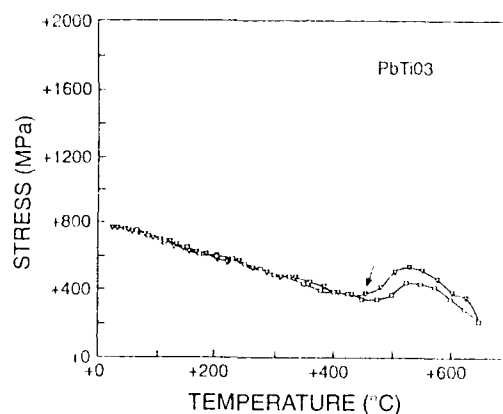
Figure 2. Film stress of the 53/47 PZT film as a function of annealing temperature.

tensile stresses would counteract this volume decrease and therefore increase the Curie temperature. For PbTiO_3 , the volume change at T_c is very high when compared with PZT films. Therefore, the effect of extrinsic stress on temperature dependence of stress is significant for PbTiO_3 . This may explain the non-linear change in stress at T_c for PbTiO_3 (Figure 3).

Table 1 Curie Temperature as a Function of CompositionComposition T_c^{exp} ($^{\circ}\text{C}$)* T_c^{ref} ($^{\circ}\text{C}$)

PbTiO ₃	507 \pm 8	490
53/47	439 \pm 10	411
75/25	356 \pm 13	335

T_c^{exp} = Curie temperature measured in this experiment ; T_c^{ref} = Curie temperature given in the literature ⁶ ; * Average of at least four measurements

**Figure 3.** Film stress of the PbTiO₃ film as a function of annealing temperature.

In summary, a novel method for determination of Curie temperature of ferroelectric films by film stress measurement is described. The Curie temperatures measured by the film stress method are in good agreement with the literature values for bulk materials. The discrepancy of Curie temperature can be explained by the large intrinsic tensile stresses present in the film.

REFERENCES

- 1) L.M. Sheppard, *Ceram. Bull.*, 71, 85 (1992).
- 2) G.H. Haertling, *Ferroelectrics*, 75, 25 (1987).
- 3) G. Arlt, D. Hennings and A. de With, *J. Appl. Phys.*, 58, 1619 (1985).
- 4) S.B. Desu, *J. Electrochem.Soc.*, in press.
- 5) G. Stoney, *Proc. R. Soc. (London)* **A82**, 172 (1909).
- 6) J. Blum and S. Gorkovich, *J. of Mat. Sci.* **20**, 4479 (1985).
- 7) Chi Kong Kwok, Ph. D. Dissertation, Virginia Polytechnic Institute & State University, July 1992.
- 8) *Landolt-Bornstein Series, Vol. 3, Ferro- and antiferroelectric substances*, K. Hellwege, ed. (Springer-Verlag, Berlin, 1969), pp.269.

STUDY OF PbTiO_3 FORMATION KINETICS BY AN IN-SITU STRESS MEASUREMENT TECHNIQUE

CHEN C. LI AND SESHU B. DESU

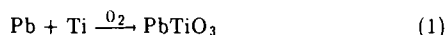
Department of Materials Science and Engineering, Virginia Polytechnic Institute and
State University, Blacksburg, VA 24061

ABSTRACT

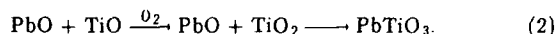
The primary objective of this study is to demonstrate an in-situ stress measurement technique for the study of formation kinetics of multicomponent thin films such as PbTiO_3 . Film stress-temperature and film stress-time plots have been successfully used to monitor the phase formation of PbTiO_3 films in an in-situ way. It is believed that the mechanism of this reaction was dominated by grain boundary diffusion of the participating cations. The activation energy of the PbTiO_3 phase formation from PbO/TiO_2 double layers was estimated to be 108 kcal/mole.

INTRODUCTION

Thin films of multicomponent oxides such as PbTiO_3 have been extensively studied due to their remarkable ferroelectric, pyroelectric, and piezoelectric properties. The applications of these thin films include opto-electronic devices, sensors, transducers, and non-volatile memory devices [1]. Variety of vapor deposition techniques have been applied to the fabrication of these thin films. Physical vapor deposition techniques such as sputtering and evaporation often encounter a problem of controlling film stoichiometry. One of the methods of overcoming this problem is the multilayer approach [2], in which the composition of the films is accurately controlled by depositing designed thickness of individual layers (e.g. $A + B \rightarrow AB$). In PbTiO_3 system, the multilayers used can be metallic layers,



or oxide layers



In order to optimize the process of thin film fabrications, it is of great importance to understand the formation kinetics of thin films. When a thin film, denoted as film A, is deposited on a substrate, the total film stress of film A can be a function of temperature, time, substrate and film thickness [3]. If a second film, denoted as film B, is deposited on top of film A, the total film stress of this bilayer can be influenced not only by the aforementioned factors but also by chemical reaction, if any, between film A and film B. Assume that film stresses of the individual layers are constant at a given temperature, when a product layer of AB is formed at the interface between A and B by chemical reaction, total film stresses of the multilayers could be defined by the thickness of films A, B, and AB. Since the extent of reaction is time-dependent at a given temperature, the total stress of the multilayer is also time-dependent. Therefore, the formation kinetics of multicomponent thin films can be studied by using the in-situ stress measurement technique.

In this report it is our goal to demonstrate this novel in-situ stress measurement technique for studying the formation kinetics of multicomponent thin films.

EXPERIMENTAL PROCEDURE

The electron beam evaporation system for film deposition was described in detailed elsewhere [4]. Before deposition, the system was pumped down to 4×10^{-8} torr, rising to $2-3 \times 10^{-7}$ torr during deposition. All the depositions were performed at ambient temperature with a deposition rate of 0.2–0.5 nm/s. Total film thickness was kept at 300nm.

High purity, vapor deposition grade oxides (PbO and TiO) were used as the evaporation sources. TiO₂ was not used due to its decomposition during deposition. Based on theoretical calculations and taking into account the loss of Pb (10 mol.% of PbO was added), the thicknesses of the PbO and TiO layers were approximately 200nm and 100nm, respectively. The 2-inch sapphire substrates were cleaned by a series of organic solutions and deionized water followed by drying in N₂ gas.

Film stress measurements as a function of temperature and time were performed for the PbO/TiO oxide multilayers, on 2-inch diameter sapphire substrates in air. The heating rate was 5°C/min. The sample curvature was calculated from the change in position of a reflected laser beam. The position was measured by a position sensitive detector while the beam was scanned across the sample. The total film stresses were calculated by comparing the substrate curvature before and after film deposition using the Stoney equation [5], which yields the biaxial stress in the thin films parallel to the substrate:

$$\sigma = \frac{E_s}{6(1-\nu_s)} \frac{t_s^2}{t_f} \frac{1}{R} \quad (3)$$

where E_s , ν_s , and t_s are Young's modulus, Poisson's ratio, and thickness of the substrate, respectively, and t_f is the film thickness. R is an effective radius of curvature of the substrate determined by $R = 1/(1/R_2 - 1/R_1)$, where R_1 and R_2 are the substrate radii of curvature before and after film deposition. This formula is applicable when t_f is far smaller than t_s and the central wafer deflection is much smaller than the diameter of the wafer. Both conditions are met in the present work.

Based on this technique, stress-temperature and stress-time plots of the PbO/TiO/sapphire specimens were obtained. In order to quantify the extent of the reaction and the morphological change associated with film stresses development, separate tests were carried out, such as x-ray diffraction analysis for phase determination and scanning and transmission electron microscopy for morphology observation.

RESULTS AND DISCUSSION

After initial deposition of the individual PbO and TiO layers, oxidation of the oxide layers would take place first. From our previous study [6] it was reported that both of the oxide layers completely oxidized at $\leq 500^\circ\text{C}$. It was also reported [7] that the reaction between lead oxide and titanium oxide could not take place below 400°C and was very slow at $\leq 500^\circ\text{C}$. Accordingly, when the temperature raised to 500°C , the diffusion couple of PbO/TiO multilayers would become PbO/TiO₂ multilayers, and the reaction between PbO and TiO₂ could be neglected. The formation of PbTiO₃ from the PbO/TiO₂ multilayers was then activated at $\geq 500^\circ\text{C}$. From now on the study concentrates on the temperature range from 550°C to 625°C .

In-Situ Study of PbTiO₃ Formation by Stress Measurement

Fig. 1 depicts a typical stress-temperature plot for the multilayers subjected to annealing in air at 575°C for 4 hours with a heating rate of $5^\circ\text{C}/\text{min}$. The as-deposited multilayers were under tension with a film stress of around 100 MPa. It was found that the as-deposited film stress was very sensitive to deposition rate. As the temperature was raised, the film stress started decreasing at around 300°C and reached a local minimum at around 400°C , then increased slightly and decreased to a state where the film was nearly stress free at 500°C . This region of the curve was attributed to the oxidation of the multilayers. The uptake of oxygen into the films may have resulted in increased film volume, generating compressive stresses. Above 500°C , the stress-temperature curve entirely fell into the compressive region. Compressive stress continued developing in the films when the temperature was above 500°C and reached a local minimum in the isothermal region. This section of the curve was attributed to the formation of the PbTiO₃ phase in the film. These compressive film stresses then started to relax. After 4 hours at 575°C the film was cooled down to room

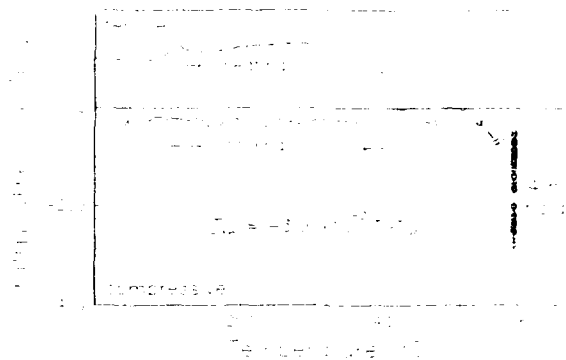


Fig. 1 Typical stress-temperature plots of PbTiO_3 formation

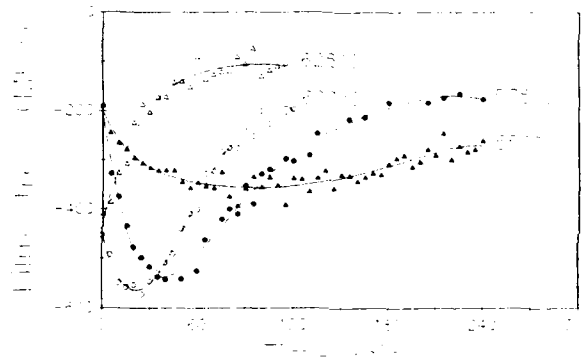


Fig. 2 Stress-time plots of PbTiO_3 formation

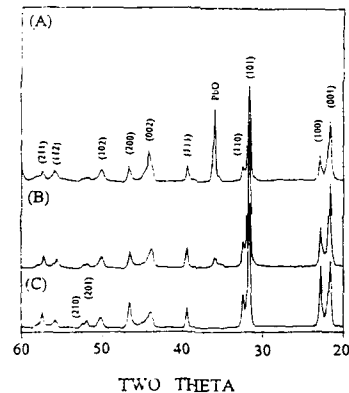


Fig. 3 XRD spectra of PbTiO_3 films annealed at 600°C for (A) 0.1 (B) 10 (C) 30 minutes

temperature. Film stresses in this region showed very good linearity against temperature. Therefore thermal stress (σ_{th}) could be calculated as:

$$\sigma_{th} = E_f \Delta \alpha \Delta T / (1 - \nu_f) \quad (4)$$

where ΔT is the difference between T and the annealing temperature and the value, $E_f \Delta \alpha / (1 - \nu_f)$, the product of the biaxial modulus of the film and the difference in thermal expansion coefficients between film and substrate, was $-3.02 \times 10^{-2} \text{ MPa} \cdot \text{K}^{-1}$.

The isothermal region in Fig. 1 could be plotted as film stress against time. Fig. 2 shows the film stress-time plots for several different temperatures. Again, film stresses reached minima in the plots. For instance, the minimum was found at around 40 minutes for 575°C . Lowering the annealing temperature increased the time to achieve a minimum, e.g. around 100 minutes for 550°C . Conversely, raising the annealing temperature decreased the time to achieve a minimum e.g. around 20 minutes for 600°C . By annealing at 625°C , the minimum occurred too quickly to appear on the plot. It was believed that the development of compressive stresses in the region where the annealing time went from 0 to the minimum point should be responsible for the compound formation of the PbTiO_3 phase. It was confirmed by x-ray diffraction analysis (as shown in Fig. 3) that the minima in the stress-time plots were reached when the formation of the PbTiO_3 phases were completed.

It is believed that formation of the PbTiO_3 phase in the diffusion couple of PbO/TiO_2 multilayers was dominated by the interdiffusion of the participating species and vacancy movement. During formation, the generation of compressive stresses in the film could be attributed to the expansion of the lateral dimension of the films, caused by the generation of vacancies and grain boundaries. After the formation was completed, the high strain energy stored by vacancies and grain boundaries needed to be released. Therefore, tensile stresses were generated by the elimination of vacancies and grain boundaries in the films, and the total film stresses were reduced.

Formation Kinetics

When sequentially deposited films are all very thin compared with the substrate, each film imposes a separate bending moment and separate curvature. Since moments are additive so are the curvatures.

$$1/R_1 + 1/R_2 + \dots = \frac{1 - \nu_s}{E_s} \frac{6}{d_s^2} (\sigma_1 d_1 + \sigma_2 d_2 + \dots) \quad (5)$$

$$\sigma d \approx \sum_{i=1}^n \sigma_i d_i, \quad (6)$$

where σ and d denote total film stress and thickness, respectively.

For the multilayers PbO/TiO_2 on the sapphire substrate, the total film stress can be written as:

$$\sigma d = \sigma_a d_a + \sigma_b d_b, \quad (7)$$

where (a) and (b) denote PbO and TiO_2 and later (ab) is PbTiO_3 .

Assume that, first, stresses of the PbO , TiO_2 and PbTiO_3 layers (σ_a , σ_b , and σ_{ab}) are constant during the formation process. Second, the total thickness (d) of the multilayers is constant, and third, initial stress is defined as $\sigma_i = (\sigma_a d_a + \sigma_b d_b) / d$, where $d_a / d_b \approx 2/1$. The value of σ_i is obtained from the stress-temperature plot where the temperature is 500°C .

At a certain fraction of reaction where a layer of PbTiO_3 (d_{ab}) is formed, the total film stress becomes

$$\begin{aligned}
 \sigma &= \frac{1}{d} \left[\sigma_a \left(d_a - \frac{2}{3} d_{ab} \right) + \sigma_b \left(d_b - \frac{1}{3} d_{ab} \right) + \sigma_{ab} d_{ab} \right] \\
 &= \frac{1}{d} \left[(\sigma_a d_a + \sigma_b d_b) + d_{ab} \left(\sigma_{ab} - \frac{2\sigma_a + \sigma_b}{3} \right) \right] \\
 &= \left(\frac{\sigma_a d_a + \sigma_b d_b}{d} \right) + \left(\sigma_{ab} - \frac{2\sigma_a + \sigma_b}{3} \right) \left(\frac{d_{ab}}{d} \right) \\
 &= \sigma_i + (\sigma_{ab} - \sigma_i) \left(\frac{d_{ab}}{d} \right)
 \end{aligned}$$

$$\text{Therefore, } \frac{d_{ab}}{d} = \frac{\sigma - \sigma_i}{\sigma_{ab} - \sigma_i} = f(T, t). \quad (8)$$

From equation (8) the thickness of the PbTiO_3 layer formed can be deduced as

$$d_{ab} = d \cdot f. \quad (9)$$

The growth of the PbTiO_3 layer is governed by the parabolic law, i.e., $(d_{ab})^2 = kt$, where k is the rate constant. Fig. 4 illustrates the kinetics of PbTiO_3 growth at three different temperatures. Since the data of Fig. 4 represents a diffusion-controlled

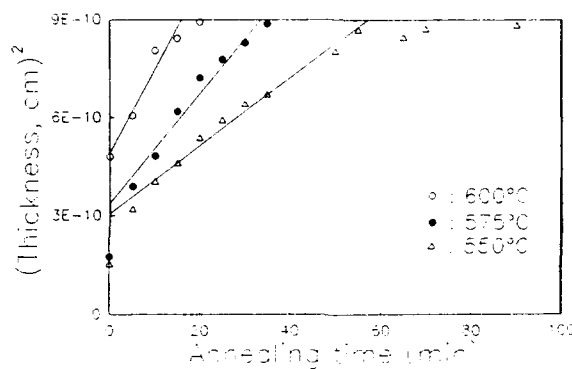


Fig. 4 Growth kinetics of PbTiO_3 at three different temperatures

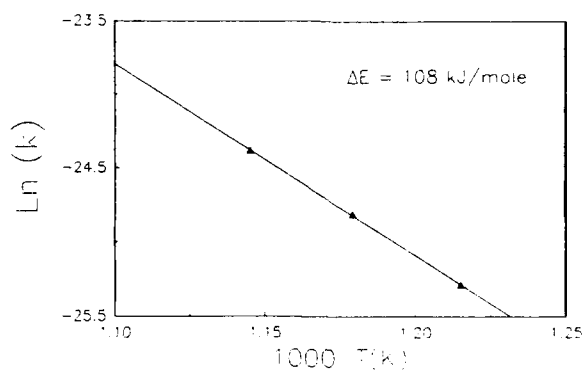


Fig. 5 Arrhenius plot of PbTiO_3 formation

growth process the chemical interdiffusion coefficient (D) can be determined from the rate constant, $k = 4D$. The rate constant, k , has an Arrhenius behavior as shown in Fig. 5. The straight line fit points to a thermally activated growth of PbTiO_3 on sapphire. The activation was estimated to be 108 kJ/mole. This value is in excellent agreement with the literature values [7].

For the formation of ionic crystals such as PbTiO_3 it is believed that the slower partner that essentially determines the reaction rate. From the rate constants, the chemical diffusion constant of PbTiO_3 formation in this work could be obtained as $6.8 \times 10^{-14} \text{ cm}^2/\text{sec}$ at 575°C . The chemical diffusion constants at this temperature were estimated to be $1 \times 10^{-12} \text{ cm}^2/\text{sec}$ for PbO [8] and $7.4 \times 10^{-16} \text{ cm}^2/\text{sec}$ for TiO_2 [8]. Our experimental value is approximately an order lower than that for PbO and two order higher than that for TiO_2 . This would suggest that transport of Ti^{4+} ions through the product layer is the rate-determining step. Furthermore it is believed that the participating components mainly diffuse through the grain boundaries. Accordingly the diffusion constant of the reaction can be written as $D_{\text{gl}} = 3 \times 10^{-7} \exp(-108,000/kT) \text{ cm}^2/\text{sec}$. From the grain boundary diffusion constant, one can extrapolate the rate constant of the PbTiO_3 formation at 500°C . The amount of reaction between PbO and TiO_2 films annealed at 500°C for 0.1 minute was calculated to be 2%. This value is neglectable and is consistent with the literature report [7].

SUMMARY

In-situ stress measurement technique has been successfully developed to study the formation kinetics of multi-component thin films such as PbTiO_3 . Using the multilayer approach, film composition can be simply controlled by the thickness of the individual layers, i.e. PbO/TiO_2 . During annealing, the TiO_2 layer converts into TiO phase at temperatures less than 500°C . Above 500°C , the formation of the PbTiO_3 layer at the interface of PbO/TiO_2 altered the total stress of the multilayers. By monitoring stress changes in the multilayers, the in-situ formation kinetics of PbTiO_3 films was successfully examined. The activation energy of PbTiO_3 formation was estimated to be 108 KJ/mole which is in excellent agreement with the literature value. It is believed that the formation of PbTiO_3 phase was dominated by grain boundary diffusion mechanism because of the very fine grain size in the films.

ACKNOWLEDGMENT

This work was financially supported by DARPA through a project from ONR, and by The Center for Advanced Ceramic Materials at Virginia Tech.

REFERENCES

1. M. Okuyama and Y. Hamakawa, *Int. J. Engng. Sci.*, 29(3), 391 (1991)
2. E. R. Myers and A. I. Kingon, "Ferroelectric Thin Films," Materials Research Society Symposium Proceedings, Vol. 200, Materials Research Society, Pittsburgh, PA, 1990
3. J. C. Braveman, W. D. Nix, D. M. Barnett, and D. A. Smith, "Thin Films: Stresses and Mechanical Properties," Materials Research Society Symposium Proceedings, Vol. 130, Materials Research Society, Pittsburgh, PA, 1989
4. C. C. Li and S. B. Desu, *Ceramic Transactions*, 25, 59 (1992)
5. G. G. Stoney, *Proc. Royal Society London*, A82, 172, (1909)
6. C. C. and S. B. Desu, unpublished work
7. G. Janson, E. Z. Freidenfelds, I. Skomorokha, and O. S. Maksimova, *Uch. Zap. Rzhsk. Politekh. Inst.* 16, 387 (1965)
8. S. Mrowec, "Defects and Diffusion in Solids: An Introduction," Elsevier Scientific Publishing Company, Amsterdam, Netherlands, 1980

ELECTRICAL PROPERTIES OF AMORPHOUS THIN FILMS OF FERROELECTRIC OXIDES PREPARED BY SOL-GEL TECHNIQUE

Yuhuan Xu, Ren Xu*, Chih-Hsing Cheng and John D. Mackenzie
Department of Materials Science and Engineering, University of California,
Los Angeles, CA 90024, USA

*Current address: Department of Materials Science and Engineering, The University of Utah,
Salt Lake City, Utah 84112

ABSTRACT

Amorphous thin films of ferroelectric oxides including lead zirconate titanate (PZT), barium titanate (BaTiO_3) and lithium niobate (LiNbO_3) on several kinds of substrates were prepared by a sol-gel technique. The heat-treatment temperatures for preparation of amorphous thin films were much lower than those for the corresponding crystalline ferroelectric thin films. Electrical properties of these amorphous thin films were measured and compared with those of corresponding crystalline films. These amorphous thin films exhibited ferroelectric-like behavior. A model of the microstructure of these films is proposed.

INTRODUCTION

A ferroelectric is normally a spontaneously polarized material with its polarization reversible under an external electric field. Unique properties of ferroelectric materials such as piezoelectric, electro-optic, electro-acoustic, and nonlinear optic effects have made possible a variety of device applications.[1] Ferroelectric thin films have received increased attention in recent years and many deposition techniques have been employed for their preparation.[2] A variety of novel devices, such as non-volatile memories, electro-acoustic transducers, pyroelectric infrared detectors, electrooptic modulators, optical waveguides, etc. have been demonstrated.[3]

One of the main obstacles between demonstrational waveguide devices and commercial applications is the optical loss due to grain boundary scattering. Consequently, effort have been directed to the fabrication of single crystal (such as LiNbO_3) waveguides by techniques such as RF sputtering, liquid phase epitaxy and ion-exchange. It is also in principle possible to avoid the problems of grain boundary scattering by completely eliminating crystallinity in these waveguides. From the materials science point of view, such endeavour involves the synthesis of an amorphous material that presents at least some of the typical ferroelectric or ferroelectric-like behavior.

Amorphous ferroelectricity was first suggested by Lines[4] and partially experimentally demonstrated[5] on rapidly quenched LiNbO_3 and LiTaO_3 glasses, where a ferroelectric or ferroelectric-like phase transition was reported at temperatures below the crystallization temperature. Other observations of ferroelectric or ferroelectric-like phase transitions in LiNbO_3 and PbTiO_3 systems[6-8] have been reported in the past where RF sputtering was also used to form amorphous films of these systems. However, there has been no report of P - E hysteresis loops and pyroelectric coefficients of these materials, mainly due to the difficulties in making these amorphous materials in large enough quantities and geometries suitable for property measurement. Despite these previous reports, the confirmation of amorphous ferroelectricity still awaits more conclusive experiments. Observation of P - E hysteresis and improvement of processing techniques are needed for this purpose.

PREPARATION OF AMORPHOUS THIN FILMS

Sol-gel processing is a demonstrated technique for fabricating amorphous and crystalline oxide thin films in the last two decades [9,10]. Not surprisingly, considerable efforts were devoted to the fabrication of crystalline ferroelectric thin films by this technique. However, there has been no effort in utilizing this technique to fabricate amorphous thin films of known ferroelectric systems. For example, amorphous LiNbO_3 thin films can be fabricated by the sol-gel technique (see the flow chart in Fig. 1). Lithium and niobium ethoxides were known to form intermolecular complexes often called double alkoxides upon refluxing for extended periods of time. [11-14]. The solution structure can be controlled by allowing complexation of LiOC_2H_5 with $\text{Nb}(\text{OC}_2\text{H}_5)_5$ forming the double alkoxide $\text{LiNb}(\text{OC}_2\text{H}_5)_6$. This is a slow reaction and needs sufficient time for completion. In ethanol solutions, the $\text{LiNb}(\text{OC}_2\text{H}_5)_6$ double alkoxide was stable and can be characterized by FTIR and NMR. [14]. This double alkoxide in its crystalline form closely resembles the local atomic configuration of crystalline LiNbO_3 . [15]. Other intermolecular complexes with different Li/Nb ratio were not found and generally not expected for alkali-Nb alkoxide complexes. [13]. It was our intention to control the formation of such double alkoxides in the solution stage and further to preserve this atomic level configuration through the gelation stage so that the resulting film consists of similar local units as those in crystalline LiNbO_3 .

Amorphous LiNbO_3 gel films were deposited on substrates (such as metal Pt, Ti, silicon and Au passivated silicon wafers) and stabilized at 100°C in air for 2 hours. X-ray diffraction and electron diffraction of the sample are showed in Fig. 2, where the diffraction patterns and diffused rings indicate the amorphous nature of the film. High resolution electron microscopy also confirmed that no crystallites with a size larger than 20 \AA were observed. [16]

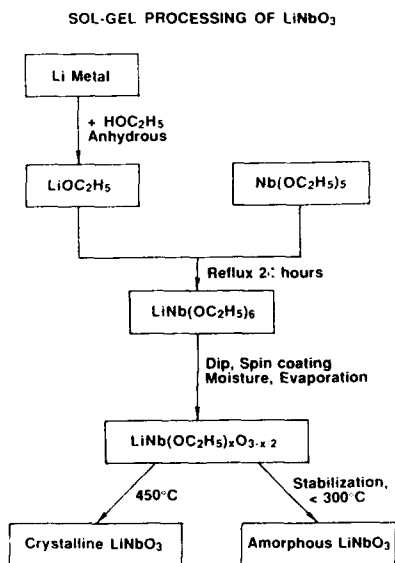


Fig. 1 A flow chart for the preparation of LiNbO_3 films by the sol-gel method.

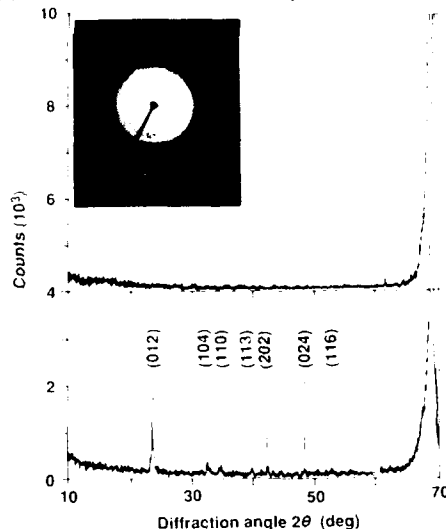


Fig. 2 X-ray (top spectrum) and electron diffraction pattern of the amorphous LiNbO_3 film heat-treated at 100°C . The diffuse ring indicated the amorphous nature of the thin film. Crystallization occurred at temperatures above 350°C . The bottom spectrum shows the indexed X-ray diffraction peaks of crystalline LiNbO_3 film on silicon (100) single crystal wafer.

Amorphous lead zirconate titanate (PZT) and amorphous barium titanate (BaTiO_3) thin films on metal Ti substrate were also prepared by using the sol-gel method. It has been confirmed by X-ray and electron diffraction that these films heated at temperatures below 400°C are still amorphous [17].

ELECTRICAL PROPERTIES

Electrical characterizations was facilitated with a Au/amorphous film/Au-passivated silicon sandwich structure. A modified Sawyer-Tower bridge was used for P - E hysteresis loop measurements. Figure 3(a) shows the 60Hz hysteresis loops of amorphous LiNbO_3 films coated on Au passivated silicon wafers (heat-treated at 100°C for 2 hours). P_r and E_c values of $7.8\mu\text{C}/\text{cm}^2$ and $110\text{KV}/\text{cm}$, respectively, were found to be in the same order of magnitude of those of single crystal LiNbO_3 . Figure 3(b) and 3(c) show the loops of amorphous PZT and amorphous BaTiO_3 thin films, respectively.

Dielectric properties of the amorphous films as a function of frequency were measured at room temperature. As an example, the dielectric spectra of amorphous LiNbO_3 is shown in Fig. 4. Four peaks caused by piezoelectric resonance absorption at 115kHz , 1.9MHz , 7.5MHz and 10.9MHz were observed.

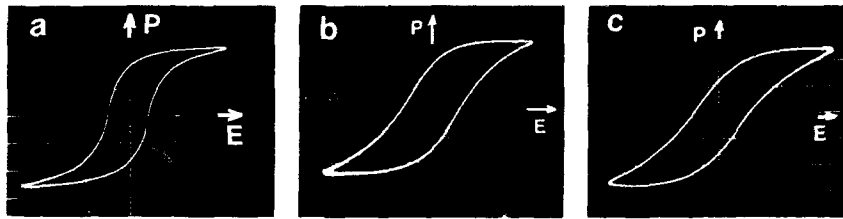


Fig.3 60Hz P - E hysteresis loops of amorphous thin films. (a) amorphous LiNbO_3 , scale of P : $5.6\mu\text{C}/\text{cm}^2/\text{div.}$ and scale of E : $14.7\text{kV}/\text{mm}/\text{div.}$; (b) amorphous PZT, scale of P : $2\mu\text{C}/\text{cm}^2/\text{div.}$ and scale of E : $6.5\text{kV}/\text{mm}/\text{div.}$; and (c) amorphous BaTiO_3 , scale of P : $1.6\mu\text{C}/\text{cm}^2/\text{div.}$ and scale of E : $11\text{kV}/\text{mm}/\text{div.}$

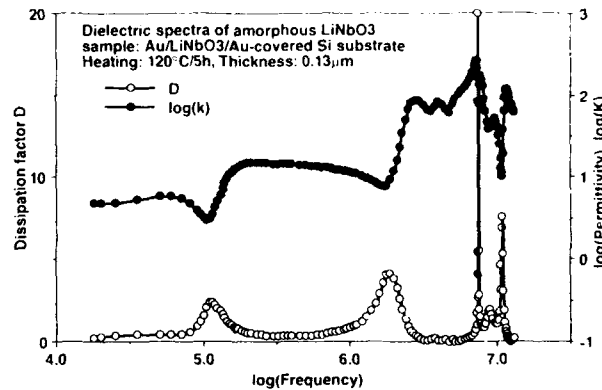


Fig. 4 Dielectric permittivity and dissipation factor change with frequency in amorphous LiNbO_3 thin film.

Fig. 5 Pyroelectric current $i_p(T)$ of Au / amorphous PZT thin film / Au sample. Measurements were made at different times after poling.

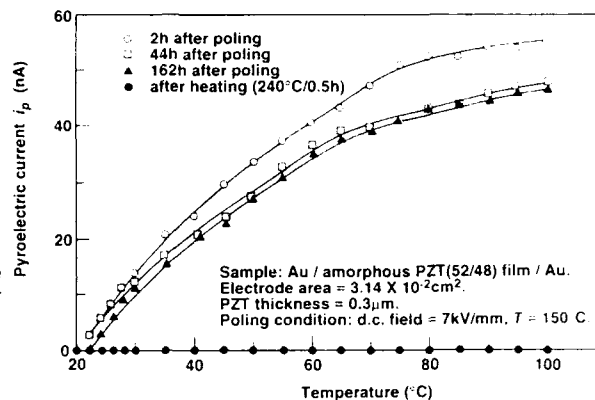


Table I Electrical Properties of Amorphous BaTiO_3 , $\text{Pb}(\text{Zr}_{0.52}\text{Ti}_{0.48})\text{O}_3$, and LiNbO_3 Thin Films at Room Temperature

Properties*	Amorphous BaTiO_3^{**} ($400^\circ\text{C}/1\text{h}$)	Amorphous PZT^{**} ($400^\circ\text{C}/1\text{h}$)	Amorphous LiNbO_3^{***} ($150^\circ\text{C}/5\text{h}$)
Film thickness t	$0.3 \mu\text{m}$	$0.3 \mu\text{m}$	$0.13 \mu\text{m}$
Dielectric permittivity ϵ (25°C)	90 (1kc) 70 (100kc)	160 (1kc) 49 (100kc)	4.8 (1kc) 3.2 (100kc)
Resistivity (d.c.) ρ ($\Omega\text{-cm}$)	1.5×10^9	1.4×10^7	1.75×10^6
Pyroelectric coefficient p ($\text{nC}/\text{cm}^2\text{K}$)	0.5	13.8	8
Remanent polarization P_r ($\mu\text{C}/\text{cm}^2$)	2.3	3.2	7.8
Coercive field E_c (kV/mm)	10.6	7.8	11
Breckdown strength E_b (kV/mm)	60	53	34

* Measured samples have the sandwich structure of Au / thin film / substrate;

** Metal Ti Substrate; *** Silicon Substrate.

Pyroelectric current was measured by a picoammeter connected in series with the sample, while the sample was heated at a moderate rate. Before the measurement, the amorphous samples were poled with a dc electric field of 7--10 kV/mm. The pyroelectric coefficients p of these samples are listed in Table I. The pyroelectric current change with time were observed. For example, in the case of an amorphous PZT film poled at 150°C , the pyroelectric current became stable after poling 162 hours (as shown in Fig. 5). After heating up the poled amorphous PZT sample to 250°C , the pyroelectric current disappeared owing to depolarization. Therefore, it was identified that the pyroelectric effect in the amorphous PZT was caused by the contribution of poled dipoles.

The above observations strongly suggest that the observed ferroelectric-like behaviour, i.e., P - E hysteresis, pyroelectricity, and piezoelectric resonance absorption, was due to the action of permanent dipoles in these amorphous ferroelectric oxides. The measured electrical properties of amorphous BaTiO_3 , PZT and LiNbO_3 thin films are summarized in Table I.

MODEL AND DISCUSSION

The structural origin of ferroelectric-like behavior in these amorphous materials can be discussed on the basis of the sol-gel fabrication process. For example, one readily identifies the basic building block of the amorphous LiNbO_3 as the polyhedral pair. One of them is a niobium-oxygen octahedron, and the other one is a highly distorted lithium-oxygen octahedron sharing a face with the niobium-oxygen octahedron. Therefore, in the amorphous LiNbO_3 the basic building block is very similar to those found in crystalline LiNbO_3 . Due to the differences in hydrolysis tendency for bidental and tridental oxygens in the ethoxides, the hydrolysis reaction can be slowed down to the extent that the octahedra pairs are preserved during hydrolysis. Since the polycondensation reaction occurs immediately after the hydrolysis of ethoxyl groups, an amorphous oxide with identifiable octahedral pairs is produced. Figure 6(a) illustrates a simplified structure of amorphous LiNbO_3 . The octahedral pairs after hydrolysis and polycondensation reactions will be interconnected through one of the following configurations: head-to-head, head-to-tail, side-by-side, or tail-to-tail. After complete hydrolysis and polycondensation, an amorphous LiNbO_3 with local structure shown in Figure 6(b) is formed. Such assemblies will be referred to here as "ferrons". In Figure 6(b) then, there are two ferrons. As a comparison, a small crystallite of LiNbO_3 of comparable size is drawn in Figure 6(c). Ferrons are the groups of octahedral pairs interconnected through polycondensation reactions of the precursor ethoxide in such a fashion that the pairs are aligned relatively along one direction. The size of the ferrons will be dependent on the processing condition. Similar to the structure of crystalline LiNbO_3 , ferrons have on the average 1/3 vacant octahedra, 1/3 lithium occupied octahedra and 1/3 niobium occupied octahedra. Within the volume of a ferron, the stoichiometry is satisfied, and the relative displacement of Nb^{5+} and Li^{+1} ions are spontaneously polarized in the same direction. Because of the randomness of the stacking sequence for the three types of octahedra, and these octahedra have slightly different sizes, each ferron is not a crystallite. Ferrons are in turn interconnected through their octahedra. The random orientation of the adjacent ferrons is expected to result in the formation of molecular size voids [see Figure 6(a)].

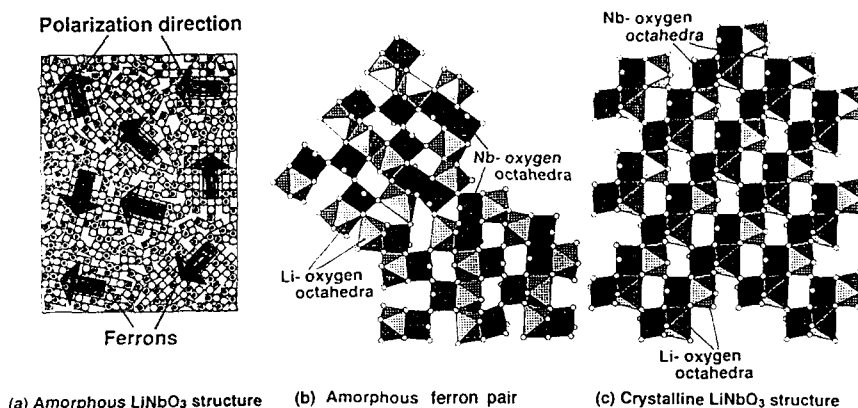


Fig. 6(a) Schematic illustration of proposed amorphous LiNbO_3 structure. The arrows indicate the spontaneous polarization directions for different ferrons; (b) Proposed structure of a ferron pair; (c) A small crystallite of LiNbO_3 constructed using the same group of building blocks from the ferron in (b).

The directions of the spontaneous polarization for ferrons are random for amorphous LiNbO_3 , and the polarization is reversible by an external electric field. Ferrons in close proximity may interact and polarize in favor of one particular direction, although in the absence of an external electric field the overall polarization of the macroscopic sample is extremely small or zero. When an external electric field is applied, a net polarization in the direction of the field is obtained. However, this net polarization is expected to be smaller than that of the crystalline ferroelectric. Although the above proposed model is still preliminary, it does explain very well the observed ferroelectric-like behavior of the amorphous oxides in this study.

The above picture is generally applicable to other amorphous phases of known ferroelectric crystals by similar sol-gel processing. The observed behavior of amorphous PZT and BaTiO_3 thin films in this study are also attributed to the ferron model.

CONCLUSIONS

- 1) Amorphous thin films of ferroelectric oxides were successfully prepared by the sol-gel method with heat-treatment at temperature below 150°C for LiNbO_3 and below 400°C for PZT and BaTiO_3 , respectively.
- 2) The electrical properties of amorphous LiNbO_3 , PZT and BaTiO_3 films were measured. It was found that these amorphous thin films showed ferroelectric-like behavior.
- 3) A structural model of "ferrons" is proposed to account for the ferroelectric-like behavior in the amorphous phase.
- 4) The advantages of ferroelectric-like amorphous materials, include low processing temperature, low dielectric permittivity and good transparency without grain boundaries.

ACKNOWLEDGEMENT

This work was supported by the Air Force Office of Scientific Research, Directorate of Chemical and Materials Science under Grant No. AFOSR-91-0096.

REFERENCES

1. Yuhuan Xu, Ferroelectric Materials and Their Applications, 1st ed. (North-Holland, Elsevier Science Publishers, Amsterdam, 1991).
2. E. R. Myers and A. I. Kingon (editors), Ferroelectric thin films, (Mater. Res. Soc. Proc. **200**, Pittsburgh, PA, 1990).
3. Yuhuan Xu and John D. Mackenzie, Integrated Ferroelectrics, **1**, 17 (1992).
4. M. E. Lines, Phys. Rev. B, **15**, 388 (1977).
5. A. M. Glass, M. E. Lines, K. Nassau and J. W. Shiever, Appl. Phys. Lett., **31** [4], 249 (1977).
6. T. Mitsuyu and K. Wasa, Japan. J. Appl. Phys., **20**, L48 (1981).
7. M. Kitabatake, T. Mitsuyu and K. Wasa, J. Non-Cryst. Solid., **53**, 1 (1982).
8. H. Engelmann, N. Kraemer and U. Gonser, Ferroelectrics, **100**, 127 (1989).
9. J. D. Mackenzie, J. Non-cryst. Solid., **48**, 1 (1982).
10. J. D. Mackenzie, Ultrastructure Processing of Advanced Ceramics (Eds. by Mackenzie, J. D. and Ulrich, D. R.), chap. 43, (John Wiley & Sons, New York, 1988).
11. S. Hirano and K. Kato, J. Non-cryst. Solid., **100**, 538 (1988).
12. S. Hirano and K. Kato, Mat. Res. Symp. Proc., **155**, 181 (1989).
13. D. C. Bradley, R. C. Mehrotra and D. P. Gaur, Metal Alkoxides (Academic Press, London, 1978).
14. S. Hirano and K. Kato, Adv. Ceram. Mater., **2**, [2], 142 (1987).
15. D. J. Eichorst, D. A. Payne, S. R. Wilson and K. E. Howard, Inorg. Chem., **29**, 1459 (1990).
16. R. Xu, Z. C. Kang, L. Eyring and J. D. Mackenzie, (Report at MRS Fall Meeting, Symposium I, 1991, Boston).
17. Yuhuan Xu, C. H. Cheng, R. Xu and J. D. Mackenzie, Mat. Res. Symp. Proc., **271**, 359 (1992).

FERROELECTRIC THIN FILMS INTENDED FOR ELECTRONIC DEVICE APPLICATIONS

A. Patel, E.A. Logan, R. Nicklin, N.B. Hasdell, R.W. Whatmore and M. Uren*

GEC-Marconi Materials Technology Ltd, Caswell, Towcester, Northants, NN12 8EQ, UK
*DRA, St Andrews Road, Malvern, Worcs, WR14 3PS

ABSTRACT

The need for integrated ferroelectrics as charge storage capacitors has increased dramatically not only for use in radiation hardened and commercial non-volatile memories, but also as possible high dielectric material suitable for capacitor applications. These properties combined with a thin film format, offer the capability of forming very compact capacitor structures suitable for MCM applications through Flip-Chip Bonding, or even integrated directly onto MMIC's. In this paper, the material $\text{PbZr}_x\text{Ti}_{1-x}\text{O}_3$, where $x=1, 0.53$, and 0.60 has been assessed. Thin films were produced using a sol-gel technique onto metallised thermally oxidised silicon. The effects on film microstructure and crystallinity with variation in the deposition process will be described. The best films were obtained by incorporating excess lead in the starting solutions, and also by the addition of acetylacetone which was used as a solution modifier. It will be demonstrated that fully perovskite films can be readily obtained at temperatures as low as 450°C . The films were normally $0.3\text{--}0.44\mu\text{m}$ thick with grain sizes of the order of $0.2\mu\text{m}$. These films exhibited dielectric constants and loss in the range $170\text{--}800$ and $1\text{--}3\%$ respectively. Measurements upto 3MHz , indicated useful performance with low dispersion. The measured P_r and E_c were in the range $16\text{--}22\mu\text{C}/\text{cm}^2$, and $60\text{--}120\text{kV}/\text{cm}$ respectively.

INTRODUCTION

The complex nature of the lead zirconate titanate (PZT) material system gives it a unique set of electrical, mechanical and optical properties which have been used or proposed for device applications¹. Recent work has developed a new set of applications for these materials involving devices for memory and logic circuits on silicon or GaAs, and requiring the use of thin films. Films ($200\text{--}300\text{nm}$) of ferroelectric allow operating voltages compatible with normal device voltages, ie, up to 5V , and compatibility of the film deposition technique with established silicon processing makes integration with planar circuit technology possible. The high dielectric constants offered by ferroelectric materials in thin film format² makes them attractive for use as high volume efficient capacitors. The space saving due to the high capacitance could be further enhanced by combining high 'K' thin layers with flip chip solder bonding technology^{3,4}, a combination, which has previously never been explored.

The flip chip technique permits the use of area array bonding and thinner substrates, giving space saving potential, but in most cases, the capacitor area is determined by the dielectric properties of the thin film material. Capacitors on GaAs presently use Si_3N_4 for MMIC RF decoupling applications. The use of ferroelectrics is expected to yield a factor of up to 1000 increase in permittivity coupled with a similar reduction in chip area. The choice of material for this application depends strongly on the area of application and the intended operating frequency range. Of the range of ferroelectric materials available, the lead zirconate titanate ($\text{PbZr}_x\text{Ti}_{1-x}\text{O}_3$) PZT solid solution system offers the greatest potential. It has been shown previously⁵ that compositions close to $x = 0.98$ can provide a dielectric constant of 115 with low dispersion and low loss out to microwave frequencies. In this paper, we report the use of sol-gel derived $\text{PbZr}_x\text{Ti}_{1-x}\text{O}_3$ $x = 0.53, 0.6$ and 1 thin films deposited onto platinum coated silicon (100) wafers with a thermal oxide barrier layer.

EXPERIMENTAL PROCEDURE

The precursors used to prepare the deposition solution consisted of lead acetate trihydrate, titanium n-butoxide and zirconium n-butoxide in 2-methoxyethanol (2ME) as a solvent. The process is shown schematically in Figure 1; the titanium and zirconium precursors were reacted separately and then added to the dehydrated lead solution. The as prepared (53/47) solution ~0.7M was further modified with acetylacetone and 2ME to give a deposition solution of about 0.1M strength. The sols for the 60/40 composition and 100/0 were not acac modified, however, they were diluted to the same extent as that used for the 53/47 sol. Best results were obtained with lead excesses of 10%, which compensated for lead loss at higher temperatures and aided sintering. The films were typically spin coated at 2000 rpm for 30 seconds, followed by a bake at 170°C to remove the solvent. This process was repeated several times and then consolidated at 450°C/2 mins. This temperature was found to be sufficient to decompose the organic groups and crystallise the perovskite phase. The thickness per layer obtained after firing was about 0.015µm. The substrates used consisted of e-beam coated Pt/Ti on SiO₂/silicon, the Pt/Ti thicknesses were 1000 and 50Å respectively and were used without any pre-annealing.

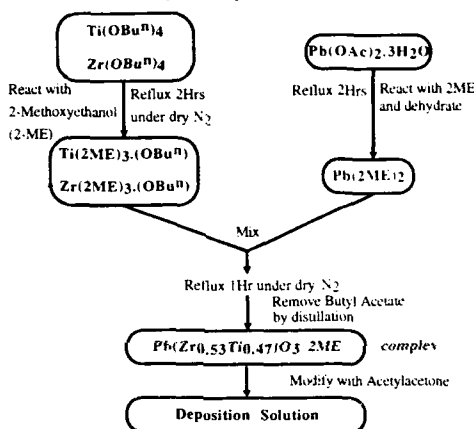


Figure 1. Solution Preparation Schematic

The films were characterised by a number of techniques, including X-ray diffraction (XRD) using Cu α radiation and scanning electron microscopy. Dielectric properties were determined using a Wayne Kerr 6425 LC meter and high frequency measurements on a Hewlett Packard 4191A impedance analyser. Hysteresis loop measurements were conducted on a Radiant Technologies RT66A thin films tester.

RESULTS AND DISCUSSION

For a film of composition 53/47 (Zr/Ti) a preferentially (111) orientated film was almost always obtained, as shown in Figure 2. Increasing Zr content, however, gave an increasing degree of preferred (100) orientation as shown by Figures 3 and 4, for a 60/40 and a 100/0 film respectively. It was noticeable that where samples were processed without a 450°C intermediate bake, conversion to the perovskite phase proved to be more difficult and required extended periods of time at 450°C or higher to fully convert.

SEM analysis of 53/47 films indicated a smooth surface (Figure 5) and showed little evidence of grain growth at 450°C. High temperature treatment at up to 700°C led to limited grain growth with 'rosette' type grains up to 0.2µm observable. It is thought that this is probably due to the acac modification, which alters the sol chemistry, leading to fine scale grain structures. In contrast, both the 60/40 and the 100/0 films gave good microstructures with rapid grain growth

even at low temperature. A typical surface is shown in Figure 6. This shows dense regions of grain growth interspersed with dark areas (matrix).

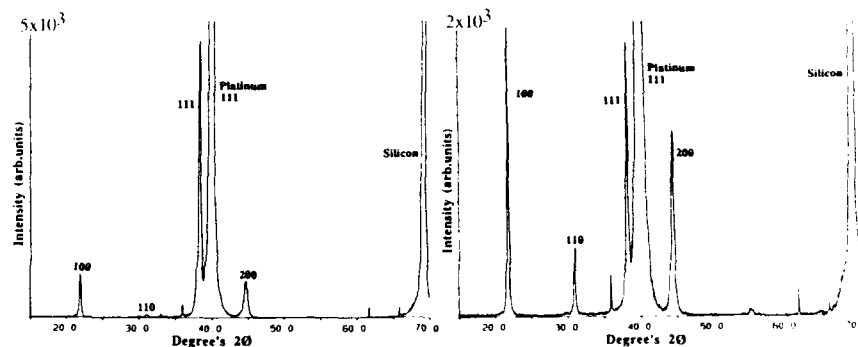


Figure 2. X-ray trace for a 53/47 PZT film

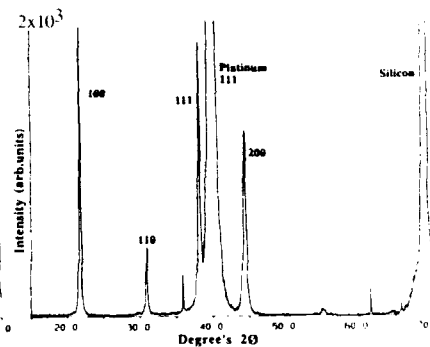


Figure 3. X-ray trace for a 60/40 PZT film

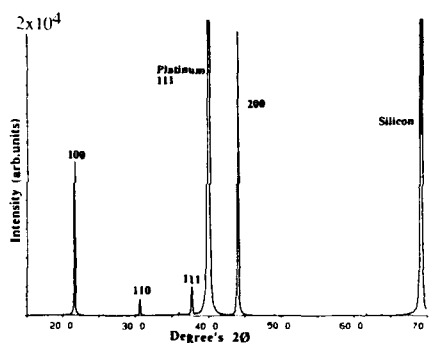


Figure 4 X-ray trace for a 100/0 PZT film

Examination by EPMA (electron probe microanalysis) concluded that the matrix region was lead deficient and Zr rich. Because no pyrochlore phase was detected by X-ray diffractometry, it is thought that the matrix probably consists of an amorphous pyrochlore phase, of a composition as yet undetermined. Further, higher temperature treatment gave limited grain growth with grains of up to $0.2\mu\text{m}$ across. It is also interesting to note that an unmodified 53/47 film also gave extensive grain growth at higher temperatures. In our investigation, we have observed a reverse trend to that seen by Klee et al⁶, who showed that pre-annealing the substrates influenced the oriented growth of PZT with reasonable grain size. In our case, the pre-annealed substrates were found to consist of a smooth surface compared with an unannealed surface which was rougher. This surface roughness we believe leads to preferred PZT crystallisation sites.

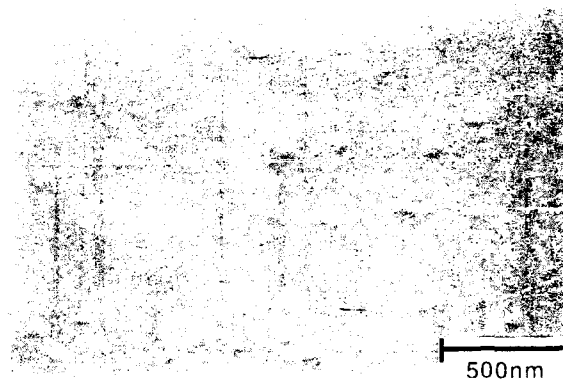


Figure 5. SEM surface of a 53/47 PZT film

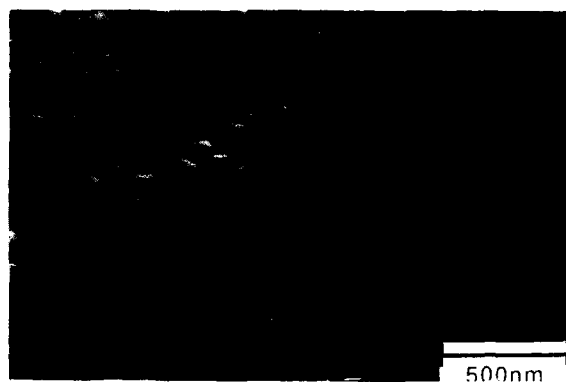


Figure 6. SEM surface of a 60/40 PZT film

The film dielectric characteristics were determined by evaporating Cr/Au electrodes onto the surface of the film through a shadow mask consisting of 200 to 1mm diameter holes. The bottom electrode was exposed by acid etching at a corner using a HF/HCl mixture. Both the 53/47 and 60/40 films were approximately $0.3\mu\text{m}$ thick, while the 100/0 was $0.44\mu\text{m}$; for films having a final anneal at 700°C . As the Zr concentration was altered, three different types of hysteresis loops were observed, as shown in Figure 7. The 53/47 films all gave a strongly asymmetric loop related to the electrode profile of the stack and also the higher Ti content. In general, this gave a P_r and E_c values in the range $24\text{--}32\mu\text{C}/\text{cm}^2$ and $95\text{--}110\text{kV}/\text{cm}$ respectively. Increasing Zr content led to slimmer loops with P_r and E_c in the range $16\text{--}22\mu\text{C}/\text{cm}^2$ and $63\text{--}112\text{kV}/\text{cm}$ for films with 60/40 composition. In contrast, PbZrO_3 which is antiferroelectric (AFE) at room-temperature, show loops typical of a dielectric. Hysteresis loops have been observed for PbZrO_3 previously⁷, but only after inducing a AFE-FE transition under a high critical electrical field. The calculated relative permittivities at 1kHz were of the order of 800, 300 and 180 for 53/47, 60/40 and 100/0 respectively. The measurement of permittivity from 1kHz to 300kHz showed a decrease from 800 to 700 for the 53/47 composition. However, both

the Zr rich films gave negligible variation with values of 250 and 170 for 60/40 and 100/0 respectively. The dielectric losses at 1kHz also show a similar decrease with increasing Zr content from ~4% to less than 1% for pure PbZrO_3 . Interestingly, the 100/0 film also gave a very high resistivity of $>10^{10}\Omega\text{m}$; compared with $10^9\Omega\text{m}$ for 53/47 and 60/40 compositions. The low dielectric constants obtained in the present films have been observed previously⁸, and may be due in part to variations in grain size, film thickness, interfaces, etc.

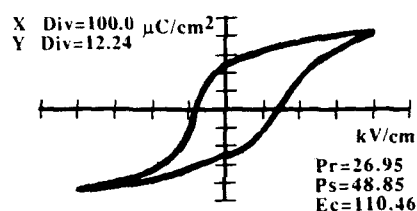


Figure 7(a). Hysteresis for a 53/47 PZT film

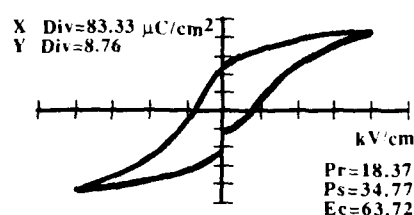


Figure 7(b). Hysteresis for a 60/40 film

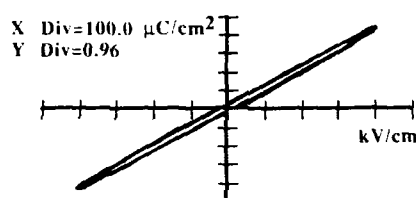


Figure 7(c). Hysteresis typical of a dielectric (PbZrO_3)

A 53/47 film was also suitably etched and electroded with Cr/Au electrodes of area's $160\mu\text{m}^2$ and $200\mu\text{m}^2$. After suitable wirebonding, measurements of permittivity and loss were performed up to a 3MHz. The observed permittivity again indicated a negligible decrease from 550 at 1kHz to 500 at 3MHz. Similarly, the dielectric loss gave value's of 6% and 3% at 1kHz and 3MHz respectively. This is not unexpected as similar behaviour has been observed in PZT ceramics⁹, where the dielectric constant was found to be independent of frequency in the range 1kHz-100MHz, with a value close to 1000. Also, the low frequency dielectric loss was found to be sensitive to dc-conduction within the film, leading to a sharp increase.

CONCLUSIONS

Highly crystalline perovskite PZT films of composition 53/47, 60/40 and 100/0 were successfully deposited on metallised silicon substrates using the sol-gel process at 450°C . It was shown that at this temperature, the preferred orientation gradually changes from (111) to (100), as the film composition was varied from 53/47 - 100/0. All the films exhibited small grain size of the order $0.2\mu\text{m}$. These films exhibited dielectric constants and loss in the range 170-800 and

1-3% respectively. The measured P_r and E_c were in the range 16-22 μ C/cm² and 60-120kV/cm. High frequency measurements up to 3MHz for a 53/47 film indicated useful performance in the lower MHz range with low dispersion.

ACKNOWLEDGEMENT

This work has been carried out with the support of the Defence Research Agency, Ministry of Defence.

We thank N.M. Shorrocks for technical assistance in the high frequency measurements.

REFERENCES

1. L.H. Parker and A.F. Tasch, IEEE Circuits and Devices Magazine, 17-26 (1990).
2. Ferroelectric Thin Films, Mat. Res. Soc. Proc., 200 (Eds. A.I. Kingon and E.R. Myers, MRS 1991).
3. D.J. Warner, K.L. Pickering, D.J. Pedder, B.J. Buck and S.J. Pike, IEE. Procs.-H, 138 (1), 74-78 (1991).
4. A. Burkhart, Surface Mount Tech., 41-44, July 1991.
5. M.T. Lanagan, J.H. Kim, S.J. Jang and R.E. Newnham, J.Amer.Cer.Soc., 71, 311(1988).
6. M. Klee, R. Eusemann, R. Waser, W. Brand and H. Van Hal, J. Appl. Phys., 72 (4), 1566-1576 (1992).
7. F. Wang, K.K. Li and G.H. Haertling, Opt.Letts., 17(16), 1122(1992).
8. S.L. Swartz, S.J. Bright, J.R. Busch and T.R. Shrout, Cer. Trans., 14, 159-178 (1990).
9. O. Kersten and G. Schmidt, Ferroelectrics, 67, 191(1986).

PART XII

Sputter Deposition

SPUTTERING OF LEAD-BASED FERROELECTRICS

K.Iijima, N.Nagao, T.Takeuchi, I.Ueda, Y.Tomita* and R.Takayama*

Central Research Laboratories, Matsushita Electric Industrial Co. Ltd., Yakumonakamachi, Moriguchi, Osaka 570, Japan

**Materials and Devices Research Laboratory, Matsushita Electric Industrial Co. Ltd., Kadoma, Osaka 570, Japan*

ABSTRACT

PbTiO_3 (PT), $\text{Pb}_{1-x}\text{La}_x\text{Ti}_{1-x/4}\text{O}_3$ (PLT) and $\text{PbZr}_x\text{Ti}_{1-x}\text{O}_3$ (PZT) thin films were prepared by rf magnetron sputtering. It was found that the thin films have remarkably large pyroelectric effect and high figures of merit for infrared sensors without poling treatment. High performance pyroelectric infrared sensors (single element and linear array) were fabricated by using the PLT ($x=0.1$) thin films with the new structures and the device process. This type of sensor is carried on the air conditioner to detect a thermal environment. The PZT thin films with $x=0.9$ showed a large remanent polarization of $46\mu\text{C}/\text{cm}^2$ and small coercive force of $28\text{kV}/\text{cm}$. In addition, good endurance behavior (no degradation of Pr after 10^{11} cycles) was observed. Recent activities of ferroelectric thin film research in Japan is also reported.

INTRODUCTION

Lead-based ferroelectrics with perovskite type structure, such as PT, PZT, PLT and $(\text{PbLa})(\text{ZrTi})\text{O}_3$ (PLZT), have interesting and beneficial properties; i.e., dielectric, ferroelectric, piezoelectric, pyroelectric, and optoelectric properties. These materials have been widely used for electric devices in bulk ceramic form. However, the preparation of a large high quality single crystal of pure Pb-based ferroelectrics is very difficult because of high volatility of Pb or PbO .

Development of high quality single crystal thin film of Pb-based ferroelectrics has been an important subject of our thin film research to obtain new or advanced properties unattainable in ceramic form with randomly oriented grain structure. The difficulties to produce high quality thin films of Pb-based ferroelectrics are mainly due to the relatively high crystallization or epitaxial temperature ($>500^\circ\text{C}$), the high volatility of PbO , the low melting point of Pb (327°C) and the necessity of high oxygen pressure for the oxidation of Pb. Progress of thin film technology in this decade make it possible to grow a high quality single crystal thin film and a film with the proper crystalline orientation [1-3]. We have reported the preparation and electric properties of PT, PLT and PZT films epitaxially grown on the single crystal substrate [3-6] and the application of these films to infrared sensors [7,8]. The progress of thin film technology is realizing the integration of ferroelectrics into semiconductor devices for non-volatile

random access memories, thermal imaging sensor, piezoelectric acoustic wave transducers and optoelectric device applications[9].

In this paper, PT, PLT and PZT films fabricated with rf-magnetron sputtering are reported. These films showed unique dielectric and ferroelectric properties. Fabrication and characteristics of the infrared sensors using PLT thin films are also reported.

FERROELECTRIC THIN FILM RESEARCH IN JAPAN

A number of companies and universities are investigating the ferroelectric and dielectric thin films. At the 1993 Spring Meeting of Japanese Society of Applied Physics(Mar. 29 to Apr.1), fifty five contributed papers on ferroelectric thin film were discussed. More than 50% of the papers were aiming at memory applications. 65% of papers were dealing with the Pb-based ferroelectrics, especially PZT having the composition of morphotropic phase boundary (MPB).

Many researchers investigated a fatigue problem. Professor Okada's group (Chubu University) examined fatigue characteristics of (001) and (111) oriented PZT(45/55) films prepared by MOCVD[10]. These PZT films were deposited on (111)Pt/SiO₂/Si and (100)Pt/MgO, respectively. The (001) oriented PZT showed excellent fatigue characteristics and the film did not degrade until almost 10¹² cycles. However, the (111) oriented PZT degrades at about 10⁹ cycle. They discussed the mechanism of fatigue from the view point of the difference of crystal orientation. Lowering of process temperature is desired for the compatibility to silicon process. Sharp Corp. reported PZT films prepared by RTA(deposited at 250°C and 15 seconds RTA) with good fatigue characteristics (10⁹ cycle)[11]. Olympus and Colorado University group discussed the fatigue mechanism from the view point of oxygen defects in the PZT film near the electrodes[12].

The pyroelectric sensor is an important application field of ferroelectric thin film. We reported almost 100% c-axis oriented PLT thin film deposited on (100)Pt/MgO by rf magnetron sputtering[13]. This film showed very high pyroelectric coefficient, γ , of 1.3x10⁻⁷C/cm²K and relatively low dielectric constant, ϵ_r , of 350.

PLT AND PZT FILMS IN MATSUSHITA

Preparation of the films by rf magnetron sputtering

The substrates used were (100)MgO and (100)oriented Pt on MgO. For the PZT films, (111)Pt coated R- and c-sapphire and SiO₂/Si substrates were also used. The compositions of sputtering target powders were given by the formula: For the PLT film, (1-Y)(Pb_{1-x}La_xTi_{1-x/4}O₃)+Y(PbO), where x=0.0-0.15 and Y=0.2. For the PZT film, (1-Y)(PbZr_xTi_{1-x}O₃)+Y(PbO), where x=0.2-0.9 and Y=0.2. The films were deposited at a substrate temperature of 500-725°C in a sputtering gas (Ar/O₂=9/1) at the pressure of around 10⁻² Torr. The deposition rate of the films was typically 6nm/min.

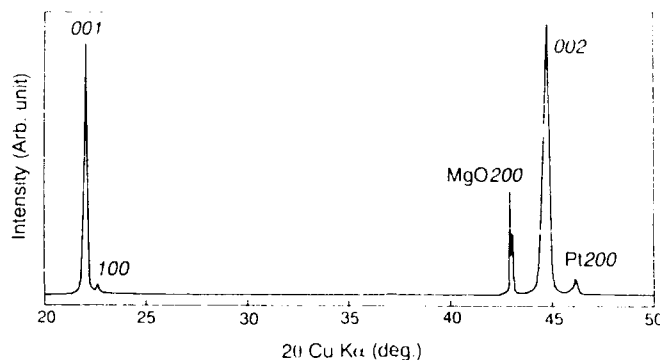


Fig. 1 X-ray diffraction pattern of PLT($x=0.15$) thin film deposited on Pt/MgO.

Characterization of PLT films

The films were examined by electron and X-ray ($\text{CuK}\alpha$) diffractometry and electron microscope. The evaluation was made in the degree of c -axis orientation α ; $\alpha = I_{001}/(I_{100} + I_{001})$, where I_{100} and I_{001} represent the diffraction intensities of 100 and 001 reflections, respectively.

c -axis oriented PLT film is important for infrared sensors, because the c -axis is the polarization axis. Highly c -axis oriented PT and PLT thin films were obtained on both the MgO and Pt/MgO substrate. Figure 1 shows the typical X-ray diffraction pattern of the c -axis oriented PLT($x=0.15$) thin film with the thickness of $5.7\mu\text{m}$. The α of this film is 0.97 and $00l$ reflections of perovskite structure are mainly observed. The $h00$ reflections are very weak and are not observed clearly. c -axis orientation of the films is due to the large thermal expansion coefficient of MgO and ferroelasticity of the PLT.

In order to investigate the film quality as well as to reveal the interface structure, the PLT films were examined by high resolution electron microscopy. TEM photographs of the cross section of the PLT ($x=0.15$) film deposited on the MgO substrate are shown in Fig. 2. Fig. 2(a) shows a low magnification image of the film in which no crack and no grain boundary is observed and the film seems to be homogeneous. The diffraction pattern of this area shows that the film is a single crystal. At the central part of the photograph, a domain structure is observed. The analysis of the diffraction pattern of this area indicates that the film is constructed by mainly the c -domain (c -axis of the film is perpendicular to the substrate) and small portion of a -domain (c -axis is almost parallel to the substrate) which have a (101) plane in common with the matrix. In the PLT film dark periodic contrasts (about 3nm intervals) are observed at the interface to the MgO substrate, indicating the existence of strong lattice distortion or strained layer.

In Fig. 2(b) of the high resolution image, the lattice image of the film and the substrate can be clearly observed. Although the surface of the MgO substrate is not flat and fairly irregular, PLT film grew epitaxially on the MgO substrate. The connection of the atomic rows in the $[001]$ direction going from the MgO substrate into the PLT film is clearly observed.



Fig. 2 (a) A low magnification image of (001) PLT ($x=0.15$) on (100) MgO.

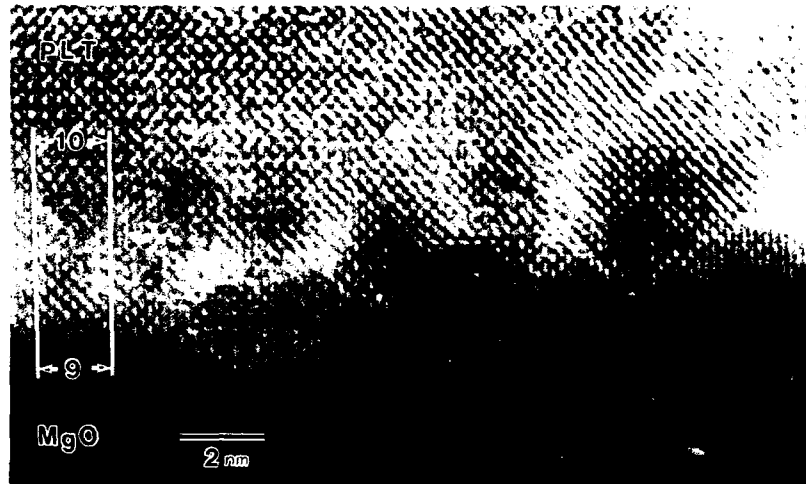


Fig. 2 (b) A high resolution image of the PLT/MgO interface.

Misfit dislocations are observed in the PLT thin film corresponding to the dark contrast of the film mentioned above. The dislocations are not located at the interface of the film and the substrate but in the PLT film about 2 nm apart from the surface. Although the lattice mismatch between PLT and MgO is very large and about 8%, the PLT seems to accommodate its crystal lattice to that of MgO.

Characterization of PZT films

(001) oriented PZT thin films were obtained on the (100) Pt/MgO

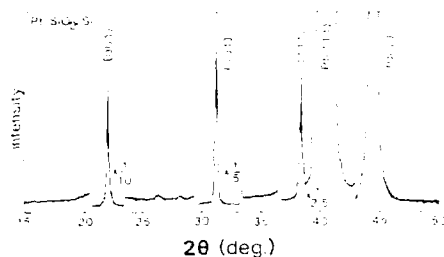


Fig. 3 X-ray diffraction pattern of PZT($x=0.8$) deposited on Pt/SiO₂/Si.

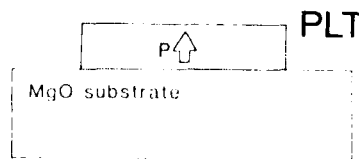


Fig. 4 Schematic drawing of c -axis oriented PLT thin film which have polarization without poling treatment.

substrates. On the (111)Pt substrate, polycrystalline PZT films were obtained. (111) oriented PZT films were obtained above 700°C. Reliable electric data were not obtained for the film deposited at such a high substrate temperature, because of low concentration of Pb in the films. The X-ray diffraction patterns indicated that the films were tetragonal when the zirconium content, x , in the target was less than 0.45. When x was greater than 0.50, there was no separation of the $h00$ and $00l$ reflections on the X-ray diffraction pattern of the films indicating that the tetragonality was too small to be detected or that the films were rhombohedral.

Figure 3 shows the X-ray diffraction pattern of a PZT thin film on Pt/SiO₂/Si deposited at 675°C using the target with $x=0.80$. It is the pattern of polycrystalline PZT indicating the film is single phase and has a perovskite structure, however 001 reflection is relatively strong.

Electric properties of PLT films

Dielectric constant, ϵ_r , and dielectric loss factor, $\tan\delta$, were measured at 1kHz applying about 25kV/cm by a multifrequency LCR meter. D-E hysteresis loops were obtained by a Sawyer-Tower circuit with sinusoidal wave of 100Hz. Pyroelectric coefficient, γ was obtained from the temperature gradient of pyroelectric current measured by a pA meter. These measurements were performed without a poling treatment. Nevertheless, significant pyroelectric currents were detected on all the thin films. The directions of currents were the same in all measured samples and from the lower electrode on the side of the MgO substrate to the upper electrode on heating. Usually, pyroelectric currents cannot be observed on ferroelectric polycrystalline ceramics and single crystal without a poling treatment. This phenomenon is named "self-polarization" and is shown schematically in Figure 4.

Figure 5 shows ϵ_r and γ of PbTiO₃ films as a function of the c -axis orientation rate α . ϵ_r decreases and γ increases upon increasing α . This behavior can be explained by the fact that ϵ_r along the c -axis is smaller than that perpendicular to the c -axis, and the c -axis is the polarization axis. The film with $\alpha=0.8$ shows an ϵ_r of 97 and γ of 2.5×10^{-8} C/cm²K. ϵ_r is smaller

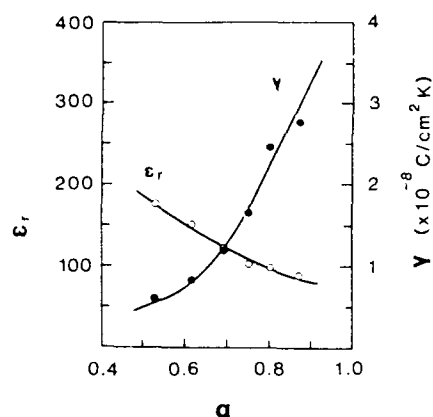


Fig. 5 Relation between pyroelectric coefficient γ , dielectric constant ϵ_r and c -axis orientation rate α .

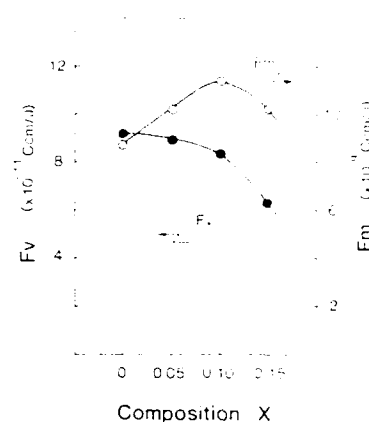


Fig. 6 Figure of merit F_v for voltage responsivity and F_m for specific detectivity as a function of composition x .

and γ is larger than those of PbTiO_3 ceramics. ($\epsilon_r=190$, $\gamma=1.8 \times 10^{-8} \text{C/cm}^2 \text{K}$) ϵ_r and γ increased with increasing La . The evaluation of pyroelectric materials was carried out using figures of merit $F_v (= \gamma / \epsilon_r C_v)$ for voltage responsivity and $F_m (= \gamma / C_v \epsilon_r \tan \delta)$ for specific detectivity D^* , where C_v is volume specific heat ($= 3.2 \text{J/cm}^3 \text{K}$). Figure 6 shows the mean values of figures of merit F_v and F_m for PLT thin films with the same thickness as a function of La content. The loss factor of $\tan \delta$ was almost constant with the variation of La content and about 0.006. The mean F_m shows a maximum at $x=0.1$. These results show that the c -axis oriented PLT thin films with $x=0.1$ are a good material for pyroelectric infrared detectors.

Electric properties of PZT films

Figure 7 shows ϵ_r of PZT thin films as a function of the target composition. A peak of ϵ_r was observed at the target composition of $x=0.65$ for the films deposited on the Pt/sapphire substrate. Chemical composition analysis showed that when the target composition x is 0.65, the film composition became 0.55. Therefore, the peak of ϵ_r in Fig. 7 corresponds to the composition of the MPB exactly.

On the other hand, a peak of ϵ_r was difficult to identify for the PZT films deposited on Pt/MgO and the value of ϵ_r is small compared with that on Pt/sapphire. It is believed that PZT has a large anisotropy in the dielectric constant as observed in PbTiO_3 , i.e., ϵ_r along the c -axis is small compared with that perpendicular to polarization axis. The PZT films on Pt/MgO substrates were oriented in (001). The differences observed in Fig. 7 are, therefore, explained by the anisotropy of ϵ_r of PZT.

Figure 8 shows remanent polarization, P_r , and coercive field, E_c , of the PZT films deposited on Pt/MgO as a function of the target composition at the

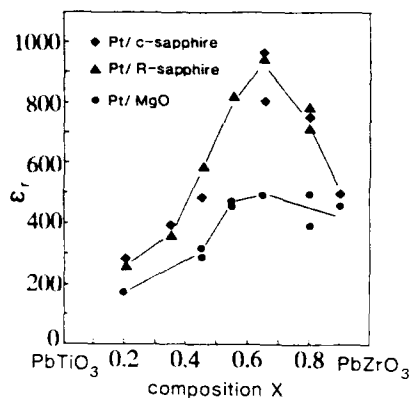


Fig. 7 Dielectric constant ϵ' of PZT film as a function of target composition.

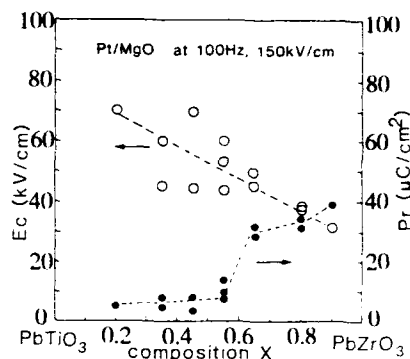


Fig. 8 Pr and Ec of PZT film as a function of target composition.

applied voltage of 150kV/cm. Ec decreased and Pr increased with increasing Zr content. The gradual change of Pr against the molar ratio of Zr in the target is observed except in the region between $x=0.55$ and $x=0.65$, where the Pr changes abruptly. The abrupt change in Fig. 8 represents the boundary between the tetragonal and the rhombohedral phase. This result indicates that PZT films in the rhombohedral region have "soft" ferroelectricity and are suitable for memories. A peak of Pr is observed at the composition of MPB for the PZT ceramics[14] and polycrystalline thin films[15]. However, in this study a peak of Pr was not observed at the MPB composition. This is due to the high (001) orientation of the films and relatively low applied field of 150kV/cm. Figure 9 shows typical D-E hysteresis loops with $x=0.9$ and $x=0.35$. The PZT film with 0.90 showed Pr of $46\mu\text{C}/\text{cm}^2$ and Ec of 28kV/cm at the applied voltage (100Hz) of 150kV/cm. These values observed on films with $x=0.90$ are expected to easily satisfy the requirement imposed by large scale random access memories.

The resistance to fatigue of PZT films is crucial for their application in advanced RAMs. As shown in Fig. 10, bipolar stressing ($\pm 10\text{V}$) resulted in no degradation of Pr of PZT($x=0.8$) film at least up to 10^{11} cycles.

The most interesting thing of our (001) oriented PLT and PZT thin film is that the spontaneous polarization of the films is directing in the same direction. Therefore, pyroelectric and piezoelectric signals can be obtained without poling treatment. After annealing treatments at above Curie temperature of those films, this "self-polarization" nature was not changed. The exact reason of "self-polarization" have not been revealed. Some researchers pointed out that it is caused by the large lattice distortion due to the difference of the thermal expansion coefficient between the film and the substrate[16]. It has been reported that the pyroelectric current decreased with increasing substrate temperature and it changed the direction at 630°C . This result indicates that the direction of the polarization changed at this substrate temperature; e.g., below 630°C , polarization was pointing from the lower electrode to the upper electrode as shown in Fig. 4, however above

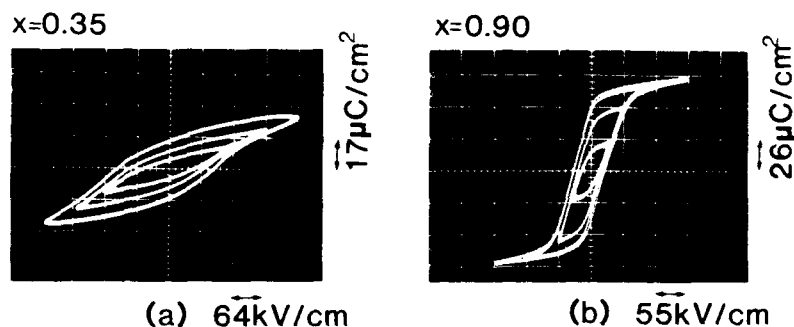


Fig. 9 D-E hysteresis loops of PZT thin films (a) $x=0.35$ and (b) $x=0.90$

630°C , it was pointing the lower electrode. Compositional analysis of the films (20nm thick) shows that Pb/Ti ratio in the films decrease with increasing substrate temperature. These facts imply that the direction of the polarization in the films is strongly related to the chemical composition, that is Pb/Ti ratio or the atom species of the first layer of the films.

INFRARED SENSORS

Several types of single element sensors and linear array sensors were fabricated using PLT ($x=0.1$) thin films. For example, a reticulated linear array sensor is illustrated in Fig. 11. This type of array sensor has separated PLT elements (element size is $0.15 \times 1\text{ mm}$, $3\text{ }\mu\text{m}$ thickness) deposited on (100)-oriented Pt film ($1 \times 25\text{ mm}$, 160 nm thickness) by using a metal mask. The Pt electrode noncoated with the PLT was etched off by Ar ion milling. The Ni-Cr top electrodes ($0.1 \times 0.3\text{ mm}^2$) were evaporated on the PLT using metal mask. The MgO substrate under the PLT was etched off by phosphoric acid. Another reticulated sensors, which are coated and supported by only the polyimide films to the MgO were fabricated. This linear array and discrete JFET chips were enclosed within a pin-grid package as shown in Fig. 12. Each read-out electrode was connected to each gate of 64 FET chips by Au wire bonding. Si window was prepared.

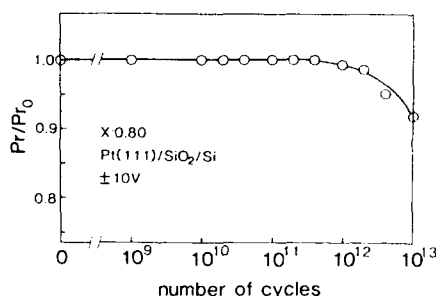


Fig. 10 Effect of fatigue on P_r under bipolar stressing ($\pm 10\text{ V}$).

The outputs were amplified by a 60dB amplifier and measured by a lock-in amplifier. The cross talk was measured by using the radiation through a slit from a He-Ne laser.

Figure 13 shows R_v and D^* of a single element of the reticulated sensor. D^* increase with increasing chopping frequency, f , when $f < 50\text{ Hz}$, because R_v almost saturate and V_n vary as f^{-1} . On the other hand, D^* is proportional to $f^{-1/2}$ when $f > 100\text{ Hz}$, because R_v vary as

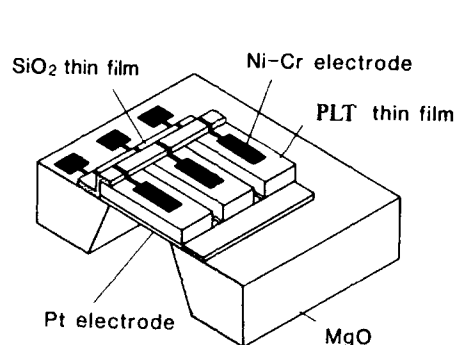


Fig. 11 Schematic structural drawing of the reticulated linear array sensor.

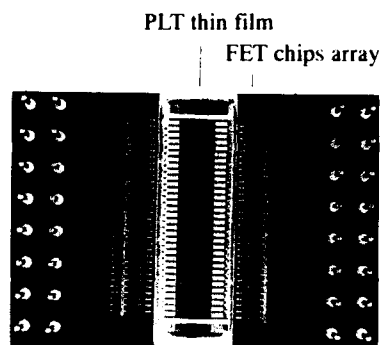


Fig. 12 A photograph of the reticulated linear array sensor with discrete JFET chips (64 elements, 5 elements/mm)

f^{-1} and V_n vary as $f^{-1/2}$. The D^* of this sensor is considerably large and $6 \times 10^8 \text{ cm}^2 \text{ Hz}^{1/2} / \text{W}$ is attained. The reticulated linear array sensor has a very low cross talk of <3% at 100 Hz compared with that of non-reticulate one (20%). The fundamental characteristics of the linear array sensor are summarized in Table I. The reticulated sensors with the resolution of 5 elements/mm can be constructed by the method of using simple metal mask process.

This type of the sensor using PLT thin film with 8 elements will be carried on the air-conditioner to instantly identify the number, location and postures—standing or sitting—of people in a room, expecting the sensor will help to provide more adequate air-conditioning by making the room more comfortable for all occupants.

FUTURE OF FERROELECTRIC THIN FILM

Oxide materials with perovskite structure have a number of interesting properties, such as ferroelectricity, piezoelectricity, ferro- or ferrimagnetism and high temperature superconductivity. Recently, the atomic layer growth and the fabrication of artificial superlattice of the oxide with perovskite structure have been attained[17]. We believe that multiple deposition layers of different type of materials or graded layers of the material on an atomic scale would open up a new path in the field of materials science.

For this purpose, preparation of a high quality substrate surface is essential to make a film with high crystallinity and a smooth surface. Recently, we succeeded in the preparation of (100) oriented Pt thin film on MgO substrate with high crystallinity and excellent surface morphology by rf magnetron sputtering. Figure 14 shows the RHEED pattern and SEM image of the surface of this film. These results show that the Pt film is a single crystal and its surface is atomically flat. Thin film materials should be investigated on such well defined surfaces.

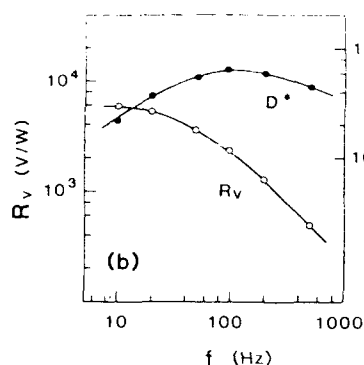


Fig. 13 Frequency dependence of R_v and D^* for the reticulated linear array sensor.

SUMMARY

Thin films of Pb-based ferroelectrics were prepared by rf magnetron sputtering. These films showed unique and excellent properties which are not obtained on the bulk ceramics. It was found that the thin films show remarkably large pyroelectric effect without poling treatment. Pyroelectric infrared sensors were fabricated using the PLT thin films. This type of sensor is carried on air-conditioners for sensing of persons. This is the first report of a thin ferroelectric film application to consumer appliances.

The PZT thin films with $x=0.9$ showed a large remanent polarization of $46\mu\text{C}/\text{cm}^2$, small coercive force of $28\text{kV}/\text{cm}$ and good endurance behavior (no degradation of Pr after 10^{11} cycles). Recent activities of ferroelectric thin film research in Japan was also reported.

Table I
Characteristics of the reticulated linear array sensor

Voltage responsivity R_v (at 50Hz)	3600V/W
Specific detectivity D^* (500K, 50Hz, 1Hz)	$5.0 \times 10^8 \text{ cm Hz}^{1/2}/\text{W}$
Cross talk (at 50Hz)	4 %
Element density	5 elements/mm
Element number	64 elements
Element size	$0.1 \times 0.3 \text{ mm}^2$

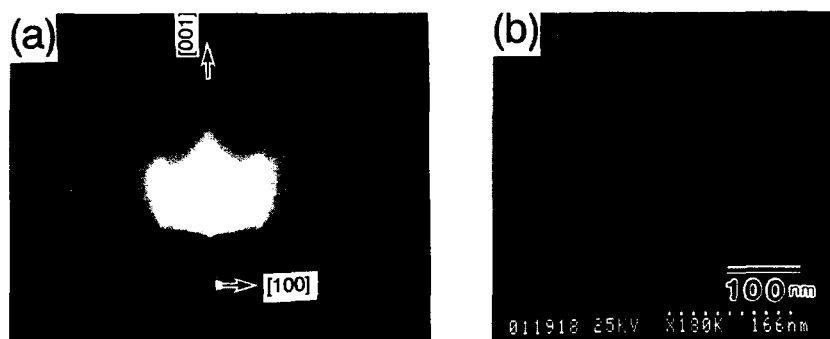


Fig. 14 (a) RHEED pattern and (b) SEM image of the newly developed (100) Pt thin film electrode.

ACKNOWLEDGEMENT

The authors would like to thank Mr. Yoshihiro Daito and Professor Yoshichika Bando of Kyoto University for taking fine TEM photographs.

REFERENCES

- 1.M.Okuyama, T.Usuki, Y.Hamakawa and T.Nakagawa, Appl. Phys., 21,339 (1980).
- 2.M.Okada,K.Tominaga,T.Araki,S.Katayama and Y.Sakashita, Jpn. J. Appl. Phys., 29, 718 (1990).
- 3.K.Iijima, Y.Tomita, T.Takayama and I.Ueda, J. Appl.Phys., 60, 361 (1986).
- 4.K.Iijima, T.Takayama, Y.Tomita and I.Ueda, ibid.,60, 2914 (1986).
- 5.K.Iijima, I.Ueda and K.Kugimiya, Jpn. J. Appl. Phys., 30,2149 (1991).
- 6.R.Takayama and Y.Tomita, J.Appl. Phys., 65,1666 (1989).
- 7.R.Takayama, Y.Tomita, K.Iijima and I.Ueda, J.Appl. Phys., 63, 5868 (1988).
- 8.R.Takayama, Y.Tomita, K.Iijima and I.Ueda, ibid., 61, 411 (1987).
- 9.Ferroelectric Thin Films Mat. Res. Soc. Proc. 243,(Eds. A.I.Kingon, E.R.Mayers and B.Tuttle) MRS (1992).
- 10.A.Shirayanagi, K.Tominaga, and M.Okada, Ext. Abstracts the 40th Spring Meeting of Jpn. Soc. Appl. Phys. Tokyo Japan (1993), Vol.2, p490.
- 11.M.Ushikubo, Y.Ito, T.Kawabe, H.Matusnaga, N.Ohtani and T. Takase, ibid., p444.
- 12.T.Mihara, H.Watanabe and C.Paz de Araujo, ibid., p448.
- 13.N.Nagao and K. Iijima, ibid., p443.
- 14.D.A.Berlincourt, C.Cmouk and H.Jaffe, Proc. IRE, 48, 220 (1960).
- 15.K.Sreenivas, M.Sayer and P.Garrett, Thin Solid Film, 251 (1989).
- 16.H.Takeuchi and K.Kushida, Proc. IEEE 7th Int. Symp. on Application of Ferroelectrics, p115.
- 17.K.Iijima, T.Terashima, Y.Bando, K.Kamigaki and H.Terauchi, J. Appl. Phys., 72, 2840 (1992).

PZT THIN FILMS ON A LEAD TITANATE INTERLAYER PREPARED BY rf MAGNETRON SPUTTERING

P. H. Ansari*, A. Safari

Department of Ceramic Engineering, Rutgers University, Piscataway NJ 08855

ABSTRACT

Ferroelectric lead zirconate titanate (PZT) films with a composition near the morphotropic phase boundary have been deposited by rf magnetron sputtering on a Si substrate coated with silicon oxide, titanium, and platinum (Si/SiO₂/Ti/Pt). Substrate temperature and oxygen partial pressure were changed during deposition to prepare films with controlled stoichiometry and perovskite structure. The effects of lead titanate (PT) as a buffer layer were investigated. Thin films of PT/PZT have a dielectric constant of 800 with a dissipation factor of 0.04 at 1 kHz. The remnant polarization of 8 $\mu\text{C}/\text{cm}^2$ and the coercive field of 50 kV/cm were measured. The effect of processing on the formation of perovskite phase and the electrical properties will be discussed.

INTRODUCTION

Ferroelectric thin films, due to their display of a spontaneous electrical polarization that can be switched between two stable states, are of considerable interest in fabricating a ferroelectric memory device¹⁻³. Such devices would require a ferroelectric material with good endurance (10^{10} - 10^{19} cycles) and retention (1-10 years), fast switching polarization of at least 5 $\mu\text{C}/\text{cm}^2$ and a switching voltage capability ranging between 3 and 5 volts. These operating conditions demand a high quality ferroelectric film with low coercive field, high remanent polarization and minimal aging and fatigue. Lead zirconate-titanate (PZT) thin film is a prime candidate for memory applications.

Thin films of PZT have been prepared by several deposition methods including sputtering^{4,6}, sol-gel^{7,8}, and pulsed laser deposition^{9,10}. Several review papers on comparing various features of common deposition techniques of ferroelectric materials can be found in the literature¹¹. In the present work, rf magnetron sputtering has been used, a method that is compatible with conventional semiconductor processing such as CMOS, and offers good control of the deposition parameters and the stoichiometry of the film.

In this work the deposition parameters such as the target-to-substrate distance and the sputtering power were optimized to grow PZT films on a Si-based multilayer substrate. The effects of a lead titanate (PT) layer on the formation of the perovskite phase were investigated extensively. Such intermediate layers were found to minimize the substrate dependencies of the crystallization of PZT thin films. PZT films deposited directly on the Si-based substrate (i.e. with no intermediate PT layer) showed a great tendency for electric short, whether or not the substrate had been annealed prior to growth. The perovskite phase formation and the electrical properties of the PT/PZT composite thin films are presented.

EXPERIMENTAL

A Sputtered Film Inc. rf magnetron sputtering machine was used to deposit thin films of PT and PZT on a multilayer substrate. The system was equipped with a Balzers turbo

*Permanent address: Physics Department, Seton Hall University, S. Orange, NJ 07079

molecular pump allowing film growth in a 100% oxygen environment, and an Angstrom Sciences sputtering gun, permitting the use of cold pressed powders as targets.

$\text{PbZr}_{0.53}\text{Ti}_{0.47}\text{O}_3$ films were prepared using targets made from a commercially synthesized powder (PZT 501A) manufactured by Ultrasonic Powders Inc. PT films were deposited using a PbTiO_3 powder made by conventional solid solution technique, i.e. by mixing the TiO_2 and PbO powders and calcining at 850°C . Additional 10 wt% excess PbO was added to both the PZT powder and the PT powder prior to target preparation. Excess PbO in the starting material compensates the PbO losses during the sputtering procedure, allowing the deposition of stoichiometric films. Target materials were cold pressed onto a shallow grooved metallic dish to a thickness of about 0.3 cm and a diameter of 5.1 cm.

A (100) oriented Si wafer coated with silicon oxide, titanium and platinum ($\text{SiO}_2/\text{Ti}/\text{Pt}$) was used as a substrate. The Ti layer improves the adhesion of the Pt-electrode on SiO_2 . The multilayer substrates were thoroughly cleaned before they were placed onto a holder facing a target at an optimized distance of 5 cm. A heating element clamped to the holder allowed the substrate reaching a temperature up to 750°C . All depositions were preceded by a pre-sputtering period of at least 30 minutes. Films of PT and PZT were reactively deposited both at room temperature and in situ up to 650°C according to the flow chart given in Fig. 1. Most films were grown in a 100% oxygen medium, whereas, others were deposited in either Ar only or a mixture of Ar/O_2 . The sputtering conditions of PT and PZT thin films are given in Table I.

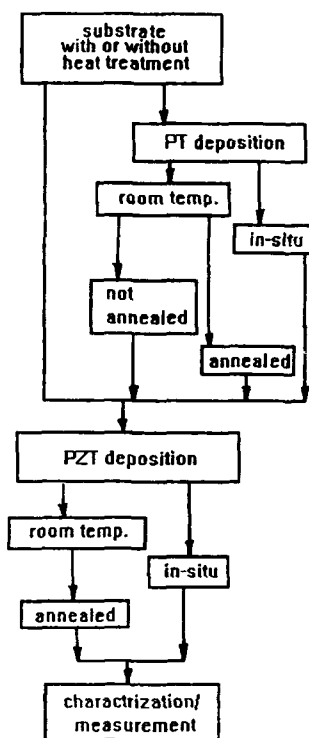


Fig. 1 Deposition flow chart.

RESULTS AND DISCUSSIONS

PZT films were prepared at both room temperature (i.e. without heating the substrate) and higher temperatures between 450°C and 650°C . The crystal structure of the sputtered films were observed to depend on the substrate temperature. While, PZT films prepared at low substrate temperatures were amorphous, those deposited at temperatures between 450°C and 600°C displayed a mixture of perovskite and pyrochlore phase. Films prepared at temperatures higher than 600°C showed a single phase perovskite structure. Films with amorphous structure required a heat treatment in order

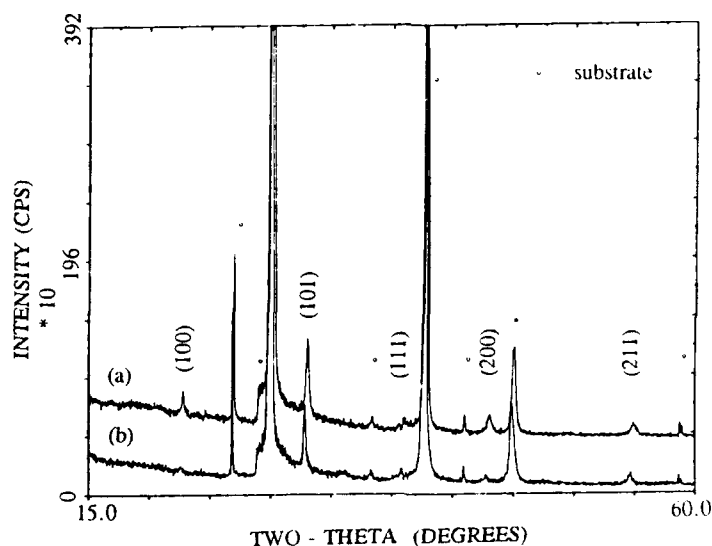
Table I The sputtering parameters.

Parameters	PT Films	PZT Films
rf Power	110 W	50-110 W
Target	Cold Pressed Powder	Cold Pressed Powder
Target Diameter	5.1 cm	5.1 cm
Target-Sub. Distance	5 cm	5 cm
Gas Flow	O ₂ : 2-5 sccm Ar: 2 sccm	O ₂ : 2-12 sccm Ar: 6-10 sccm
Gas Pressure	14-30 mtorr	14-120 mtorr
Substrate Temp.	up to 625°C	up to 650°C
Deposition Rate	15-20 Å/min	15-20 Å/min

to transform their structure into a perovskite phase. This was achieved by rapid thermal processing (RTP) as well as the conventional annealing method. RTP at 600°C for up to 20 seconds and conventional annealing at 500°C for up to one hour were examined.

Room temperature deposited PZT films (with no PT layer) annealed at 600°C for (a) 30 minutes and (b) 20 seconds are compared in Fig. 2. While both patterns represent single phase perovskite structure, the annealed film displays an XRD pattern with peaks that are slightly shifted to the lower 2-theta values and are less intense than those annealed for a longer time. Shift of the XRD lines in Fig. 2 maybe due to stress in the film studied.

Single phase perovskite structure is also obtained when PZT films are deposited on

**Fig. 2** PZT films annealed at 600°C for (a) 30 minutes and (b) 20 seconds.

PT layers at room temperature and subsequently annealed at 600°C for 30 minutes. In Fig. 3, a typical XRD pattern of a PZT film deposited on an annealed PT layer is compared to that of a film deposited on a PT layer with no prior heat treatment. While the two films demonstrate essentially identical XRD patterns, PZT deposited on an annealed PT layer displays a more intense pattern than that deposited on a not heat treated PT layer.

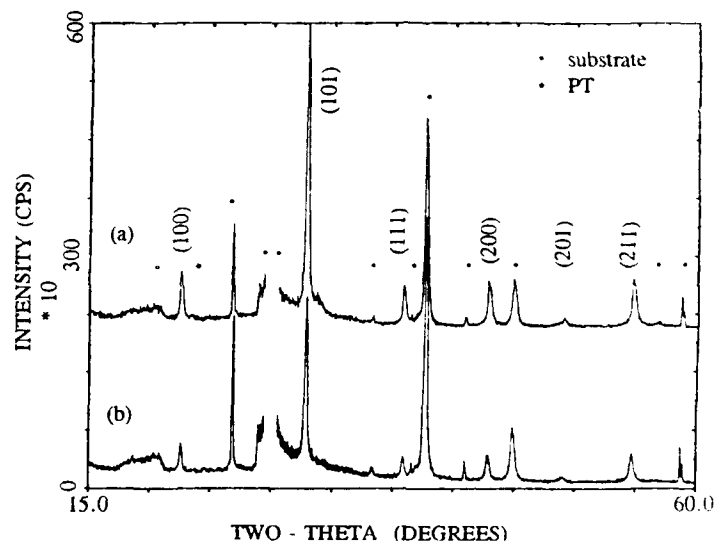


Fig. 3 PZT films deposited on (a) an annealed PT layer and (b) a not heat treated PT layer.

Fig. 4 displays the XRD patterns of two PT/PZT composite films with PT films grown at room temperature followed by (a) no further heat treatment, and (b) annealed at 600°C for 30 minutes, prior to the in-situ deposition of PZT at 600°C. Both patterns display single phase perovskite structure. However, the XRD peaks for the PZT films deposited on not-heat treated PT layers are found to be more intense than those grown on annealed PT layers. In addition, the XRD peaks for Pt (the bottom electrode) are more intense for the PZT films deposited on annealed PT layers. This maybe due to the partial diffusion of Pt in the PT buffer layer due to excessive heating. Therefore, for application purposes one would prefer to grow PZT on a as grown PT layer than annealed PT films.

In all films prepared, the (110) diffraction peak is the main XRD peak of the perovskite PZT, which corresponds to a lattice distance $d_{hkl} = 4.036 \text{ \AA}$. This peak was used to estimate the PZT grain size using Cauchy and Pseudo-Voight models. The grain size of in-situ deposited PZT films at 600°C is averaged at 60nm. This estimate is in line with the findings of other scholars who had used no buffer layer⁴.

The microstructure of thin films was examined using the scanning electron microscopy (SEM). The films are generally crack-free and have a smooth surface feature (not shown here). Some very small dark dots on otherwise bright backgrounds were observed on some PZT films. The elemental analysis of both regions revealed no obvious differences.

When PZT films were deposited directly on Pt-electrodes they showed a great

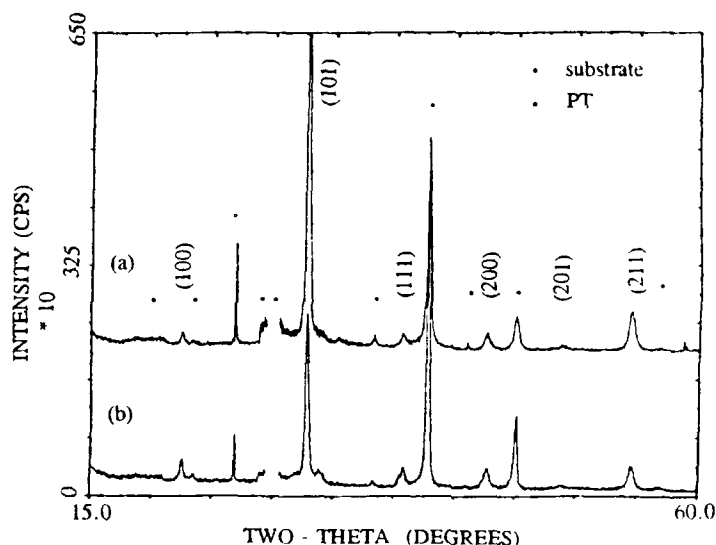


Fig. 4 In-situ deposited PZT films on (a) a not heat treated PT layer and (b) an annealed PT layer.

tendency for electric short, whether or not the substrate had been heated prior to growth. Observations of similar nature are also found in the literature ¹¹.

To minimize the electric short, a PT buffer layer was deposited on Pt-electrode. PT as a buffer layer is a preferred material since it crystallizes into the perovskite phase with a lattice constant similar to that of PZT. The effective role of PT as an interlayer in growth of PLZT by sol-gel has been reported ¹². Interlayers have been found to minimize the substrate dependencies of the crystallization of PZT thin films. However, it is found to be necessary to minimize the buffer layer since its thickness affects the film properties such as polarization and permittivity. We use a PT layer of a thickness, minimized at about 300 Å. However, the electrical properties of thin films like capacitance, dielectric constant, and polarization are inevitably influenced by thin films of PT.

In our study, Pt as top electrode was sputtered onto the films and together with the bottom electrode, they sandwiched the ferroelectric thin films forming a capacitor cell. Here, PZT films are between 2000 Å to 5000 Å thick.

At 1 kHz, the capacitance of the composite films was found to be at least 3 nF, and the dielectric constant was measured to vary in the range of 750-990 at room temperature with an averaged dissipation factor of 0.04.

A Sawyer-Tower circuit was used to measure the ferroelectric properties of the sputtered films. Hysteresis loops such as that shown in Fig. 5 are obtained at a driving frequency of 100 Hz. Remanent polarizations of up to 10 $\mu\text{C}/\text{cm}^2$ and coercive field of about 50 kV/cm were measured. The hysteresis loops are asymmetric due to an internal bias field. Such fields are found to be about 4 kV/cm.

CONCLUSION

In this work, the feasibility of growing high quality films of PZT on Si has been

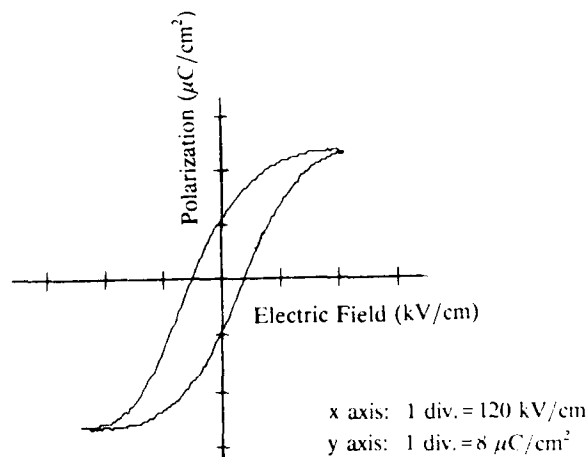


Fig. 5 A typical hysteresis loop for the PT/PZT composite films.

demonstrated using PT buffer layers. These films display high dielectric constants and remanent polarizations which make them very attractive for integrated Si non-volatile memories.

ACKNOWLEDGEMENT

The authors would like to thank the support of the National Science Foundation.

REFERENCES

1. Carlos A. Paz de Araujo, Larry D. McMillan, Bradley M. Melnick, Joseph D. Cuchiario, and James F. Scott, *Ferroelectrics* **104**, 241 (1990).
2. Leonard J. Schewe, *Ferroelectrics* **116**, 157 (1991).
3. B. P. Maderic, L. E. Sanchez, and S. Y. Wu, *Ferroelectrics* **116**, 65 (1991).
4. S. B. Krupanidhi, N. Maffei, M. Sayer, and K. El-Assal, *J. Appl. Phys.* **54** (11), 6601 (1983).
5. Takashi Hase, and Tadashi Shiosaki, *Japanese J. Appl. Phys.* **30** (9B), 2159 (1991).
6. Ryoichi Takayama, and Yoshihiro Tomita, *J. Appl. Phys.* **65** (4), 1666 (1989).
7. B. M. Melnick, J. D. Cuchiario, L. D. McMillan, C. A. Paz de Araujo, and J. F. Scott, *Ferroelectrics* **112**, 329 (1990).
8. L. E. Sanchez, D. T. Dion, S. Y. Wu, and I. K. Naik, *Ferroelectrics* **116**, 1 (1991).
9. R. Ramesh, A. Inam, W. K. Chan, F. Tillerot, B. Wilkens, C. C. Chang, T. Sands, J. M. Tarascon, and V. G. Keramidas, *Appl. Phys. Lett.* **59** (27), 3542 (1991).
10. K. S. Grabowski, J. S. Horwitz, and D. B. Chrisey, *Ferroelectrics* **116**, 19 (1991).
11. See for example, R. A. Roy, K. F. Etzold, and J. J. Cuomo, *Mat. Res. Soc. Symp. Proc.* **200**, 141 (1990).
12. S. L. Swartz, S. J. Bright, P. J. Melling, and T. R. Shrout, *Ferroelectrics* **108**, 71 (1990).

ULTRA-THIN SPUTTERED PZT FILMS FOR ULSI DRAMs

JYOUNG KIM, C. SUDHAMA, R. JESH KHAMANKAR and JACK LEE
Microelectronics Research Center, The University of Texas at Austin, Austin, TX 78712

ABSTRACT

In this work, a high-temperature deposition technique has been developed for ultra-thin sputtered PZT films for ULSI DRAM (>256Mb) storage capacitor applications. In contrast to the previously developed low-temperature (200°C) deposition, deposition at high-temperature (400°C) yields a desirable reduction in grain size of the perovskite phase. The thickness of PZT films has been reduced to less than 30nm with high charge storage density ($\sim 30 \mu\text{C}/\text{cm}^2$) and low leakage current density. An optimized 65nm PZT thin film was found to have an equivalent SiO_2 thickness of 1.9Å and a leakage current density of less than $10^{-6} \text{ A}/\text{cm}^2$ under 2V operation.

INTRODUCTION

As the area of a dynamic random access memory (DRAM) cell keeps decreasing, complicated capacitor cell technologies (trench, stack or rugged-stack) have been developed to meet the required charge storage density [1, 2]. Materials with very high dielectric constants allow for a reduction in device area permitting a higher level of integration with satisfactory requirements, and avoid having to scale down conventional SiO_2 thickness to extremely low values. Therefore, there is a strong need for alternative dielectric materials for ULSI DRAM cells, and ferroelectric thin films, such as PZT ($\text{Pb}(\text{Zr,Ti})\text{O}_3$), are potential candidates for next generation memory cells. An ability to scale down the thickness while maintaining high dielectric constants for these materials has a twofold advantage: thinner films will, in general, require lower operating voltages for the same performance, thereby allowing a reduction in power supply voltages and power consumption. Secondly, thinner dielectrics will simplify the conformal deposition of passivation layers by avoiding large non-planarities on the chip.

In previous work, we have optimized a low-temperature deposition technique (at 200°C), which is followed by a high-temperature ($\sim 550^\circ\text{C}$ - 600°C) crystallization of the perovskite phase in order to obtain large charge storage densities Q_c [3, 4]. Note that the crystallization temperature of 550°C is relatively low in comparison to other PZT processes. One disadvantage with large grain size ($30 \mu\text{m}$) may cause potential on-chip Q_c non-uniformities (cell-to-cell variation in Q_c might actually not be a severe problem as long as each cell maintains a minimum Q_c). Thus the main impetus for high-temperature deposition is a reduction in grain size, which also results in a drop in the perovskite grain size. As is discussed below, it also becomes possible to simultaneously scale the thickness down to less than 300Å. Material and electrical characteristics of the ultra-thin films are reported.

EXPERIMENTAL DETAILS

Test devices used in this study were metal-insulator-metal capacitors (with a platinum electrode thickness of 4000Å) fabricated on $\text{TiO}_2/\text{SiO}_2/\text{Si}$ multi-layered substrates. The PZT films were deposited by reactive DC-magnetron sputtering from a multi-component Pb/Zr/Ti metal target (PZT target) in a pure oxygen ambient. The PZT metal target was designed to provide a compositional ratio of $\frac{[\text{Ti}]}{[\text{Ti}]+[\text{Zr}]} = 0.35$. Pb content in the films was adjusted by sputtering simultaneously from a separate Pb target. This was used to compensate for the Pb lost during deposition and annealing [3]. With PZT gun power of 30W, the compositional ratio $\frac{[\text{Pb}]}{[\text{Ti}]+[\text{Zr}]}$ was 0.95, 1.04, 1.10 and 1.15 for Pb compensation powers of 9W, 12W, 15W and 17W respectively after 550°C crystallization in a nitrogen ambient. In this study, the PZT film was annealed at various temperatures. Annealing time and ambient were fixed at 1hr

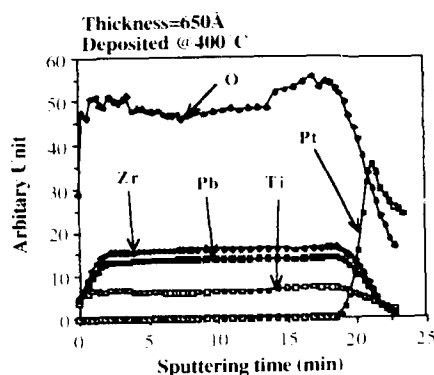


Figure 1. AES depth profile of a PZT film deposited at 400 °C and annealed at 575 °C. PZT and Pb gun powers were 30W and 9W, respectively. Approximate sputtering rate is 30 Å/min.

and pure nitrogen. Devices with different thicknesses were obtained by varying deposition times. The top electrode (area = $87 \times 87 \mu\text{m}^2$) was patterned using a lift-off process.

A pulsed-polarization test (with triangular pulses) generated using the RT66A tester was used to measure charge-storage density [5]. Leakage current measurements were made on an HP 4140B pico-ammeter interfaced to an HP computer. A Tencor Alpha-step profilometer was used to measure thickness after selective-area etching. Compositional analysis was done using a Physical Electronics Scanning Auger Microprobe with a single-pass cylindrical mirror analyzer; composition was calculated by multiplying the peak-to-peak height of each component by an appropriate weight-factor [3]. Phase-content was analyzed using a grazing angle X-ray diffractometer. Nomarski phase-contrast microscopy for the microstructural analysis of the films was performed on an Olympus BH-2 microscope.

RESULTS AND DISCUSSIONS

In our previous attempt to scale down the film thickness using low temperature (200 °C) sputter-deposition, anomalous phase transformation at the interface between the PZT and bottom Pt electrode was observed. This resulted in diminished charge storage densities for

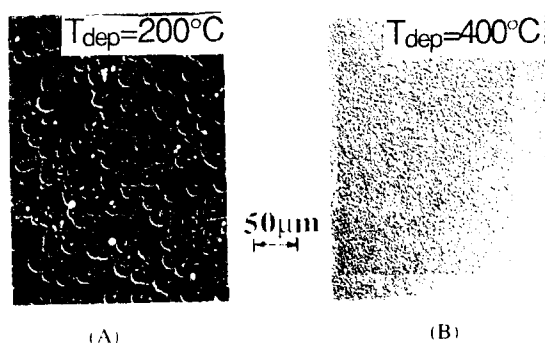


Figure 2. Nomarski pictures for optimized 1000 Å PZT films deposited at (a) 200 °C and (b) 400 °C. Both were annealed at 575 °C.

the same operating voltage in films thinner than 3500Å. This was due to a low dielectric constant interfacial layer arising from significant diffusion of Pb into the bottom Pt [6, 7]. Careful control of Pb compensation during deposition and annealing results in good electrical characteristics in films as thin as 1000Å [4]. However, a 300Å thick interfacial layer is still observed in these films using cross-sectional TEM. It is difficult to scale down thickness beyond 100nm with the low temperature deposition technique. On the other hand, the formation of a relatively thick interface layer in the PZT film deposited at high temperature (400°C) is apparently avoided. Figure 1 depicts the concentration of each element as a function of sputtering time from a 650Å thick PZT film deposited at 400°C and subsequently annealed at 575°C. Note that the range of interdiffusion between PZT and Pt is much narrower than previously reported. The thinner interface layer helps avoid a series capacitor and results in a high charge storage density for the 650Å thick PZT films. For films thinner than 300Å, significant Pb depletion is observed due to diffusion into the Pt substrate.

Another problem with low-temperature sputter-deposition is the inevitable evolution of large sized perovskite grains commonly reported in PZT thin films [3, 4, 8]. A large grain size is believed to possibly lead to cell-to-cell non-uniformity on the gigabit DRAM chip, where the storage capacitor area is expected to be as small as $0.2\mu\text{m}^2$. Figure 2(a) shows rosettes as large as $30\mu\text{m}$ crystallized after annealing a film deposited at a low temperature. Figure 2(b) shows the relatively smooth surface of a film sputtered at high temperature which has a grain size smaller than 1000Å (this is confirmed by SEM). In the low temperature deposition case, the as-deposited film is a mixture of amorphous and pyrochlore phases. Post-deposition crystallization annealing involves two steps of phase transformation: first from amorphous to pyrochlore phase and subsequently to the perovskite phase. The pyrochlore phase thus provides potential nucleation sites for the perovskite phase formation [9, 10]. In comparison with low temperature deposited films, more nucleation sites exist in those deposited at high-temperatures. A large number of nuclei lead to a small grain size after phase transformation annealing.

The films used in this study were deposited at fairly low deposition rates; the deposition rate is easily increased by increasing the power to the magnetron gun that houses the PZT target. Figure 3 shows a comparison of effective dielectric constants of films sputtered at high (50W) and low (30W) powers. Deposition rates for the low and high power techniques are 2.7Å/min and 7.1Å/min, respectively. Further, for each PZT power the lead-compensation power (i.e. the power supplied to the gun containing the metallic lead target) was optimized. Pb concentration in the PZT films is a critical parameter which determines not only material but electrical characteristics as well [11]. The effective dielectric constant is

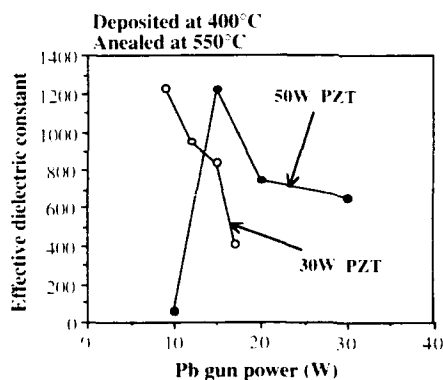


Figure 3. Effective dielectric constant as a function of a Pb-compensation power with different PZT powers. Effective dielectric constants are obtained by applying large signal (0V to 3V) pulses.

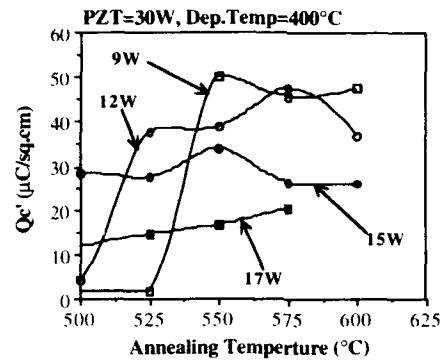


Figure 4. Charge storage density as a function of annealing temperature for various Pb-compensation powers. Film thickness is 650 \AA .

obtained using a large signal pulse (from 0V to -3V), in order to simulate DRAM operation as closely as possible. Charge storage density (and hence the effective dielectric constant) for films with a PZT power of 50W exhibits a single peak at 15W lead compensation (near stoichiometric PZT composition, as evident from AES) while the lower PZT power yields the highest charge storage density of 51 $\mu\text{C}/\text{cm}^2$ with 9W lead compensation. Unfortunately, due to plasma stability issues, 9W is the lowest practical Pb gun power. It was observed that while both PZT gun powers achieved nearly identical effective dielectric constants at a near-stoichiometric composition, the lower power yields a lower leakage current density (J_L). Figure 4 shows the variation of charge storage density as a function of annealing temperature for different Pb-compensation levels (for the low PZT gun power). 9W compensation yields the highest Q_c . The abrupt increase in Q_c with increasing anneal-temperature for low Pb compensation is understood to be due to the onset of phase transformation. Since the phase transformation temperature window is very narrow due to the low thickness, Q_c does not increase beyond a certain critical annealing temperature and instead saturates (for all Pb compensation levels), as also reported in [6]. For higher Pb compensation powers, the as-deposited films exhibit fairly high charge storage densities. This is possibly because a high

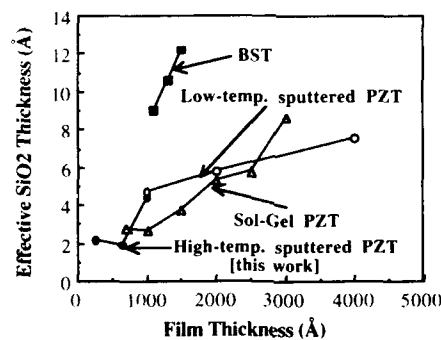


Figure 5. Comparison of effective SiO_2 thickness as a function of dielectric film thickness between different materials and deposition techniques.

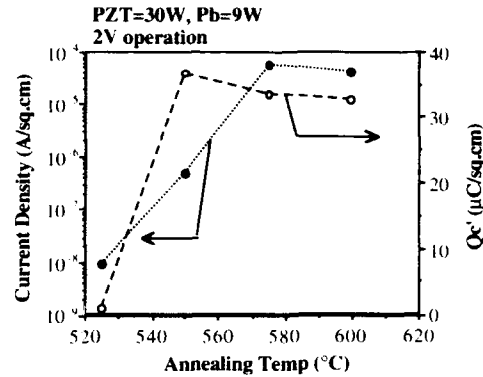


Figure 6. 2V DRAM operation on 650Å PZT films deposited at 400°C with PZT and Pb powers of 30W and 9W respectively.

Pb concentration (for 15W and 17W, $\frac{[Pb]}{[Ti]+[Zr]} = 1.1$ & 1.15 respectively) enhances phase transformation such that the perovskite phase is obtained at lower annealing temperature. It must be noted that the leakage current density increased significantly with the Pb compensation level (possibly due to segregation of extra metallic Pb and PbO in grain-boundaries), thereby diminishing the usefulness of as-deposited perovskite films (Figure 4).

Figure 5 shows the variation of effective SiO₂ thickness as a function of film thickness for very thin films of two dielectric materials obtained from various deposition techniques (calculated from ref. [4, 12 and 13]). An optimized low-temperature sputter-deposited 1000Å PZT film has an equivalent SiO₂ thickness of 4.7Å [4] while Moazzami, et al. have reported sol-gel derived PZT films of 700Å with an equivalent SiO₂ thickness of 2.1Å for 0.75V operation [12]. A 1000Å BST ((Ba,Sr)TiO₃) film equivalent to 13Å of SiO₂ has been reported recently [13]. In comparison, an optimized 650Å thick sputtered PZT film deposited at a high temperature is equivalent to 1.9Å of SiO₂, with a leakage current density of less than 10⁻⁶A/cm² for 2V operation. Furthermore, the 270Å film exhibits a value close to that of the

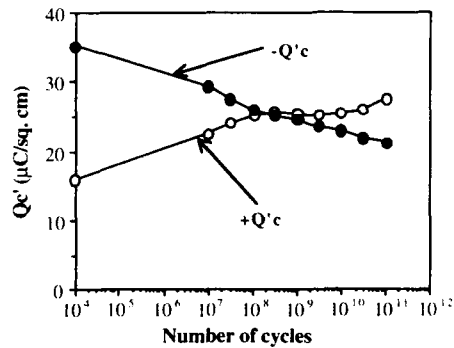


Figure 7. Fatigue behavior of a 650Å PZT film (PZT=30W, Pb=9W) under unipolar stress (0V to -2V) to 10¹¹ cycles. 1MHz square pulses were used.

650Å film. This implies that effective dielectric constant decreases as the film thickness is reduced. It is observed by AES that in the 270Å film there is severe depletion of Pb near the interface between PZT and the bottom Pt electrode. On the other hand, the Pb concentration is uniform throughout the 650Å PZT film. The anomalous interface in the 270Å film may act as a series capacitor and thereby reduce the effective dielectric constant. Even though scaling down the thickness to less than 300Å causes a reduction in dielectric constant, the charge storage density ($Q_c = 31 \mu\text{C}/\text{cm}^2$) and leakage current density (less than $10^{-6} \text{A}/\text{cm}^2$ at 2V) satisfy requirements of 256Mb DRAMs.

Leakage current density and charge storage density of films deposited with 30W PZT and 9W Pb gun power under 2V DRAM operation are shown in Figure 6 as a function of annealing temperature. As annealing temperature increases, leakage current density rises steeply, possibly due to thermal stress between PZT film and bottom electrode Pt [14]. Thus when leakage current density is taken into account, an annealing temperature of 550°C is optimum under 2V operation ($Q_c = 37 \mu\text{C}/\text{cm}^2$ and $J_l = 4 \times 10^{-7} \text{A}/\text{cm}^2$). Figure 7 shows the fatigue behavior under unipolar stress for the 650Å film. Unipolar fatigue testing (0 to -2V, 1MHz) to 10^{11} cycles indicates significant degradation of Q_c for the negative test polarity and an increase in the positive Q_c . This was seen to be related to hysteresis relaxation as well as the reduction in zero-voltage relaxation [15].

SUMMARY AND CONCLUSIONS

A high temperature deposition technique has been developed for ultrathin sputtered PZT films with very low equivalent SiO_2 thicknesses ($\sim 2\text{\AA}$). An increase in deposition temperature from 200°C to 400°C leads to a reduction in grain size, which in turn might improve the cell-to-cell uniformity of thin film device characteristics. PZT films with thicknesses of less than 300Å show high charge storage density ($\sim 30 \mu\text{C}/\text{cm}^2$) and low leakage current density ($< 10^{-6} \text{A}/\text{cm}^2$). Fatigue endurance to unipolar pulses needs to be improved before the films can be used in ULSI DRAMs.

References

1. J. H. Ahn et al., Tech. Dig. VLSI Tech. Symp., p.12, 1992
2. P. C. Fazan et al., IEDM Tech. Dig., p. 263, 1992
3. V. Chikarmane et al., J. Electron. Mater., 21(5), p. 503, 1992
4. C. Sudhama et al., J. Electron. Mater., to be published
5. RT66A Ferroelectric Tester Operation Manual, Version 2.0, Radiant Technologies, Albuquerque, New Mexico
6. V. Chikarmane et al., Mat. Res. Soc. Symp. Proc., 243, p. 367, 1992
7. K. Kugimiya et al., Mat. Res. Soc. Symp. Proc., 243, p. 179, 1992
8. S. A. Myers et al., Mat. Res. Soc. Symp. Proc., 200, p. 231, 1990
9. K. C. Chen et al., Mat. Res. Soc. Symp. Proc., 73, p. 731, 1986
10. C. V. R. Vassant Kumar et al., J. Appl. Phys., 71, p. 864, 1992
11. V. Chikarmane et al., Mat. Res. Soc. Symp. Proc., 230, p. 297, 1992
12. R. Moazzami et al., IEDM Tech. Dig., p. 973, 1992
13. E. Fujit et al., IEDM Tech. Dig., p.267, 1992
14. J. Lee et al., Integrated Ferroelectrics, to be published
15. C. Sudhama et al., J. Vac. Sci. Technol., to be published

PART XIII

**Pulsed Laser and Other
Vapor Deposition Techniques**

EFFECTS OF PROCESS PARAMETERS ON THE ABLATED FLUX CHARACTERISTICS DURING PULSED-LASER ABLATION OF LEAD ZIRCONATE TITANATE (PZT)

D. I. LICHTENWALNER¹, O. AUCIELLO^{1,4}, R. DAT¹, R. BARNES², A.F. SCHREINER², O.E. HANKINS³, and A.I. KINGON¹, North Carolina State University, Raleigh, NC 27695.

¹Dept. of Mat. Sci. and Eng., ²Dept. of Chemistry, and ³Dept. of Nuclear Engineering.

⁴MCNC Center for Microelectronics, Research Triangle Park, NC 27709.

ABSTRACT

We have investigated the ablated flux characteristics of $\text{PbZr}_x\text{Ti}_{1-x}\text{O}_3$ as a function of deposition process parameters. The ablation-deposition rate, angular distribution, and type of ablated species are all affected by the oxygen gas pressure. Visually, a change in the shape and color of the ablation plume are evident upon adding oxygen gas. The ablated flux distribution narrows as the oxygen pressure is increased, from a $\cos^{40}\theta$ distribution in a low gas pressure, up to a $\cos^{260}\theta$ distribution at an oxygen pressure of 300 mTorr. This narrowing, or focusing, of the ablated plume also results in an increased deposition rate along the plume centerline for high laser power. However, at low laser power the deposition rate decreases as the pressure is increased, due to gas scattering effects. The energy of depositing species and the ratio of deposition flux to O_2 flux will then be very different in each of these two regimes. The species in the plume have been examined using optical emission spectroscopy. We have found that mostly atomic species are present, but the ratio of ions to neutrals is very different for the Pb, Zr, and Ti atoms. Therefore, the application of electric fields near the substrate would affect the film composition to some degree.

INTRODUCTION

Pulsed laser ablation-deposition (PLAD) has been shown by many researchers to be a useful technique for depositing epitaxial films of multicomponent materials. Recent reports suggest that epitaxial films of $\text{PbZr}_x\text{Ti}_{1-x}\text{O}_3$ (PZT) deposited using PLAD show little loss of remnant polarization after 10^{10} switching cycles¹. This indicates that epitaxial films may be desirable to meet the operational goals envisioned for ferroelectric RAM devices. However, there are many aspects of the PLAD process that are not completely understood, or have not been thoroughly studied. Understanding the deposition process for PZT film growth is important in order to minimize Pb loss during film growth, eliminate formation of pyrochlore phases, eliminate surface particulates, and control the film microstructure. Knowledge and control of the ablated flux distribution is also important for scale-up to larger substrate areas.

Numerous studies of the pulsed laser ablation process have been performed,²⁻⁹ although most studies have concentrated on the ablation of $\text{YBa}_2\text{Cu}_3\text{O}_{7-\delta}$ [Refs. 4-7]. Studies of PZT ablation have focused on examining the Pb incorporation as a function of oxygen pressure,⁸ or on the energy distributions of ablated species.⁹ In this study, we have investigated the effect of the oxygen pressure during ablation on: 1) the angular distribution of deposited species, 2) the deposition rate at the substrate position, and 3) the type of species in the plume. Evidence that the oxygen pressure affects the deposition dynamics is clearly observed by visual inspection of the plume. The deposition flux characteristics were examined using a quartz crystal thickness monitor positioned at the substrate location, and the species in the plume were examined using optical emission spectroscopy.

EXPERIMENTAL PROCEDURE

The vacuum system used for film deposition consists of a stainless steel chamber pumped by a 510 l/s turbomolecular pump. During film deposition, a conductance limiting aperture is inserted which allows chamber pressures to be as high as 1 Torr with the pump on. The oxygen gas flow is controlled using an MKS mass flow meter in series with a solenoid control valve, and the chamber pressure is monitored using a Granville Phillips Convectron

gauge. A load-lock chamber with a magnetically-coupled transfer rod enables substrates and targets to be exchanged without breaking vacuum. The substrate heater and the target holder assembly are each mounted on linear motion drives for positioning during deposition, and for load-lock transfer.

Substrates are heated radiatively using a quartz lamp mounted in a ceramic holder. Substrates are bonded to a silicon backing piece (using silver paste) to obtain good thermal contact to the radiatively heated Si. A type R thermocouple is used to measure the temperature near the substrate. The thermocouple temperature is calibrated by melting Pb (MP 327°C) and Al (MP 660°C) pellets, and scaling the thermocouple readings appropriately within this range. The target holder assembly has the capability to hold six separate targets, each of which can be tilted to a fixed angle and rotated continuously about its center. The entire assembly can also be rotated to position each target in the path of the laser. This holder has been described in detail previously [10]. Sputtering targets have been prepared using conventional pressing and sintering techniques, or purchased from commercial suppliers.

A pulsed KrF excimer laser (Lambda Physik LPX 301, 25 ns pulse) is used to impact the target material. The laser impacts 45° from the target normal, while the substrate is positioned along the normal. The laser beam is focused using an appropriate lens, and enters the chamber through a quartz suprasil window. The beam energy at the target location was measured using a Coherent Labmaster-E energy meter, and the focused beam area was measured on a mark produced on a Polaroid type 55 negative impacted with one laser pulse. The average laser energy density is thus obtained from the ratio of the measured energy over the impacted area.

The angular distribution of deposited species was measured by depositing PZT onto unheated glass slides, and using Rutherford Backscattering Spectrometry (RBS) to measure the thickness profile across the glass. Average deposition rates at the substrate position were measured using an Inficon XTC quartz crystal monitor. Optical emission spectra of excited species in the plasma were monitored using a computer-controlled optical multichannel analyzer (OMA) with a 512-element photodiode array located at the focal plane of a 0.25 m monochromator with a 150 grooves/mm grating (0.5 nm spectral resolution). Light was collected from the plasma through a 0.4 mm diam optical fiber, positioned perpendicular to the ablated plume axis, and mounted on a linear motion feedthrough. The fiber was sheathed in a SS tube, to prevent deposition on the fiber end, and to use the tube aperture as a light acceptance slit. This enabled light to be sampled from fixed cross sections of the plume, and at various distances from the target surface.

RESULTS AND DISCUSSION

The effects of increasing the oxygen pressure during ablation of PZT are clearly visible by observation of the plume. The photographs in Fig. 1 show the ablation of a PZT target ($\text{PbZr}_{0.52}\text{Ti}_{0.48}\text{O}_3 + 10\%\text{PbO}$) using 900 mJ laser energy ($\sim 1.95 \text{ J/cm}^2$) in: a) vacuum, b) 50 mTorr, c) 300 mTorr and d) 900 mTorr oxygen. The plume is that of one laser pulse, with the camera shutter open much longer than the plume lifetime. Narrowing of the plume is clearly visible as the oxygen pressure is increased. Note that at the higher pressures, a narrow stream of dense emission is observed along the centerline of the plume, indicating a concentration of species there. The color of the PZT plume is a strong blue in vacuum. When oxygen is added, the plume becomes yellow/orange/red at the plasma periphery, while still bluish inside. Observations of the plume (visually, photographically) in argon gas show a similar effect on the plasma shape, but the plasma color remains totally blue. Therefore, the change in the plasma color must be due to chemical interactions between the oxygen and the ablated species. The blue in the center suggests that this region has not interacted substantially with oxygen.

To determine if the change in the plasma shape correlated to an actual change in the angular distribution of deposited species, the film thickness uniformity was examined for PZT films deposited on unheated glass slides in pressures of 10, 100, 300, and 900 mTorr oxygen. Films were deposited using a laser energy of 900 mJ ($\sim 1.95 \text{ J/cm}^2$), 3 Hz repetition rate, 6 cm distance, and a 2 min. deposition time. The film thickness distributions, measured using RBS, are shown in Fig. 2. Note that the deposition rate at the center position increases as oxygen pressure is increased, but then begins to decrease at very high pressures. Most importantly,

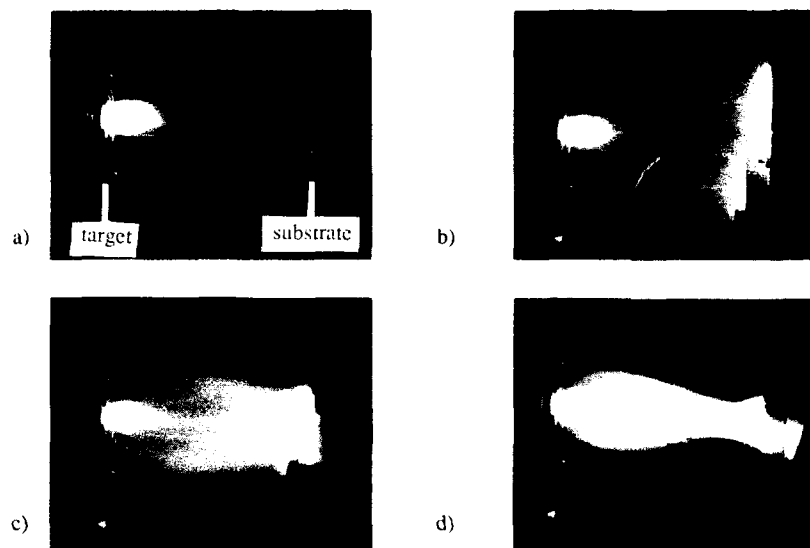


Figure 1. Photographs of the PZT ablation plume produced by a 900 mJ laser pulse in a) vacuum, b) 50 mTorr, c) 300 mTorr, and d) 900 mTorr oxygen. The actual target - substrate distance is 6 cm.

the angular distribution of ablated species is significantly affected by the pressure. We have fit the data using a sum of two cosine functions, taking into account the change in distance from the target as the angle θ is increased. The complete expression for the deposition rate is

$$t(\text{\AA}) = (A/r^2)\cos\theta + (B/r^2)\cos^n\theta, \quad (1)$$

where t is the film thickness, θ is the angle from the target normal, r is the target-to-substrate distance (which is a function of θ), and A and B are constants. The first term in eq. (1) accounts for any evaporation-like component of the flux distribution, and the second term accounts for the ablated flux distribution.

Note from Fig. 2 that the angular distribution, characterized mainly by the exponent 'n', rises from a $\cos^{40}\theta$ in 10 mTorr oxygen, up to $\cos^{260}\theta$ in 300 mTorr, and decreases back to $\cos^{120}\theta$ by 900 mTorr. Also, the magnitude of the evaporation-like component (the constant A) increases with oxygen pressure. These findings reveal that the ablated species are actually tending to converge, or focus, as oxygen gas is added. However, once the pressure is too high, gas scattering effects will tend to broaden the distribution out again. Gas scattering effects appear to be the origin of most of the $\cos\theta$ component of the flux at high pressures, with an evaporation component probably contributing the rest. (Due to the high fields generated in the plume, plasma ions repelled back to the target could possibly produce a sputtered component as well.) These angular distributions are much narrower than those observed by Venkatesan et al.⁴ for $\text{YBa}_2\text{Cu}_3\text{O}_{7-\delta}$ (YBCO) deposition, probably due to differences in the ablation conditions.

Measurements of the PZT deposition rate (after target equilibration) as a function of the laser energy and oxygen pressure reveal two distinct regimes. This is shown in Fig. 3. At low laser powers, the deposition rate drops as the pressure is increased, presumably due to gas scattering. At higher laser power, the deposition rate increases with oxygen pressure. Based

on the plume photographs and the measured narrowing flux distribution, we believe that the rate increase indicates a focusing type of effect. (When the oxygen pressure is increased beyond 300 mTorr, the rate again begins to drop even at high power due to the gas scattering effects.) Note that the deposition rate of PZT shows no obvious ablation threshold in vacuum; the gas interaction effects result in an apparent ablation threshold only, but not a true threshold. This behavior has also been observed using Ar or Kr as the background gas.

The functional dependence of this change from gas scattering to focusing depends on the laser energy, the gas pressure, the target surface condition, and the measuring distance. The focusing is expected to occur when the ablated flux density and the background gas density are near the viscous flow level. The leading edge of the plume must push aside the background gas, which has less energy, from the front of the plume (the plume front has the highest flux density). The following ejected species, which are slower or ejected at a later time,^{6,9} are channeled by collisions with the background gas into this low pressure region in the center of the plume. The photographs of the plume in Fig. 1 indicate that no background oxygen interacts with the central portion of the plume, consistent with this explanation. We believe that this plume focusing is a general phenomena, and will always be observed if the laser power and gas pressure are high enough (will be dependent on the target material and gas type).

Figure 2. Angular distribution of deposited species during ablation of PZT. The laser energy is 900 mJ, and the oxygen pressures are 10 mTorr, 100 mTorr, 300 mTorr, and 900 mTorr oxygen. The lines are fits using eq. (1).

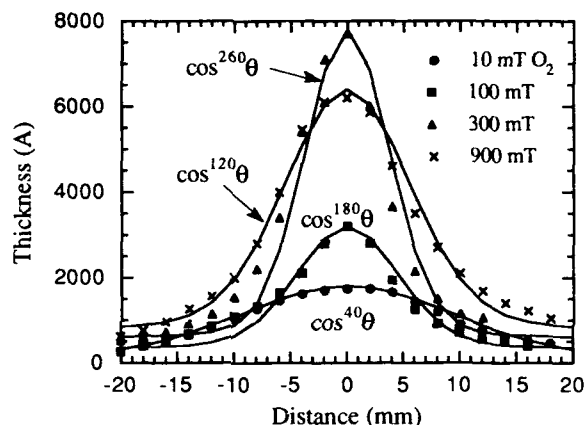
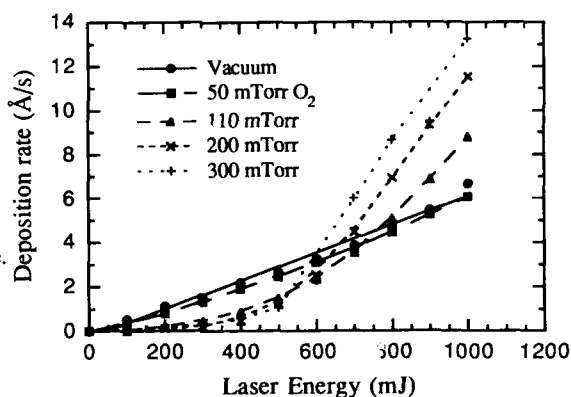


Figure 3. Deposition rate of PZT as a function of the laser energy and the oxygen pressure. The substrate-target distance is 6 cm. The lines are smoothed fits to the data points.



Optical emission spectroscopy of the plasma plume was performed to identify the type and state of the species in the plume, as well as to reveal effects caused by interaction with oxygen. Figure 4 shows optical emission spectra from PZT ablated using 400 mJ laser energy, and 10 Hz repetition rate. The oxygen pressure was 900 mTorr, for the top curve, while the bottom curve shows the spectra obtained in vacuum. The optical fiber was positioned 0.5 cm from the target surface (parallel to the surface, aiming through the plume). Note the abundance of emission lines, especially in the blue region of the spectrum. The peak at 496 nm is due to a reflection of the laser from the target surface (a 248 nm "ghost" line). Emission spectra of individual PbO, TiO₂, and ZrO₂ targets were investigated to aid in the line identification. Only a few lines do not contain significant overlaps from more than one element; these have been marked in Fig. 4 on the 900 mTorr oxygen spectrum. This PZT spectrum, as well as those of the separate oxides, reveal that nearly all of the excited Pb species are neutral atoms (Pb I), while the Zr consists of mostly singly ionized species (Zr II) plus some neutral atoms. The Ti species are a mixture of singly ionized and neutral atoms, with the neutral species appearing to outnumber the ions (Ti neutral and ion lines often overlap, making positive identification not always possible). These results indicate that attempts to alter the energy or direction of ionized species by electric fields will have little effect on the Pb atoms, but will affect the Ti and Zr atoms, because many are ionized. The abundance of atomic species over larger molecules agrees with results of other studies of the ablation flux.^{2,5,7,9} The absence of ionized Pb (Pb II) emission is probably due to two factors: Pb has a higher ionization potential than Ti or Zr, and it bonds more weakly to oxygen (which would strip the electron upon vaporization or gas-phase collisions).

The emission intensity increases sharply with oxygen pressure, as seen by comparing the vacuum and 900 mTorr oxygen emission spectra in Fig. 4. A similar effect was seen by Fried et al.⁷ for YBCO ablation. Because the deposition rate does not increase with oxygen pressure under these conditions (400 mJ energy, shown in Fig. 3), the increase in emission is due to some interaction with the oxygen gas. The interaction is most likely a combination of an increased density of species caused by the focusing effect (which would occur near the target, but scattering would dominate at greater distances), and some chemical interaction with the oxygen. The plume photographs show that the plume periphery does chemically react with the added oxygen (color change), although the emission intensity in the red part of the spectrum is too weak for positive identification of the peaks (molecular species are expected to be present in the high oxygen pressures).

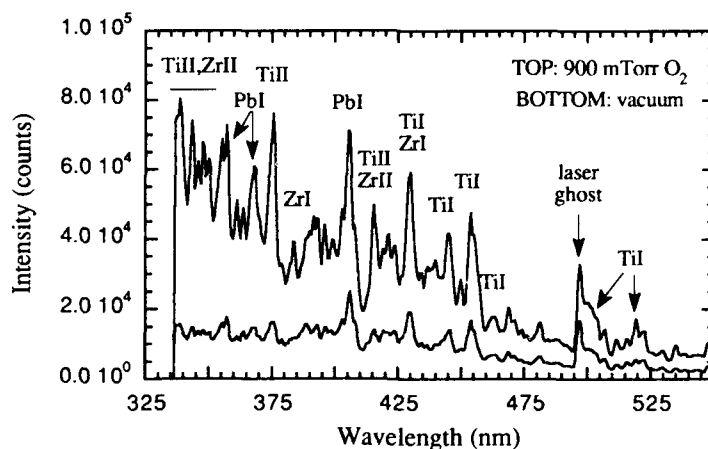


Figure 4. Optical emission spectra of PZT ablated in vacuum (bottom curve) and 900 mTorr oxygen (top). Excited neutral atoms are marked 'I' (e.g., PbI) while excited ions are marked 'II'.

CONCLUSIONS

These studies reveal that the ablated flux characteristics of PZT are a strongly dependent on the oxygen pressure. RBS measurements show that as the oxygen pressure is increased, the angular distribution of species narrows sharply, going from a $\cos^{40}\theta$ distribution to as high as $\cos^{260}\theta$ in 300 mTorr oxygen. At higher pressures, the distribution begins to widen, and a larger portion of the deposited flux fits a $\cos\theta$ distribution, compared to those in lower pressures. This indicates that gas scattering begins to be significant at very high pressure. The narrowing (focusing) of the ablated flux distribution in oxygen corresponds with photographs which show the plasma plume narrowing.

Measurements of the PZT deposition rate as a function of both the laser energy and oxygen pressure show two distinct regimes. At low laser power, increasing the oxygen pressure decreases the deposition rate due to gas scattering effects. At high laser power, the oxygen pressure causes an increase in the deposition rate, due to a plume focusing effect. We believe that this focusing is caused by the leading edge of the ablation plume front physically pushing away the background gas, creating a low pressure channel for the ablated species which follow (those having a lower energy, or ablated later in time). These effects were also observed in argon and krypton gas, verifying that these are not simply chemical reaction effects.

Optical emission spectroscopy of the plume reveals that most of the excited species are atoms. The Pb atoms are mostly neutrals, while the Ti and Zr atoms are mixtures of ions and neutrals. Therefore, efforts to change the energy or direction of ablated species with electric fields (biased filaments or rings) will alter the film composition somewhat.

ACKNOWLEDGMENTS

We would like to thank Craig Near of Morgan Matrock, Inc., for supplying the PZT powder used to fabricate the PZT target. This work was funded by the Defense Advanced Research Projects Agency, grant # 90F131300.

REFERENCES

- [1] R. Ramesh, W.K. Chan, B. Wilkens, H. Gilchrist, T. Sands, J.M. Tarascon, V.G. Keramides, D.K. Fork, J. Lee, and A. Safari, *Appl. Phys. Lett.* **61**, 1537 (1992).
- [2] J.T. Cheung and H. Sankur, *CRC Critical Rev. in Sol. State and Mat. Sci.*, **15**(1), 63 (1988).
- [3] C.L. Chan and J. Mazumder, *J. Appl. Phys.* **62**, 4579 (1987).
- [4] T. Venkatesan, X.D. Wu, A. Inam, and J.B. Wachtman, *Appl. Phys. Lett.* **52**, 1193 (1988).
- [5] O. Auciello, S. Athavale, O.E. Hankins, M. Sito, A.F. Schreiner, and N. Biunno, *Appl. Phys. Lett.* **53**, 72 (1988).
- [6] D.B. Geohegan, *Appl. Phys. Lett.* **60**, 2732 (1992).
- [7] D. Fried, G.P. Reck, T. Kushida, and E.W. Rothe, *J. Phys. D: Appl. Phys.* **24**, 1065 (1991).
- [8] J.S. Horwitz, K.S. Grabowski, D.B. Chrisey, and R.E. Leuchtner, *Appl. Phys. Lett.* **59**, 1565 (1991).
- [9] R.E. Leuchtner, J.S. Horwitz, and D.B. Chrisey, in *Ferroelectric Thin Films II*, edited by A.I. Kingon, E.R. Myers, and B. Tuttle, *Mater. Res. Soc. Proc.* **243**, Pittsburgh PA 1992, pp 525-530.
- [10] O. Auciello, J. Emerick, J. Duarte, and A. Illingworth, *J. Vac. Sci. Technol. A* **11**, 267 (1993).

PREPARATION OF SrTiO_3 THIN FILMS BY ECR AND THERMAL MOCVD

P.-Y. LESAICHERRE *, H. YAMAGUCHI **, T. SAKUMA **, Y. MIYASAKA **,
M. YOSHIDA **, A. ISHITANI *

* ULSI Device Development Laboratories, NEC Corporation, Sagamihara, Kanagawa 229,

** Fundamental Research Laboratories, NEC Corporation, Kawasaki, Kanagawa 216, Japan

ABSTRACT

SrTiO_3 thin films were prepared by ECR and thermal MOCVD. In thermal-CVD mode, Sr content and Ti content were at a maximum at 0.56 Torr. Results showed that SrO deposition is a surface reaction limited process between 500 and 650 °C, whereas TiO_2 deposition is surface reaction limited between 500 and 600 °C, and diffusion limited above 600 °C. At a low pressure of 8 mTorr, ECR oxygen plasma was found to help decompose $\text{Ti}(\text{i-OC}_3\text{H}_7)_4$. In ECR-CVD mode, the deposition temperature could be lowered to 400 °C. TEM and SEM analyses showed that SrTiO_3 thin films have a columnar structure. The size of the grains depends on film thickness, and their shape on film composition (Sr/Ti). Films prepared by thermal-CVD had a lateral step coverage of 50 %. 40 nm SrTiO_3 thin films (Sr/Ti = 1.0) prepared by thermal-CVD on $\text{Pt/TaO}_x/\text{Si}$ and annealed for 2 hours in O_2 had a maximum dielectric constant of 139 ($C_s = 31$ fF/ μm^2 and $t_{\text{eq}} = 1.1$ nm) and a leakage current density of 6×10^{-8} A/ cm^2 at 1.0 V.

INTRODUCTION

Because of their high dielectric constants, good chemical stability and good insulating properties, ferroelectric thin films are considered as promising materials to replace Si_3N_4 and Ta_2O_5 for use as capacitor dielectrics in future high density DRAMs, designed with a simple cell structure. Among the great variety of ferroelectrics, two families of materials have emerged recently as the most promising candidates: the lead titanate family, comprising mostly ferroelectric-phase materials such as PbTiO_3 , PZT and PLZT, and the barium-strontium titanate family, comprising mostly paraelectric-phase materials, such as SrTiO_3 and $(\text{Ba},\text{Sr})\text{TiO}_3$.

The dielectric properties of ferroelectric PZT were shown recently to be considerably altered at high frequencies, with a particularly sharp decrease in the dielectric constant occurring at 1 MHz or a few hundred MHz [1,2]. Thus, for high frequency applications such as ULSI DRAMs (clock rate ≥ 100 MHz), paraelectric SrTiO_3 and $(\text{Ba},\text{Sr})\text{TiO}_3$ seem to be more suitable materials.

Several deposition techniques, such as rf-sputtering [3-6], ion-beam sputtering [7-9], pulsed laser ablation [10], metal organic decomposition [11], co-evaporation [12-13] and chemical vapor deposition (CVD) [14-22] have been reported to prepare SrTiO_3 and $(\text{Ba},\text{Sr})\text{TiO}_3$ thin films. Among these techniques, CVD is often considered the most interesting, with characteristic features such as a good step coverage, high deposition rates, an easy control of composition, and good thickness and composition uniformities over large size wafers.

In this paper, the preparation of SrTiO_3 thin films by ECR and thermal MOCVD is reported.

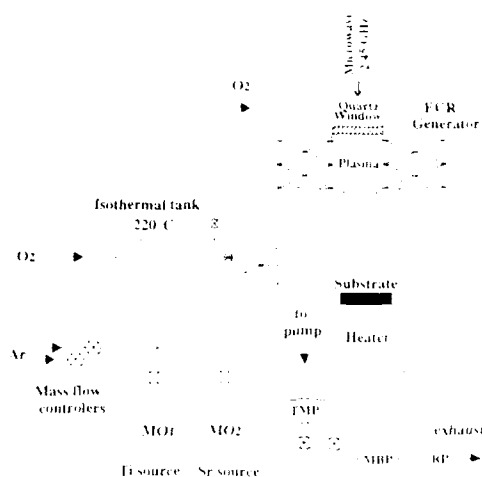
EXPERIMENTAL

A schematic representation of the MOCVD system is shown in Figure 1. Using a single apparatus, SrTiO_3 thin films were prepared either by ECR-CVD, or by thermal-CVD. Titanium isopropoxide $\text{Ti}(\text{i-OC}_3\text{H}_7)_4$ (or TIP) and strontium dipivaloylmethanate $\text{Sr}(\text{DPM})_2$ were used as the metalorganic sources, and oxygen was used as the oxidant. The bottle containing liquid TIP was maintained at 20 °C in a water bath, and the bottle containing solid $\text{Sr}(\text{DPM})_2$ was heated at 190 °C. Argon was used as the carrier gas to transport the metalorganic vapors. The gas lines between the source bottles and the reaction chamber were maintained at 220 °C. Argon gas flow was regulated by mass flow controllers placed upstream from the source bottles. Argon flow rates were varied between 50 and 300 sccm for TIP and $\text{Sr}(\text{DPM})_2$, and oxygen flow rates ranged from 100 to 500 sccm (100 sccm in ECR mode). In both the ECR and Thermal-CVD modes, the total gas flow rate was maintained between 400 and 840 sccm. Pressure in the TIP bottle was monitored by a pressure sensor acting on a pressure control valve, placed downstream from the bottle. TIP and $\text{Sr}(\text{DPM})_2$ vapors were mixed just before injection into the reaction chamber. In thermal-CVD mode, oxygen was mixed with the metalorganics prior to injection.

and in ECR-CVD mode, an ECR oxygen plasma was generated above the substrate, as shown in Figure 1. The coil current was 18.5 A, and a power of 550-600 W was maintained throughout the deposition. Substrates were placed on a rotating holder and heated by a backside resistance, at temperatures ranging from 400 to 650 °C. Silicon, sapphire and Pt/TaO₂/Si 4" wafers were used as substrates. The pumping system consisted of a series of a turbomolecular pump, a mechanical booster pump and a rotary pump. In ECR-CVD mode, typical operating pressures were in the range of 5 to 10 mTorr. In Thermal-CVD mode, the turbomolecular pump was bypassed. Using the mechanical booster pump and rotary pump only, operating pressures were in the range of 0.5 to 10 Torr. A circular stainless steel piece, surrounding wafers and comprising 12 uniformly distributed holes, was installed in the deposition chamber to allow uniform pumping from the bottom of the wafers. In thermal-CVD mode, a supplementary quartz piece was installed above the substrates, in order to reduce the volume of the reaction chamber. Film thicknesses were measured by ellipsometry for films deposited on silicon and sapphire, and using a surface profiler (Dektak-3030) for films prepared on Pt/TaO₂/Si substrates. Film composition (Sr/Ti) was estimated by Rutherford backscattering spectrometry (RBS), inductively coupled plasma atomic emission spectroscopy (ICP-AES) or energy dispersion X-ray analysis (EDX). Electrical properties were evaluated using Au/SrTiO₃/Pt/TaO₂/Si capacitors. Only the gold top electrodes were patterned. For electrical measurement, contact was made to the Au top electrode and on the Au/Ti metallized backside of the wafers. Capacitance and tan δ were measured in the 100 Hz to 10 MHz frequency range, and values retained for the dielectric constant were obtained at 10 kHz.

In both CVD modes, deposition rates of 5 to 10 Å/min were obtained, and composition and thickness uniformities were about 10% across 4" silicon wafers.

Fig. 1 Schematic diagram of the MOCVD system



RESULTS AND DISCUSSION

1. Reactions in the TiP-Sr(DPM)₂-O₂ system

The effect of the total pressure and substrate temperature on the deposition rate and composition of SrTiO₃ thin films were investigated in thermal-CVD mode on silicon substrates. Sr and Ti counts are presented in Figure 2 as a function of pressure and temperature.

First, the pressure in the reactor was varied from 0.56 to 6.00 Torr (75 to 800 Pa), by introducing ballast gas in the exhaust line before the mechanical booster pump, reducing the pumping capacity of the reaction chamber. All other parameters were kept constant, with a total gas flow of 840 sccm (420 sccm O₂) and a substrate temperature of 600 °C. The results show that Sr and Ti deposition rates are maximum at the lowest investigated pressure of 0.56 Torr. An increase in the total pressure induces a reduction in the gas flow velocity, and an increase in the residence time of the reactants in the deposition chamber. As a result, the concentration of reactive species in the gas phase is increased, and this possibly leads to increased extraneous deposition on the walls of the reaction chamber. It is thus preferable to operate at the low pressure of 0.56 Torr, for which the best thickness and composition uniformities of 10% and 2% respectively were obtained.

In a second series of experiments, the chamber pressure was set at 0.56 Torr and the substrate temperature was varied between 500 and 650 °C, all other parameters being unchanged. As can be seen in Figure 2, in thermal-CVD mode, the deposition of SrO on silicon from Sr(DPM)₂

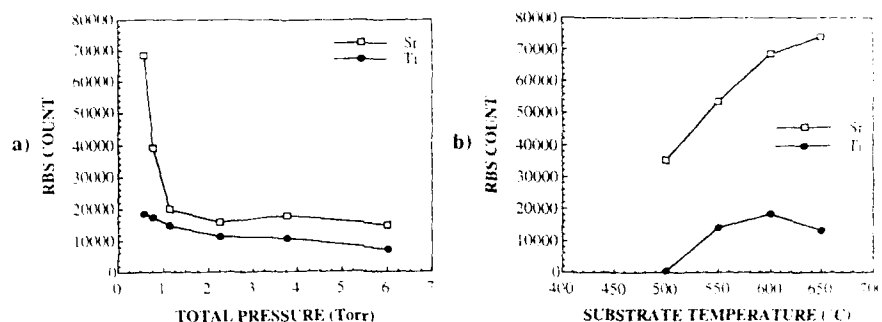


Fig. 2 Thermal-CVD on Si. Variation of the Sr and Ti RBS counts with a) pressure (at 600 °C) and b) substrate temperature (at 0.56 Torr).

vapor and oxygen is a surface reaction controlled process between 500 and 650 °C. As for titanium, no deposition occurred at a temperature of 500 °C. The deposition of TiO_2 has been reported to occur at temperatures as low as 300 °C, under a total pressure of 6 Torr [23]. A low operating pressure of 0.56 Torr and other operating parameters, such as the gas flow rates, the distance between the injector and the substrate, as well as the overall design of the reactor could explain the difference observed between our results and the reported results. Titanium deposition occurs when the temperature is increased to 550 °C, but levels off above 600 °C. TiO_2 deposition from TIP vapor and oxygen thus appears to be a surface reaction controlled process between 500 and 600 °C, and a diffusion limited process above 600 °C. In the diffusion limited regime, the titanium deposition rate can be raised by increasing the supplying rate of titanium species to the substrate surface, in order to adjust composition (Sr/Ti) [23]. In our system, composition was adjusted by changing the pressure in the TIP bottle, changing the partial pressure of TIP vapor in the gas transport line. In the ECR-CVD mode, the pumping system configuration did not allow large variations in the operating pressure, which was maintained at a few mTorr. The substrate temperature was varied between 400 and 700 °C. As shown in Figure 3, the growth of crystallized SrTiO_3 thin films occurred at temperatures as low as 400 °C on sapphire. At 400 °C, only a low intensity 110 peak of cubic perovskite SrTiO_3 could be detected. At 600 and 700 °C, for films prepared with a composition ratio $\text{Sr/Ti} \approx 1.0$ on Si and $\text{Pt/TaO}_x/\text{Si}$ by both ECR and thermal-CVD, 100 and 200 SrTiO_3 peaks were also detected, and still no other phase than SrTiO_3 (Sr_2TiO_4 for example) was observed.

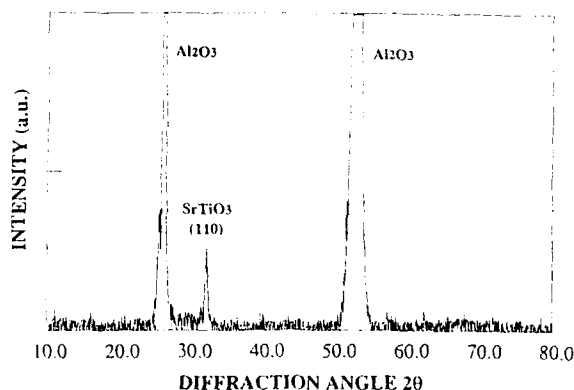


Fig. 3 XRD spectrum of 900 Å SrTiO_3 films ($\text{Sr/Ti} \approx 0.9$) by ECR-CVD on Al_2O_3 at 400 °C.

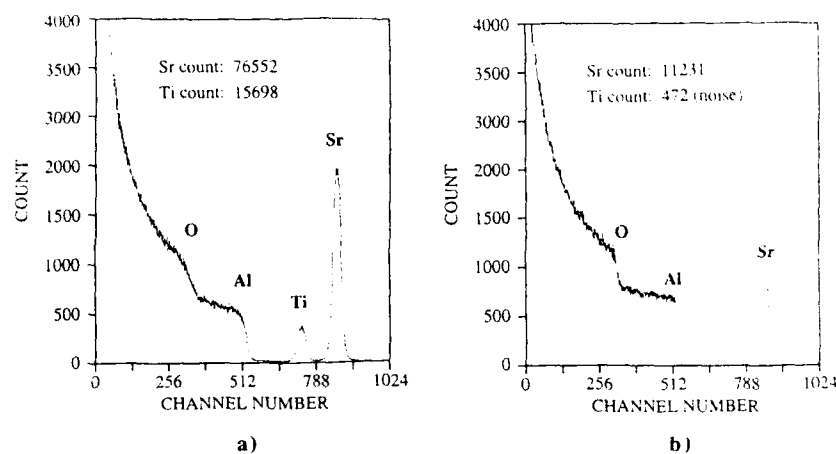


Fig. 4 RBS spectra of samples prepared in ECR-CVD mode at 600 °C on Al_2O_3 . With ECR plasma (a) and without (b).

With characteristic features such as a high plasma density and low ion energy, ECR plasma is known to allow deposition of high quality films at low substrate temperatures [24]. The low-energy ion bombardment interacts with the gas phase and the substrate surface. As a result, the mobility of adsorbed species is enhanced, and reactions otherwise impossible can occur. In order to investigate the effect of the ECR plasma on the deposition efficiency of Sr and Ti, an experiment was performed in ECR-CVD mode at 8 mTorr and 600 °C using a sapphire substrate, without generating the ECR plasma. Oxygen was injected between the coils of the ECR generator, but no plasma was produced. The results are presented in Figure 4, and a comparison is made with an experiment performed in similar conditions but with producing the oxygen plasma. The suppression of the ECR plasma induced a reduction in the strontium count by a factor of 7, and titanium almost completely disappeared. The film thickness was reduced from 1100 Å to about 250 Å. Thus, a low pressure of 8 mTorr, the ECR plasma strongly assists the decomposition of TIP, and to a lesser extent the decomposition of $\text{Sr}(\text{DPM})_2$. When plasma is produced in the ECR-CVD mode, $\text{Ti}(\text{i-OC}_3\text{H}_7)_4$ decomposition might occur in the vapor phase, assisted by the ECR plasma, whereas $\text{Sr}(\text{DPM})_2$ decomposition would mainly occur at the substrate surface, and be less affected by the ECR plasma.

2. $\text{Sr}_x\text{Ti}_{1-x}\text{O}_3$ microstructure

The microstructure of $\text{Sr}_x\text{Ti}_{1-x}\text{O}_3$ thin films was investigated by transmission and scanning electron microscopy. A TEM cross-section of a sample prepared by ECR-CVD at 600 °C on Pt/TaO_x/Si is shown in Figure 5a. SrTiO_3 films grow with a crystallized columnar structure on platinum, and no amorphous layer is observed at the interface with the platinum. An SEM top view of the same sample is shown in Figure 5b. The grain size of these films ranges from 10 to 20 nm. An extensive study of the surface morphology showed that the microstructure of the films prepared by both ECR and thermal-CVD does not depend on the substrate, but on the thickness and composition, when films are thicker than 400 Å. An amorphous layer of 200 to 300 Å can be formed for films prepared on Si and SiO₂ (but not on Pt) [6], depending on the composition of the films, as is discussed later (see § 3). Similar to the results obtained by Feil et al. [14], the grain size was observed to depend on the film thickness. For 400 Å thick films, the grain size ranged from 10 to 20 nm (Figure 5c), for 600 Å thick films the grain size ranged from 20 to 30 nm (Figure 5d), and for 2000 Å thick films, the grain size was between 30 and 60 nm (Figure 5e). The shape of the grains changed with composition. Grains had a round shape for Ti-rich films ($\text{Sr}/\text{Ti} < 1.0$ - Figure 5f), a triangular shape for $\text{Sr}/\text{Ti} \approx 1.0$ (Figure 5g), and a stretched triangular shape for strontium-rich films ($\text{Sr}/\text{Ti} > 1.0$ - Figure 5h).

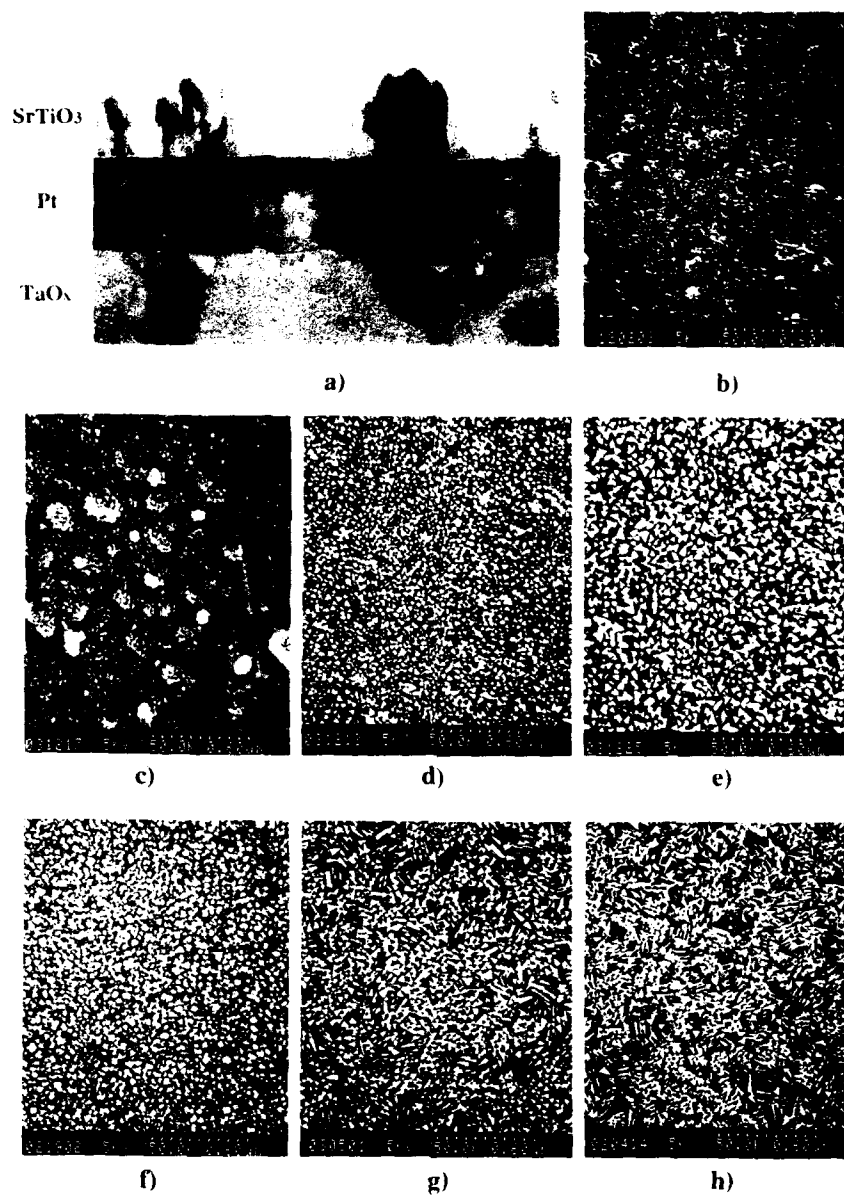


Fig. 5 $\text{Sr}_x\text{Ti}_{1-x}\text{O}_3$ structure a) TEM cross-section (Pt thickness = 600 Å) and b) SEM top view of 500 Å thick films ($\text{Sr}/\text{Ti} \approx 0.9$) prepared at 600 °C on Pt/TaO_x/Si by ECR-CVD. c) to h) surface morphology of films prepared at 75 Pa and 600 °C on Si by thermal-CVD. c) 400 Å - $\text{Sr}/\text{Ti} = 0.9$, d) 600 Å - $\text{Sr}/\text{Ti} = 0.9$, e) 2000 Å - $\text{Sr}/\text{Ti} = 0.9$, f) $\text{Sr}/\text{Ti} = 0.8$ - 1000 Å, g) $\text{Sr}/\text{Ti} = 1.0$ - 1000 Å, h) $\text{Sr}/\text{Ti} = 1.2$ - 900 Å.

3. Step coverage

Step coverage of SrTiO_3 thin films prepared by thermal-CVD on silicon substrates with SiO_2 steps at 100 Pa and 600 °C was investigated, and the results are presented in Figure 6. Films with a composition ratio of $\text{Sr/Ti} = 0.4$ (Figure 6a) and $\text{Sr/Ti} = 0.8$ (Figure 6b) were prepared. In order to facilitate the SEM observation, the SrTiO_3 layer was encapsulated by a 3000 Å sputtered tantalum layer. The minimum lateral step coverage was about 50 % for both films. This value is lower than the one obtained for films prepared by liquid-source CVD [22], but is much higher than results obtained using physical deposition techniques such as evaporation or sputtering. In Figure 6a, an amorphous layer of about 200 to 400 Å is observed at the SrTiO_3 -silicon interface, and a thinner layer of about 100 to 200 Å is observed at the SrTiO_3 - SiO_2 interface. No amorphous layer can be observed in Figure 6b. This result would indicate that the presence of an amorphous layer, possibly a titanium rich oxide phase, depends on the Sr/Ti ratio. More data need to be gathered to confirm this explanation.

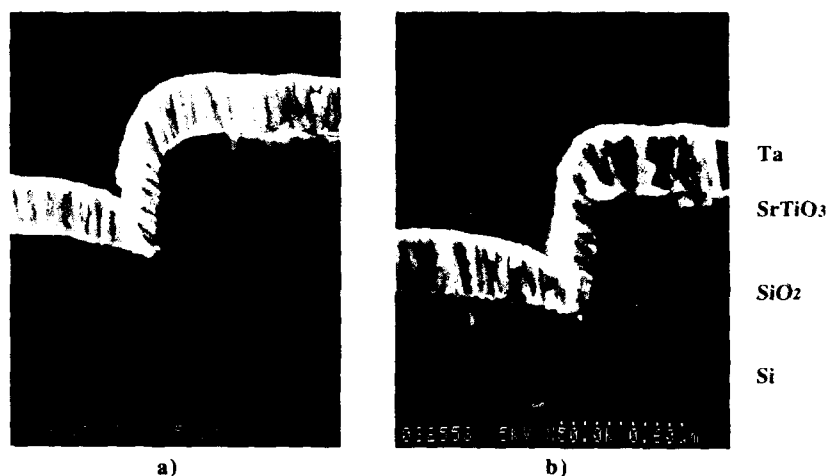


Fig. 6 Step coverage of 3000 Å SrTiO_3 films prepared by thermal-CVD at 100 Pa and 600 °C on Si-SiO_2 (step) a) $\text{Sr/Ti} = 0.4$, b) $\text{Sr/Ti} = 0.8$.

4. Electrical results

As was shown above, in thermal-CVD, at a pressure of 0.56 Torr (75 Pa), thickness and composition uniformities are good, and the Sr and Ti deposition rates are at a maximum. When the temperature is raised above 600 °C, hillocks appeared on the platinum surface. Electrical properties were measured for films prepared by thermal-CVD at a pressure of 0.56 Torr and a temperature of 600 °C. 40 nm and 100 nm thick SrTiO_3 films ($\text{Sr/Ti} = 1.0$) were prepared on $\text{Pt/TaO}_x/\text{Si}$ substrates. After deposition, the films were annealed for 2 hours at 600 °C in an oxygen ambient at atmospheric pressure. C-V, C-freq. and I-V characteristics were measured for as-deposited and annealed films, using 0.09 mm² square electrodes. As seen in Figure 7a, a capacitance of 2.7 nF and a dielectric loss of 0.01 were measured for the 40 nm annealed films. The corresponding dielectric constant, SiO_2 equivalent thickness and total charge capacity were $\epsilon_r = 139$, $t_{eq} = 1.1$ nm and $C_s = 31$ fF/ μm^2 . The increase in $\tan \delta$ observed in Figure 7a is due to a parasitic resistance in the measurement system, and more precise measurements showed that capacitance and dielectric loss remain constant over the range of 100 Hz to 100 MHz. The I-V characteristics of 40 nm and 100 nm annealed films are shown in Figure 7b and 7c. A leakage current density of 6×10^{-8} A/cm² was measured at 1.0 V for the 40 nm annealed films.

As-deposited 40 nm films had a dielectric constant 112 and a leakage current density of 1.2×10^{-5} A/cm² at 1.0 V. The annealing treatment helped increase the dielectric constant and improve the I-V characteristics. The main effects of the annealing treatment in oxygen ambient are considered to be desorption of carbon incorporated in the films during deposition, and improvement of the crystalline structure of the films. As-deposited 100 nm films had a dielectric constant of 96 and a leakage current density of 1×10^{-7} A/cm², the same films when annealed had a dielectric constant of 210 ($t_{eq} = 1.9$ nm) and a leakage current density of 1×10^{-7} A/cm². The best charge storage capacity was obtained for the 40 nm films. As the leakage current density did not vary with annealing for thicker films, the present annealing process is probably not optimum.

45 nm SrTiO₃ thin films (Sr/Ti = 1.0) were prepared by ECR-CVD on Pt/TaO_x/Si electrodes at 600 °C and 8.5 mTorr. Films were annealed at 600 °C, either by rapid thermal annealing (RTA) for 1 minute in oxygen, or by furnace annealing for 30 minutes in oxygen. Leakage current densities were about 10^{-6} A/cm² for all samples, and the dielectric constants were 20, 140 and 150, for as-deposited, furnace annealed and RTA-annealed films, respectively. For ECR-CVD films, the best results were obtained for RTA annealed films ($\epsilon_r = 150$ and $t_{eq} = 1.1$ nm), similar to the best results obtained by thermal-CVD. Optimization of the annealing process is needed to further improve these results.

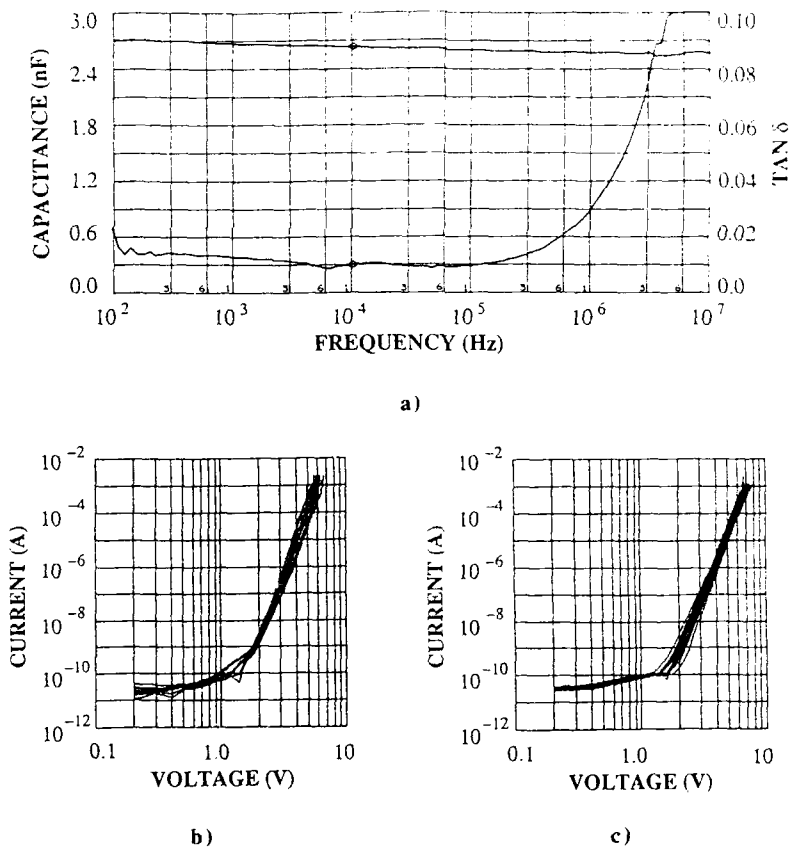


Fig. 7 a) C-f and b) I-V characteristics of 40 nm SrTiO₃ on Pt/TaO_x/Si by thermal-CVD at 600 °C c) I-V characteristics of 100 nm SrTiO₃ in same conditions (all annealed 2 hours in O₂).

CONCLUSION

SrTiO₃ thin films were prepared by ECR and thermal MOCVD. The effect of the total pressure and the substrate temperature on the deposition rates of strontium and titanium were investigated. In thermal-CVD mode at 0.56 Torr, results showed that SrO deposition is surface reaction limited between 500 and 600 °C, whereas TiO₂ deposition is surface reaction limited between 500 and 600 °C, and diffusion limited above 600 °C. At a low pressure of 8 mTorr, ECR oxygen plasma was found to help decompose Ti(OC₂H₅)₄. The deposition temperature could be lowered to 400 °C, using ECR oxygen plasma. SEM analysis showed that the microstructure of SrTiO₃ thin films depends on the film thickness and the Sr/Ti composition ratio. The step coverage results showed that SrTiO₃ thin films prepared by thermal-CVD have a minimum lateral coverage of 50 %. 40 nm SrTiO₃ thin films (Sr/Ti = 1.0) prepared by ECR and thermal-CVD at 600 °C, and annealed for 2 hours at 600 °C in O₂ at atmospheric pressure had a maximum charge storage capacity of 31 fF/μm² (t_{eq} = 1.1 nm). Results indicated a leakage current density two orders lower for thermal-CVD films than for ECR-CVD films, with a value of 6x10⁻⁸ A/cm² at 1.0 V.

ACKNOWLEDGEMENTS

The authors wish to express their gratitude to Drs. R. Lang, N. Shohata, M. Kamoshida and O. Kudo for their encouragement and continuous support in this study. Thanks are also due to K. Takemura, S. Yamamichi, T. Hase, H. Yabuta, N. Tawarayama, and A. Nakai for technical assistance and helpful discussions.

REFERENCES

1. J. F. Scott et al., Proceedings of the 8th ISAF, 356, August 31-September 2, 1992.
2. J. Chen et al., *ibid.*, p 182.
3. W. B. Pennebaker, IBM J. Res. Develop., 686, November 1969.
4. S. Matsubara et al., Mat. Res. Soc. Symp. Proc., Vol. 200, 243, 1990.
5. Y. Miyasaka et al., Proceedings of the 7th ISAF, 121, June 6-8, 1990.
6. T. Sakuma et al., Appl. Phys. Lett., Vol. 57 (23), 2431, December 1990.
7. S. Yamamichi et al., Jap. J. Appl. Phys., Vol. 30, No. 9B, 2193, September 1991.
8. S. Yamamichi et al., Mat. Res. Soc. Symp. Proc., Vol. 243, 297, 1992.
9. C. J. Peng et al., Proceedings of the 8th ISAF, 305, August 31-September 2, 1992.
10. R. F. Pinizzotto et al., Mat. Res. Soc. Symp. Proc., Vol. 243, 463, 1992.
11. E. Fujii et al., IEDM 1992, p 267.
12. H. Yamaguchi et al., Jap. J. Appl. Phys., Vol. 30, No. 9B, 2197, September 1991.
13. H. Yamaguchi et al., Proceedings of the 8th ISAF, 285, August 31-September 2, 1992.
14. W. A. Feil et al., J. Appl. Phys., Vol. 67 (8), 3858, April 1990.
15. L. A. Wills et al., J. Cryst. Growth, Vol. 107, Nos. 1-4, 712, January 1991.
16. E. J. Donahue et al., Mat. Res. Bull., Vol. 26, 1119, November 1991.
17. A. Greenwald et al., Mat. Res. Soc. Symp. Proc., Vol. 243, 457, 1992.
18. P. C. Van Buskirk et al., presented at the 4th ISIF, Monterey, CA, March 9-11, 1992.
19. L. D. McMillan et al., presented at the 4th ISIF, Monterey, CA, March 9-11, 1992.
20. S. Matsuno et al., Ext. abstr. 9th FMA, Kyoto, May 27-29, 1992, p111 (in Japanese).
21. H. Funakubo et al., J. Chem. Vap. Dep., Vol. 1, 73, July 1992.
22. J. F. Scott et al., Ferroelectrics, Vol. 133, 47, August 1992.
23. M. Okada et al., Jap. J. Appl. Phys., Vol. 28, No. 6, 1030, June 1989.
24. S. B. Krupanidhi, J. Vac. Sci. Technol. A, Vol. 10 (4), 1569, July-August 1992.

Author Index

- Achard, H., 23
 Adams, P.M., 339
 Agius, B., 23
 Aitchison, K.A., 339
 Aizawa, Kouji, 313
 Anderson, G.B., 113
 Ansari, P.H., 467
 Asahi, Ryouji, 79
 Auciello, O., 481

 Baertlein, C.D., 423
 Bai, G., 235
 Barnes, R., 481
 Baron, Cynthia J., 201
 Barrie, J.D., 339
 Barrow, D., 37
 Baude, P.F., 139
 Beach, D., 189
 Beckage, P., 157
 Beetz, Jr., C.P., 345
 Bentley, J., 345
 Bierlein, J.D., 29
 Bihari, B., 119
 Bindloss, W., 29
 Birnie III, D.P., 423
 Borrego, J.M., 157
 Boulton, J.M., 369, 423
 Bullington, J.A., 3

 Caballero, Celia R., 375
 Campbell, Andrew C., 151, 209
 Carris, Michael W., 375
 Cattani, E., 23
 Cava, R.J., 145
 Chan, S.-K., 403
 Chandler, C.D., 351, 357
 Chang, H.L.M., 235, 403
 Charlet, Barbara, 363
 Chen, C.H., 145
 Chen, J., 47
 Cheng, Chih-Hsing, 441
 Cheng, L.K., 29
 Chiarello, R.P., 403
 Cho, Yong Soo, 397
 Chow, A.F., 301
 Cima, M.J., 325
 Claus, R.O., 65
 Cochrane, S., 157
 Cross, L.E., 47
 Cui, Guang-Ji, 249, 345

 Dat, R., 481
 Davies, Kerrie E., 363
 de Keijser, M., 223
 Derderian, G.J., 339
 Desu, Seshu B., 65, 133, 165, 241, 429, 435
 Dexter, Kathleen F., 99
 Dimos, D., 59, 87

 Dormans, G.J.M., 127, 223
 Dudley, M., 29

 Eakim, B., 23
 Eatough, M.O., 15
 Eichorst, Dennis J., 201
 Endo, Hidehiro, 325
 Eom, C.B., 145
 Esayan, S., 107
 Evans, Joseph T., 3, 71

 Fleming, R.M., 145
 Fork, D.K., 113, 145, 195
 Foster, C.M., 403
 Francis, Lorraine Falter, 281
 Fuenzalida, V.M., 333
 Fujimoto, Masashi, 255
 Fukagawa Mitsuru, 255

 Gallatin, G., 119
 Gao, Y., 235
 Gardiner, Robin, 119
 Garino, Terry J., 71
 Goedken, Virgil L., 375
 Gong, X., 179
 Goodnow, D.C., 3, 15
 Gordon, Douglas, 249
 Graettinger, Thomas M., 301
 Grill, A., 189

 Hammetter, W.F., 3
 Hampden-Smith, M.J., 351, 357
 Hance, Robert, 209
 Hankins, O.E., 481
 Hasdell, N.B., 447
 Headley, T.J., 15
 Helfrich, J.A., 319
 Hendricks, Warren C., 241
 Hesse, Werner, 375
 Huang, Y., 391
 Hutchins, D.A., 37

 Ichiki, Tatsuya, 313
 Iijima, K., 455
 Ishitani, A., 487
 Ishiwara, Hiroshi, 313

 Jones, Robert E., 151, 209
 Joshi, Vikram, 287
 Jung, Hyung Jin, 397

 Kamath, G.S., 9
 Kane, W., 189
 Katayama, Takuma, 255
 Kaushik, Vidya, 209
 Keramidas, V.G., 195
 Ketterson, J.B., 319
 Khamankar, Rajesh, 473
 Kim, Jiyoung, 473

- Kingon, A.I., 301, 481
 Kingston, J.J., 113
 Kirilin, Peter S., 119
 Knapik, D.A., 37
 Knorr, D.B., 157
 Kodas, T.T., 351
 Kumar, J., 119
 Kwok, Chi Kong, 429

 Lam, D.J., 235, 403
 Lampa, D.L., 15
 Larsen, P.K., 127
 Lee, Dong Heon, 397
 Lee, J., 107
 Lee, Jack, 473
 Lee, Jeon Kook, 397
 Lesaichere, P.-Y., 487
 Lewis, Keith L., 99
 Li, Chen C., 435
 Lichtenwalner, D.J., 481
 Liu, W.-T., 157
 Lockwood, Steven J., 59, 275
 Logan, E.A., 447
 Lu, H.A., 319
 Lu, T.-M., 157
 Luten, Henry A., 375

 Mackenzie, John D., 441
 Madsen, Lynnette D., 385
 Maniar, Papu, 151, 209
 Marshall, J.H., 145
 McIntyre, Dale C., 71
 McCartney, Martha L., 287, 339
 Merkle, K.L., 235
 Merklein, S., 263
 Miyasaka, Y., 487
 Moazzami, Reza, 151, 209
 Mochizuki, Midori, 79
 Mogab, C. Joseph, 151, 209
 Momoda, L.A., 9
 Morris, P.A., 301

 Nagao, N., 455
 Nakaya, Kenichi, 255
 Narayan, J., 215
 Nashimoto, Keiichi, 293
 Nicklin, R., 447
 Noteboom, R., 37

 Orr, M.N., 423

 Pan, Wei, 133
 Patel, A., 53, 447
 Payne, David A., 269, 391
 Peng, Chien H., 241
 Phillips, Julia M., 145
 Pilleux, M.E., 333
 Polla, D.L., 139
 Pompe, W., 179
 Powell, Q., 351
 Prohaska, J., 107
 Pyle, Ronald, 209

 Ramesh, R., 195
 Rees, Jr., William S., 375
 Roy, Debasis, 287
 Rymaszewski, E.J., 157

 Safari, A., 107, 467
 Sakata, Jiro, 79
 Sakuma, T., 487
 Sands, T., 195
 Sayer, M., 37
 Schindel, D.W., 37
 Schmidt, Lanny D., 281
 Schönecker, A., 263
 Schreiner, A.F., 481
 Schwartz, Joseph M., 281
 Schwartz, Robert W., 3, 59, 275, 357
 Seager, Carleton H., 71
 Seraphin, Supapan, 369
 Shimizu, Masaru, 255
 Shiosaki, Tadashi, 255
 Shorrocks, N.M., 53
 Si, Jie, 241
 Smart, C., 189
 Speck, J.S., 113, 179
 Spierings, G.A.C.M., 127
 Sporn, D., 263
 Stauf, Gregory T., 119
 Steinbeck, John, 249, 345
 Sudarshanam, V.S., 65
 Sudhama, C., 473
 Sugiyama, Susumu, 79
 Sun, B.N., 391
 Suo, Z., 179

 Tabata, Osamu, 79
 Taga, Yasunori, 79
 Takayama, R., 455
 Takeuchi, T., 455
 Tani, Toshihiko, 269
 Tanikawa, Eiki, 255
 Tarsa, E.J., 113
 Teowee, G., 369, 415, 423
 Thomas, E.V., 275
 Tiwari, P., 215
 Tomita, Y., 455
 Torres, V.M., 59
 Tossell, D.A., 53
 Tuttle, Bruce A., 3, 15, 71, 87, 275, 391

 Ueda, I., 455
 Uhlmann, D.R., 369, 415, 423
 Ulenaers, M.J.E., 127
 Uren, M., 447

 Vajo, John J., 9
 Van Buskirk, Peter C., 119, 249, 345
 Van Dover, R.B., 145
 Van Glabbeek, J.J., 127
 van Veldhoven, P.J., 223
 Varniere, F., 23
 Vasant Kumar, C.V.R., 37
 Vijay, Dilip P., 133
 Voigt, James A., 15

- Wade, R.K., 423
Waldman, Robert W., 71
Wang, S., 29
Wang, Z.L., 345
Warren, William L., 3, 71, 87, 391
Watton, R., 53
Weaver, Louise, 385
Werder, D.J., 145
Wessels, B.W., 319, 409
Whatmore, R.W., 53, 447
Wills, L.A., 319, 409
Wong, S.B., 9
Woolcott, R.R., 301

Xing, Jimmy, 165
Xu, Ren, 441

Xu, Yuhuan, 441
Xu, Zhengkui, 269

Yamaguchi, H., 487
Ye, C., 139
Yoo, In K., 165
Yoshida, M., 487

Zhan, X., 319
Zhang, Jiming, 249, 345
Zhang, Q., 47
Zheleva, Tsvetanka, 215
Zhou, Dan, 369
Zou, L., 37
Zumsteg, F.C., 301

Subject Index

- ablated flux distribution, 481
- aerosol, 351
- ageing, 165
- alkoxide, 325, 375
- amorphous films, 441
- anisotropic dielectric, 403
- atomic layer epitaxy, 397
- Avrami method, 15
- β -diketonates, 375
- BaMgF₄, 313
- barium
 - hydroxide, 333
 - titanate, 119, 157, 249, 319, 333, 375, 397, 409, 441
- barrier layer, 281
- bias voltage, 363
- bismuth titanate, 241
- capacitive sensor, 37
- capacitor, 157
 - decoupling, 59
 - (Pt/PZT/PT) stack, 127
- carbon, 3
- charge storage
 - capacitors, 447
 - density, 473
 - traps, 87
- chemical vapor deposition, 119, 375
 - low pressure metallorganic, 385
 - metallorganic, 319, 403, 493
 - organometallic, 223, 235, 241, 255
 - plasma enhanced organo-metallic, 249
- Cl₂, 363
- CMOS, 151
- conductive oxides, 249
- crystallinity, 313
- crystallization, 15, 189, 287
 - behavior, 263, 357
 - solid phase, 313
- Curie temperature, 429
- cyclopentadienides, 375
- decoupling capacitor, 59
- defects, 3
 - Fe⁺³ defects, 391
 - Pb⁺³, 3
 - Pt⁺³ defects, 391
 - structure, 409
- deflections, static, 37
- degradation properties, 165
- dielectric
 - constants, 319
 - properties, 47, 157
- domains, 179
- walls, 29
- donor doping, 59
- DRAM, 151, 473, 493
- ECR, 493
 - microwave reactor, 363
- electrical
 - characterization, 263
 - measurements, 333
- electrodes, 189, 249, 345
- electroluminescence displays, 397
- electron paramagnetic resonance (EPR), 3, 391
- electro-spray, 79
- electrostrictive processes, 99
- epitaxial, 345, 403
 - growth, 293
 - platinum, 345
- epitaxy, 107, 113, 119
- etching
 - plasma, 127, 133
 - PZT, 363
- excess PbO, 369
- fatigue, 145, 423
- Fe⁺³ defects, 391
- ferroelectric
 - domains, 29
 - like behavior, 441
 - relaxor, 47
- fiber optic modulation, 65
- field-induced displacement, 99
- formation kinetics, 435
- GaAs, 113
- grain size, 473
- Group 2 elements, 375
- HBr, 363
- heteroepitaxial growth, 269, 287, 325
- heterostructures, 145, 195, 345
- high dielectric, 189
- hillocks, 201
- hydrothermal technique, 333
- infrared sensor, 79, 455
- interferometry, 99
- ion-beam etching, 139
- isotropic metallic oxide, 145
- I-V characteristics, 415
- KTiOPO₄, 29
- lattice-matched epitaxy, 179
- lead
 - bis-tetramethylheptadione, 241
 - lanthanum titanate, 53
 - magnesium niobate titanate, 47
 - oxide, 385

- vac (continued)
 - titanate, 53, 235, 281, 385, 435, 467
 - zirconate titanate, 241
 - leakage current, 59
 - Lewis base stabilization, 375
 - lithium
 - niobate, 113, 287, 293, 441
 - tantalate, 139
 - LSCO, 195, 249
- metal oxide powders, 351
- metallo-organic decomposition, 201
- metalorganic precursors, 397
- MFV capacitors, 415, 447
- MgO, 113
- microstructure, 209, 281, 339
- modelling, 415
- molecular beam epitaxy, 313
- NF₃, 363
- niobium pentaethoxide, 325
- non-switched polarization, 195
- non-volatile memory, 71, 145, 151
- nondestructive readout, 71
- nonlinear optical properties, 301
- nuclear reaction analysis, 23
- nucleation, 15, 339
- optical
 - emission spectroscopy, 481
 - memory, 87
 - scatterometer, 119
 - waveguide, 403
- orientation, 313
- oxygen
 - ¹⁸O, 9
 - partial pressure, 467
 - tracer, 9
 - vacancies, 9, 409
- Pb⁺³, 3
 - defects, 391
- perovskite, 209, 255, 351, 357
- sol-gel, 53, 59, 151, 189, 263, 269, 275, 293, 325, 339, 357, 369, 423, 441, 447
- spin coating, 357
- spray pyrolysis, 351
- sputter deposition
 - high temperature, 473
 - ion beam, 53, 301
 - magnetron, 23
 - RF magnetron, 455, 467
 - thin films, 145
- statistical experimental design, 275
- step coverage, 255
- strain energy, 179
- stress
 - in-situ measurements, 435
 - thermal, 429
- strontium titanate, 493
- switched polarization, 195
- tetra-ethyl-lead, 223
- textured growth, 269
- titanium
 - ethoxide, 241
 - oxide, 385
 - tetra-isopropoxide, 223
- transient photocapacitance spectroscopy, 409
- Transmission Electron Microscopy, 209, 235, 281, 287, 339, 369
 - high resolution, 215
- triphenyl bismuth, 241
- twins, 179
- ultrasonic transducers, 37
- waveguide, 113
- X-ray
 - diffraction, 215, 235, 385
 - topography, 29
- YBCO, 195, 215, 249
- zinc oxide, 71
- zirconium
 - tetrakis-tetramethylheptadione, 241
 - tetra-tertiarybutoxide, 223